frontiers | Research Topics

How large igneous provinces (LIPs) during the triassic shaped modern-day ecosystems

Edited by
Jacopo Dal Corso, Sara Callegaro and Haijun Song

Published in
Frontiers in Earth Science
Frontiers in Ecology and Evolution

ISSN 1664-8714
ISBN 978-2-8325-3879-1
DOI 10.3389/978-2-8325-3879-1

About Frontiers

Frontiers is more than just an open access publisher of scholarly articles: it is a pioneering approach to the world of academia, radically improving the way scholarly research is managed. The grand vision of Frontiers is a world where all people have an equal opportunity to seek, share and generate knowledge. Frontiers provides immediate and permanent online open access to all its publications, but this alone is not enough to realize our grand goals.

Frontiers journal series

The Frontiers journal series is a multi-tier and interdisciplinary set of open-access, online journals, promising a paradigm shift from the current review, selection and dissemination processes in academic publishing. All Frontiers journals are driven by researchers for researchers; therefore, they constitute a service to the scholarly community. At the same time, the *Frontiers journal series* operates on a revolutionary invention, the tiered publishing system, initially addressing specific communities of scholars, and gradually climbing up to broader public understanding, thus serving the interests of the lay society, too.

Dedication to quality

Each Frontiers article is a landmark of the highest quality, thanks to genuinely collaborative interactions between authors and review editors, who include some of the world's best academicians. Research must be certified by peers before entering a stream of knowledge that may eventually reach the public - and shape society; therefore, Frontiers only applies the most rigorous and unbiased reviews. Frontiers revolutionizes research publishing by freely delivering the most outstanding research, evaluated with no bias from both the academic and social point of view. By applying the most advanced information technologies, Frontiers is catapulting scholarly publishing into a new generation.

What are Frontiers Research Topics?

Frontiers Research Topics are very popular trademarks of the *Frontiers journals series*: they are collections of at least ten articles, all centered on a particular subject. With their unique mix of varied contributions from Original Research to Review Articles, Frontiers Research Topics unify the most influential researchers, the latest key findings and historical advances in a hot research area.

Find out more on how to host your own Frontiers Research Topic or contribute to one as an author by contacting the Frontiers editorial office: frontiersin.org/about/contact

How large igneous provinces (LIPs) during the triassic shaped modern-day ecosystems

Topic editors

Jacopo Dal Corso — China University of Geosciences Wuhan, China

Sara Callegaro — University of Oslo, Norway

Haijun Song — China University of Geosciences Wuhan, China

Citation

Corso, J. D., Callegaro, S., Song, H., eds. (2023). *How large igneous provinces (LIPs) during the triassic shaped modern-day ecosystems*. Lausanne: Frontiers Media SA. doi: 10.3389/978-2-8325-3879-1

Table of contents

frontiers | Frontiers in Earth Science

TYPE Editorial
PUBLISHED 23 October 2023
DOI 10.3389/feart.2023.1302216

OPEN ACCESS

EDITED AND REVIEWED BY
Bruce S. Lieberman,
University of Kansas, United States

*CORRESPONDENCE
Sara Callegaro,
sara.callegaro@geo.uio.no

RECEIVED 26 September 2023
ACCEPTED 10 October 2023
PUBLISHED 23 October 2023

CITATION
Callegaro S, Dal Corso J and Song H (2023), Editorial: How Large Igneous Provinces (LIPs) during the Triassic shaped modern-day ecosystems. *Front. Earth Sci.* 11:1302216. doi: 10.3389/feart.2023.1302216

Editorial: How Large Igneous Provinces (LIPs) during the Triassic shaped modern-day ecosystems

Sara Callegaro[1]*, Jacopo Dal Corso[2] and Haijun Song[2]

[1]Centre for Planetary Habitability, University of Oslo, Oslo, Norway, [2]State Key Laboratory of Biogeology and Environmental Geology, China University of Geosciences, Wuhan, China

KEYWORDS

Triassic, Permian-Triassic boundary mass extinction (PTME), Carnian pluvial episode (CPE), end Triassic extinction, large igneous province (LIP), ecosystem change drivers, mass extinction

Editorial on the Research Topic
How Large Igneous Provinces (LIPs) during the Triassic shaped modern-day ecosystems

The Triassic (250–200 Ma) was an extremely intriguing period in Earth's history, marked by profound changes in ocean and land biota, which laid the foundations of modern-style ecosystems. Notably, the roots of *Homo sapiens* go back deep into the Triassic, when the first mammals appeared. The biological changes are marked by three major events. At the beginning and at the end of the Triassic, two of the five major known mass extinctions, also known as the "Big Five," occurred (Raup and Sepkoski, 1982). The Permian–Triassic boundary mass extinction (PTME) was by far the largest extinction of the Phanerozoic, "*when life nearly died*" (Benton, 2003), with the disappearance of 81%–94% of marine species and a massive turnover in terrestrial ecosystems (Erwin, 1993; Jin et al., 2000; Song et al., 2013; Stanley, 2016; Dal Corso et al., 2022). About 50 Myr later, the end-Triassic mass extinction (ETME) wiped out 60%–70% of marine species and severely perturbed terrestrial ecosystems (Raup and Sepkoski, 1982; Kiessling et al., 2007). Between these two major biological crises, other smaller extinctions took place. Amongst these, the "Carnian crisis" (234–232 Ma) is gaining increasing attention from the scientific community: a smaller extinction event, but apparently linked to a major diversification of important groups of animals and plants. This was the geological interval when dinosaurs rose to dominance and within which the first mammals' remains were found (Simms and Ruffell, 1989; Bernardi et al., 2018; Dal Corso et al., 2020). The rise of new groups had profound impacts on global biogeochemical cycles, such as calcifying nannoplankton, which since then have been major players in regulating global ocean chemistry (Ridgwell, 2005). The recent discovery of an Early Triassic lagerstätte (Guiyang biota, 1.08 Ma after the PTME; Dai et al., 2023) suggests that the PTME facilitated the replacement of the Paleozoic evolutionary fauna by the Modern evolutionary fauna in the oceans.

Three major Triassic global environmental crises, at the Permian–Triassic boundary, during the Carnian Pluvial Episode (CPE), and at the Triassic–Jurassic boundary, are coeval with the biological turnovers. The environmental perturbations included, e.g., global warming, ozone depletion, changes in the hydrological cycle, marine anoxia, ocean acidification, and acid rain (e.g., (Wignall, 2001)). The magnitudes of these

changes differ from case to case and this could be the reason for different extinction rates between the events (e.g., (Song et al., 2021)). Nevertheless, they share similar triggers, as they are all temporally linked to the emplacement of large igneous provinces (LIPs), i.e., the Siberian Traps (STLIP) across the Permian–Triassic boundary (Burgess and Bowring, 2015; Burgess et al., 2017), the Wrangellia during the Carnian (Greene et al., 2010), and the Central Atlantic magmatic province (CAMP) during the end of the Triassic (Blackburn et al., 2013; Davies et al., 2017; Lindström et al., 2021). LIPs are volcanic provinces with areal extents of more than 0.1 million km^2 and volumes of more than 0.1 million km^3 that were emplaced in less than <1–5 Ma (e.g., (Ernst et al., 2021)). While ascending toward the surface intruding crustal rocks (intrusive activity) and erupting enormous volumes of magma (effusive and explosive activity), LIPs release large quantities of volcanic gases—namely CO_2, CH_4, SO_2, metals, and halogens—which can induce massive perturbations for the global climate and ecosystems. Vast input of volcanic CO_2 into the atmosphere could indeed result in global warming, ocean acidification, and extreme droughts and rainfall events. These environmental perturbations sound familiar today, when we are witnessing increasing atmospheric pCO_2 levels, global temperatures, ozone depletion, etc. Gaining a deep understanding of such events of the past is therefore crucial to understand future climate scenarios. Hence, this Research Topic of *Frontiers in Earth Science* and *Frontiers in Ecology and Evolution* aimed at gathering an article Research Topic of studies and reviews on the biological turnovers, environmental changes, and LIP eruptions that marked the latest Permian–earliest Jurassic interval.

The two columns of this Research Topic, i.e., Triassic biological turnovers and LIP volcanism, are presented by Benton and Wu and Boscaini et al. Benton and Wu describe the profound ecosystem revolution occurring in the Triassic as a recovery from the PTME, which started in the Early Triassic, but really peaked at the CPE. Also, the Mesozoic marine revolution may have started at the CPE, i.e., earlier than previously reported, contributing to the appreciation of the Carnian as a fundamental tipping point for life on Earth. Boscaini et al. reconstruct CO_2 emissions from the Siberian Traps, Wrangellia, and CAMP LIPs by using Nb concentration in magmas and melt inclusions as a proxy. The CO_2 load of these LIPs can vary significantly across magma units, and thermogenic gases mobilized by magma–sediment interaction contributed importantly to the total mass of volatiles released.

A relevant feature of this Research Topic is the attention dedicated to terrestrial ecosystem changes, which are often overlooked in mass extinction literature. Volcanically induced changes in rain patterns and conditions played a key role in shaping land plant biota. The effect of increasing humidity is portrayed in the contribution by Roghi et al. focused on conifer taxa preserved in amber from the Heiligkreuz Formation in the Dolomites (Italy). Here, and in other sections of the western Tethys realm, the CPE is recognized as the volcanic-driven stressor of conifers and lycophytes in a complex coastal and tidal setting. Mancuso et al. present a study of the terrestrial Carnian of the Ischigualasto-Villa Unión Basin in northwestern Argentina. Clay mineralogy and paleosol geochemistry are coupled with information on changes among terrestrial tetrapods and plants. The authors found that environmental change from warmer, drier conditions to more temperate humid conditions can explain pseudosuchian archosaur diversity and rhynchosaur relative abundance. Zeh et al. report new detrital zircon laser ablation inductively coupled plasma mass spectrometry (LA-ICP-MS) U–Pb ages from the Carnian Stuttgart Formation (Schilfsandstein), revealing tephra fallout from the Olenekian to Carnian in the Central European Basin. The products of this volcanism were re-worked into the Stuttgart Formation and give a maximum LA-ICP-MS U-Pb depositional age for the Stuttgart Formation of 231.1 ± 1. 6 Ma, which is a very important unit representing the terrestrial CPE. Zhang et al. show how an increase in dry conditions and widespread wildfires can cause generic losses of up to 45% in land plants. They present a multi-proxy study of lacustrine deposits of the Jiyuan Basin (North China), which straddle the ETME interval. The turnovers can be attributed to CAMP volcanism, and associated mercury records evidence a distribution of volcanic activity in two major pulses. The palynological record from the Late Triassic–Early Jurassic sequence in the Danish Basin presented by Lindström shows two pulses of mass rarity in the coastal and near-coastal lowland mire vegetation during the ETME. These two pulses occur in correspondence to major environmental changes, including higher temperatures, sea-level fluctuations, wildfire activity, and soil erosion, which can be ascribed to the eruption of the coeval CAMP LIP.

Alongside changes in plant communities, Triassic climate changes affected animal evolution. Zhang et al. describe a new insect species (*Chauliodites tongchuanensis)* from the Middle Triassic Tongchuan Formation of Shaanxi, northwestern China. This finding combined with the occurrence of *Chauliodites* in the Lower and Middle Triassic of South China suggests that the bloom of *Chauliodites* is associated with low-productivity terrestrial ecosystems following the Permian–Triassic mass extinction. Langer and Cordoy studied the diversification and body size evolution of terrestrial pan-avians along the Triassic and Early Jurassic. Occurrence data show increased diversity, high diversification rates, and body size disparity of terrestrial pan-avians in the Carnian, supporting the hypothesis that the CPE played an important role in the early radiation of the group. Pan-avian macroevolution shows no marked shift across the Triassic–Jurassic boundary.

Hohn et al. and Todaro et al. present a marine perspective on Triassic biological and environmental changes. One of the major evolutionary innovations of the Triassic was the appearance of calcifying nannoplankton, which had a massive impact on ocean chemistry. Hohn et al. show that the rise of intracellular calcification was linked to cellular calcium metabolism and control of the accumulation of calcium in the cytoplasm. Gene-tree analysis indicates that ancestral non-calcifiers already possessed the physiological machinery

to calcify, and modeling suggests that there is no difference in energy demands between calcifying and non-calcifying cells. Hence, calcifying nannoplankton could have appeared at any time, but only the peculiar environmental conditions of the Triassic, which still require further research to be fully understood, drove their rise. Todaro et al. use isotopic data of C, O, S, Zn, Pb, and Sr near the Triassic–Jurassic boundary at Mt Sparagio in north-western Sicily to link the marine ETME to the CAMP LIP. A warming event in the upper part of the Rhaetian beds coincided with the reduction in diversity and body size of the megalodontoids. The negative carbon isotope excursions suggest that ocean acidification affected the benthic community.

The theorized volcanic forcing on marine and terrestrial environments, and hence on biota, needs confirmation from studies of geochemical perturbations in the sedimentary record, and quantitative studies of volatile release from LIPs. Müller et al. test the effects of end-Permian global warming on the primary productivity, by investigating phosphorous speciation, sedimentary total organic carbon, and nickel concentrations in low-latitude Tethyan carbonate sections. They found that primary productivity collapsed 30 kyr before the main marine extinction pulse. Huang et al. present high-resolution carbon isotopic data in the microbialite formation across the Permian–Triassic boundary at Dajiang, South China. The results show a general decrease in $\delta^{13}C$ followed by an increase, suggesting that multiple sources of dissolved carbon are required to explain the carbon isotopic pattern in the microbialite profile. Cho et al. analyze a pelagic sequence of bedded chert encompassing the CPE from the Inuyama area (Japan). The new geochemical data show an increase in terrigenous supply to the deep-sea depositional environment around the Julian–Tuvalian boundary (i.e., the boundary between early and late Carnian). This terrigenous material was delivered to the site as aeolian dust and could indicate extensive aridification in the interior Pangea during the CPE interval, showing that the changes in the hydrological cycle during the event were likely highly heterogeneous.

Author contributions

SC: Writing–original draft, Writing–review and editing. JC: Writing–original draft, Writing–review and editing. HS: Writing–original draft, Writing–review and editing.

Funding

The author(s) declare financial support was received for the research, authorship, and/or publication of this article. SC is supported by the Research Council of Norway (Young Talent Grant 301096). JC and HS are supported by the National Natural Science Foundation of China (NSFC Grants: 42172031 and 42325202).

Acknowledgments

We thank all the authors that contributed to this Research Topic and the journal managers for their invaluable support. Editor Bruce S. Lieberman is thanked for providing constructive feedback and prompt editorial handling.

Conflict of interest

The authors declare that the research was conducted in the absence of any commercial or financial relationships that could be construed as a potential conflict of interest.

Publisher's note

References

Benton, M. J. (2003). *When life nearly died: the greatest mass extinction of all time*. London, UK: Thames and Hudson.

Bernardi, M., Gianolla, P., Petti, F. M., Mietto, P., and Benton, M. J. (2018). Dinosaur diversification linked with the carnian pluvial episode. *Nat. Commun.* 9, 1499. doi:10.1038/s41467-018-03996-1

Blackburn, T. J., Olsen, P. E., Bowring, S. A., McLean, N. M., Kent, D. V., Puffer, J., et al. (2013). Zircon U-Pb geochronology links the end-triassic extinction with the central Atlantic magmatic province. *Science* 340, 941–945. doi:10.1126/science.1234204

Burgess, S. D., and Bowring, S. A. (2015). High-precision geochronology confirms voluminous magmatism before, during, and after Earth's most severe extinction. *Sci. Adv.* 1, e1500470. doi:10.1126/sciadv.1500470

Burgess, S. D., Muirhead, J. D., and Bowring, S. A. (2017). Initial pulse of Siberian Traps sills as the trigger of the end-Permian mass extinction. *Nat. Commun.* 8, 164. doi:10.1038/s41467-017-00083-9

Dai, X., Davies, J. H. F. L., Yuan, Z., Brayard, A., Ovtcharova, M., Xu, G., et al. (2023). A Mesozoic fossil lagerstätte from 250.8 million years ago shows a modern-type marine ecosystem. *Science* 379 (6632), 567–572. doi:10.1126/science.adf1622

Dal Corso, J., Bernardi, M., Sun, Y., Song, H., Seyfullah, L. J., Preto, N., et al. (2020). Extinction and dawn of the modern world in the carnian (late triassic). *Sci. Adv.* 6, eaba0099. doi:10.1126/sciadv.aba0099

Dal Corso, J., Song, H., Callegaro, S., Chu, D., Sun, Y., Hilton, J., et al. (2022). Environmental crises at the Permian–Triassic mass extinction. *Nat. Rev. Earth Environ.* 3, 197–214. doi:10.1038/s43017-021-00259-4

Davies, J. H. F. L., Marzoli, A., Bertrand, H., Youbi, N., Ernesto, M., and Schaltegger, U. (2017). End-Triassic mass extinction started by intrusive CAMP activity. *Nat. Commun.* 8, 15596. doi:10.1038/ncomms15596

Ernst, R. E., Dickson, A. J., and Bekker, A. (2021). *Large igneous provinces: a driver of global environmental and biotic changes*. Cambridge, MA, USA: MIT Press.

Erwin, D. H. (1993). *The great paleozoic crisis: life and death in the permian*. New York, NY, USA: Columbia University Press.

Greene, A. R., Scoates, J. S., Weis, D., Katvala, E. C., Israel, S., and Nixon, G. T. (2010). The architecture of oceanic plateaus revealed by the volcanic stratigraphy of the accreted Wrangellia oceanic plateau. *Geosphere* 6, 47–73. doi:10.1130/GES00212.1

Jin, Y. G., Wang, Y., Wang, W., Shang, Q. H., Cao, C. Q., and Erwin, D. H. (2000). Pattern of marine mass extinction near the Permian-Triassic boundary in South China. *Science* 289, 432–436. doi:10.1126/science.289.5478.432

Kiessling, W., Aberhan, M., Brenneis, B., and Wagner, P. J. (2007). Extinction trajectories of benthic organisms across the Triassic-Jurassic boundary. *Palaeogeogr. Palaeoclimatol. Palaeoecol.* 244, 201–222. doi:10.1016/j.palaeo.2006.06.029

Lindström, S., Callegaro, S., Davies, J., Tegner, C., van de Schootbrugge, B., Pedersen, G. K., et al. (2021). Tracing volcanic emissions from the central atlantic magmatic province in the sedimentary record. *Earth Sci. Rev.* 212, 103444. doi:10.1016/j.earscirev.2020.103444

Raup, D. M., and Sepkoski, J. J. (1982). Mass extinctions in the marine fossil record. *Science* 215, 1501–1503. doi:10.1126/science.215.4539.1501

Ridgwell, A. (2005). A Mid Mesozoic Revolution in the regulation of ocean chemistry. *Mar. Geol.* 217, 339–357. doi:10.1016/j.margeo.2004.10.036

Simms, M. J., and Ruffell, A. H. (1989). Synchroneity of climatic change and extinctions in the Late Triassic. *Geology* 17, 265–268. doi:10.1130/0091-7613(1989)017<0265:SOCCAE>2.3.CO;2

Song, H., Kemp, D. B., Tian, L., Chu, D., Song, H., and Dai, X. (2021). Thresholds of temperature change for mass extinctions. *Nat. Commun.* 12, 4694. doi:10.1038/s41467-021-25019-2

Song, H., Wignall, P. B., Tong, J., and Yin, H. (2013). Two pulses of extinction during the Permian-Triassic crisis. *Nat. Geosci.* 6, 52–56. doi:10.1038/ngeo1649

Stanley, S. M. (2016). Estimates of the magnitudes of major marine mass extinctions in earth history. *Proc. Natl. Acad. Sci. U. S. A.* 113, E6325–E6334. doi:10.1073/pnas.1613094113

Wignall, P. B. (2001). Large igneous provinces and mass extinctions. *Earth Sci. Rev.* 53, 1–33. doi:10.1016/S0012-8252(00)00037-4

frontiers in Earth Science

ORIGINAL RESEARCH
published: 17 November 2021
doi: 10.3389/feart.2021.780343

Two-phased Mass Rarity and Extinction in Land Plants During the End-Triassic Climate Crisis

Sofie Lindström *

GEUS—Geological Survey of Denmark and Greenland, Copenhagen, Denmark

Greenhouse gas emissions from large-scale volcanism in the Central Atlantic Magmatic Province is considered to have caused the end-Triassic mass extinction (201.5 million years ago), but the impact on land plants has been debated. Here, abundance changes in spores and pollen record the devastating effects this volcanic induced climate crisis had on coastal and near-coastal lowland mire vegetation around the European epicontinental sea and the European Tethys margin. Combined stress from rising air temperatures and changing climate at the onset of the crisis was exacerbated by a rapidly rising sea-level resulting in fragmentation and destruction of coastal and near-coastal lowland mire habitats, causing mass rarity and extinctions primarily in gymnosperm trees and shrubs adapted to these environments. The devastation of these habitats was further amplified by a subsequent sea-level fall leaving pioneering opportunists and herbaceous survivors to colonize disturbed areas in an environment stressed by increased wildfire activity and enhanced soil erosion. The pioneering flora was severely decimated in a second mass rarity phase and ultimately extirpated. The second mass rarity phase occurred just prior to and at the onset of a prominent negative excursion in $\delta^{13}C_{org}$. A subsequent sea-level rise appears to have restored some of the near-coastal mire habitats allowing some of the plants to recover. The supraregional mass rarity during the end-Triassic crisis affected both previously dominant as well as rare plants and this resonates with ongoing and future climate change and attests to the vulnerability of coastal and lowland vegetation, especially rare plant species, to climatic and environmental disturbances, where rising sea-level threatens entire ecosystems.

Keywords: palynology, palaeoclimate, global warming, sea-level, mass extinction, Triassic—Jurassic boundary, spores, pollen

OPEN ACCESS

Edited by:
Jacopo Dal Corso,
China University of Geosciences, China

Reviewed by:
Evelyn Kustatscher,
Museum of Nature South Tyrol, Italy
Annette Götz,
State Authority for Mining, Energy and Geology, Germany

***Correspondence:**
Sofie Lindström
sli@geus.dk

Specialty section:
This article was submitted to Paleontology, a section of the journal Frontiers in Earth Science

Received: *20 September 2021*
Accepted: *27 October 2021*
Published: *17 November 2021*

Citation:
Lindström S (2021) Two-phased Mass Rarity and Extinction in Land Plants During the End-Triassic Climate Crisis. Front. Earth Sci. 9:780343. doi: 10.3389/feart.2021.780343

1 INTRODUCTION

The end-Triassic mass extinction is generally recognized as one of the five major mass extinctions of the Phanerozoic (Sepkoski, 1996; McGhee et al., 2013), but the severity of the crisis on the vegetation is still debated. Amongst the land plants only seed ferns of the family Peltaspermaceae became extinct during the end-Triassic crisis (McElwain and Punyasena, 2007). However, on lower taxonomic levels extinctions are estimated to be higher, with up to 95% of species locally (McElwain et al., 1999). Estimating the severity of the crisis in land plants is complicated by provinciality and conflicting records between extinctions based on fossil leaf taxa and those based on spores and pollen (Bond and Wignall, 2014; Lindström, 2016; Barbacka et al., 2017). However, extinctions in spore and pollen taxa

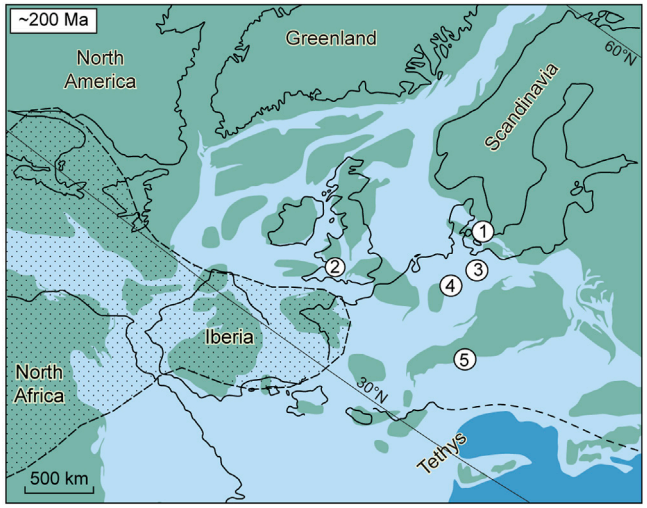

FIGURE 1 | Palaeogeographic map (after Blakey, 2014) of the European epicontinental sea and the northern Tethys margin, showing the location of the studied cored wells Stenlille-1 and -4, and other localities compared with in the text.

vary globally between 17 and 73% and for most of the taxa that went extinct, the parent plant affinity is not fully resolved or even unknown (Lindström, 2016). Likely, many of the spore-producing plants that disappeared at the end of the Rhaetian or in the earliest Hettangian were plants with ecological preferences that resulted in low preservation potential for their macroscopic remains, e.g. epiphytic plants or plants growing in sites with little potential for fast burial. From an ecological perspective, the crisis amongst land plants at the end of the Triassic was profound, with replacement or major disruptions of the terrestrial ecosystems (McGhee et al., 2013; Lindström, 2016). Recently, mass rarity, i.e. the reduction in the numerical abundances and/or the reduction in geographic ranges of several species, was suggested as a more robust measure of the severity of a biotic crisis than taxonomic extinction (Hull et al., 2015). In plant ecology and ecosystem analysis, rarity is a key factor when establishing whether a taxon is at risk of becoming endangered or extinct (Stohlgren and Kumar, 2013), but it is not often discussed for the big five biotic crises.

Here, two high resolution palynological records of the Danish Basin are used to assess whether mass rarity amongst land plants played a role in the end-Triassic crisis scenario. The marine TJB succession of the cored Stenlille-1 and -4 wells on Sjælland, Denmark (**Figure 1**), are well constrained by palynology, $\delta^{13}C_{org}$-isotopes and other geochemical proxies, and can be correlated primarily with other NW European TJB strata, but also globally (Lindström et al., 2017b). Deposition took place in a shoreface to offshore setting in the northwestern part of an epicontinental sea that covered large parts of Europe. The two wells are situated 3.5 km apart on opposite sides of a gentle salt dome and exhibit minor variations in the sedimentary record. Two negative excursions in $\delta^{13}C_{org}$, the Marshi CIE and the Spelae CIE, can be correlated with TJB sections in the Tethys and Panthallassic oceans, where the last occurrence of typical Triassic and the first occurrence of typical Jurassic ammonoids bracket the marine mass extinction interval (Lindström et al., 2017b, 2021). Both these excursions have been interpreted to reflect massive volcanic degassing of ^{12}C to the atmosphere from the CAMP, which could have acted as a trigger for the extinction (Hesselbo et al., 2002; Ruhl and Kürschner, 2011). In addition, Hg-anomalies in the succession provide a link to other Hg-records across the TJB and to the CAMP volcanism (Lindström et al., 2019; Lindström et al., 2021).

2 RESULTS

2.1 From Terrestrial Ecosystem Stability to Mass Rarity

The palynological records show that terrestrial vegetation of the extensive coastal areas and lowlands of the Danish Basin was remarkably stable during the middle Rhaetian (**Figure 2**). Variations in climate and sea level likely influenced vegetation changes on land as well as changes in depositional environment (Nielsen, 2003), contributing to abundance variations in the palynological records of the Gassum Formation (**Figure 2**). The pollen records show that cheirolepidiacean and taxodiacean/cupressacean conifers dominated the vegetation (**Figure 2**), occupying the upper canopy tier in drier and wetter environments, respectively (**Tables 1** and **2**; **Figure 3A**). Apart from these and *Ricciisporites tuberculatus*, most other typical Rhaetian tree pollen taxa were less common, but their parent plants were still important contributors to the upper canopy. The Rhaetian mire forests were most likely multi-storeyed and lush, with mid-canopy elements including very rare Erdtmannithecales, rare Bennettitales and Ginkgoales/Cycadales, and common Caytoniales (**Tables 1** and **2**; **Figure 3A**), similar in composition to macroplant assemblages described from Greenland, southern Sweden and Germany (McElwain et al., 2007; Pott and McLoughlin, 2011; Van Konijnenburg-Van Cittert et al., 2018). Understorey plants, including ferns, lycophytes, bryophytes and sphenophytes, were generally rare to common and many of these plants were probably adapted to living in the shade of the trees or even as epiphytes on the trees (**Figure 3A**).

Two phases of mass rarity are evident in the Stenlille pollen records, here referred to as MR1 and MR2, respectively (**Figure 2**). MR1 occurs within the lowermost part of the Fjerritslev Formation (**Figure 2**) and encompasses the upper part of a black shale and the lowermost part of the succeeding "grey siltstone" interval of the Fjerritslev Formation (Lindström et al., 2017b) (**Figure 2**). At MR1, upper canopy plants appear to have been particularly hard hit. Both the coastal, salinity tolerant and xerophytic cheirolepidiacean conifers, as well as the taxodiacean/cupressacean conifers that preferred wet habitats like mires and estuaries (Mussard et al., 1997), were severely

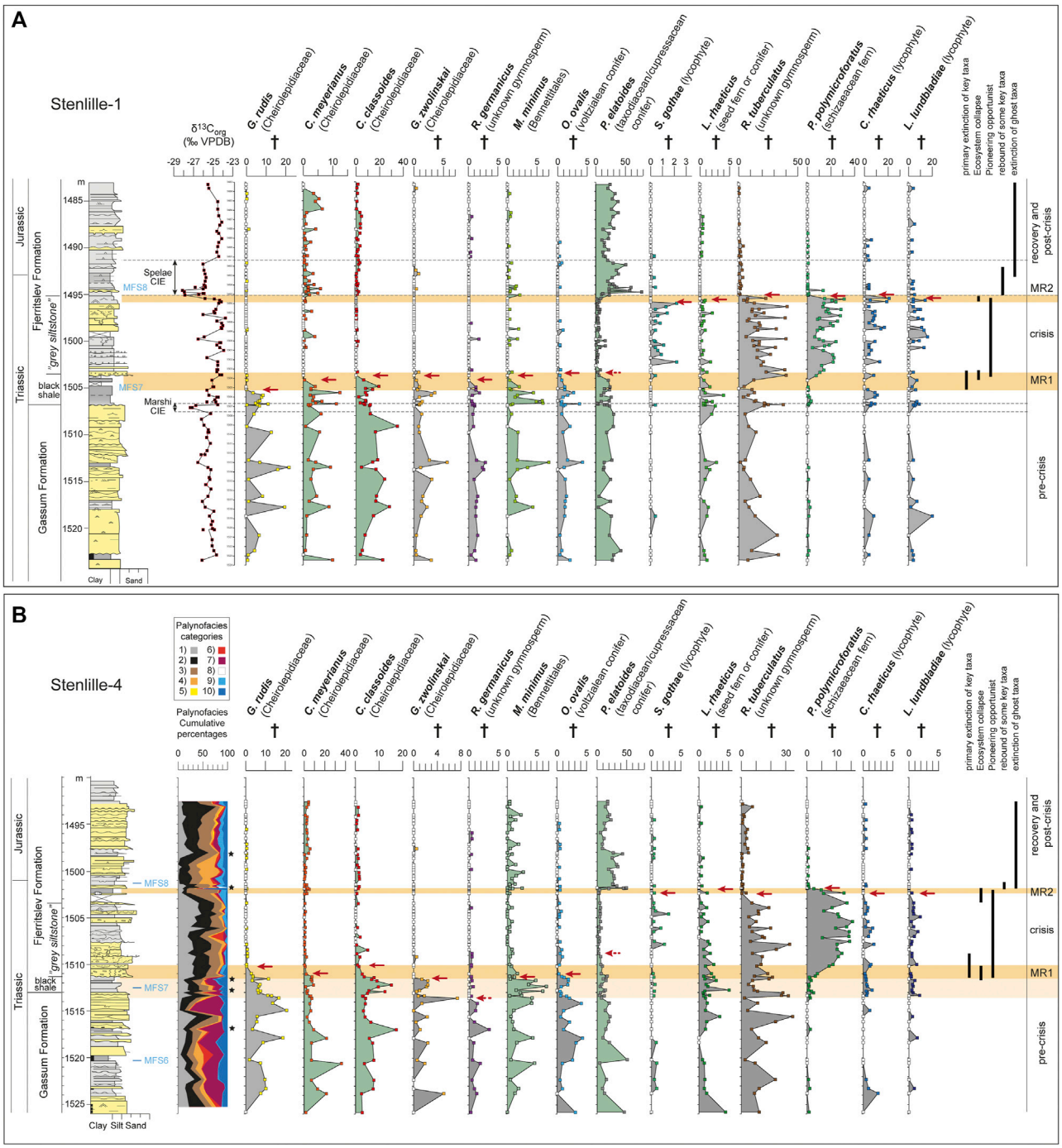

FIGURE 2 | Abundances of selected representative spore-pollen taxa in the Triassic–Jurassic boundary successions of the **(A)** Stenlille-1 and **(B)** Stenlille-4 cored wells. **(A)** also displays the $\delta^{13}C_{org}$ record of Stenlille-1, the position of the Marshi and Spelae CIEs, and of the maximum flooding surfaces (Nielsen, 2003, Lindström et al., 2021). **(B)** also shows the cumulative percentages of palynofacies categories: 1) black opaque clasts, 2) black wood remains, 3) brown wood remains, 4) plant tissue, 5) cuticles, 6) Amorphous organic matter, 7) marine phytoplankton, 8) freshwater microalgae, 9) spores, 10) pollen. The spore-pollen counts for Stenlille-1 and -4 are listed in **Supplementary Tables S1, S2**, respectively. Black stars mark observations of char.

reduced in abundances within a c. 2 m thick interval from the middle of the black shale in the Stenlille-1 record (**Figure 2A**; **Table 1**). Four different cheirolepidiacean pollen species exhibit rarity at this level commencing with *Granuloperculatipollis rudis*, followed in ascending order by *Classopollis meyerianus*, *Geopollis zwolinskai* and *C. classoides* (**Figure 2**). Rarity is also registered in *Rhaetipollis germanicus, Monosulcites minimus, Ovalipollis ovalis* and *Perinopollenites elatoides,* showing that other tree taxa were

TABLE 1 | Botanical affinity, habit, leaf morphology, pollination strategy, and environmental preferences for the parent plants affected at MR1 and MR2.

Spore or pollen taxon	Mother plant Order Family	Habit	Leaf morphology	Pollen dispersal	Ecological preference	MR1	MR2
Classopollis classoides	Conifer Coniferales Cheirolepidiaceae	Upper canopy	Scaly leaf shoots	Wind	Xerophytic, salinity tolerant	Non-permanent rarity	Recovery
Classopollis meyerianus	Conifer Coniferales Cheirolepidiaceae	Upper canopy	Scaly leaf shoots	Wind	Xerophytic, salinity tolerant	Non-permanent rarity	Recovery
Granuloperculatipollis rudis	Conifer Coniferales Cheirolepidiaceae	Upper canopy	Scaly leaf shoots	Wind	Xerophytic, salinity tolerant	Permanent rarity	Extirpation
Geopollis zwolinskai	Conifer Coniferales Cheirolepidiaceae	Upper canopy	Scaly leaf shoots	Wind	Xerophytic, salinity tolerant	Permanent rarity + Extirpation	—
Rhaetipollis germanicus	Gymnosperm Unknown	Unknown, here placed in mid-canopy	Unknown	Unknown	Unknown	Permanent rarity + Extirpation	—
Perinopollenites elatoides	Conifer Coniferales Taxodiaceae/ Cupressaceae	Upper canopy	Needle-like leaves	Wind	Moisture loving, mire	Non-permanent rarity	Recovery
Ovalipollis ovalis	Conifer Voltziales Unknown	Upper canopy	Needle-like leaves	Wind	Xerophytic	Permanent rarity	Extirpation
Monosulcites minimus	Seed fern Bennettitales Unknown	Mid canopy	Segmented or entire-margined	Insect	Deltaic and disturbed environments, mire	Non-permanent rarity	Recovery
Lunatisporites rhaeticus	Seed fern or Conifer Voltziales Unknown	Upper canopy	?Needle-like leaves	Wind	?Xerophytic	Permanent rarity	Permanent rarity + Extirpation
Semiretisporis gothae	Lycophyte	Ground cover	—	Water	Lowlands, hygrophytic	—	Permanent rarity + Extirpation
Cingulizonates rhaeticus	Lycophyte	Ground cover	—	Water	Lowlands, hygrophytic	—	Permanent rarity + Extirpation
Limbosporites lundbladiae	Lycophyte	Ground cover	—	Water	Lowlands, hygrophytic	—	Permanent rarity + Extirpation
Polypodiisporites polymicroforatus	Fern Filicales Schizaeaceae	Ground cover	—	Water	Disturbed environments, ? hygrophytic	—	Permanent rarity + Extirpation
Ricciisporites tuberculatus	Gymnosperm	Unknown, here placed in mid-canopy	Unknown	Insect? Animal?	Unknown	—	Permanent rarity + Extirpation

also affected (**Figure 2A**). The affinity of *R. germanicus* is unknown, but *O. ovalis* may have been produced by voltzialean conifers (Scheuring, 1970), and *M. minimus* by a bennettitalean parent plant (Pott et al., 2016). The Cheirolepidiacean, taxodiacean/cupressacean and voltzialean conifers had scale- or needle-like leaves that would make them more fire prone than e.g., bennettitaleans that had elongated entire-margined or segmented leaves (Belcher et al., 2010) (**Table 1**). Wildfires under high temperatures indicative of crown fires in fire-prone vegetation are known to have occurred in the mid-Rhaetian mires (Petersen and Lindström, 2012). Palynofacies analyses of the Stenlille-4 samples show some intervals in the Gassum Formation where increased amounts of black phytoclasts and wood remains indicate that more intense wildfires may have occurred at times (**Figure 2B**). Rhaetian bennettitaleans seem to have had an ecological preference for highly disturbed and deltaic habitats (Pott, 2014), and *M. minimus* was found to be common to abundant in the fire struck Rhaetian mires of the Danish Basin (Petersen and Lindström, 2012). Except for the Bennettitales that may have been insect pollinated (Pott, 2014), the tree taxa affected at MR1 are all considered to have been wind pollinated (**Table 1**). In the Stenlille-4 record MR1 appears to be extended from the uppermost part of the Gassum Formation to lower part of the "grey siltstone" interval (**Figure 2B**). Discrepancies between the upper part of MR1 in this record and Stenlille-1 likely relates to the fact that the base of the "grey siltstone" in Stenlille-4 contains clay clasts probably derived from the black shale (**Figure 2**). Apart from the probable reworking of black shale material into the lowermost "grey siltstone", the overall pattern is similar in the two wells. Although neither the parent plants of *Classopollis classoides, C. meyerianus, Perinopollenites elatoides* nor

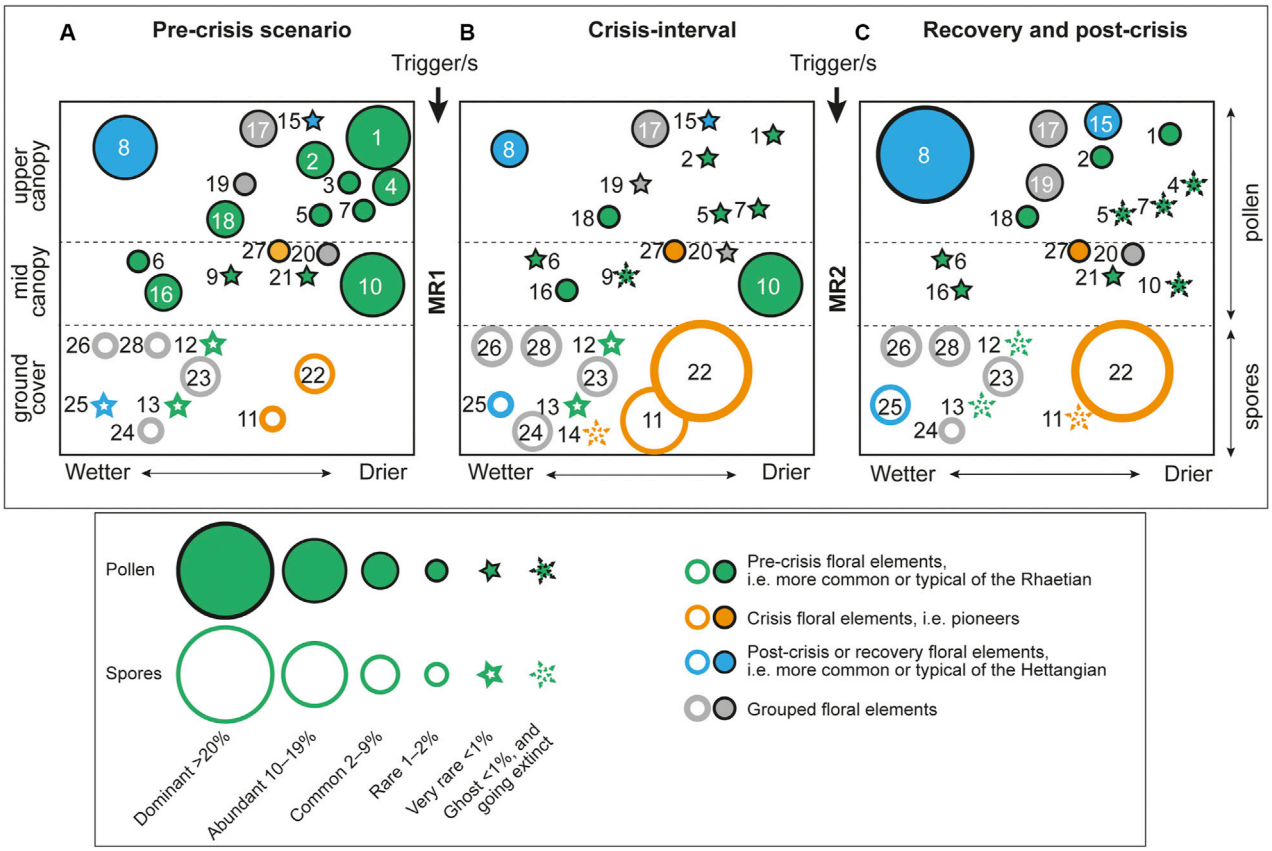

FIGURE 3 | Schematic bubble diagrams illustrating vegetation composition in the Danish Basin during **(A)** the pre-MR1 interval, **(B)** the floral crisis interval, **(C)** the post-MR2 and recovery interval, based on mean relative spore-pollen abundances in Stenlille-1. Numbers in the diagrams refer to twenty-eight specific spore-pollen taxa, namely: 1. *Classopollis classoides*, 2. *Classopollis meyerianus*, 3. *Geopollis zwolinskai*, 4. *Granuloperculatipollis rudis* (all cheirolepidiacean conifers), 5. *Lunatisporites rhaeticus* (seed fern of conifer); 6. *Monosulcites minimus* (Bennettitales); 7. *Ovalipollis ovalis* (voltzialean conifer); 8. *Perinopollenites elatoides* (taxodiacean/cupressacean conifer); 9. *Rhaetipollis germanicus* (unknown affinity); 10. *Ricciisporites tuberculatus* (unknown gymnosperm); 11. *Polypodiisporites polymicroforatus* (schizaeacean fern); 12. *Cingulizonates rhaeticus* (unknown lycophyte); 13. *Limbosporites lundbladiae* (unknown lycophyte); 14. *Semiretisporis gothae* (unknown lycophyte); 15. *Pinuspollenites minimus* (pinacean conifer); 16. *Vitreisporites pallidus* and *V. bjuvensis* (both Caytoniales); 17. Bisaccates (other than specified), 18. *Alisporites* spp. (seed ferns), 19. Non-saccate conifers (other than specified), 20. Monosulcate non-conifer pollen (other than specified), 21. *Eucommiidites* spp. (Erdtmannithecales), 22. *Deltoidospora* spp. (dipterid and matoniacean ferns), 23. Fern spores (other than specified), 24. Lycophytes (other than specified), 25. *Calamospora* spp. (Equisetales), 26. Bryophytes, 27. *Chasmatosporites* spp. (Ginkgo or Cycads), and 28. *Osmundacidites/Baculatisporites/Punctatisporites* spp. (osmundacean ferns). Mean abundance values can be found in **Table 2**.

Monosulcites minimus were extirpated in the end-Triassic extinction, the cheirolepidiacean conifers that produced *G. zwolinkai* and *G. rudis*, as well as the voltzialean conifer that shed *O. ovalis* and the unknown parent plant of *R. germanicus*, were all victims of the crisis.

2.2 Ecological Upheaval and Pioneering Plants

The ecological disruption during MR1 resulted in a major reduction of the upper and mid-canopy tree elements, suggesting major deforestation in the area and a marked shift towards a more open landscape (**Tables 1** and **2**; **Figure 3B**). Marked and consistently increased levels of black phytoclasts and black wood remains, and significantly decreased amounts of spores and pollen compared to prior to MR1 may indicate that increased wildfire (**Figure 2B**). Both the vegetation density and volume were likely severely decreased during this floral crisis interval as indicated by low TOC values (Lindström et al., 2019), and by significantly lower amounts of spores and pollen during this interval (**Figure 2B**). The deforestation allowed some previously less prominent taxa to flourish during the deposition of the "grey siltstone" (**Figures 1**, **2**). In particular the understorey spore-producing schizaeacean (*Polypodiisporites polymicroforatus* spores) and dipterid and/or matoniaceous ferns (Van Konijnenburg-Van Cittert et al., 2020) (*Deltoidospora* spores; not shown on **Figure 2**) seem to have benefitted from the open landscape (**Table 2**; **Figure 3B**). These opportunistic ferns had a significantly faster life cycle than trees and could perhaps reproduce both sexually and through asexual spreading via rhizomes. These ferns flourished together with an unknown, possibly ruderal, gymnosperm (*Ricciisporites*

tuberculatus pollen) (Kürschner et al., 2014) that also increased in abundance compared to in the Gassum Formation. A similar vegetation response has been documented across Europe and interpreted as reflecting widespread distribution of pioneering plant communities after deforestation (van de Schootbrugge et al., 2009; Lindström, 2016; Lindström et al., 2017b; Gravendyck et al., 2020). Interestingly, *Monosulcites minimus* is significantly decreased during the deforestation interval, i.e. the "grey siltstone" beds, despite the parent plants possible preference to disturbed habitats (Pott, 2014) (**Figure 2**). Some typical Rhaetian spore-pollen taxa, e.g., the lycophyte spores *Limbosporites lundbladiae* and *Cingulizonates rhaeticus*, and the probable conifer or seed fern pollen *Lunatisporites rhaeticus*, show none or only marginal changes in abundance during this interval (**Figure 2**). Another typical Rhaetian lycophyte spore, *Semiretisporis gothae*, even increased in abundance during the deposition of the "grey siltstone" beds.

2.3 Mass Rarity and Recovery

In the uppermost part of the "grey siltstone" beds, a second mass rarity event, MR2, was instigated with the virtual disappearance of the low-abundance species *S. gothae*, *L. rhaeticus, C. rhaeticus,* and *L. lundbladiae* (**Figures 2**, **3C**). Two of the opportunistic palynofloral elements in the "grey siltstone" beds, *P. polymicroforatus* and *R. tuberculatus,* also show marked abundance losses, reflecting that the collapse of the pioneering ecosystem occurred during MR2 (**Figure 2**). MR2 coincided with the onset and first negative peak of the Spelae CIE (**Figure 2**), which coincides with a sudden relative increase in the equisetalean spore *Calamospora tener* and in the freshwater algae *Botryococcus braunii* (CCM zone in (Lindström et al., 2017b). As equisetaleans preferred wet environments like riverbanks or lake shores, this signals an increase in freshwater input at that time. After this there was a return of, in particular, the taxodiacean/cupressacean (*P. elatoides* pollen), but also to a lesser extent cheirolepidiacean (*C. meyerianus* and *C. classoides* pollen) and bennettitalean (*M. minimus* pollen) trees (**Figure 2**). Although cupressacean conifers appear to have returned in large numbers signalling re-establishment of coastal mires, the drier coastal habitats that supported the cheirolepidiacean conifers appear to have been greatly diminished (**Tables 1** and **2**; **Figure 3C**). In general, the post-crisis vegetation appears less dense in the upper canopy while the mid-canopy tier seems almost eradicated, similar to macroplant fossil observations in East Greenland (McElwain et al., 2007). The post-crisis vegetation contained several rare or ghost taxa, the latter including e.g., *G. rudis, O. ovalis, L. rhaeticus, P. polymicroforatus* and *R. tuberculatus,* that were victims of the crisis (**Figure 3C**). Later, *Pinuspollenites minimus,* a previously rare pinacean conifer pollen increased in abundance during the post-crisis and recovery interval, probably inhabiting hinterland or drier areas (Lindström, 2016) (**Figure 3C**).

2.4 Diversity Patterns Reveal Onset of Disturbances

Diversity indices provide additional clues to the timing and severity of the environmental changes that led to the mass rarity phases. In accordance with the intermediate disturbance hypothesis (IDH) (Svensson et al., 2012), two intervals where species richness increased and peaked indicate that the ecosystem was subjected to disturbances of intermediate magnitude and/or frequency; namely intermediate disturbance 1 (ID1) and 2 (ID2) (**Figure 4**). At ID1 species richness increased and peaked just prior to and during the lower part of MR1 (**Figure 4**), indicating an intermediate level of disturbance that hindered competitive exclusion by supressing species that were previously dominant and allowing new species to colonize free space (Svensson et al., 2012). This is reflected by the initial increase in richness coinciding with a minimum in dominance, <0.1, and an increase in evenness to >0.8 (**Figure 4**). Just prior to MR1, while species richness was still high, evenness dropped continuously to the top of MR1 (**Figure 4**), indicating high level disturbances promoting dominance of a few disturbance specialists, namely *P. polymicroforatus*, *R. tuberculatus* and *Deltoidospora* spp. (**Figure 2**). The decline in evenness continued to the top of MR1 as species richness also declines, reflecting a subsequent loss in biodiversity (**Figure 4**).

At ID2 in the upper part of the "grey siltstone" beds, richness again reached maximum levels indicating intermediate disturbance (**Figure 4**). At the top of the beds, richness fell successively and reached a minimum during MR2 (**Figure 4**). This coincided with a fall in dominance and a rise in evenness, suggesting that the taxa that were ecologically dominant during the "grey siltstone" beds were now suffering, whereas other species were recovering or establishing. The diversity indices suggest that conditions improved after the Spelae CIE and the palynology suggests that some of the previously lost coastal habitats were restored, as primarily taxodiacean/cupressacean, but also to lesser extent cheirolepidiacean, conifers increase in abundance (**Figures 1**–**3**).

3 DISCUSSION

3.1 Comparison With Other Records

3.1.1 St. Audrie's Bay, United Kingdom

The St. Audrie's Bay succession (**Figures 1**, **5**) is one of the extensively studied key localities for the TJB, and it is well constrained by palynology, ammonoids and organic C-isotopes (Hesselbo et al., 2002; Hesselbo et al., 2004). Hesselbo et al. (2004) indicated that a maximum flooding surface (MFS) is present in the middle of the Westbury formation, around the level of the Marshi CIE, but they could not specify the exact location. Maximum abundances of dinoflagellate cysts (Bonis et al., 2010) indicate that the MFS could be located higher, in the uppermost part of the Westbury Formation and lower to upper Cotham Member of the Lilstock Formation. It is within this interval that several spore-pollen taxa begin to decline markedly in abundance. *Granuloperculatipollis rudis* is the first taxon to exhibit rarity already in the uppermost Westbury Formation. Then *Perinopollenites* elatoides, which was never common, declines in abundance and *Ovalipollis ovalis* becomes rare in the uppermost lower Cotham Member and at this level *Classopollis meyerianus* also shows a marked decline in abundance, although it never becomes rare (Bonis et al., 2010,

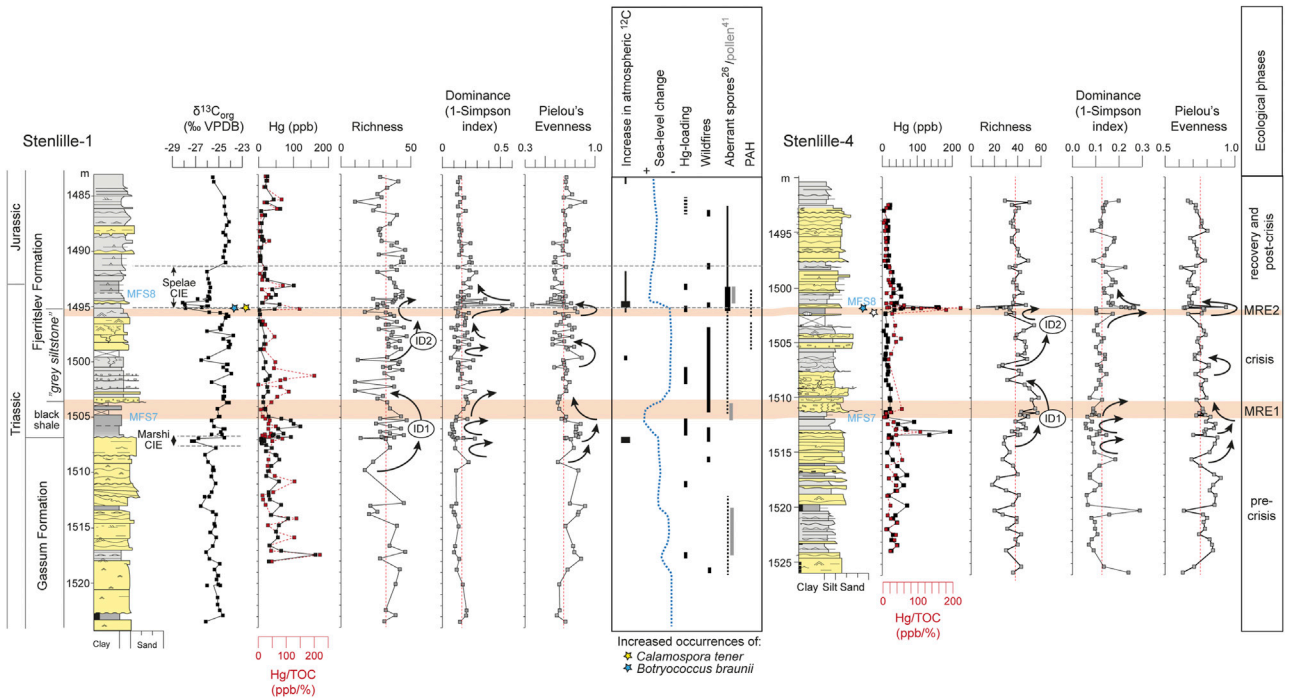

FIGURE 4 | Comparison of species richness, dominance (1-Simpson index), and Pielou's evenness in Stenlille-1 and Stenlille-4. ID1 and ID 2 refer to two intervals with increased to maximum values in species richness indicate intermediate disturbance (Connell, 1978; Svensson et al., 2012). Hg and Hg/TOC records have been interpreted to reflect volcanic pulses of the CAMP (Lindström et al., 2021). Thin stippled red lines indicate mean level of the respective diversity indices.

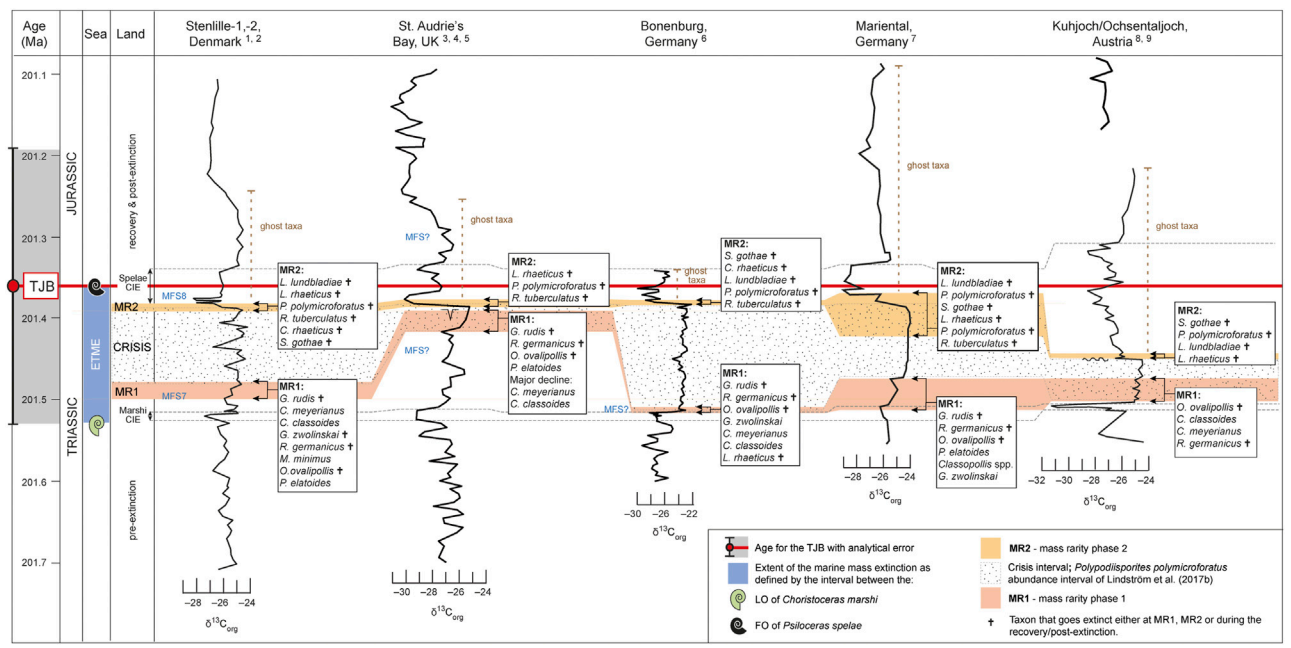

FIGURE 5 | Correlation of $\delta^{13}C_{org}$-records, mass rarity phases (MR1 and 2) and crisis interval [i.e. *Polypodiisporites polymicroforatus* abundance interval of Lindström et al. (2017b)] in Stenlille-1, St. Audrie's Bay, Bonenburg, Mariental and Kuhjoch. The recorded taxa are also shown in **Table 3**. Numbers after the localities refer to the following references: 1. Lindström et al. (2017b), 2. Lindström et al. (2021), 3. Hesselbo et al. (2002), 4. Hesselbo et al. (2004), 5. Bonis et al. (2010), 6. Gravendyck et al. (2020); Heunisch et al. (2010), 8. Bonis et al. (2009), 9. Hillebrandt et al. (2013). The correlation is based on Lindström et al. (2017b), Lindström et al. (2021).

TABLE 2 | Mean percentage data for the various spore-pollen taxa or groups of taxa shown in **Figure 3** as well as assumed forest level and climate preference.

Nr. on Figure 3	—	Taxon or group of taxa	Pre-extinction	Crisis	Recovery and post-extinction	Forest level	Climate preference
1	Pollen	*Classopollis classoides*	12.4%	0.2%	1.3%	Upper canopy	Xerophytic
2	Pollen	*Classopollis meyerianus*	3.9%	0.3%	1.8%	Upper canopy	Xerophytic
3	Pollen	*Geopollis zwolinskai*	1.3%	0.0%	0.0%	Upper canopy	Xerophytic
4	Pollen	*Granuloperculatipollis rudis*	5.5%	0.0%	0.1%	Upper canopy	Xerophytic
5	Pollen	*Lunatisporites rhaeticus*	1.0%	0.3%	0.1%	Upper canopy	Xerophytic
6	Pollen	*Monosulcites minimus*	1.8%	0.2%	0.3%	Mid canopy	Wet
7	Pollen	*Ovalipollis ovalis*	1.2%	0.1%	0.1%	Upper canopy	Xerophytic
8	Pollen	*Perinopollenites elatoides*	18.8%	4.2%	27.4%	Upper canopy	Wet
9	Pollen	*Rhaetipollis germanicus*	0.9%	0.1%	0.0%	Unknown	Unknown
10	Pollen	*R. tuberculatus*	14.1%	16.9%	0.7%	Unknown	Xerophytic
11	Spores	*Polypodiisporites polymicroforatus*	1.0%	15.9%	0.6%	Ground cover	Drier
12	Spores	*Cingulizonates rhaeticus*	0.3%	0.6%	0.1%	Ground cover	Wet
13	Spores	*Limbosporites lundbladiae*	0.3%	0.4%	0.1%	Ground cover	Wet
14	Spores	*Semiretisporis gothae*	0.0%	0.4%	0.0%	Ground cover	Wet
15	Pollen	*Pinuspollenites minimus*	0.7%	0.4%	8.1%	Upper canopy	Xerophytic
16	Pollen	*Vitreisporites* spp.	3.3%	1.3%	0.9%	Mid canopy	Xerophytic
17	Pollen	Other bisaccates	8.0%	5.7%	2.9%	Upper canopy	Xerophytic
18	Pollen	*Alisporites* spp.	2.3%	1.8%	1.1%	Upper canopy	Xerophytic
19	Pollen	Other non-saccate conifers	1.7%	0.6%	2.0%	Upper canopy	Xerophytic
20	Pollen	*Monosulcites* spp. other	1.3%	0.7%	1.9%	Upper canopy	Unknown
21	Pollen	*Eucommiidites* spp.	0.4%	0.0%	0.1%	?Mid canopy	Drier
22	Spores	*Deltoidospora* spp.	8.7%	25.5%	23.8%	Ground cover	Drier
23	Spores	Other ferns (minus *Osmundaceae*)	3.9%	8.3%	7.2%	Ground cover	Wet
24	Spores	Other lycophytes	1.7%	2.2%	1.9%	Ground cover	Wet
25	Spores	*Calamospora* spp.	0.5%	1.9%	5.0%	Ground cover	Wet
26	Spores	Bryophytes total	1.8%	2.2%	4.9%	Ground cover	Wet
27	Pollen	*Chasmatosporites* spp.	1.2%	1.7%	1.2%	Upper canopy	Drier
28	Spores	*Osmundaceae* total	1.3%	3.9%	6.0%	Ground cover	Wet

Figures 3, **4** therein). *Rhaetipollis germanicus* becomes rare just at the level marked by desiccation cracks (see below) and this is also where *C. classoides* first drops markedly in abundance (Bonis et al., 2010) (**Figure 5**). The presence of an erosion surface with prominent desiccation cracks up to 90 cm deep at the top of the lower Cotham member indicates a hiatus at that level in the succession (Hesselbo et al., 2004) (**Figure 5**). Sedimentary structures including flat-topped ripples indicate water depth of just a few meters in the upper Cotham Member of the Lilstock Formation and thus the culmination of a regressive event (Hesselbo et al., 2004). This corresponds stratigraphically to the sea-level fall in the Danish and North German Basins. Thus, a first phase of mass rarity (MR1) can be recognized in the lower Cotham Member, below the desiccation cracks (**Table 3**; **Figure 5**). It is possible that most of the crisis interval at St. Audrie's Bay is missing Lindström et al. (2017b). In addition, several of the taxa reviewed herein where not listed in the palynological record from St. Audrie's Bay, namely *Cingulizonates rhaeticus*, *Limbosporites lundbladiae*, *Semiretisporis gothae*, and *Geopollis zwolinskai* (Bonis et al., 2010) (**Table 3**), so their responses cannot be assessed. A second mass rarity phase (MR2) can be distinguished within a narrow interval above the desiccation cracks, encompassing the onset of the Spelae CIE, with rarity in *Lunatisporites rhaeticus, Perinopollenites elatoides, Polypodiisporites polymicroforatus* and *Ricciisporites tuberculatus* (**Table 3**; **Figure 5**). The MR2 interval in St. Audrie's Bay corresponds more or less to the interval referred to as the "lower CIE" in by Fox et al. (2020), interpreted to represent a dramatic perturbation to the ecosystem by shallowing with increasing freshwater conditions and development of microbial mats. The onset of the Spelae CIE is in St. Audrie's Bay also associated with an increased abundance of the equisetalean spore *Calamospora tener*, which may suggest increased runoff from a nearby freshwater source where equisetalean plants may have thrived along riverbanks or lake shores.

3.1.2 Bonenburg, Germany

In the Bonenburg section (**Figures 1**, **5**), located in the German Basin, six taxa exhibit mass rarity during an interval stratigraphically equivalent with MR1, namely *Classopollis classoides, C. meyerianus, Geopollis zwolinskai, Granuloperculatipollis rudis, Ovalipollis ovalis* and *Rhaetipollis germanicus* (Gravendyck et al., 2020) (**Table 3**; **Figure 5**). The abundance drops in these taxa occur at or immediately after a peak in marine phytoplankton abundance, in particular the fully marine dinoflagellate cyst taxon *Rhaetogonyaulax rhaetica* in the upper part of the Contorta Beds, which suggests that this level represents a maximum transgression (Gravendyck et al., 2020). Only *G. rudis* disappears at this level. *Perinopollenites elatoides* is rare throughout the section and appears to have been unaffected. *Lunatisporites rhaeticus* is also rare but drops in abundance within the crisis interval (Triletes beds) (Gravendyck et al., 2020) (**Table 3**; **Figure 5**). At a level equivalent to MR2,

TABLE 3 | Comparison of mass rarities, extinctions and recoveries of the selected taxa on **Figure 1**, for Stenlille-1 and -4 (this paper), St. Audrie's Bay (United Kingdom; Bonis et al., 2010), Bonenburg (Germany; Gravendyck et al., 2020), Mariental (Germany; Heunisch et al., 2010), Kuhjoch (Austria; Bonis et al., 2009; Hillebrandt et al., 2013). The localities are correlated according to ref. 10[10]. In the case of Mariental, only *Classopollis* spp. is listed. Numbers for the seven lowest lines in the table refer to number of taxa affected during each phase.

	Stenlille-1				Stenlille-4				St. Audrie's bay				Bonenburg				Mariental				Kuhjoch			
Selected taxa	**MR1**	**Crisis**	**MR2**	**Post-crisis**	**MR1**	**Crisis**	**MR2**	**Post-crisis**	**MR1**	**Crisis**	**MR2**	**Post-crisis**	**MR1**	**Crisis**	**MR2**	**Post-crisis**	**MR1**	**Crisis**	**MR2**	**Post-crisis**	**MR1**	**Crisis**	**MR2**	**Post-crisis**
Classopollis classoides	x	—	—	R	x	—	—	R	(x)	—	—	R	x	—	R	—	x	—	R	—	—	(x)	R	—
Classopollis meyerianus	x	—	—	R	x	—	—	R	(x)	—	R	—	x	—	R	—	x	—	R	—	x	—	—	—
Geopollis zwolinskai	x	—	—	†	x, †	—	—	—	not listed				x	—	R	—	x	—	—	—	not listed			
Granuloperculatipollis rudis	x, †	—	—	—	x	†	—	—	x, †	—	—	—	x, †	—	—	—	†	—	—	—	x, †	—	—	—
Rhaetipollis germanicus	x, †	—	—	—	x	†	—	—	x	—	†	—	x	—	—	†	x, †	—	—	—	x, †	—	—	—
Monosulcites minimus	x	—	—	R	x	—	R	—	not listed				not specified				not listed				not listed			
Ovalipollis ovalis	x	—	—	†	x	—	—	†	x	—	†	—	x	—	—	†	x	—	—	†	x	—	—	†
Perinopollenites elatoides	x	—	R	—	—	X	R	—	x	—	—	R	not affected				x	—	R	—	not affected			—
Limbosporites lundbladiae	—	—	x	†	—	—	x	†	not listed				—	—	x	†	x	—	†	—	—	—	x	†
Lunatisporites rhaeticus	—	—	x	†	—	—	x	†	—	—	x, †		—	x		†	—	x	†	—	—	x, †	—	—
Polypodiisporites polymicroforatus	—	—	x	†	—	—	x	†	—	—	x	†	—	—	x, †	—	—	—	x	†	—	—	x	†
Ricciisporites tuberculatus	—	—	x	†	—	—	x	†	—	—	x	†	—	—	x	†	—	x	—	†	not affected			
Cingulizonates rhaeticus	—	—	x	†	—	—	x	†	not listed				—	—	x	†	not listed				—	—	x	†
Semiretisporis gothae	—	—	x	†	—	—	x	†	not listed				—	—	x, †	—	—	—	x	†	x	—	—	†
MR1 mass rarity	8	—	—	—	7	—	—	—	4	—	—	—	6	—	—	—	6	—	—	—	5	—	—	—
MR1 extinction	2	—	—	—	1	—	—	—	1	—	—	—	1	—	—	—	2	—	—	—	2	—	—	—
Crisis interval mass rarity	—	—	—	—	—	1	—	—	—	—	—	—	—	1	—	—	—	2	—	—	—	1	—	—
Crisis interval extinction	—	—	—	—	—	2	—	—	—	—	—	—	—	—	—	—	—	—	—	—	—	1	—	—
MR2 mass rarity	—	—	6	—	—	—	6	—	—	—	3	—	—	—	5	—	—	—	2	—	—	—	3	—
MR2 extinction	—	—	—	—	—	—	—	—	—	—	3	—	—	—	2	—	—	—	2	—	—	—	—	—
Post-crisis extinction	—	—	—	8	—	—	—	7	—	—	—	2	—	—	—	6	—	—	—	4	—	—	—	5

R = recovery.
x = rarity.
(x) = major decline.
†= extinction.

Limbosporites lundbladiae, Polypodiisporites polymicroforatus, Semiretisporis gothae and *Ricciisporites tuberculatus* exhibit mass rarity, while *Classopollis classoides, C. meyerianus* and *G. zwolinskai* again increase in abundance (**Table 3**; **Figure 5**). The recovery of *G. zwolinskai* is surprising, but this has also been documented in Mariental (see below). This contrasts to records further north where this taxon appears to have gone extinct during MR1 (Lund, 2003; Lindström et al., 2017a; this paper). *Semiretisporis gothae* and *R. germanicus* went extinct at this level. *Ovalipollis ovalis, Lunatisporites rhaeticus* and *Limbosporites lundbladiae* lingered on but disappeared during the post-crisis interval (**Table 2**; **Figure 5**). *Ricciisporites tuberculatus* increased again towards the top of the record (Gravendyck et al., 2020) similar to what is seen in Stenlille (**Figure 2**), and most likely went extinct at a higher level.

3.1.3 Mariental, Germany

In the Mariental succession (**Figure 1**), six taxa show marked abundance drops at a level equivalent to MR1 in the upper part of the Contorta Beds, namely *Classopollis* spp., *G. zwolinskai, Limbosporites lundbladiae, Ovalipollis ovalis, Perinopollenites elatoides* and *Rhaetipollis germanicus* (Heunisch et al., 2010). The latter as well as *Granuloperculatipollis rudis* went extinct at that level (**Figure 5**). A similar pattern was also noted by Lund (2003) in the German well Eitzendorff 8 located in the Bremen area, where a MFS in the upper part of the Mittel-Rhät Contorta Beds is marked by an acme of *R. rhaetica*, and succeeded by the last occurrences of *G. rudis*, *G. zwolinskai* and *R. germanicus* (Lund, 2003). During the middle part of the crisis interval (the Triletes beds) *Ricciisporites tuberculatus* and *Lunatisporites rhaeticus* exhibited mass rarity (Heunisch et al., 2010) (**Table 3**; **Figure 5**). The latter as well as *Limbosporites lundbladiae* disappeared at a level equivalent to MR2, where also *Polypodiisporites polymicroforatus* and *Semiretisporis gothae* show mass rarity. Four taxa, *O. ovalis, P. polymicroforatus, R. tuberculatus* and *Semiretisporis gothae* went extinct during the post-crisis interval (Heunisch et al., 2010) (**Table 2**; **Figure 5**). *Classopollis* spp., *Perinopollenites elatoides* and *Geopollis zwolinskai* all recovered during MR2 (Heunisch et al., 2010).

3.1.4 Kuhjoch, Austria

The Triassic–Jurassic boundary succession at Kuhjoch (**Figure 1** and) is the Global Stratigraphic Section and Point (GSSP) for the base of the Jurassic (Hillebrandt et al., 2013). Several of the herein compared taxa were not listed in the Kuhjoch record, including *G. zwolinskai, G. rudis, M. minimus* and *S. gothae* (**Table 3**; **Figure 5**), and two taxa, *P. elatoides* and *R. tuberculatus* were seemingly unaffected (Hillebrandt et al., 2013). The open marine Kössen Formation in succeeded by a sea-level fall and the deposition of the grey Tiefengraben Member of the Kendlback Formation (Hillebrandt et al., 2013). Major drops in abundances occur within an interval corresponding to MR1 affecting e.g. *C. meyerianus, C. classoides,* while *G. rudis* and *R. germanicus* exhibit mass rarity (Bonis et al., 2009) (**Table 3**; **Figure 5**). During the subsequent crisis interval, i.e. the Schattwald beds deposited during continued sea-level fall, mass rarity is registered in *L. lundbladiae, O. ovalis* and *L. rhaeticus*. There instead, *Polypodiisporites polymicroforatus* and other spores dominated the assemblages (Bonis et al., 2009). *Granuloperculatipollis rudis* and *R. germanicus* went extinct during MR1, while *Lunatisporites rhaeticus* was extirpated during the crisis interval (**Table 3**; **Figure 5**). At a narrow interval at the base of the Spelae CIE, *Polypodiisporites polymicroforatus, Limbosporites lundbladiae, Lunatisporites rhaeticus* and *Semiretisporis gothae* became rare and later disappeared during the earliest Jurassic (**Table 3**; **Figure 5**).

3.1.5 A Supraregional Pattern

The comparison with other high-resolution palynological records from the European epicontinental sea and the northern Tethys margin clearly shows that mass rarity in coastal and near-coastal lowland plants occurred in two phases on a supraregional scale. Although significant differences in the pollen records occur for some species, e.g. for *P. elatoides*, the taxodiacean/cupressacean parent plant of which is known to have survived the end-Triassic crisis. However, while it was severely suppressed during MR1 and in both the "grey siltstone" beds in the Stenlille wells and the Triletes beds of the German well Mariental (Heunisch et al., 2010), the parent plant of *P. elatoides* occurred consistently in low numbers and appeared unaffected at the other localities (**Table 3**). This is most likely related to the ecological and climatological preference of the taxodiacean/cupressacean parent plant, which was never abundant during the Rhaetian in the United Kingdom or Austria (Bonis et al., 2010) (Hillebrandt et al., 2013), as well as the depositional environment at each site.

3.2 The Onset of an Ecological Crisis

The magmatic activity in the Central Atlantic Magmatic Province may have affected the terrestrial ecosystem in multiple ways, following the flow chart in **Figure 6**. The successive abundance losses at MR1 were unprecedented during the Rhaetian of NW Europe. The preceding increase in richness, ID1, which signals intermediate levels of ecosystem stress, coincided with and immediately succeeded the Marshi CIE, believed to reflect added excess of light carbon to the carbon cycle as greenhouse gases (Hesselbo et al., 2002; Ruhl and Kürschner, 2011; Lindström et al., 2021), which may have included methane from magma-sediment interaction (Ruhl et al., 2011; Capriolo et al., 2021) (**Figure 4**). The local/regional effects of the subsequent global warming would likely have varied depending on the prevailing palaeoclimatic conditions at each site. The maximum values in species richness also coincided with increased Hg-loading and moderately increased occurrences of mutated fern spores (Lindström et al., 2019) interpreted to reflect volcanic emissions from CAMP volcanism (Thibodeau et al., 2016; Percival et al., 2017; Lindström et al., 2019; Lindström et al., 2021). Increased occurrences of mutated *Classopollis* pollen at a corresponding stratigraphical level in Germany (Gravendyck et al., 2020) further suggests that mutagenic stress also affected the cheirolepidiacean conifers. The mutagenesis could have been caused by Hg-toxicity as suggested for the ferns (Lindström et al., 2019), however, other heavy metal toxicities or increased UV-B

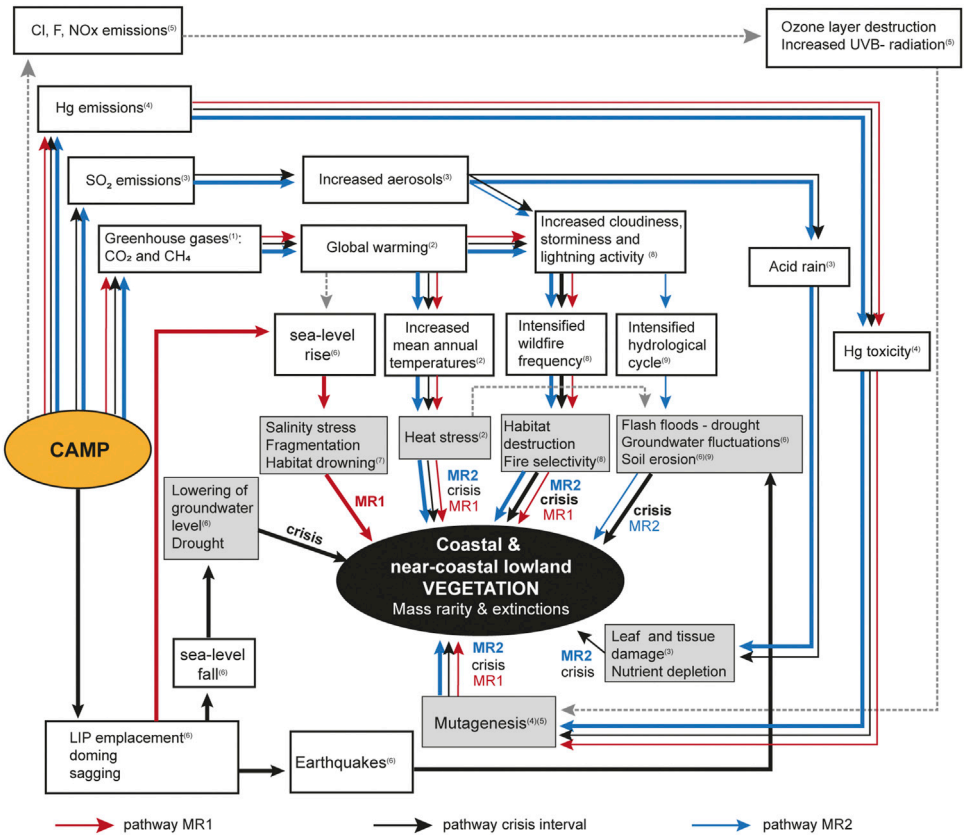

FIGURE 6 | Flow chart illustrating cause-and-effect relationships between the CAMP and the terrestrial vegetation. White boxes exemplify causes and primary physical effects of these, while secondary effects (physiological or directly affecting habitats) are marked with grey boxes. Different coloured arrows illustrate known or herein hypothesized pathways: red arrows = MR1; black arrows = crisis interval; and blue arrows = MR2. The thickness of the arrows emphasizes importance during the different intervals, with thicker lines being more important. Grey stippled arrows illustrate hypothesized pathways not discussed in detail in the text. Numbers in brackets refer to references that either hypothesise or have shown these possible pathways: 1) Hesselbo et al. (2002), Ruhl et al. (2011), Capriolo et al. (2021); 2) McElwain et al. (1999), Steinthorsdottir et al. (2011); 3) Guex et al. (2004), Lindström et al. (2012), Callegaro et al. (2014), Steinthorsdottir et al. (2018), Landwehrs et al. (2020); 4) Thibodeau et al. (2016), Percival et al. (2017), Lindström et al. (2019); 5) Heimdal et al. (2019), Benca et al. (2018); 6) Hallam and Wignall (1999), Hallam (1997), Nielsen (2003), Lindström et al. (2015), Weibel et al. (2016); 7) this paper; 8) Belcher et al. (2010), Petersen and Lindström (2012); 9) Steinthorsdottir et al. (2012), van de Schootbrugge et al. (2020).

radiation, as suggested for plant mutagenesis at the end-Permian event (Benca et al., 2018; Chu et al., 2021), cannot be excluded at this time (**Figure 6**).

3.3 The Effects of Rapid Sea-Level Changes

The coastal and near-coastal lowland terrestrial ecosystems along the margins of the European continental sea and the northern Tethys margin were vulnerable to sea-level changes, but the vegetation appears to have remained relatively stable during the middle Rhaetian. The black shale at the base of the Fjerritslev Formation was deposited during the late Rhaetian transgression (marked by a maximum flooding surface, MFS7; **Figure 2**) (Nielsen, 2003; Lindström and Erlström, 2006) which in contrast to previous transgressive events was associated with massive abundance losses in trees growing in coastal habitats or near-coastal lowlands during MR1 (**Figure 2**). The fact that this mass rarity occurred just prior to, during and after the culmination of this late Rhaetian transgression indicates that the rate of sea level rise outpaced the organic and inorganic sediment supply in the coastal region, leading to habitat fragmentation of the terrestrial coastal and lowland ecosystems to such an extent that it instigated the mass rarity (**Figure 6**). The fast relative sea-level rise in combination with global warming (Ruhl et al., 2011), increased wildfire frequency (Petersen and Lindström, 2012) and heavy metal pollution (Lindström et al., 2019) likely exerted profound stress on the terrestrial ecosystem at that time (**Figure 6**).

The late Rhaetian transgression was succeeded by a prominent regression during which the "grey siltstone beds" were deposited (**Figure 2**). This major drop in sea-level in the late Rhaetian was part of a regression-transgression couplet that can be recognized over large parts of Europe (Hallam, 1997; Hallam and Wignall, 1999), but the mechanism behind this sea-level drop remains to be explained. Hallam (1997) favoured a tectono-eustatic

mechanism other than sea-floor spreading, comparing it in pace and magnitude to glacio-eustacy. Hallam and Wignall (1999) suggested that the regression-transgression couplet was linked to the formation of the CAMP, and widespread occurrences of seismites in co-eval strata across Europe (Simms, 2003; Lindström et al., 2015) seem to support this. In the Danish Basin, this regression culminated with coastal deposition far into the basin, and in some marginal areas fluvial erosion and incision took place (Nielsen, 2003). As a consequence of this regression, a marked lowering of the base-level groundwater table would have had devastating effects on the remaining fragmented coastal mires and lowland ecosystems (**Figure 6**). Normally, sea-level changes affect the relative abundances of spores and pollen in such a way that wind-transported pollen increase in relative abundance compared to water-transported spores with increasing distance from the shore, i.e. the "Neves effect" (Chaloner and Muir, 1968). The fact that the opportunistic palynoflora dominated by *P. polymicroforatus, Deltoidospora* spp. and *Ricciisporites tuberculatus,* has been recovered from various terrestrial to marine settings (Lindström and Erlström, 2006; Lindström et al., 2017b) without major changes in the relative abundances, suggests that the floral shift was not due to the "Neves effect" (Chaloner and Muir, 1968), but that the deforestation on land was extensive (van de Schootbrugge et al., 2009).

On land, in northwest Scania in southern Sweden, the spore-pollen records indicate decreasing tree density from the middle to late Rhaetian, coincident with increased wildfire frequency but decreasing burning temperatures, where the latter may also reflect decreased tree density (Petersen and Lindström, 2012). In fluvial terrestrial strata, stratigraphically equivalent to the "grey siltstone" beds, perfectly zoned sphaerosiderite suggest strong seasonal climate variations with major fluctuations between high groundwater levels and drought (Weibel et al., 2016) (**Figure 6**). Fluctuations in groundwater levels could have been the result of extreme weather, with alternations between drought and excessive rain fall and flash floods during storms. It is also possible that changes in groundwater level was directly related to the on-going seismic activity (Weibel et al., 2016) (**Figure 6**). Both increased wildfire activity and deforestation would exacerbate sediment loads due to lack of vegetation stabilizing channel-margins and could potentially have hindered colonization of newly emerged surfaces by other than opportunistic plants. An abundance of reworked palynomorphs within the grey siltstone beds and equivalent strata in NW Europe, further suggest rapid ongoing soil erosion (van de Schootbrugge et al., 2020) (**Figure 6**).

Towards the top of this interval, increased species richness during ID2 (**Figure 4**) again indicate intermediate disturbance to the ecosystem. However, ID2 neither coincided with or immediately succeeded a negative $\delta^{13}C_{org}$ excursion or Hg-loading (Lindström et al., 2019) (**Figure 4**), hence disturbance stressing the opportunistic ecosystem at this level must have been something else. Multiple records provide evidence of further intensification of storminess and wildfire frequency at this level, as evidenced by charcoal records (Belcher et al., 2010; Petersen and Lindström, 2012), and pyrolytic polycyclic aromatic hydrocarbons (PAHs) (van de Schootbrugge et al., 2009; Lindström et al., 2021). In addition, PAH formed by incomplete combustion of organic matter suggest that intrusive coking of organic-rich sediments in the CAMP area also occurred (van de Schootbrugge et al., 2009). At the same level (Lindström et al., 2021), cuticles from bennettitaleans and ginkgoaleans in Greenland exhibit lesions and distortions typical of sulfuric acid deposition and this was further intensified across the TJB (Steinthorsdottir et al., 2018), suggesting ongoing sulphur-rich volcanic emissions from the CAMP, in line with that some CAMP lavas contained especially high levels sulphur compared to other LIPs (Callegaro et al., 2014). Acid rain would have exacerbated the physiological responses that TJB plants had to ongoing heat and water stress, possibly further increasing the hydrological cycle (Steinthorsdottir et al., 2012), which could explain why the opportunistic plants adapted to drought began to decline in abundance. MR2 preceded the prominent Spelae CIE (**Figures 2**, **4**). This negative excursion has been interpreted to reflect atmospheric increase in light carbon either through degassing of volcanic CO_2 or methane (Hesselbo et al., 2002; Ruhl et al., 2011). However, this was recently questioned by Fox et al. (2020) who instead suggested that the negative CIEs at the Spelae level were regional phenomena caused by fractionation by microbial mats under brackish water conditions. An increase in freshwater algae in the Stenlille record also seems to indicate enhanced runoff (Lindström et al., 2012), but because negative CIEs at the Spelae level are also present outside the European epicontinental sea, e.g. in Argentina (Ruhl et al., 2020), further studies are needed to resolve this issue. Regardless of which, the Spelae CIE did not instigate the MR2 mass rarity in land plants. Instead, living conditions for some of the plants that had suffered during MR1 (e.g. *Classopollis, Perinopollenites elatoides*) appear to have improved during the Spelae CIE, perhaps due to stabilizing climatic conditions. A second relative sea-level rise may have helped to restore some of the coastal and near-coastal lowland habitats that were lost during and after MR1 (**Figures 2–5**). Thus, at least in the northern hemisphere both the destruction and resurrection of coastal and near-coastal terrestrial ecosystems were tightly linked to relative sea-level changes.

3.4 Rare Species Are Especially Vulnerable to Climate and Environmental Change

Today, areas with long term stable climatic conditions have been found to contain higher numbers of rare plants, because of the reduced extinction risks (Enquist et al., 2019). However, because rare plants species are more susceptible to reductions in populations size, they are more likely to go extinct by orders of magnitude than more abundant species during times of rapid climate change (Enquist et al., 2019). The geographical and numerical reduction of plant species during the two end-Triassic mass rarity phases attest to the severe impact of this crisis on the vegetation in NW Europe.

The causality behind the mass rarity amongst the plants was clearly complex, including both direct effects of the volcanic activity in the CAMP, as well as subsequent feedback mechanisms. The volcanic activity of the CAMP emitted multiple stressors, including greenhouse gases, SO_2, Hg-pollution, PAHs, and likely also halocarbons (**Figure 6**). The results emphasize that rapid sea-level changes, probably driven by tectono-eustatic activity in the CAMP area, severely affected the coastal and near-coastal lowland vegetation, to the extent that many species already stressed by climate change and volcanic pollution, may have had difficulties coping with fragmentation of habitats and changes groundwater levels. The mass rarity was profound as it affected both already rare as well as previously abundant species and must have had a cascading negative impact on the terrestrial ecosystem as a whole, altering the conditions for a range of organisms from the lowest to the highest trophic levels. The mass rarity in plants was supraregional across NW Europe (**Table 2**), although small populations of typical Rhaetian plant taxa lingered without recovery into the earliest Jurassic (early Hettangian) in some areas. Most of these ghost taxa are only known by their spores or pollen and have not been identified as macroplant fossils, thus they were rare already prior to the crisis. Their extirpation in the aftermath of the end-Triassic crisis attest to the vulnerability of plant species to reductions in abundance and geographic range, especially in coastal regions. This should resonate when considering present day anthropogenic ecosystem disturbances and ongoing and future climate change scenarios (IPCC, 2021) that, similar to the end-Triassic crisis include rapid sea-level rise (De Conto et al., 2021) in combination with increased frequency and intensity of climate extremes such as prolonged heatwaves and drought, wildfires, major storms and heavy precipitation.

4 METHODS

4.1 Sampling, Palynological Processing and Analysis

109 sedimentary rock samples from Stenlille-1 and 87 ones from Stenlille-4 were processed using standard palynological methods at the Palynology Laboratory at GEUS. Approximately 20 g of each sample was crushed and treated with hydrochloric and hydrofluoric acids to remove carbonate and silicate minerals, respectively. Heavy minerals were removed from the residues using heavy liquid separation. The organic residues were mildly oxidized using nitric acid and filtered on 11 μm mesh filters. Strew slides were prepared after each step in the preparation after the hydrofluoric acid treatment, using glycerine gel as mounting medium. The palynomorph content of the samples were assessed by counting 300 specimens in one representative strew slide from each sample. Spore and pollen taxa abundances were normalized against the total spore-pollen count in each sample. It is important to remember that spore/pollen production in a plant is not necessarily related to the actual abundance of that plant in the ecosystem, and the parent plant of continuously rare spore/pollen taxa may still have played an important role in the ecosystem. In addition, plants that rely on insect or animal assistance with dispersal and pollination may have a more restrained pollen production compared to those that rely on wind for dispersal. In the late Triassic, prior to the diversification of the angiosperms, possible insect pollination has only been suggested for the Bennettitales (Labandeira et al., 2007).

Seventy-five samples from Stenlille-4 were analysed for palynofacies. Two-hundred particles or more were counted from each sample on the slide prepared after heavy liquid separation but prior to swirling. The palynodebris and palynomorphs were divided into ten different categories: *Black opaque phytoclasts* which include opaque usually rounded particles; *black wood* encompasses all black wood remains, both blade shaped, needle shaped and equidimensional ones; *plant tissue* includes all non-woody and non-cuticular plant remains; *cuticles* include translucent to semi-translucent tissue with cellular structures with or without stomata; *Amorphous organic matter (AOM)* encompasses degraded material either as structureless amorphous or structured amorphous matter; *marine phytoplankton* includes acritarchs, dinoflagellate cysts and prasinophytes, however, for graphic purposes unidentifiable palynomorphs were also included in this group but are listed separately in **Supplementary Table S3**; *freshwater microalgae* primarily include *Botryococcus braunii* and zygnematacean cysts; *Spores* also include rare fragments of clitellate cocoon fragments; and finally *pollen*. The counts are listed in **Supplementary Table S3**.

4.2 Mass Rarity Assessment

In palynology, loss of species abundance has often been used as an indicator of biotic crises without specifically referring this to mass rarity (Twitchett et al., 2001; Lindström and McLoughlin, 2007; van de Schootbrugge et al., 2009). The mass rarity of a taxon was determined as either: 1) a marked shift from consistently common to abundant abundance values to consistently or inconsistently rare occurrences, i.e. the last common occurrence (LCO), or 2) as a marked shift from consistently present in low abundances to inconsistently present in low or lower abundances, i.e. the last consistent occurrence (LCon). In fact, mass rarity is routinely used in palynostratigraphy as the last common occurrence (LCO) of a taxon, or for taxa of low abundance the last consistent occurrence (LCon) may also reflect mass rarity in the parent plant.

4.3 Diversity Patterns

Diversity trends in the successions were analyzed using species richness, dominance (1-Simpson index) and Pielou's evenness calculated using the software PAST4.05. Because many of the spore- and pollen-genera at the Triassic–Jurassic boundary are monospecific, species richness is only marginally higher than genus richness. Reworked taxa were excluded from the diversity analyses. The diversity patterns were assessed primarily according to the intermediate disturbance hypothesis (Connell, 1978; Svensson et al., 2012).

DATA AVAILABILITY STATEMENT

The original contributions presented in the study are included in the article/**Supplementary Material**, further inquiries can be directed to the corresponding author.

AUTHOR CONTRIBUTIONS

SL designed the project, produced and analysed the data, and wrote the manuscript.

FUNDING

This work was partly supported by the Geocenter Denmark grant 2013–6 to SL and the CCUS2020-project for providing support to the analyses of additional samples and compilation of data.

ACKNOWLEDGMENTS

SL would like to thank Gunver K. Pedersen and Lars Henrik Nielsen for comments on an early version of the manuscript. SL gratefully acknowledges the recent constructive reviews of Evelyn Kustatscher and Annette Götz.

SUPPLEMENTARY MATERIAL

The Supplementary Material for this article can be found online at: https://www.frontiersin.org/articles/10.3389/feart.2021.780343/full#supplementary-material

REFERENCES

Barbacka, M., Pacyna, G., Kocsis, Á. T., Jarzynka, A., Ziaja, J., and Bodor, E. (2017). Changes in Terrestrial Floras at the Triassic-Jurassic Boundary in Europe. *Palaeogeogr. Palaeoclimatol. Palaeoecol.* 480, 80–93. doi:10.1016/j.palaeo.2017.05.024

Belcher, C. M., Mander, L., Rein, G., Jervis, F. X., Haworth, M., Hesselbo, S. P., et al. (2010). Increased Fire Activity at the Triassic/Jurassic Boundary in Greenland Due to Climate-Driven floral Change. *Nat. Geosci* 3, 426–429. doi:10.1038/ngeo871

Benca, J. P., Duijnstee, I. A. P., and Looy, C. V. (2018). UV-B-induced forest Sterility: Implications of Ozone Shield Failure in Earth's Largest Extinction. *Sci. Adv.* 4, e1700618. doi:10.1126/sciadv.1700618

Bond, D. P. G., and Wignall, P. B. (2014). "Large Igneous Provinces and Mass Extinctions: An Update," in *Volcanism, Impacts, and Mass Extinctions: Causes and Effects* (Boulder, CO: G. Keller & A.C. Kerr.), 29–55. doi:10.1130/2014.2505(02)

Bonis, N. R., Kürschner, W. M., and Krystyn, L. (2009). A Detailed Palynological Study of the Triassic-Jurassic Transition in Key Sections of the Eiberg Basin (Northern Calcareous Alps, Austria). *Rev. Palaeobotany Palynology* 156, 376–400. doi:10.1016/j.revpalbo.2009.04.003

Bonis, N. R., Ruhl, M., and Kürschner, W. M. (2010). Milankovitch-scale Palynological Turnover across the Triassic-Jurassic Transition at St. Audrie's Bay, SW UK. *J. Geol. Soc.* 167, 877–888. doi:10.1144/0016-76492009-141

Callegaro, S., Baker, D. R., De Min, A., Marzoli, A., Geraki, K., Bertrand, H., et al. (2014). Microanalyses Link Sulfur from Large Igneous Provinces and Mesozoic Mass Extinctions. *Geology* 42, 895–898. doi:10.1130/g35983.1

Capriolo, M., Marzoli, A., Aradi, L. E., Ackerson, M. R., Bartoli, O., Callegaro, S., et al. (2021). Massive Methane Fluxing from Magma-Sediment Interaction in the End-Triassic Central Atlantic Magmatic Province. *Nat. Commun.* 12, 5534. doi:10.1038/s41467-021-25510-w

Chaloner, W. G., and Muir, M. (1968). "Spores and Floras," in *Coal and Coal-Bearing Strata*. Editors D. Murchison and T. S. Westall (Edinburgh: Oliver & Boyd), 127–146.

Chu, D., Dal Corso, J., Shu, W., Haijun, S., Wignall, P. B., Grasby, S. E., et al. (2021). Metal-induced Stress in Survivor Plants Following the End-Permian Collapse of Land Ecosystems. *Geology* 49, 657–661. doi:10.1130/g48333.1

Connell, J. H. (1978). Diversity in Tropical Rain Forests and Coral Reefs. *Science* 199, 1302–1310. doi:10.1126/science.199.4335.1302

De Conto, R. M., Pollard, D., Alley, R. B., Velicogna, I., Gasson, E., Gomez, N., et al. (2021). The Paris Climate Agreement and Future Sea-Level Rise from Antarctica. *Nature* 593, 83–89. doi:10.1038/s41586-021-03427-0

Enquist, B. J., Feng, X., Boyle, B., Maitner, B., Newman, E. A., Jørgensen, P. M., et al. (2019). The Commonness of Rarity: Global and Future Distribution of Rarity across Land Plants. *Sci. Adv.* 5, eaaz0414. doi:10.1126/sciadv.aaz0414

Fox, C. P., Cui, X., Whiteside, J. H., Olsen, P. E., Summons, R. E., and Grice, K. (2020). Molecular and Isotopic Evidence Reveals the End-Triassic Carbon Isotope Excursion Is Not from Massive Exogenous Light Carbon. *Proc. Natl. Acad. Sci. USA* 117, 30171–30178. doi:10.1073/pnas.1917661117

Gravendyck, J., Schobben, M., Bachelier, J. B., and Kürschner, W. M. (2020). Macroecological Patterns of the Terrestrial Vegetation History during the End-Triassic Biotic Crisis in the central European Basin: A Palynological Study of the Bonenburg Section (NW-Germany) and its Supra-regional Implications. *Glob. Planet. Change* 194, 103286. doi:10.1016/j.gloplacha.2020.103286

Guex, J., Bartolini, A., Atudorei, V., and Taylor, D. (2004). High-resolution Ammonite and Carbon Isotope Stratigraphy across the Triassic-Jurassic Boundary at New York Canyon (Nevada). *Earth Planet. Sci. Lett.* 225, 29–41. doi:10.1016/j.epsl.2004.06.006

Hallam, A. (1997). Estimates of the Amount and Rate of Sea-Level Change across the Rhaetian-Hettangian and Pliensbachian-Toarcian Boundaries (Latest Triassic to Early Jurassic). *J. Geol. Soc.* 154, 773–779. doi:10.1144/gsjgs.154.5.0773

Hallam, A., and Wignall, P. B. (1999). Mass Extinctions and Sea-Level Changes. *Earth-Science Rev.* 48, 217–250. doi:10.1016/s0012-8252(99)00055-0

Heimdal, T. H., Callegaro, S., Svensen, H. H., Jones, M. T., Pereira, E., and Planke, S. (2019). Evidence for Magma-Evaporite Interactions during the Emplacement of the Central Atlantic Magmatic Province (CAMP) in Brazil. *Earth Planet. Sci. Lett.* 506, 476–492. doi:10.1016/j.epsl.2018.11.018

Hesselbo, S. P., Robinson, S. A., Surlyk, F., and Piasecki, S. (2002). Terrestrial and marine Extinction at the Triassic-Jurassic Boundary Synchronized with Major Carbon-Cycle Perturbation: A Link to Initiation of Massive Volcanism? *Geol* 30, 251–254. doi:10.1130/0091-7613(2002)030<0251:tameat>2.0.co;2

Hesselbo, S. P., Robinson, S. A., and Surlyk, F. (2004). Sea-level Change and Facies Development across Potential Triassic-Jurassic Boundary Horizons, SW Britain. *J. Geol. Soc.* 161, 365–379. doi:10.1144/0016-764903-033

Heunisch, C., Luppold, F. W., Reinhardt, L., and Röhling, H.-G. (2010). Palynofazies, Bio- und Lithostratigrafie im Grenzbereich Trias/Jura in der Bohrung Mariental 1 (Lappwaldmulde, Ostniedersachsen). *zdgg* 161, 51–98. doi:10.1127/1860-1804/2010/0161-0051

Hillebrandt, A. v., Krystyn, L., Kürschner, W. M., Bonis, N. R., Ruhl, M., Richoz, S., et al. (2013). The Global Stratotype Sections and Point (GSSP) for the Base of the Jurassic System at Kuhjoch (Karwendel Mountains, Northern Calcareous Alps, Tyrol, Austria). *Episodes* 36, 162–198. doi:10.18814/epiiugs/2013/v36i3/001

Hull, P. M., Darroch, S. A. F., and Erwin, D. H. (2015). Rarity in Mass Extinctions and the Future of Ecosystems. *Nature* 528, 345–351. doi:10.1038/nature16160

Kürschner, W. M., Mander, L., and Mcelwain, J. C. (2014). A Gymnosperm Affinity for Ricciisporites Tuberculatus Lundblad: Implications for Vegetation and

Environmental Reconstructions in the Late Triassic. *Palaeobio Palaeoenv* 94, 295–305. doi:10.1007/s12549-014-0163-y

Labandeira, C. C., Kvaček, J., and Mostovski, M. B. (2007). Pollination Drops, Pollen, and Insect Pollination of Mesozoic Gymnosperms. *Taxon* 56, 663–695. doi:10.2307/25065852

Landwehrs, J. P., Feulner, G., Hofmann, M., and Petri, S. (2020). Climatic Fluctuations Modeled for Carbon and Sulfur Emissions from End-Triassic Volcanism. *Earth Planet. Sci. Lett.* 537, 116174. doi:10.1016/j.epsl.2020.116174

Lindström, S., Sanei, H., Van De Schootbrugge, B., Pedersen, G. K., Lesher, C. E., Tegner, C., et al. (2019). Volcanic Mercury and Mutagenesis in Land Plants during the End-Triassic Mass Extinction. *Sci. Adv.* 5, eaaw4018. doi:10.1126/sciadv.aaw4018

Lindström, S., Callegaro, S., Davies, J., Tegner, C., Van De Schootbrugge, B., Pedersen, G. K., et al. (2021). Tracing Volcanic Emissions from the Central Atlantic Magmatic Province in the Sedimentary Record. *Earth-Science Rev.* 212, 103444. doi:10.1016/j.earscirev.2020.103444

Lindström, S., Erlström, M., Piasecki, S., Nielsen, L. H., and Mathiesen, A. (2017a). Palynology and Terrestrial Ecosystem Change of the Middle Triassic to Lowermost Jurassic Succession of the Eastern Danish Basin. *Rev. Palaeobotany Palynology* 244, 65–95. doi:10.1016/j.revpalbo.2017.04.007

Lindström, S., and Erlström, M. (2006). The Late Rhaetian Transgression in Southern Sweden: Regional (And Global) Recognition and Relation to the Triassic-Jurassic Boundary. *Palaeogeogr. Palaeoclimatol. Palaeoecol.* 241, 339–372. doi:10.1016/j.palaeo.2006.04.006

Lindström, S., and McLoughlin, S. (2007). Synchronous Palynofloristic Extinction and Recovery after the End-Permian Event in the Prince Charles Mountains, Antarctica: Implications for Palynofloristic Turnover across Gondwana. *Rev. Palaeobotany Palynology* 145, 89–122. doi:10.1016/j.revpalbo.2006.09.002

Lindström, S. (2016). Palynofloral Patterns of Terrestrial Ecosystem Change during the End-Triassic Event - a Review. *Geol. Mag.* 153, 223–251. doi:10.1017/s0016756815000552

Lindström, S., Pedersen, G. K., Van De Schootbrugge, B., Hansen, K. H., Kuhlmann, N., Thein, J., et al. (2015). Intense and Widespread Seismicity during the End-Triassic Mass Extinction Due to Emplacement of a Large Igneous Province. *Geology* 43, 387–390. doi:10.1130/g36444.1

Lindström, S., Van De Schootbrugge, B., Dybkjaer, K., Pedersen, G. K., Fiebig, J., Nielsen, L. H., et al. (2012). No Causal Link between Terrestrial Ecosystem Change and Methane Release during the End-Triassic Mass Extinction. *Geology* 40, 531–534. doi:10.1130/g32928.1

Lindström, S., Van De Schootbrugge, B., Hansen, K. H., Pedersen, G. K., Alsen, P., Thibault, N., et al. (2017b). A New Correlation of Triassic-Jurassic Boundary Successions in NW Europe, Nevada and Peru, and the Central Atlantic Magmatic Province: A Time-Line for the End-Triassic Mass Extinction. *Palaeogeogr. Palaeoclimatol. Palaeoecol.* 478, 80–102. doi:10.1016/j.palaeo.2016.12.025

Lund, J. J. (2003). Rhaetian to Pliensbachian Palynostratigraphy of the central Part of the NW German Basin Exemplified by the Eitzendorf 8 Well. *CFS Courier Forschungsinstitut Senckenberg* 2003, 69–83.

McElwain, J. C., Beerling, D. J., and Woodward, F. I. (1999). Fossil Plants and Global Warming at the Triassic-Jurassic Boundary. *Science* 285, 1386–1390. doi:10.1126/science.285.5432.1386

McElwain, J. C., Popa, M. E., Hesselbo, S. P., Haworth, M., and Surlyk, F. (2007). Macroecological Responses of Terrestrial Vegetation to Climatic and Atmospheric Change across the Triassic/Jurassic Boundary in East Greenland. *Paleobiology* 33, 547–573. doi:10.1666/06026.1

McElwain, J. C., and Punyasena, S. W. (2007). Mass Extinction Events and the Plant Fossil Record. *Trends Ecol. Evol.* 22, 548–557. doi:10.1016/j.tree.2007.09.003

McGhee, G. R., Clapham, M. E., Sheehan, P. M., Bottjer, D. J., and Droser, M. L. (2013). A New Ecological-Severity Ranking of Major Phanerozoic Biodiversity Crises. *Palaeogeogr. Palaeoclimatol. Palaeoecol.* 370, 260–270. doi:10.1016/j.palaeo.2012.12.019

Mussard, J. M., Ducazeaux, J., and Cugny, P. (1997). Statistical Analyses of Palynomorph Assemblages in Middle Jurassic Deposits (Lower to Middle Bathonian, Brent Group, Norway). *Bull. Des Centres De Recherches Exploration-Production Elf Aquitaine* 21, 265–277.

Nielsen, L. H. (2003). Late Triassic - Jurassic Development of the Danish Basin and the Fennoscandian Border Zone, Southern Scandinavia. *GEUS Bull.* 1, 459–526. doi:10.34194/geusb.v1.4681

Percival, L. M. E., Ruhl, M., Hesselbo, S. P., Jenkyns, H. C., Mather, T. A., and Whiteside, J. H. (2017). Mercury Evidence for Pulsed Volcanism during the End-Triassic Mass Extinction. *Proc. Natl. Acad. Sci. USA* 114, 7929–7934. doi:10.1073/pnas.1705378114

Petersen, H. I., and Lindström, S. (2012). Synchronous Wildfire Activity Rise and Mire Deforestation at the Triassic-Jurassic Boundary. *Plos One* 7, e47236. doi:10.1371/journal.pone.0047236

Pott, C. (2014). A Revision of Wielandiella Angustifolia, a Shrub-Sized Bennettite from the Rhaetian-Hettangian of Scania, Sweden, and Jameson Land, Greenland. *Int. J. Plant Sci.* 175, 467–499. doi:10.1086/675577

Pott, C., and McLoughlin, S. (2011). The Rhaetian flora of Rögla, Northern Scania, Sweden. *Palaeontology* 54, 1025–1051. doi:10.1111/j.1475-4983.2011.01090.x

Pott, C., Schmeissner, S., Dütsch, G., and Van Konijnenburg-Van Cittert, J. H. A. (2016). Bennettitales in the Rhaetian flora of Wüstenwelsberg, Bavaria, Germany. *Rev. Palaeobotany Palynology* 232, 98–118. doi:10.1016/j.revpalbo.2016.04.010

Ruhl, M., Bonis, N. R., Reichart, G.-J., Damsté, J. S. S., and Kürschner, W. M. (2011). Atmospheric Carbon Injection Linked to End-Triassic Mass Extinction. *Science* 333, 430–434. doi:10.1126/science.1204255

Ruhl, M., Hesselbo, S. P., Al-Suwaidi, A., Jenkyns, H. C., Damborenea, S. E., Manceñido, M. O., et al. (2020). On the Onset of Central Atlantic Magmatic Province (CAMP) Volcanism and Environmental and Carbon-Cycle Change at the Triassic-Jurassic Transition (Neuquén Basin, Argentina). *Earth-Science Rev.* 208, 103229. doi:10.1016/j.earscirev.2020.103229

Ruhl, M., and Kürschner, W. M. (2011). Multiple Phases of Carbon Cycle Disturbance from Large Igneous Province Formation at the Triassic-Jurassic Transition. *Geology* 39, 431–434. doi:10.1130/g31680.1

Scheuring, B. W. (1970). Palynologische und palynostratigraphische Untersuchungen des Keupers im Bölchentunnel (Solothurner Jura). *Schweizerische Paläontologische Abhandlungen* 88, 119pp.

Sepkoski, J. J. (1996). "Patterns of Phanerozoic Extinction: a Perspective from Global Data Bases," in *Global Events and Event Stratigraphy*. Editor O. H. Walliser (Berlin: Springer-Verlag), 35–51. doi:10.1007/978-3-642-79634-0_4

Simms, M. J. (2003). Uniquely Extensive Seismite from the Latest Triassic of the United Kingdom: Evidence for Bolide Impact? *Geol* 31, 557–560. doi:10.1130/0091-7613(2003)031<0557:uesftl>2.0.co;2

Steinthorsdottir, M., Elliott-Kingston, C., and Bacon, K. L. (2018). Cuticle Surfaces of Fossil Plants as a Potential Proxy for Volcanic SO2 Emissions: Observations from the Triassic-Jurassic Transition of East Greenland. *Palaeobio Palaeoenv* 98, 49–69. doi:10.1007/s12549-017-0297-9

Steinthorsdottir, M., Jeram, A. J., and Mcelwain, J. C. (2011). Extremely Elevated CO2 Concentrations at the Triassic/Jurassic Boundary. *Palaeogeogr. Palaeoclimatol. Palaeoecol.* 308, 418–432. doi:10.1016/j.palaeo.2011.05.050

Steinthorsdottir, M., Woodward, F. I., Surlyk, F., and Mcelwain, J. C. (2012). Deep-time Evidence of a Link between Elevated CO2 Concentrations and Perturbations in the Hydrological Cycle via Drop in Plant Transpiration. *Geology* 40, 815–818. doi:10.1130/g33334.1

Stohlgren, T. J., and Kumar, S. (2013). "Endangered Plants," in *Encyclopedia of Biodiversity*. Editor S. A. Levin. Second ed (Academic Press Elsevier), 205–215. doi:10.1016/b978-0-12-384719-5.00241-0

Svensson, J. R., Lindegarth, M., Jonsson, P. R., and Pavia, H. (2012). Disturbance-diversity Models: what Do They Really Predict and How Are They Tested? *Proc. R. Soc. B.* 279, 2163–2170. doi:10.1098/rspb.2011.2620

Thibodeau, A. M., Ritterbush, K., Yager, J. A., West, A. J., Ibarra, Y., Bottjer, D. J., et al. (2016). Mercury Anomalies and the Timing of Biotic Recovery Following the End-Triassic Mass Extinction. *Nat. Commun.* 7, 11147. doi:10.1038/ncomms11147

Twitchett, R. J., Looy, C. V., Morante, R., Visscher, H., and Wignall, P. B. (2001). Rapid and Synchronous Collapse of marine and Terrestrial Ecosystems during the End-Permian Biotic Crisis. *Geol* 29, 351–354. doi:10.1130/0091-7613(2001)029<0351:rascom>2.0.co;2

van de Schootbrugge, B., Quan, T. M., Lindström, S., Püttmann, W., Heunisch, C., Pross, J., et al. (2009). Floral Changes across the Triassic/Jurassic Boundary Linked to Flood basalt Volcanism. *Nat. Geosci* 2, 589–594. doi:10.1038/ngeo577

van de Schootbrugge, B., Van Der Weijst, C. M. H., Hollaar, T. P., Vecoli, M., Strother, P. K., Kuhlmann, N., et al. (2020). Catastrophic Soil Loss Associated with End-Triassic Deforestation. *Earth-Science Rev.* 210, 103332. doi:10.1016/j.earscirev.2020.103332

Van Konijnenburg-Van Cittert, J. H. A., Pott, C., Schmeissner, S., Dütsch, G., and Kustatscher, E. (2020). Ferns and Fern Allies in the Rhaetian flora of Wüstenwelsberg, Bavaria, Germany. *Rev. Palaeobotany Palynology* 273, 104147. doi:10.1016/j.revpalbo.2019.104147

Van Konijnenburg-Van Cittert, J. H. A., Pott, C., Schmeissner, S., Dütsch, G., and Kustatscher, E. (2018). Seed Ferns and Cycads in the Rhaetian flora of Wüstenwelsberg, Bavaria, Germany. *Rev. Palaeobotany Palynology* 258, 190–214. doi:10.1016/j.revpalbo.2018.08.005

IPCC (2021). "Sixth Assessment Report," in *Climate Change 2021: The Physical Science Basis. Contribution of Working Group I to the Sixth Assessment Report of the Intergovernmental Panel on Climate Change*. Editors V. Masson-Delmotte, P. Zhai, A. Pirani, S. C. P. L. Connors, S. Berger, N. Caud, and et al (Cambridge: IPCC).

Weibel, R., Lindström, S., Pedersen, G. K., Johansson, L., Dybkjær, K., Whitehouse, M. J., et al. (2016). Groundwater Table Fluctuations Recorded in Zonation of Microbial Siderites from End-Triassic Strata. *Sediment. Geology.* 342, 47–65. doi:10.1016/j.sedgeo.2016.06.009

Conflict of Interest: The author declares that the research was conducted in the absence of any commercial or financial relationships that could be construed as a potential conflict of interest.

Publisher's Note: All claims expressed in this article are solely those of the authors and do not necessarily represent those of their affiliated organizations, or those of the publisher, the editors and the reviewers. Any product that may be evaluated in this article, or claim that may be made by its manufacturer, is not guaranteed or endorsed by the publisher.

frontiers in Earth Science

ORIGINAL RESEARCH
published: 15 December 2021
doi: 10.3389/feart.2021.778820

Zircon of Triassic Age in the Stuttgart Formation (Schilfsandstein)—Witness of Tephra Fallout in the Central European Basin and New Constraints on the Mid-Carnian Episode

Armin Zeh[1,2]*, *Matthias Franz*[3] and *Karsten Obst*[4]

[1]Mineralogy and Petrology, Institute for Applied Geosciences, Karlsruhe Institute of Technology (KIT), Karlsruhe, Germany, [2]Frankfurt Isotope and Element Research Center (FIERCE), Goethe-University, Frankfurt, Germany, [3]Abteilung Angewandte Geologie, Geowissenschaftliches Zentrum der Georg-August-Universität Göttingen, Göttingen, Germany, [4]Geological Survey of Mecklenburg-Western Pomerania, LUNG M-V, Güstrow, Germany

The Carnian Stuttgart-Formation (Schilfsandstein) of the Central European Basin contains relics of Triassic volcanic detritus in form of euhedral zircon grains and authigenic analcime. Multiple LA-ICP-MS spot analyses of single zircon crystals from an outcrop near Heilbronn (SW Germany) yielded weighted average $^{206}Pb/^{238}U$ ages between 250 and 230 Ma, providing evidence for tephra fallout in the southern part of the Central European Basin related to Olenekian, Anisian–Ladinian and Carnian volcanic activity. The tephra was probably transported by monsoonal circulations from volcanic centres of the NW Tethys to the Central European Basin. The four youngest zircon crystals gave a weighted average $^{206}Pb/^{238}U$ age of 231.1 ± 1.6 Ma (10 analyses), which is interpreted to date syn-depositional tephra fallout into the fluvial Lower Schilfsandstein Member of the Stuttgart Formation. This new maximum depositional age provides the first evidence that deposition of the Stuttgart Formation, which represents the type-example of the mid-Carnian episode, a global episode of enhanced flux of siliciclastic detritus and related environmental perturbations, occurred during the Tuvalian 2 substage at ca. 231 Ma, about 3 million years later than suggested by previous correlations. Zircon grains with weighted average $^{206}Pb/^{238}U$ ages of 236.0 ± 1.2 Ma (n = 17) and 238.6 ± 1.5 Ma (n = 6) and $^{206}Pb/^{238}U$ ages between 241 ± 6 and 250 ± 3 Ma point to the presence of tephra in early Carnian to Olenekian strata of the Keuper to Buntsandstein Groups. Traces of these reworked tephra were incorporated into the Stuttgart Formation due to fluvial erosion in the southern Central European Basin and at its margins.

Keywords: zircon, U-Pb data, tephra, Keuper, Stuttgart Formation (Schilfsandstein), Carnian

OPEN ACCESS

Edited by:
Jacopo Dal Corso,
China University of Geosciences Wuhan, China

Reviewed by:
Joshua Davies,
Université du Québec à Montréal, Canada
Lawrence Henry Tanner,
Le Moyne College, United States

***Correspondence:**
Armin Zeh
armin.zeh@kit.edu

Specialty section:
This article was submitted to Sedimentology, Stratigraphy and Diagenesis, a section of the journal Frontiers in Earth Science

Received: *17 September 2021*
Accepted: *29 November 2021*
Published: *15 December 2021*

Citation:
Zeh A, Franz M and Obst K (2021) Zircon of Triassic Age in the Stuttgart Formation (Schilfsandstein)—Witness of Tephra Fallout in the Central European Basin and New Constraints on the Mid-Carnian Episode. Front. Earth Sci. 9:778820. doi: 10.3389/feart.2021.778820

1 INTRODUCTION

Presently, correlations of the terrestrial-marine Keuper Group of the Germanic Upper Triassic with stages of the international Triassic standard (overviews in Bachmann and Kozur, 2004; Franz et al., 2018a) are based on biostratigraphic control using spinicaudatans (conchostracans) and palynomorphs (Heunisch, 1999; Kozur and Weems, 2007; Kozur and Weems, 2010; Geyer and

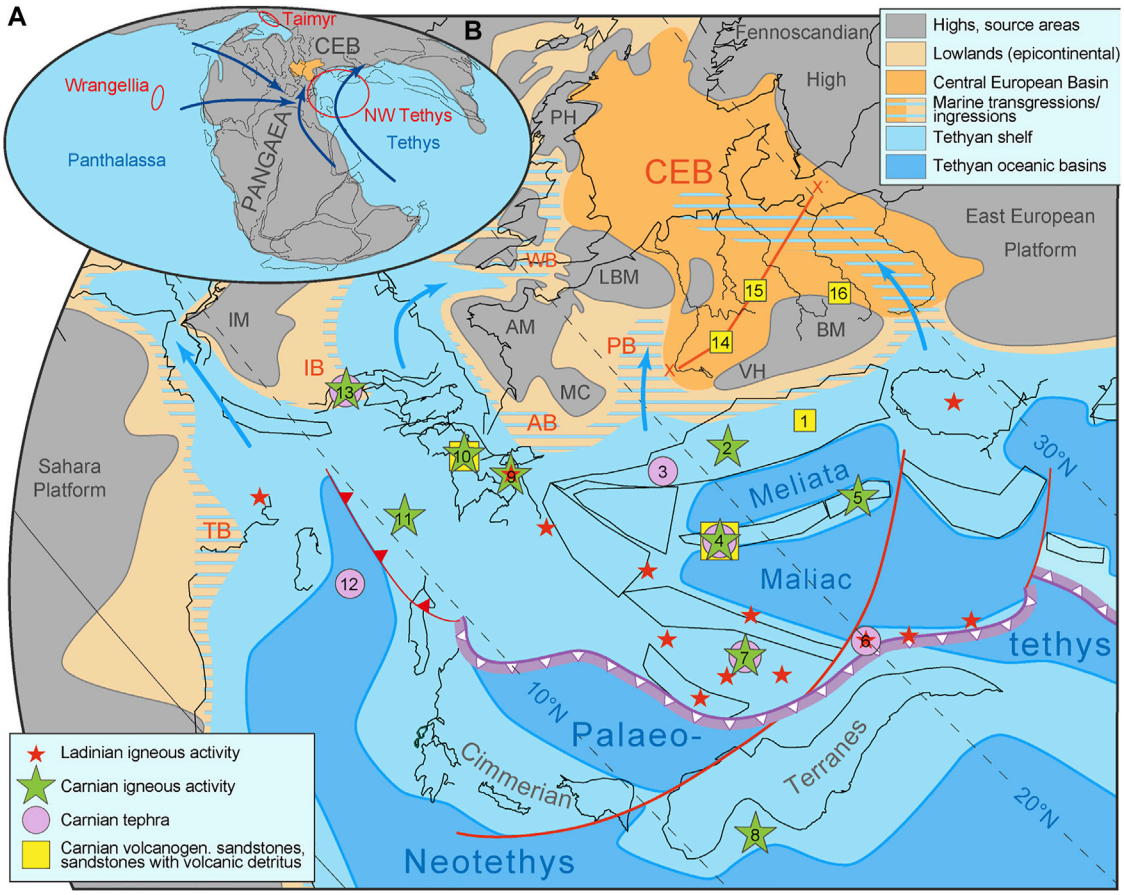

FIGURE 1 | Ladinian–Carnian global and regional palaeogeography. A. Global palaeogeography with the positions of the Central European Basin (CEB), the NW Tethys igneous province, and the Taimyr and Wrangellia Large Igneous Provinces; circulation pattern of northern summer monsoon (blue arrows) after Parrish (1999). B. Regional palaeogeography of the NW Tethys and peri-Tethyan lowlands (modified from Stampfli and Borel, 2004). The CEB is shown at the stage of the Lower Schilfsandstein Member; for cross-section X–X′ see **Figure 2**. Centres of Ladinian and Carnian igneous activity were adopted from Stampfli and Borel (2004): 1—W Carpathians (Lunz Sandstone: Kohut et al., 2018); 2—North Karawank Mountains (Eisenkappel: Dunkl et al., 2019); 3—Drau Range (Nötsch tuff: Dunkl et al., 2019); 4—Transdanubian Range (Dunkl et al., 2019); 5—Bükk Mountains (Dunkl et al., 2019); 6—Huğlu-Pindos (SW Turkey, Lycian nappes: Moix et al., 2013); 7—Pindos basal sequence (E Crete, Priolithos Fm: Stampfli et al., 2003); 8—Kara Dere Basalt (SW Turkey, Antalya nappes: Maury et al., 2008); 9—Dolomites (Predazzo: e.g., Dunkl et al., 2019); 10—Lombardy (Val Sabbia sandstone: e.g. Garzanti, 1985; Cassinis et al., 2008); 11—"Southern mobile belt" (Brusca et al., 1982); 12—Lagonegro Basin (Aglianico ash bed: Furin et al., 2006); 13—Mallorca (e.g. López-Gómez et al., 2017); 14—CEB (Schilfsandstein at Heilbronn: this study); 15—CEB (Schilfsandstein at Großmonra,Thuringia: Hofmann et al., 2018); 16—CEB (Lisowice bone-bearing horizon, Lipie Śląskie: Kowal-Linka et al., 2019). AM, Amorican Massif; AB, Aquitaine Basin; BM, Bohemian Massif; IM, Iberian Massif; LBM, London-Brabant Massif; MC, Massif Central; PB, Paris Basin; PH, Pennine High; TB, Tunis Basin; VH, Vindelician High; WB, Wessex Basin.

Kelber, 2018; Heunisch and Wierer, 2021), partly supplemented by magnetostratigraphy and sequence-stratigraphy (e.g., Zhang et al., 2020). However, a more refined correlation with substages of the Triassic standard is limited due to the lack of any Tethyan marker fossils within the Central German Basin (CEB). Furthermore, exact depositional ages of individual formations remain vague owing to the apparent absence of tuff horizons with datable minerals like zircon, commonly used for precise dating of sedimentary successions. This absence is surprising considering the fact that intense Triassic volcanic activity is known from the NW Tethys realm (e.g., Brusca et al., 1982; Cassinis et al., 2008; Marocchi et al., 2008; Beltran-Trivino et al., 2016; Bianchini et al., 2018; Dunkl et al., 2019; Lustrino et al., 2019; Storck et al., 2019), and also postulated for the northern margin of the CEB (e.g., Fisher and Mudge, 1990; Ziegler, 1990; van Bergen and Sissingh, 2007; Larsen et al., 2008). Significant input of Carnian volcanism has recently been reported from marine sandstones of NW Tethyan basins (Kohut et al., 2018; Dunkl et al., 2019), and scarce traces also from a terrestrial sandstone of the Keuper Group in South Poland (Kowal-Linka et al., 2019), while nothing is known so far from wide parts of the CEB.

In this study, we present the first set of Triassic U-Pb ages obtained from euhedral zircon grains of the Stuttgart Formation (Schilfsandstein) from the classical locality Jägerhaus quarry near Heilbronn in SW Germany. Weighted mean $^{206}Pb/^{238}U$ ages obtained from these zircon grains provide the first precise radiometric constraints on the timing of pre- to syn-depositional tephra fallout within the southern part of the

CEB, and on the maximum depositional age of the Stuttgart Formation. As the Stuttgart Formation represents the type-example of the mid-Carnian episode, a global phase of environmental perturbations and related ecosystem responses (reviews by Arche and López-Gómez, 2014; Ogg, 2015; Ruffell et al., 2015; Dal Corso et al., 2018; Dal Corso et al., 2020, and references therein), the results also have implications for the interpretation of the mid-Carnian episode, in particular for its timing, duration, and international correlation, as will also be discussed here.

2 GEOLOGICAL SETTING AND STRATIGRAPHIC CONTROL

2.1 Geological Setting

In Triassic times, the CEB was part of the NW peri-Tethys realm, a belt of lowlands bordering the NW Tethys shelf (**Figure 1**). The basin was filled with detritus delivered from surrounding highs, mainly from Fennoscandian sources to the North and Variscan sources to the South, such as the Vindelician High and/or the Bohemian Massif (**Figure 1**; e.g., Wurster, 1968; Stollhofen et al., 2008; Bachmann et al., 2010). The tripartite Germanic Triassic is composed from bottom to top of the terrestrial–marine Buntsandstein Group, the marine Muschelkalk Group and the terrestrial–marine Keuper Group (overviews in DSK (Deutsche Stratigraphische Kommission), 2005; DSK (Deutsche Stratigraphische Kommission), 2013; DSK (Deutsche Stratigraphische Kommission), 2020).

Within the Keuper Group, the shaly–sandy Stuttgart Formation (Schilfsandstein) is of basin-wide occurrence and represents a distinct break in the otherwise shaly–evaporitic Keuper sedimentation (e.g., Wurster, 1964; Schröder, 1977; Beutler in DSK (Deutsche Stratigraphische Kommission), 2005; Kozur and Bachmann, 2010). The Stuttgart Formation also represents the type-example of the mid-Carnian episode (Simms and Ruffell, 1989), a global phase characterized by the enhanced influx of siliciclastic detritus into different depositional settings ranging from terrestrial to deep-marine. Various phenomena are considered to be associated with the mid-Carnian episode, such as pronounced sea-level fluctuations and related oceanographic responses, climate change, faunal turnovers of marine and partly terrestrial groups, and perturbations of the global carbon cycle (see reviews by Arche and López-Gómez, 2014; Ogg, 2015; Ruffell et al., 2015; Dal Corso et al., 2018; Dal Corso et al., 2020 and references therein). The perturbations of the carbon cycle, i.e., sharp negative C-isotope excursions, are considered to have been caused by substantial carbon dioxide exhalations, due to ubiquitous volcanism related to the Wrangellia Large Igneous Province (e.g., Dal Corso et al., 2012; Xu et al., 2014; Dal Corso et al., 2015) and contemporaneous sources like the Taimyr LIP or volcanism in the Tethys realm (Sun et al., 2016; Dal Corso et al., 2018; Lu et al., 2021). Methan release is also discussed as a possible source (Miller et al., 2017).

Due to continuous northwards drift of Pangaea, the latitudinal position of the CEB changed from c. 15°N to c. 30°N between the Early and Late Triassic (Stampfli and Borel, 2004). Contemporaneously, the NW Tethys domain underwent fundamental plate tectonic reorganization, resulting from sea-floor spreading of the Neotethys, subduction and closure of the Palaeotethys, and opening of back-arc basins (e.g., Stampfli and Borel, 2004). These plate tectonic processes were accompanied by widespread volcanic activity, which is well preserved in the Triassic stratigraphic record, e.g., by the omnipresent Anisian to earliest Carnian Pietra verde ash beds in the Tethys realm (**Figure 1**; overviews in Lustrino et al., 2019; De Min et al., 2020), and by the middle to late Carnian tuffs and volcanogenic sandstones reported from the NW Tethys domain, i.e., from the Drau Range, North Karawank Mountains, Transdanubian Mountains, South Alpine, and others (e.g., Brusca et al., 1982; Garzanti, 1985; Cassinis et al., 2008; Kohut et al., 2018; Dunkl et al., 2019). One of the best-known example of late Carnian volcanic activity is the Aglianico ash bed of the Calcari con Selce Formation (Lagonegro Basin), which was deposited at 230.91 ± 0.33 Ma, as indicated by high-precision CA-ID-TIMS dating (Furin et al., 2006). Despite the temporally intense volcanic activity in the NW Tethys domain, ash beds currently have not been found so far in the early to late Triassic strata of the Buntsandstein to Keuper Groups of the CEB.

The Late Triassic climate was controlled by the Tethys and Panthalassa Oceans and the supercontinent Pangaea (**Figure 1**), which stretched from the northern to southern polar region and blocked W-E directed exchange of global sea current systems (e.g., Stampfli and Borell, 2004). The stable palaeogeographical configuration and differential heating between the summer hemisphere of Pangaea and the Tethys are considered to have driven monsoonal circulation systems (e.g., Kutzbach and Gallimore, 1989; Parrish, 1993; Wilson et al., 1994; Preto et al., 2010). The lowlands of the NW peri-Tethys realm, including the CEB, were particularly affected by the summer monsoon, which carried moisture from the NW Tethys to the North where Variscan highs acted as orographic barrier (**Figure 1**; Reinhardt and Ricken, 2000; Kendall et al., 2003; Feist-Burkhardt et al., 2008; Vollmer et al., 2008; McKie, 2017).

2.2 Stratigraphic Control on the Stuttgart Formation

Bachmann et al. (1999) and Beutler in DSK (Deutsche Stratigraphische Kommission) (2005) introduced the formal lithostratigraphic term Stuttgart-Formation for the prominent shaly–sandy interval of the Keuper Group traditionally referred to as Schilfsandstein (Jäger, 1827). The Stuttgart Formation comprises a layer-cake architecture of the fluvio-deltaic Lower and Upper Schilfsandstein Members, which are intercalated with the transgressive brackish-marine Neubrandenburg, Gaildorf and Beaumont Members (**Figure 2**; Franz et al., 2014). The Stuttgart Formation attains an average thickness of 60–70 m in the northern CEB, but increases locally to more than 100 m (Beutler and Häusser, 1982; Franz et al., 2018b). Towards the South, the thickness successively decreases to 15–50 m in Thuringia (e.g., locality Großmonra) and to 3–40 m in the southern parts of the basin (**Figure 2**; Dockter and Schubert

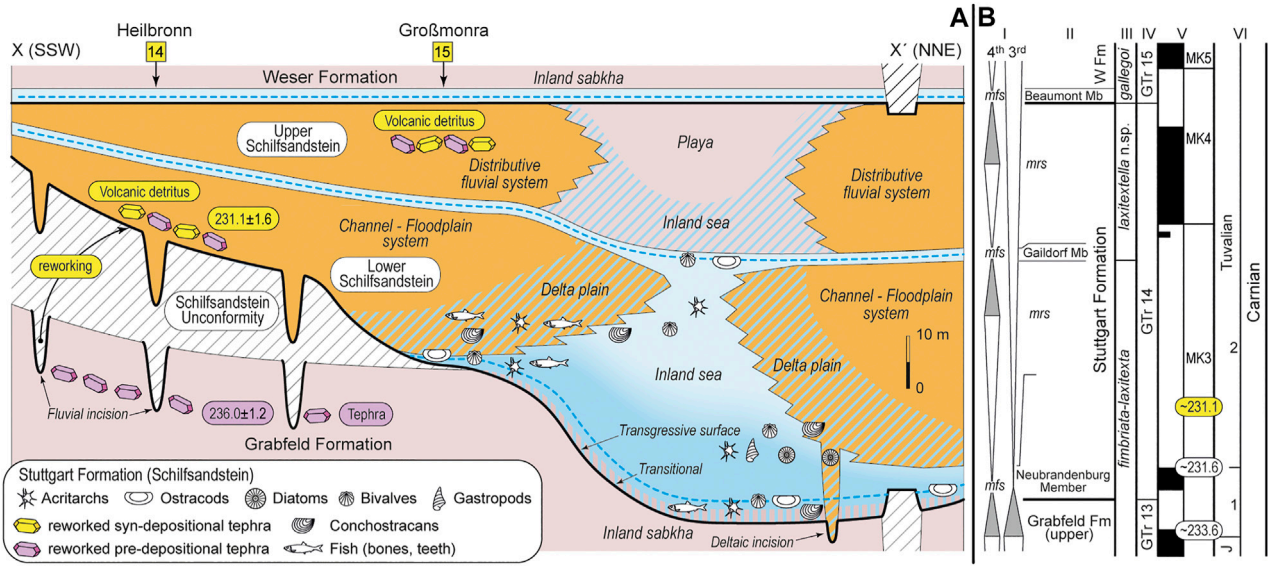

FIGURE 2 | Schematic SSW-NNE cross-section through the Central European Basin summarizing depositional environments **(A)** and stratigraphy **(B)** of the Stuttgart Formation (modified from Franz et al., 2018b). Additionally, the stratigraphic position of tephra is shown deposited at 236.0 ± 1.2 Ma (early Carnian Grabfeld Fm), at 231.1 ± 1.6 Ma (late Carnian Lower Schilfsandstein Member at Heilbronn, this study), and 231 ± 5 Ma **(Upper** Schilfsandstein Member at Großmonra, Hofmann et al., 2018). Due to fluvial incision and reworking of older strata, remnants of pre-depositional tephra were incorporated into fluvial sandstones of the Stuttgart Formation and mixed with syn-depositional tephra. For profile line X–X′ see **Figure 1**. I—third- and fourth-order sequences, II—lithostratigraphy of the Stuttgart Formation (Franz et al., 2014), III—conchostracan biostratigraphy (Kozur and Bachmann, 2010; Geyer and Kelber, 2018), IV—palynostratigraphy (Heunisch, 1999), V—magnetostratigraphy (reinterpreted from Zhang et al., 2020), VI—correlation with Carnian substages, tentatively recalibrated according to the new age presented herein; white boxes—ages substage boundaries (according to Zhang et al., 2020); J-Julian, yellow box: maximum depositional age of the Lower Schilfsandstein Member in SW Germany (this study).

in DSK (Deutsche Stratigraphische Kommission), 2005; Etzold and Schweitzer in DSK (Deutsche Stratigraphische Kommission), 2005). The fluvio-deltaic Lower and Upper Schilfsandstein Members are subject to pronounced lateral facies shifts from sand-prone fluvio-deltaic channels to shaly floodplain, delta plain and inland sea environments (overviews in Wurster, 1964; Kozur and Bachmann, 2010; Franz et al., 2018b). These shaly successions are 3–15 m thick in the southern CEB but up to 70 m thick in the northern CEB and yielded remnants of terrestrial to marine vertebrate and invertebrate faunas (overviews in Etzold and Schweitzer in DSK (Deutsche Stratigraphische Kommission), 2005; Kozur and Bachmann, 2010; Franz et al., 2018b). Apart from authigenic analcime, considered the diagenetic product of volcanic ash (e.g., Hay, 1966; Füchtbauer, 1974; Kühn, 1976), remnants of tephra or ash beds could not be observed, neither in sandstones of the channel facies nor in shales of overbank environments.

Corresponding to the higher thickness in the northern CEB, the change from the shaly–evaporitic Grabfeld Formation to the Stuttgart Formation is transitional and therefore, can be considered continuous (overviews in Franz et al., 2018b; Franz and Barnasch, 2021). In contrast to this, the transitional interval and the transgressive brackish-marine Neubrandenburg Member are missing in the southern CEB resulting in a sharp and discontinuous boundary between the Grabfeld and Stuttgart Formations. The gap associated to this boundary increases when fluvial channels of the Lower Schilfsandstein Member are incised into the upper Grabfeld Formation (**Figure 2**). A particular good example of an incised valley fill (c.f. Aigner and Bachmann, 1992) is exposed at Heilbronn where a fluvial channel cuts about 9 m deep into the upper Grabfeld Formation (Bachmann and Wild, 1976). Comparable erosional gaps associated to the Schilfsandstein Unconformity (Franz et al., 2018b) were described from the northern basin margins and from basin-internal swells (overviews in Beutler, 1995; Franz, 2008; Barnasch, 2010).

As marine index fossils of Tethyan biozones are lacking in the Stuttgart Formation, biostratigraphic control is provided by conchostracans, ostracods and palynomorphs (**Figure 2**; Heunisch, 1999; Kozur and Bachmann, 2010; Kozur and Weems, 2010). The zonations based on conchostracans and palynomorphs are only valid in the CEB (Heunisch, 1999; Kozur and Weems, 2010; Geyer and Kelber, 2018), but the occurrence of the ostracod *Simeonella alpina* enables the tentative correlation with Tethyan strata. As *S. alpina* is restricted to the late Julian *Austrotrachyceras austriacum* Zone of the NW Tethys, Bachmann and Kozur (2004), and Kozur and Bachmann (2010) correlated the Stuttgart Formation with the North Alpine Reingraben Shales/Lunz Formation and contemporaneous Tethyan strata. Since, this preliminary correlation has been accepted and provided the basis for sequence-stratigraphic and magnetostratigraphic correlations of the Stuttgart Formation (Franz et al., 2014; Zhang et al., 2020). Recently, Zhang et al. (2020) proposed a composite

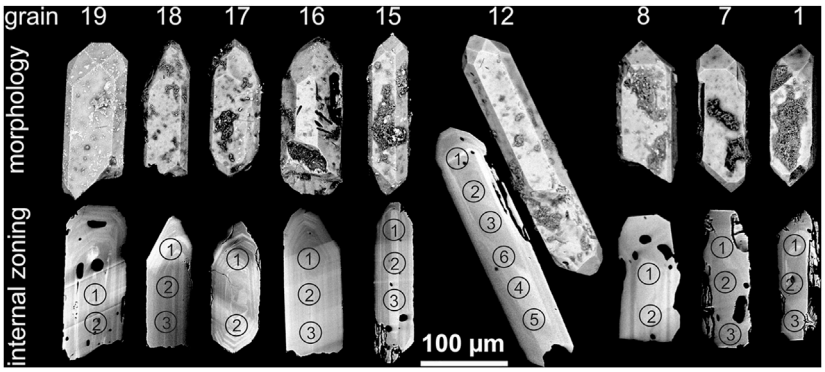

FIGURE 3 | Morphology and internal zoning of dated zircon grains of sandstone sample Heilb-1 from the Jägerhaus quarry near Heilbronn (all back scattered electron images). Circles mark laser spot positions; numbers refer to **Table 1**.

Carnian magnetostratigraphy covering larger parts of the Keuper Group including the Stuttgart Formation. Zhang et al. (2020) correlated the biostratigraphically calibrated magnetic polarity pattern of the Stuttgart Formation with an about 1 myr long interval between c. 234–233 Ma ranging from the Julian 2 to lower Tuvalian 1, which largely corresponds to previous correlations (Kozur and Bachmann 2010; Franz et al., 2014). The short time-span of the Stuttgart Formation is in congruence with estimated durations of about 0.8 Ma according to Kozur and Bachmann (2010) and about 1.2 Ma according to Miller et al. (2017).

3 SAMPLES AND METHODS

3.1 Sample Description

The investigated sample Heilb-1 represents a medium-to fine-grained, brownish, homogeneous sandstone of the Lower Schilfsandstein Member exposed in the Jägerhaus quarry east of Heilbronn in SW Germany (co-ordinates: N 48°08′07.96″, E 9°16′02.70″). The detritus of the sample is immature and consists mostly of angular, poorly rounded fragments of monocrystalline quartz, K-feldspar, plagioclase, white micas and lithic components, thoroughly cemented by interstitial quartz, illite/smectite and Fe-oxides/hydroxides, and contains accessory zircon, apatite and ilmenite. These minerals are confirmed by detailed thin section survey and XRD analyses. Evidence for the existence of authigenic analcime has not been found in our sample, but is described from many other localities in the Central European Basin (see Kühn, 1976; Förster et al., 2010; Franz et al., 2018b; Franz et al., 2019).

3.2 Methods

The sample was crushed with a jaw crusher and disc mill to <500 µm, and the heavy minerals enriched by panning, Frantz magnetic separator, and finally handpicked under ethanol (all at KIT Karlsruhe). The separated zircon grains were mounted on double-sided tape, coated with gold and their morphologies photographed by means of scanning electron microscope (TESCAN VEGA2 SBH with Oxford SwiftED EDX-system). Subsequently, the grains were embedded with epoxy resin in 1-inch plastic rings, ground and polished to expose their center parts, and the internal structures analyzed by back scattered electron imaging (**Figure 3**). During a first session, about 130 zircon grains, independent of their shapes (ranging from round to needle-like euhedral) were analyses for U-Th-Pb isotopes using single laser spots to get information about general age variations. During a second session, up to five additional laser spots were placed on single zircon crystals already measured during the first session, in particular grains of Triassic age. In addition, a new set of 30 euhedral zircon crystals, most of needle-like shape (aspect ratios = 2 to 5; **Table 1**) were measured by up to four spot analyzes. The multiple analyses were done with the aim to gain information about intra-grain age variations related to Pb loss. All U-Th-Pb isotopes were measured by means of a Resonetics M50 193 nm Excimer laser system, coupled to a Thermo-Scientific ELEMENT XR at Goethe University Frankfurt, Germany, using the same methods as described by Gerdes and Zeh (2009) with modifications given in Zeh and Gerdes (2012). During both sessions, data were acquired with 20- and 16-s measurements for background and sample ablation, respectively. Laser spot-size was 26 µm for unknown and primary reference material (zircon GJ1), as well as secondary reference materials (zircon BB and Plesoviče). Ablation was performed in a He stream (0.33 L/min), which was mixed directly after the ablation cell with N_2 and Ar, 0.006 L/min and 0.89 L/min, respectively, prior to introduction into the Ar plasma of the SF–ICP–MS. The signal was tuned for maximum sensitivity for Pb and U while keeping oxide production, monitored as $^{254}(UO)/^{238}U$, below 0.3%. The sensitivity achieved was in the range of 9,900 cps $(\mu g/g)^{-1}$ for ^{238}U with a 26-µm spot size, at 5.5 Hz and about 2.8 J/cm^2 laser energy. The typical penetration depth was about 15 µm. Detailed instrument and processing parameters are presented in **Supplementary Table S1**.

Raw data were corrected offline for background signal, common Pb, laser-induced elemental fractionation, instrumental mass discrimination, and time-dependent elemental fractionation of Pb/U using an in-house MS Excel© spreadsheet program (Gerdes and Zeh, 2006; Gerdes and Zeh, 2009). A common-Pb correction was carried out based on the interference- and

TABLE 1 | Results of U-Pb zircon dating and zircon size measurements.

Grain/ analysis	$^{207}Pb^{a}$ (cps)	U^{b} (ppm)	Pb^{b} (ppm)	Th^{b}/U	$^{206}Pbc^{c}$ (%)	$^{206}Pb^{d}/^{238}U$	± 2σ (%)	$^{207}Pb^{d}/^{235}U$	± 2σ (%)	$^{207}Pb^{d}/^{206}Pb$	± 2σ (%)	rho[e]	$^{206}Pb/^{238}U$	± 2σ (Ma)	$^{207}Pb/^{235}U$	± 2σ (Ma)	$^{207}Pb/^{206}Pb$	± 2σ (Ma)	Conc.[f] (%)	Length µm	Width µm	Aspect ratio
1-a22-s1	45,298	568	25	0.92	b.d.	0.03954	1.3	0.2784	1.5	0.05106	0.6	0.91	250	3	249	3	244	14	103	123	60	2.1
1-a11-s1	22,440	258	13	1.66	b.d.	0.03949	1.5	0.2925	6.2	0.05373	6.0	0.24	250	4	261	14	360	136	69			
1-a324	10,941	236	11	1.00	0.81	0.03918	2.9	0.2775	16.2	0.05137	16	0.18	248	7	249	36	258	366	96			
2-a289	17,915	284	13	0.86	1.56	0.03906	2.9	0.2724	9.9	0.05057	9.5	0.29	247	7	245	22	221	220	112	189	55	3.5
2-a288	14,034	320	14	0.92	0.23	0.03723	2.5	0.2625	2.8	0.05114	1.2	0.90	236	6	237	6	247	28	95			
2-a282	12,753	306	13	0.81	b.d.	0.03709	2.5	0.2607	2.6	0.05097	0.9	0.94	235	6	235	6	240	21	98			
3-a06-s1	15,579	168	8	1.12	0.63	0.03880	1.5	0.3	3.1	0.05607	2.7	0.50	245	4	266	7	455	60	54	188[g]	62	3.1
4-a304	21,363	510	22	0.78	b.d.	0.03829	2.4	0.2692	2.6	0.05099	0.9	0.94	242	6	242	6	240	20	101	154[g]	60	2.6
4-a305	25,027	576	23	0.49	0.11	0.03735	2.5	0.2665	2.8	0.05176	1.2	0.91	236	6	240	6	275	27	86			
4-a303	32,173	782	33	1.09	b.d.	0.03628	2.4	0.257	2.5	0.05139	0.7	0.96	230	6	232	5	258	16	89			
5-a299	11,413	263	12	1.15	0.18	0.03802	2.5	0.2673	2.9	0.05099	1.3	0.89	241	6	241	6	240	30	100	197	75	2.6
5-a301	8,532	193	8	0.81	0.19	0.03697	2.5	0.2658	3.1	0.05216	1.8	0.80	234	6	239	7	292	42	80			
5-a300	9,174	224	10	1.07	0.16	0.03666	2.6	0.2541	2.8	0.05028	1.1	0.92	232	6	230	6	208	26	112			
6-a41-s1	18,761	220	10	1.30	0.10	0.03786	1.8	0.2723	2.0	0.05216	0.9	0.90	240	4	245	4	293	20	82	133[g]	53	2.5
7-a41	19,799	399	17	0.88	0.77	0.03799	1.4	0.2662	5.8	0.05081	5.7	0.24	240	3	240	13	232	131	104	168	51	3.3
7-a42	19,114	378	16	0.68	1.38	0.03795	1.6	0.256	7.1	0.04891	6.9	0.23	240	4	231	15	144	161	167			
7-a40	19,709	410	17	0.80	b.d.	0.03734	1.2	0.2651	1.4	0.05148	0.7	0.85	236	3	239	3	263	17	90			
8-a318	12,939	312	13	0.58	b.d.	0.03774	2.4	0.2657	2.6	0.05107	0.9	0.94	239	6	239	6	244	21	98	211[g]	67	3.2
8-a317	5,847	141	6	0.63	0.07	0.03748	2.5	0.2637	3.0	0.05103	1.8	0.81	237	6	238	6	242	40	98			
9-a27	19,634	355	15	0.86	0.48	0.03771	1.3	0.2639	5.5	0.05075	5.3	0.24	239	3	238	12	230	123	104	211	68	3.1
9-a26	25,725	525	22	0.91	0.55	0.03748	1.2	0.2585	5.3	0.05003	5.2	0.23	237	3	233	11	197	120	121			
9-a64-s1	20,935	374	15	0.57	1.99	0.03742	1.6	0.2605	5.9	0.05048	5.7	0.27	237	4	235	12	217	131	109			
9-a28	39,309	493	20	0.72	0.13	0.03653	1.4	0.2584	1.7	0.05129	0.8	0.86	231	3	233	4	254	20	91			
10-a89-s1	54,254	688	28	0.62	b.d.	0.03768	1.5	0.268	1.7	0.05159	0.8	0.88	238	4	241	4	267	19	89	134[g]	67	2.0
10-a24	35,482	749	29	0.64	1.10	0.03659	1.2	0.241	5.2	0.04777	5	0.23	232	3	219	10	88	119	263			
11-a101-s1	7,724	96	4	0.57	2.26	0.03759	2.6	0.2641	4.9	0.05095	4.2	0.53	238	6	238	11	239	97	100	122[g]	68	1.8
12-a16	10,178	205	9	0.92	0.01	0.03765	1.3	0.2645	1.7	0.05096	1	0.80	238	3	238	4	239	23	100	368	71	5.2
12-a19	7,747	161	7	0.86	0.01	0.03740	1.5	0.2628	2.0	0.05096	1.4	0.75	237	4	237	4	239	31	99			
12-a18	8,651	187	8	0.85	0.01	0.03718	1.2	0.2607	1.6	0.05084	1.1	0.75	235	3	235	3	234	25	101			
12-a17	9,695	207	9	0.88	0.07	0.03701	1.2	0.2585	1.7	0.05065	1.2	0.71	234	3	233	4	225	28	104			
12-a15	18,128	363	15	1.05	2.61	0.03659	1.4	0.2467	8.8	0.04889	8.7	0.15	232	3	224	18	143	205	162			
12-a127-s1	12,949	142	6	0.86	b.d.	0.03545	2.4	0.2474	2.8	0.05062	1.4	0.86	225	5	224	6	223	33	101			
13-a57	9,254	195	8	0.82	2.11	0.03767	2.0	0.2604	11.5	0.05014	11	0.17	238	5	235	24	202	264	118	145[g]	72	2.0
13-a56	11,252	176	7	0.76	4.06	0.03745	2.2	0.2623	13.2	0.05081	13	0.17	237	5	237	28	232	301	102			
13-a55	17,220	302	13	0.82	1.58	0.03718	1.7	0.2614	8.9	0.05099	8.8	0.19	235	4	236	19	240	202	98			
14-a94-s1	31,878	374	16	0.87	0.50	0.03747	1.5	0.2664	2.0	0.05156	1.4	0.74	237	3	240	4	266	31	89	156[g]	61	2.6
15-a322	10,142	220	9	0.97	1.13	0.03730	2.8	0.2623	15.1	0.05101	15	0.18	236	6	237	32	241	343	98	206	54	3.9
15-a321	18,589	327	15	1.09	1.80	0.03707	2.5	0.2931	3.8	0.05735	2.9	0.65	235	6	261	9	505	63	46			
15-a320	18,223	458	20	1.18	b.d.	0.03625	2.4	0.2559	2.5	0.0512	0.7	0.96	230	5	231	5	250	16	92			
16-a310	9,218	227	10	1.39	0.01	0.03675	2.5	0.2575	2.6	0.05083	1	0.93	233	6	233	6	233	23	100	220[g]	89	2.5
16-a311	10,120	256	11	1.19	0.05	0.03660	2.4	0.2562	2.7	0.05076	1.2	0.89	232	6	232	6	230	28	101			
16-a312	14,869	357	15	1.07	0.02	0.03672	2.4	0.2599	2.6	0.05133	0.9	0.94	232	6	235	5	255	20	91			
17-a342	26,801	678	26	0.58	b.d.	0.03662	2.4	0.2563	2.5	0.05076	0.7	0.96	232	6	232	5	230	15	101	189	69	2.7
17-a343	16,847	405	15	0.43	0.09	0.03614	2.5	0.2556	2.6	0.05128	1	0.93	229	6	231	5	253	22	90			
18-a295	39,309	493	20	0.72	0.13	0.03653	1.4	0.2584	1.7	0.05129	0.8	0.86	231	3	233	4	254	20	91	180[g]	59	3.0
18-a296	7,868	197	9	1.35	b.d.	0.03643	2.5	0.2558	2.7	0.05092	1.1	0.92	231	6	231	6	237	24	97			
18-a297	7,977	175	8	1.29	0.09	0.03642	2.5	0.2553	3.0	0.05084	1.5	0.85	231	6	231	6	233	36	99			

(Continued on following page)

TABLE 1 | (*Continued*) Results of U-Pb zircon dating and zircon size measurements.

Grain/ analysis	^{207}pb[a] (cps)	U[b] (ppm)	pb[b] (ppm)	Th[b] U	^{206}pbc[c] (%)	^{206}pb[d] ^{238}U	± 2σ (%)	^{207}pb[d] ^{235}U	± 2σ (%)	^{207}pb[d] ^{206}pb	± 2σ (%)	rho[e]	^{206}pb ^{238}U	± 2σ (Ma)	^{207}pb ^{235}U	± 2σ (Ma)	^{207}pb ^{206}pb	± 2σ (Ma)	Conc.[f] (%)	Length µm	Width µm	Aspect ratio
19-a341	11,699	292	12	0.74	0.07	0.03644	2.5	0.2553	2.7	0.05081	1.1	0.91	231	6	231	6	232	26	99	221[g]	86	2.6
19-a340	11,565	286	12	0.91	0.02	0.03632	2.4	0.2541	2.6	0.05074	0.9	0.94	230	6	230	5	229	21	100			

^{206}Pb/^{238}U error is the quadratic additions of the within run precision (2 SE) and the external reproducibility (2 SD) of the reference zircon. ^{207}Pb/^{206}Pb error propagation.

(^{207}Pb signal dependent) following Gerdes and Zeh (2009). ^{207}Pb/^{235}U error is the quadratic addition of the ^{207}Pb/^{206}Pb and ^{206}Pb/^{238}U uncertainty.

[a]*Within run background-corrected mean ^{207}Pb signal in cps (counts per second).*

[b]*U and Pb content and Th/U ratio were calculated relative to GJ-1 reference zircon.*

[c]*Percentage of the common Pb on the ^{206}Pb. b.d. = below detection limit.*

[d]*Corrected for background, within-run Pb/U fractionation (in case of ^{206}Pb/^{238}U) and common Pb using Stacy and Kramers (1975) model Pb composition and subsequently normalised to GJ-1 (ID-TIMS value/measured value); ^{207}Pb/^{235}U calculated using ^{207}Pb/^{206}Pb/(^{238}U/^{206}Pb*1/137.88).*

[e]*rho is the ^{206}Pb/^{238}U/^{207}Pb/^{235}U error correlation coefficient.*

[f]*Degree of concordance = ^{206}Pb/^{238}U age/^{207}Pb/^{206}Pb age x 100.*

[g]*s1-session 1 (otherwise session 2).*

[g]*Fragmented grain (minimum length).*

background-corrected ^{204}Pb signal and a model Pb composition (Stacey and Kramers, 1975). Calculated common ^{206}Pb contents in samples is mostly <0.2% of the total ^{206}Pb, but in rare cases exceeded 1.5% (**Table 1**). Laser-induced elemental fractionation and instrumental mass discrimination were corrected by normalization to the reference zircon GJ-1 (Jackson et al., 2004), as well as inter-elemental fractionation (^{206}Pb*/^{238}U) during sample ablation. Corrected drift during the analytical sessions was between 2 and 6%. Reported uncertainties (2σ) of the ratio were propagated by quadratic addition of the external reproducibility (2 S.D., standard deviation), obtained from the reference zircon GJ-1 and the within-run precision of each analysis (2 S.E., standard error). For the ratio ^{207}Pb/^{206}Pb, we used a^{207}Pb-signal-dependent uncertainty propagation (Gerdes and Zeh, 2009). The ratio ^{207}Pb/^{235}U is derived from the normalized and error-propagated ratios ^{207}Pb/^{206}Pb* and ^{206}Pb*/^{238}U, assuming a natural abundance ratio of ^{238}U/^{235}U = 137.818 (Hiess et al., 2012) and the uncertainty derived by quadratic addition of the propagated uncertainties of both ratios.

Accuracy was verified by multiple analyses of two secondary reference materials, which yielded Concordia ages for the Plesoviče zircon of 337.9 ± 1.1 Ma (session 1: $MSWD_{C.+E.}$ = 0.97, $Probability_{C.+E.}$ = 0.52, n = 26; C. + E. – concordance and equivalence) and 337.8 ± 2.3 Ma (session 2: $MSWD_{C.+E.}$ = 0.76, $Probability_{C.+E.}$ = 0.75, n = 10), and for BB zircon of 563.5 ± 2.5 Ma (session 1: $MSWD_{C.+E.}$ = 0.89, $Probability_{C.+E.}$ = 0.60, n = 10), and 561.1 ± 1.2 Ma (session 2: $MSWD_{C.+E.}$ = 1.08, $Probability_{C.+E.}$ = 0.29, n = 38), in agreement with the quoted LA–ICP–MS value of 562 ± 9 Ma for the BB zircon (^{206}Pb/^{238}U; Santos et al., 2017), and with the quoted TIMS value of 337.13 ± 0.37 Ma for the Plesoviče zircon (Sláma et al., 2008). Data were plotted using the software ISOPLOT (Ludwig, 2001). Results of U-Th-Pb isotope measurements are presented in **Table 1**, and of the reference zircons in **Supplementary Table S2**.

4 RESULTS

During this study about 160 zircon grains, comprising 50 grains of euhedral habitus were analyzed for U-Th-Pb isotope compositions. Nineteen of these grains yielded Triassic ages. These are the ones that will be discussed further in this study. The shapes of the Triassic zircon grains vary from short-prismatic stubby to needle-like, with lengths ranging from c. 125–370 µm, and aspect ratios from 1.8 to 5.2, although some elongated grains represent broken fragments (**Figure 3**; **Table 1**). Most grains show oscillatory or banded internal zoning (**Figure 3**), and Th/U ratios between 0.43 and 1.66 (**Table 1**), both features typical for zircon crystals formed in magmatic environments. The ^{206}Pb/^{238}U ages obtained by single-spot analyses from the Triassic zircon grains range from 250 ± 3 Ma to 230 ± 6 Ma (**Table 1**). Multiple analyses carried out on individual zircon crystals, i.e., 2–6 analyses per grain, gave in most cases identical dates, within error, allowing calculation of weighted average ^{206}Pb/^{238}U ages (**Figure 4**). Significant differences between the oldest and youngest ^{206}Pb/^{238}U age values were only observed in a few grains (e.g., grains 10, 12). For these crystals, the youngest ages were

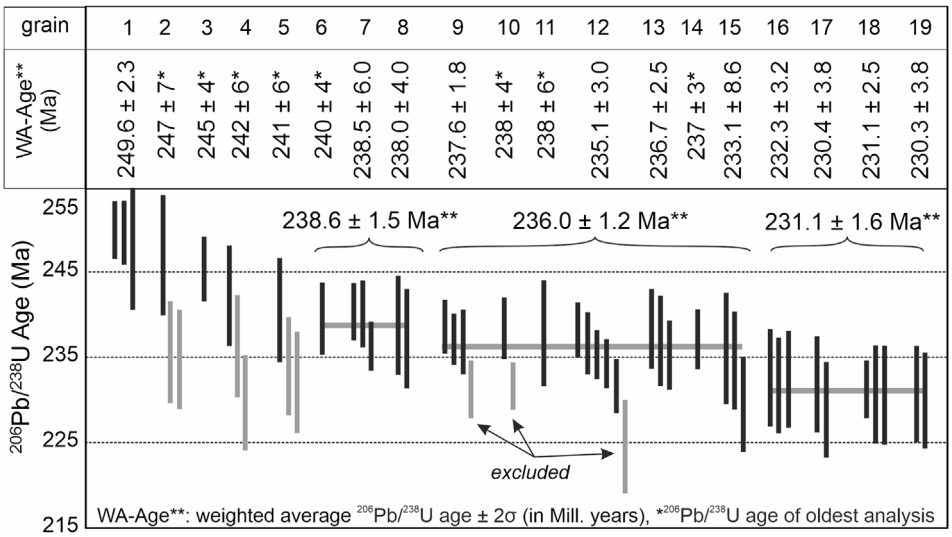

FIGURE 4 | Results of U-Pb dating of the nineteen youngest detrital zircon grains of euhedral shape separated from the sandstone sample Heilb-1. Weighted average ages were calculated from multiple analyses of individual zircon grains (*), or from analyses of several grains (**). Excluded analyses (grey bars) are assumed to represent outliers due to significant Pb loss.

considered to have been reset by Pb loss and excluded from weighted average $^{206}Pb/^{238}U$ age calculations.

Analyses of the four youngest zircon crystals (grains 16–19) yield weighted average $^{206}Pb/^{238}U$ ages of 230.3 ± 3.8 Ma (grain 19; $n = 2$), 230.4 ± 3.8 Ma (grain 17; $n = 2$), 231.1 ± 2.5 Ma (grain 18; $n = 3$), and 232.3 ± 3.2 Ma (grain 16; $n = 3$). All ten analyses together reveal a weighted average $^{206}Pb/^{238}U$ age of 231.1 ± 1.6 Ma (**Figure 4**), identical to a Concordia age of 231.5 ± 1.6 Ma ($MSWD_{C.+E.}$ = 0.85, $Probability_{C.+E.}$ = 0.65; C. + E. − concordance and equivalence; **Figure 5A**). This age is significantly younger than that calculated for the seven next older zircon grains (9–15). These give a weighted average $^{206}Pb/^{238}U$ age of 236.0 ± 1.2 Ma ($n = 17$), identical to a Concordia age of 236.6 ± 0.9 Ma ($MSWD_{C.+E.}$ = 1.4, $Probability_{C.+E.}$ = 0.16, $n = 15$) (**Figure 5B**). Individual weighted average $^{206}Pb/^{238}U$ ages obtained from the grains 9 to 15 range from 233.1 ± 8.6 Ma to 237.6 ± 1.8 Ma (**Figure 4**). The $^{206}Pb/^{238}U$ ages of the three zircon grains (6–8) range from 238.0 ± 4.0 Ma (grain 8, n = 2) to 240 ± 4 Ma (grain 6, $n = 1$), with all six analyses yielding a weighted average $^{206}Pb/^{238}U$ age of 238.6 ± 1.5 Ma ($n = 6$), identical to a Concordia age of 238.4 ± 1.9 Ma ($MSWD_{C.+E.}$ = 1.7, $Probability_{C.+E.}$ = 0.11, $n = 4$) (**Figure 5C**). The five oldest grains (1–5) show $^{206}Pb/^{238}U$ ages between 241 ± 6 (grain 5, $n = 1$) and 249.6 ± 2.3 Ma (grain 1, $n = 3$). Most of these grains are disturbed, as indicated by significant variations of their $^{206}Pb/^{238}U$ ages, preventing calculation of single grain weighted average $^{206}Pb/^{238}U$ ages (**Figure 4**).

5 DISCUSSION

5.1 Triassic Zircon Grains in the Schilfsandstein

The weighted mean $^{206}Pb/^{238}U$ ages obtained during this study by multiple dating of nineteen zircon crystals range between 249.6 ± 2.3 Ma and 230.3 ± 3.8 Ma, and provide the first hard evidence for the occurrence of Triassic zircon grains within the Stuttgart Formation. These ages in combination with the euhedral habitus of the analyzed zircon crystals suggest a volcanogenic origin. According to the Carnian depositional age of the Stuttgart Formation, these zircon grains are herein considered traces of pre- and syn-depositional tephra fall out related to Olenekian to late Carnian volcanic activity within the NW Tethys domain. This interpretation is in good agreement with the prevailing North-directed wind regime of the northern summer monsoon proposed by Parrish (1999) for central Europe during the Triassic (**Figure 1**), and with U-Pb ages between 242.01 ± 0.05 and 221.2 ± 1.6 Ma estimated for volcanic events in the NW Tethys domain (see **Figures 1**, **6**). We note that the three weighted average $^{206}Pb/^{238}U$ ages of 238.6 ± 1.5 Ma, 236.0 ± 1.2 Ma, and 231.1 ± 1.6 Ma obtained during this study (**Figure 4**) overlap with the majority of zircon ages estimated for igneous rocks, tuffs and volcanogenic sandstones of the Transdanubian Range, southern Alps, N-Karawank Mountains, Drau Range, W Carpathians and Lagonegro Basin (for compilation and references see **Figure 6**). However, they are significantly older than U-Pb ages of 211 ± 3 Ma and 222 ± 2 Ma (concordance level 90–110%), recently dated by SHRIMP on zircon grains of the Lisowice bone-bearing horizon at Lipie Śląskie (Silesia, Poland) by Kowal-Linka et al. (2019). These young ages are interpreted to date tephra fall out around the Carnian/Norian boundary interval, which was probably related to volcanic sources in the West Carpathians (**Figure 6**), much younger than the Carnian volcanism being the source for the Schilfsandstein detrital zircons. Two older ages at 230 ± 2 Ma and 237 ± 3 Ma, also reported by Kowal-Linka et al. (2019), provide evidence for the additional contribution of volcanic detritus related to late Ladinian to late Carnian volcanism. These two dates overlap those produced in this

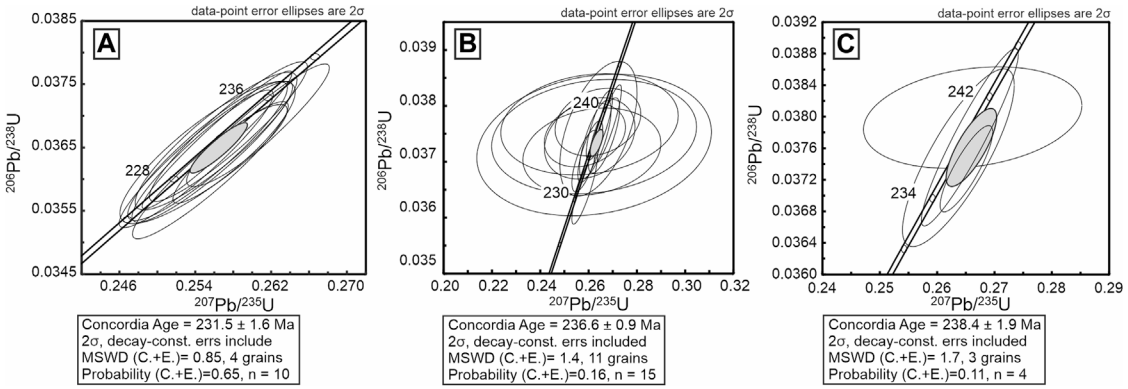

FIGURE 5 | Concordia diagrams showing the results of 29 analyses of the nineteen youngest zircon grains of sample Heilb-1 pooled in three clusters based on $^{206}Pb/^{238}U$ ages. **(A)** results of multiple analyses of the four youngest zircon crystals (grains 16–19), **(B)** of the seven second oldest zircon grains (9–15), and **(C)** of the three oldest grains (6–8). MSWD, Mean squared weighted deviation, C.+E., concordance and equivalence.

study, and provide evidence that wide parts of the CEB were affected by Ladinian-Carnian tephra fall out, and that older volcanic detritus was re-deposited during late Carnian/early Norian sedimentation leading to formation of the Lisowice bone-bearing horizon. Evidence for tephra fall out during deposition of the Stuttgart Formation is, apart from the late Carnian age of 231.1 ± 1.6 Ma obtained from euhedral zircon grains, additionally provided by the occurrence of authigenic analcime, commonly considered to represent a diagenetic product of volcanic ashes (Hay, 1966; Füchtbauer, 1974; Kühn, 1976). Authigenic analcime cement occurs ubiquitously in sandstones of the Stuttgart Formation in North Germany as shown by Kühn (1976) and Förster et al. (2010), and more recently by Franz et al. (2018b) and Franz et al. (2019). However, it seems to be absent in South Germany (see Heling, 1965), as confirmed by the herein investigated sample from Heilbronn, in which analcime could not be found, neither by thin section survey nor XRD analyses. The reasons and consequences of this are discussed in **Section 5.2**.

The findings of Triassic zircon grains with ages between 249.6 ± 2.3 Ma and 230.3 ± 3.8 Ma provide evidence that the Stuttgart Formation contains traces of reworked tephra deposits of Olenekian to early Carnian age. We note that Hofmann et al. (2018) reported ten zircon crystals from Großmonra (Thuringia) showing $^{206}Pb/^{238}U$ ages between 250 ± 7 and 234 ± 7 Ma ($n = 10$) and two zircon crystals from Bodenmühle (Franconia) with $^{206}Pb/^{238}U$ ages between 248 ± 7 and 247 ± 7 Ma ($n = 2$), similar to the age spectrum reported herein (**Figure 4**). All these Triassic zircon grains were most probably incorporated into the Stuttgart Formation due to erosion of older Triassic strata in the southern CEB and at its margins.

Zircon grains which gave weighted average $^{206}Pb/^{238}U$ ages of 236.0 ± 1.2 Ma and 238.6 ± 1.5 Ma suggest the presence of tephra deposits in the Grabfeld and Erfurt Formations of the Keuper Group (**Figures 2**, **6**). As the Upper Grabfeld Formation is biostratigraphically constrained to the early Carnian (for details see Bachmann and Kozur, 2004), the erosion of early Carnian tephra with an age of 236.0 ± 1.2 Ma could be explained by fluvial incision of the Stuttgart Formation into the Upper Grabfeld Formation, which is well documented in South Germany (overview in Etzold and Schweizer in DSK (Deutsche Stratigraphische Kommission), 2005). But, as the fluvial incision of Schilfsandstein rivers in South Germany is limited to a few decametres (Etzold and Schweizer in DSK (Deutsche Stratigraphische Kommission), 2005), the erosion of late Ladinian tephra with an age of 238.6 ± 1.5 Ma must have been located at the southern margins of the CEB. The same interpretation can be applied to Triassic zircon grains of Olenekian to Anisian tephra. The fact that tephra deposits are unknown in Triassic strata of the CEB may be attributed to (fluvial) reworking after deposition, intense pedogenesis and modification due to diagenetic processes (see **Section 5.2**).

5.2 Maximum Depositional Age of the Stuttgart Formation

The four youngest zircon grains dated during this study yielded a weighted average $^{206}Pb/^{238}U$ age of 231.1 ± 1.6 Ma. These euhedral zircons are herein considered remnants of tephra, which was deposited in the active fluvial system of the Lower Schilfsandstein Member. After fall out in active channels, the tephra was mixed with detrital grains, dispersed downstream and stable tephra grains, such as zircon, became finally deposited within fluvial sands. At overbank environments, such as backswamps, wetlands and floodplains, distinct ash beds may have formed, but were disintegrated during the next flood stage or became finally preserved. The weighted average $^{206}Pb/^{238}U$ age of 231.1 ± 1.6 Ma is identical, within error, with the two youngest zircon grains with $^{206}Pb/^{238}U$ ages of 231 ± 5 Ma and 232 ± 6 Ma (concordance level 97–99%), reported by Hofmann et al. (2018) from a sample of the Upper Schilfsandstein Member at Großmonra. This outcrop is located in Thuringia ca. 250 km northeast of Heilbronn (**Figure 1**). Even though not interpreted in detail by Hofmann et al. (2018), and unconfirmed by multiple zircon spot analyses, the presence of these zircon grains in Thuringia points to a wider distribution of syn-depositional

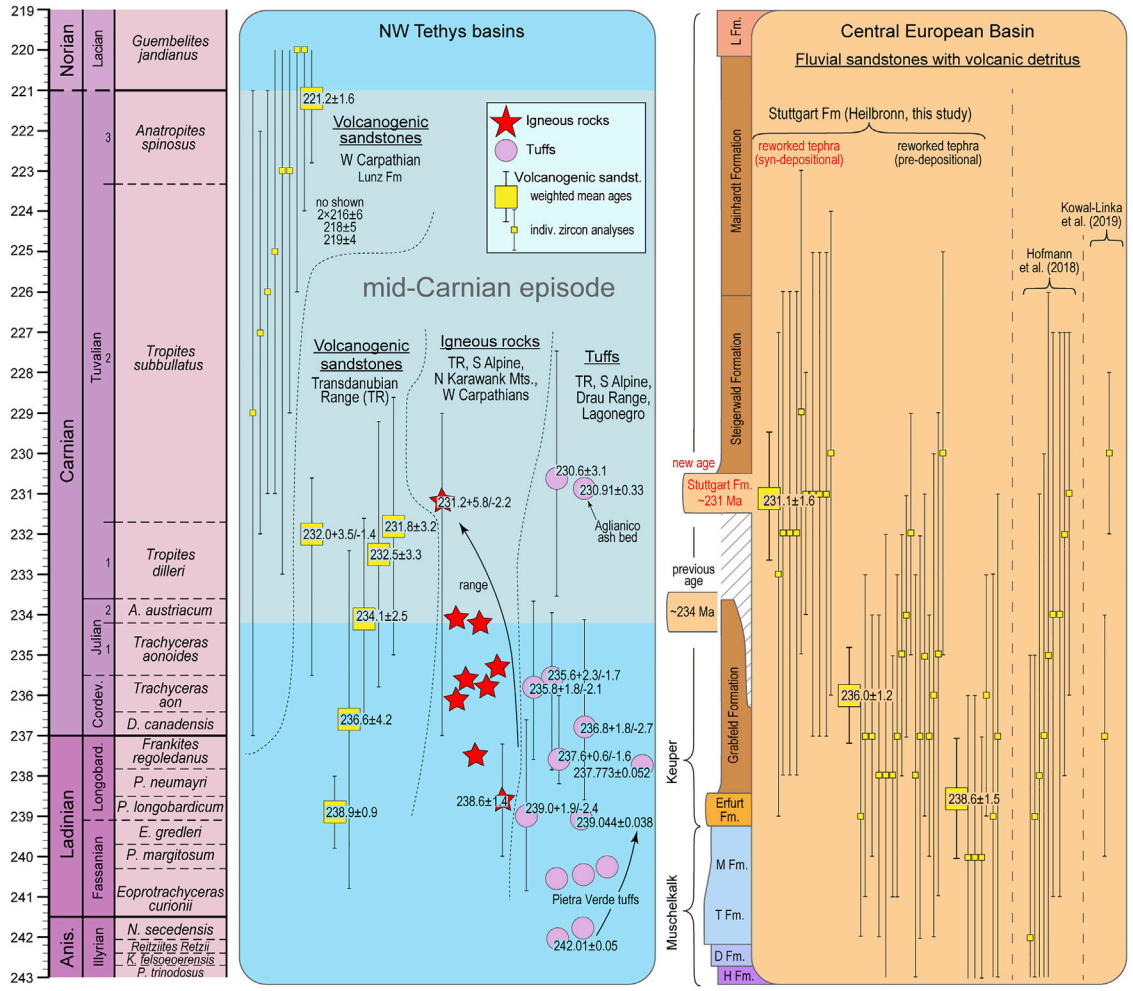

FIGURE 6 | Compilation of zircon U-Pb ages of igneous rocks, tuffs and volcanogenic sandstones of NW Tethys basins (published dates) compared with volcanic detritus found in fluvial sandstones of the Stuttgart Formation (this study; Hofmann et al., 2018) and the Upper Keuper (Kowal-Linka et al., 2019). Chronostratigraphy according to Zhang et al. (2020), base Norian at 221.0 Ma adopted from Kohut et al. (2018). Published dates were compiled from Furin et al. (2006), Mietto et al. (2012), Wotzlaw et al. (2018), Kohut et al. (2018), and Dunkl et al., 2019. The data presented herein suggest that detrital zircon grains in the Lower Schilfsandstein Member in SW Germany result from syn- and pre-depositional tephra fall out. Syn-depositional fall out occurred at 231.1 ± 1.6 Ma coeval to ash beds reported from the Lagonegro Basin (Furin et al., 2006) and the Transdanubian Range (Dunkl et al., 2019), and pre-depositional fall out mainly at 238.6 ± 1.5 Ma and 236.0 ± 1.2 Ma coeval to widespread Ladinian–early Carnian igneous activity in the NW Tethys. The occurrence of pre-depositional tephra within the Stuttgart Formation is explained by reworking of older ash beds, due to erosion of older strata and fluvial incision. Note, the stratigraphic column for the Central European Basin (right) shows the subdivision of the Upper Muschelkalk to Middle Keuper in the Heilbronn area located in the southern part of CEB, where the contact of the Stuttgart Formation to the underlying Grabfeld Formation is discontinuous (see **Figure 2**): H Fm., Heilbronn-Formation; D Fm., Diemel Formation; T Fm., Trochitenkalk Formation; M Fm., Meissner Formation; L Fm., Löwenstein Formation. Further shown is the previously suggested age for the Stuttgart Formation, based on bio-magneto-sequence stratigraphic record (Zhang et al., 2020).

tephra in the Stuttgart Formation. Considering this and the short time-span of 0.8–1.2 Ma estimated for the Stuttgart Formation (Kozur and Bachmann, 2010; Miller et al., 2017), the weighted average $^{206}Pb/^{238}U$ age of 231.1 ± 1.6 Ma is taken as the best current estimate for the maximum depositional age (e.g., Rainbird et al., 2001; Brown and Gehrels, 2007) of the Stuttgart Formation in South Germany.

Syn-depositional tephra fall out is supported by the occurrence of authigenic analcime cement in the Stuttgart Formation, representing the diagenetic product of volcanic ash (Kühn, 1976; Förster et al., 2010; Franz et al., 2018b; Franz et al. (2019)). But the ubiquitous presence of analcime in the northern CEB, it's absence in the southern CEB, and the fact that ash beds have not been observed in the Stuttgart Formation needs to be explained. As the diagenetic stability of detrital minerals is mainly a function of pore-water chemistry, depositional environments directly impact diagenetic pathways of volcanic detritus in sediments (Hay, 1966; Hurst and Irwin, 1982; Burley et al., 1985). As shown by Hay (1966), the presence of moderate saline depositional water leads to authigenesis of analcime during diagenetic alteration of volcanic ash, whereas interaction with meteoric (freshwater) depositional water leads to

authigenesis of montmorillonite. This is in congruence with the palaeogeographic situation and authigenic mineralogy of the Stuttgart Formation. The present-day occurrence of authigenic analcime in the northern CEB corresponds to the extension of the marine-brackish inland sea (Kühn, 1976; Förster et al., 2010; Franz et al., 2018b) and its absence in the southern CEB (Heling, 1965; Kühn, 1976; Nürnberger, 2010) corresponds to the presence of fluvial environments in this part of the basin (**Figure 2**). However, montmorillonite was only reported from a single locality at the southern margin of the CEB, where it occurs at a very low abundance (Salger, 1982). The apparent absence is most probably related to illitization of montmorillonite, a common mesodiagenetic dehydration reaction associated to burial temperatures between 50 and 135°C (e.g., Patrick Muffler and White, 1969; De Segonzac, 1970; Perry and Hower, 1970; Dypvik, 1983). This is in general agreement with the dominance of illite in clay mineral assemblages of the Stuttgart Formation in the southern CEB (Heling, 1965; Dockter and Kühn, 1974; Häusser and Kurze, 1975; Salger, 1982) and maximum burial temperatures of up to 100°C estimated for the Keuper Group in Thuringia (Voigt et al., 2010; Beyer, 2015).

Intense burial diagenesis at depths of >2,000 m, in particular in the northern CEB, and related maximum burial temperatures of >100°C (e.g., Neunzert et al., 1996; Hoth, 1997; Thomson and Zeh, 2000; Friberg, 2001; Rodon and Littke, 2005), may explain why ash beds were not observed within fine-grained successions of the Stuttgart Formation so far. As described from Mesozoic strata elsewhere in the CEB, fine-grained ash underwent argillization during early diagenesis before cementation could preserve typical textures (Jeans et al., 2000). Further modifications during burial diagenesis, i.e., the alteration of volcanic glass and transitions of clay minerals (e.g., Segonzac, 1970; Cuadros et al., 2013; Gong et al., 2018), contribute to the obliteration of volcanic minerals and overprint of typical textures.

5.3 Correlation and Timing of the Mid-Carnian Episode

The new weighted average $^{206}Pb/^{238}U$ age of 231.1 ± 1.6 Ma constrains the Stuttgart Formation to the Tuvalian two substage of the Carnian (**Figure 6**). Accepting this new age as maximum depositional age, the Stuttgart Formation is c. 3 myr younger compared to the age of about 234 Ma as proposed by Zhang et al. (2020). Noteworthy, the depositional age of Zhang et al. (2020), obtained from the correlation with the Global Polarity Time Scale, relies on a rather preliminary biostratigraphic correlation of the Stuttgart Formation with Tethyan strata (see **Section 2.2**).

We note that the new maximum depositional age of the Stuttgart Formation overlaps, within error, with the high-precision $^{206}Pb/^{238}U$ TIMS age of 230.91 ± 0.33 Ma reported by Furin et al. (2006) for the Aglianico ash bed (Lagonegro Basin, southern Italy), which is biostratigraphically constrained to the Tuvalian two substage. It further overlaps with Concordia ages of 232.5 ± 3.3 and 230.6 ± 3.1 Ma reported by Dunkl et al. (2019) from pebbles of reworked tuffs and volcanogenic sandstones of the Transdanubian Range in Hungary (**Figure 6**). Whether these records are related to a phase of volcanic activity or if they can be attributed to a single volcanic event has to be verified by further investigations, including the application of high precision dating techniques.

Since the Schilfsandstein (Stuttgart Formation) represents the type-example of the mid-Carnian episode (Simms and Ruffell, 1989), the new maximum depositional age has significant impact on the timing of the mid-Carnian episode. The correlation of the Stuttgart Formation with the Aglianico ash bed, biostratigraphically dated as Tuvalian 2 (Furin et al., 2006), and contemporaneous strata of NW Tethyan basins, contradicts a synchronous onset of the mid-Carnian episode in the late Julian at around 234 Ma as reconstructed previously (e.g., Simms and Ruffell, 1989; Hornung et al., 2007a,; Hornung et al., 2007b; Roghi et al., 2010; Franz et al., 2014; Dal Corso et al., 2015, Dal Corso et al., 2020; Jin et al., 2020; Li et al., 2020; Mancuso et al., 2020). The new depositional age of the Stuttgart Formation indicates that the onset of the mid-Carnian episode in the CEB was delayed by about 3 myr compared to basins of the NW Tethys domain. If this is also the case for other basins of the peri-Tethyan realm, such as the Paris Basin or the Iberian Basins, needs to be verified by further investigations.

The end of the mid-Carnian episode ranges from the late Julian 2 in the Transdanubian Range (Dal Corso et al., 2015) to the early Tuvalian 2 in the Southern Alps and other basins (Dal Corso et al., 2018; Dal Corso et al., 2020). But the recently reported maximum depositional age of 221.2 ± 1.6 Ma for the top of the Lunz Formation in the western Carpathians (Kohut et al., 2018) points to a much longer range of clastic input in this part of the Tethys (**Figure 6**). Considering the lower limit at 234 Ma and accepting the upper limit of the mid-Carnian episode at c. 221 Ma, as proposed by Kohut et al. (2018), results in a maximum duration of about 13 myr; the multiple of 1.5–1.7 myr as previously reconstructed by Bernardi et al. (2018) and Li et al. (2020).

6 CONCLUSION

Multiple LA-ICP-MS spot analyses of euhedral zircon grains, recovered from the Schilfsandstein (Stuttgart Formation) at Heilbronn (SW Germany), provide the first robust evidence of Triassic tephra fallout in the Central European Basin. The following conclusions can be drawn from this reconnaissance study.

1) The presence of volcanic zircon grains with $^{206}Pb/^{238}U$ ages between 250 ± 3 Ma and 230 ± 4 Ma evidences repeated tephra fallout from the Olenekian to late Carnian in the Central European Basin.
2) Representing detritus of dispersed syn-depositional tephra, the four youngest zircon grains of euhedral habitus gave a weighted average $^{206}Pb/^{238}U$ age of 231.1 ± 1.6 Ma (10 analyses). This new maximum depositional age of the Stuttgart Formation is about 3 myr younger than previously suggested.
3) The late Carnian volcanic zircon grains from Heilbronn, but also the volcanic zircon grains with $^{206}Pb/^{238}U$ ages of 231 ±

5 Ma and 232 ± 6 Ma from Großmonra/Thuringia, and the ubiquitous presence of authigenic analcime reveals a wider distribution of syn-depositional tephra in the Stuttgart Formation.

4) The new maximum depositional age of the Stuttgart Formation indicates that the onset of the mid-Carnian episode in the Central European Basin occurred about 3 myr later than compared to basins of the NW Tethys domain.
5) The finding of volcanic zircon grains of Olenekian to early Carnian age in the Stuttgart Formation points to the presence of tephra beds in the Buntsandstein to Keuper Groups, which were previously overlooked. The detritus of these pre-depositional tephra beds was incorporated into the Stuttgart Formation due to fluvial incision and reworking at the southern margins of the Central European Basin.
6) The congruence of herein reported $^{206}Pb/^{238}U$ ages of volcanic zircons with published $^{206}Pb/^{238}U$ ages of tephra beds and volcanogenic sandstones from Tethyan basins suggest a common source in the NW Tethys domain and transport of tephra to the Central European Basin by monsoonal circulation systems.

DATA AVAILABILITY STATEMENT

The original contributions presented in the study are included in the article/**Supplementary Material**, further inquiries can be directed to the corresponding author.

AUTHOR CONTRIBUTIONS

AZ did sampling, zircon separation, U-Pb dating and data processing, BSE—imaging. MF and KO compiled literature data and produced half of the figures. AZ and MF wrote the first draft of the manuscript. All authors contributed to manuscript revision, read, and approved the submitted version.

SUPPLEMENTARY MATERIAL

The Supplementary Material for this article can be found online at: https://www.frontiersin.org/articles/10.3389/feart.2021.778820/full#supplementary-material

REFERENCES

Aigner, T., and Bachmann, G. H. (1992). Sequence-stratigraphic Framework of the German Triassic. *Sediment. Geology* 80, 115–135. doi:10.1016/0037-0738(92)90035-p

Arche, A., and López-Gómez, J. (2014). The Carnian Pluvial Event in Western Europe: New Data from Iberia and Correlation with the Western Neotethys and Eastern North America-NW Africa Regions. *Earth-Science Rev.* 128, 196–231. doi:10.1016/j.earscirev.2013.10.012

Bachmann, G. H., Beutler, G., Hagdorn, H., and Hauschke, N. (1999). "Stratigraphie der Germanischen Trias," in *Trias – eine ganz andere Welt*. Editors N. Hauschke and V. Wilde (München: Pfeil), 81–104.

Bachmann, G. H., Geluk, M. C., Warrington, G., Becker-Roman, A., Beutler, G., Hagdorn, H., et al. (2010). "Triassic," in *Petroleum Geological Atlas of the Southern Permian Basin Area*. Editors J. C. Doornenbal and A. G. Stevenson (Houten: EAGE Publication), 149–173.

Bachmann, G. H., and Kozur, H. (2004). The Germanic Triassic: Correlations with the International Chronostratigraphic Scale, Numerical Ages and Milankovitch Cyclicity. *Hallesches Jahrbuch für Geowissenschaften B.* 26, 17–62.

Bachmann, G. H., and Wild, H. (1976). Die Grenze Gipskeuper/Schilfsandstein (Mittlerer Keuper) bei Heilbronn/Neckar. *Jahresberichte des Oberrheinischen geologischen Vereins,* N. F. 58, 137–152. doi:10.1127/jmogv/58/1976/137

Barnasch, J. (2010). Der Keuper im Westteil des Zentraleuropäischen Beckens (Deutschland, Niederlande, England, Dänemark): diskontinuierliche Sedimentation, Litho-, Zyklo- und Sequenzstratigraphie. *Schriftenreihe der Deutschen Gesellschaft für Geowissenschaften* 71, 170. doi:10.1127/sdgg/71/2010/7

Beltrán-Triviño, A., Winkler, W., von Quadt, A., and Gallhofer, D. (2016). Triassic Magmatism on the Transition from Variscan to Alpine Cycles: Evidence from U-Pb, Hf, and Geochemistry of Detrital Minerals. *Swiss J. Geosci.* 109, 309–328. doi:10.1007/s00015-016-0234-3

Bernardi, M., Gianolla, P., Petti, F. M., Mietto, P., and Benton, M. J. (2018). Dinosaur Diversification Linked with the Carnian Pluvial Episode. *Nat. Commun.* 9, 1–10. doi:10.1038/s41467-018-03996-1

Beutler, G., and Häusser, I. (1982). Über den Schilfsandstein der DDR. *Z. für Geologische Wissenschaften* 10, 511–525.

Beutler, G. (1995). Quantifizierung der altkimmerischen Bewegungen in Nordwestdeutschland. *Ber. Archiv-nr.* 113087, 1–147. Hannover (Bundesanstalt für Geowissenschaften und Rohstoffe).

Beyer, D. (2015). Evolution of Reservoir Properties in the Lower Triassic Aquifer Sandstones of the Thuringian Syncline in Central Germany. Disseration thesis. Friedrich-Schiller-Universität Jena, 124. Available at: https://www.db-thueringen.de/servlets/MCRFileNodeServlet/dbt_derivate_00031526/Diss/Dissertation%20Beyer.pdf.

Bianchini, G., Natali, C., Shibata, T., and Yoshikawa, M. (2018). Basic Dykes Crosscutting the Crystalline Basement of Valsugana (Italy): New Evidence of Early Triassic Volcanism in the Southern Alps. *Tectonics* 37, 2080–2093. doi:10.1029/2017tc004950

Brown, E. H., and Gehrels, G. E. (2007). Detrital Zircon Constraints on Terrane Ages and Affinities and Timing of Orogenic Events in the San Juan Islands and North Cascades, Washington. *Can. J. Earth Sci.* 44, 1375–1396. doi:10.1139/e07-040

Brusca, C., Gaetani, M., Jadoul, F., and Viel, G. (1982). Paleogeografia Ladino-Carnica e metallogenesi nel Sudalpino. *Mem. Soc. Geol. It.* 22, 65–82.

Burley, S. D., Kantorowicz, J. D., and Waugh, B. (1985). *Clastic Diagenesis*. Geological Society, London, Special Publications, 189–226. doi:10.1144/gsl.sp.1985.018.01.10

Cassinis, G., Cortesogno, L., Gaggero, L., Perotti, C. R., and Buzzi, L. (2008). Permian to Triassic Geodynamic and Magmatic Evolution of the Brescian Prealps (Eastern Lombardy, Italy). *Boll. Soc. Geol. It.* 127, 501–518.

Cuadros, J., Afsin, B., Jadubansa, P., Ardakani, M., Ascaso, C., and Wierzchos, J. (2013). Pathways of Volcanic Glass Alteration in Laboratory Experiments through Inorganic and Microbially-Mediated Processes. *Clay Miner.* 48, 423–445. doi:10.1180/claymin.2013.048.3.01

Dal Corso, J., Bernardi, M., Sun, Y., Song, H., Seyfullah, L. J., Preto, N., et al. (2020). Extinction and Dawn of the Modern World in the Carnian (Late Triassic). *Sci. Adv.* 6, eaba0099. doi:10.1126/sciadv.aba0099

Dal Corso, J., Gianolla, P., Newton, R. J., Franceschi, M., Roghi, G., Caggiati, M., et al. (2015). Carbon Isotope Records Reveal Synchronicity between Carbon Cycle Perturbation and the "Carnian Pluvial Event" in the Tethys Realm (Late Triassic). *Glob. Planet. Change* 127, 79–90. doi:10.1016/j.gloplacha.2015.01.013

Dal Corso, J., Gianolla, P., Rigo, M., Franceschi, M., Roghi, G., Mietto, P., et al. (2018). Multiple Negative Carbon-Isotope Excursions during the Carnian Pluvial Episode (Late Triassic). *Earth-Science Rev.* 185, 732–750. doi:10.1016/j.earscirev.2018.07.004

Dal Corso, J., Mietto, P., Newton, R. J., Pancost, R. D., Preto, N., Roghi, G., et al. (2012). Discovery of a Major Negative $\delta^{13}C$ Spike in the Carnian (Late Triassic) Linked to the Eruption of Wrangellia Flood Basalts. *Geology* 40, 79–82. doi:10.1130/g32473.1

De Min, A., Velicogna, M., Ziberna, L., Chiaradia, M., Alberti, A., and Marzoli, A. (2020). Triassic Magmatism in the European Southern Alps as an Early Phase of Pangea Break-Up. *Geol. Mag.* 157, 1800–1822. doi:10.1017/s0016756820000084

Dockter, J., and Kühn, W. (1974). "Fazies und Sedimentologie des Keupers im Thüringer Becken," in *Sedimentäre Fazies – Fortschritte der Sedimentationsanalyse; Exkursionsf. Tagg. Gesellsch. geol. Wiss. DDR vom 16.–18. Mai 1974 in Gera*. Berlin, 48–59.

DSK (Deutsche Stratigraphische Kommission) (2005). "Stratigraphie von Deutschland, IV: Keuper," in *Courier Forschungsinstitut Senckenberg*. Schweizerbart Science Publishers, 253, 296.

DSK (Deutsche Stratigraphische Kommission) (2013). "Stratigraphie von Deutschland, XI: Buntsandstein," in *Schriftenreihe der Deutschen Gesellschaft für Geowissenschaften*, 69, 657.

DSK (Deutsche Stratigraphische Kommission) (2020). "Stratigraphie von Deutschland, XIII: Muschelkalk," in *Schriftenreihe der Deutschen Gesellschaft für Geowissenschaften*, 91, 1256.

Dunkl, I., Farics, É., Józsa, S., Lukács, R., Haas, J., and Budai, T. (2019). Traces of Carnian Volcanic Activity in the Transdanubian Range, Hungary. *Int. J. Earth Sci. (Geol Rundsch)* 108, 1451–1466. doi:10.1007/s00531-019-01714-w

Dypvik, H. (1983). Clay mineral Transformations in Tertiary and Mesozoic Sediments from North Sea. *Bull. Am. Ass. Petrol. Geol.* 67, 160–165. doi:10.1306/03b5acdc-16d1-11d7-8645000102c1865d

Feist-Burkhardt, S., Götz, A. E., Szulc, J., Borkhataria, R., Geluk, M., Haas, J., et al. (2008). "Triassic," in *The Geology of Central Europe: Mesozoic and Cenozoic*. Editor A. McCann (London: Geological Society of London), 749–821.

Fisher, M. J., and Mudge, D. C. (1990). "Triassic," in *Introduction to the Petroleum Geology of the North Sea*. Editor K.W. Glennie (Oxford: Blackwell), 191–218.

Förster, A., Schöner, R., Förster, H.-J., Norden, B., Blaschke, A.-W., Luckert, J., et al. (2010). Reservoir Characterization of a CO2 Storage Aquifer: The Upper Triassic Stuttgart Formation in the Northeast German Basin. *Mar. Pet. Geology.* 27, 2156–2172. doi:10.1016/j.marpetgeo.2010.07.010

Franz, M., Bachmann, G. H., Barnasch, J., Heunisch, C., and Röhling, H.-G. (2018a). Der Keuper in der Stratigraphischen Tabelle von Deutschland 2016 - kontinuierliche Sedimentation in der norddeutschen Beckenfazies (Variante B). *Zeitschrift der Deutschen Gesellschaft für Geowissenschaften* 169, 203–224. doi:10.1127/zdgg/2018/0114

Franz, M., and Barnasch, J. (2021). "Der Keuper im zentralen Germanischen Becken," in *Trias – Aufbruch in das Erdmittelalter*. Editors N. Hauschke, M. Franz, and G. H. Bachmann (München: Pfeil), 83–108.

Franz, M., Kustatscher, E., Heunisch, C., Niegel, S., and Röhling, H.-G. (2019). The Schilfsandstein and its flora; Arguments for a Humid Mid-carnian Episode? *J. Geol. Soc.* 176, 133–148. doi:10.1144/jgs2018-053

Franz, M. (2008). Litho- und Leitflächenstratigraphie, Chronostratigraphie, Zyklo- und Sequenzstratigraphie des Keupers im östlichen Zentraleuropäischen Becken (Deutschland, Polen) und Dänischen Becken (Dänemark, Schweden). Ph.D. Thesis. Germany: Martin-Luther-Universität Halle-Wittenberg, 198. Available at: http://sundoc.bibliothek.uni-halle.de/diss-online/08/09H048/index.htm.

Franz, M., Nowak, K., Berner, U., Heunisch, C., Bandel, K., Röhling, H.-G., et al. (2014). Eustatic Control on Epicontinental Basins: the Example of the Stuttgart Formation in the Central European Basin (Middle Keuper, Late Triassic). *Glob. Planet. Change* 122, 305–329. doi:10.1016/j.gloplacha.2014.07.010

Franz, M., Nowak, K., Niegel, S., Seidel, E., Wolf, M., and Wolfgramm, M. (2018b). Deep Geothermal Resources of the North German Basin: The Hydrothermal Reservoirs of the Stuttgart Formation (Schilfsandstein, Upper Triassic). *Zeitschrift der Deutschen Gesellschaft für Geowissenschaften* 169, 353–387. doi:10.1127/zdgg/2018/0164

Friberg, L. J. (2001). Untersuchungen zur Temperatur- und Absenkungsgeschichte sowie zur Bildung und Migration von Methan und molekularem Stickstoff im Nordostdeutschen Becken. *Berichte Forschungszentrum Jülich* 3914, 226.

Füchtbauer, H. (1974). Zur Diagenese Fluviatiler Sedimente. *Geologische Rundschau* 63, 904–925.

Furin, S., Preto, N., Rigo, M., Roghi, G., Gianolla, P., Crowley, J. L., et al. (2006). High-precision U-Pb Zircon Age from the Triassic of Italy: Implications for the Triassic Time Scale and the Carnian Origin of Calcareous Nannoplankton and Dinosaurs. *Geol* 34, 1009–1012. doi:10.1130/g22967a.1

Garzanti, E. (1985). The sandstone Memory of the Evolution of a Triassic Volcanic Arc in the Southern Alps, Italy. *Sedimentology* 32, 423–433. doi:10.1111/j.1365-3091.1985.tb00521.x

Gerdes, A., and Zeh, A. (2006). Combined U-Pb and Hf Isotope LA-(MC-)ICP-MS Analyses of Detrital Zircons: Comparison with SHRIMP and New Constraints for the Provenance and Age of an Armorican Metasediment in Central Germany. *Earth Planet. Sci. Lett.* 249, 47–61. doi:10.1016/j.epsl.2006.06.039

Gerdes, A., and Zeh, A. (2009). Zircon Formation versus Zircon Alteration - New Insights from Combined U-Pb and Lu-Hf *In-Situ* LA-ICP-MS Analyses, and Consequences for the Interpretation of Archean Zircon from the Central Zone of the Limpopo Belt. *Chem. Geology.* 261, 230–243. doi:10.1016/j.chemgeo.2008.03.005

Geyer, G., and Kelber, K.-P. (2018). Spinicaudata ("Conchostraca," Crustacea) from the Middle Keuper (Upper Triassic) of the Southern Germanic Basin, with a Review of Carnian-Norian Taxa and Suggested Biozones. *PalZ* 92, 1–34. doi:10.1007/s12542-017-0363-7

Gong, N., Hong, H., Huff, W. D., Fang, Q., Bae, C. J., Wang, C., et al. (2018). Influences of Sedimentary Environments and Volcanic Sources on Diagenetic Alteration of Volcanic Tuffs in South China. *Sci. Rep.* 8, 7616. doi:10.1038/s41598-018-26044-w

Häusser, I., and Kurze, M. (1975). Sedimentationsbedingungen und Schwermineralführung im Mesozoikum des Nordteils der DDR. *Z. Geol. Wiss.* 3, 1317–1332.

Hay, R. L. (1966). *Zeolites and Zeolitic Reactions in Sedimentary Rocks*, 85. Geological Society of America, Special Paper, 180.

Heling, D. (1965). Zur Petrographie des Schilfsandsteins. *Beitr Mineral. u Petrogr* 11, 272–296. doi:10.1007/bf01172137

Heunisch, C. (1999). "Die Bedeutung der Palynologie für Biostratigraphie und Fazies in der Germanischen Trias," in *Trias: eine ganz andere Welt*. Editors N. Hauschke and V. Wilde (München: Pfeil), 207–220.

Heunisch, C., and Wierer, F. (2021). "Palynomorphe der Germanischen Trias," in *Trias – Aufbruch in das Erdmittelalter*. Editors N. Hauschke, M. Franz, and G. H. Bachmann (München: Pfeil), 205–217.

Hiess, J., Condon, D. J., McLean, N., and Noble, S. R. (2012). $^{238}U/^{235}U$ Systematics in Terrestrial Uranium-Bearing Minerals. *Science* 335, 1610–1614. doi:10.1126/science.1215507

Hofmann, M., Voigt, T., Bittner, L., Gärtner, A., Zieger, J., and Linnemann, U. (2018). Reworked Middle Jurassic Sandstones as a Marker for Upper Cretaceous basin Inversion in Central Europe-A Case Study for the U-Pb Detrital Zircon Record of the Upper Cretaceous Schmilka Section and Their Implication for the Sedimentary Cover of the Lausitz Block (Saxony, Germany). *Int. J. Earth Sci. (Geol Rundsch)* 107, 913–932. doi:10.1007/s00531-017-1552-z

Hornung, T., Brandner, R., Krystyn, L., Joachimski, M. M., and Keim, L. (2007a). Multistratigraphic Constraints on the NW Tethyan "Carnian Crisis". *New Mexico Mus. Nat. Hist. Bulletins* 4, 9–67.

Hornung, T., Krystyn, L., and Brandner, R. (2007b). A Tethys-wide Mid-carnian (Upper Triassic) Carbonate Productivity Crisis: Evidence for the Alpine Reingraben Event from Spiti (Indian Himalaya)? *J. Asian Earth Sci.* 30, 285–302. doi:10.1016/j.jseaes.2006.10.001

Hoth, P. (1997). *Fazies und Diagenese von Präperm-Sedimenten der Geotraverse Harz – Rügen*. Schriftenreihe für Geowissenschaften. Ostklüne: Verlag Störr 4, 139.

Hurst, A., and Irwin, H. (1982). Geological Modelling of clay Diagenesis in Sandstones. *Clay Miner.* 17, 5–22. doi:10.1180/claymin.1982.017.1.03

Jackson, S. E., Pearson, N. J., Griffin, W. L., and Belousova, E. A. (2004). The Application of Laser Ablation-Inductively Coupled Plasma-Mass Spectrometry to *In Situ* U-Pb Zircon Geochronology. *Chem. Geology.* 211, 47–69. doi:10.1016/j.chemgeo.2004.06.017

Jäger, F. (1827). *Über Pflanzenversteinerungen welche in dem Bausandstein von Stuttgart vorkommen*. Stuttgart: Metzler, 40.

Jeans, C. V., Wray, D. S., Merriman, R. J., and Fisher, M. J. (2000). Volcanogenic Clays in Jurassic and Cretaceous Strata of England and the North Sea Basin. *Clay Miner.* 35, 25–55. doi:10.1180/000985500546710

Jin, X., Gianolla, P., Shi, Z., Franceschi, M., Caggiati, M., Du, Y., et al. (2020). Synchronized Changes in Shallow Water Carbonate Production during the Carnian Pluvial Episode (Late Triassic) throughout Tethys. *Glob. Planet. Change* 184, 103035. doi:10.1016/j.gloplacha.2019.103035

Kendall, G. C. S. C., Lake, P., Weathers, H. D., III, Lakshmi, V., Althausen, J., and Alsharan, A. S. (2003). "Evidence of Rain Shadow in the Geologic Record: Repeated Evaporite Accumulation at Extensional and Compressional Plate Margins," in *Desertification in the Third Millennium*. Editors A.S. Alsharan, W.W.A.S. WoodGoudie, A. Fowler, and E.M. Abdellatif (Netherlands: Swets & Zeitlinger), 45–52.

Kohút, M., Hofmann, M., Havrila, M., Linnemann, U., and Havrila, J. (2018). Tracking an Upper Limit of the "Carnian Crisis" And/or Carnian Stage in the Western Carpathians (Slovakia). *Int. J. Earth Sci. (Geol. Rundsch)* 107, 321–335. doi:10.1007/s00531-017-1491-8

Kowal-Linka, M., Krzemińska, E., and Czupyt, Z. (2019). The Youngest Detrital Zircons from the Upper Triassic Lipie Śląskie (Lisowice) continental Deposits (Poland): Implications for the Maximum Depositional Age of the Lisowice Bone-Bearing Horizon. *Palaeogeogr. Palaeoclimatol. Palaeoecol.* 514, 487–501. doi:10.1016/j.palaeo.2018.11.012

Kozur, H. W., and Bachmann, G. H. (2010). The Middle Carnian Wet Intermezzo of the Stuttgart Formation (Schilfsandstein), Germanic Basin. *Palaeogeogr. Palaeoclimatol. Palaeoecol.* 290, 107–119. doi:10.1016/j.palaeo.2009.11.004

Kozur, H. W., and Weems, R. E. (2010). "The Biostratigraphic Importance of Conchostracans in the continental Triassic of the Northern Hemisphere," in *The Triassic Timescale*. Editor S. G. Lucas (Geol. Soc. London, Special Pub), 334, 315–417. doi:10.1144/sp334.13

Kozur, H. W., and Weems, R. E. (2007). "Upper Triassic Conchostracan Biostratigraphy of the continental Rift Basins of Eastern North America: its Importance for Correlating Newark Supergroup Events with the German Basin and the International Geological Time Scale," in *The Global Triassic*. Editors S. G. Lucas and J. A. Spielmann (New Mexico: Museum of Natural History & Science Bulletins), 41, 137–188.

Kühn, W. (1976). Einige Bemerkungen zum Auftreten von Analcim im Keuper. *Jahrbuch für Geologie*. 5/6 (1969/1970), 269–276.

Kutzbach, J. E., and Gallimore, R. G. (1989). Pangaean Climates: Megamonsoons of the Megacontinent. *J. Geophys. Res.* 94 (D3), 3341–3357. doi:10.1029/jd094id03p03341

Larsen, B. T., Olaussen, S., Sundvoll, B., and Heeremans, M. (2008). The Permo-Carboniferous Oslo Rift through Six Stages and 65 Million Years. *Episodes* 31, 52–58. doi:10.18814/epiiugs/2008/v31i1/008

Li, Z., Chen, Z.-Q., Zhang, F., Ogg, J. G., and Zhao, L. (2020). Global Carbon Cycle Perturbations Triggered by Volatile Volcanism and Ecosystem Responses during the Carnian Pluvial Episode (Late Triassic). *Earth-Science Rev.* 211, 103404. doi:10.1016/j.earscirev.2020.103404

López-Gómez, J., Escudero-Mozo, M. J., Martín-Chivelet, J., Arche, A., Lago, M., and Galé, C. (2017). Western Tethys continental-marine Responses to the Carnian Humid Episode: Palaeoclimatic and Palaeogeographic Implications. *Glob. Planet. Change* 148, 79–95. doi:10.1016/j.gloplacha.2016.11.016

Lu, J., Zhang, P., Dal Corso, J., Yang, M., Wignall, P. B., Greene, S. E., et al. (2021). Volcanically Driven Lacustrine Ecosystem Changes during the Carnian Pluvial Episode (Late Triassic). *Proc. Natl. Acad. Sci. USA* 118, e2109895118. doi:10.1073/pnas.2109895118

Ludwig, K. (2001). "Isoplot/Ex, Rev. 2.49," in *A Geochronological Toolkit for Microsoft Excel* (Berkeley Geochronology Center, Special Publication No. 1a).

Lustrino, M., Abbas, H., Agostini, S., Caggiati, M., Carminati, E., and Gianolla, P. (2019). Origin of Triassic Magmatism of the Southern Alps (Italy): Constraints from Geochemistry and Sr-Nd-Pb Isotopic Ratios. *Gondwana Res.* 75, 218–238. doi:10.1016/j.gr.2019.04.011

Mancuso, A. C., Benavente, C. A., Irmis, R. B., and Mundil, R. (2020). Evidence for the Carnian Pluvial Episode in Gondwana: New Multiproxy Climate Records and Their Bearing on Early dinosaur Diversification. *Gondwana Res.* 86, 104–125. doi:10.1016/j.gr.2020.05.009

Marocchi, M., Morelli, C., Mair, V., Klötzli, U., and Bargossi, G. M. (2008). Evolution of Large Silicic Magma Systems: New U-Pb Zircon Data on the NW Permian Athesian Volcanic Group (Southern Alps, Italy). *J. Geology.* 116, 480–498. doi:10.1086/590135

Maury, R. C., Lapierre, H., Bosch, D., Marcoux, J., Krystyn, L., Cotten, J., et al. (2008). The Alkaline Intraplate Volcanism of the Antalya Nappes (Turkey): a Late Triassic Remnant of the Neotethys. *Bull. Soc. Géol. Fr.* 179, 397–410. doi:10.2113/gssgfbull.179.4.397

McKie, T. (2017). "Paleogeographic Evolution of Latest Permian and Triassic Salt Basins in Northwest Europe," in *Permo-Triassic Salt Provinces of Europe, North Africa and the Atlantic Margins – Tectonics and Hydrocarbon Potential*. Editors J.I. Soto, J.F. Flinch, and G. Tari (Elsevier), 159–173. doi:10.1016/b978-0-12-809417-4.00008-2

Mietto, P., Manfrin, S., Preto, N., Rigo, M., Roghi, G., Furin, S., et al. (2012). The Global Boundary Stratotype Section and Point (GSSP) of the Carnian stage (Late Triassic) at Prati di Stuores/Stuores Wiesen section (Southern Alps, NE Italy). *Episodes* 35, 414–430. doi:10.18814/epiiugs/2012/v35i3/003

Miller, C. S., Peterse, F., da Silva, A.-C., Baranyi, V., Reichart, G. J., and Kürschner, W. M. (2017). Astronomical Age Constraints and Extinction Mechanisms of the Late Triassic Carnian Crisis. *Sci. Rep.* 7, 2557. doi:10.1038/s41598-017-02817-7

Moix, P., Vachard, D., Allibon, J., Martini, R., Wernli, R., Kozur, H. W., et al. (2013). "Paleotethyan, Neotethyan and Huğlu–Pindos Series in the Lycian Nappes (SW Turkey): Geodynamical Implications," in *The Triassic System*. Editors L.H. Tanner, J.A. Spielmann, and SG. Lucas (New Mexico: Museum of Natural History & Science Bulletins), 61, 401–444.

Neunzert, G. H., Gaupp, R., and Littke, R. (1996). Burial and Temperature of Paleozoic and Mesozoic Rocks in the Northwest German Basin. *Zeitschrift der Deutschen Gesellschaft für Geowissenschaften* 147, 183–208. doi:10.1127/zdgg/147/1996/183

Nürnberger, T. (2010). Fazies und Genese der Stuttgart-Formation (Schilfsandstein) im Thüringer Becken und Thüringer Grabfeld. Diploma thesis. University of Jena, 92.

Ogg, J. G. (2015). The Mysterious Mid-carnian "Wet Intermezzo" Global Event. *J. Earth Sci.* 26, 181–191. doi:10.1007/s12583-015-0527-x

Parrish, J. T. (1993). Climate of the Supercontinent Pangea. *J. Geology* 101, 215–233. doi:10.1086/648217

Parrish, J. T. (1999). "Pangaea und das Klima der Trias," in *Trias – eine ganz andere Welt*. Editors N. Hauschke and V. Wilde (München: Pfeil), 81–104.

Patrick Muffler, L. J., and White, D. E. (1969). Active Metamorphism of Upper Cenozoic Sediments in the Salton Sea Geothermal Field and the Salton Trough, southeastern California. *Geol. Soc. America Bull.* 80, 157–182. doi:10.1130/0016-7606(1969)80[157:amoucs]2.0.co;2

Perry, E., and Hower, J. (1970). Burial Diagenesis in Gulf Coast Pelitic Sediments. *Clays and Clay Minerals* 18, 165–177. doi:10.1346/ccmn.1970.0180306

Preto, N., Kustatscher, E., and Wignall, P. B. (2010). Triassic Climates - State of the Art and Perspectives. *Palaeogeogr. Palaeoclimatol. Palaeoecol.* 290, 1–10. doi:10.1016/j.palaeo.2010.03.015

Rainbird, R. H., Hamilton, M. A., and Young, G. M. (2001). Detrital Zircon Geochronology and Provenance of the Torridonian, NW Scotland. *J. Geol. Soc.* 158, 15–27. doi:10.1144/jgs.158.1.15

Reinhardt, L., and Ricken, W. (2000). The Stratigraphic and Geochemical Record of Playa Cycles: Monitoring a Pangaean Monsoon-like System (Triassic, Middle Keuper, S. Germany). *Palaeogeogr. Palaeoclimatol. Palaeoecol.* 161, 205–227. doi:10.1016/s0031-0182(00)00124-3

Rodon, S., and Littke, R. (2005). Thermal Maturity in the Central European Basin System (Schleswig-Holstein Area): Results of 1D basin Modelling and New Maturity Maps. *Int. J. Earth Sci. (Geol Rundsch)* 94, 815–833. doi:10.1007/s00531-005-0006-1

Roghi, G., Gianolla, P., Minarelli, L., Pilati, C., and Preto, N. (2010). Palynological Correlation of Carnian Humid Pulses throughout Western Tethys. *Palaeogeogr. Palaeoclimatol. Palaeoecol.* 290, 89–106. doi:10.1016/j.palaeo.2009.11.006

Ruffell, A., Simms, M. J., and Wignall, P. B. (2015). The Carnian Humid Episode of the Late Triassic: a Review. *Geol. Mag.* 153, 271–284. doi:10.1017/s0016756815000424

Salger, M. (1982). Mineralogie der Forschungsbohrung Dinkelsbühl 1001. *Geologica Bavarica* 83, 57–66.

Santos, M. M., Lana, C., Scholz, R., Buick, I., Schmitz, M. D., Kamo, S. L., et al. (2017). A New Appraisal of Sri Lankan BB Zircon as a Reference Material for LA-ICP-MS U-Pb Geochronology and Lu-Hf Isotope Tracing. *Geostand Geoanal Res.* 41, 335–358. doi:10.1111/ggr.12167

Schröder, B., (1977). Unterer Keuper und Schilfsandstein im germanischen Trias-Randbecken. *Zentralblatt für Geologie und Paläontologie*, Teil I 1976, 1030–1056.

Segonzac, G. D. (1970). The Transformation of Clay Minerals during Diagenesis and Low-Grade Metamorphism: A Review. *Sedimentology* 15, 281–346. doi:10.1111/j.1365-3091.1970.tb02190.x

Simms, M. J., and Ruffell, A. H. (1989). Synchroneity of Climatic Change and Extinctions in the Late Triassic. *Geol* 17, 265–268. doi:10.1130/0091-7613(1989)017<0265:soccae>2.3.co;2

Sláma, J., Košler, J., Condon, D. J., Crowley, J. L., Gerdes, A., Hanchar, J. M., et al. (2008). Plešovice Zircon — A New Natural Reference Material for U–Pb and Hf Isotopic Microanalysis. *Chem. Geol.* 249, 1–35. doi:10.1016/j.chemgeo.2007.11.005

Stacey, J. S., and Kramers, J. D. (1975). Approximation of Terrestrial lead Isotope Evolution by a Two-Stage Model. *Earth Planet. Sci. Lett.* 26, 207–221. doi:10.1016/0012-821x(75)90088-6

Stampfli, G. M., and Borel, G. D. (2004). "The TRANSMED Transects in Space and Time: Constraints on the Paleotectonic Evolution of the Mediterranean Domain," in *The TRANSMED Atlas. The Mediterranean Region from Crust to Mantle*. Editors W. Cavazza, F. Roure, W. Spakman, G.M. Stampfli, and P.A. Ziegler (Berlin, Heidelberg: Springer), 53–80. doi:10.1007/978-3-642-18919-7_3

Stampfli, G. M., Vavassis, I., De Bono, A., Rosselet, F., Matti, B., and Bellini, M. (2003). Remnants of the Paleotethys Oceanic Suture-Zone in the Westem Tethyan Area. *Boll. Soc. Geol. It.,* Vol Spec. 2, 1–23.

Stollhofen, H., Bachmann, G. H., Barnasch, J., Bayer, U., Beutler, G., Franz, M., et al. (2008). "Upper Rotliegend to Lower Cretaceous basin Development," in *Dynamics of Complex Sedimentary Basins: The Example of the Central European Basin System*. Editors R. Littke, U. Bayer, D. Gajewski, and S. Nelskamp (Heidelberg: Springer), 157–180.

Storck, J.-C., Brack, P., Wotzlaw, J.-F., and Ulmer, P. (2019). Timing and Evolution of Middle Triassic Magmatism in the Southern Alps (Northern Italy). *J. Geol. Soc.* 176, 253–268. doi:10.1144/jgs2018-123

Sun, Y. D., Wignall, P. B., Joachimski, M. M., Bond, D. P. G., Grasby, S. E., Lai, X. L., et al. (2016). Climate Warming, Euxinia and Carbon Isotope Perturbations during the Carnian (Triassic) Crisis in South China. *Earth Planet. Sci. Lett.* 444, 88–100. doi:10.1016/j.epsl.2016.03.037

Thomson, S. N., and Zeh, A. (2000). Fission-track Thermochronology of the Ruhla Crystalline Complex: New Constraints on the post-Variscan thermal Evolution of the NW Saxo-Bohemian Massif. *Tectonophysics* 324, 17–35. doi:10.1016/s0040-1951(00)00113-x

van Bergen, M. J., and Sissingh, W. (2007). "Magmatism in the Netherlands: Expression of the north-west European Rifting History," in *Geology of the Netherlands*. Editors T. E. Wong, D.A.J. Batjes, and J. de Jager (Royal Netherlands Academy of Arts and Sciences), 197–221.

Voigt, T., Grobleben, J., Schöner, R., and Gaupp, R. (2010). Die thermische Reife permokarboner Ablagerungen in Thüringen – Schlussfolgerungen für die Versenkungsgeschichte der Thüringer Mulde. *Beitr. Geol. Thüringen*, N.F. 17, 83–100.

Vollmer, T., Werner, R., Weber, M., Tougiannidis, N., Röhling, H.-G., and Hambach, U. (2008). Orbital Control on Upper Triassic Playa Cycles of the Steinmergel-Keuper (Norian): A New Concept for Ancient Playa Cycles. *Palaeogeogr. Palaeoclimatol. Palaeoecol.* 267, 1–16. doi:10.1016/j.palaeo.2007.12.017

Wilson, K. M., Pollard, D., Hay, W. W., Thompson, S. L., and Wold, C. N. (1994). General Circulation Model Simulations of Triassic Climates: Preliminary Results. *Geol. Soc. Am. Spec. Paper* 288, 91–116. doi:10.1130/spe288-p91

Wotzlaw, J.-F., Brack, P., and Storck, J.-C. (2018). High-resolution Stratigraphy and Zircon U-Pb Geochronology of the Middle Triassic Buchenstein Formation (Dolomites, Northern Italy): Precession-Forcing of Hemipelagic Carbonate Sedimentation and Calibration of the Anisian-Ladinian Boundary Interval. *J. Geol. Soc.* 175, 71–85. doi:10.1144/jgs2017-052

Wurster, P. (1964). Geologie des Schilfsandstein. *Mitteilungen des Geologischen Staatsinstituts Hamburg* 33, 140.

Wurster, P. (1968). Paläogeographie der deutschen Trias und die paläogeographische Orientierung der Lettenkohle in Südwestdeutschland. *Eclogae Geologicae Helv.* 61, 157–166.

Xu, G., Hannah, J. L., Stein, H. J., Mørk, A., Vigran, J. O., Bingen, B., et al. (2014). Cause of Upper Triassic Climate Crisis Revealed by Re-Os Geochemistry of Boreal Black Shales. *Palaeogeogr. Palaeoclimatol. Palaeoecol.* 395, 222–232. doi:10.1016/j.palaeo.2013.12.027

Zeh, A., and Gerdes, A. (2012). U-Pb and Hf Isotope Record of Detrital Zircons from Gold-Bearing Sediments of the Pietersburg Greenstone Belt (South Africa)-Is There a Common Provenance with the Witwatersrand Basin? *Precambrian Res.* 204-205, 46–56. doi:10.1016/j.precamres.2012.02.013

Zhang, Y., Ogg, J. G., Franz, M., Bachmann, G. H., Szurlies, M., Röhling, H.-G., et al. (2020). Carnian (Late Triassic) Magnetostratigraphy from the Germanic Basin Allowing Global Correlation of the Mid-carnian Episode. *Earth Planet. Sci. Lett.* 541, 116275. doi:10.1016/j.epsl.2020.116275

Ziegler, P. A. (1990). *Geological Atlas of Western and Central Europe*. Den Haag: Shell International Petroleum Maatschapij BV.

Conflict of Interest: The authors declare that the research was conducted in the absence of any commercial or financial relationships that could be construed as a potential conflict of interest.

frontiers in Earth Science

ORIGINAL RESEARCH
published: 09 March 2022
doi: 10.3389/feart.2022.832308

Phosphorus Cycle and Primary Productivity Changes in the Tethys Ocean During the Permian-Triassic Transition: Starving Marine Ecosystems

Johann Müller[1]*, *Yadong Sun*[1]*, *Fen Yang*[2], *Alicia Fantasia*[3] and *Michael Joachimski*[1]

[1]GeoZentrum Nordbayern, Friedrich-Alexander University Erlangen-Nürnberg (FAU), Erlangen, Germany, [2]State Key Laboratory of Biogeology and Environmental Geology, China University of Geosciences, Wuhan, China, [3]University Lyon, UCBL, ENSL, UJM, CNRS, LGL-TPE, Villeurbanne, France

The ultimate cause(s) of the end-Permian mass extinction (~252 Ma ago) has been disputed. A complex interplay of various effects, rather than a single, universal killing mechanism, were most likely involved. Climate warming as consequence of greenhouse gas emissions by contemporaneous Siberian Traps volcanism is widely accepted as an initial trigger. Synergetic effects of global warming include increasing stratification of the oceans, inefficient water column mixing, and eventually low marine primary productivity culminating in a series of consequences for higher trophic levels. To explore this scenario in the context of the end-Permian mass extinction, we investigated sedimentary total organic carbon, phosphorus speciation as well as nickel concentrations in two low-latitude Tethyan carbonate sections spanning the Permian-Triassic transition. Total organic carbon, reactive phosphorus and nickel concentrations all decrease in the latest Permian and are low during the Early Triassic, pointing to a decline in primary productivity within the Tethyan realm. We suggest that the productivity collapse started in the upper *C. yini* conodont Zone, approximately 30 ka prior to the main marine extinction interval. Reduced primary productivity would have resulted in food shortage and thus may serve as explanation for pre-mass extinction perturbations among marine heterotrophic organisms.

Keywords: phosphorus cycle, primary productivity, nutrients, food shortage, Permian-Triassic, end-Permian mass extinction, phosphorus speciation

OPEN ACCESS

Edited by:
Sara Callegaro,
University of Oslo, Norway

Reviewed by:
Stephen Grasby,
Geological Survey of Canada, Canada
William J. Foster,
University of Hamburg, Germany

***Correspondence:**
Johann Müller
johann.jm.mueller@fau.de
Yadong Sun
yadong.sun@fau.de

Specialty section:
This article was submitted to Biogeoscience, a section of the journal Frontiers in Earth Science

Received: *09 December 2021*
Accepted: *10 February 2022*
Published: *09 March 2022*

Citation:
Müller J, Sun Y, Yang F, Fantasia A and Joachimski M (2022) Phosphorus Cycle and Primary Productivity Changes in the Tethys Ocean During the Permian-Triassic Transition: Starving Marine Ecosystems. Front. Earth Sci. 10:832308. doi: 10.3389/feart.2022.832308

INTRODUCTION

Anthropogenic global warming is expected to decline marine primary productivity with severe consequences for global ecosystems as well as for mankind (Mora et al., 2013). This is because climate warming likely slows down the meridional overturning circulation, decreases wind-driven coastal and equatorial upwelling intensity but increases thermal stratification thereby inhibiting the mixing of shallow and deep waters (Behrenfeld et al., 2006). Bulk primary production in today's oceans is mainly confined to equatorial and shelf areas where upwelling systems replenish nutrients to the euphotic zone (Boyd et al., 2014). In general, there is a complex interplay between water column mixing, oxygen saturation of sea water, nutrient levels

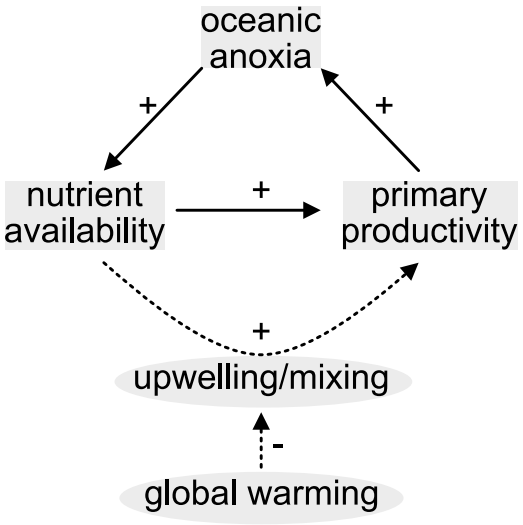

FIGURE 1 | Positive feedback mechanism promoting high primary productivity. Global warming may impede the feedback from operating efficiently by weakening the mixing module.

in the euphotic zone, primary productivity, and organic carbon export to deep waters and the sediment. For example, 1) upwelling systems replenish phosphorus (P) to the euphotic zone 2) organic matter remineralization consumes oxygen and 3) seafloor hypoxia favors P recycling from sediments (**Figure 1**; e.g., Ingall et al., 1993). Under normal climatic conditions, this eutrophication feedback mechanism is able to maintain high levels of productivity in coastal shelf areas, e.g., in the euphotic zone along the modern Peruvian margin (Burnett et al., 1982). However, if vertical mixing weakens due to warming, the nutrient P will be trapped in deeper waters where it cannot be utilized by phytoplankton (Behrenfeld et al., 2006), ultimately leading to a food shortage for higher trophic levels.

To better understand the marine nutrient cycling in the context of ongoing global warming, it is of prime importance to investigate intervals of potent warming in the geological past. Among the so called "big five" mass extinctions, the end-Permian mass extinction stands out being regarded as the most devastating in the Phanerozoic (Newell, 1967; Raup and Sepkoski, 1982; Bambach et al., 2004; Stanley, 2016; Bond and Grasby, 2017). Several coinciding ecological changes were inferred from the geological record using different sedimentological, paleontological, and geochemical methods and many controversial hypotheses exist concerning their causal relationships with no consensus having been reached hitherto. For example, stable oxygen isotope studies of conodont apatite indicate that the Earth has experienced significant and relatively rapid global warming during the latest Permian (e.g., Joachimski et al., 2012; Sun et al., 2012; Schobben et al., 2014; Chen et al., 2020; Joachimski et al., 2020). Low latitude sea surface temperatures increased by ~10°C within ~40 ka from the latest Changhsingian into the Induan. The contemporaneity of Siberian Traps volcanism suggests that volcanogenic greenhouse gas emissions raised atmospheric pCO_2 to high levels (Svensen et al., 2009; Burgess et al., 2017). Additionally, the injection of isotopically light, volcanogenic carbon to the atmosphere

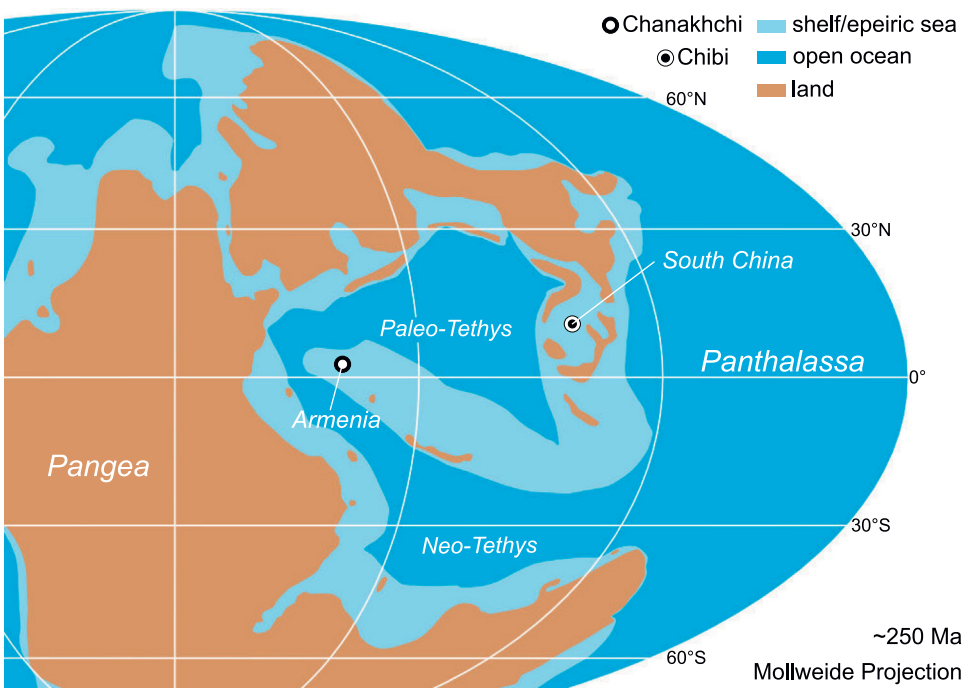

FIGURE 2 | Changhsingian paleogeographic reconstruction after Kocsis and Scotese (2021) with locations of studied sections.

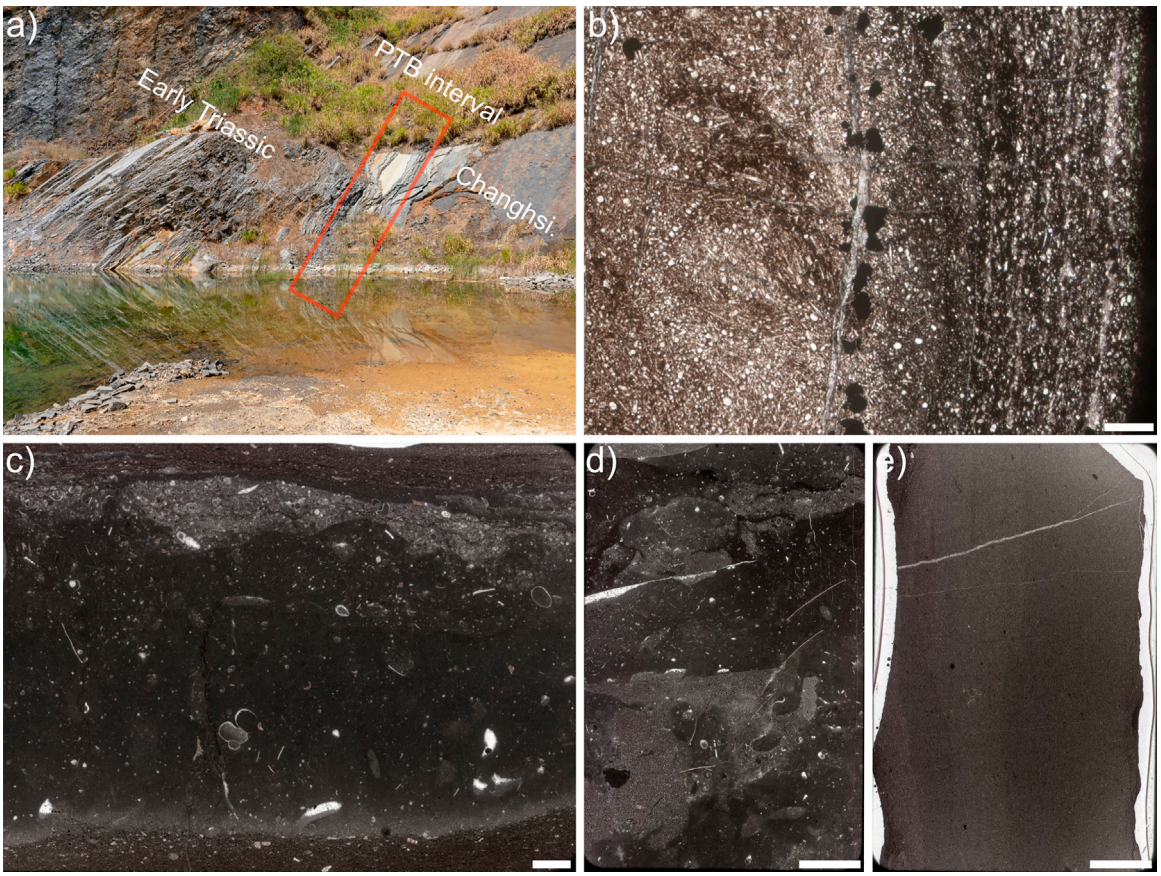

FIGURE 3 | Chibi section and microfacies of Changhsingian and Early Triassic carbonates. **(A)** Chibi section, **(B)** Changhsingian spiculite (sample Y12; scale is 5 mm), **(C,D)** basal Early Triassic bioturbated limestone rich in gastropods with prominent burrows (sample Z10 and Z11; scale is 2 and 5 mm, respectively), **(E)** Griesbachian laminated limestone (sample Z33; scale is 5 mm).

potentially generated the prominent negative carbon isotope excursion at the Permian-Triassic (P-T) boundary (Korte et al., 2010; Korte and Kozur, 2010; Shen et al., 2012). Intense ocean anoxia during the crisis interval was recognized early based on the widespread occurrence of sedimentary facies typical for deposition under hypoxic conditions (Wignall and Hallam, 1992; Wignall and Twitchett, 1996; Isozaki, 1997). This was confirmed by various proxies such as framboidal pyrite analysis, trace metal concentrations, stable sulfur and uranium isotopes and iron speciation further refining the record of P-T ocean anoxia (e.g., Riccardi et al., 2006; Grasby et al., 2013; Clarkson et al., 2016; Lau et al., 2016; Wignall et al., 2020). In contrast to the previously proposed P-T superanoxia, the current understanding is that of a spatially and temporally heterogenous anoxic event that initiated ~70 ka prior to the main marine extinction level (Zhang et al., 2018).

While climate warming and ocean anoxia are reasonably well-established for the end-Permian mass extinction, marine primary productivity levels at the time remain intensively debated. Studies arguing for a boost in marine primary productivity through enhanced continental input of nutrients (i.e., eutrophication; e.g., Algeo and Twitchett, 2010; Schobben et al., 2020) are opposed to studies pointing towards a productivity collapse due to strong ocean stratification and/or weak upwelling with inefficient nutrient shuttling to the euphotic zone (i.e., oligotrophication; e.g., Schoepfer et al., 2012; Grasby et al., 2016; Sun et al., 2021). Other authors point out that a loss of nitrate under anoxic conditions more likely resulted in an ammonium ocean during the end-Permian mass extinction and P was possibly not the limiting nutrient at the time (Sun et al., 2019; Grasby et al., 2020). The oligotrophication scenario is in better accordance with modelling results for the near future and changes we have already observed in the recent past (e.g., Bopp et al., 2013; Roxy et al., 2016). Furthermore, Earth system modelling for the P-T interval predicts a decline in net primary productivity (−40% globally) especially in low latitudes and a large P reservoir in the deep water column (Supplementary Figure S4 in Penn et al., 2018).

In order to document marine P cycling and associated changes of primary productivity in the Tethys Ocean during the critical P-T boundary interval, we investigated sedimentary P distributions, total organic carbon (TOC) and nickel (Ni) concentrations in two carbonate successions from South China and Armenia (**Figure 2**). A sequential P extraction method was applied to reconstruct bioavailable, reactive P (P_{react}). C/P molar

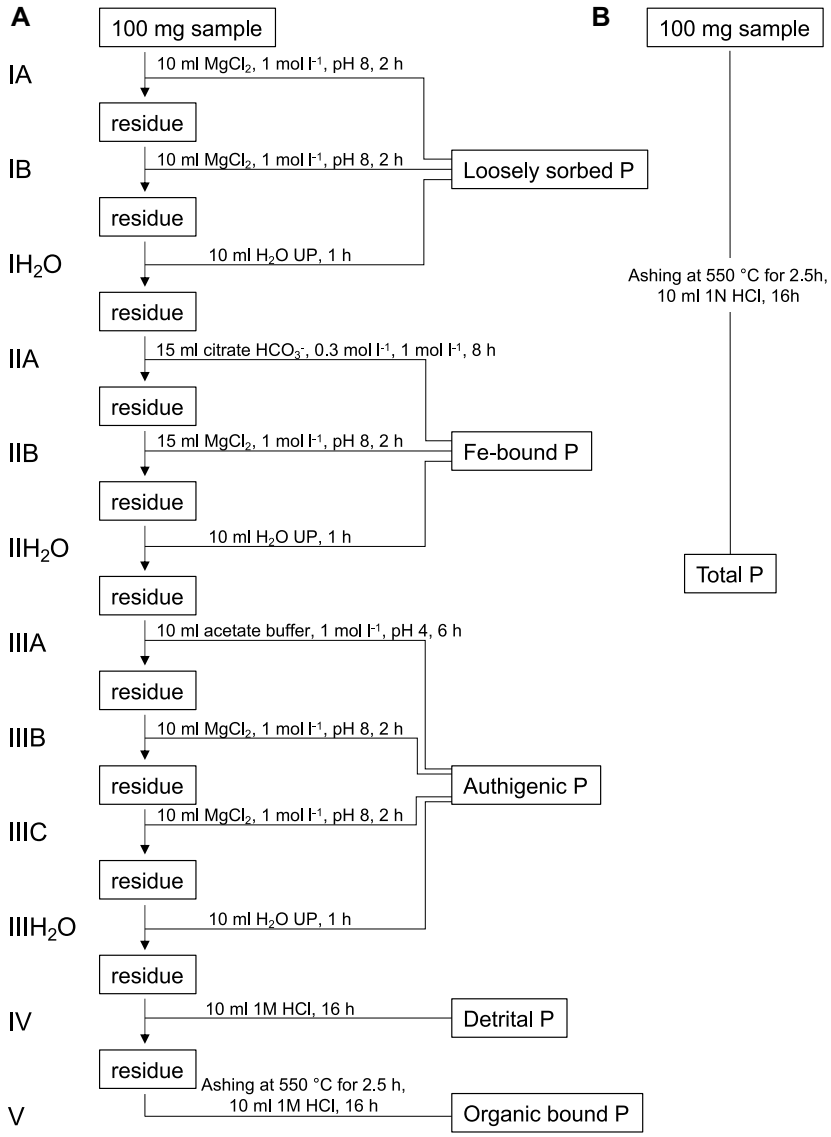

FIGURE 4 | (A) Sequential phosphorus extraction scheme used based on the original SEDEX method developed by Ruttenberg (1992). **(B)** Method for the extraction of total P (Aspila et al., 1976).

ratios are used to evaluate early diagenetic P transfer processes (sink switching) as well as the degree of P burial versus benthic P release (i.e., the P burial efficiency). The geochemical records from both studied sections suggest a decrease in primary productivity in the Tethyan region starting well before the end-Permian mass extinction.

MATERIALS AND METHODS

Geological Setting

Studied P-T boundary successions were deposited across the Paleotethys ocean at tropical latitudes between 0 and 20°N (Kocsis and Scotese, 2021; **Figure 2**). The studied Chibi Section (29.7515 N, 113.9519 E) is located in South China about 100 km south of the city of Wuhan (Hubei Province). The study area is part of the South China Block which was situated in tropical latitudes at the eastern margin of the Paleotethys Ocean during the Lopingian. At that time, the South China Block was characterized by a vast carbonate platform (Yangtze Platform) passing into a deeper basin with siliceous carbonate and chert deposition further north. During the Wuchiapingian, the Chibi section was located on a shallow water platform, but as consequence of a relative sea level rise, the depositional setting changed to a deeper slope setting in the latest Changhsingian. The continuous sedimentary succession is

represented by the Lopingian Wujiaping and Dalong Formations as well as the Early Triassic Daye Formation. With the depositional environment deepening during the Changhsingian, dark gray to black siliceous carbonates and cherts with sponge spicules and radiolarian tests (Dalong Formation) were deposited. The P-T transition is characterized by a volcanic ash bed followed by thinly bedded, in part dolomitic light gray carbonates and marls of the Early Triassic (Daye Formation). While some latest Permian and Early Triassic beds are rich in gastropods and show signs of bioturbation, most carbonates are laminated and lack fossils (**Figure 3**).

The Chanakhchi (former Sovetashen) section (39.8412 N, 45.0491 E) is located in Central Armenia close to the village of Zangakatun about 60 km southeast of the capital Yerevan. The area is part of the South Armenian Block belonging to the Anatolide-Tauride South Armenian microplate, which rifted northward from North Gondwana in the late Paleozoic (Meijers et al., 2015). During the P-T transition, the Cimmerian terranes were located at tropical latitudes and separated the opening Neo-Tethys to the south from the closing Paleo-Tethys to the north. The Changhsingian is characterized by irregularly bedded to nodular gray to reddish limestones (Paratirolites Beds) followed by thin reddish marls with thin lenticular limestone beds ("Boundary Clay") of the Akhura Formation. The latest Permian and basal Early Triassic are characterized by microbialites interfingering with reddish to gray micritic limestones. These are overlain by the Karabaglyar Formation, a monotonous succession of platy, non-bioturbated and partially laminated limestones of Griesbachian to Dienerian age. The prominent Early Triassic sponge microbial buildups suggest a platform environment between fair-weather and storm wave base during the earliest Triassic (Baud et al., 2007; Friesenbichler et al., 2018; Foster et al., 2020).

Samples

The sampling of the Chibi section started at the boundary between the Lopingian Wujiaping and Dalong Formations and reaches up a few meters into the Early Triassic Daye Formation (~14 m; **Figure 3**). Only fresh and unweathered hand specimens were collected bed by bed. One part of the samples was sent for thin section preparation while the other part was powdered for geochemical analyses. For the latter, weathered or altered surfaces as well as parts of the samples comprising diagenetic features like calcite veins were removed with a rock saw. After this, samples were crushed with a jaw crusher and ground to powder using an agate disc mill. Finally, powders were sieved passing through 125 µm and stored in polypropylene beakers.

Armenian samples were selected from an existing sample set taken in the Chanakhchi section during earlier field campaigns in 2011 and 2013 (Joachimski et al., 2020). The sampled interval covers the Lopingian Akhura Formation and the lower member of the Early Triassic Karabaglyar Formation (~44 m). Because samples were taken at a very high resolution, around 300 specimens were available. For this study 66 samples were selected in even intervals. Samples were put in a polypropylene sleeve and then crushed with a hammer. From the resulting rock chips fresh and unaltered rock pieces were picked manually. Selected rock chips were powdered with an agate ball mill. To ensure that no coarse grains remained within the powder, samples were sieved through 125 µm and stored in polypropylene beakers.

Stable Carbon Isotope Analyses

Carbonate powders of samples from the Chibi section were reacted with phosphoric acid at 70°C using a Gasbench II connected to a ThermoFisher Delta V Plus isotope ratio mass spectrometer (IRMS) at the GZN Erlangen. Reproducibility and accuracy were monitored by replicate analysis of in-house standards calibrated against NBS19 (1.95‰) and LSVEC (−46.6‰). Reproducibility for $\delta^{13}C$ was ±0.03‰ (1σ; n = 18). All values are reported in per mil ‰ using the standard delta notation ($\delta^{13}C$) relative to Vienna—Pee Dee Belemnite (V-PDB).

Quantification of Total Organic Carbon

For the determination of TOC contents, carbonate was removed by treating bulk rock powders with hydrochloric acid. About 5 g of each powdered sample were weighed into 250 ml glass beakers and approximately 200 ml of 10% HCl was added while carefully stirring with a glass rod. The beakers were then covered with a watch glass and placed on a hotplate at 50°C for a minimum of 12 h. The procedure was repeated in case there was still reaction observable after this time. Insoluble and carbonate free residues were repeatedly washed with deionized H_2O until the supernatant had a pH between 6 and 7. The insoluble residues were then transferred into pre-weighed evaporating dishes which were then placed into an oven at 50°C until they were dry and weights were constant. At last, the dry residues were homogenized with an agate pestle and mortar and stored in glass vials.

The organic carbon concentration of the insoluble residues was measured with a ThermoFisher Flash 2000 elemental analyzer connected to a Delta V Plus IRMS at the GZN Erlangen. Precision determined from replicate analyses of laboratory standards OAS (1.61% C) and Jon1 (0.44% C) was ±0.09% (1σ, n = 23) and ±0.05% (1σ, n = 5), respectively.

The TOC content of the original sample (TOC_{sample}) in % was calculated by multiplying the organic carbon concentration of the insoluble residues (OC_{res}) in % with the ratio between the weight of the insoluble residues (m_{res}) and the original samples (m_{sample}):

$$TOC_{sample} = OC_{res} \cdot \frac{m_{res}}{m_{sample}} \quad (1)$$

Sequential Phosphorus Extraction

In order to determine the concentration of bio-available or reactive P (P_{react}), we used the sequential phosphorus extraction method (SEDEX) developed by Ruttenberg (1992). The SEDEX technique enables to extract loosely adsorbed phosphorus (P_{ex}), P bound to Fe-oxyhydroxides (P_{Fe}), authigenic apatite-P (P_{auth}), detrital apatite-P (P_{det}), and P bound to organic matter (P_{org}) by treating sample powders with reagents of increasing "aggressivity" in five steps

TABLE 1 | Mean P concentrations in ppm of the different P species in replicate analyses of internal standard X1 (n = 8). 1σ - standard deviation, CV - coefficient of variation.

n = 8	Step I (sorbed)	Step III (authigenic)	Step IV (detrital)	Step V (organic)	P_{tot} (total)	P_{react} (reactive)
Mean	12.1	885.1	47.9	11.4	931.8	883.8
1σ	±9	±36	±17	±2	±46	±56
CV	73%	4%	36%	20%	5%	6%

(**Figure 4**). To avoid contamination only *p.a.* grade reagents and ultrapure (UP) H_2O (Merk MilliQ) were used. Additionally, all used glassware was cleaned in a 10% HCl bath for a minimum of 24 h and then rinsed three times with UP H_2O.

First, sample splits of about 100 mg were weighed into clean 50 ml polypropylene centrifuge tubes. To extract the P_{ex} fraction, the samples were treated with 10 ml $MgCl_2$ solution (1 mol L^{-1}, pH 8) twice for 2 h followed by a rinsing step with 10 ml UP H_2O for 1 h. After this, 15 ml of a citrate-bicarbonate solution (0.3 mol L^{-1}, 1 mol L^{-1}, pH 7.6) and 0.375 g sodium dithionite were added and centrifuge tubes were shaken for 8 h to extract P_{Fe}. Subsequently the residues were rinsed with 15 ml $MgCl_2$ solution for 2 h and with 10 ml UP H_2O for 1 h. This was followed by the extraction of P_{auth} using 10 ml of a sodium acetate buffer solution (1 mol L^{-1}, pH 4) for 6 h. Next, samples were rinsed with 10 ml $MgCl_2$ for 2 h and 10 ml UP H_2O for 1 h. After this, P_{det} was extracted from the residue by treating the residue with 1 M HCl for 16 h. Finally, the residues were transferred from the centrifuge tubes into glass vials and evaporated at 80°C in an oven. Once dry, 0.4 ml $MgNO_3$ solution (50% w v^{-1}) was added and the vials were placed in a furnace at 550°C for 2.5 h. Eventually, the ashed residues were treated with 10 ml 1 M HCl for another 16 h to extract P_{org}. To determine total P (P_{tot}) 0.4 ml $MgNO_3$ solution (50% w v^{-1}) was added to 100 mg sample splits in glass vials. Vials were placed in a furnace and samples were ashed for 2.5 h at 550°C. Residues were then treated with 1 M HCl for 16 h to extract P_{tot} (Aspila et al., 1976). It should be noted here that the P-fractions of the different steps are operationally defined and do not necessarily represent chemically discriminable entities.

To ensure that samples were in contact with the reagents throughout the procedure the powders must be kept suspended. This was accomplished by placing the centrifuge tubes onto a shaker table at a suitable speed. After each step the tubes were centrifuged at 4,000*g for 10 min and the supernatant solutions were decantated and filtered through 0.45 µm nylon syringe filters into clean 20 ml polyethylene bottles. The supernatants were then acidified with concentrated HCl and stored in a fridge until analysis.

Photometric Analyses

Concentrations of phosphate in the solutions generated by the SEDEX method (steps I, III, IV and V) were determined with the photometric ascorbic acid method developed by Murphy and Riley (1962). This method is based on the formation of a blue colored molybdate complex with the intensity of the blue color being proportional to the phosphate concentration in the solution.

For this, 100 µL of a mixing reagent (4.5 N sulfuric acid, 0.001 mol L^{-1} antimony potassium tartrate, 0.01 mol L^{-1} ammonium heptamolybdate) and 100 µL of an ascorbic acid solution (0.4 mol L^{-1}) were added to 3 ml of the diluted sample solution. Blue color was allowed to develop for 30 min and absorbance values were measured with a Hach & Lange, DR 2800 spectrophotometer at 880 nm in 1 cm disposable PS cells. Because of the reducing property of dithionite and the interfering organic ligands from the sodium citrate in the solution generated in step II (P_{Fe}), it is not possible to measure the phosphate concentrations using the ascorbic acid method (Ruttenberg, 1992). Instead P_{Fe} was obtained by subtraction (see below).

To calculate the phosphate concentrations from the measured absorbance values a standard calibration curve was established. Because interferences caused by the different reagents used in the SEDEX procedure may influence the measurement, matrix matched standard solutions were prepared from a phosphate stock solution (1,000 mg L^{-1} PO_4^{3-}). Linear regression analysis was performed by relating the concentration of phosphate in the standard solutions to the measured absorbance value. The resulting equation was used to calculate the concentrations in the sample solutions (fit better than R^2 = 0.99 in all cases). Sample solutions were diluted with 0.1 M HCl or H_2O UP to be bracketed by the concentrations of the respective standard solutions. Finally, the concentrations of the different phosphate fractions in the sample powders (c_{sample} in mg g^{-1}) were obtained from the concentration of the respective solutions (c_{sol} in mg L^{-1}), the volume of the solutions (V_{sol} in L) and the sample weights (m_{sample} in g) by following equation:

$$c_{sample} = \frac{c_{sol} \cdot V_{sol}}{m_{sample}} \quad (2)$$

To perform a background correction and to check for potential contamination during the SEDEX procedure two procedural blanks were included in each run of twelve samples. Average absorbance of the blank solutions was subtracted from the absorbance values of the samples prior to calculating concentrations. In order to estimate precision of the whole method an internal standard was processed and measured along every twelve samples (**Table 1**). Reproducibility for the concentration of P_{react} was ±0.06 mg g^{-1} (n = 8; RSD = 6%).

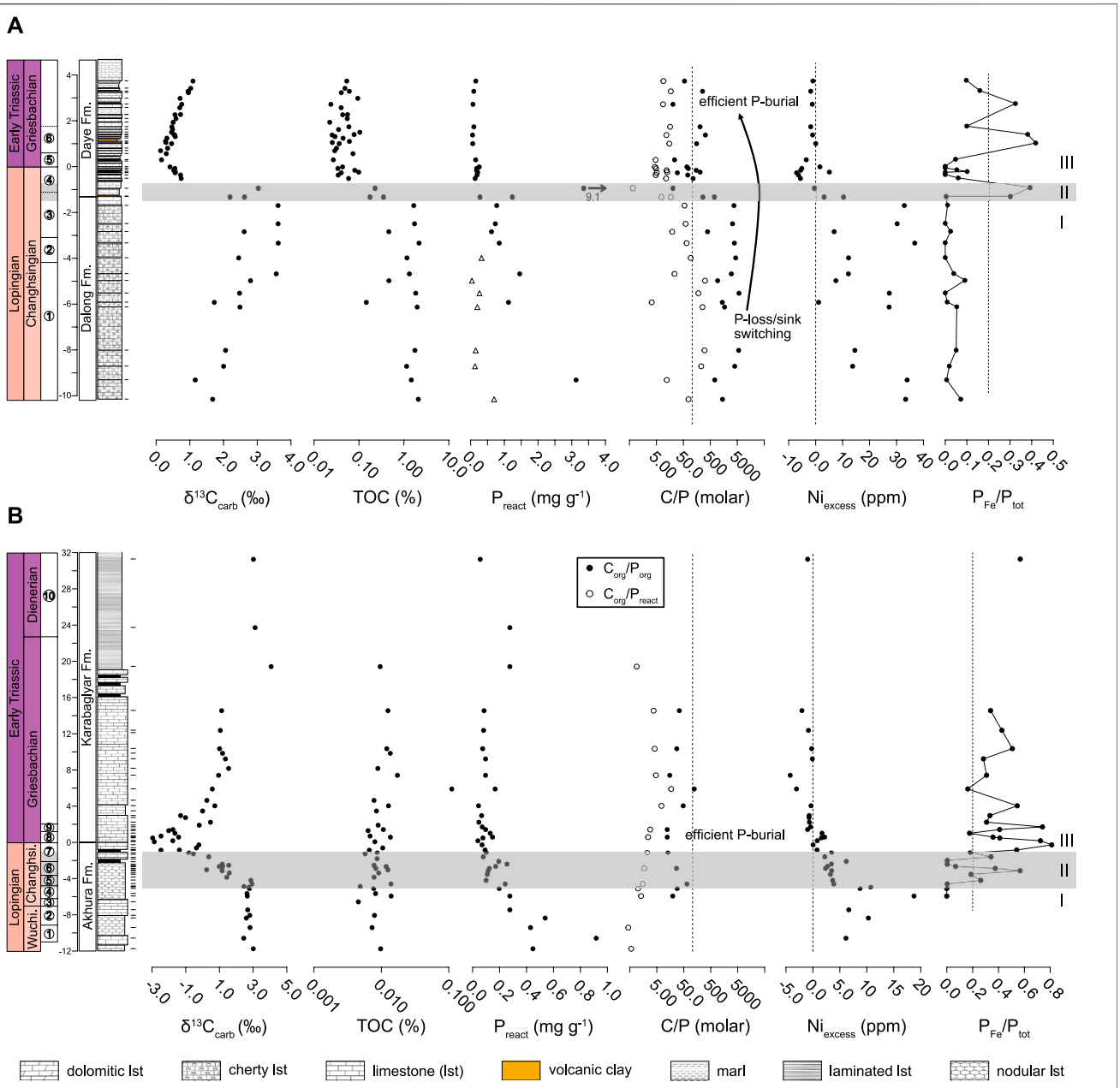

FIGURE 5 | $\delta^{13}C_{carb}$, TOC, P_{react}, C/P molar ratio, Ni_{excess} and P_{Fe}/P_{tot} for **(A)** Chibi and **(B)** Chanakhchi. Vertical dashed lines in C/P plots indicate average C/P of marine organic matter of 106 (Redfield et al., 1963). Grey bars represent transitional phase II defined by intermediate Ni_{excess} separating phase I and III. Conodont zonation and carbon isotopes for Chanakhchi from Joachimski et al. (2020). Conodont Zones at Chibi: 1 - *C. subcarinata*, 2 - *C. changxingensis*, 3 - *C. yini*, 4 - *H. praeparvus*, 5 - *H. parvus*, 6 - *I isarcica*. Conodont Zones at Chanakhchi: 1 - *C. transcaucasia*, 2 - *C. orientalis*, 3 - *C. subcarinata*, 4 - *C. bachmanni*, 5 - *C. nodosa*, 6 - *C. zhangi* to *C. hauschkei*, 7 - *H. praeparvus*, 8 - *H. parvus*, 9 - *I. isarcica*, 10 - *N. dieneri*. Vertical dashed lines in P_{Fe}/P_{tot} plot marks the defined 20% threshold. Triangles in the P_{react} plot for the Chibi section are samples affected by strong P loss indicated by high C/P_{react}.

Major and Trace Element Analyses and Calculation of Ni_{excess}

Bulk major and trace element concentrations were measured via ICP-AES and ICP-MS on bulk rock powders after lithium borate fusion and four acid digestion at ALS Global Ltd. Analytical precision was better than 10% (RSD). For the presentation of the Ni data, we used Ni_{excess} which is the concentration of bulk Ni minus terrigenous Ni. This was done because Ni in bulk rock samples should be comprised of a terrigenous and an authigenic fraction. Enrichment factors (EF = $(Ni/Al_{sample})/(Ni/Al_{PAAS})$) were not calculated because our samples were mainly carbonates and cherts and because the

TABLE 2 | Average geochemical values for phase I (*C. transcaucasia* to lower *C. yini*) and III (upper *H. praeparvus* to *N. dieneri*) in the Chibi section and inferred P burial efficiency and primary productivity states. Samples with negative Ni_{excess} are interpreted to reflect no enrichment.

	TOC (%)	Ni_{excess} (ppm)	P_{react} (mg/g)	P_{Fe}/P_{tot}	C/P_{org}	P burial eff.	Productivity
Phase I	1.4	20.7	0.8	0.03	~2,900	–	High
Phase III	0.05	–2.4	0.1	0.12	~130	+	Low

PAAS reference for EF calculation is a shale. Ni_{excess} values were calculated as

$$Ni_{excess} = Ni_{sample} - \left(Al_{sample} \cdot \left(Ni/Al\right)_{PAAS}\right) \quad (3)$$

where $(Ni/Al)_{PAAS}$ is the Ni to Al ratio of average Post-Archean Australian shale ($Ni/Al_{PAAS} = 5.49 \times 10^{-4}$; Taylor and McLennan, 1985). In principle, the calculation of excess contents assumes that the Ni content of the terrigenous input was close to PAAS and that there was no variation in Ni/Al over the studied time interval. Values <0 are interpreted to reflect no authigenic Ni enrichment.

Calculation of Reactive Phosphorus (P_{react}), Fe-Oxyhydroxide Bound Phosphorus (P_{Fe}), and C/P Molar Ratios

Assuming that all P species, except for P_{det}, were bioavailable before sedimentation, the concentration of P_{react} was calculated by subtracting the concentration of P_{det} from the concentration of P_{tot}:

$$P_{react} = P_{tot} - P_{det} \quad (4)$$

P_{Fe} was determined by subtracting all P fractions determined via the ascorbic acid method (steps I, III, IV and V) from P_{tot}:

$$P_{Fe} = P_{tot} - \left(P_{ex} + P_{auth} + P_{det} + P_{org}\right) \quad (5)$$

C/P molar ratios were calculated as follows:

$$C/P_{react} = \frac{C/M(C)}{P_{react}/M(P)} \quad (6)$$

$$C/P_{org} = \frac{C/M(C)}{P_{org}/M(P)} \quad (7)$$

where M(C) and M(P) are the molar masses of carbon and phosphorus, respectively.

RESULTS

Stable Carbon Isotopes

Changhsingian $\delta^{13}C_{carb}$ values in the Chibi section vary between 1.2 and 2.5‰ (avg. = 1.85‰, 1σ = ±0.45‰, *n* = 6; **Figure 5A**; **Supplementary Table S1**) until they start to increase at 5.83 m below the P-T boundary to values between 2.2 and 3.6‰ (avg. = 2.97‰, 1σ = ±0.55‰, *n* = 11). Values start to decrease sharply by almost 3‰ at 1.2 m below the P-T boundary (upper *C. yini* conodont Zone) to a minimum value of 0.1‰ at 0.63 m above the P-T boundary (*I. isarcica* Zone). This negative shift is followed by a gradual increase in $\delta^{13}C_{carb}$ in the Early Triassic with the stratigraphically highest sample showing a value of 1.1‰. For a discussion of the Chanakhchi carbon isotope record the reader is referred to Joachimski et al. (2020).

Total Organic Carbon and Ni_{excess}

In the lower part of the Chibi section, TOC values range from 0.15 to 2.17% (avg. = 1.39%, 1σ = ±0.64%, *n* = 14; **Figure 5A**; **Supplementary Table S1**). After this, they start to decrease 1.4 m below the P-T boundary (upper *C. yini* Zone) with average contents of 0.05% (1σ = ±0.02%, *n* = 32) measured from 0.6 m below the P-T boundary to the Early Triassic. Samples from the Chanakhchi section show average TOC contents of 0.01% (1σ = ±0.016%, *n* = 42) with only minor, statistically insignificant variation throughout the studied interval (**Figure 5B**; **Supplementary Table S2**). In general, such extremely low TOC contents should be treated with caution. Potentially, small flaws during sample preparation using the above-described method could result in artificially low values. Hence the TOC record from Chanakhchi is not interpreted in terms of relative changes because they are obviously below reproducibility of the data.

Ni_{excess} values in the Chibi section are between 1.1 and 36.7 ppm (avg. = 18.9 ppm, 1σ = ±12.4 ppm, *n* = 16; **Figure 5A**; **Supplementary Table S1**) in the lower part of the studied section (Changhsingian) and decrease to <0 at 1.2 m below the P-T boundary (*C. yini* to *H. praeparvus* Zone). Upsection Ni_{excess} increases slightly and values stabilize close to 0. High and variable Ni_{excess} values between 6.1 and 18.7 ppm (avg. = 10.2 ppm, 1σ = ±4.6 ppm, *n* = 6) are observed in the Chanakhchi section in the *C. transcaucasia* to *C. bachmanni* Zone (**Figure 5B**; **Supplementary Table S2**). Ni_{excess} starts to decrease 4.7 m below the P-T boundary and reaches values <0 in the uppermost *H. praeparvus* Zone. Upwards Ni_{excess} stays below 0 with two samples (Ch217 and Ch207) showing very negative values between the *I. isarcica* and *N. dieneri* zones.

Reactive Phosphorus (P_{react})

P_{react} in the latest Changhsingian of the Chibi section is highly variable with values between 0.04 and 1.46 mg g^{-1} (**Figure 5A**; **Supplementary Table S1**). Two exceptionally high values of 3.13 and 9.14 mg g^{-1} are observed at 9.4 and 1 m below the P-T boundary, respectively (samples Y14 and Z2). P_{react} contents decrease at 0.8 m below the P-T boundary (*H. praeparvus* Zone) and vary between 0.06 and 0.26 mg g^{-1} (avg. = 0.14 mg g^{-1}, 1σ = ±0.06 mg g^{-1}; *n* = 14) in the uppermost Changhsingian and Griesbachian. P_{react} in the Chanakhchi

TABLE 3 | Average geochemical values for phase I (*C. transcaucasia* to lower *C. yini*) and III (upper *H. praeparvus* to *N. dieneri*) in the Chanakhchi section and inferred P burial efficiency and primary productivity states.

	TOC (%)	Ni_{excess} (ppm)	P_{react} (mg/g)	P_{Fe}/P_{tot}	C/P_{org}	P burial eff.	Productivity
Phase I	0.01	10.2	0.4	0	~24	+	High
Phase III	0.01	−0.2	0.1	0.42	~40	+	Low

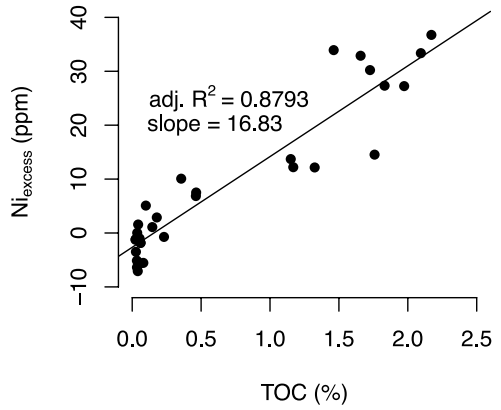

FIGURE 6 | Ni_{excess} versus TOC for the samples from Chibi section. Correlation suggests association of Ni with sedimentary organic matter, regression slope of ~16.8 indicates preferential preservation of Ni over organic matter.

section also exhibits a downward trend towards the P-T boundary, albeit the decrease in P_{react} appears more gradual than in the Chibi section (**Figure 5B**; **Supplementary Table S2**). The highest value of 0.92 mg g^{-1} is observed 10.6 m below the P-T boundary in the *C. transcaucasia* Zone (sample Ch37). Above this level, values decline gradually and vary around an average of 0.11 mg g^{-1} (1σ = ±0.06 mg g^{-1}, n = 36) in the *H. praeparvus* Zone and the Early Triassic. Hence, both sections show a significant decrease in P_{react} from the Lopingian into the Early Triassic.

Fe-Oxyhydroxide Bound Phosphorus (P_{Fe})

In both sections, the proportion of P_{Fe} relative to P_{tot}, expressed as the ratio P_{Fe}/P_{tot}, is elevated in specific time intervals (**Figure 5**). We used a P_{Fe}/P_{tot} ratio >0.2 to characterize intervals where P_{Fe} represents an important P fraction. This estimate is based on modern, global P burial flux calculations showing that P_{Fe} contributes ~20% to the total reactive P flux to the sediment (Ruttenberg, 1993). In the Chibi section, P_{Fe}/P_{tot} ratios >0.2 are observed in the *C. yini* to *H. praeparvus* Zones (1.4–1 m below the P-T boundary) and in the *I. isarcica* Zone (0.9–2.7 m above the P-T boundary). At Chanakhchi, $P_{Fe}/P_{tot} > 0.2$ are registered in the *C. nodosa* and *C. zhangi* Zones (4.1 and 2.9 m below the P-T boundary) and in an interval starting 1.6 m below the P-T boundary, from the *H. praeparvus* to the *N. dieneri* Zone (avg. = 0.42, 1σ = ±0.19, n = 22). In the latter interval, three samples show $P_{Fe}/P_{tot} < 0.2$. In all other samples, P_{Fe} is a minor fraction of P_{tot} with $P_{Fe}/P_{tot} < 0.2$.

C/P Molar Ratios

At Chibi, C/P_{org} ratios range from 254 to 5,780 (avg. = 2,576, 1σ = ±1861, n = 16) in the Changhsingian and start to decrease at 1.2 m below the P-T boundary (*C. yini* to *H. praeparvus* Zone; **Figure 5A**; **Supplementary Table S1**). Values in the uppermost Changhsingian and Griesbachian fluctuate between 20 and 328 (avg. = 119, 1σ = ±96, n = 15). C/P_{react} ratios are lower than the C/P_{org} ratios. C/P_{react} values are between 3 and 318 (avg. = 108, 1σ = ±112, n = 16) and decrease in parallel with C/P_{org} to low values between 1 and 17 (avg. = 9, 1σ = ±5, n = 15). At Chanakhchi, C/P ratios show no significant change but C/P_{org} values of 12–122 (avg. = 39, 1σ = ±31, n = 14) are higher than C/P_{react} values between 0 and 17 (avg. = 4, 1σ = ±4, n = 19) throughout the studied interval (**Figure 5B**; **Supplementary Table S2**).

DISCUSSION

For the discussion of the dataset, three temporal intervals are defined based on the stratigraphic variation in Ni_{excess}. Phase I (*C. transcaucasia* to lower *C. yini* Zone) is characterized by high TOC in the Chibi section and generally high Ni_{excess} values in both sections. Phase II (upper *C. yini* to lower *H. praeparvus* Zone) represents a transitional interval with decreasing, intermediate Ni_{excess} values, while during phase III (upper *H. praeparvus* to *N. dieneri* Zone), low TOC and low Ni_{excess} values are observed in both sections (see **Tables 2**, **3**).

Nickel as Paleoproductivity Proxy

TOC as a paleoproductivity proxy has major shortcomings since the TOC contents might be biased due to remineralization of organic matter in the water column, anaerobic decomposition of organic matter during diagenesis, and the dilution effect (e.g., Schoepfer et al., 2015). Thus, only a fraction of organic matter exported from surface waters sinks to the seafloor and is preserved in sediments. Ni_{excess} is used as another productivity proxy as it shows a nutrient-like distribution in the water column and, in case of anoxic conditions, is less prone to co-precipitation with sulfides compared to Cu, Cd, or Zn (Piper and Calvert, 2009). Furthermore, stable Ni isotope data suggests that the distribution of Ni in the water column is not affected by redox cycling (Yang et al., 2021). Recent studies showed that Ni and TOC are positively correlated in modern, superficial sediments regardless of redox conditions making Ni a robust and reliable productivity proxy (Böning et al., 2015; Steiner et al., 2017). For example, Steiner et al. (2017) were able to link anthropogenic nutrient fluxes and associated

productivity changes to sedimentary Ni concentrations in oxic sediments of the Gulf of Aqaba.

Ni_{excess} shows decreasing concentrations from phase I to phase III in both study sections (**Figure 5**). Ni_{excess} is positively correlated with TOC in the Chibi section (R^2 = 0.88, p < 0.001; **Figure 6**) suggesting that Ni was mainly shuttled to the sediment by sinking organic matter. The slope of the linear regression is 16.8 and thus higher than for modern core top sediments (~6–9; Böning et al., 2015) suggesting preferential preservation of Ni over TOC during sinking, burial, and diagenesis. Furthermore, this correlation indicates that the preservation factor of organic matter remained invariant over the studied interval in case of the Chibi section. In contrast, samples from the Chanakhchi section point towards lower preservation of organic matter in phase I, since we observe no change in TOC (~0.01%) but a decrease in Ni_{excess} from phase I to III. The decrease in Ni_{excess} in both sections is interpreted as the result of declining primary productivity in the Tethys Ocean starting in the *C. yini* Zone. For the following discussion Ni_{excess} values from Chanakhchi serve as a surrogate for the primary TOC content of the sediment, i.e., Chanakhchi samples with high Ni_{excess} are interpreted to reflect a high organic matter sinking flux and vice versa.

In this study we use Ni contents as a proxy for the sinking flux of organic matter because Ni is an essential nutrient for photosynthesizing organisms. However, an alternative source of Ni could be through the deposition of Ni-rich aerosols released to the atmosphere during Siberian Traps volcanism (Le Vaillant et al., 2017). Indeed, peaks in Ni contents coinciding with the negative shift in $\delta^{13}C$ were reported for several P-T sections (Rothman et al., 2014; Rampino et al., 2017; Li et al., 2021). Furthermore, Li et al. (2021) found that Ni-rich beds of the Buchanan Lake section exhibit extremely light Ni stable isotopic compositions corroborating a volcanogenic signature ($\delta^{60}Ni$ down to −1.09‰). In contrast the Ni-records from Chibi and Chanakhchi are not showing such a relationship, i.e., Ni contents are already low when the negative excursion in $\delta^{13}C$ starts (**Figure 5**). Hence, we argue that the Lopingian high Ni_{excess} values of this study are unrelated to P-T volcanism and reflect high organic matter sinking fluxes.

P Scavenging From the Water Column

In the case of anoxic conditions and Fe-oxide reduction, P bound to Fe-oxides will be released to the water column or porewaters and potentially reprecipitated as authigenic P-minerals (sink switching; Paytan and McLaughlin, 2007). The increase in P_{Fe}/P_{tot} from phase I to II (**Figure 5**) coincides with the observed decrease in Ni_{excess} in both sections. At Chibi, TOC decreases with rising P_{Fe}/P_{tot}. Hence the data show an inverse relationship and two cases can be differentiated. Samples from Chanakhchi with low P_{Fe}/P_{tot} show high Ni_{excess} while high P_{Fe}/P_{tot} appears together with low Ni_{excess} and TOC. At Chibi the same relationship is observed for P_{Fe}/P_{tot} and Ni_{excess} and additionally samples with low P_{Fe}/P_{tot} show high TOC contents.

This pattern has been observed as well in modern sediments from the California continental margin where sediments are deposited in low O_2 bottom waters and P is either released or sequestered with Fe-oxides depending on the amount of organic matter remineralization (McManus et al., 1997). P is sequestered into the sediment when little organic matter is available for decomposition and vice versa. McManus et al. (1997) attribute this to the presence of a ferric layer within the upper part of the sediments providing sites for P adsorption. The ferric layer only develops if O_2 consumption through organic matter remineralization is not too high and the depth of O_2 penetration is intermediate.

Relatively high TOC and/or Ni_{excess} values in combination with minor or absent P_{Fe} contents in phase I samples indicate the release of P_{Fe} during the reductive dissolution of Fe-oxides in a sediment where free oxygen was effectively consumed by organic matter degradation which shifted sediment redox conditions below the zone of Fe^{3+} reduction (further supported by high C/P_{react} at Chibi). In contrast, O_2 consumption through organic matter remineralization was likely minor in phases II and III as signaled by low sedimentary TOC and/or Ni_{excess}. Redox conditions not below the zone of nitrate or Mn^{4+} reduction would have favored the formation of ferric layers which served as an efficient P sink (further supported by low C/P_{react}). This can explain the preservation of high P_{Fe} proportions in the phase III samples.

Benthic P Regeneration and/or Reduced P-Shuttle

Both sections show a significant decrease in average P_{react} concentrations from phase I to phase III (**Figure 5**; **Tables 2**, **3**). This decrease can be explained either by benthic P regeneration causing a decrease in the P burial efficiency and therefore low P contents in sediments (Ingall and Jahnke, 1994) or a lower primary productivity since, besides Fe-oxyhydroxide, organic matter is the main shuttle of reactive P to the sediment (Paytan and McLaughlin, 2007).

Studies on modern, subrecent and deep time sediments have shown that P is preferentially released from the sediment to the water column under anoxic conditions (e.g., Van Cappellen and Ingall, 1994; Filippelli et al., 2003; Mort et al., 2007; Fantasia et al., 2018; Schobben et al., 2020). While the release of P_{Fe} is in the form of reductive dissolution of Fe-oxides, the enhanced release of P_{org} seems to be microbially mediated; i.e., the bacterial sequestration of P into stable polyphosphates is less efficient under anoxic conditions because only some P-accumulating bacteria are able to utilize nitrate as an electron acceptor for this process (Kerrn-Jespersen and Henze, 1993). In the case where dissolved P is transferred to the euphotic zone e.g., by diffusion, mixing of the water column or upwelling, it can be utilized by phytoplankton. In such case, P may increase primary productivity, expand the oxygen-minimum zone, and reinforce the sinking flux of organic carbon in a positive feedback loop (Van Cappellen and Ingall, 1994; Mort et al., 2007). The efficiency of water column mixing depends on the wind intensity, the depth of the thermocline, and the degree of thermal stratification (Kämpf and Chapman, 2016). Substantial warming from the latest Permian into the Early Triassic (e.g., Joachimski et al., 2012; Joachimski et al., 2020) likely resulted in decreased wind stress, a deeper thermocline, and

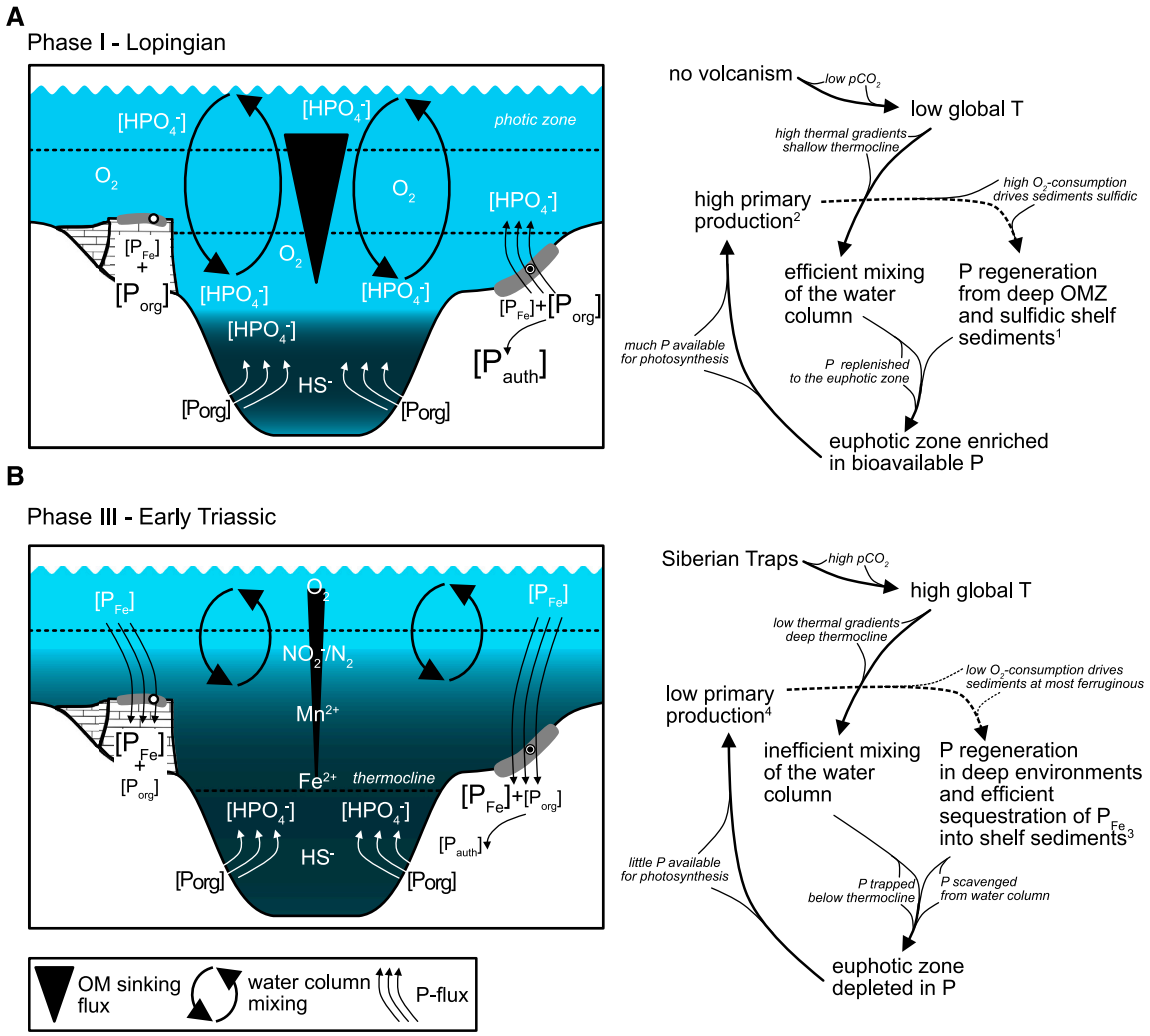

FIGURE 7 | Model for P cycling illustrating inferred decrease in primary productivity in the latest Permian. **(A)** Phase I - Lopingian: efficient mixing of the water column and nutrient recycling sustaining primary productivity. **(B)** Phase III - Early Triassic: redox stratified water column with inefficient nutrient recycling and low levels of primary production. Superscripts refer to geochemical evidence: 1) $C/P_{org} > 106$ and low P_{Fe}/P_{tot}; 2) high TOC, P_{react}, and Ni_{excess}; 3) $C/P_{org} \approx 106$, $C/P_{react} < 106$, and high P_{Fe}/P_{tot}; 4) low TOC, P_{react}, and Ni_{excess}.

enhanced stratification of the water column (e.g., Hotinski et al., 2001; Kidder and Worsley, 2004). Hence, we argue that the vertical P-shuttle was likely less efficient during the latest Permian to Early Triassic, leading to P-trapping in a large deep water P-reservoir (Penn et al., 2018).

P_{react} concentrations are comparably variable (0.04–1.46 mg g^{-1}) during phase I in the Chibi section (**Figure 5A**). Filippelli et al. (2003) explained varying P_{react} concentrations in late Miocene sapropels as a consequence of precessional wind systems resulting in alternating water column stratification (low productivity, low particulate organic matter (POM)-shuttle, low net P-burial, high P-release, low P_{react}, P accumulation in deep water) and intense upwelling (high productivity, high POM-shuttle, high net P-burial, low P-release, P recycled to euphotic zone). This scenario is likely an analogue for phase I at Chibi. Accordingly, low P_{react} values would correspond to intervals with low productivity and P accumulation whereas higher P_{react} values would correspond to intervals with high productivity where deep-water P was effectively replenished to the euphotic zone through water column mixing. In phase III, P_{react} is low (avg. = 0.14 mg g^{-1}) and less variable, again, pointing to enhanced water column stratification in the tropical Tethyan realm.

The molar ratio of organic carbon versus P_{org} and P_{react} (C/P_{org} and C/P_{react}) is used as an additional proxy to reconstruct benthic P-regeneration, the transfer of P into authigenic phases and hence the burial efficiency of P. While sinking organic matter has a stoichiometrical C/P ratio of 106 (Redfield et al., 1963), after sedimentation under anoxic conditions, P might be preferentially released increasing the C/P ratio of refractory organic matter to

>106 (Ingall et al., 1993). Released P can either be transferred to the upper water column where it can be re-used by primary production or precipitated as authigenic phosphate in the sediment (Paytan and McLaughlin, 2007). The latter mechanism is able to decrease C/P_{react} ratios to <106 since authigenic phosphate contributes to the P_{react} pool.

C/P_{org} ratios from the Chibi section are consistently >106 in phase I, indicating P loss during the deposition and burial of organic matter (**Figure 5A**). Intervals with C/P_{org} > 106 and C/P_{react} < 106 are characterized by sink switching processes, i.e., the transfer of P_{org} and P_{Fe} to authigenic carbonate fluorapatite. C/P_{org} and C/P_{react} > 106 can be attributed to intervals with strong P loss to the water column continuously depleting refractory organic matter with respect to P. P_{react} values below stoichiometrically possible concentrations of sinking organic matter are generated by this process in samples showing relatively high C/P_{react} ratios. Hence efficient P-recycling likely sustained high primary productivity levels in phase I. C/P_{org} ratios ≤106 in phase III suggest that efficient burial of P_{org} with benthic P-regeneration was likely inhibited. Low P_{react} concentrations together with C/P_{react} < 106 in phase III document a reduced organic matter shuttle. The high proportion of P_{Fe} in phase III can explain C/P_{react} < 106 because the P_{Fe} sink is decoupled from carbon cycling (see *P Scavenging From the Water Column*; McManus et al., 1997; Paytan and McLaughlin, 2007).

In Chanakhchi C/P_{org} is <106 and C/P_{react} is <106 throughout the sampled interval (**Figure 5B**). Like in Chibi, the latter is explained by the relatively high proportion of P_{Fe}. C/P_{org} < 106 indicates that there was neither an active sink switch nor P loss to the water column, thus burial efficiency was high at any given time. As previously noted, sample preparation as well as organic matter remineralization might have affected C/P ratios by lowering TOC contents. However, if TOC contents were 10 times higher the calculation of C/P ratios would still give values indicative of efficient P burial.

Changes in Primary Productivity Across the P-T Boundary

A conceptual model was developed to explain changes in marine P cycling in the Tethys across the P-T boundary (**Figure 7**). Primary productivity was comparably high during the Lopingian (phase I), started to decline in the upper *C. yini* conodont Zone (phase II) and was at lower levels during the final Changhsingian and subsequent Early Triassic (phase III; Jiang et al., 2007; Chen et al., 2015). This interpretation is based on the observation that TOC and Ni_{excess} (at Chanakhchi only Ni_{excess}) contents decrease significantly across the transitional phase II and the assumption that the two proxies behave proportional to the organic matter sinking flux and thus primary productivity.

High productivity in the tropical Tethys Ocean during the Lopingian is indicated by high P_{react} concentrations in both sections. P burial efficiency was low at Chibi but high at Chanakhchi as suggested from C/P ratios. This suggests that at Chibi a large part of the sedimentary P delivered by sinking organic matter and Fe-oxides was lost to the water column or transferred to authigenic P phases under O_2 deficient conditions driven by organic matter remineralization. Because mixing of surface and bottom waters was likely more efficient during the cooler climatic conditions of the Permian, recycled P was replenished to the euphotic zone, fueling photosynthesis and sustaining productivity on equatorial shelfs. This eventually led to the observed enrichment of authigenic P. However, low C/P ratios at Chanakhchi indicate that sedimentary P was not recycled but buried efficiently in shallow platform environments.

Low P_{react} concentrations together with low C/P_{org} ratios indicate efficient P burial, corroborating the latest Permian to Early Triassic low productivity scenario for the tropical Tethys. Although there was no P loss from the sediment, concentrations of P_{react} are low at both sites. Under the exceptional warmth of the Early Triassic, vertical mixing in the water column was probably inhibited when a deep thermocline was developed (Kidder and Worsley, 2004; Grasby et al., 2016; Grasby et al., 2020). Hence, although it is possible that P-regeneration occurred in other euxinic deeper water settings, P still would have been trapped in bottom waters.

P_{Fe} became a relatively important P sink in the latest Permian to Early Triassic (phase III). P trapping in bottom waters combined with Fe-oxide associated scavenging of bioavailable P from the water column and efficient burial in shelf and platform sediments possibly caused P depletion in the euphotic zone of the Tethys Ocean. A prerequisite for such scenario is that bottom waters and sediment redox conditions did not exceed the ferruginous zone. This is plausible since there was probably no significant O_2 consumption via organic matter remineralization to shift redox conditions into the sulfidic zone (TOC is low; anoxia is controlled by stratification). Furthermore, this interpretation is consistent with modeling and geochemical studies pointing towards less severe O_2 depletion in the upper water column of the tropical oceans (Clarkson et al., 2016; Penn et al., 2018). These conditions might have been similar to pre-Cryogenian oceans when pervasive ferruginous conditions resulted in enhanced scavenging of P from surface waters and low P burial on continental margins in the form of authigenic phosphates (Reinhard et al., 2017). Accordingly, we argue that, during the latest Permian to Early Triassic (phase III), the water column in the low-latitude Tethys was characterized by warm oligotrophic surface waters with nutrient trapping occurring in deeper anoxic waters (Grasby et al., 2016). P shuttling to the sediment diminished with the decrease in marine primary productivity (Algeo et al., 2013).

According to this model, an eutrophication scenario in the Tethys Ocean is untenable. Schobben et al. (2020) argued for a boost in primary productivity followed by eutrophication as a consequence of enhanced nutrient input and P recycling. The dataset, spanning the extinction interval to the Early Triassic, was acquired in a mid-latitude setting at the northern margin of Pangea (Deltadalen and Festningen, Spitsbergen). On the

other hand, stable nitrogen isotopes from the same region (Festningen; Grasby et al., 2020) and from virtually all P-T boundary sections exhibit a significant decrease in $\delta^{15}N$ across the extinction interval, indicating a shift to dominance of diazotrophic metabolism and a substantial decrease in the oceanic nutrient-N inventory, leading to oligotrophic oceans (e.g., Schoepfer, 2013; Sun et al., 2019). This discrepancy in interpretations is due to either the application of different proxies, or simply to the fact that there are contrasts between distal and proximal sites in respect to nutrient influx. However, a collapse of primary productivity is documented not only in northern low- and mid-latitudes, but also in the southern mid-latitude oceans (Sun et al., 2021). In general, regional differences in the effect of global warming on marine primary productivity are to be expected, given that climate models predictions for the modern ocean are spatially heterogenous (e.g., Mora et al., 2013).

Decline of Primary Production and its Effects on Marine Food Webs

In both sections, the transitional phase II starts slightly earlier than the onset of the negative carbon isotope excursion and ends before the $\delta^{13}C_{carb}$ curves reach their minima in the *H. parvus* Zone (**Figure 5**). Thus, in both sections, the decline in primary productivity coincides with the major part of the negative shift in $\delta^{13}C_{carb}$. Using the radiometric ages from the Meishan GSSP section, conodont biozonation and assuming constant sedimentation rate, it can be estimated that primary productivity started to decrease approximately 30 ka before the main extinction interval (Jiang et al., 2007; Burgess et al., 2014; Chen et al., 2015). Since marine primary producers constitute the base of marine food webs, their decline likely imposed negative effects on higher trophic levels.

Body size reduction and biodiversity losses among marine heterotrophic organisms have been reported for the pre-extinction interval. For example, brachiopods from South China show miniaturization starting in the *C. yini* Zone and community turnover occurred prior to the onset of the main phase of marine extinction (Zhang et al., 2016). Besides higher water temperatures or lower oxygen levels, declining primary productivity serves as an explanation for miniaturization since reduced body size can be an adaptation to a decrease in food supply (e.g., Yasuda et al., 2016). Sponge spicules exhibit a significant decline in abundance, size and morphological diversity in an interval corresponding to the upper *C. yini* conodont Zone (Liu et al., 2013). Radiolarians suffered significant diversity loss before the extinction with ~53% of species and ~22% of genera going extinct in the *C. yini* Zone (Meishan Bed 24d; Feng et al., 2007). A first extinction pulse among *Albaillella* observed in pelagic sections from Japan can be correlated with the aforementioned event (Wenchen et al., 2004). In the western Tethys, ammonoids from Iran exhibit an extinction pulse as well as declining morphological complexity and body size (pedomorphosis) in the *Paratirolites kittli* ammonoid Zone which is equivalent to the *C. yini* conodont Zone (Kiessling et al., 2018). However, the authors erroneously claimed that this deterioration started 700 ka before the extinction not taking into account radiometric ages from the Meishan section indicating that the onset of the *C. yini* Zone is significantly younger (Burgess et al., 2014).

Hence, the decrease in primary productivity in the tropical Tethys can be temporally correlated with the prelude of the extinction. However, at least in some regions, oxygen availability in the water column decreased at the same time (e.g., Clarkson et al., 2016). Hence, the expansion of oxygen minimum zones is an equally valid explanation. In general, anoxia directly stresses marine organisms by narrowing suitable habitats for sensitive species. Considering an inverse relationship between marine primary productivity and anoxia under warming climatic conditions it turns out that both are inextricably connected (Keeling et al., 2010). This is because mixing of oxygenated and nutrient-poor surface waters with deoxygenated and nutrient-rich deeper waters is diminished when water column stratification becomes stronger.

SUMMARY

Downward trends in sedimentary productivity proxies (TOC, Ni_{excess}, and P_{react}) from two Tethyan successions suggest a reduction of the organic matter sinking flux due to a decrease of marine primary productivity from the Lopingian to the Early Triassic. This commenced in the upper *C. yini* conodont Zone 30 ka before the main marine extinction level. C/P ratios indicate a switch from efficient P-recycling during the Lopingian normal productivity interval to efficient P-burial during the low productivity interval with Fe-oxides becoming a major P sink in the Early Triassic.

The decrease in primary productivity in the equatorial Tethyan realm can be explained by the concomitant effects of global warming across the P-T boundary, in particular enhanced stratification of the water column and a deepened thermocline leading to a state of inefficient P recycling. Hence, the latest Permian and Early Triassic Tethys was characterized by nutrient-poor surface waters while deep waters were probably enriched in P released from pelagic euxinic sediments. Potentially, the described developments reflect the onset of the Early Triassic Phosphorite gap, i.e., the lacking deposition of P-rich marine sediments for almost 5 Ma due to nutrient stress (Trappe, 1994). While this was demonstrated for the western, northern and eastern margins of Pangea (Schoepfer, 2013; Grasby et al., 2016; Grasby et al., 2020; Sun et al., 2021) our results suggest a similar oligotrophication scenario for the tropical Tethys Ocean.

The resulting food shortage may explain coincident extinction pulses, reductions in body size and pedomorphosis among heterotrophic organisms particularly in the tropical Tethys before and during the end-Permian mass extinction interval as well as during the protracted recovery phase.

DATA AVAILABILITY STATEMENT

The original contributions presented in the study are included in the article/**Supplementary Material**, further inquiries can be directed to the corresponding authors.

AUTHOR CONTRIBUTIONS

JM designed the study, generated, and analyzed the datasets and wrote the manuscript. YS designed the study and revised the manuscript. FY and AF generated and analyzed data. MJ designed the study, revised the manuscript, and is the project administration.

FUNDING

The National Natural Science Foundation of China (grant no. 41821001) supported this study. This is a contribution to German Research Foundation (DFG) Research Unit TERSANE (FOR 2332: Temperature-related stressors as a unifying principle in ancient extinctions; Project Jo 219/16-1).

ACKNOWLEDGMENTS

We acknowledge logistic support and advice during fieldwork in South China by Prof. Y.B. Wang (CUG Wuhan) who sadly passed away in early 2021 before this study was accomplished. We thank Thierry Adatte (University of Lausanne/Switzerland) for kindly granting access to the phosphorus lab at UNIL and Daniele Lutz (FAU Erlangen-Nürnberg) for measuring carbon isotopes and organic carbon contents. Tan Wang and Yujun Bao (CUG Wuhan) are acknowledged for great help with collecting samples from the Chibi section. Johannes Barth, Christian Hanke, and Robert van Geldern (FAU Erlangen-Nürnberg) are thanked for analytical support. Furthermore, we thank two reviewers for their constructive comments.

SUPPLEMENTARY MATERIAL

The Supplementary Material for this article can be found online at: https://www.frontiersin.org/articles/10.3389/feart.2022.832308/full#supplementary-material

REFERENCES

Algeo, T. J., and Twitchett, R. J. (2010). Anomalous Early Triassic Sediment Fluxes Due to Elevated Weathering Rates and Their Biological Consequences. *Geology* 38, 1023–1026. doi:10.1130/G31203.1

Algeo, T. J., Henderson, C. M., Tong, J., Feng, Q., Yin, H., and Tyson, R. V. (2013). Plankton and Productivity during the Permian-Triassic Boundary Crisis: An Analysis of Organic Carbon Fluxes. *Glob. Planet. Change* 105, 52–67. doi:10.1016/j.gloplacha.2012.02.008

Aspila, K. I., Agemian, H., and Chau, A. S. Y. (1976). A Semi-automated Method for the Determination of Inorganic, Organic and Total Phosphate in Sediments. *Analyst* 101, 187–197. doi:10.1039/an9760100187

Bambach, R. K., Knoll, A. H., and Wang, S. C. (2004). Origination, Extinction, and Mass Depletions of marine Diversity. *Paleobiology* 30, 522–542. doi:10.1666/0094-8373(2004)030<0522:oeamdo>2.0.co;2

Baud, A., Richoz, S., and Pruss, S. (2007). The Lower Triassic Anachronistic Carbonate Facies in Space and Time. *Glob. Planet. Change* 55, 81–89. doi:10.1016/j.gloplacha.2006.06.008

Behrenfeld, M. J., O'Malley, R. T., Siegel, D. A., McClain, C. R., Sarmiento, J. L., Feldman, G. C., et al. (2006). Climate-Driven Trends in Contemporary Ocean Productivity. *Nature* 444, 752–755. doi:10.1038/nature05317

Böning, P., Shaw, T., Pahnke, K., and Brumsack, H.-J. (2015). Nickel as Indicator of Fresh Organic Matter in Upwelling Sediments. *Geochim. Cosmochim. Acta* 162, 99–108. doi:10.1016/j.gca.2015.04.027

Bond, D. P. G., and Grasby, S. E. (2017). On the Causes of Mass Extinctions. *Palaeogeogr. Palaeoclimatol. Palaeoecol.* 478, 3–29. doi:10.1016/j.palaeo.2016.11.005

Bopp, L., Resplandy, L., Orr, J. C., Doney, S. C., Dunne, J. P., Gehlen, M., et al. (2013). Multiple Stressors of Ocean Ecosystems in the 21st century: Projections with CMIP5 Models. *Biogeosciences* 444, 6225–6245. doi:10.5194/bg-10-6225-2013

Boyd, P. W., Sundby, S., and Pörtner, H.-O. (2014). "Cross-Chapter Box on Net Primary Production in the Ocean," in *Climate Change 2014: Impacts, Adaptation, and Vulnerability. Part A: Global and Sectoral Aspects. Contribution of Working Group II to the Fifth Assessment Report of the Intergovernmental Panel of Climate Change* (Cambridge University Press), 133–136.

Burgess, S. D., Bowring, S., and Shen, S.-z. (2014). High-precision Timeline for Earth's Most Severe Extinction. *Proc. Natl. Acad. Sci. USA* 111, 3316–3321. doi:10.1073/pnas.1317692111

Burgess, S. D., Muirhead, J. D., and Bowring, S. A. (2017). Initial Pulse of Siberian Traps Sills as the Trigger of the End-Permian Mass Extinction. *Nat. Commun.* 8, 164. doi:10.1038/s41467-017-00083-9

Burnett, W. C., Beers, M. J., and Roe, K. K. (1982). Growth Rates of Phosphate Nodules from the Continental Margin off Peru. *Science* 215, 1616–1618. doi:10.1126/science.215.4540.1616

Chen, Z.-Q., Yang, H., Luo, M., Benton, M. J., Kaiho, K., Zhao, L., et al. (2015). Complete Biotic and Sedimentary Records of the Permian-Triassic Transition from Meishan Section, South China: Ecologically Assessing Mass Extinction and its Aftermath. *Earth-Science Rev.* 149, 67–107. doi:10.1016/j.earscirev.2014.10.005

Chen, J., Shen, S.-z., Zhang, Y.-c., Angiolini, L., Gorgij, M. N., Crippa, G., et al. (2020). Abrupt Warming in the Latest Permian Detected Using High-Resolution *In Situ* Oxygen Isotopes of Conodont Apatite from Abadeh, central Iran. *Palaeogeogr. Palaeoclimatol. Palaeoecol.* 560, 109973. doi:10.1016/j.palaeo.2020.109973

Clarkson, M. O., Wood, R. A., Poulton, S. W., Richoz, S., Newton, R. J., Kasemann, S. A., et al. (2016). Dynamic Anoxic Ferruginous Conditions during the End-Permian Mass Extinction and Recovery. *Nat. Commun.* 7, 12236. doi:10.1038/ncomms12236

Fantasia, A., Föllmi, K. B., Adatte, T., Spangenberg, J. E., and Montero-Serrano, J.-C. (2018). The Early Toarcian Oceanic Anoxic Event: Paleoenvironmental and Paleoclimatic Change across the Alpine Tethys (Switzerland). *Glob. Planet. Change* 162, 53–68. doi:10.1016/j.gloplacha.2018.01.008

Feng, Q., He, W., Gu, S., Meng, Y., Jin, Y., and Zhang, F. (2007). Radiolarian Evolution during the Latest Permian in South China. *Glob. Planet. Change* 55, 177–192. doi:10.1016/j.gloplacha.2006.06.012

Filippelli, G. M., Sierro, F. J., Flores, J. A., Vázquez, A., Utrilla, R., Pérez-Folgado, M., et al. (2003). A Sediment-Nutrient-Oxygen Feedback Responsible for Productivity Variations in Late Miocene Sapropel Sequences of the Western Mediterranean. *Palaeogeogr. Palaeoclimatol. Palaeoecol.* 190, 335–348. doi:10.1016/S0031-0182(02)00613-2

Foster, W. J., Heindel, K., Richoz, S., Gliwa, J., Lehrmann, D. J., Baud, A., et al. (2020). Suppressed Competitive Exclusion Enabled the Proliferation of Permian/Triassic Boundary Microbialites. *Depositional Rec.* 6, 62–74. doi:10.1002/dep2.97

Friesenbichler, E., Richoz, S., Baud, A., Krystyn, L., Sahakyan, L., Vardanyan, S., et al. (2018). Sponge-microbial Build-Ups from the Lowermost Triassic Chanakhchi Section in Southern Armenia: Microfacies and Stable Carbon Isotopes. *Palaeogeogr. Palaeoclimatol. Palaeoecol.* 490, 653–672. doi:10.1016/j.palaeo.2017.11.056

Grasby, S. E., Beauchamp, B., Embry, A., and Sanei, H. (2013). Recurrent Early Triassic Ocean Anoxia. *Geology* 41, 175–178. doi:10.1130/g33599.1

Grasby, S. E., Beauchamp, B., and Knies, J. (2016). Early Triassic Productivity Crises Delayed Recovery from World's Worst Mass Extinction. *Geology* 44, 779–782. doi:10.1130/G38141.1

Grasby, S. E., Knies, J., Beauchamp, B., Bond, D. P. G., Wignall, P., and Sun, Y. (2020). Global Warming Leads to Early Triassic Nutrient Stress across Northern Pangea. *Geol. Soc. Am. Bull.* 132, 943–954. doi:10.1130/b32036.1

Hotinski, R. M., Bice, K. L., Kump, L. R., Najjar, R. G., and Arthur, M. A. (2001). Ocean Stagnation and End-Permian Anoxia. *Geology* 29, 7. doi:10.1130/0091-7613(2001)029<0007:osaepa>2.0.co;2

Ingall, E., and Jahnke, R. (1994). Evidence for Enhanced Phosphorus Regeneration from marine Sediments Overlain by Oxygen Depleted Waters. *Geochim. Cosmochim. Acta* 58, 2571–2575. doi:10.1016/0016-7037(94)90033-7

Ingall, E. D., Bustin, R. M., and Van Cappellen, P. (1993). Influence of Water Column Anoxia on the Burial and Preservation of Carbon and Phosphorus in marine Shales. *Geochim. Cosmochim. Acta* 57, 303–316. doi:10.1016/0016-7037(93)90433-W

Isozaki, Y. (1997). Permo-Triassic Boundary Superanoxia and Stratified Superocean: Records from Lost Deep Sea. *Science* 276, 235–238. doi:10.1126/science.276.5310.235

Jiang, H., Lai, X., Luo, G., Aldridge, R., Zhang, K., and Wignall, P. (2007). Restudy of Conodont Zonation and Evolution across the P/T Boundary at Meishan Section, Changxing, Zhejiang, China. *Glob. Planet. Change* 55, 39–55. doi:10.1016/j.gloplacha.2006.06.007

Joachimski, M. M., Lai, X., Shen, S., Jiang, H., Luo, G., Chen, B., et al. (2012). Climate Warming in the Latest Permian and the Permian-Triassic Mass Extinction. *Geology* 40, 195–198. doi:10.1130/G32707.1

Joachimski, M. M., Alekseev, A. S., Grigoryan, A., and Gatovsky, Y. A. (2020). Siberian Trap Volcanism, Global Warming and the Permian-Triassic Mass Extinction: New Insights from Armenian Permian-Triassic Sections. *Geol. Soc. Am. Bull.* 132, 427–443. doi:10.1130/B35108.1

Kämpf, J., and Chapman, P. (2016). *Upwelling Systems of the World*. Cham: Springer International Publishing. doi:10.1007/978-3-319-42524-5

Keeling, R. F., Körtzinger, A., and Gruber, N. (2010). Ocean Deoxygenation in a Warming World. *Annu. Rev. Mar. Sci.* 2, 199–229. doi:10.1146/annurev.marine.010908.163855

Kerrn-Jespersen, J. P., and Henze, M. (1993). Biological Phosphorus Uptake under Anoxic and Aerobic Conditions. *Water Res.* 27, 617–624. doi:10.1016/0043-1354(93)90171-D

Kidder, D. L., and Worsley, T. R. (2004). Causes and Consequences of Extreme Permo-Triassic Warming to Globally Equable Climate and Relation to the Permo-Triassic Extinction and Recovery. *Palaeogeogr. Palaeoclimatol. Palaeoecol.* 203, 207–237. doi:10.1016/S0031-0182(03)00667-9

Kiessling, W., Schobben, M., Ghaderi, A., Hairapetian, V., Leda, L., and Korn, D. (2018). Pre-mass Extinction Decline of Latest Permian Ammonoids. *Geology* 46, 283–286. doi:10.1130/G39866.1

Kocsis, Á. T., and Scotese, C. R. (2021). Mapping Paleocoastlines and continental Flooding during the Phanerozoic. *Earth-Science Rev.* 213, 103463. doi:10.1016/j.earscirev.2020.103463

Korte, C., and Kozur, H. W. (2010). Carbon-isotope Stratigraphy across the Permian-Triassic Boundary: A Review. *J. Asian Earth Sci.* 39, 215–235. doi:10.1016/j.jseaes.2010.01.005

Korte, C., Pande, P., Kalia, P., Kozur, H. W., Joachimski, M. M., and Oberhänsli, H. (2010). Massive Volcanism at the Permian-Triassic Boundary and its Impact on the Isotopic Composition of the Ocean and Atmosphere. *J. Asian Earth Sci.* 37, 293–311. doi:10.1016/j.jseaes.2009.08.012

Lau, K. V., Maher, K., Altiner, D., Kelley, B. M., Kump, L. R., Lehrmann, D. J., et al. (2016). Marine Anoxia and Delayed Earth System Recovery after the End-Permian Extinction. *Proc. Natl. Acad. Sci. USA* 113, 2360–2365. doi:10.1073/pnas.1515080113

Le Vaillant, M., Barnes, S. J., Mungall, J. E., and Mungall, E. L. (2017). Role of Degassing of the Noril'sk Nickel Deposits in the Permian-Triassic Mass Extinction Event. *Proc. Natl. Acad. Sci. USA* 114, 2485–2490. doi:10.1073/pnas.1611086114

Li, M., Grasby, S. E., Wang, S.-J., Zhang, X., Wasylenki, L. E., Xu, Y., et al. (2021). Nickel Isotopes Link Siberian Traps Aerosol Particles to the End-Permian Mass Extinction. *Nat. Commun.* 12, 2024. doi:10.1038/s41467-021-22066-7

Liu, G., Feng, Q., Shen, J., Yu, J., He, W., and Algeo, T. J. (2014). Decline of Siliceous Sponges and Spicule Miniaturization Induced by Marine Productivity Collapse and Expanding Anoxia during the Permian-Triassic Crisis in South China. *PALAIOS* 28, 664–679. doi:10.2110/palo.2013.p13-035r

McManus, J., Berelson, W. M., Coale, K. H., Johnson, K. S., and Kilgore, T. E. (1997). Phosphorus Regeneration in continental Margin Sediments. *Geochim. Cosmochim. Acta* 61, 2891–2907. doi:10.1016/S0016-7037(97)00138-5

Meijers, M. J. M., Smith, B., Kirscher, U., Mensink, M., Sosson, M., Rolland, Y., et al. (2015). A Paleolatitude Reconstruction of the South Armenian Block (Lesser Caucasus) for the Late Cretaceous: Constraints on the Tethyan Realm. *Tectonophysics* 644-645, 197–219. doi:10.1016/j.tecto.2015.01.012

Mora, C., Wei, C. L., Rollo, A., Amaro, T., Baco, A. R., Billett, D., et al. (2013). Biotic and Human Vulnerability to Projected Changes in Ocean Biogeochemistry over the 21st Century. *PLOS Biol.* 11, e1001682. doi:10.1371/journal.pbio.1001682

Mort, H. P., Adatte, T., Föllmi, K. B., Keller, G., Steinmann, P., Matera, V., et al. (2007). Phosphorus and the Roles of Productivity and Nutrient Recycling during Oceanic Anoxic Event 2. *Geol* 35, 483. doi:10.1130/G23475A.1

Murphy, J., and Riley, J. P. (1962). A Modified Single Solution Method for the Determination of Phosphate in Natural Waters. *Analytica Chim. Acta* 27, 31–36. doi:10.1016/S0003-2670(00)88444-5

Newell, N. D. (1967). "Revolutions in the History of Life," in *Geological Society of America Special Paper*. Boulder 89, 63–91. doi:10.1130/SPE89-p63

Paytan, A., and McLaughlin, K. (2007). The Oceanic Phosphorus Cycle. *Chem. Rev.* 107, 563–576. doi:10.1021/cr0503613

Penn, J. L., Deutsch, C., Payne, J. L., and Sperling, E. A. (2018). Temperature-dependent Hypoxia Explains Biogeography and Severity of End-Permian marine Mass Extinction. *Science* 362, eaat1327. doi:10.1126/science.aat1327

Piper, D. Z., and Calvert, S. E. (2009). A marine Biogeochemical Perspective on Black Shale Deposition. *Earth-Science Rev.* 95, 63–96. doi:10.1016/j.earscirev.2009.03.001

Rampino, M. R., Rodriguez, S., Baransky, E., and Cai, Y. (2017). Global Nickel Anomaly Links Siberian Traps Eruptions and the Latest Permian Mass Extinction. *Sci. Rep.* 7, 12416. doi:10.1038/s41598-017-12759-9

Raup, D. M., and Sepkoski, J. J. (1982). Mass Extinctions in the Marine Fossil Record. *Science* 215, 1501–1503. doi:10.1126/science.215.4539.1501

Redfield, A. C., Ketchum, B. H., and Richards, F. A. (1963). The Influence of Organisms on the Composition of Seawater. *The sea* 2, 26–77.

Reinhard, C. T., Planavsky, N. J., Gill, B. C., Ozaki, K., Robbins, L. J., Lyons, T. W., et al. (2017). Evolution of the Global Phosphorus Cycle. *Nature* 541, 386–389. doi:10.1038/nature20772

Riccardi, A. L., Arthur, M. A., and Kump, L. R. (2006). Sulfur Isotopic Evidence for Chemocline Upward Excursions during the End-Permian Mass Extinction. *Geochim. Cosmochim. Acta* 70, 5740–5752. doi:10.1016/j.gca.2006.08.005

Rothman, D. H., Fournier, G. P., French, K. L., Alm, E. J., Boyle, E. A., Cao, C., et al. (2014). Methanogenic Burst in the End-Permian Carbon Cycle. *Proc. Natl. Acad. Sci.* 111, 5462–5467. doi:10.1073/pnas.1318106111

Roxy, M. K., Modi, A., Murtugudde, R., Valsala, V., Panickal, S., Prasanna Kumar, S., et al. (2016). A Reduction in marine Primary Productivity Driven by Rapid Warming over the Tropical Indian Ocean. *Geophys. Res. Lett.* 43, 826–833. doi:10.1002/2015GL066979

Ruttenberg, K. C. (1992). Development of a Sequential Extraction Method for Different Forms of Phosphorus in marine Sediments. *Limnol. Oceanogr.* 37, 1460–1482. doi:10.4319/lo.1992.37.7.1460

Ruttenberg, K. C. (1993). Reassessment of the Oceanic Residence Time of Phosphorus. *Chem. Geology.* 107, 405–409. doi:10.1016/0009-2541(93)90220-D

Schobben, M., Joachimski, M. M., Korn, D., Leda, L., and Korte, C. (2014). Palaeotethys Seawater Temperature Rise and an Intensified Hydrological Cycle Following the End-Permian Mass Extinction. *Gondwana Res.* 26, 675–683. doi:10.1016/j.gr.2013.07.019

Schobben, M., Foster, W. J., Sleveland, A. R. N., Zuchuat, V., Svensen, H. H., Planke, S., et al. (2020). A Nutrient Control on marine Anoxia during the End-Permian Mass Extinction. *Nat. Geosci.* 13, 640–646. doi:10.1038/s41561-020-0622-1

Schoepfer, S. D., Henderson, C. M., Garrison, G. H., and Ward, P. D. (2012). Cessation of a Productive Coastal Upwelling System in the Panthalassic Ocean at the Permian-Triassic Boundary. *Palaeogeogr. Palaeoclimatol. Palaeoecol.* 313-314, 181–188. doi:10.1016/j.palaeo.2011.10.019

Schoepfer, S. D., Shen, J., Wei, H., Tyson, R. V., Ingall, E., and Algeo, T. J. (2015). Total Organic Carbon, Organic Phosphorus, and Biogenic Barium Fluxes as Proxies for Paleomarine Productivity. *Earth-Sci. Rev.* 149, 23–52. doi:10.1016/j.earscirev.2014.08.017

Schoepfer, S. D. (2013). Termination of a Continent-Margin Upwelling System at the Permian–Triassic Boundary (Opal Creek, Alberta, Canada). *Glob. Planet. Change* 15, 21–35. doi:10.1016/j.gloplacha.2012.07.005

Shen, J., Algeo, T. J., Hu, Q., Zhang, N., Zhou, L., Xia, W., et al. (2012). Negative C-Isotope Excursions at the Permian-Triassic Boundary Linked to Volcanism. *Geology* 40, 963–966. doi:10.1130/G33329.1

Stanley, S. M. (2016). Estimates of the Magnitudes of Major marine Mass Extinctions in Earth History. *Proc. Natl. Acad. Sci. USA* 113, E6325–E6334. doi:10.1073/pnas.1613094113

Steiner, Z., Lazar, B., Torfstein, A., and Erez, J. (2017). Testing the Utility of Geochemical Proxies for Paleoproductivity in Oxic Sedimentary marine Settings of the Gulf of Aqaba, Red Sea. *Chem. Geol.* 473, 40–49. doi:10.1016/j.chemgeo.2017.10.012

Sun, Y., Joachimski, M. M., Wignall, P. B., Yan, C., Chen, Y., Jiang, H., et al. (2012). Lethally Hot Temperatures during the Early Triassic Greenhouse. *Science* 338, 366–370. doi:10.1126/science.1224126

Sun, Y. D., Zulla, M. J., Joachimski, M. M., Bond, D. P. G., Wignall, P. B., Zhang, Z. T., et al. (2019). Ammonium Ocean Following the End-Permian Mass Extinction. *Earth Planet. Sci. Lett.* 518, 211–222. doi:10.1016/j.epsl.2019.04.036

Sun, Y. D., Richoz, S., Krystyn, L., Grasby, S. E., Chen, Y. L., Banerjee, D., et al. (2021). Integrated Bio-Chemostratigraphy of Lower and Middle Triassic marine Successions at Spiti in the Indian Himalaya: Implications for the Early Triassic Nutrient Crisis. *Glob. Planet. Change* 196, 103363. doi:10.1016/j.gloplacha.2020.103363

Svensen, H., Planke, S., Polozov, A. G., Schmidbauer, N., Corfu, F., Podladchikov, Y. Y., et al. (2009). Siberian Gas Venting and the End-Permian Environmental Crisis. *Earth Planet. Sci. Lett.* 277, 490–500. doi:10.1016/j.epsl.2008.11.015

Taylor, S. R., and McLennan, S. M. (1985). *The Continental Crust: Its Composition and Evolution*. 1st ed. Oxford: Blackwell Scientific Publications.

Trappe, J. (1994). *Pangean Phosphorites - Ordinary Phosphorite Genesis in an Extraordinary World?* Editors Embry, A. F., Beauchamp, B., and Glass, D. J. (Pangea: Global Environments and Resources. Canadian Society of Petroleum Geologists), 469–478.

Van Cappellen, P., and Ingall, E. D. (1994). Benthic Phosphorus Regeneration, Net Primary Production, and Ocean Anoxia: A Model of the Coupled marine Biogeochemical Cycles of Carbon and Phosphorus. *Paleoceanography* 9, 677–692. doi:10.1029/94PA01455

Wenchen, X., Ning, Z., Guoqing, W., and Kakuwa, Y. (2004). Pelagic Radiolarian and Conodont Biozonation in the Permo-Triassic Boundary Interval and Correlation to the Meishan GSSP. *Micropaleontology* 50, 27–44. doi:10.1661/0026-2803(2004)050[0027:pracbi]2.0.co;2

Wignall, P. B., and Hallam, A. (1992). Anoxia as a Cause of the Permian/Triassic Mass Extinction: Facies Evidence from Northern Italy and the Western United States. *Palaeogeogr. Palaeoclimatol. Palaeoecol.* 93, 21–46. doi:10.1016/0031-0182(92)90182-5

Wignall, P. B., and Twitchett, R. J. (1996). Oceanic Anoxia and the End Permian Mass Extinction. *Science* 272, 1155–1158. doi:10.1126/science.272.5265.1155

Wignall, P. B., Bond, D. P. G., Grasby, S. E., Pruss, S. B., and Peakall, J. (2020). Controls on the Formation of Microbially Induced Sedimentary Structures and Biotic Recovery in the Lower Triassic of Arctic Canada. *GSA Bull.* 132, 918–930. doi:10.1130/B35229.1

Yang, S.-C., Kelly, R. L., Bian, X., Conway, T. M., Huang, K.-F., Ho, T.-Y., et al. (2021). Lack of Redox Cycling for Nickel in the Water Column of the Eastern Tropical North Pacific Oxygen Deficient Zone: Insight from Dissolved and Particulate Nickel Isotopes. *Geochim. Cosmochim. Acta* 309, 235–250. doi:10.1016/j.gca.2021.07.004

Yasuda, N., Miyamoto, N., Fujiwara, Y., Yamamoto, T., and Yusa, Y. (2016). Effects of Food Availability on Growth and Reproduction of the Deep-Sea Pedunculate Barnacle Heteralepas Canci. *Deep Sea Res. Oceanogr. Res. Pap.* 108, 53–57. doi:10.1016/j.dsr.2015.12.008

Zhang, Y., Shi, G. R., He, W.-h., Wu, H.-t., Lei, Y., Zhang, K.-x., et al. (2016). Significant Pre-Mass Extinction Animal Body-Size Changes: Evidences from the Permian-Triassic Boundary Brachiopod Faunas of South China. *Palaeogeogr. Palaeoclimatol. Palaeoecol.* 448, 85–95. doi:10.1016/j.palaeo.2015.11.020

Zhang, F., Algeo, T. J., Romaniello, S. J., Cui, Y., Zhao, L., Chen, Z.-Q., et al. (2018). Congruent Permian-Triassic δ238U Records at Panthalassic and Tethyan Sites: Confirmation of Global-Oceanic Anoxia and Validation of the U-Isotope Paleoredox Proxy. *Geology* 46, 327–330. doi:10.1130/G39695.1

Conflict of Interest: The authors declare that the research was conducted in the absence of any commercial or financial relationships that could be construed as a potential conflict of interest.

frontiers in Ecology and Evolution

ORIGINAL RESEARCH
published: 28 March 2022
doi: 10.3389/fevo.2022.853404

Volcanically-Induced Environmental and Floral Changes Across the Triassic-Jurassic (T-J) Transition

Peixin Zhang[1], Jing Lu[1], Minfang Yang[2], David P. G. Bond[3], Sarah E. Greene[4], Le Liu[1], Yuanfu Zhang[5], Ye Wang[1], Ziwei Wang[1], Shan Li[1], Longyi Shao[1] and Jason Hilton[4]**

[1] State Key Laboratory of Coal Resources and Safe Mining, College of Geoscience and Surveying Engineering, China University of Mining and Technology, Beijing, China, [2] Research Institute of Petroleum Exploration and Development, PetroChina, Beijing, China, [3] Department of Geography, Geology and Environment, University of Hull, Hull, United Kingdom, [4] School of Geography, Earth and Environmental Sciences, University of Birmingham, Birmingham, United Kingdom, [5] School of Energy Resources, China University of Geosciences, Beijing, China

The End-Triassic Mass Extinction (ETME) saw the catastrophic loss of *ca.* 50% of marine genera temporally associated with emplacement of the Central Atlantic Magmatic Province (CAMP). However, the effects of the ETME on land is a controversial topic. Evaluation of the disparate cause(s) and effects of the extinction requires additional, detailed terrestrial records of these events. Here, we present a multidisciplinary record of volcanism and environmental change from an expanded Triassic-Jurassic (T-J) transition preserved in lacustrine sediments from the Jiyuan Basin, North China. High-resolution chemostratigraphy, palynological, kerogen, and sedimentological data reveal that terrestrial conditions responded to and were defined by large-scale volcanism. The record of sedimentary mercury reveals two discrete CAMP eruptive phases during the T-J transition. Each of these can be correlated with large, negative C isotope excursions (CIE-I of −4.7‰; CIE-II of −2.9‰), significantly reduced plant diversity (with *ca.* 45 and 44% generic losses, respectively), enhanced wildfire (marked by increased fusinite or charcoal content), and major climatic shifts toward drier and hotter conditions (indicated by the occurrence of calcareous nodules, increased *Classopollis* pollen content, and PCA analysis). Our results show that CAMP eruptions may have followed a bimodal eruptive model and demonstrate the powerful ability of large-scale volcanism to alter the global C cycle and profoundly affect the climate, in turn leading to enhanced wildfires and a collapse in land plant diversity during the T-J transition.

Keywords: End-Triassic Mass Extinction, palynology, volcanism, paleoenvironment, paleoclimate, carbon cycle, North China

OPEN ACCESS

Edited by:
Sara Callegaro, University of Oslo, Norway

Reviewed by:
Simonetta Cirilli, University of Perugia, Italy
Guillaume Paris, UMR 7358 Centre de Recherches Pétrographiques et Géochimiques (CRPG), France

***Correspondence:**
Jing Lu
lujing@cumtb.edu.cn
Jason Hilton
J.M.Hilton@bham.ac.uk

Specialty section:
This article was submitted to Paleontology, a section of the journal Frontiers in Ecology and Evolution

Received: *12 January 2022*
Accepted: *24 February 2022*
Published: *28 March 2022*

Citation:
Zhang P, Lu J, Yang M, Bond DPG, Greene SE, Liu L, Zhang Y, Wang Y, Wang Z, Li S, Shao L and Hilton J (2022) Volcanically-Induced Environmental and Floral Changes Across the Triassic-Jurassic (T-J) Transition. Front. Ecol. Evol. 10:853404. doi: 10.3389/fevo.2022.853404

INTRODUCTION

As one of the five biggest Phanerozoic extinctions in Earth history, the End-Triassic Mass Extinction (ETME, *ca.* 201.51 Ma) during the Triassic-Jurassic (T-J) transition resulted in the loss of *ca.* 50% of marine genera (Raup and Sepkoski, 1982; Dal Corso et al., 2014; Miller and Baranyi, 2021). However, the impact of this crisis on terrestrial plant diversity is poorly understood. Studies of plant macrofossils and palynological (spore-pollen) assemblages reveal that plant diversity and many dominant species suffered severe losses in the Tethys ocean domain of the northern

hemisphere in Europe (McElwain et al., 1999, 2007; Kuerschner et al., 2007; Bonis et al., 2009, 2010; Pieńkowski et al., 2012; Lindström, 2016, 2021; Lindström et al., 2019; Wignall and Atkinson, 2020), North America (Olsen et al., 2002), South China (Wang et al., 2010; Li et al., 2020; Zhou et al., 2021), and northwest (NW) China (Lu and Deng, 2005; Deng et al., 2010; Sha et al., 2015; Fang et al., 2021). Similar losses are known from southern hemisphere Australia and New Zealand (De Jersey and McKellar, 2013). However, this is not completely supported by data from the Fundy Basin in North America (Marzoli et al., 2008; Cirilli et al., 2009; Cirilli, 2010) or southern Europe (Cirilli et al., 2015, 2018; Vilas-Boas et al., 2021) where low biodiversity losses are recorded across the T-J boundary (TJB). Similarly, recent studies from Poland and other western Tethyan locations found no significant changes in plant diversity and community succession through the T-J transition (Lucas and Tanner, 2015; Barbacka et al., 2017; Lucas, 2021). In Morocco, palynological assemblages record losses in the Rhaetian that suggest the terrestrial crisis was slightly older than the TJB (Panfili et al., 2019). Evaluation of the fate of terrestrial plants during the ETME requires further detailed records of floral diversity and associated environmental and climate changes from continental successions across different latitudes and climatic zones.

The Central Atlantic Magmatic Province (CAMP) is one of the most voluminous large igneous provinces (LIPs) on Earth and its emplacement was near-synchronous with the ETME (Schoene et al., 2010; Wotzlaw et al., 2014). The close temporal association between CAMP and the extinction losses has led to volcanism being implicated as a driver of the ETME (Bond and Wignall, 2014; Percival et al., 2017; Lindström et al., 2019; Panfili et al., 2019). The massive input of CAMP greenhouse gases (e.g., CO_2 and CH_4) into the atmosphere-ocean system would likely have driven rapid global warming (Hesselbo et al., 2002; Marzoli et al., 2004; Cirilli et al., 2009, 2015, 2018; Svensen et al., 2009; Dal Corso et al., 2014; Percival et al., 2017; Panfili et al., 2019; Heimdal et al., 2020; Ruhl et al., 2020; Capriolo et al., 2021a,b). Some studies from West Tethys and South China demonstrate wildfires associated with global warming played an important role for changes in terrestrial vegetation and ecosystems (Belcher et al., 2010; Petersen and Lindström, 2012; Lindström et al., 2019, 2021; Song et al., 2020), with enhanced wildfire leading to catastrophic soil erosion following vegetation loss (van de Schootbrugge et al., 2020; Lindström et al., 2021). However, it remains unknown whether wildfire during the T-J transition was localized or extended across the world as it appears to have done during the Permian-Triassic terrestrial mass extinction (e.g., Glasspool et al., 2015; Lu et al., 2020a; Dal Corso et al., 2022). As a result, further study is needed to enhance our understanding of the relationship between volcanic activity, wildfire, and terrestrial plant evolution across this key geological time interval.

We investigate a terrestrial succession from the Zuanjing-1 (ZJ-1) borehole in the Jiyuan Basin of the southern North China Plate (NCP). We use fossil plant biostratigraphy and organic C isotope ($\delta^{13}C_{org}$) chemostratigraphy together with Hg concentrations to correlate changes in plant composition and diversity with volcanic activity during the T-J transition.

GEOLOGICAL SETTING

During the Late Triassic, the NCP was located at approximately 30–40°N in the eastern Tethys Ocean (Greene et al., 2012; **Figures 1A,B**). The Yinshan paleoland lay to the north and the Qinling-Dabie Orogenic Belt (QDOB) to the south (Liu et al., 2013; **Figure 1B**). The Ordos Basin occupied the central and southwestern parts of the NCP and incorporated the smaller Jiyuan Basin at its southeast margin (Liu et al., 2013; **Figure 1B**). From the Late Triassic to the Jurassic the Jiyuan Basin was a lake (Li et al., 2014) that received sediment from the QDOB and southern NCP (Yang et al., 2012; **Figures 1A,B**).

The stratigraphic and lithologic succession and fossil plant assemblages from the Late Triassic to the Middle Jurassic of the Jiyuan Basin are shown in **Figure 1C**. The age of the Jiyuan succession is constrained by its flora and through zircon dating (see Lu et al., 2021a). The Tanzhuang Formation and the lower part of the Anyao Formation are considered to be Late Triassic in age based on the presence of the *Danaeopsis-Bernoullia* fossil plant assemblage (Hu, 1991; **Figure 1C**). Zircon U-Pb ages from two tuffaceous claystone horizons in the topmost part of the Tanzhuang Formation (233.1 ± 1.3 and 232.9 ± 2.1 Ma; Lu et al., 2021a) confirm this age assignment. The upper part of the Anyao Formation lacks biostratigraphically informative megafossils (Hu, 1991) but it can be assigned to the T-J transition based on its position between underlying Triassic strata and the overlying Jurassic-aged Yangshuzhuang Formation based on biostratigraphy and the presence of the *Coniopteris–Phoenicopsis* floral plant assemblage (Hu, 1991; **Figure 1C**).

MATERIALS AND METHODS

Fifty fresh mudstone drill core samples from the Anyao Formation were taken from the ZJ-1 borehole (35.07001°N, 112.47338°E) that was drilled in the Jiyuan Basin (**Figures 1A,B**; sampling locations are shown in **Figure 2**). These samples were analyzed for their geochemistry and palynology. Each sample was first divided into two parts of which one was crushed into particles *ca.* 1 mm in diameter for analysis of (1) kerogen enrichment and (2) palynological isolation. The remaining part of the sample was crushed to pass through a 200 μm mesh and then divided into seven subparts for analysis of (1) $\delta^{13}C_{org}$, (2) total organic carbon (TOC), (3) total nitrogen (TN), (4) mercury (Hg) content, (5) total sulfur (TS), (6) major elements, and (7) Rock-Eval pyrolysis.

Hg concentrations were measured at the State Key Laboratory of Coal Resources and Safe Mining (Beijing). $\delta^{13}C_{org}$, TS, and major elements were measured at the Beijing Research Institute of Uranium Geology, and TOC and TN were measured at the Research Institute of Petroleum Exploration and Development Research (RIPED). Hg concentration was undertaken using a mercury analyzer (Lumex RA-915 +) with lower detection limits of 2 ng/g (2 ppb). The mercury analyzer was calibrated before use with standards of China National Certified Reference Material soil (CRMs; GBW07427) with Hg concentration of 52 ± 6 ppb, and analytic precision was within 5%. $\delta^{13}C_{org}$ analysis was

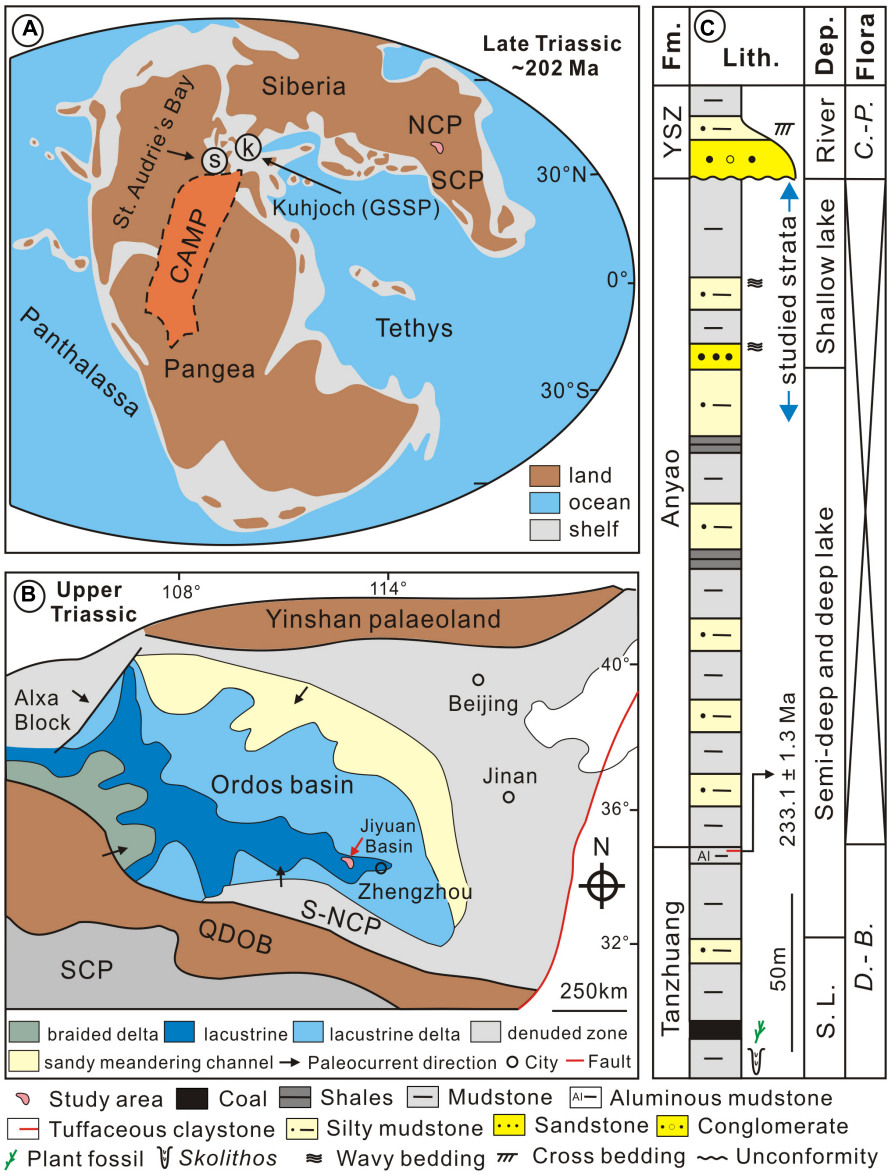

FIGURE 1 | Location and geological context for the study area. **(A)** Paleogeographic reconstruction for the Late Triassic (~202 Ma) showing the location of the NCP and approximate extent of CAMP (revised after Greene et al., 2012); **(B)** simplified tectonic map of the southern NCP during the Late Triassic showing the location of the study area (modified from Liu et al., 2013); **(C)** stratigraphic framework of the Tanzhuang Formation to the Lower Yangshuzhuang (YSZ) Formation from the Jiyuan Basin (modified from Yang et al., 2012). Depositional environments come from Li et al. (2014). Note that U-Pb dating (233.1 ± 1.3 Ma) come from Lu et al. (2021a). CAMP, Central Atlantic Magmatic Province; NCP, North China Plate; SCP, South China Plate; QDOB, Qinling-Dabie Orogenic Belt; S-NCP, southern North China Plate; Fm., Formation; Lith., Lithology; Dep., Depositional environment; *C.-P.*, *Coniopteris-Phoenicopsis*.

performed using a stable isotope mass spectrometer (MAT253), and $\delta^{13}C_{org}$ values are expressed in per mil (‰) with respect to the Vienna Pee Dee Belemnite (VPDB) standard, with an absolute analysis error of ± 0.1‰. TS analysis was performed using a carbon-sulfur analyzer (Eltra CS580-A) with the lower detection limits of 30 ppm, yielding an analytical accuracy within 5% of the reported values. Major elements analysis was undertaken with an X-ray fluorescence spectrometer (PW2404). The spectrometer was calibrated before use with standards of CRMs (GBW07427), and analytic precision was within 5%. TOC and TN analysis was performed using an elemental analyzer (Vario MICRO Cube). To quantify the analytical results of TOC and TN, a certified reference material (L-alanine) was used during the analysis, yielding an analytical accuracy of 1.5 and 2% of the reported values, respectively. The analytic precision or error of all samples is based on reproducibility and repeats of the standard sample and standard samples were run after every five sample analyses. Detailed descriptions of analytical methods and errors used are available following those of Lu et al. (2020a,b, 2021a,b).

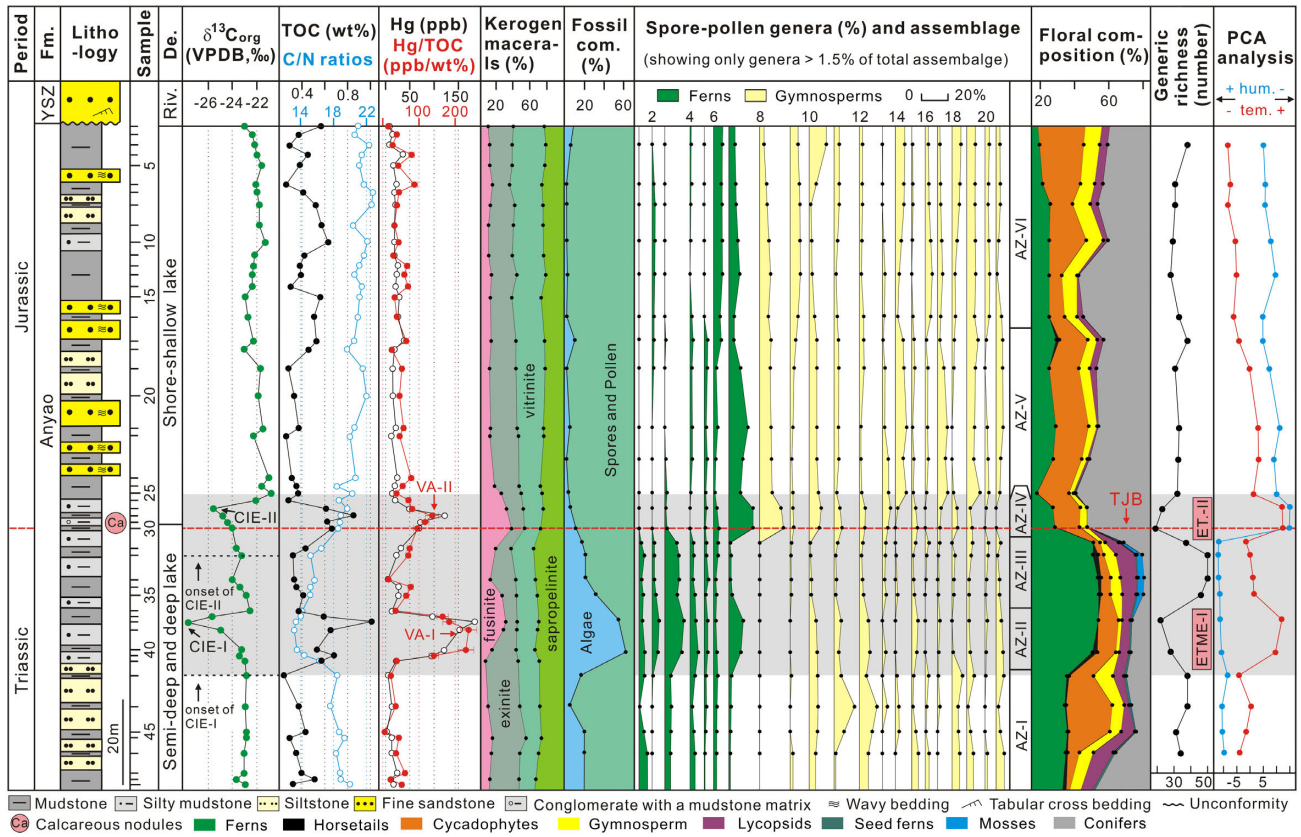

FIGURE 2 | Results of $\delta^{13}C_{org}$ values, TOC contents, C/N ratios, Hg concentrations, Hg/TOC ratios, kerogen macerals, fossil component, spore-pollen genera and palynology assemblage, floral composition, generic richness (number of different genera, excluding rework taxa), and principal components analysis (PCA) from the studied borehole in the Jiyuan Basin. Note that error bars on Hg/TOC plots represent the propagated error on Hg (± 5%) and TOC (± 0.2%) content measurements, and spore-pollen species more than 1.5% are plotted (more detailed data are shown in **Supplementary Table 1**). Fm., Formation; YSZ, Yangshuzhuang; De., Depositional environment; Riv., River; VPDB, Vienna Pee Dee Belemnite; CIE-I to CIE-II, from the first organic carbon isotope excursion to the second organic carbon isotope excursion; VA-I, first pulse of volcanic activity; VA-II, second pulse of volcanic activity; floral com., floral composition; 1, *Crassispora* (reworked); 2, *Triquitrites* (reworked); 3, *Anapiculatisporites*; 4, *Cyclogranisporites*; 5, *Dictyophyllidites*; 6, *Punctatisporites*; 7, *Leiotriletes*; 8, *Classopollis*; 9, *Cyathidites*; 10, *Pinuspollenites*; 11, *Osmundacidites*; 12, *Concentrisporites*; 13, *Cycadopites*; 14, *Chasmstosporites*; 15, *Psophosphaera*; 16, *Inaperturopollenites*; 17, *Vesicaspora*; 18, *Callialasporites*; 19, *Quadraeculina*; 20, *Rotundipollis*; 21, *Pseudopicea*; 22, *Protopinus*; 23, *Paleoconiferus*; AZ-I to AZ-VI, from the first palynology assemblage zone (AZ) I to the sixth palynology assemblage zone VI; TJB, Triassic-Jurassic boundary; ETME-I, the first stage of the end Triassic mass extinction; ET.-II, the second stage of the end Triassic mass extinction; PCA, principal component analysis; hum., humidity; tem., temperature.

Ten mudstone samples were selected for Rock-Eval pyrolysis at RIPED using an Oil and Gas Evaluation workstation (OEG-II) according to China National Standard (GB/T18602-2012). Kerogen enrichment and identification was performed on 30 of the 50 mudstone samples according to China national standard (SY/T5125–2014) at RIPED, with no less than 300 effective points per sample analyzed. Palynological isolation and identifications were undertaken for 23 of the 50 mudstone samples. Samples were subjected to acid digestion in 30% hydrochloric acid (HCl) and 38% hydrofluoric acid (HF). Heavy mineral separation was used to concentrate the sporomorphs and separate them from other components of the residue. For each spore-pollen sample, more than 100 sporomorphs were identified by the point-counting method under transmitted light microscopy (Olympus BX 41). All palynological slides are housed at the State Key Laboratory of Coal Resources and Safe Mining (Beijing). Percentages of spore and pollen taxa were calculated based on the sum of total sporomorphs. Palynological assemblages were identified by stratigraphically constrained cluster analysis (CONISS) using the Tilia software.

In this study, Hg concentration is used as a proxy for volcanism (e.g., Percival et al., 2017; Lu et al., 2020b, 2021a,b,c; Shen et al., 2020, 2022). Variations in spore-pollen composition through the studied strata were used to reconstruct paleoclimatic conditions (excluding reworked taxa, see **Supplementary Material**) based on the climatic preferences of the parent plants (e.g., Bonis et al., 2010; Lindström, 2016; Li et al., 2020; Lu et al., 2021a). Principal Components Analysis (PCA) by CANOCO software was performed to transform the relative abundances of spore-pollen (excluding reworked taxa, see **Supplementary Material**) into climatic parameters including temperature and humidity (e.g., Bonis et al., 2010; Li et al., 2020). Fusinite (charcoal) content is used as a proxy for paleo-wildfire activity (e.g., Glasspool et al., 2015; Lu et al., 2020a).

RESULTS AND ANALYSIS

Paleofloral Reconstruction and Paleoclimatological Inferences of Palynological Assemblages

From the samples 34 spore, 32 pollen, and 8 algae genera have been identified (**Supplementary Table 1**, **Figure 2**, and **Supplementary Figures 1, 2**) that are typical of Late Triassic and Early Jurassic palynological assemblages (see section "The Stratigraphic Position of the TJB in the Jiyuan Basin"). They are assigned to six palynological assemblage zones (AZ) based on the palynomorph abundance variations and CONISS: *Psophosphaera—Chasmatosporites—Cycadopites* assemblage zone (AZ–I; samples #JY 23—#JY 20), the *Punctatisporites—Cyathidites—Psophosphaera* assemblage zone (AZ–II, #JY 19—#JY 18), the *Punctatisporites—Verrucosisporites—Triquitrites* assemblage zone (AZ–III, #JY 17—#JY 14), the *Classopollis—Cyathidites—Cycadopites* assemblage zone (AZ–IV, #JY 13—#JY 12), the *Cyathidites—Classopollis—Pseudopicea* assemblage zone (AZ–V, #JY 11—#JY 7), and the *Pinuspollenites—Cycadopites—Classopollis* assemblage zone (AZ–VI, #JY 6—#JY 1) (**Figure 2** and **Supplementary Figure 1**). The composition of AZ-I is dominated by gymnosperm pollen (mean ($\bar{x}$) = 56.5%, including *Psophosphaera* and *Chasmstosporites*), followed by fern spores ($\bar{x}$ = 43.5%, including *Punctatisporites* and *Crassispora*). The compositions of AZ-II and AZ-III are noticeably different, although fern spores (including *Cyathidites* and *Punctatisporites*) dominate followed by gymnosperm pollen (including *Psophosphaera* and *Cycadopites*), but in AZ-II algae dominate ($\bar{x}$ = 57.6%) and the proportion of spores and pollens decreases by ca. 45% from 38 to 21 genera (**Figure 2**). Nine of the fern spore genera (dominated by *Verrucosisporites* and *Laevigatosporites*) and eight gymnosperm pollen genera (mainly *Rotundipollis*, *Podocarpidites* and *Callialasporites*) decreased in abundance (**Supplementary Table 1** and **Figure 2**). The compositions of AZ-IV, AZ-V, and AZ-VI are generally similar and are dominated by gymnosperm pollen ($\bar{x}$ = 72.0, 71.7, and 72.8%, respectively) including *Classopollis*, *Cycadopites,* and *Pseudopicea*. AZ-IV, AZ-V, and AZ-VI have low proportions of ferns ($\bar{x}$ = 28.0, 28.3, and 27.2%, respectively) including *Cyathidites* and *Osmundacidtes*, while algal composition is uniformly low ($\bar{x}$ = 7.1, 3.4, and 1.6%, respectively). In AZ-IV, the proportion of spores and pollens decreases by ca. 44% and from 50 to 28 genera. In this assemblage 14 fern spore genera (mainly *Verrucosisporites*, *Punctatisporites*, *Triquitrites,* and *Triporoletes*) and eight gymnosperm pollen genera (mainly *Paleoconiferus*, *Protopinus,* and *Callialasporites*) each decreased in abundance (**Supplementary Table 1** and **Figure 2**). In addition, AZ-IV (sample #JY 13) sees a decrease in diversity but a rapid increase in the abundance of *Classopollis* and *Cythidites*, and includes the first appearance of *Cerbropollenites* (**Figure 2**).

The parent plants of the palynological taxa have been evaluated to reconstruct the floral successions of the Jiyuan Basin (**Supplementary Tables 1, 2** and **Figure 2**). Diverse plant groups are recognized in the study area from the Late Triassic to Early Jurassic including mosses ($\bar{x}$ = 0.6%), lycopsids ($\bar{x}$ = 3.2%), horsetails ($\bar{x}$ = 0.7%), "filicalean" ferns ($\bar{x}$ = 34.0%), conifers ($\bar{x}$ = 39.9%), cycads ($\bar{x}$ = 14.7%), and pteridosperms (seed ferns; $\bar{x}$ = 0.4%) (**Supplementary Tables 1, 2** and **Figure 2**). These taxa mainly grow in temperate to subtropical, warm and humid climates (Liu et al., 2015; Li et al., 2020; Lu et al., 2021a). In AZ-I, AZ-II, and AZ-III, ferns are dominant ($\bar{x}$ = 34.8, 52.9, and 52.1%, including the Osmundaceae, Dicksoniaceae/Cyatheaceae, and Dipteridaceae/Matoniaceae), followed by conifers ($\bar{x}$ = 31.4, 28.8, and 24.1%, including Taxodiaceae and Podocarpaceae) and cycads. Horsetails and lycopsids are less abundant, while pteridosperms appear sporadically (**Supplementary Tables 1, 2**, **Figure 2**, and **Supplementary Figure 1**). In AZ-IV, AZ-V, and AZ-VI, conifers are dominant ($\bar{x}$ = 47.3, 49.4, and 47.3%, including Cheirolepidiaceae, Taxodiaceae, and Pinaceae), followed by ferns ($\bar{x}$ = 28.0, 25.9, and 23.8%, including Dicksoniaceae/Cyatheaceae and Osmundaceae), while cycads, horsetails, lycopsids, and seed ferns appear sporadically and mosses are absent (**Supplementary Tables 1, 2**, **Figure 2**, and **Supplementary Figure 1**).

Results of PCA analysis based on the relative abundance of spore-pollen genera are shown in **Figures 2–4**. Two main ordination axes representing the largest variance in palynological composition are used to explain the two most dominant environmental gradients that control the dataset (e.g., Bonis et al., 2010; Li et al., 2020). In this study, axis 1 and axis 2 separately account for 42.28 and 16.75% of the sporomorph spectra difference (**Figure 3**). On the positive side of axis 1, the xerophytic *Classopollis*, *Pinuspollenites,* and *Quadraeculina* pollen and hygro-mesophytic *Cyathidites* spores (e.g., Lindström, 2016; Li et al., 2020) have high scores, and the hygrophytic *Punctatisporites* spores (e.g., Lindström, 2016; Li et al., 2020) show high scores on the negative side of axis 1. Relatively cool, temperate conifer pollen including *Pinuspollenites* and *Pseudopicea* have high scores on the negative side of axis 2, and the relatively warm condition spores *Cyathidites* and *Punctatosporites* (e.g., Li et al., 2020) and the pollen *Classopollis* (e.g., Lindström, 2016) have high scores on the positive side of axis 2. Thus, the first and the second axes are interpreted to reflect the changes in relative humidity and temperature, respectively (**Figures 2**, **3**). The PCA results indicate stable cool-humid conditions prevailed during AZ-I, and cool-dry paleoclimate during AZ-V and AZ-VI, while mixed or fluctuating climatic conditions prevailed from AZ-II to AZ-IV, especially during two warming intervals in AZ-II and AZ-IV (**Figures 2**, **3**).

Total Organic Carbon and $\delta^{13}C_{org}$ Chemostratigraphy

Results for TOC and $\delta^{13}C_{org}$ are shown in **Figure 2** and **Supplementary Table 3**. TOC values vary from 0.24 to 1.01 wt% ($\bar{x}$ = 0.46 wt%). At the base of the succession TOC values are low and have a gradually decreasing trend in the mudstones and yellow siltstones (samples 50–43; $\bar{x}$ = 0.39 wt%), followed by an interval of fluctuating values and including two TOC peaks of 1.01 and 0.85 wt% in the latest Triassic-earliest Jurassic mudstones and gray siltstones (samples 42–25; $\bar{x}$ = 0.56 wt%). TOC values show a generally increasing

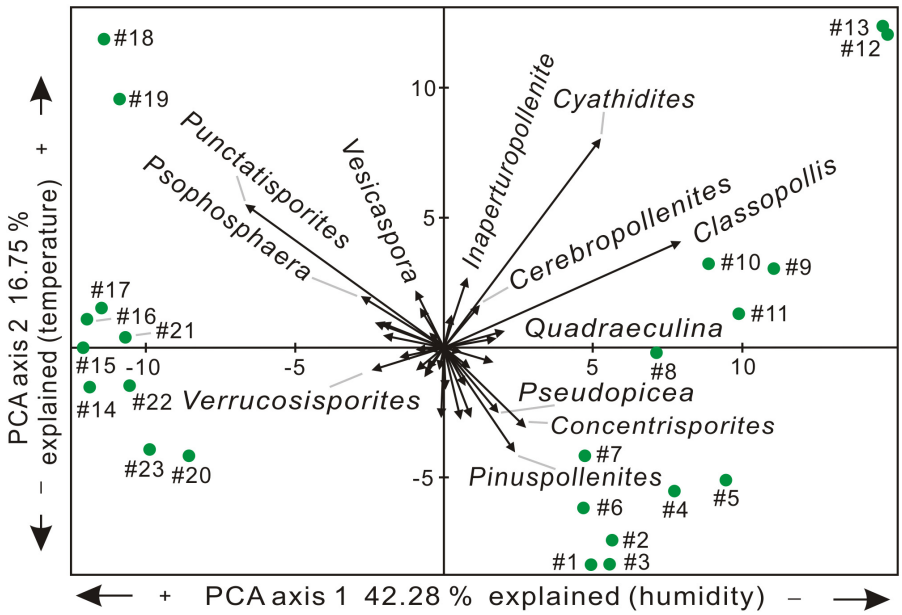

FIGURE 3 | Principal Component Analysis (PCA) ordination plot of sporomorph relative abundances (excluding reworked taxa) from the studied borehole in the Jiyuan Basin.

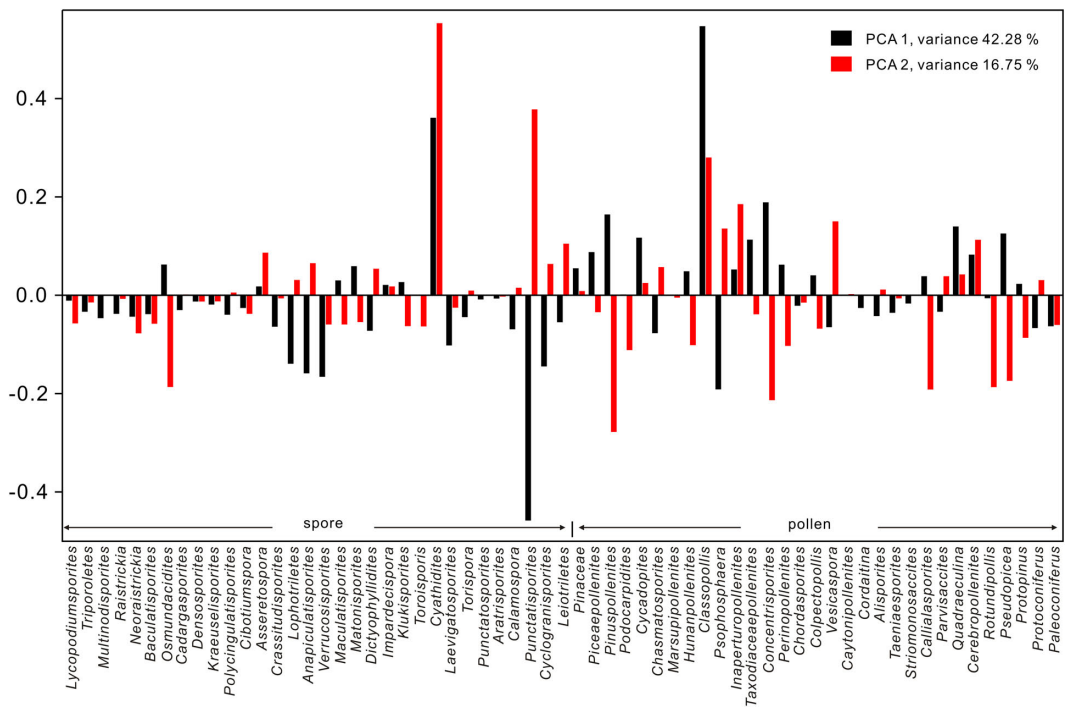

FIGURE 4 | Loading plots of PCA1 and PCA2 for spore and pollen genera (excluding rework taxa) from the studied borehole in the Jiyuan Basin.

trend through the Jurassic mudstones, siltstones, and sandstone to the top of our succession (samples 24–1; $\bar{x}$ = 0.44 wt%) (**Figure 2**). From samples through the complete succession, peak temperature of rock pyrolysis (T_{max}) values vary from 442 to 446°C ($\bar{x}$ = 444.1°C) (**Supplementary Table 3**) and indicate that kerogen maturity varies from low-maturity to mature as defined by the China National Standard (SY/T 5477-2003) (**Supplementary Table 5**).

$\delta^{13}C_{org}$ values vary from −27.5 to −20.8‰ ($\bar{x}$ = −22.8‰; **Figure 2**) and stratigraphically have two heavier plateaus either

side of a phase of lighter values around the T-J transition (**Figure 2**). In the earlier plateau (samples 50–43, roughly corresponding to AZ-I), $\delta^{13}C_{org}$ values are stable and average −22.9‰. In the phase of lighter values between the two plateaus (samples 42–25, roughly corresponding to AZ-II to AZ-IV) values vary from −29.0 to −22.5‰ ($\bar{x}$ = −24.3‰) and this part includes two negative $\delta^{13}C_{org}$ excursions (CIEs) with magnitudes of −4.7‰ (CIE-I) and −2.9‰ (CIE-II) relative to the background mean. These CIEs are near-synchronous with two falls in plant diversity in AZ-II and AZ-IV (**Figure 2**). Above CIE-II (samples 24–1, corresponding to AZ-V to AZ-VI), $\delta^{13}C_{org}$ values return to a heavier and stable plateau and average −22.0‰, including a slight decrease between samples 24 and 10 (**Figure 2**).

Kerogen Macerals as a Proxy for Wildfire

Kerogen macerals mainly comprise exinite ($\bar{x}$ = 29.1%), sapropelinite ($\bar{x}$ = 28.5%) and vitrinite ($\bar{x}$ = 26.4%), followed by fusinite ($\bar{x}$ = 16.1%) (**Supplementary Table 4** and **Figure 2**). Exinite content varies from 19.2 to 39.3% ($\bar{x}$ = 29.1%) and mainly comprises sporopollenite, cutinite, and subertinite (**Figures 2**, **5**). Sapropelinite content varies from 21.9 to 38.9% ($\bar{x}$ = 28.5%) (**Figures 2**, **5**). Vitrinite content varies from 12.4 to 37.8% ($\bar{x}$ = 26.4%) and comprises non-fluorescent telinite and collinite (**Figures 2**, **5**). Fusinite content varies from 6.7 to 39.6% ($\bar{x}$ = 16.1%) and is entirely fragmental fusinite which is opaque, pure black, does not fluoresce under fluorescence illumination, and is mostly long and thin or fragmental in shape with sharp edges (**Figures 2**, **5**). Fusinite enrichment in the studied strata (**Figure 2**) corresponds to the emergence of a large number of charcoal particles in sediments (**Figure 5**), with fusinite representing the product of incomplete combustion from wildfire (e.g., Goodarzi, 1985; Bustin and Guo, 1999; Lu et al., 2020a). We therefore use fusinite content as a proxy for wildfire. In this study, two obvious fusinite peaks with the values of 37.0 and 39.6% in the uppermost Triassic and earliest Jurassic strata (samples 38 and 30, respectively) correspond to the falls in plant diversity in AZ-II and AZ-IV (**Figure 2**).

Hg Anomalies as a Proxy for Volcanism

Results for Hg concentrations are shown in **Figure 2** and **Supplementary Table 3**. Hg concentrations show considerable variation, ranging from 2.23 to 183.42 ppb ($\bar{x}$ = 34.33 ppb) and have a distribution that is broadly anticorrelated to $\delta^{13}C_{org}$ values (**Figure 2**). The Hg concentrations show stronger covariation with TOC (r = + 0.67) than with Al (r = + 0.17) or TS (r = −0.03) (**Supplementary Figure 3**), suggesting Hg is mostly hosted by organic matter (OM) (e.g., Shen et al., 2020; Lu et al., 2021a,b,c). As a result, we present Hg/TOC values as a proxy for volcanism. Hg/TOC varies from 5.19 to 234.72 ppb/wt% ($\bar{x}$ = 66.16 ppb/wt%) with distribution broadly similar to the raw Hg concentrations (**Figure 2**). There are two Hg/TOC peaks with values of 234.72 ppb/wt% in AZ-II (from which we infer pulses of volcanic activity = VA-I) and 144.93 ppb/wt% in AZ-IV (VA-II; **Figure 2**). The intervals of Hg/TOC enrichment roughly correspond to the position of the CIEs, enhanced wildfire, and decreases in plant diversity (**Figure 2**).

DISCUSSION

The Stratigraphic Position of the T-J Boundary in the Jiyuan Basin

The TJB has been tentatively placed in the upper part of the Anyao Formation in the Jiyuan Basin (see Lu et al., 2021a and section "Geological Setting"). Palynological composition can be effective in determining stratigraphic age (e.g., Lu and Deng, 2005; Sha et al., 2015; Lindström et al., 2017; Li et al., 2020; Wignall and Atkinson, 2020). In western Tethys, floral changes near the TJB are characterized by: (1) an end-Triassic fern peak (including *Polypodiisporites polymicroforatus*, and trilete megaspores in some areas); (2) the earliest Jurassic first appearance (FO) of *Cerbropollenites thiergartii* and the last occurrence (LO) of *Lunatisporites rhaeticus*; and (3) a brief earliest Jurassic proliferation of *Classopollis* pollen (Cheirolepidiaceae) and the subsequent restoration and dominance of conifers (e.g., Olsen et al., 2002; Whiteside et al., 2007; Bonis et al., 2009, 2010; van de Schootbrugge et al., 2009; Pieńkowski et al., 2012; Vajda et al., 2013; Lindström et al., 2017; Wignall and Atkinson, 2020; Boomer et al., 2021). In eastern Tethys, a fern spore spike occurs in the Haojiaggou section from NW China during the T-J transition and is followed by the FO of *Cerbropollenites thiergartii*, the LO of *Lunatisporites rhaeticus*, and the co-dominance of *Classopollis* and *Cythidites* in Lower Jurassic strata (Lu and Deng, 2005; Deng et al., 2010; Sha et al., 2015; Fang et al., 2021); a fern spore spike also occurs in the Qilixia section of South China during T-J transition, followed by the co-dominance of *Classopollis* and *Cythidites* in the overlying Lower Jurassic strata (Wang et al., 2010; Li et al., 2020).

The combined records from the Haojiagou and Qilixia sections allow the development of an integrated stratigraphic TJB framework for the terrestrial eastern Tethys region (e.g., Lu and Deng, 2005; Li et al., 2020; Fang et al., 2021). In this study, similar changes in palynological assemblages allows us to correlate these two sections (see **Supplementary Material**). Significantly, the fern spore spike occurs in AZ-II and AZ-III in our study, but it lacks some of the usual fern elements including trilete type spores and *Polypodiisporites polymorphoratus*, which are key palynostratigraphic markers for the TJB in western Tethys (e.g., Lindström et al., 2017; Wignall and Atkinson, 2020). Similar patterns are also seen in the Haojiagou and Qilixia sections, which have been interpreted as the fern peak associated with global records from the T-J transition interval (see **Supplementary Material**). In our study, the spore and pollen composition of AZ-IV is very similar to that from the Badaowan Formation of NW China and the Zhenzhuchong Foamation of South China, with the co-dominance of *Cyathidites* (Dicksoniaceae/Cyatheaceae) and *Classopollis* (Cheirolepidiaceae), the common occurrence of *Cycadopites*, and the presence of *Dictyophyllidites*, *Chasmatosporites,* and *Quadraeculina*, which indicate an Early Jurassic age (e.g., Lu and Deng, 2005; Li et al., 2020). This is further supported by the disappearance at the base of AZ-IV of the Triassic taxa *Aratrisporites*, *Taeniaesporites*, and *Kraeuselisporites* (e.g., Fu and Yuan, 1998; Li et al., 2020). Furthermore, AZ-IV in the study

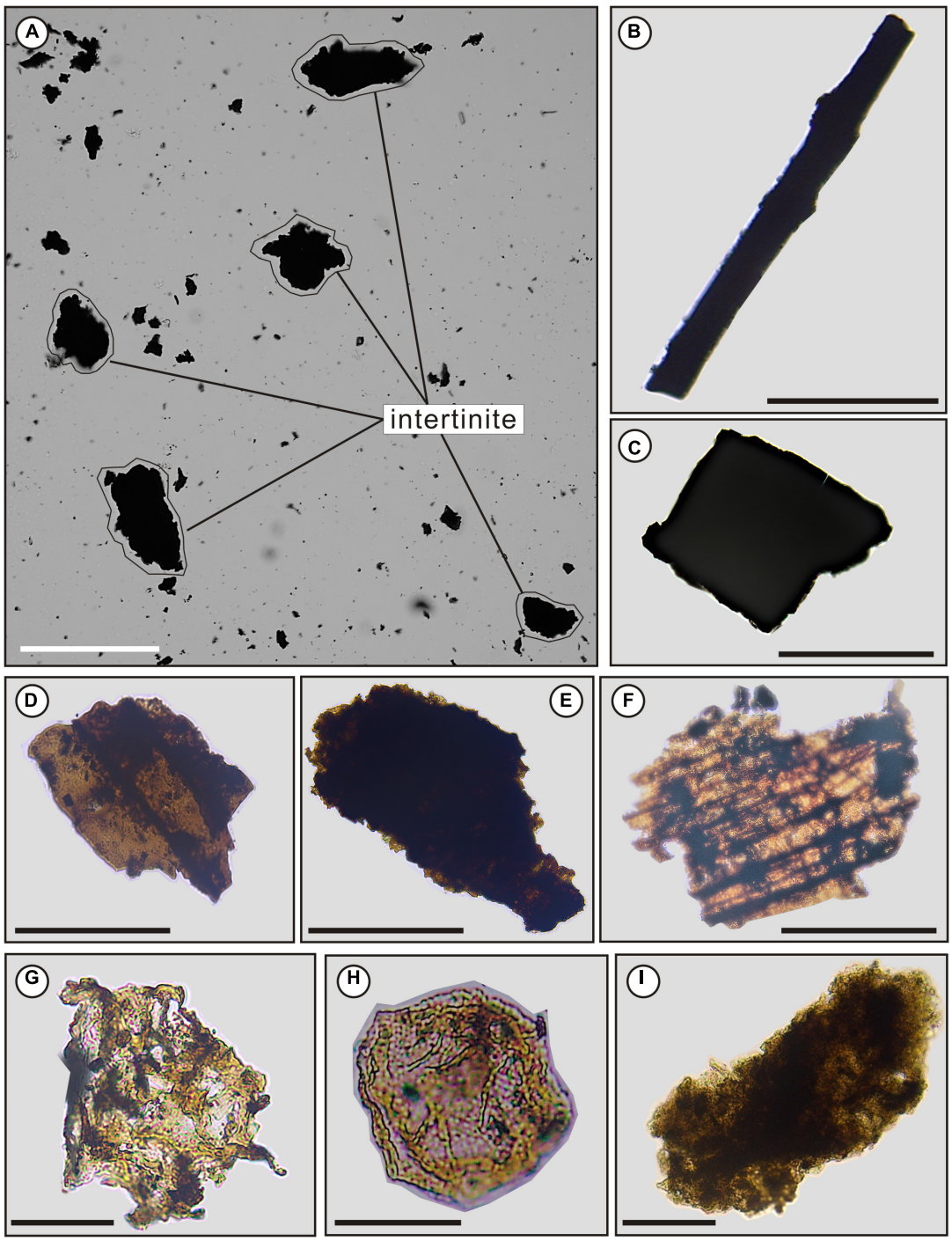

FIGURE 5 | Photomicrographs showing microstructure characteristics of kerogen macerals in the Jiyuan Basin (all scale bars = 50 μm). **(A)** Overview showing characteristics of inertinite (transmitted light, sample #38); **(B,C)** inertinite (transmitted light, samples #39 and #30); **(D,E)** vitrinite (transmitted light, sample #47); **(F)** suberinite (transmitted light, sample #19); **(G)** cutinite (transmitted light, sample #25); **(H)** saporopollenite (transmitted light, sample #42); **(I)** sapropelinite (transmitted light, sample #40).

area records the rapid proliferation of *Classopollis* pollen, and the subsequent restoration and dominance of conifers at the top of the assemblage zone (**Supplementary Table 1**, **Figure 2**, and **Supplementary Figure 1**). Similar records are known from the Early Jurassic of western Tethys (see above; e.g., Wignall and Atkinson, 2020). Collectively, these observations are consistent with the placement of the TJB at the base of AZ-IV (**Figure 2** and **Supplementary Figure 1**). As a result, we consider that the

fern spike recorded in the study area is representative of the global TJB record.

The T-J transition, beginning with the onset of the ETME, is one of the most ecologically significant intervals of the past 200 Ma and is characterized by dramatic global C cycle perturbations together with major changes in climate and ecosystem composition on land and in the oceans. Across the T-J transition, in particular where fossils or other diagnostic age markers are absent, chemostratigraphy and in particular C isotope stratigraphy can be used to correlate strata deposited in a diverse range of depositional environments (e.g., Korte et al., 2019; Pieńkowski et al., 2020; Ruhl et al., 2020; Fang et al., 2021).

In our study, Rock-Eval pyrolysis indicates that OM Rock-Eval pyrolysis data suggests that diagenetic processes are unlikely to be responsible for the observed shifts in the $\delta^{13}C$ signature of the OM, because such changes occur in late diagenetic to metamorphic burial stages that our material has not been subjected to (Dal Corso et al., 2018; Lu et al., 2021a). The two CIEs in the studied strata are also unlikely to have occurred through proportionate changes in terrestrial and algal organic carbon sources, which can be isotopically distinct from one another (Cloern et al., 2002). Variations in kerogen macerals reveal that the OM in the studied strata was from mixed sources of terrestrial plants and lacustrine plankton (see **Supplementary Material**). However, the proportion of OM sources did not change significantly during the two CIEs. Similarly, relatively high C/N ratios (see **Supplementary Material**) suggest that the OM throughout the succession is predominantly terrestrial with lower C/N ratios supporting a proportional increase in algal production during AZ-II and AZ-III (the shift to lower C/N ratios occurs between samples 42 and 41) (Cloern et al., 2002). Crucially no apparent relationship exists between C/N and $\delta^{13}C$ values across the CIEs. Furthermore, the $\delta^{13}C_{org}$ is largely limited by the pathway of plant photosynthesis and varies with plant types (e.g., Collister et al., 1994; Diefendorf and Freimuth, 2017). The two CIEs in the studied strata are synchronous with changes in fern spore and gymnosperm pollen abundances and the decreased plant diversity, indicating that whatever drove the CIEs might have affected the plant composition (e.g., van de Schootbrugge et al., 2008). However, changes in plant types is unlikely to be the driver of the observed CIEs in this study because those CIEs are remarkably similar to those in T-J transition $\delta^{13}C$ records in carbonates and in bulk marine and terrestrial OM (e.g., Bacon et al., 2011; **Figure 6** and **Supplementary Figure 4**). Compilation of global carbon isotope data has revealed a pattern of three isotopic excursions in both marine and continental strata. These comprise an initial excursion, then a small (unnamed) secondary excursion after a positive plateau, and finally a globally widespread main excursion (e.g., Hesselbo et al., 2002; Ruhl et al., 2009, 2010, 2020; Kovács et al., 2020; Wignall and Atkinson, 2020; Fang et al., 2021; Shen et al., 2022; **Figure 6**). In this study, the C isotope record exhibits similar features with two negative excursions comprising an initial CIE and an unnamed small CIE (**Figure 6**), that permit correlation with other TJB sections globally. The amplitude of the two CIEs in this study is consistent with those recorded in marine (–4 to –6.5‰) and continental (–2 to –4‰) strata in the Western Tethys Ocean in the middle and low latitudes of the northern hemisphere (**Figure 6** and **Supplementary Figure 4**). Therefore, we consider that CIE-I and CIE-II in this study reflect the changes to the global carbon cycle, namely the massive input carbon from an isotopically depleted carbon source.

In our study, CIE-I (−4.7‰) is characterized by a 45% reduction in plant diversity, the proliferation of fern spores, and an Hg/TOC peak (234.72 ppb/wt%, VA-I) during a phase of climatic warming (**Figures 2**, **6**). Similar features also characterize the former candidate global stratotype section and point (GSSP) at St. Audrie's section in the United Kingdom and the GSSP at Kuhjoch in Austria (**Figures 1A**, **6**). Here we use the candidate GSSP St. Audrie's section and the GSSP Kuhjoch section records as reference points (**Figures 1A**, **6**) since almost all other global T-J sections have been correlated with these (e.g., Ruhl et al., 2009, 2010, 2020; Lindström et al., 2017; Percival et al., 2017; Zaffani et al., 2018; Kovács et al., 2020; Pieńkowski et al., 2020; Wignall and Atkinson, 2020; Fang et al., 2021). However, numerous studies provide a range of interpretations in stratigraphic correlation, although in general the global C isotope curves are similar (Hesselbo et al., 2002; Ruhl et al., 2009, 2010, 2020; Lindström et al., 2017; Percival et al., 2017; Zaffani et al., 2018; Kovács et al., 2020; Wignall and Atkinson, 2020; Fang et al., 2021). The interpretation of Wignall and Atkinson (2020) is used here as it is the most representative and up to date. In their scheme, the initial CIE corresponds to the first extinction pulse that includes plant extinctions (see below) and Hg enrichment. A secondary unnamed CIE corresponds to a secondary extinction pulse that saw further losses within the plant record and Hg enrichment (e.g., Percival et al., 2017; Wignall and Atkinson, 2020). This indicates that the mass extinction history in Europe is pulsed and synchronous with C isotope excursions, facilitating global correlation of these phenomena (Wignall and Atkinson, 2020). Furthermore, the fern spore peaks in our study coincide with the initial CIE and the ETME. This observation has been reported in numerous sections (see references above) and further supports the placement of the onset of the ETME in the study area around CIE-I.

The younger CIE-II in the Jiyuan Basin succession is also widely known from marine and terrestrial records as the unnamed minor CIE in other areas (Hesselbo et al., 2002; Ruhl et al., 2009, 2010, 2020; Percival et al., 2017; Pieńkowski et al., 2020; Wignall and Atkinson, 2020; Fang et al., 2021; **Figure 6**). Like CIE-I, CIE-II is accompanied by a significant reduction in plant diversity in which 44% of genera are lost, and similar losses are known from other terrestrial records near the TJB (e.g., Wignall and Atkinson, 2020; Lindström, 2021). CIE-II is also accompanied by a minor Hg/TOC peak (144.93 ppb/wt%, VA-II). Warmer and drier climates persisted at this level in the study area indicated by the occurrence of calcareous nodules that formed through groundwater evaporation (e.g., Lu et al., 2020a and references therein) (**Figures 2**, **6**). Therefore, we consider it reasonable to place the TJB during the CIE-II interval based on (i) changes in biotic composition as reflected in biostratigraphy and palynofloral assemblage composition, and (ii) C isotope stratigraphy. This is supported by the ammonite-defined TJB at

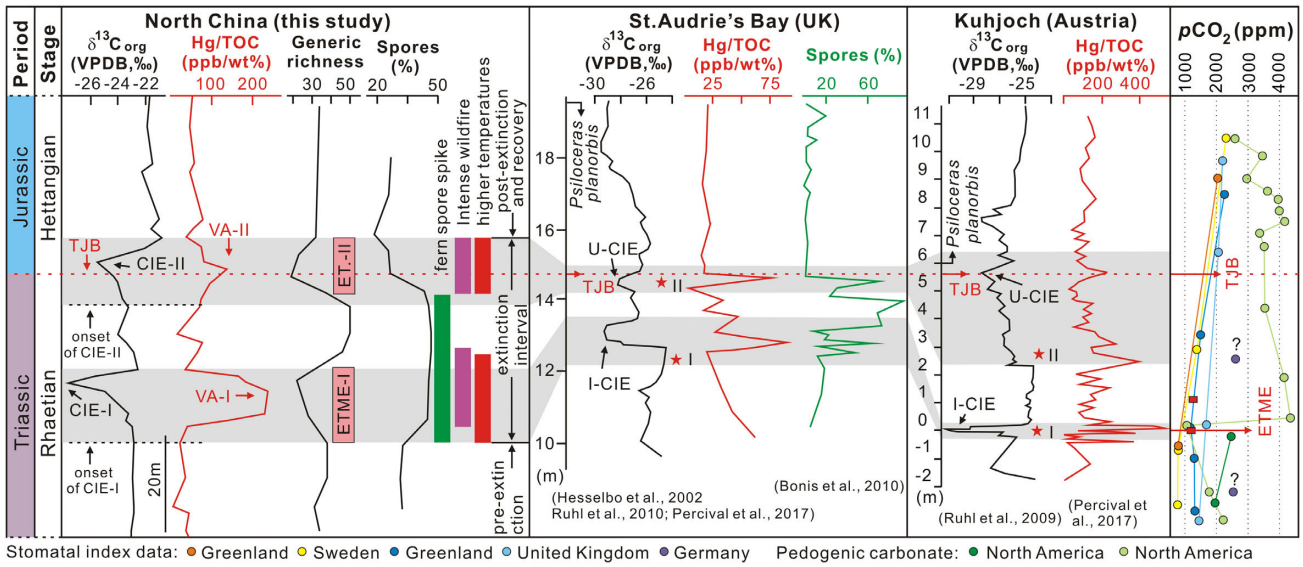

FIGURE 6 | Correlations of $\delta^{13}C_{org}$, Hg/TOC ratios, wildfire, spores (%), plant generic richness (number), and pCO_2 across the Triassic-Jurassic transition. Paleoclimate change inferred from palynology data. $\delta^{13}C_{org}$, Hg/TOC ratios, and spore data from the St. Audrie's Bay and Kuhjoch sections by Hesselbo et al. (2002), Ruhl et al. (2009), Bonis et al. (2010), Ruhl et al. (2010), and Percival et al. (2017) respectively; pCO_2 curves modified from Slodownik et al. (2021) and references therein. TJB, Triassic-Jurassic boundary; VPDB, Vienna Pee Dee Belemnite; CIE-I to CIE-II, from the first organic carbon isotope excursion to the second organic carbon isotope excursion; I-CIE, Initial CIE; U-CIE, Unnamed CIE; VA-I to VA-II, from the first volcanic activity to the second volcanic activity; ETME-I to ETME-II, from the first phase to the second phase of the end-Triassic mass extinction (ETME); Stars I and II mark the level of the first and second phase of extinction.

the GSSP at Kuhjoch, Austria (Ruhl et al., 2009) and other well-studied sections (e.g., Hesselbo et al., 2002; Percival et al., 2017; Pieńkowski et al., 2020; Ruhl et al., 2020; Wignall and Atkinson, 2020; Boomer et al., 2021; Fang et al., 2021; Shen et al., 2022) in which the TJB is below the main CIE and corresponds with a unnamed small negative CIE above the initial CIE (**Figure 6**).

Carbon cycle perturbations in the Jiyuan succession appear to have ended in the latter part of AZ-IV and the AZ-V interval is characterized by relatively stable C isotopic composition. This interval also saw stability return to climates and floral compositions (**Figures 2**, **6**), marking the end of the perturbations of the T-J transition. This can be correlated with records such as the Qilixia section in South China and the Haojiagou section in NW China, suggesting that the T-J transition approximately corresponds to the end of the secondary minor CIE, after the initial CIE (Fang et al., 2021; Shen et al., 2022).

Lacustrine Environmental and Floral Changes During the End-Triassic Mass Extinction

The timing and causal mechanism(s) of the ETME are controversial (e.g., van de Schootbrugge et al., 2009; Barbacka et al., 2017; Lindström et al., 2019; Wignall and Atkinson, 2020; Lindström, 2021; Lucas, 2021). Wignall and Atkinson (2020) document two pulses of extinction in marine and terrestrial settings, with pulses occurring during the initial and the minor (unnamed) negative CIEs during the T-J transition. On land, the first pulse of extinction is manifest as a decline in conifer pollen abundance and an overall plant diversity decline. This was followed by an interlude during which terrestrial assemblages were dominated by ferns, whose spores dominate the record from that interval. The second pulse of extinction caused another abrupt, palynological change, resulting in the loss of further pollen taxa and a brief proliferation of *Classopollis* pollen (Wignall and Atkinson, 2020). Our study also identifies a bimodal reduction in plant diversity, suggesting that the two-step extinction pattern is a globally widespread phenomenon (e.g., Wignall and Atkinson, 2020; Lindström, 2021). A rapid recovery of fern spores and their floral dominance (reaching 68.2% of all palynomorphs) (**Figure 2**) occurred in the interlude between ETME-I and ETME-II in the Jiyuan Basin. A similar pattern is known from both the southern and northern hemisphere including the Western Tethys ocean and the southern margins of Pangea (van de Schootbrugge et al., 2009; Lindström, 2016; Wignall and Atkinson, 2020).

The two pulses of plant diversity loss in the Jiyuan Basin (ETME-I and ETME-II) occurred during warming intervals indicated by the PCA analysis (**Figures 2**, **6**). Warming during the main CIE is supported by oxygen isotope data from oysters at Lavernock Point (United Kingdom) in the northwestern Tethys (Korte et al., 2009) and pCO_2 increases are recorded at both CIE levels are documented elsewhere in the record of pedogenic carbonates from the Newark Basin (Schaller et al., 2011) and the stomatal index (plant fossil cuticles) in Greenland and Sweden (McElwain et al., 1999; Slodownik et al., 2021), Germany (Bonis et al., 2010), and Northern Ireland (Steinthorsdottir et al., 2011; **Figure 6**).

Our data suggests that the two pulses of plant diversity collapse in the Jiyuan Basin are associated with significantly

different atmospheric humidities. ETME-I and the subsequent recovery occurred during humid conditions indicated by the proliferation of hygrophytic floral elements (including all spores, *Alisporites*, and *Cycadopites*) (**Figure 2** and **Supplementary Figure 1**). Similar records have been observed in Western Tethys (e.g., Hungary, Britain, Denmark, Greenland, and Canada) and southern Pangea (e.g., New Zealand, Western Australia, and Eastern Australia) and this has been interpreted as a result of increased humidity (van de Schootbrugge et al., 2009; Lindström, 2016). In contrast, ETME-II is associated with the development of an arid paleoclimate with high evaporation, as evidenced by decreased fern spore content, increasing Cheirolepidiaceae conifer content (*Classopollis* pollen), and the widespread occurrence of calcareous nodules in the core and in terrestrial outcrops (**Figures 2**, **7** and **Supplementary Figure 1**). Similar declines in fern spores and increases in gymnosperm pollen (e.g., *Classopollis* pollen) have been described for South China where they were interpreted as marking a shift toward warmer and drier conditions during the earliest Jurassic (Srivastava, 1976; Huang, 2001; Wang et al., 2010; Zhou et al., 2021).

In the Jiyuan Basin, ETME-I and ETME-II are also accompanied by enhanced paleo-wildfire indicated by the enrichment of fusinite (charcoal), as well as the appearance of a large number of charcoal particles in sediments (**Figures 3**, **7**). Enhanced wildfires during the T-J transition appears to be a global phenomenon (**Supplementary Figure 4**) as similar observations are known for other regions including North America (Jones et al., 2002), East Greenland (Belcher et al., 2010), Poland (Marynowski and Simoneit, 2009), Denmark and Sweden (Petersen and Lindström, 2012), and South China (Song et al., 2020).

A Volcanic Driver of Floral Change During the End-Triassic Mass Extinction

The emplacement of the CAMP is widely implicated as the ultimate driver of the ETME (Hesselbo et al., 2002; Schaltegger et al., 2008; Clémence et al., 2010; Bartolini et al., 2012; Percival et al., 2017; Lindström et al., 2019; Heimdal et al., 2020; Ruhl et al., 2020; Capriolo et al., 2021a,b; Shen et al., 2022). We have identified two Hg and Hg/TOC peaks in AZ-II and AZ-IV that are significantly higher than background levels seen in the other Assemblage Zones (**Figure 2** and **Supplementary Figure 5**). The behavior of Hg is complicated by depositional environment (Yager et al., 2021) and in terrestrial lake settings Hg can be sourced from the atmosphere (i.e., that associated with LIP volcanism) as well as from hydrological runoff (e.g., Shen et al., 2020; Lu et al., 2021a,b). The Hg preserved in the core material in this study is associated with OM derived from a mixture of terrestrial higher plants and lacustrine plankton in AZ-II and AZ-IV. Minor increases in TOC pre- and post-ETME are not accompanied by Hg peaks (**Figure 2**), supporting the notion that where terrestrial OM is enriched in Hg this was due to the effects of contemporaneous large-scale volcanism. Previous studies have shown that two or three Hg or Hg/TOC enrichment anomalies with likely origins in CAMP can be correlated across various sedimentary facies, from marine to terrestrial, during the T-J transition (Thibodeau et al., 2016; Percival et al., 2017; Lindström et al., 2019; Ruhl et al., 2020; Yager et al., 2021; Shen et al., 2022). Although the values of Hg and Hg/TOC enrichment anomalies vary spatially across different studied sections (**Figure 6**), Hg isotope data further support a CAMP source for elevated Hg contents across the ETME interval (Yager et al., 2021). Furthermore, two Hg enrichment anomalies in our study are synchronous with two pulses in terrestrial plant diversity, carbon cycle, enhanced wildfire and elevated temperature (**Figures 2**, **6**). Therefore, we consider the Hg/TOC ratios in this study as a reliable proxy for CAMP volcanism.

Volcanic activity can release copious amounts of isotopically light CO_2 into the reservoirs of the exogenic carbon cycle and can drive major global warming. As shown here and elsewhere (**Figure 6**), the close correspondence of Hg or Hg/TOC enrichment anomalies and CIEs during the T-J transition suggests that a large amount of isotopically light CO_2 entered the land atmosphere-ocean system during this interval. CLIMBER-3α + C Earth System model simulations suggest that pulses of CAMP volcanism potentially increased the global temperature by more than 4°C and might have triggered the disruption of the global end-Triassic carbon cycle (Landwehrs et al., 2020). Conservative estimates suggest that the emplacement of CAMP released between $\sim 1.4 \times 10^3$ Pg and 2.1×10^4 Pg of mantle C (Heimdal et al., 2020 and references therein). However, the isotope composition of volcanogenic CO_2 (mantle carbon $\sim -6‰$) means that the mass derived from CAMP emplacement is insufficient to drive the large negative CIEs associated with the ETME (e.g., Paris et al., 2016; Lindström et al., 2021). cGENIE model simulations (Vervoort et al., 2019) indicate that a negative CIE of $\geq 3‰$ (i.e., of similar magnitudes to those associated with the ETME), lasting ∼10–100 s of kyr, would require $> 3 \times 10^4$ PgC if the C mantle source had a $\delta^{13}C$ composition of $-6‰$. Similarly, GEOCLIM model simulations suggest that a CAMP-related negative CIE up to $\sim -6‰$ could be achieved by the release of repeated pulses of volcanic CO_2 if its isotopic signature was significantly light (–20‰; Paris et al., 2016). As a result, the ETME CIEs were likely in part driven by the addition of strongly ^{13}C-depleted C to the land atmosphere-ocean system from sources other than volcanic eruptions themselves. There is growing consensus that thermogenic C release was a contributing factor for the ETME CIEs (Svensen et al., 2009; van de Schootbrugge et al., 2009; Dal Corso et al., 2014; Heimdal et al., 2018, 2020). In addition, terrestrial or rock-bound organic C oxidation and methane release may have further contributed to the negative carbon isotope excursions (e.g., Ruhl et al., 2020; Capriolo et al., 2021a). In our study, two CIEs were contemporaneous with wildfires (**Figures 2**, **6**), raising the possibility that increased wildfire associated with volcanic activity provided a positive feedback in the global carbon cycle that further increased the magnitude of CIEs by releasing isotopically light carbon through combustion of biomass (e.g., Ivany and Salawitch, 1993; Belcher et al., 2010). Indeed, these hypotheses are not mutually exclusive and the different contributory factors probably acted in tandem to drive two major negative CIEs in the T-J interval. As a result, we favor a scenario in which repeated episodic light ^{13}C CO_2 release related

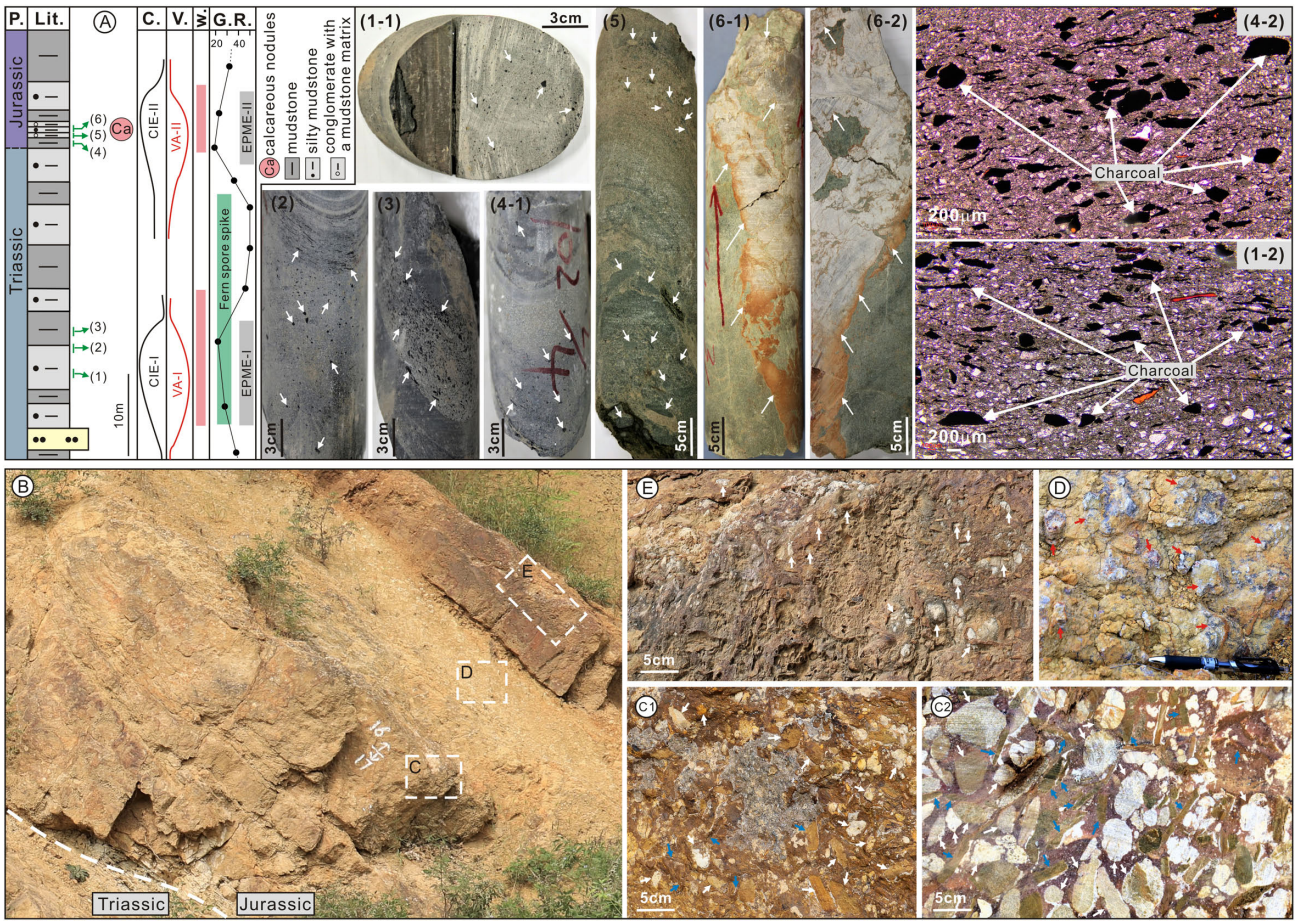

FIGURE 7 | Examples of abundant charcoal, conglomerate, mudstone clasts, and calcareous nodules from the borehole ZJ-1 and Sanhuang village section in the Jiyuan Basin during the Triassic-Jurassic transition. **(A)** Lithology, stratigraphic sequence, negative $\delta^{13}C_{org}$ excursions, volcanism, wildfire, and generic richness (number of difference genera) in the ZJ-1 borehole during the Triassic-Jurassic transition. Note (1-1), (2), (3), and (4-1) show abundant charcoal fossils in the middle Anyao Formation in the ZJ-1 borehole; (1-2) and (4-2) show microscopic images of charcoal fossils in the middle Anyao Formation in the ZJ-1 borehole; (5) shows mudstone clasts in the middle Anyao Formation in the ZJ-1 borehole; (6-1) and (6-2) show calcareous nodules in the middle Anyao Formation in the ZJ-1 borehole. **(B)** Lithology in the Sanhuang village section during the Triassic-Jurassic transition. **(C1,C2,D,E)** Abundant conglomerate, mudstone clasts, and calcareous nodules from the Sanhuang village section during the Triassic-Jurassic transition. Note the white arrows represent conglomerate, blue arrows represent mudstone clasts, red arrows represent calcareous nodules. P., Period; Lit., Lithology; C., Carbon cycle; V., Volcanism; W., Wildfire; G. R., Generic richness; CIE, carbon isotope excursion; VA, interval of volcanic activity; ETME-I, first phase to the second phase of the end-Triassic mass extinction; ETME-II, second phase to the second phase of the end-Triassic mass extinction.

to CAMP volcanism and its direct effects was responsible for the CIEs (e.g., Capriolo et al., 2021b), and drove contemporaneous global warming, as suggested by the PCA results.

Though global warming as a result of large-scale volcanism could be expected to have a major impact on plants, it appears that the development of intense wildfires—an indirect function of volcanism—seems to have the most profound impact on terrestrial plant ecosystems (**Figure 8** and **Supplementary Figure 6**). We suggest that the warming climate resulting from pulsed CAMP eruptions increased the frequency of lightning and wildfires (see **Supplementary Material**), resulting in the deterioration of terrestrial ecosystems (e.g., soil erosion) and associated reductions in plant diversity (**Figures 2**, **6**, **8** and **Supplementary Figure 6**). Frequent and intense wildfires were not only the direct cause of changes in terrestrial plant ecosystems and species diversity but also represent a vital link between the lake and terrestrial ecological crisis (e.g., Lu et al., 2020a; Mays et al., 2021). Thus, wildfire disruption to land surface vegetation would cause increased soil erosion, itself increasing nutrient runoff, but also further exposing bedrock and increasing continental weathering leading to siltation (Glasspool et al., 2015; Lu et al., 2020a). These processes can lead to large amounts of OM (including charcoal and un-charred material), and other substances entering the lake system through surface runoff (**Supplementary Figure 6**), promoting eutrophication and blooms of cyanobacteria and algae in freshwater environments, just as shown in the Jiyuan Basin. In this case, oxygen circulation between freshwater and atmosphere would have been inhibited by floating inert organic particles, cyanobacteria and algae in surface waters (e.g., Lu et al., 2020a). Cyanobacterial and algal

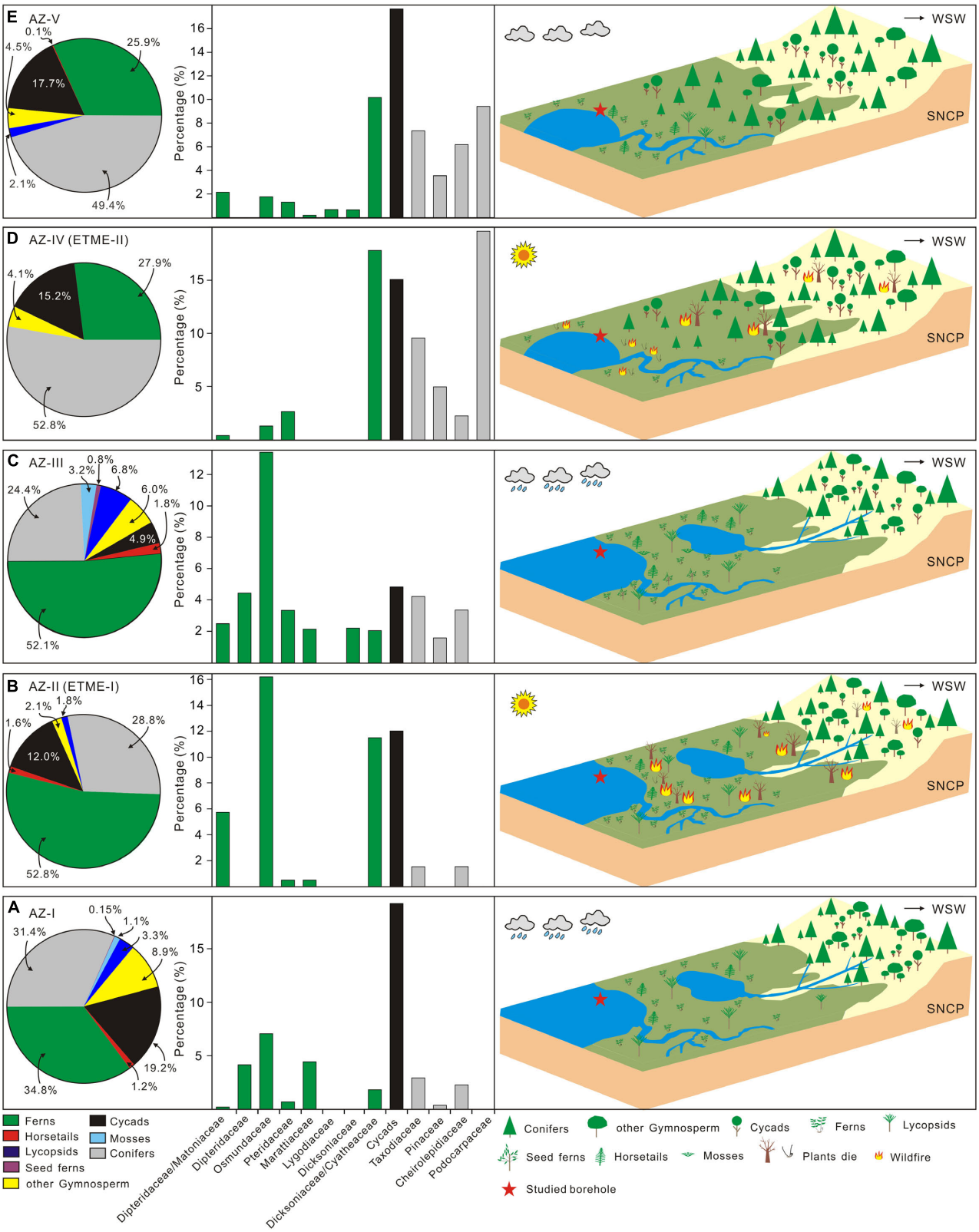

FIGURE 8 | Paleovegetation composition and paleoenvironmental reconstruction of the Jiyuan Basin illustrating five distinct **(A–E)** floral assemblages across the Triassic-Jurassic transition. AZ-I to AZ-V, palynology assemblage zone (AZ) I to the V; ETME-I, first stage of the end Triassic mass extinction; ETME-II, second stage of the end Triassic mass extinction; WSW, west-southwest; SNCP, southern North China Plate.

blooms would likely have contributed to the consumption of dissolved oxygen through decomposition post-mortem. It is possible that they produced secondary metabolites toxic to animals, impeding the recovery of lake freshwater ecosystems (Mays et al., 2021) in a scenario, similar to that proposed for the Carnian Pluvial Episode (Lu et al., 2021a) and the end-Permian extinction (Mays et al., 2021).

DATA AVAILABILITY STATEMENT

The original contributions presented in the study are included in the article/**Supplementary Material**, further inquiries can be directed to the corresponding author/s.

AUTHOR CONTRIBUTIONS

PZ, JL, MY, LS, and JH designed the research. JL, PZ, MY, LS, LL, and JH analyzed the data. PZ, JL, MY, LS, DB, SG, LL, and JH wrote the manuscript. All authors contributed to the interpretation of the data and to the final manuscript.

FUNDING

Financial support was provided from the National Key Research and Development Program of China (2021YFC2902000), the Natural Environment Research Council's Biosphere Evolution, Transition and Resilience (BETR) Program (NE/P0137224/1), the National Natural Science Foundation of China (Grant nos. 42172196, 41772161, and 41472131), and the National Science and Technology Major Project (Award no. 2017ZX05009-002).

ACKNOWLEDGMENTS

We are grateful to Suping Peng and Shifeng Dai (China University of Mining and Technology Beijing) for comments on earlier versions of the manuscript. We thank Simonetta Cirilli and Guillaume Paris for constructive and helpful reviews of the manuscript.

SUPPLEMENTARY MATERIAL

The Supplementary Material for this article can be found online at: https://www.frontiersin.org/articles/10.3389/fevo.2022.853404/full#supplementary-material

REFERENCES

Bacon, K. L., Belcher, C. M., Hesselbo, S. P., and McElwain, J. C. (2011). The Triassic-Jurassic boundary carbon-isotope excursions expressed in taxonomically identified leaf cuticles. *Palaios* 26, 461–469. doi: 10.2110/palo.2010.p10-120r

Barbacka, M., Pacyna, G., Kocsis, Á. T., Jarzynka, A., Ziaja, J., and Bodor, E. (2017). Changes in terrestrial floras at the Triassic-Jurassic Boundary in Europe. *Palaeogeogr. Palaeoclimatol. Palaeoecol.* 480, 80–93. doi: 10.1016/j.palaeo.2017.05.024

Bartolini, A., Guex, J., Spangenberg, J. E., Schoene, B., Taylor, D. G., Schaltegger, U., et al. (2012). Disentangling the Hettangian carbon isotope record: implications for the aftermath of the end-Triassic mass extinction. *Geochem. Geophys. Geosyst.* 13:Q01007. doi: 10.1029/2011GC003807

Belcher, C. M., Mander, L., Rein, G., Jervis, F. X., Haworth, M., Hesselbo, S. P., et al. (2010). Increased fire activity at the Triassic/Jurassic boundary in Greenland due to climate-driven floral change. *Nat. Geosci.* 3, 426–429. doi: 10.1038/ngeo871

Bond, D. P. G., and Wignall, P. B. (2014). "Large igneous provinces and mass extinctions: an update," in *Volcanism, Impacts, and Mass Extinctions: Causes and Effects*, eds G. Keller and A. C. Kerr (Boulder, CO: Geological Society of America), 29–55.

Bonis, N. R., Kürschner, W. M., and Krystyn, L. (2009). A detailed palynological study of the Triassic-Jurassic transition in key sections of the Eiberg Basin (Northern Calcareous Alps, Austria). *Rev. Palaeobot. Palynol.* 156, 376–400. doi: 10.1016/j.revpalbo.2009.04.003

Bonis, N. R., Ruhl, M., and Kürschner, W. M. (2010). Milankovitch-scale palynological turnover across the Triassic-Jurassic transition at St. Audrie's Bay, SW UK. *J. Geol. Soc. Lond.* 167, 877–888. doi: 10.1144/0016-76492009-141

Boomer, I., Copestake, P., Raine, R., Azmi, A., Fenton, J. P. G., Page, K. N., et al. (2021). Stratigraphy, palaeoenvironments and geochemistry across the Triassic-Jurassic boundary transition at Carnduff, County Antrim, Northern Ireland. *Proc. Geol. Assoc.* 132, 667–687. doi: 10.1016/j.pgeola.2020.05.004

Bustin, R., and Guo, Y. (1999). Abrupt changes (jumps) in reflectance values and chemical compositions of artificial charcoals and inertinite in coals. *Int. J. Coal Geol.* 38, 237–260. doi: 10.1016/S0166-5162(98)00025-1

Capriolo, M., Marzoli, A., Aradi, L. E., Ackerson, M. R., Bartoli, O., Callegaro, S., et al. (2021a). Massive methane fluxing from magma–sediment interaction in the end-Triassic Central Atlantic Magmatic Province. *Nat. Commun.* 12:5534. doi: 10.1038/s41467-021-25510-w

Capriolo, M., Mills, B. J. W., Newton, R. J., Corso, J. D., Dunhill, A. M., Wignall, P. B., et al. (2021b). Anthropogenic-scale CO_2 degassing from the Central Atlantic Magmatic Province as a driver of the end-Triassic mass extinction. *Glob. Planet. Change* 209:103731. doi: 10.1016/j.gloplacha.2021.103731

Cirilli, S. (2010). Upper Triassic-lowermost Jurassic palynology and palynostratigraphy: a review. *Geol. Soc. Spec. Publ.* 334, 285–314. doi: 10.1144/SP334.12

Cirilli, S., Buratti, N., Gugliotti, L., and Frixa, A. (2015). Palynostratigraphy and palynofacies of the Upper Triassic Streppenosa Formation (SE Sicily, Italy) and inference on the main controlling factors in the organic rich shale deposition. *Rev. Palaeobot. Palynol.* 218, 67–79. doi: 10.1016/j.revpalbo.2014.10.009

Cirilli, S., Marzoli, A., Tanner, L., Bertrand, H., Buratti, N., Jourdan, F., et al. (2009). Latest Triassic onset of the Central Atlantic Magmatic Province (CAMP) volcanism in the Fundy Basin (Nova Scotia): new stratigraphic constraints. *Earth Planet. Sci. Lett.* 286, 514–525. doi: 10.1016/j.epsl.2009.07.021

Cirilli, S., Panfili, G., Buratti, N., and Frixa, A. (2018). Paleoenvironmental reconstruction by means of palynofacies and lithofacies analyses: an example from the Upper Triassic subsurface succession of the Hyblean Plateau Petroleum System (SE Sicily, Italy). *Rev. Palaeobot. Palynol.* 253, 70–87. doi: 10.1016/j.revpalbo.2018.04.003

Clémence, M., Bartolini, A., Gardin, S., Paris, G., Beaumont, V., and Page, K. N. (2010). Early Hettangian benthic–planktonic coupling at Doniford (SW England). *Palaeogeogr. Palaeoclimatol. Palaeoecol.* 295, 102–115. doi: 10.1016/j.palaeo.2010.05.021

Cloern, J. E., Canuel, E. A., and Harris, D. (2002). Stable carbon and nitrogen isotope composition of aquatic and terrestrial plants of the San Francisco Bay estuarine system. *Limnol. Oceanogr.* 47, 713–729. doi: 10.4319/lo.2002.47.3.0713

Collister, J. W., Rieley, G., Stern, B., Eglinton, G., and Fry, B. (1994). Compound-specific δ13C analyses of leaf lipids from plants with differing carbon dioxide metabolisms. *Org. Geochem.* 21, 619–627. doi: 10.1016/0146-6380(94)90008-6

Dal Corso, J., Gianolla, P., Rigo, M., Franceschi, M., Roghi, G., Mietto, P., et al. (2018). Multiple negative carbon-isotope excursions during the Carnian Pluvial Episode (Late Triassic). *Earth Sci. Rev.* 185, 732–750. doi: 10.1016/j.earscirev.2018.07.004

Dal Corso, J., Marzoli, A., Tateo, F., Jenkyns, H. C., Bertrand, H., Youbi, N., et al. (2014). The dawn of CAMP volcanism and its bearing on the end-Triassic carbon cycle disruption. *J. Geol. Soc. Lond.* 171, 153–164. doi: 10.1144/jgs2013-063

Dal Corso, J., Song, H. J., Callegaro, S., Chu, D. L., Sun, Y. D., Hilton, J., et al. (2022). Environmental crises at the Permian–Triassic mass extinction. *Nat. Rev. Earth Environ.* doi: 10.1038/s43017-021-00259-4

De Jersey, N. J., and McKellar, J. L. (2013). The palynology of the Triassic-Jurassic transition in southeastern Queensland, Australia, and correlation with New Zealand. *Palynology* 37, 77–114. doi: 10.1080/01916122.2012.718609

Deng, S. H., Lu, Y. Z., Fan, R., Pan, Y. H., Cheng, X. S., Fu, G. B., et al. (2010). *The Jurassic System of Northern Xinjiang, China*. Hefei: University of Science and Technology of China Press. (in Chinese with English abstract).

Diefendorf, A. F., and Freimuth, E. J. (2017). Extracting the most from terrestrial plant-derived n-alkyl lipids and their carbon isotopes from the sedimentary record: a review. *Org. Geochem.* 103, 1–21. doi: 10.1016/j.orggeochem.2016.10.016

Fang, Y., Fang, L., Deng, S., Lu, Y., Wang, B., Zhao, X., et al. (2021). Carbon isotope stratigraphy across the Triassic-Jurassic boundary in the high-latitude terrestrial Junggar Basin, NW China. *Palaeogeogr. Palaeoclimatol. Palaeoecol.* 577:110559. doi: 10.1016/j.palaeo.2021.110559

Fu, Z., and Yuan, X. (1998). Late Triassic sporopollen assemblage from Liupanshan Basin of Ningxia and their stratigraphical significance. *Acta Palaeontol. Sin.* 37, 446–454.

Glasspool, I. J., Scott, A. C., Waltham, D., Pronina, N., and Shao, L. (2015). The impact of fire on the late Paleozoic Earth System. *Front. Plant Sci.* 6:756. doi: 10.3389/fpls.2015.00756

Goodarzi, F. (1985). Optically anisotropic fragments in a Western Canadian subbituminous coal. *Fuel* 64, 1294–1300. doi: 10.1016/0016-2361(85)90191-7

Greene, S. E., Martindale, R. C., Ritterbush, K. A., Bottjer, D. J., Corsetti, F. A., and Berelson, W. M. (2012). Recognising ocean acidification in deep time: an evaluation of the evidence for acidification across the Triassic-Jurassic boundary. *Earth Sci. Rev.* 113, 72–93. doi: 10.1016/j.earscirev.2012.03.009

Heimdal, T. H., Jones, M. T., and Henrik, H. S. (2020). Thermogenic carbon release from the Central Atlantic magmatic province caused major end-Triassic carbon cycle perturbations. *Proc. Natl. Acad. Sci. U.S.A.* 117, 11968–11974. doi: 10.1073/pnas.2000095117

Heimdal, T. H., Svensen, H. H., Ramezani, J., Iyer, K., Pereira, E., Rodrigues, R., et al. (2018). Large-scale sill emplacement in Brazil as a trigger for the end-Triassic crisis. *Sci. Rep.* 8:141. doi: 10.1038/s41598-017-18629-8

Hesselbo, S. P., Robinson, S. A., Surlyk, F., and Piasecki, S. (2002). Terrestrial and marine extinction at the Triassic-Jurassic boundary synchronized with major carbon-cycle perturbation: a link to initiation of massive volcanism? *Geology* 30, 251–254. doi: 10.1130/0091-7613(2002)030<0251:tameat>2.0.co;2

Hu, B. (1991). The late Triassic and middle Jurassic continental strata in Jiyuan basin, Henan Province. *J. Stratigr.* 15, 48–52.

Huang, Q. (2001). Early Jurassic flora and paleoenvironment in Daxian and Kaixian counties, northern border of Sichuan basin (in Chinese with English abstract). *Earth Sci. China Univ. Geosci.* 26, 221–227.

Ivany, L. C., and Salawitch, R. J. (1993). Carbon isotopic evidence for biomass burning at the K-T boundary. *Geology* 21:487. doi: 10.1130/0091-7613(1993)021<0487:ciefbb>2.3.co;2

Jones, T. P., Ash, S., and Figueiral, I. (2002). Late Triassic charcoal from Petrified Forest National Park, Arizona, USA. *Palaeogeogr. Palaeoclimatol. Palaeoecol.* 188, 127–139. doi: 10.1016/S0031-0182(02)00549-7

Korte, C., Hesselbo, S. P., Jenkyns, H. C., Rickaby, R. E. M., and Spötl, C. (2009). Palaeoenvironmental significance of carbon- and oxygen-isotope stratigraphy of marine Triassic–Jurassic boundary sections in SW Britain. *J. Geol. Soc. Lond.* 166, 431–445. doi: 10.1144/0016-76492007-177

Korte, C., Ruhl, M., Pálfy, J., Ullmann, C. V., and Hesselbo, S. P. (2019). "Chemostratigraphy across the Triassic-Jurassic boundary," in *Chemostratigraphy Across Major Chronological Boundaries*, eds A. N. Sial, C. Gaucher, M. Ramkumar, and V. P. Ferreira (Washington, DC: American Geophysical Union (AGU)), 183–210. doi: 10.1002/9781119382508.ch10

Kovács, E. B., Ruhl, M., Demény, A., Fórizs, I., Hegyi, I., Horváth-Kostka, Z. R., et al. (2020). Mercury anomalies and carbon isotope excursions in the western Tethyan Csővár section support the link between CAMP volcanism and the end-Triassic extinction. *Glob. Planet. Change* 194:103291. doi: 10.1016/j.gloplacha.2020.103291

Kuerschner, W. M., Bonis, N. R., and Krystyn, L. (2007). Carbon-isotope stratigraphy and palynostratigraphy of the Triassic–Jurassic transition in the Tiefengraben section – Northern Calcareous Alps (Austria). *Palaeogeogr. Palaeoclimatol. Palaeoecol.* 244, 257–280. doi: 10.1016/j.palaeo.2006.06.031

Landwehrs, J. P., Feulner, G., Hofmann, M., and Petri, S. (2020). Climatic fluctuations modeled for carbon and sulfur emissions from end-Triassic volcanism. *Earth Planet. Sci. Lett.* 537:116174. doi: 10.1016/j.epsl.2020.116174

Li, L., Wang, Y., Kürschner, W. M., Ruhl, M., and Vajda, V. (2020). Palaeovegetation and palaeoclimate changes across the Triassic – Jurassic transition in the Sichuan Basin, China. *Palaeogeogr. Palaeoclimatol. Palaeoecol.* 556:109891. doi: 10.1016/j.palaeo.2020.109891

Li, M., Zheng, D., Dai, G., Liu, C., and Zhou, L. (2014). Geochemical characteristics of the Jurassic argillaceous rocks of the Jiyuan Basin, Western Henan and the implications for environments and provenances. *Acta Geol. Sin.* 88, 229–238.

Lindström, S. (2016). Palynofloral patterns of terrestrial ecosystem change during the end-Triassic event – a review. *Geol. Mag.* 153, 223–251. doi: 10.1017/S0016756815000552

Lindström, S. (2021). Two-phased mass rarity and extinction in land plants during the end-Triassic climate crisis. *Front. Earth Sci.* 9:780343. doi: 10.3389/feart.2021.780343

Lindström, S., Callegaro, S., Davies, J., Tegner, C., van de Schootbrugge, B., Pedersen, G. K., et al. (2021). Tracing volcanic emissions from the Central Atlantic Magmatic Province in the sedimentary record. *Earth Sci. Rev.* 212:103444. doi: 10.1016/j.earscirev.2020.103444

Lindström, S., Sanei, H., van de Schootbrugge, B., Pedersen, G. K., Lesher, C. E., Tegner, C., et al. (2019). Volcanic mercury and mutagenesis in land plants during the end-Triassic mass extinction. *Sci. Adv.* 5:eaaw4018. doi: 10.1126/sciadv.aaw4018

Lindström, S., van de Schootbrugge, B., Hansen, K. H., Pedersen, G. K., Alsen, P., Thibault, N., et al. (2017). A new correlation of Triassic–Jurassic boundary successions in NW Europe, Nevada and Peru, and the Central Atlantic Magmatic Province: a time-line for the end-Triassic mass extinction. *Palaeogeogr. Palaeoclimatol. Palaeoecol.* 478, 80–102. doi: 10.1016/j.palaeo.2016.12.025

Liu, S., Su, S., and Zhang, G. (2013). Early Mesozoic basin development in North China: indications of cratonic deformation. *J. Asian Earth Sci.* 62, 221–236. doi: 10.1016/j.jseaes.2012.09.011

Liu, Z., Li, L., and Wang, Y. (2015). Late Triassic spore-pollen assemblage from Xuanhan of Sichuan,China. *Acta Micropala Eontol. Sin.* 32, 43–62. doi: 10.16087/j.cnki.1000-0674.20150407.006

Lu, J., Zhang, P., Dal Corso, J., Yang, M., Wignall, P. B., Greene, S. E., et al. (2021a). Volcanically driven lacustrine ecosystem changes during the Carnian Pluvial Episode (Late Triassic). *Proc. Natl. Acad. Sci. U.S.A.* 118:e2109895118. doi: 10.1073/pnas.2109895118

Lu, J., Zhou, K., Yang, M., Zhang, P., Shao, L., and Hilton, J. (2021b). Records of organic carbon isotopic composition ($\delta^{13}C_{org}$) and volcanism linked to changes in atmospheric pCO_2 and climate during the Late Paleozoic Icehouse. *Glob. Planet. Change* 207:103654. doi: 10.1016/j.gloplacha.2021.103654

Lu, J., Wang, Y., Yang, M., Shao, L., and Hilton, J. (2021c). Records of volcanism and organic carbon isotopic composition ($\delta^{13}C_{org}$) linked to changes in atmospheric pCO_2 and climate during the Pennsylvanian icehouse interval. *Chem. Geol.* 570:120168. doi: 10.1016/j.chemgeo.2021.120168

Lu, J., Zhang, P., Yang, M., Shao, L., and Hilton, J. (2020a). Continental records of organic carbon isotopic composition ($\delta^{13}C_{org}$), weathering, paleoclimate and wildfire linked to the End-Permian Mass Extinction. *Chem. Geol.* 558:119764. doi: 10.1016/j.chemgeo.2020.119764

Lu, J., Zhou, K., Yang, M., Eley, Y., Shao, L., and Hilton, J. (2020b). Terrestrial organic carbon isotopic composition ($\delta^{13}C_{org}$) and environmental

perturbations linked to Early Jurassic volcanism: evidence from the Qinghai-Tibet Plateau of China. *Glob. Planet. Change* 195:103331. doi: 10.1016/j.gloplacha.2020.103331

Lu, Y., and Deng, S. (2005). Triassic-Jurassic sporopollen assemblages on the Southern Margin of the Junggar Basin, Xinjiang and the T-J Boundary. *Acta Geol. Sin.* 1, 15–28. doi: 10.3321/j.issn:0001-5717.2005.01.003

Lucas, S. G. (2021). "End-triassic extinctions," in *Encyclopedia of Geology*, eds D. Alderton and S. A. Elias (Amsterdam: Elsevier), 653–664. doi: 10.1016/B978-0-12-409548-9.12013-5

Lucas, S. G., and Tanner, L. H. (2015). End-Triassic nonmarine biotic events. *J. Palaeogeogr.* 4, 331–348. doi: 10.1016/j.jop.2015.08.010

Marynowski, L., and Simoneit, B. R. T. (2009). Widespread upper Triassic to lower Jurassic wildfire records from poland: evidence from charcoal and pyrolytic polycyclic aromatic hydrocarbons. *Palaios* 24, 785–798. doi: 10.2110/palo.2009.p09-044r

Marzoli, A., Bertrand, H., Knight, K. B., Cirilli, S., Buratti, N., Vérati, C., et al. (2004). Synchrony of the Central Atlantic magmatic province and the Triassic-Jurassic boundary climatic and biotic crisis. *Geology* 32, 973–976. doi: 10.1130/G20652.1

Marzoli, A., Bertrand, H., Knight, K. B., Cirilli, S., Nomade, S., Renne, P. R., et al. (2008). Comment on "Synchrony between the Central Atlantic magmatic province and the Triassic-Jurassic mass-extinction event? By Whiteside et al. (2007)." *Palaeogeogr. Palaeoclimatol. Palaeoecol.* 262, 189–193. doi: 10.1016/j.palaeo.2008.01.016

Mays, C., McLoughlin, S., Frank, T. D., Fielding, C. R., Slater, S. M., and Vajda, V. (2021). Lethal microbial blooms delayed freshwater ecosystem recovery following the end-Permian extinction. *Nat. Commun.* 12:5511. doi: 10.1038/s41467-021-25711-3

McElwain, J. C., Beerling, D. J., and Woodward, F. I. (1999). Fossil plants and global warming at the Triassic-Jurassic boundary. *Science* 285, 1386–1390. doi: 10.1126/science.285.5432.1386

McElwain, J. C., Popa, M. E., Hesselbo, S. P., Haworth, M., and Surlyk, F. (2007). Macroecological responses of terrestrial vegetation to climatic and atmospheric change across the Triassic/Jurassic boundary in East Greenland. *Paleobiology* 33, 547–573. doi: 10.1666/06026.1

Miller, C. S., and Baranyi, V. (2021). "Triassic climates," in *Encyclopedia of Geology*, eds D. Alderton and S. A. B. T. Elias (Oxford: Elsevier), 514–524. doi: 10.1016/B978-0-12-409548-9.12070-6

Olsen, P. E., Kent, D. V., Sues, H. D., Koeberl, C., Huber, H., Montanari, A., et al. (2002). Ascent of dinosaurs linked to an iridium anomaly at the Triassic-Jurassic boundary. *Science* 296, 1305–1307. doi: 10.1126/science.1065522

Panfili, G., Cirilli, S., Corso, J. D., Bertrand, H., Medina, F., Youbi, N., et al. (2019). New biostratigraphic constraints show rapid emplacement of the Central Atlantic Magmatic Province (CAMP) during the end-Triassic mass extinction interval. *Glob. Planet. Change* 172, 60–68. doi: 10.1016/j.gloplacha.2018.09.009

Paris, G., Donnadieu, Y., Beaumont, V., Fluteau, F., and Goddéris, Y. (2016). Geochemical consequences of intense pulse-like degassing during the onset of the Central Atlantic Magmatic Province. *Palaeogeogr. Palaeoclimatol. Palaeoecol.* 441, 74–82. doi: 10.1016/j.palaeo.2015.04.011

Percival, L. M. E., Ruhl, M., Hesselbo, S. P., Jenkyns, H. C., Mather, T. A., and Whiteside, J. H. (2017). Mercury evidence for pulsed volcanism during the end-Triassic mass extinction. *Proc. Natl. Acad. Sci. U.S.A.* 114, 7929–7934. doi: 10.1073/pnas.1705378114

Petersen, H. I., and Lindström, S. (2012). Synchronous wildfire activity rise and mire deforestation at the Triassic–Jurassic boundary. *PLoS One* 7:e47236. doi: 10.1371/journal.pone.0047236

Pieńkowski, G., Hesselbo, S. P., Barbacka, M., and Leng, M. J. (2020). Non-marine carbon-isotope stratigraphy of the Triassic-Jurassic transition in the Polish Basin and its relationships to organic carbon preservation, pCO_2 and palaeotemperature. *Earth Sci. Rev.* 210:103383. doi: 10.1016/j.earscirev.2020.103383

Pieńkowski, G., Niedźwiedzki, G., and Waksmundzka, M. (2012). Sedimentological, palynological and geochemical studies of the terrestrial Triassic-Jurassic boundary in northwestern Poland. *Geol. Mag.* 149, 308–332. doi: 10.1017/S0016756811000914

Raup, D. M., and Sepkoski, J. J. (1982). Mass extinctions in the marine fossil record. *Science* 215, 1501–1503. doi: 10.1126/science.215.4539.1501

Ruhl, M., Deenen, M. H. L., Abels, H. A., Bonis, N. R., Krijgsman, W., and Kürschner, W. M. (2010). Astronomical constraints on the duration of the early Jurassic Hettangian stage and recovery rates following the end-Triassic mass extinction (St Audrie's Bay/East Quantoxhead, UK). *Earth Planet. Sci. Lett.* 295, 262–276. doi: 10.1016/j.epsl.2010.04.008

Ruhl, M., Hesselbo, S. P., Al-Suwaidi, A., Jenkyns, H. C., Damborenea, S. E., Manceñido, M. O., et al. (2020). On the onset of Central Atlantic Magmatic Province (CAMP) volcanism and environmental and carbon-cycle change at the Triassic–Jurassic transition (Neuquén Basin, Argentina). *Earth Sci. Rev.* 208:103229. doi: 10.1016/j.earscirev.2020.103229

Ruhl, M., Kürschner, W. M., and Krystyn, L. (2009). Triassic–Jurassic organic carbon isotope stratigraphy of key sections in the western Tethys realm (Austria). *Earth Planet. Sci. Lett.* 281, 169–187. doi: 10.1016/j.epsl.2009.02.020

Schaller, M. F., Wright, J. D., and Kent, D. V. (2011). Atmospheric PCO_2 perturbations associated with the central Atlantic magmatic province. *Science* 331, 1404–1409. doi: 10.1126/science.1199011

Schaltegger, U., Guex, J., Bartolini, A., Schoene, B., and Ovtcharova, M. (2008). Precise U-Pb age constraints for end-Triassic mass extinction, its correlation to volcanism and Hettangian post-extinction recovery. *Earth Planet. Sci. Lett.* 267, 266–275. doi: 10.1016/j.epsl.2007.11.031

Schoene, B., Guex, J., Bartolini, A., Schaltegger, U., and Blackburn, T. J. (2010). Correlating the end-Triassic mass extinction and flood basalt volcanism at the 100 ka level. *Geology* 38, 387–390. doi: 10.1130/G30683.1

Sha, J., Olsen, P. E., Pan, Y., Xu, D., Wang, Y., Zhang, X., et al. (2015). Triassic–Jurassic climate in continental high-latitude Asia was dominated by obliquity-paced variations (Junggar Basin, Ürümqi, China). *Proc. Natl. Acad. Sci. U.S.A.* 112, 3624–3629. doi: 10.1073/pnas.1501137112

Shen, J., Feng, Q., Algeo, T. J., Liu, J., Zhou, C., Wei, W., et al. (2020). Sedimentary host phases of mercury (Hg) and implications for use of Hg as a volcanic proxy. *Earth Planet. Sci. Lett.* 543:116333. doi: 10.1016/j.epsl.2020.116333

Shen, J., Yin, R., Zhang, S., Algeo, T. J., Bottjer, D. J., Yu, J., et al. (2022). Intensified continental chemical weathering and carbon-cycle perturbations linked to volcanism during the Triassic–Jurassic transition. *Nat. Commun.* 13:299. doi: 10.1038/s41467-022-27965-x

Slodownik, M., Vajda, V., and Steinthorsdottir, M. (2021). Fossil seed fern *Lepidopteris ottonis* from Sweden records increasing CO_2 concentration during the end-Triassic extinction event. *Palaeogeogr. Palaeoclimatol. Palaeoecol.* 564:110157. doi: 10.1016/j.palaeo.2020.110157

Song, Y., Algeo, T. J., Wu, W., Luo, G., Li, L., Wang, Y., et al. (2020). Distribution of pyrolytic PAHs across the Triassic-Jurassic boundary in the Sichuan Basin, southwestern China: evidence of wildfire outside the Central Atlantic Magmatic Province. *Earth Sci. Rev.* 201:102970. doi: 10.1016/j.earscirev.2019.102970

Srivastava, S. K. (1976). The fossil pollen genus *Classopollis*. *Lethaia* 9, 437–457. doi: 10.1111/j.1502-3931.1976.tb00985.x

Steinthorsdottir, M., Jeram, A. J., and McElwain, J. C. (2011). Extremely elevated CO_2 concentrations at the Triassic/Jurassic boundary. *Palaeogeogr. Palaeoclimatol. Palaeoecol.* 308, 418–432. doi: 10.1016/j.palaeo.2011.05.050

Svensen, H., Planke, S., Polozov, A. G., Schmidbauer, N., Corfu, F., Podladchikov, Y. Y., et al. (2009). Siberian gas venting and the end-Permian environmental crisis. *Earth Planet. Sci. Lett.* 277, 490–500. doi: 10.1016/j.epsl.2008.11.015

Thibodeau, A. M., Ritterbush, K., Yager, J. A., West, A. J., Ibarra, Y., Bottjer, D. J., et al. (2016). Mercury anomalies and the timing of biotic recovery following the end-Triassic mass extinction. *Nat. Commun.* 7:11147. doi: 10.1038/ncomms11147

Vajda, V., Calner, M., and Ahlberg, A. (2013). Palynostratigraphy of dinosaur footprint-bearing deposits from the Triassic-Jurassic boundary interval of Sweden. *GFF* 135, 120–130. doi: 10.1080/11035897.2013.799223

van de Schootbrugge, B., Payne, J. L., Tomasovych, A., Pross, J., Fiebig, J., Benbrahim, M., et al. (2008). Carbon cycle perturbation and stabilization in the wake of the Triassic-Jurassic boundary mass-extinction event. *Geochem. Geophys. Geosyst.* 9:Q04028. doi: 10.1029/2007GC001914

van de Schootbrugge, B., Quan, T. M., Lindström, S., Püttmann, W., Heunisch, C., Pross, J., et al. (2009). Floral changes across the Triassic/Jurassic boundary linked to flood basalt volcanism. *Nat. Geosci.* 2, 589–594. doi: 10.1038/ngeo577

van de Schootbrugge, B., van der Weijst, C. M. H., Hollaar, T. P., Vecoli, M., Strother, P. K., Kuhlmann, N., et al. (2020). Catastrophic soil loss associated

with end-Triassic deforestation. *Earth Sci. Rev.* 210:103332. doi: 10.1016/j.earscirev.2020.103332

Vervoort, P., Adloff, M., Greene, S. E., and Kirtland Turner, S. (2019). Negative carbon isotope excursions: an interpretive framework. *Environ. Res. Lett.* 14:085014. doi: 10.1088/1748-9326/ab3318

Vilas-Boas, M., Pereira, Z., Cirilli, S., Duarte, L. V., and Fernandes, P. (2021). New data on the palynology of the Triassic–Jurassic boundary of the Silves Group, Lusitanian Basin, Portugal. *Rev. Palaeobot. Palynol.* 290:104426. doi: 10.1016/j.revpalbo.2021.104426

Wang, Y. D., Fu, B. H., Xie, X. P., Huang, Q. S., Li, K., Li, G., et al. (2010). *The Terrestrial Triassic and Jurassic Systems in the Sichuan Basin, China*. Hefei: University of Science and Technology of China Press, 1–216. (in Chinese with English abstract).

Whiteside, J. H., Olsen, P. E., Kent, D. V., Fowell, S. J., and Et-Touhami, M. (2007). Synchrony between the Central Atlantic magmatic province and the Triassic–Jurassic mass-extinction event? *Palaeogeogr. Palaeoclimatol. Palaeoecol.* 244, 345–367. doi: 10.1016/j.palaeo.2006.06.035

Wignall, P. B., and Atkinson, J. W. (2020). A two-phase end-Triassic mass extinction. *Earth Sci. Rev.* 208:103282. doi: 10.1016/j.earscirev.2020.103282

Wotzlaw, J. F., Guex, J., Bartolini, A., Gallet, Y., Krystyn, L., McRoberts, C. A., et al. (2014). Towards accurate numerical calibration of the Late Triassic: high-precision U-Pb geochronology constraints on the duration of the Rhaetian. *Geology* 42, 571–574. doi: 10.1130/G35612.1

Yager, J. A., West, A. J., Thibodeau, A. M., Corsetti, F. A., Rigo, M., Berelson, W. M., et al. (2021). Mercury contents and isotope ratios from diverse depositional environments across the Triassic–Jurassic Boundary: towards a more robust mercury proxy for large igneous province Magmatism. *Earth Sci. Rev.* 223:103775. doi: 10.1016/j.earscirev.2021.103775

Yang, W., Yang, J., Wang, X., and Du, Y. (2012). Geochronology from Middle Triassic to Middle Jurassic detrital zircons in Jiyuan basin and its implications for the Qinling Orogen. *Earth Sci. China Univ. Geosci.* 37, 489–500. doi: 10.3799/dqkx.2012.055

Zaffani, M., Jadoul, F., and Rigo, M. (2018). A new Rhaetian $\delta^{13}C_{org}$ record: carbon cycle disturbances, volcanism, End-Triassic mass Extinction (ETE). *Earth Sci. Rev.* 178, 92–104. doi: 10.1016/j.earscirev.2018.01.004

Zhou, N., Xu, Y., Li, L., Lu, N., An, P., Popa, M. E., et al. (2021). Pattern of vegetation turnover during the end-Triassic mass extinction: trends of fern communities from South China with global context. *Glob. Planet. Change* 205:103585. doi: 10.1016/j.gloplacha.2021.103585

Conflict of Interest: MY was employed by the company PetroChina.

The remaining authors declare that the research was conducted in the absence of any commercial or financial relationships that could be construed as a potential conflict of interest.

Publisher's Note: All claims expressed in this article are solely those of the authors and do not necessarily represent those of their affiliated organizations, or those of the publisher, the editors and the reviewers. Any product that may be evaluated in this article, or claim that may be made by its manufacturer, is not guaranteed or endorsed by the publisher.

frontiers in Earth Science

ORIGINAL RESEARCH
published: 28 March 2022
doi: 10.3389/feart.2022.853833

Widespread Grylloblattid Insects After the End-Permian Mass Extinction

Qianqi Zhang[1,2]*, *Edmund A. Jarzembowski*[1,3] *and Bo Wang*[1,2]

[1]State Key Laboratory of Palaeobiology and Stratigraphy, Nanjing Institute of Geology and Palaeontology and Center for Excellence in Life and Paleoenvironment, Chinese Academy of Sciences, Nanjing, China, [2]University of the Chinese Academy of Sciences, Beijing, China, [3]Department of Earth Sciences, The Natural History Museum, London, United Kingdom

The end-Permian mass extinction (EPME) led to a severe terrestrial ecosystem collapse. However, the ecological response of insects to the EPME remains poorly understood. Here, we report a new species assigned to *Chauliodites*, *Chauliodites tongchuanensis* sp. nov. (Grylloblattida: Chaulioditidae), from the Middle Triassic Tongchuan Formation of Shaanxi, northwestern China, and redescribe *Chauliodites fuyuanensis* (Lin, 1978) from the Lower Triassic Kayitou Formation of Yunnan and *Chauliodites nanshenghuensis* (Lin, 1978) comb. nov. from the Middle Triassic of Guizhou, southwestern China. Our results show that *Chauliodites* widely distributed after the EPME is probably related to the rise of isoetalean-dominated low-productivity terrestrial ecosystems.

OPEN ACCESS

Edited by:
Haijun Song,
China University of Geosciences Wuhan, China

Reviewed by:
Dagmara Zyla,
Zoological Museum Hamburg, Germany
Olivier Béthoux,
UMR7207 Centre de recherche sur la paléobiodiversité et les paléoenvironnements (CR2P), France

***Correspondence:**
Qianqi Zhang
qianqizhang@nigpas.ac.cn

Specialty section:
This article was submitted to Paleontology, a section of the journal Frontiers in Earth Science

Received: *13 January 2022*
Accepted: *16 February 2022*
Published: *28 March 2022*

Citation:
Zhang Q, Jarzembowski EA and Wang B (2022) Widespread Grylloblattid Insects After the End-Permian Mass Extinction. Front. Earth Sci. 10:853833. doi: 10.3389/feart.2022.853833

Keywords: *Chauliodites tongchuanensis* (Lin, 1978) comb. nov., *Chauliodites nanshenghuensis* comb. nov., grylloblattida, Tongchuan Formation, China

INTRODUCTION

The end-Permian mass extinction (EPME: approximately 252 million years ago) witnessed the most severe biodiversity crisis during Earth history (Shen et al., 2011). How terrestrial ecosystems were affected during the EPME is still highly controversial (Benton and Newell, 2014; Gastaldo, 2019). In the terrestrial realm, insects were the earliest and most successful flying animals, which could spread and disperse globally in a relatively short time. Their often small size, powered flight, and metamorphosic development could have helped insects to survive extreme events such as the EPME (Condamine et al., 2016; Montagna et al., 2019). Nearly all Permian insect families decreased from the Middle to Late Permian, and approximately one-third of families became extinct at the Permian/Triassic (P/T) boundary, while overall insect diversity was probably stabilized because of the emergence of new families (Ponomarenko, 2016). However, the ecological response of insects to the EPME remains poorly understood due to the rather low number of species described (Labandeira and Sepkoski, 1993; Béthoux et al., 2005; Benton and Newell, 2014; Schachat and Labandeira, 2020; Zhao et al., 2021).

Grylloblattida (Paraplecoptera) is comparatively abundant during the Permian, with three families continuing into the Mesozoic (Ponomarenko, 2016). Among them, the family Chaulioditidae (composing subfamilies Chaulioditinae and Kargalellinae) ranges from the Middle Permian to Middle Triassic and is represented near the Permo-Triassic boundary (Bashkuev et al., 2012; Aristov et al., 2013). These grylloblattidans were stonefly-like extinct insects, but most of their nymphs apparently lived on land (Ponomarenko, 2006) and probably played an important role in Early Triassic terrestrial ecosystems (Ponomarenko, 2016) with biostratigraphical potential (Aristov, 2008). *Chauliodites*, the type genus of Chaulioditidae, is the most widespread genus in this family and is also among the most important insectan index fossils during the Late Permian and Early Triassic (Aristov, 2008; Shcherbakov, 2008; Bashkuev et al., 2012).

FIGURE 1 | Geographical map showing the distributions of the Triassic Chaulioditidae in China. 1, Tongchuan City, Shaanxi Province; 2, Taijiang County, Guizhou Province; 3, Fuyuan County, Yunnan Province.

Therefore, we investigated the fossil record of *Chauliodites* to help provide new insights into how insects were affected by the EPME.

Here, we report one new species assigned to *Chauliodites* from the Middle Triassic Tongchuan Formation of northwestern China and redescribe *Chauliodites fuyuanensis* (Lin, 1978) from the Early Triassic Kayitou Formation and *Chauliodites nanshenghuensis* comb. nov. from the Middle Triassic of southwestern China.

MATERIALS AND METHODS

The Triassic grylloblattidan specimens (registration numbers NIGP51619, NIGP51620, and NIGP162048) were collected from the Middle Triassic Tongchuan Formation in Tongchuan City, Shaanxi Province, NW China (Zheng et al., 2018); the Lower Triassic Kayitou Formation in Fuyuan County, Yunnan Province, SW China (Lin, 1978; Liu and Yao, 2002); and unnamed Middle Triassic strata at Nanshenghu in Guizhou Province, SW China (Lin, 1978), respectively (**Figure 1**). All specimens are housed at the Nanjing Institute of Geology and Palaeontology, Chinese Academy of Sciences (NIGPAS), and were observed and photographed using a stereomicroscope system (ZEISS Stereo Discovery V16). Line drawings and interpretations were prepared using CorelDRAW 2019. The terminology of the tegminal venation is based on Kukalová (1964) and Storozhenko (1998): Sc, subcosta; RA, radius anterior; RP, radius posterior; MA, median anterior; MP, median posterior; CuA, cubitus anterior; CuP, cubitus posterior. However, M5, which is considered as strengthened crossvein, is not adopted here (Cui et al., 2021).

SYSTEMATIC PALEONTOLOGY

Family Chaulioditidae Handlirsch, 1906.

Type genus. *Chauliodites* Heer, 1865.

Diagnosis (revised from Aristov, 2004). Tegmen oval; costal area wider than postcostal area, crossed by simple branches of Sc; M bifurcated beyond RP base; CuA1 simple and curved, area between CuA and CuP basally narrow.

Composition. *Chauliodites* Heer, 1865; *Paratomia* Aristov, 2003; and *Yontala* Aristov, 2005.

Genus *Chauliodites* Heer, 1865.

Type species. *Chauliodites picteti* Heer, 1865.

Revised diagnosis. RA usually with several branches fewer than Sc; RP with more than two branches, area between RA and RP wide in mid-tegmen; RA and RP initially divided in apical mid-tegmen; MA and MP usually with two–six branches in total. CuA first fork basal of R dividing.

Age and occurrence. Middle and Late Permian of Russian Federation; Early Triassic of China, Mongolia, and Russia; Middle Triassic of China, France, Germany, Poland, and Russia.

Species included. Twenty-six species: *Chauliodites afonini* Aristov, 2008, *C. anisicus* Grauvogel-Stamm et Marchal-Papier, 2011, *C. antiquus* (Aristov, 2003) Aristov, 2004 (Ansorge and Brauckmann, 2008), *C. babiy* Aristov, 2020a, *C.* (*T.*) *cancellata* (Aristov, 2003) Aristov, 2004, *C. circumornatus* Aristov et al., 2013 (Aristov et al., 2013a), *C. costalis* (Martynov, 1936) Aristov,

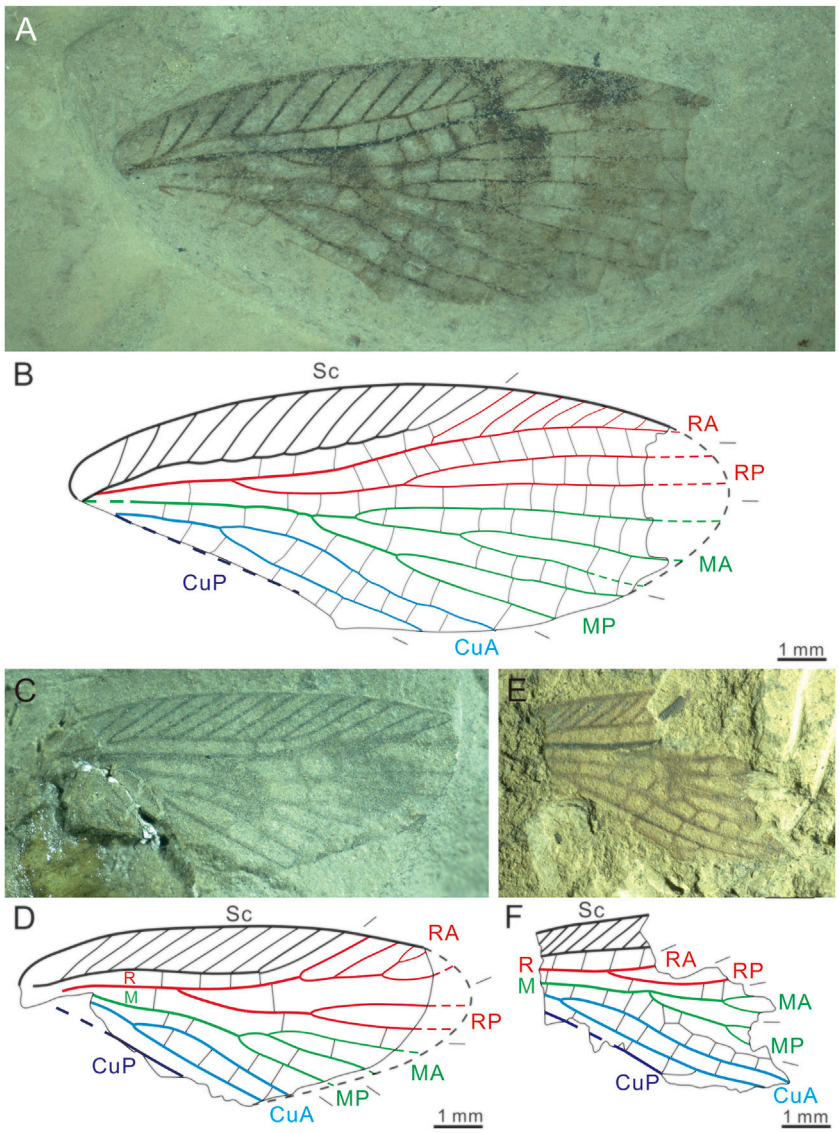

FIGURE 2 | (A) Reversed photograph of *Chauliodites tongchuanensis* sp. nov. Holotype, NIGP162048a; **(B)** venational interpretation of **(A)**; **(C)** reversed photograph of *Chauliodites nanshenghuensis* (Lin, 1978) comb. nov., Holotype, NIGP51620; **(D)** venational interpretation of **(C)**; **(E)** photograph of *Chauliodites fuyuanensis* (Lin, 1978) Aristov, 2004, holotype, NIGP51619; **(F)** venational interpretation of **(E)**.

2004, *C. durus* (Aristov, 2003) Aristov, 2004 (Ansorge and Brauckmann, 2008), *C. eskovi* Aristov, 2011, *C. esperstedtensis* van Eldijk et al., 2017, *C. fuyuanensis* (Lin, 1978) Aristov, 2004 (Ansorge and Brauckmann, 2008), *C. geniatus* Aristov et al., 2013 (Aristov et al., 2013a), *C. gomankovi* Aristov, 2008, *C. incanus* Aristov, 2015, *C. issadensis* Aristov, 2009, *C. kitshmengensis* Aristov, 2013, *C. monglicus* Aristov, 2005, *C. nedubrovensis* Aristov, 2013, *C. niedzwiedzkii* Aristov et al., 2013, *C. picteti* Heer, 1865, *C. ponomarenkoi* Aristov, 2008, *C. ramosa* (Aristov, 2003) Aristov, 2004, *C. sakmaris* Aristov, 2020b, *C. sennikovi* (Aristov, 2003) Aristov, 2004, and two new species [*C. nanshenghuensis* (Lin, 1978) comb. nov. and *C. tongchuanensis* sp. nov.] proposed here.

Chauliodites tongchuanensis sp. nov. (**Figures 2A,B**).

2018 *Chauliodites*: Zheng et al., p. 3, Fig 3H.

Etymology. The specific epithet comes from the name of the city of Tongchuan in the fossil-bearing area.

Holotype. NIGP162048a, b; a forewing without clavus and apex; part and counterpart.

Type locality. Hejiafang Village, Tongchuan City, Shaanxi Province, northwestern China.

Age and horizon. Ladinian, late Middle Triassic; top bed of the lower Tongchuan Formation.

Diagnostic characters. Costal/postcostal width ratio more than 2:1, no crossveins connecting branches of Sc in costal area; initial division of RP basal of RA dividing; branches of RA developed; M with five branches in total; dark-colored stripes present.

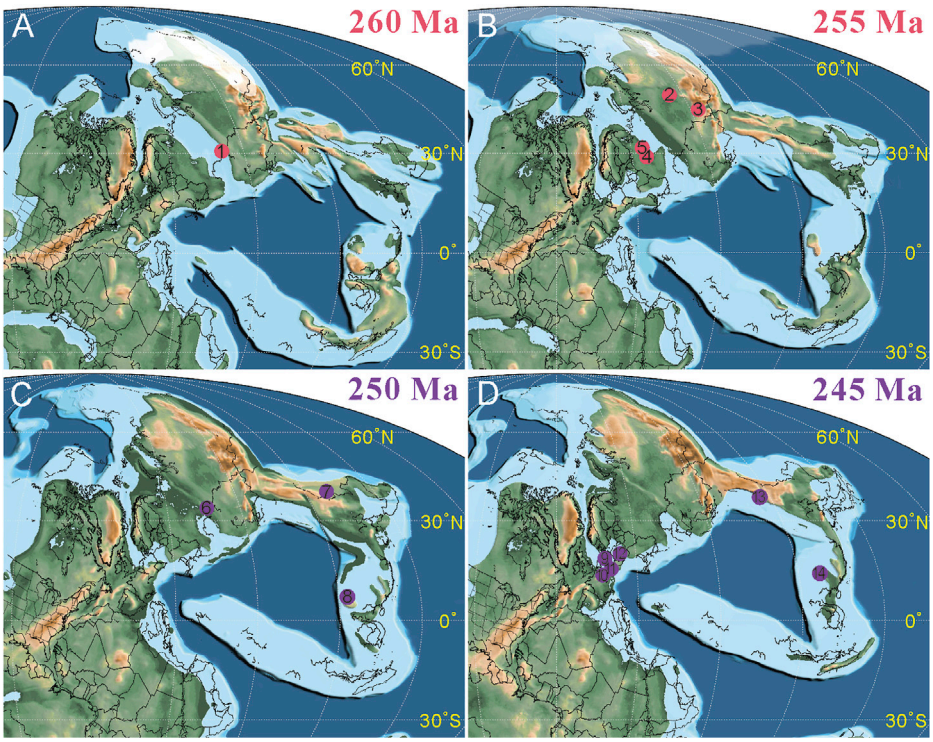

FIGURE 3 | Paleogeographic distribution of *Chauliodites* during the Middle Permian to Middle Triassic: **(A)** (1) Orenburg, Russia; **(B)** (2) Krasnoyarsk, Russia; (3) Kemerovo, Russia; (4) Vladimir, Russia; (5) Vologda, Russia; **(C)** (6) Orenburg, Russia; (7) Nomgon Sum, Mongolia; (8) Yunnan, China; **(D)** (9) Lower Saxony, Germany; (10) Vosges, France; (11) Bavaria, Lower Franconia and Thurngia of Germany; (12) Mniów, Poland; (13) Shaanxi, China; (14) Guizhou, China. Paleogeographic maps modified from Scotese (2021).

Description: Tegmen preserved length 12.2 mm, maximum width 4.7 mm, slightly convex in middle of anterior margin; maximum width of costal margin three times greater than subcostal area width. Twelve simple anterior branches of vein Sc present and seven of RA, nearly parallel and crossed to anterior margin. RA coalesced with Sc at tegminal base with six crossveins connecting Sc and RA in mid-forewing; RA long and curved without forks; stem R divided in basal quarter of tegminal length; RP curved posteriorly, two-forked apical of mid-tegminal length. M straight, possibly coalesced with Sc, divided into MA and MP at two-fifths of tegminal length; MA forked into MA1 and MA2 near mid-tegminal length; MA2 two-divided at apical third of tegminal length; MP two-divided at level of RP forking. CuA straight, nearly parallel to basal part of M, forked into CuA1 and CuA2 near RP base; two branches of CuA present, simple and extended towards posterior margin, CuA1 more curved than CuA2. CuP straight and thin. Crossveins short, simple, and developed between branches of main veins and veinlets. Ornament: three transverse dark-colored stripes of irregular shape across tegmen.

Chauliodites nanshenghuensis (Lin, 1978) comb. nov. (**Figures 2C,D**).

1978 *Tomia nanshenhuensis* Lin, p. 316; pl. 1; Fig 5.

1997 *Shurabia nanshenhuensis* (Lin, 1978): Storozhenko, pp. 1, 15.

2003 *Nivopteria nanshenhuensis* (Lin, 1978): Aristov, pp. 31, 33, 37, 38.

Holotype. NIGP51620; a forewing with clavus and apical part missing; only partly preserved. Housed at NIGPAS.

Type locality. Nanshenghu Village, Taijiang County, Guizhou Province, southwestern China.

Age and horizon. Middle Triassic.

Diagnostic characters. Costal/postcostal width ratio more than 3:1, no crossveins connected by veinlets in costal area; initial division of RA basal of RP; branches of RA well developed; area between RA and RP widened; M with three branches; CuA two-branched, CuA1 S-shaped; dark-colored stripes present on tegmen.

Description: Tegmen without apical and claval part, length 8.4 mm, 2.6 mm in maximum width. Oval in shape with anterior margin slightly convex; maximum width of costal area about 3.6 times greater than subcostal width. Sc with 10 simple, straight anterior branches without crossveins, R long and curved, parallel to Sc, and connected with Sc by four crossveins, divided into RA and RP at about two-thirds of tegminal length from base; stems RA and RP simple and curved, RA divided four times and forming at least five terminals. RP two-forked at about 0.63 of tegminal length. Area between RA and RP becomes wider distinctly near mid-tegmen. Basal part of M missing, slightly curved, and initially divided into MA and MP at about 0.45 of tegminal length; MA short, two-forked at 0.54 of tegminal length; MP simple. Base of CuA not preserved, nearly straight, forking into simple CuA1 and CuA2 about 0.25 of tegminal length; CuA1 more curved than CuA2. CuP straight, partly preserved.

TABLE 1 | Floristic compositions of *Chauliodites* species bearing strata.

Species	Formation (Age)	Floral	References
C. babiy Aristov, 2020a	Maltsevo Fm. (P3)	*Lepidopteris*	Karasev (2015)
C. cancellata (Aristov, 2003) Aristov, 2004			
C. costalis (Martynov, 1936) Aristov, 2004			
C. ramosa (Aristov, 2003) Aristov, 2004			
C. circumornatus Aristov, 2013	Poldarsa Fm. (P3)	Conifer shoots	Karasev et al. (2019)
C. geniatus Aristov, 2013			
C. issadensis Aristov, 2009			
C. ponomarenkoi Aristov, 2008			
C. durus (Aristov, 2003) Aristov, 2004	Bugarikta Fm. (P3)	Ferns, peltasperms, and conifers	Shcherbakov et al. (2021)
C. eskovi Aristov, 2011	Agitkan Fm. (P3)	*Todites, Acrostichides, Pecopteris, Rhipidopsis, Lepidopteris*	Sadovnikov, (2008)
C. kitshmengensis Aristov, 2013	Vokhma Fm. (P3)	*Tatarina*	Aristov, (2013)
C. nedubrovensis Aristov, 2013			
C. fuyuanensis (Lin, 1978) Aristov, 2004	Kayitou Fm. (T1)	*Gigantopteris*	Feng et al. (2020)
C. sakmaris Aristov, 2020b	Petropavlovka Fm. (T1)	*Densoisporites, Pleuromeia*	Shcherbakov et al. (2020)
C. anisicus Aristov, 2011	Grès à Voltzia Fm. (T2)	*Lycopsids*	Gall and Grauvogel-Stamm, (2005)
C. esperstedtensis van Eldijk et al., 2017	Vossenveld Fm. (T2)	*Triadispora*	Herngreen et al. (2005)
C. niedzwiedzkii Aristov, 2013	Samsonów Fm. (T2)	*Punctatisporites, Cyclotriletes, Cycloverrutriletes Densoisporites*	Żyła et al. (2013)
C. picteti Heer, 1865	Solling Fm. (T2)	*Pleuromeia*	Kustatscher et al. (2014)
C. tongchuanensis sp. nov.	Tongchuan Fm. (T2)	*Annalepis-Tongchuanophyllum* assemblage	Zhou and Zhou, (1983)
C. incanus Aristov, 2015	Amanak Fm. (P2)	Unknown	—
C. sennikovi Aristov, 2003 Aristov, 2004	Rybinsk Fm. (P3)	Unknown	—
C. antiqua (Aristov, 2003) Aristov, 2004	Salarevo Fm. (P3)	Unknown	—
C. monglicus Aristov, 2005	Yamaan-Us Fm. (T1)	Unknown	—
C. nanshenghuensis (Lin, 1978) comb. nov.	Unnamed	Unknown	—
C. afonini Asristov, 2008			
C. gomankovi Asristov, 2008			

Crossveins short, simple, and vertically linking main veins and veinlets. Two dark-colored patches on middle and medial areas of tegmen.

Remarks: *Nivopteria* Lin, 1978 is a doubtful genus due to incomplete venational information about the type specimen (Aristov, 2003). Re-examination of the *Nivopteria nanshenghuensis* Lin, 1978 revealed that this species should be assigned to *Chauliodites* Heer, 1865 from characters including costal area wide with developed veinlets on Sc; RP and CuA both two-branched; MP first forked apical of R forking; initial forking of CuA basad of R dividing, and thus suggest that *Nivopteria* Lin, 1978 is a synonym of *Chauliodites* Heer, 1865.

Chauliodites fuyuanensis (Lin, 1978) Aristov, 2004 (**Figures 2E,F**).

1978 *Tomia fuyuanensis* Lin, p. 316; pl. 1; Figs. 4-6.

1997 *Shurabia fuyuanensis* (Lin, 1978): Storozhenko, pp. 1, 14.

2004 *Chauliodites fuyuanensis* (Lin, 1978): Aristov, S147

2008 *Chauliodites fuyuanensis* (Lin, 1978): Ansorge and Brauckmann, p. 255.

Holotype. NIGP51619; a forewing with mid-wing preserved; part and countpart.

Type locality. Qingyun Village, Fuyuan County, Yunnan Province, southwestern China.

Age and horizon. Olenekian, Early Triassic; Kayitou Formation.

Diagnostic characters. Costal/postcostal width ratio less than 2:1, no crossveins connected by veinlets in costal area; secondary crossveins present between MP2 and CuA1; M with four branches at least; CuA two-branched, CuA1 S-shaped; dark-colored stripes present.

Description: Middle part of tegmen preserved, 5.2 mm in maximum length, 3.3 mm in maximum width. Eight anterior branches of Sc present, nearly straight and parallel to each other. Costal/postcostal width ratio 1.4:1. R simple, slightly curved posteriorly, connected with Sc by four crossveins; RP simple, more curved than R; M divided into MA and MP apically at level of R forking. MA and MP both two-branched, forking nearly at the same level, secondary crossveins between MP and CuA developed. CuA forked basal of R dividing, CuA1 and CuA2 curved and parallel. CuP simple and straight.

DISCUSSION

The stratigraphical range of *Chauliodites* varies within Laurasia from the Middle Permian (Guadalupian) to Middle Triassic (**Figure 3**). In the Middle Permian, there are only two species reported from one fossil site in Russia (**Figure 3A**); in the Late Permian (Lopingian), *Chauliodites* bloomed with 15 species reported from four sites in Russia (**Figure 3B**); only three from sites around the Neo-Tethys during the Early Triassic (**Figure 3C**), and during the Middle Triassic, six species are known from six sites in total (**Figure 3D**). This genus disappeared from the fossil record by the late Middle

Triassic. The extinction of this taxon may result from the turnover of flora or competition from new types of insects (e.g., holometabolan), and further research is still needed to confirm the hypothesis.

Plant/insect interaction in terrestrial ecosystems is also a consideration, especially in the light of the EPME. The dominant flora in the latest Permian to Early Triassic turnover changed dramatically from gymnosperm to isoetalean lycophyte communities (mainly genera *Annalepis*, *Pleuromeria*, and *Tomiostrobus*) according to the palynological and megafloral record (Grauvogel-Stamm and Ash, 2005; Hermann et al., 2012; Feng et al., 2020; Liu et al., 2020; Looy et al., 2021). The Permo-Triassic transitional Kayitou Formation is widely exposed in southwestern China and, when yielding *Chauliodites fuyuanensis*, is dominated by isoetaleans (*Annalepis*) in the *Gigantopteris* floral (Yu et al., 2008; Chen et al., 2011; Feng et al., 2020). Rainforest on land is considered to have been replaced by herbaceous vegetation in the tropics, but the response of land plants to the Permo-Triassic crisis is variable due to latitudinal gradient (Feng et al., 2020). However, *Chauliodites*, spread across the floras of Angara, Euramerica, and Cathaysia, was little affected by latitude. The occurrence of isoetaleans is up to 12.5% in the megaflora and 24.0% in the microflora in the Olenekian (Early Triassic) (Looy et al., 2021). Floristic compositions of the *Chauliodites* bearing strata are listed (**Table 1**). Our study suggests that *Chauliodites* possibly become abundant with the rise of an isoetalean (lycophyte)-dominated flora, considered environmentally and climatically tolerant plants in the low-productivity terrestrial ecosystems after the end-Permian terrestrial crisis (Feng et al., 2020).

DATA AVAILABILITY STATEMENT

The original contributions presented in the study are included in the article/Supplementary Material, further inquiries can be directed to the corresponding author.

AUTHOR CONTRIBUTIONS

Designing the project: BW. Preparing the fossil material and performing morphological analyses: QZ and BW. Preparing photographs and figures: QZ. Analyzing the data: QZ, BW, and EJ. Writing the manuscript: QZ, BW, and EJ.

FUNDING

This research was supported by the National Natural Science Foundation of China (Nos 41730317, 42125201, and 41688103) and the Strategic Priority Research Program of the Chinese Academy of Sciences (XDB26000000). This is a Leverhulme Emeritus Fellowship contribution for EJ.

REFERENCES

Ansorge, J., and Brauckmann, C. (2008). Chaulioditidae from Germany with a description of a new specimen from the early Middle Triassic of Gambach/Main, Bavaria (Insecta: Grylloblattida). *Entomol. Gen.* 31 (3), 251–260. doi:10.1127/entom.gen/31/2008/251

Aristov, D. S. (2004). Grylloblattids of the Family Chaulioditidae (= Tomiidae Syn. nov.) (Insecta: Grylloblattida) from the Upper Permian of the Orenburg Region. *Paleontol. J.* 38 (Suppl. 2), S146–S149.

Aristov, D. S. (2005). New Grylloblattids (Insecta: Grylloblattida) from the Triassic of Eastern Europe, Eastern Kazakhstan and Mongolia. *Paleontol. J.* 39 (2), 173–177.

Aristov, D. S. (2009). New Permian Grylloblattids (Insecta: Grylloblattida) from Isady Locality (Severovdvinian Stage of Vologda Region). *Russ. Entomol. J.* 18 (1), 17–22.

Aristov, D. S. (2003). Revision of the Family Tomiidae (Insecta: Grylloblattida). *Paleontol. J.* 37 (1), 31–38.

Aristov, D. S., Grauvogel-Stamm, L., and Marchal-Papier, F. (2011). New grylloblattid insects (Insecta: Grylloblattida) from the Grès à Voltzia of the Vosges (Middle Triassic of France). *Paleontol. J.* 45 (2), 159–166. doi:10.1134/s0031030111020043

Aristov, D. S. (2011). New and Little Known Grylloblattida (Insecta) from Intertrappean Deposits of the Tunguska Basin of Sibiria. *Paleontol. J.* 45 (5), 537–545. doi:10.1134/s0031030111050030

Aristov, D. S. (2020b). New and Little Known Gryllones Insects (Insecta: Gryllones: Cnemidolestida, Reculida) from the Triassic of Eurasia. *Paleontol. J.* 54, 524–530. doi:10.1134/S0031030120050020

Aristov, D. S. (2013). New Grylloblattida (Insecta) from the Upper Permian and Lower Triassic of European Russia and Kazakhstan. *Paleontol. J.* 47, 66–76. doi:10.1134/S0031030113010024

Aristov, D. S. (2015). New Gryllones (Insecta) from the Permian of Russia. *Paleontol. J.* 49, 1310–1333. doi:10.1134/S0031030115120023

Aristov, D. S. (2020a). New Gryllones Insects (Insecta: Gryllones) from the Babii Kamen' Locality (Upper Permian of Russia). 2. Order Reculida and Gryllones Ordinis Incertis. *Paleontol. J.* 54, 132–142. doi:10.1134/S0031030120020021

Aristov, D. S. (2008). New Tatarian Representatives of the Subfamily Chaulioditinae (Insecta: Grylloblattida: Chaulioditidae) from European Russia. *Paleontol. J.* 42 (1), 32–35. doi:10.1007/s11492-008-1004-0

Aristov, D. S., Bashkuev, A. S., Golubev, V. K., Gorochov, A. V., Karasev, E. V., and Kopylov, D. S. (2013a). Fossil Insects of the Middle and Upper Permian of European Russia. *Paleontol. J.* 47 (7), 641–832. doi:10.1134/S0031030113070010

Aristov, D. S., Żyła, D., and Wegierek, P. (2013b). *Chauliodites niedzwiedzkii* sp. n. (Grylloblattida: Chaulioditidae) from Triassic Sediments of Poland. *Zootaxa* 3721 (3), 281–285. doi:10.11646/zootaxa.3721.3.4

Bashkuev, A., Sell, J., Aristov, D., Ponomarenko, A., Sinitshenkova, N., and Mahler, H. (2012). Insects from the Buntsandstein of Lower Franconia and Thuringia. *Paläontol. Z.* 86 (2), 175–185. doi:10.1007/s12542-011-0119-8

Benton, M. J., and Newell, A. J. (2014). Impacts of Global Warming on Permo-Triassic Terrestrial Ecosystems. *Gondwana Res.* 25 (4), 1308–1337. doi:10.1016/j.gr.2012.12.010

Béthoux, O., Papier, F., and Nel, A. (2005). The Triassic Radiation of the Entomofauna. *Comptes Rendus Palevol* 4 (6-7), 609–621. doi:10.1016/j.crpv.2005.06.005

Chen, J. H., Yu, J. X., Huang, Q. S., Broutin, J., Song, Q. Q., and Chen, B. (2011). New Research Progress on the Paleoflora in the Earliest Triassic of Western Guizhou and Eastern Yunnan, South China. *Earth Sci. – J. China Univ. Geosci.* 36 (3), 500–510. in Chinese with English abstract. doi:10.3799/dqkx.2011.051

Condamine, F. L., Clapham, M. E., and Kergoat, G. J. (2016). Global Patterns of Insect Diversification: towards a Reconciliation of Fossil and Molecular Evidence? *Sci. Rep.* 6 (1), 19208–19213. doi:10.1038/srep19208

Feng, Z., Wei, H.-B., Guo, Y., He, X.-Y., Sui, Q., Zhou, Y., et al. (2020). From Rainforest to Herbland: New Insights into Land Plant Responses to the End-Permian Mass Extinction. *Earth-Science Rev.* 204, 103153. doi:10.1016/j.earscirev.2020.103153

Gall, J. C., and Grauvogel-Stamm, L. (2005). The early Middle Triassic 'Grès à Voltzia' Formation of eastern France: a model of environmental refugium. *Comptes Rendus Palevol.* 4 (6-7), 637–652. doi:10.1016/j.crpv.2005.04.007

Gastaldo, R. A. (2019). Ancient Plants Escaped the End-Permian Mass Extinction. *Nature* 567, 38–39. doi:10.1038/d41586-019-00744-3

Grauvogel-Stamm, L., and Ash, S. R. (2005). Recovery of the Triassic Land flora from the End-Permian Life Crisis. *Comptes Rendus Palevol* 4, 593–608. doi:10.1016/j.crpv.2005.07.002

Handlirsch, A. (1906). *Die Fossilen Insekten und die Phylogenie der Rezenten Formen, parts I-IV*. LeipzigGerman: Ein Handbuch fur Palaontologen und Zoologen, 1–1092.

Heer, O. (1865). Über die fossilen Kakerlaken. *Vierteljahresschrift der Naturforschenden Gesellschaft, Zürich* 9, 273–302.

Hermann, E., Hochuli, P. A., Bucher, H., and Roohi, G. (2012). Uppermost Permian to Middle Triassic Palynology of the Salt Range and Surghar Range, Pakistan. *Rev. Palaeobotany Palynology* 169, 61–95. doi:10.1016/j.revpalbo.2011.10.004

Herngreen, G. F. W., van Konijnenburg - van Cittert, J. H. A., and Oosterink, H. W. (2005). New Geological Data (Middle Triassic, Rhaetian-Liassic and Oligocene) of the Winterswijk Quarry, the Eastern Netherlands. *Neth. J. Geosciences* 84 (4), 409–413. doi:10.1017/S0016774600021223

Karasev, E. (2015). On Small Pinnate Leaves of Peltasperm Pteridosperms from the Early Triassic of the Kuznetsk Basin (Mal'tsevo Formation, Babii Kamen Locality). *Botanica Pacifica* 4 (2), 131–136. doi:10.17581/bp.2015.0411710.17581/bp.2015.04217

Karasev, E., Forte, G., Coiro, M., and Kustatscher, E. (2019). *Mutoviaspermum krassilovii* gen. et sp. nov.: A Peculiar Compound Ovuliferous Conifer Cone from the Lopingian (Late Permian) of European Russia (Vologda Region). *Int. J. Plant Sci.* 180 (8), 779–799. doi:10.1086/704944

Kukalová, J. (1964). Permian Insects of Moravia. Part II–Liomopteridae. *Sborník geologických věd, Paleontonologie* 3, 3–118.

Kustatscher, E., Franz, M., Heunisch, C., Reich, M., and Wappler, T. (2014). Floodplain Habitats of Braided River Systems: Depositional Environment, flora and Fauna of the Solling Formation (Buntsandstein, Lower Triassic) from Bremke and Fürstenberg (Germany). *Palaeobio Palaeoenv* 94 (2), 237–270. doi:10.1007/s12549-014-0161-0

Labandeira, C. C., and Sepkoski, J. J. (1993). Insect Diversity in the Fossil Record. *Science* 261, 310–315. doi:10.1126/science.11536548

Lin, Q. B. (1978). Upper Permian and Triassic Fossil Insects of Guizhou. Acta Palaeontol. *Sin* 17 (3), 313–317. in Chinese with English abstract.

Liu, F., Peng, H., Bomfleur, B., Kerp, H., Zhu, H., and Shen, S. (2020). Palynology and Vegetation Dynamics across the Permian-Triassic Boundary in Southern Tibet. *Earth-Science Rev.* 209, 103278. doi:10.1016/j.earscirev.2020.103278

Liu, L. J., and Yao, Z. Q. (2002). Geological Age of the Kayitou Formation. *J. Stratigr.* 26 (3), 235–237. in Chinese with English abstract.

Looy, C. V., van Konijnenburg-van Cittert, J. H., and Duijnstee, I. A. (2021). Proliferation of Isoëtalean Lycophytes during the Permo-Triassic Biotic Crises: a Proxy for the State of the Terrestrial Biosphere. *Front. Earth Sci.* 9, 55. doi:10.3389/feart.2021.615370

Martynov, A. V. (1936). On Some New Materials of Arthropoda from Kuznetsk-Basin. *Izvestiya Akademii Nauk SSSR: Seriya Biologicheskaya* 6, 1251-1264.

Montagna, M., Tong, K. J., Magoga, G., Strada, L., Tintori, A., Ho, S. Y. W., et al. (2019). Recalibration of the Insect Evolutionary Time Scale Using Monte San Giorgio Fossils Suggests Survival of Key Lineages through the End-Permian Extinction. *Proc. R. Soc. B.* 286 (1912), 20191854. doi:10.1098/rspb.2019.1854

Ponomarenko, A. G. (2006). Changes in Terrestrial Biota before the Permian-Triassic Ecological Crisis. *Paleontol. J.* 40 (Suppl. 4), S468–S474. doi:10.1134/S0031030106100066

Ponomarenko, A. G. (2016). Insects during the Time Around the Permian-Triassic Crisis. *Paleontol. J.* 50 (2), 174–186. doi:10.1134/S0031030116020052

Sadovnikov, G. N. (2008). On the Global Stratotype Section and point of the Triassic Base. *Stratigr. Geol. Correl.* 16 (1), 31–46. doi:10.1007/s11506-008-1003-1

Schachat, S. R., and Labandeira, C. C. (2020). Are Insects Heading toward Their First Mass Extinction? Distinguishing Turnover from Crises in Their Fossil Record. *Ann. Entomol. Soc. Am.* 114 (2), 99–118. doi:10.1093/aesa/saaa042

Scotese, C. R. (2021). An Atlas of Phanerozoic Paleogeographic Maps: the Seas Come in and the Seas Go Out. *Annu. Rev. Earth Planet. Sci.* 49, 679–728. doi:10.1146/annurev-earth-081320-064052

Shcherbakov, D. E. (2008). On Permian and Triassic Insect Faunas in Relation to Biogeography and the Permian-Triassic Crisis. *Paleontol. J.* 42 (1), 15–31. doi:10.1007/s11492-008-1003-1

Shcherbakov, D. E., Timm, T., Tzetlin, A. B., Vinn, O., and Zhuravlev, A. Y. (2020). A Probable Oligochaete from an Early Triassic Lagerstätte of the Southern Cis-Urals and its Evolutionary Implications. *Acta Palaeontol. Pol.* 65 (2), 219–233. doi:10.4202/app.00704.2019

Shcherbakov, D. E., Vinn, O., and Zhuravlev, A. Y. (2021). Disaster Microconchids from the Uppermost Permian and Lower Triassic Lacustrine Strata of the Cis-Urals and the Tunguska and Kuznetsk Basins (Russia). *Geol. Mag.* 158 (8), 1335–1357. doi:10.1017/S0016756820001375

Shen, S.-z., Crowley, J. L., Wang, Y., Bowring, S. A., Erwin, D. H., Sadler, P. M., et al. (2011). Calibrating the End-Permian Mass Extinction. *Science* 334 (6061), 1367–1372. doi:10.1126/science.1213454

Storozhenko, S. Yu. (1997). Classification of Order Grylloblattida (Insecta), with Description of New Taxa. *Far East. Entomol.* 42, 1.–20

Storozhenko, S. Yu. (1998). *Systematics, Phylogeny and Evolution of the Grylloblattids (Insecta: Grylloblattida)*. Russian: Dal'nauka, Vladivostok, 1–207.

van Eldijk, T., Goris, G., Haarhuis, A., Lankamp, J., Winkelhorst, H., Reumer, J., et al. (2017). New Fossil Insects from the Anisian (Lower to Middle Muschelkalk) from the Central European Basin (Germany and The Netherlands). *PalZ* 91, 185–194. doi:10.1007/s12542-017-0343-y

Yu, J. X., Huang, Q. S., Broutin, J., and Yang, F. Q. (2008). The Early Triassic *Annalepis* from Western Guizhou and Eastern Yunnan, South China. Acta Palaeontol. *Sin* 47 (3), 292–300. in Chinese with English abstract.

Zhao, X. Y., Yu, Y. L., Clapham, M. E., Yan, E., Chen, J., Jarzembowski, E. A., et al. (2021). Early Evolution of Beetles Regulated by the End-Permian Deforestation. *eLife* 10, e72692. doi:10.7554/eLife.72692

Zheng, D. R., Chang, S-C., Wang, H., Fang, Y., Wang, J., Feng, C. Q., et al. (2018). Middle-Late Triassic Insect Radiation Revealed by Diverse Fossils and Isotopic Ages from China. Sci. *Adv* 4 (9), eaat1380. doi:10.1126/sciadv.aat1380

Zhou, T. S., and Zhou, H. Q. (1983). Triassic Non-marine Strata and flora of China. *Bull. Chin. Acad. Geol. Sci.* 5, 95–108. in Chinese with English abstract.

Żyła, D., Wegierek, P., Owocki, K., and Niedźwiedzki, G. (2013). Insects and Crustaceans from the Latest Early–Early Middle Triassic of Poland. *Palaeogeogr. Palaeoclimatol. Palaeoecol.* 371, 136–144. doi:10.1016/j.palaeo.2013.01.002

Conflict of Interest: The authors declare that the research was conducted in the absence of any commercial or financial relationships that could be construed as a potential conflict of interest.

Publisher's Note: All claims expressed in this article are solely those of the authors and do not necessarily represent those of their affiliated organizations, or those of the publisher, the editors, and the reviewers. Any product that may be evaluated in this article, or claim that may be made by its manufacturer, is not guaranteed or endorsed by the publisher.

frontiers | Frontiers in Earth Science

MINI REVIEW
published: 12 April 2022
doi: 10.3389/feart.2022.887632

Late Permian to Late Triassic Large Igneous Provinces: Timing, Eruptive Style and Paleoenvironmental Perturbations

Andrea Boscaini[1], *Sara Callegaro*[2], *Yadong Sun*[3] *and Andrea Marzoli*[4]*

[1]Dipartimento di Geoscienze, Università di Padova, Padova, Italy, [2]Centre for Earth Evolution and Dynamics, University of Oslo, Oslo, Norway, [3]GeoZentrum Nordbayern, Universität Erlangen-Nurnberg, Erlangen, Germany, [4]Dipartimento Territorio e Sistemi Agro-Forestali, Università di Padova, Legnaro, Italy

The emplacement of the Siberian Traps, the Central Atlantic Magmatic Province (CAMP) and the Wrangellia have been linked to the end-Permian, the end-Triassic mass extinctions, and to the Carnian Pluvial Episode (CPE), respectively. Exploring the timing, eruptive styles, and volatile degassing of these Large Igneous Provinces (LIPs) is crucial to understand their causal link to the catastrophic environmental crises that punctuated the Triassic. In this study we review the main characteristics of these LIPs, emphasizing common features and differences, and discussing aspects that are still in debate. Estimates of CO_2 budgets and emissions from the three LIPs are based on the Nb content of little evolved basalts and highlight that early Siberian Traps and CAMP and high-Ti Wrangellia volcanics were quite CO_2-rich. On the contrary, other volcanics from the three LIPs probably emitted relatively low amounts of CO_2, which reinforces the possibility that thermogenic reactions between sills and sediments were additional fundamental suppliers of climate-modifying gases.

Keywords: triassic, siberian traps, central atlantic magmatic province (CAMP), carnian crisis, wrangellia LIP, large igneous province, mass extinction

OPEN ACCESS

Edited by:
Hossein Azizi,
University of Kurdistan, Iran

Reviewed by:
Federico Lucci,
University of Bari Aldo Moro, Italy
Orhan Karsli,
Karadeniz Technical University, Turkey

***Correspondence:**
Andrea Marzoli
andrea.marzoli@unipd.it

Specialty section:
This article was submitted to Petrology, a section of the journal Frontiers in Earth Science

Received: *01 March 2022*
Accepted: *23 March 2022*
Published: *12 April 2022*

Citation:
Boscaini A, Callegaro S, Sun Y and Marzoli A (2022) Late Permian to Late Triassic Large Igneous Provinces: Timing, Eruptive Style and Paleoenvironmental Perturbations. Front. Earth Sci. 10:887632. doi: 10.3389/feart.2022.887632

INTRODUCTION

The Triassic was a crucial period for shaping the modern world, in terms of the evolution of both the biosphere and the geosphere. While successful faunas and floras spread over Pangea, in the Panthalassa and Tethys oceans, the Triassic biosphere was devastated by two extreme extinctions at its dawn (ca. 252 Ma) and its end (ca. 201 Ma) and by a combined extinction and significant radiation episode at ca. 232 Ma, during the Carnian (e.g., Tanner et al., 2004; Song et al., 2013; Bernardi et al., 2018; Dal Corso et al., 2020, 2022; Wignall and Atkinson 2020). The three main biocrises coincided with the emplacement of three Large Igneous Provinces (LIPs), namely, the Siberian Traps, the Central Atlantic Magmatic Province (CAMP), and the Wrangellia (**Figure 1**). In this article, we review the main features of these LIPs, with a focus on their timing, emplacement styles, and CO_2 budgets. This is followed by an in-depth discussion of their critical roles in the Triassic environmental crises.

CONTINENTAL LARGE IGNEOUS PROVINCES: THE SIBERIAN TRAPS AND THE CAMP

High-precision geochronology proves that the main activity of the Siberian Traps and the CAMP (main pulses at 252.3–251.4 Ma and 201.6–201.0 Ma, respectively; for the Siberian Traps: Kamo

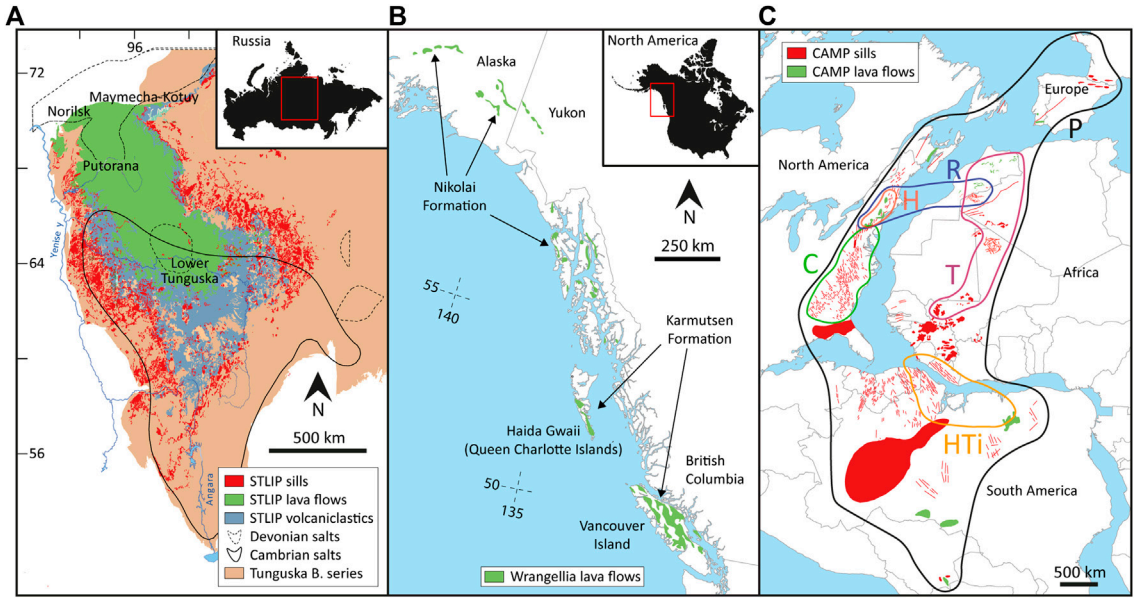

FIGURE 1 | Simplified sketches of **(A)** the Siberian Traps (modified after Svensen et al., 2018) **(B)** the Wrangellia (modified after Lassiter et al., 1995), and **(C)** the CAMP (modified after Capriolo et al., 2020). **(C)** Coloured lines represent the geographic distribution of the six geochemical groups of the CAMP magmas identified by Marzoli et al. (2018): P=Prevalent, HTi=high-Ti, T=Tiourjdal, R=Recurrent, C=Carolina, H=Holyoke.

et al., 2003; Burgess and Bowring, 2015; Burgess et al., 2017; Augland et al., 2019; for the CAMP: Blackburn et al., 2013; Davies et al., 2017, 2021; Marzoli et al., 2019) spanned the end-Permian and end-Triassic extinction intervals, respectively (251.94–251.88 Ma and 201.51–201.36 Ma; Schoene et al., 2010; Burgess et al., 2014; Wotzlaw et al., 2014). The pulsed nature of these LIPs was inferred from magnetostratigraphy and biostratigraphy (e.g., Knight et al., 2004; Panfili et al., 2019; Latyshev et al., 2020), yielding eruption rates possibly two orders of magnitude greater than the most voluminous present-day eruptions, such as those at Hawai'i (e.g., Patrick et al., 2020). The Siberian Traps and the CAMP are among the most voluminous known LIPs (both ca. 3 ± 1 million km^3; Saunders and Reichow, 2009; Marzoli et al., 2018), although a precise estimate of the original and preserved magma volume remains challenging. Large parts of the Siberian Traps are intrusive, subaerial, and huge volumes of volcanics were likely removed by erosion. The best-studied part of the province is on the Siberian Craton, at a paleolatitude of ca. 50–60°N, over an area of ca. 2.5 million km^2 (**Figure 1A**). The CAMP was emplaced over 10 million km^2 straddling the equator, and has been similarly partly eroded away, as demonstrated by the sparsely preserved lava piles (**Figure 1C**).

The first emplacement stage of the Siberian Traps started shortly before 252.24 ± 0.12 Ma with initial pyroclastic eruptions followed by effusive activity emplaced in ca 0.30 Ma. From 251.91 ± 0.07 Ma, the extrusive activity waned and shifted to dominantly intrusive for ca. 0.40 Ma, building the vast network of sills in the Tunguska Basin. These tholeiitic magmas were produced by shallower and extensive melting of a mixed peridotitic-pyroxenitic mantle (Sobolev et al., 2011; Callegaro et al., 2021). Renewed extrusive activity is recognized from 251.48 ± 0.09 Ma, marking the beginning of the third phase of the Siberian Traps. During this phase, tholeiitic extrusive and intrusive activities were accompanied by mafic to felsic alkaline intrusions in Maymecha-Kotuy and Taimyr areas (Elkins-Tanton et al., 2007; Sobolev et al., 2009; Augland et al., 2019). Alkaline melts were produced from a deep (5.5 GPa) and volatile-rich (carbonated) mantle source (Elkins-Tanton et al., 2007). The youngest sill dated in Tunguska (251.35 ± 0.09 Ma; Burgess and Bowring, 2015), and the Guli carbonatitic complex in the Maymecha-Kotuy region (250.20 ± 0.30 Ma; Kamo et al., 2003) represent the youngest known Siberian Traps products.

The beginning of the second (intrusive) phase is considered as the deadly subinterval of the Siberian Traps (Burgess et al., 2017), since it coincides with the beginning of the extinction horizon at Meishan (251.94 ± 0.04 Ma; Burgess et al., 2014), Dongpan and Penglaitan (251.94 ± 0.03 Ma and 251.98 ± 0.03 Ma; Baresel et al., 2017), China. Even if these tholeiitic magmas were probably volatile poor (Sibik et al., 2015), the interaction between the sills and the sedimentary host-rocks (i.e., evaporites, carbonates, marlstones, and coal) likely produced large amounts of thermogenic carbon, sulfur and halocarbon species (Svensen et al., 2018; Callegaro et al., 2021; Sibik et al., 2021).

The end of the Triassic witnessed the emplacement of the CAMP mainly between 201.64 ± 0.03 Ma and 201.36 ± 0.02 Ma (Blackburn et al., 2013; Davies et al., 2017, 2021; Marzoli et al., 2019), coincident with the main end-Triassic extinction interval (201.51 ± 0.15 to 201.36 ± 0.15 Ma; Schoene et al., 2010; Wotzlaw et al., 2014). Basaltic magmas erupted as short-lived pulses (Knight et al., 2004; Marzoli et al., 2019) during this magmatic phase have been shown to be rich in CO_2 and SO_2 (Callegaro

et al., 2014a; Capriolo et al., 2020) and possibly triggered the dramatic increase in CO_2, the rise of temperature and the climatic perturbations heralding the end of the Triassic (Landwehrs et al., 2020; Lindström et al., 2021; Capriolo et al., 2022). Later erupted magmas, for example, in North America and Africa (Holyoke and Recurrent groups; Blackburn et al., 2013; Marzoli et al., 2018, 2019) appear to be less voluminous and possibly had limited environmental effects.

Similar to the Siberian Traps, CAMP magmas are mainly preserved as large sills intruding Paleozoic terrestrial sediments in South America and North-western Africa, and Triassic terrestrial sediments in North America and Europe (Marzoli et al., 2018 and references therein). The CAMP basalts mobilized large amounts of organic carbon and possibly halogens from evaporitic deposits (Heimdal et al., 2018, 2019; Capriolo et al., 2021). Available geochronological data indicate that some CAMP intrusions are older than the preserved (and dated) erupted basalts (Davies et al., 2017). However, the intrusion of sills in Amazonia and north-western Africa seems to be relatively prolonged from ca. 201.53 ± 0.07 Ma to ca. 201.35 ± 0.03 Ma (Davies et al., 2017, 2021), i.e., spanning the entire end-Triassic extinction interval (Schoene et al., 2010). However, it is still unclear whether CAMP intrusions occurred in pulses, thus emitting thermogenic volatiles at high rates, and playing a catastrophic role in the end-Triassic crisis.

Unlike the Siberian Traps, CAMP magmas are relatively uniform in composition, mainly being tholeiitic basalts. Whether such relatively high degree mantle melts originated from the deep or shallow mantle is still disputed (e.g., Ruiz-Martinez et al., 2012; Tegner et al., 2019; Boscaini et al., 2022). CAMP basalts lack geochemical signatures of a mantle plume originating from the deep mantle but show a subduction signature, which is best interpreted as reflecting the presence of recycled subducted continental rocks (sediments, mainly; Callegaro et al., 2013; Merle et al., 2014; Shellnutt et al., 2018; Marzoli et al., 2019). The absence of alkaline mafic rocks or carbonatites in the CAMP calls against a significant contribution from particularly CO_2-rich metasomatized mantle portions. In contrast to the Siberian Traps, evidence for explosive volcanic activity is rare for the CAMP, whose lavas are mostly compound pahoehoe flows (e.g., El Hacimi et al., 2011) and therefore occurred as fissure eruptions like the historical Laki eruption in Iceland.

Oceanic Large Igneous Province: The Wrangellia

The Wrangellia LIP presently crops out along the north-western margin of North America (**Figure 1B**). It represents one of the best-preserved accreted oceanic plateaus on Earth, which contrast starkly with continental LIPs in terms of mantle processes, emplacement style and, possibly, environmental implications (Kerr, 2005).

The origin of the Wrangellia tholeiitic basalts has been attributed to deep mantle processes (i.e., mantle plume; Richards et al., 1991; Lassiter et al., 1995; Greene et al., 2009a; Greene et al., 2009b; Shellnutt et al., 2021). The early emplaced low-Ti basalts (0.4–1.2 TiO_2 wt%) were probably sourced from partial melting of a rising mantle plume and show a significant contribution from the subduction-modified lithospheric mantle (Greene et al., 2009a; Greene et al., 2009b). Conversely, the later high-Ti basalts (1.4–2.4 TiO_2 wt%) were sourced chiefly from the mantle plume (Greene et al., 2009a; Greene et al., 2009b).

As an oceanic plateau, the magmatic products of the Wrangellia are considerably different from those of continental LIPs like the Siberian Traps and the CAMP and include tholeiitic submarine and subaerial flows. Few sills beneath and interbedded with the lavas are also present. A total volume of at least 1 million km^3 was estimated for the entire LIP (Greene et al., 2010). Pillow lavas at the base of the volcanic succession are ubiquitous over the entire province. However, they form thinner sequences (~500 vs. ~2,500 m) and are highly vesicular in Alaska and Yukon compared to south-western Canada (Vancouver Island), suggesting a southward deepening of the emplacement depth (Greene et al., 2010). This is consistent with subaerial pahoehoe lavas being relatively more abundant in Alaska and Yukon, where they pile up to 3,500 m (Greene et al., 2010).

The age of the Wrangellia is poorly constrained. A maximum time span of ca. 2 Ma has been inferred from magnetostratigraphic studies (Greene et al., 2010 and references therein). Valuable constraints are offered by biostratigraphy. *Daonella*-bearing shales unconformably underlie the lowest basalts of the volcanic sequence. *Daonella* would indicate a maximum Ladinian age (Smith and MacKevet, 1970; Brack et al., 2005), but *Daonella* is also known from younger Triassic strata (e.g., Fürsich and Wendt, 1977). The termination of Wrangellia volcanism was marked by the establishment of stable carbonate production on top of volcanic successions and was geographically diachronous. On Vancouver Island, the uppermost basalts of the Karmutsen Formation are interbedded with sediments bearing ammonoids and bivalve *Halobia* of the Tuvalian 1 *dilleri* Zone (Upper Carnian; Carlisle and Susuki, 1974). On Haida Gwaii (Queen Charlotte Islands), the volcanic sequence is overlain by the carbonate-dominated Kunga Group that yields conodonts and ammonoids of the Tuvalian 2-3 *welleri* Zone (Desrochers and Orchard, 1991). In south-western Yukon, the volcanism continued to at least the early Norian, evidenced by conodonts recovered from interbedded limestones in the Nikolai Formation (Israel et al., 2006). Ar/Ar and U-Pb ages for the Wrangellia magmatic rocks span between 232 and 226 Ma (Greene et al., 2010 and references therein). However, samples selected for Ar/Ar dating showed widespread alteration leading to large age uncertainties (up to 11 Ma), disturbed spectra, and excess argon. Zircons and baddeleyite selected for U-Pb dating were not chemically abraded, likely yielding ages younger than the actual crystallization ages.

The lack of high precision radioisotopic ages for the Wrangellia precludes the possibility to constrain the onset of magmatism, and to distinguish different pulses in the volcanic activity, in turn hindering reconstruction of rates of volcanic or thermogenic gas discharges. This is crucial as the Wrangellia has been tentatively linked to a period of significant climate changes and biological turnover during the Late Triassic, known as CPE

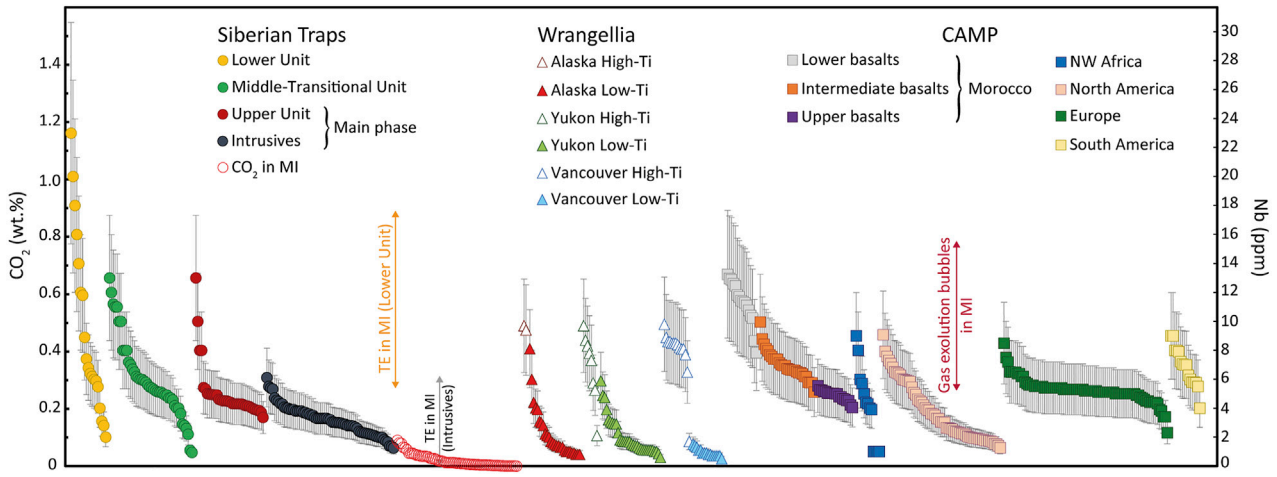

FIGURE 2 | Initial maximum CO_2 budgets obtained from Nb whole-rock concentrations of magmas for the Siberian Traps (circles), the Wrangellia (triangles) and the CAMP (squares). Following Rosenthal et al. (2015), we assumed CO_2/Nb = 505 ± 168, which corresponds to mantle source CO_2 of 75 ± 25 ppm. Data are filtered for MgO > 7wt%. Maximum and minimum MgO contents are 22.9–7.1 wt% (average 10.2 wt%) for the Siberian Traps, 17.5–7.1 wt% (average 9.8 wt%) for the Wrangellia, and 16.6–7.0 wt% (average 8.7 wt%) for the CAMP. Data are plotted in ranked order. Siberian Traps: data from GEOROC Database (http://georoc.mpch-mainz.gwdg.de/); Hawkesworth et al. (1995); Sobolev et al. (2009, 2011); Sibik et al. (2015); Callegaro et al. (2021). Wrangellia: data from Greene et al. (2009a), Greene et al. (2009b), Greene et al. (2010). CAMP: data from De Min et al. (2003); Jourdan et al. (2003); Deckart et al. (2005); Verati et al. (2005); Merle et al. (2011, 2014); Callegaro et al. (2013, 2014b); Bertrand et al. (2014); Marzoli et al. (2019). All data are reported in the **Supplementary Appendix Table**. CO_2 concentrations measured from melt inclusions (MI) for the Siberian Traps (Black et al., 2014; Sibik et al., 2015) are reported for comparison (open circles). Yellow and grey arrows represent CO_2 estimates obtained from trace element (TE) concentrations in melt inclusions following the same approach as whole-rock data. CO_2 concentrations obtained from MI of the Gudchikhinsky Formation (yellow colour; Lower Unit) and of intrusives of the main phase of the Siberian Traps (grey colour; Sibik et al., 2015) are ca. 0.3–0.9 wt% and ca. 0–0.3 wt%, respectively, consistent with the results obtained from whole-rock data. Red arrow represents CO_2 concentrations estimated from gas exsolution bubbles preserved in melt inclusion of CAMP magmas (Capriolo et al., 2020).

(Dal Corso et al., 2020). The finding of four negative carbon isotope excursions (NCIEs) correlated with Hg spikes in sedimentary strata across the CPE suggest a volcanic origin for this event (Dal Corso et al., 2018, 2020; Lu et al., 2021; Mazaheri-Johari et al., 2021). The duration of the CPE was inferred to be of ca. 1.2 to 1.7 Ma based on magnetostratigraphic, biostratigraphic and cyclostratigraphic studies (Zhang et al., 2015; Miller et al., 2017; Bernardi et al., 2018; Dal Corso et al., 2020). Accordingly, two tuffaceous claystones intercalated with CPE-related rocks of the Jiyuan Basin (China) were dated at 233.10 ± 1.30 and 232.90 ± 2.10 Ma (LA-ICP-MS U-Pb zircon ages; Lu et al., 2021). However, although the ages of the Wrangellia and the CPE partially overlap, their relative timing remains highly debated.

DISCUSSION AND CONCLUDING REMARKS

Eruptions of the Siberian Traps, the CAMP, and the Wrangellia LIPs deeply reshaped the Triassic world. In particular, the Siberian Traps and the CAMP emplaced in continental settings as pulsed magmatic events, and both bear strong evidence of interaction between magmas and sedimentary country rocks. A clear difference between these LIPs is shown by the widespread explosive volcanism and abundant alkaline magmatism marking the early and final phases of the Siberian Traps, but unknown for the CAMP. On the other hand, the Wrangellia presents substantial differences as it was emplaced in an oceanic setting, and partially consists of subaqueous lava flows. Due to the lack of high-precision geochronology it is also impossible to clarify whether its magmatic activity was pulsed or continuous.

A recurrent aspect of the Triassic period is that multiple NCIEs were reported worldwide for the end-Permian (e.g., Wu et al., 2021) and end-Triassic mass extinction intervals (Ruhl et al., 2020), as well as for the CPE (Sun et al., 2019; Dal Corso et al., 2018, 2020). NCIEs would testify for the injection of large quantities of isotopically depleted CO_2 into the atmosphere and oceans. Likely, CO_2 (and other greenhouse and poisonous gases) would have been released either from the erupted magmas (Capriolo et al., 2020) or from devolatilization of the intruded host-rocks (Svensen et al., 2009; Capriolo et al., 2021), implying that LIPs-related magmatism was the main driver for catastrophic environmental changes of the Triassic. Since the magnitude of these global crises is also related to the rates at which volatiles were generated, quantifying the process of magma degassing is crucial. Direct estimates of released CO_2 were obtained from fresh, non-recrystallized melt inclusions (e.g., Sobolev et al., 2009; Black et al., 2014; Sibik et al., 2015; Capriolo et al., 2020). However, these are few (and potentially not entirely representative) for the Siberian Traps and the CAMP, and completely lacking for the Wrangellia. We therefore adopted here the approach of Rosenthal et al. (2015) to estimate the initial CO_2 contents of basaltic magmas from their incompatible trace element compositions. In fact, Nb and CO_2 behave similarly

during partial mantle melting, both strongly partitioning into the melt phase. However, at shallow depth in the crust, CO_2 is degassed as magma ascends towards the surface (Capriolo et al., 2020), while Nb remains in the melt. We applied this proxy to whole-rock compositions of the three Triassic LIPs (**Figure 2**) filtered for basalts with MgO >7 wt% to consider only those magmas closer to the composition of mantle-derived primitive melts, as suggested by Hernandez Nava et al. (2021).

CO_2 concentrations estimated for magmas of the Siberian Traps are significantly variable within the three magmatic phases previously described (**Figure 2**). High-Ti lava flows of the Lower Unit and the low-Ti magmas of the Middle-Transitional Unit yielded the highest calculated CO_2 contents (ca. 0.1–1.2 and 0.05–0.7 wt%, respectively; **Figure 2**). In contrast, lavas of the Upper Unit and correlated intrusions, which characterize the second and more voluminous Siberian main phase, yielded lower CO_2 contents (ca. 0.1–0.3 wt%; **Figure 2**). Within CAMP, the earliest erupted basalts from north-western Africa are relatively enriched in CO_2 (0.4–0.7 wt%), while the slightly later and ubiquitous low-Ti magmas of the Prevalent group (Callegaro et al., 2013; Merle et al., 2014; Marzoli et al., 2018, 2019) yielded slightly lower CO_2 concentrations (ca. 0.1 to 0.5 wt%; **Figure 2**). These results would imply that, for both the Siberian Traps and the CAMP, the highest concentrations of mantle-derived CO_2 were produced from magmas of the initial phases. Interestingly, the end-Permian extinction coincides with the initial emplacement of the volatile-poor sills of the Siberian Traps, while the end-Triassic extinction coincides with the effusive activity of the CAMP, whose lavas are relatively CO_2-rich (Capriolo et al., 2020). The fact that variable amounts of mantle-derived CO_2 from the magmas produced similar environmental consequences suggests that additional isotopically depleted CO_2 was likely released during the intrusive Siberian Traps activity. In this case, a significant part of the emitted CO_2 (and possibly other gases, e.g., CH_4, SO_2 and halocarbons) may have been produced thermogenically from the intruded host rocks (e.g., Svensen et al., 2009, 2018; Capriolo et al., 2021) highlighting the crucial role of sedimentary basins as additional suppliers of climate-modifying gases. Noteworthy, the early terrestrial onset of the end-Permian extinction seems to suggest that mantle-derived halogens were key environmental impactors during the first phase of the Siberian Traps (Sobolev et al., 2011; Dal Corso et al., 2022).

Geochemical data for the Wrangellia are relatively scarce. However, the high-Ti basalts have the highest Nb and thus possibly the highest CO_2 contents (ca. 0.3–0.5 wt%), while the low-Ti basalts were relatively Nb and thus CO_2-depleted (≤0.3 wt %). This difference may imply that the overall production of CO_2 increased when magmas were predominantly sourced from the mantle plume source, i.e., with minor or no contribution from the lithospheric mantle.

To summarize, in this study, we reviewed the main features of the Siberian Traps, the Wrangellia and the CAMP LIPs, which impacted the Triassic world. High-precision geochronology strongly links the Siberian Traps and the CAMP to the end-Permian and the end-Triassic mass extinctions, respectively. A similar cause-and-effect scenario between the Wrangellia and the CPE seems plausible based on paleontological, biostratigraphic and geochemical studies. However, further high-precision dating on both lava flows and intrusions is necessary to constrain the onset, evolution, and cessation of this LIP, as well as its emplacement mechanisms.

Using previously published data, we estimated maximum CO_2 contents for magmas of the three Triassic LIPs. Even if these estimates are based on proxy data, our results highlight that the mantle-related CO_2 budgets of the more primitive basalts seem to vary during the overall life cycle of each LIP, suggesting that different mantle sources or melting regimes came into play to produce these exceptionally voluminous volcanic events. These observations stress the fact that each LIP is a unique case-study and building paradigms that apply to all LIPs when discussing their relationship to concurrent Earth crises is not straightforward.

AUTHOR CONTRIBUTIONS

AB wrote the review on Wrangellia, compiled data from the literature and produced the figures. SC wrote the review on the Siberian Traps. AM designed the project and wrote the review on the CAMP. YS contributed to the review on Wrangellia.

FUNDING

Financial support was provided by the Italian Ministry of University and Research (PRIN 20178LPCP to AM). SC acknowledges support from the Research Council of Norway (Grant 301096, Young Research Talents).

SUPPLEMENTARY MATERIAL

The Supplementary Material for this article can be found online at: https://www.frontiersin.org/articles/10.3389/feart.2022.887632/full#supplementary-material

REFERENCES

Augland, L. E., Ryabov, V. V., Vernikovsky, V. A., Planke, S., Polozov, A. G., and Callegaro, S. (2019). The Main Pulse of the Siberian Traps Expanded in Size and Composition. *Sci. Rep.* 9, 1–12. doi:10.1038/s41598-019-54023-2

Baresel, B., Bucher, H., Brosse, M., Cordey, F., Guodun, K., and Schaltegger, U. (2017). Precise Age for the Permian – Triassic Boundary in South China from High-Precision U-Pb Geochronology and Bayesian Age – Depth Modeling. *Solid Earth* 8, 361–378. doi:10.5194/se-8-361-2017

Bernardi, M., Gianolla, P., Petti, F. M., Mietto, P., and Benton, M. J. (2018). Dinosaur Diversification Linked with the Carnian Pluvial Episode. *Nat. Commun.* 9. doi:10.1038/s41467-018-03996-1

Bertrand, H., Fornari, M., Marzoli, A., García-Duarte, R., and Sempere, T. (2014). The Central Atlantic Magmatic Province Extends into Bolivia. *Lithos* 188, 33–43. doi:10.1016/j.lithos.2013.10.019

Black, B. A., Hauri, E. H., Elkins-Tanton, L. T., and Brown, S. M. (2014). Sulfur Isotopic Evidence for Sources of Volatiles in Siberian Traps Magmas. *Earth Planet. Sci. Lett.* 394, 58–69. doi:10.1016/j.epsl.2014.02.057

Blackburn, T. J., Olsen, P. E., Bowring, S. A., McLean, N. M., Kent, D. V., Puffer, J., et al. (2013). Zircon U-Pb Geochronology Links the End-Triassic Extinction with the Central Atlantic Magmatic Province. *Science* 340, 941–945. doi:10.1126/science.1234204

Boscaini, A., Marzoli, A., Bertrand, H., Chiaradia, M., Jourdan, F., Faccenda, M., et al. (2022). Cratonic Keels Controlled the Emplacement of the Central Atlantic Magmatic Province (CAMP). *Earth Planet. Sci. Lett.* 584. doi:10.1016/j.epsl.2022.117480

Brack, P., Rieber, H., Nicora, A., and Mundil, R. (2005). The Global Boundary Stratotype Section and Point (GSSP) of the Ladinian Stage (Middle Triassic) at Bagolino (Southern Alps, Northern Italy) and its Implications for the Triassic Time Scale. *Episodes* 28, 233–244. doi:10.18814/epiiugs/2005/v28i4/001

Burgess, S. D., and Bowring, S. A. (2015). High-precision Geochronology Confirms Voluminous Magmatism before, during, and after Earth's Most Severe Extinction. *Sci. Adv.* 1, 1–14. doi:10.1126/sciadv.1500470

Burgess, S. D., Bowring, S. A., and Shen, S. (2014). High-precision Timeline for Earth's Most Severe Extinction. *Proc. Natl. Acad. Sci. U. S. A.* 111, 3316–3321. doi:10.1073/pnas.140419611110.1073/pnas.1317692111

Burgess, S. D., Muirhead, J. D., and Bowring, S. A. (2017). Initial Pulse of Siberian Traps Sills as the Trigger of the End-Permian Mass Extinction. *Nat. Commun.* 8, 1–4. doi:10.1038/s41467-017-00083-9

Callegaro, S., Baker, D. R., de Min, A., Marzoli, A., Geraki, K., Bertrand, H., et al. (2014a). Microanalyses Link Sulfur from Large Igneous Provinces and Mesozoic Mass Extinctions. *Geology* 42, 895–898. doi:10.1130/G35983.1

Callegaro, S., Marzoli, A., Bertrand, H., Chiaradia, M., Reisberg, L., Meyzen, C., et al. (2013). Upper and Lower Crust Recycling in the Source of CAMP Basaltic Dykes from southeastern North America. *Earth Planet. Sci. Lett.* 376, 186–199. doi:10.1016/j.epsl.2013.06.023

Callegaro, S., Rapaille, C., Marzoli, A., Bertrand, H., Chiaradia, M., Reisberg, L., et al. (2014b). Enriched Mantle Source for the Central Atlantic Magmatic Province: New Supporting Evidence from Southwestern Europe. *Lithos* 188, 15–32. doi:10.1016/j.lithos.2013.10.021

Callegaro, S., Svensen, H. H., Neumann, E. R., Polozov, A. G., Jerram, D. A., Deegan, F. M., et al. (2021). Geochemistry of Deep Tunguska Basin Sills, Siberian Traps: Correlations and Potential Implications for the End-Permian Environmental Crisis. *Contrib. Mineral. Petrol.* 176, 1–30. doi:10.1007/s00410-021-01807-3

Capriolo, M., Marzoli, A., Aradi, L. E., Ackerson, M. R., Bartoli, O., Callegaro, S., et al. (2021). Massive Methane Fluxing from Magma–Sediment Interaction in the End-Triassic Central Atlantic Magmatic Province. *Nat. Commun.* 12, 1–9. doi:10.1038/s41467-021-25510-w

Capriolo, M., Marzoli, A., Aradi, L. E., Callegaro, S., Dal Corso, J., Newton, R. J., et al. (2020). Deep CO_2 in the End-Triassic Central Atlantic Magmatic Province. *Nat. Commun.* 11, 1–11. doi:10.1038/s41467-020-15325-6

Capriolo, M., Mills, B. J. W., Newton, R. J., Dal Corso, J., Dunhill, A. M., Wignall, P. B., et al. (2022). Anthropogenic-scale CO_2 Degassing from the Central Atlantic Magmatic Province as a Driver of the End-Triassic Mass Extinction. *Glob. Planet. Change* 209. doi:10.1016/j.gloplacha.2021.103731

Carlisle, D., and Suzuki, T. (1974). Emergent basalt and Submergent Carbonate-Clastic Sequences Including the Upper Triassic Dilleri and Welleri Zones on Vancouver Island. *Can. J. Earth Sci.* 11, 254–279. doi:10.1139/e74-023

Dal Corso, J., Bernardi, M., Sun, Y., Song, H., Seyfullah, L. J., Preto, N., et al. (2020). Extinction and Dawn of the Modern World in the Carnian (Late Triassic). *Sci. Adv.* 6, 1–13. doi:10.1126/sciadv.aba0099

Dal Corso, J., Callegaro, S., Sun, Y., Hilton, J., Grasby, S. E., Joachimski, M. M., et al. (2022). Environmental Crises at the Permian–Triassic Mass Extinction. *Nat. Rev. Earth Environ.*. doi:10.1038/s43017-021-00259-4

Dal Corso, J., Gianolla, P., Rigo, M., Franceschi, M., Roghi, G., Mietto, P., et al. (2018). Multiple Negative Carbon-Isotope Excursions during the Carnian Pluvial Episode (Late Triassic). *Earth-science Rev.* 185, 732–750. doi:10.1016/j.earscirev.2018.07.004

Davies, J. H. F. L., Marzoli, A., Bertrand, H., Youbi, N., Ernesto, M., Greber, N. D., et al. (2021). Zircon Petrochronology in Large Igneous Provinces Reveals Upper Crustal Contamination Processes: New U–Pb Ages, Hf and O Isotopes, and Trace Elements from the Central Atlantic Magmatic Province (CAMP). *Contrib. Mineral. Petrol.* 176, 1–24. doi:10.1007/s00410-020-01765-2

Davies, J. H. F. L., Marzoli, A., Bertrand, H., Youbi, N., Ernesto, M., and Schaltegger, U. (2017). End-Triassic Mass Extinction Started by Intrusive CAMP Activity. *Nat. Commun.* 8, 1–8. doi:10.1038/ncomms15596

De Min, A., Piccirillo, E. M., Marzoli, A., Bellieni, G., Renne, P. R., Ernesto, M., et al. (2003). The Central Atlantic Magmatic Province (CAMP) in Brazil: Petrology, Geochemistry, $^{40}Ar/^{39}Ar$ Ages, Paleomagnetism and Geodynamic Implications. *Geophys. Monogr. Ser.* 136, 91–128. doi:10.1029/136GM06

Deckart, K., Bertrand, H., and Liégeois, J. P. (2005). Geochemistry and Sr, Nd, Pb Isotopic Composition of the Central Atlantic Magmatic Province (CAMP) in Guyana and Guinea. *Lithos* 82, 289–314. doi:10.1016/j.lithos.2004.09.023

Desrochers, A., and Orchard, M. J. (1991). "The Kunga Group (Late Triassic-Early Jurassic), Queen Charlotte Islands, British Columbia: Stratigraphic Revisions and Carbonate Sedimentology," in *Evolution and Hydrocarbon Potential of the Queen Charlotte Basin, British Columbia*. Editor G. W. Woodsworth (Ottawa: Can. Geol. Surv.), 163–172.

El Hachimi, H., Youbi, N., Madeira, J., Bensalah, M. K., Martins, L., Mata, J., et al. (2011). Morphology, Internal Architecture and Emplacement Mechanisms of Lava Flows from the Central Atlantic Magmatic Province (CAMP) of Argana Basin (Morocco). *Geol. Soc. Spec. Publ.* 357, 167–193. doi:10.1144/SP357.9

Elkins-Tanton, L. T., Draper, D. S., Agee, C. B., Jewell, J., Thorpe, A., and Hess, P. C. (2007). The Last Lavas Erupted during the Main Phase of the Siberian Flood Volcanic Province: Results from Experimental Petrology. *Contrib. Mineral. Petrol.* 153, 191–209. doi:10.1007/s00410-006-0140-1

Fürsich, F. T., and Wendt, J. (1977). Biostratinomy and Palaeoecology of the Cassian Formation (Triassic) in the Southern Alps. *Palaeogeogr. Palaeoclimatol. Palaeoecol.* 22, 257–323.

Greene, A. R., Scoates, J. S., Weis, D., and Israel, S. (2009a). Geochemistry of Triassic Flood Basalts from the Yukon (Canada) Segment of the Accreted Wrangellia Oceanic Plateau. *Lithos* 110, 1–19. doi:10.1016/j.lithos.2008.11.010

Greene, A. R., Scoates, J. S., Weis, D., Katvala, E. C., Israel, S., and Nixon, G. T. (2010). The Architecture of Oceanic Plateaus Revealed by the Volcanic Stratigraphy of the Accreted Wrangellia Oceanic Plateau. *Geosphere* 6, 47–73. doi:10.1130/GES00212.1

Greene, A. R., Scoates, J. S., Weis, D., Nixon, G. T., and Kieffer, B. (2009b). Melting History and Magmatic Evolution of Basalts and Picrites from the Accreted Wrangellia Oceanic Plateau, Vancouver Island, Canada. *J. Petrol.* 50, 467–505. doi:10.1093/petrology/egp008

Hawkesworth, C. J., Lightfoot, P. C., Fedorenko, V. A., Blake, S., Naldrett, A. J., Doherty, W., et al. (1995). Magma Differentiation and Mineralisation in the Siberian continental Flood Basalts. *Lithos* 34, 61–88. doi:10.1016/0024-4937(95)90011-x

Heimdal, T. H., Callegaro, S., Svensen, H. H., Jones, M. T., Pereira, E., and Planke, S. (2019). Evidence for Magma–Evaporite Interactions during the Emplacement of the Central Atlantic Magmatic Province (CAMP) in Brazil. *Earth Planet. Sci. Lett.* 506, 476–492. doi:10.1016/j.epsl.2018.11.018

Heimdal, T. H., Svensen, H. H., Ramezani, J., Iyer, K., Pereira, E., Rodrigues, R., et al. (2018). Large-scale Sill Emplacement in Brazil as a Trigger for the End-Triassic Crisis. *Sci. Rep.* 8, 1–12. doi:10.1038/s41598-017-18629-8

Hernandez Nava, A., Black, B. A., Gibson, S. A., Bodnar, R. J., Renne, P. R., and Vanderkluysen, L. (2021). Reconciling Early Deccan Traps CO_2 Outgassing and Pre-KPB Global Climate. *Proc. Natl. Acad. Sci. U. S. A.* 118, 1–9. doi:10.1073/pnas.2007797118

Israel, S., Tizzard, A., and Major, J. (2006). "Bedrock Geology of the Duke River Area, Parts of NTS 115G/2, 3, 4, 6 and 7, Southwestern Yukon," in *Yukon Exploration and Geology 2005*. Editors D. S. Emond,

G. D. Bradshaw, L. L. Lewis, and L. H. Weston (Whitehorse: Yukon Geological Survey), 139–154.

Jourdan, F., Marzoli, A., Bertrand, H., Cosca, M., and Fontignie, D. (2003). The Northernmost CAMP: $^{40}Ar/^{39}Ar$ Age, Petrology and Sr-Nd-Pb Isotope Geochemistry of the Kerforne Dike, Brittany, France. *Geophys. Monogr. Ser.* 136, 209–226. doi:10.1029/136GM011

Kamo, S. L., Czamanske, G. K., Amelin, Y., Fedorenko, V. A., Davis, D. W., and Trofimov, V. R. (2003). Rapid Eruption of Siberian Flood-Volcanic Rocks and Evidence for Coincidence with the Permian-Triassic Boundary and Mass Extinction at 251 Ma. *Earth Planet. Sci. Lett.* 214, 75–91. doi:10.1016/S0012-821X(03)00347-9

Kerr, A. C. (2005). Oceanic LIPs: The Kiss of Death. *Elements* 1, 289–292. doi:10.2113/gselements.1.5.289

Knight, K. B., Nomade, S., Renne, P. R., Marzoli, A., Bertrand, H., and Youbi, N. (2004). The Central Atlantic Magmatic Province at the Triassic-Jurassic Boundary: Paleomagnetic and $^{40}Ar/^{39}Ar$ Evidence from Morocco for Brief, Episodic Volcanism. *Earth Planet. Sci. Lett.* 228, 143–160. doi:10.1016/j.epsl.2004.09.022

Landwehrs, J. P., Feulner, G., Hofmann, M., and Petri, S. (2020). Climatic Fluctuations Modelled for Carbon and Sulfur Emissions from End-Triassic Volcanism. *Earth Planet. Sci. Lett.* 537, 116174. doi:10.1016/j.epsl.2020.116174

Lassiter, J. C., DePaolo, D. J., and Mahoney, J. J. (1995). Geochemistry of the Wrangellia Flood basalt Province: Implications for the Role of continental and Oceanic Lithosphere in Flood basalt Genesis. *J. Petrol.* 36, 983–1009. doi:10.1093/petrology/36.4.983

Latyshev, A. V., Rad'ko, V. A., Veselovskiy, R. V., Fetisova, A. M., and Pavlov, V. E. (2020). Correlation of the Permian-Triassic Ore-Bearing Intrusions of the Norilsk Region with the Volcanic Sequence of the Siberian Traps Based on Paleomagnetic Data. *Econ. Geol.* 115, 1173–1193. doi:10.5382/ECONGEO.4746

Lindström, S., Callegaro, S., Davies, J., Tegner, C., van de Schootbrugge, B., Pedersen, G. K., et al. (2021). Tracing Volcanic Emissions from the Central Atlantic Magmatic Province in the Sedimentary Record. *Earth-science Rev.* 212. doi:10.1016/j.earscirev.2020.103444

Lu, J., Zhang, P., Corso, J. D., Yang, M., Wignall, P. B., Greene, S. E., et al. (2021). Volcanically Driven Lacustrine Ecosystem Changes during the Carnian Pluvial Episode (Late Triassic). *Proc. Natl. Acad. Sci. U. S. A.* 118, 1–8. doi:10.1073/pnas.2109895118

Marzoli, A., Bertrand, H., Youbi, N., Callegaro, S., Merle, R., Reisberg, L., et al. (2019). The Central Atlantic Magmatic Province (CAMP) in Morocco. *J. Petrol.* 60, 945–996. doi:10.1093/petrology/egz021

Marzoli, A., Callegaro, S., Dal Corso, J., Davies, J. H. F. L., Chiaradia, M., Youbi, N., et al. (2018). "The Central Atlantic Magmatic Province (CAMP): A Review," in *The Late Triassic World*. Editor L. H. Tanner (Springer International Publishing), 91–125. doi:10.1007/978-3-319-68009-5_4

Mazaheri-Johari, M., Gianolla, P., Mather, T. A., Frieling, J., Chu, D., and Dal Corso, J. (2021). Mercury Deposition in Western Tethys during the Carnian Pluvial Episode (Late Triassic). *Sci. Rep.* 11, 1–10. doi:10.1038/s41598-021-96890-8

Merle, R., Marzoli, A., Bertrand, H., Reisberg, L., Verati, C., Zimmermann, C., et al. (2011). $^{40}Ar/^{39}Ar$ Ages and Sr–Nd–Pb–Os Geochemistry of CAMP Tholeiites from Western Maranhão basin (NE Brazil). *Lithos* 122, 137–151. doi:10.1016/j.lithos.2010.12.010

Merle, R., Marzoli, A., Reisberg, L., Bertrand, H., Nemchin, A., Chiaradia, M., et al. (2014). Sr, Nd, Pb and Os Isotope Systematics of CAMP Tholeiites from Eastern North America (ENA): Evidence of a Subduction-Enriched Mantle Source. *J. Petrol.* 55, 133–180. doi:10.1093/petrology/egt063

Miller, C. S., Peterse, F., Silva, A.-C., Baranyi, V., Reichart, G. J., and Kürschner, W. M. (2017). Astronomical Age Constraints and Extinction Mechanisms of the Late Triassic Carnian Crisis. *Sci. Rep.* 7, 1–7. doi:10.1038/s41598-017-02817-7

Panfili, G., Cirilli, S., Dal Corso, J., Bertrand, H., Medina, F., Youbi, N., et al. (2019). New Biostratigraphic Constraints Show Rapid Emplacement of the Central Atlantic Magmatic Province (CAMP) during the End-Triassic Mass Extinction Interval. *Glob. Planet. Change* 172, 60–68. doi:10.1016/j.gloplacha.2018.09.009

Patrick, M. R., Houghton, B. F., Anderson, K. R., Poland, M. P., Montgomery-Brown, E., Johanson, I., et al. (2020). The Cascading Origin of the 2018 Kīlauea Eruption and Implications for Future Forecasting. *Nat. Commun.* 11, 1–13. doi:10.1038/s41467-020-19190-1

Richards, M. A., Jones, D. L., Duncan, R. A., and DePaolo, D. J. (1991). A Mantle Plume Initiation Model for the Wrangellia Flood basalt and Other Oceanic Plateaus. *Science* 254, 263–267. doi:10.1126/science.254.5029.263

Rosenthal, A., Hauri, E. H., and Hirschmann, M. M. (2015). Experimental Determination of C, F, and H Partitioning between Mantle Minerals and Carbonated basalt, CO_2/Ba and CO_2/Nb Systematics of Partial Melting, and the CO_2 Contents of Basaltic Source Regions. *Earth Planet. Sci. Lett.* 412, 77–87. doi:10.1016/j.epsl.2014.11.044

Ruhl, M., Hesselbo, S. P., Al-Suwaidi, A., Jenkyns, H. C., Damborenea, S. E., Manceñido, M. O., et al. (2020). On the Onset of Central Atlantic Magmatic Province (CAMP) Volcanism and Environmental and Carbon-Cycle Change at the Triassic–Jurassic Transition (Neuquén Basin, Argentina). *Earth-science Rev.* 208, 103229. doi:10.1016/j.earscirev.2020.103229

Ruiz-Martínez, V. C., Torsvik, T. H., van Hinsbergen, D. J. J., and Gaina, C. (2012). Earth at 200 Ma: Global Palaeogeography Refined from CAMP Palaeomagnetic Data. *Earth Planet. Sci. Lett.* 331–332, 67–79. doi:10.1016/j.epsl.2012.03.008

Saunders, A., and Reichow, M. (2009). The Siberian Traps and the End-Permian Mass Extinction: A Critical Review. *Chin. Sci. Bull.* 54, 20–37. doi:10.1007/s11434-008-0543-7

Schoene, B., Guex, J., Bartolini, A., Schaltegger, U., and Blackburn, T. J. (2010). Correlating the End-Triassic Mass Extinction and Flood basalt Volcanism at the 100 Ka Level. *Geology* 38, 387–390. doi:10.1130/G30683.1

Shellnutt, J. G., Dostal, J., and Lee, T. Y. (2021). Linking the Wrangellia Flood Basalts to the Galápagos Hotspot. *Sci. Rep.* 11. doi:10.1038/s41598-021-88098-7

Shellnutt, J. G., Dostal, J., and Yeh, M.-W. (2018). Mantle Source Heterogeneity of the Early Jurassic basalt of Eastern North America. *Int. J. Earth Sci.* 107, 1033–1058. doi:10.1007/s00531-017-1519-0

Sibik, S., Edmonds, M., Maclennan, J., and Svensen, H. (2015). Magmas Erupted during the Main Pulse of Siberian Traps Volcanism Were Volatile-Poor. *J. Petrol.* 56, 2089–2116. doi:10.1093/petrology/egv064

Sibik, S., Edmonds, M., Villemant, B., Svensen, H. H., Polozov, A. G., and Planke, S. (2021). Halogen Enrichment of Siberian Traps Magmas during Interaction with Evaporites. *Front. Earth Sci.* 9, 1–14. doi:10.3389/feart.2021.741447

Smith, J. G., and MacKevett, E. M., Jr. (1970). The Skolai Group in the McCarthy B-4, C-4, C-5 Quadrangles, Wrangell Mountains, Alaska. *Bull. U.S. Geol. Surv.* 1274-Q, Q1–Q26.

Sobolev, A. V., Krivolutskaya, N. A., and Kuzmin, D. V. (2009). Petrology of the Parental Melts and Mantle Sources of Siberian Trap Magmatism. *Petrology* 17, 253–286. doi:10.1134/S0869591109030047

Sobolev, S. V., Sobolev, A. V., Kuzmin, D. V., Krivolutskaya, N. A., Petrunin, A. G., Arndt, N. T., et al. (2011). Linking Mantle Plumes, Large Igneous Provinces and Environmental Catastrophes. *Nature* 477, 312–316. doi:10.1038/nature10385

Song, H., Wignall, P. B., Tong, J., and Yin, H. (2013). Two Pulses of Extinction during the Permian-Triassic Crisis. *Nat. Geosci.* 6, 52–56. doi:10.1038/ngeo1649

Sun, Y. D., Richoz, S., Krystyn, L., Zhang, Z. T., and Joachimski, M. M. (2019). Perturbations in the Carbon Cycle during the Carnian Humid Episode: Carbonate Carbon Isotope Records from Southwestern China and Northern Oman. *J. Geol. Soc. Lond.* 176, 167–177. doi:10.1144/jgs2017-170

Svensen, H. H., Frolov, S., Akhmanov, G. G., Polozov, A. G., Jerram, D. A., Shiganova, O. V., et al. (2018). Sills and Gas Generation in the Siberian Traps. *Philos. Trans. R. Soc. A.* 376. doi:10.1098/rsta.2017.0080

Svensen, H., Planke, S., Polozov, A. G., Schmidbauer, N., Corfu, F., Podladchikov, Y. Y., et al. (2009). Siberian Gas Venting and the End-Permian Environmental Crisis. *Earth Planet. Sci. Lett.* 277, 490–500. doi:10.1016/j.epsl.2008.11.015

Tanner, L. H., Lucas, S. G., and Chapman, M. G. (2004). Assessing the Record and Causes of Late Triassic Extinctions. *Earth-science Rev.* 65, 103–139. doi:10.1016/S0012-8252(03)00082-5

Tegner, C., Michelis, S. A. T., McDonald, I., Brown, E. L., Youbi, N., Callegaro, S., et al. (2019). Mantle Dynamics of the Central Atlantic Magmatic Province (CAMP): Constraints from Platinum Group, Gold and Lithophile Elements in Flood Basalts of Morocco. *J. Petrol.* 60, 1621–1652. doi:10.1093/petrology/egz041

Verati, C., Bertrand, H., and Féraud, G. (2005). The Farthest Record of the Central Atlantic Magmatic Province into West Africa Craton: Precise $^{40}Ar/^{39}Ar$ Dating

and Geochemistry of Taoudenni basin Intrusives (Northern Mali). *Earth Planet. Sci. Lett.* 235, 391–407. doi:10.1016/j.epsl.2005.04.012

Wignall, P. B., and Atkinson, J. W. (2020). A Two-phase End-Triassic Mass Extinction. *Earth-science Rev.* 208, 103282. doi:10.1016/j.earscirev.2020.103282

Wotzlaw, J.-F., Guex, J., Bartolini, A., Gallet, Y., Krystyn, L., Mcroberts, C. A., et al. (2014). Towards Accurate Numerical Calibration of the Late Triassic: High-Precision U-Pb Geochronology Constraints on the Duration of the Rhaetian. *Geology* 42, 571–574. doi:10.1130/G35612.1

Wu, Y., Chu, D., Tong, J., Song, H., Dal Corso, J., Wignall, P. B., et al. (2021). Six-fold Increase of Atmospheric pCO_2 during the Permian–Triassic Mass Extinction. *Nat. Commun.* 12. doi:10.1038/s41467-021-22298-7

Zhang, Y., Li, M., Ogg, J. G., Montgomery, P., Huang, C., Chen, Z., et al. (2015). Cycle-calibrated Magnetostratigraphy of Middle Carnian from South China: Implications for Late Triassic Time Scale and Termination of the Yangtze Platform. *Palaeogeogr. Palaeoclimatol. Palaeoecol.* 436, 135–166. doi:10.1016/j.palaeo.2015.05.033

Conflict of Interest: The authors declare that the research was conducted in the absence of any commercial or financial relationships that could be construed as a potential conflict of interest.

frontiers | Frontiers in Earth Science

ORIGINAL RESEARCH
published: 26 April 2022
doi: 10.3389/feart.2022.875466

End-Triassic Extinction in a Carbonate Platform From Western Tethys: A Comparison Between Extinction Trends and Geochemical Variations

Simona Todaro[1], Manuel Rigo[2,3], Pietro Di Stefano[1], Alessandro Aiuppa[1] and Massimo Chiaradia[4]*

[1]Department of Earth and Marine Sciences, University of Palermo, Palermo, Italy, [2]Department of Geosciences, University of Padova, Padova, Italy, [3]IGG—CNR, Padova, Italy, [4]Department of Earth Sciences, University of Geneva, Geneva, Switzerland

The Triassic/Jurassic boundary section cropping out at Mt Sparagio in north-western Sicily (Italy) consists of a thick and continuous peritidal succession typical of a Tethyan carbonate platform. The combined chemostratigraphic and biostratigraphic study of this section allowed us to parallel the environmental variations inferred by the isotopic records and the extinction trends recorded by the benthic organisms. In the studied section, the isotope data of C, O, and S are indicative of serious environmental perturbations related to the Central Atlantic Magmatic Province (CAMP) activity, as recorded worldwide. Two negative excursions in the C-curve (Initial-CIE and Main-CIE) confirm the acidification processes that affected the benthic community. Moreover, the oxygen isotopes curve indicates a strong warming-trend that corresponds to the reduction in biodiversity and size of the megalodontoids in the upper part of the Rhaetian beds, probably due to the deterioration of the photosymbiotic relationships of these pelecypods. We here present some novel isotope data (Zn, Pb, Sr) from the Mt Sparagio section that offer additional clues on a tight control of CAMP volcanism on the End-Triassic Extinction.

Keywords: Triassic-Jurassic boundary, end Triassic extinction, large igneous province, mass extinction, Zn-Sr-Pb isotope, Sicily

OPEN ACCESS

Edited by:
Haijun Song,
China University of Geosciences Wuhan, China

Reviewed by:
Huyue Song,
China University of Geosciences Wuhan, China
Shijun Jiang,
Hohai University, China

****Correspondence:***
Simona Todaro
simona.todaro@unipa.it

Specialty section:
This article was submitted to Sedimentology, Stratigraphy and Diagenesis, a section of the journal Frontiers in Earth Science

Received: *14 February 2022*
Accepted: *24 March 2022*
Published: *26 April 2022*

Citation:
Todaro S, Rigo M, Di Stefano P, Aiuppa A and Chiaradia M (2022) End-Triassic Extinction in a Carbonate Platform From Western Tethys: A Comparison Between Extinction Trends and Geochemical Variations. Front. Earth Sci. 10:875466. doi: 10.3389/feart.2022.875466

INTRODUCTION

The End-Triassic Extinction (ETE) is one of the Big Five mass extinction events documented during the Phanerozoic, which occurred close to the Triassic/Jurassic boundary (TJB) at about 201 Ma (Sepkoski Jr, 1994; Hesselbo et al., 2002; Blackburn et al., 2013; Lindström, 2016). Several climate and environmental perturbations occurred at the end of Triassic: a global warming estimated at 3°–4°C seems to be the result of CO_2 and CH_4 release in the atmosphere by volcanism (McElwain et al., 1999; Beerling and Berner, 2002; Todaro et al., 2018; Song et al., 2021); subaerial deposits covered the end-Triassic platform deposits implying a sea level fall (Hallam, 1997), even if its global extent is still under discussion; a decrease of ocean water circulation (Huynh and Poulsen, 2005) and widespread anoxia involved many semi-enclosed basins of Europe (Luo et al., 2018) and the mid-depth waters of oceans (Jost et al., 2017; He et al., 2020); a low oxygen conditions also in shallow water setting from western Tethys (He et al., 2022); a perturbation in the carbon cycle induced by an increase in atmospheric pCO_2 (Capriolo et al., 2021), resulted in a acidification of the ocean involved mainly bio-calcifiers organisms, such as corals, sponges and benthic bivalves, causing their extinction (Greene et al., 2012; Todaro et al., 2018). A decrease in carbonate

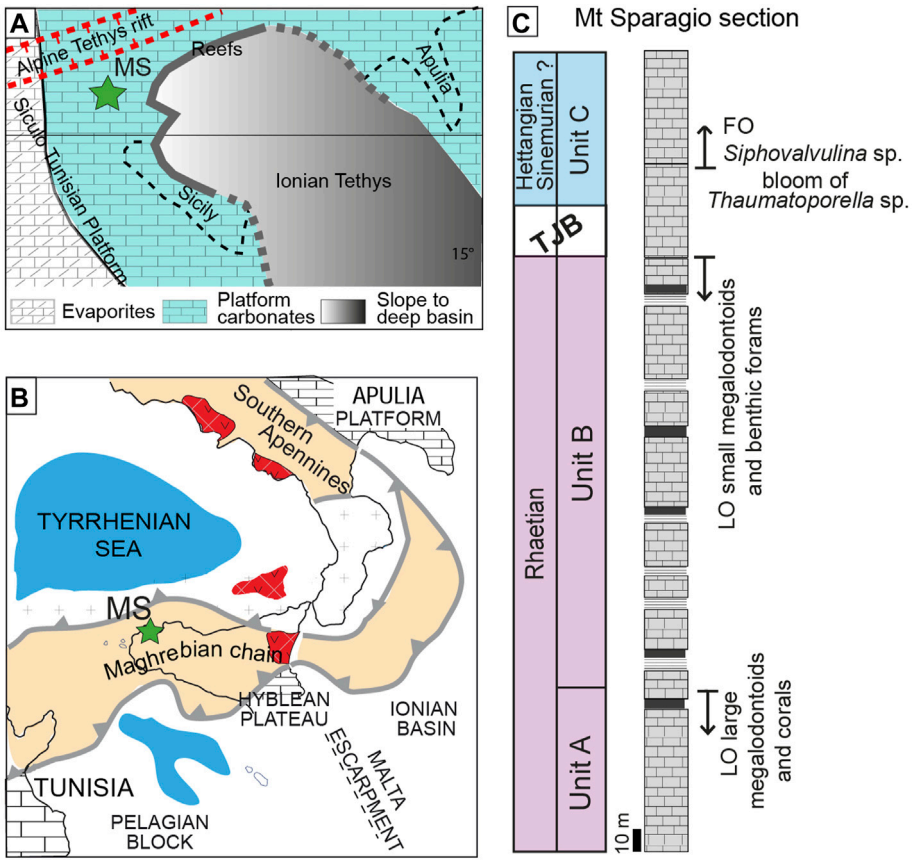

FIGURE 1 | (A) Paleogeography of the central Mediterranean area during the Late Triassic (modified after Di Stefano et al., 2015; paleolatitude after Muttoni et al., 2015). **(B)** Schematic structural map of the Central Mediterranean area. **(C)** The three informal units described in the Mt Sparagio section differentiated on the basis of the fossil associations in the subtidal facies (Modified after Todaro et al., 2018).

productivity is also observed in several stratigraphic sections from Panthalassa (Guex et al., 2004; Ciarapica, 2007; Galli et al., 2007; Wignall et al., 2007; Ruhl et al., 2009) and the Tethyan realm in which the lithologies show a decrease of wt% carbonate at TJB. All of these events might have contributed to the end Triassic mass extinction (ETE). However, the causes of the ETE are still unclear and debated, and it is largely accepted that this mass extinction is linked to the emplacement of a large igneous province known as Central Atlantic Magmatic Province (CAMP) (Marzoli et al., 1999, 2004; Wignall, 2001; Deenen et al., 2010; Schaller et al., 2011; Callegaro et al., 2014; Davies et al., 2017).

The biotic response to the environmental changes during the Late Triassic is recorded both in marine and terrestrial successions. Recent studies have demonstrated in detail two extinction pulses recorded by both marine and terrestrial realms (Wignall and Atkinson, 2020; Lindström, 2021). If on land the climatic changes led to a turnover of megaflora (McElwain et al., 1999; Lindstrom, 2021), in the marine realm high rates of extinction were recorded by benthic biocalcifiers such as bivalves, foraminifers, corals and sponges (e.g., Kiessling et al., 2007; Greene et al., 2012; Todaro et al., 2018). The main cause of the biocalcification crises was correlated to CO_2-induced acidification processes triggered by CAMP volcanism (Van De Schootbrugge et al., 2008; Todaro et al., 2018). Increasing CO_2 in the atmosphere is thought to have caused an alteration of the carbon cycle recorded by negative trends of the $\delta^{13}C$ curve (Ruhl et al., 2011; Bachan et al., 2012; Larina et al., 2021). Three major negative excursions known in literature as "Precursor" (Ruhl and Kürschner, 2011), "Initial" and "Main" CIEs (Hesselbo et al., 2002) were associated to the multiple volcanic pulses that characterized CAMP emplacement (Marzoli et al., 2004; Deenen et al., 2010; Davies et al., 2017; Zaffani et al., 2018).

This study aims to couple published data on the climatic changes, marine environmental perturbations and biotic crises recorded by a continuous Triassic-Jurassic peritidal carbonate succession from northwestern Sicily (Italy) to new isotopic data from Sr, Zn and Pb. These new results support the idea of a tight correlation between the CAMP volcanism pulses and the extinction trend at the end of Triassic.

GEOLOGICAL SETTING

The Mt Sparagio section is located in the north-western sector of Sicily (southern Italy, **Figure 1**). From the structural point of view this area, named as San Vito Peninsula, is a segment of the

Maghrebian chain and consists of a south-verging nappe pile (Giunta and Liguori, 1972; Abate et al., 1991). Each individual thrust is floored by Upper Triassic to Lower Jurassic shallow water carbonates transitional upward to pelagic carbonates of Middle Jurassic-Eocene age, with local intercalations of slope rudist limestones (Randazzo et al., 2020a; 2020b). The Upper Triassic to Lower Jurassic shallow water carbonates were part of a wide carbonate shelf that floored the south-western sector of the Tethys (i.e., Siculo-Tunisian Platform *sensu* Di Stefano et al., 2015). Part of this carbonate shelf was not involved in the Maghrebian orogeny, and today is preserved in the subsurface of the foreland areas of Sicily, e.g., the Sicily Channel and the Hyblean Plateau (Patacca et al., 1979; Antonelli et al., 1988; Todaro et al., 2021).

The internal part of the shelf was characterized by a wide subsiding peritidal area in which up to 3 km of carbonates were accumulated during Late Triassic and Early Jurassic (Patacca et al., 1979). These were transitional to evaporitic (sabkha-type) environments cropping out in the Egadi Islands, westernmost Sicily (Lo Cicero, 1986; Martini et al., 2007; Todaro et al., 2022) and are known by wells in the subsurface of the Tunisian offshore (Kamoun et al., 2001). During the Late Triassic the extensive lagoons were rimmed by a barrier reef dominated by hypercalcified coralline sponges that are recorded in several thrust sheets from Palermo to the Madonie Mountains (Senowbari Daryan et al., 2015 and references therein) (**Figure 1**). According to Zarcone et al. (2010) and Di Stefano et al. (2015) the Triassic carbonate shelf was flanked toward east by a deep and wide basin (Imerese-Sicanian Basin, *sensu* Di Stefano et al., 2015), connected to the Ionian Tethys (Finetti et al., 2005). However, due to the severe shortening induced by the Maghrebian orogeny during Neogene times, the paleogeographic relationship of this platform with the adjacent deep-water basin is subjected to different interpretations (Catalano et al., 2001).

Even if the carbonate successions pertaining to the Upper Triassic/Lower Jurassic platform are well exposed in several areas of western Sicily, a continuous section encompassing the TJB is not easy to find due to a deep erosional truncation that affected mostly the marginal sector of the rimmed platform (e.g., Palermo and Madonie Mountais, Zarcone and Di Stefano, 2010) or to local effects of dolomitization that do not allow to assess reliable bio-chronostratigraphic evaluations.

Only in boreholes from the Hyblean foreland, clear Rhaetian beds have been recognized on the base of the presence of *Triasina hantkeni* (Patacca et al., 1979). More recently the presence of Rhaetian shallow water carbonates with *Triasina hantkeni* has been reported from the Sciacca area and Mt Sparagio (Cacciatore et al., 2010). However, a careful description of the TJB section at Mt Sparagio, was first performed by Todaro et al. (2017). In this light the Mt Sparagio section can be considered as unique in Sicily.

METHODS

The descriptions of the most common macro and microfacies was based on the classification of carbonate rocks of Dunham 1969) integrated by Embry and Klovan (1972). About 200 thin sections were analysed through a Leitz Laborlux 12 Pol optical microscope under transmitted light for the petrographic and biostratigraphic characterization of the microfacies. The biostratigraphic analysis of the Mt Sparagio section was based on the biozonal schemes adopted for the Upper Triassic-Lower Jurassic sections of Tethyan inner-carbonate platform realms (Gazdzicki, 1983; De Castro, 1990; Chiocchini et al., 1994; Barattolo and Romano, 2005; Mancinelli et al., 2005; Romano et al., 2008; Coskun Tunaboylu et al., 2014).

The stable isotopic analyses were obtained from 70 samples of micritic limestone exclusively collected in the subtidal facies. O and C analyses were performed at the Department of Geosciences of the University of Padova by using GasBench II connected to the continuous flow system of a DELTA V Advantage mass spectrometer (Thermo Scientific) while S isotope analyses were performed at the Cohen Geochemistry Laboratory using an Elementar PYRO cube coupled to an IsoPrime continuous flow mass spectrometer following the procedure described by He et al. (2020) (for detailed methodology see **Supplementary Materials**).

Several laboratory analyses were carried out in order to identify any diagenetic alteration of the collected samples, including possible dolomitization. SEM (FESEM-JEOL) analyses data, performed at the Department of Chemical Engineering of University of Palermo, allowed to calculate the wt% of Mg^{2+} (0.2–0.7) confirming the absence of dolomite in the bulk samples. Cathodoluminescence observations, carried out at the School of Earth, Atmospheric and Environmental Science of Manchester University by an Olympus CCL 8200 mk3 and elemental indicators (Mn/Sr, Mg/Ca) analysed by He et al. (2022) demonstrated a minor influence of dolomitization or diagenetic processes.

These data confirm the primary nature of the collected bulk samples, supporting the use of stable isotopic analyses (O, C, S) for the Mt Sparagio section (Todaro et al., 2018; He et al., 2020; He et al., 2022).

Strontium, lead and zinc isotope analyses were carried out at the Department of Earth Sciences (University of Geneva) by Thermo Neptune PLUS Multi-Collector ICP-MS in static mode following procedures described by Chiaradia et al. (2020) for Sr and Pb and by Chiaradia et al. (2018) for Zn (see **Supplementary Materials** for detailed description).

THE MT SPARAGIO SECTION

This section is exposed along the northern slope of an east-west trending ridge about 20 km long that is part of a major thrust sheet in the southern zone of the San Vito Peninsula. This ridge is a south-dipping ramp anticline that is crosscut by NW-SE and NE-SW oriented Plio-Quaternary extensional and strike-slip faults (Nigro and Renda, 2002). However, a clear continuous sector crops out in the western part of the ridge (Mt Cocuccio, 38°3′ 44.18″ N, 12°43′9.19″ E) about 5 km north-east from the village of Custonaci. The section consists of parallel beds, the thickness of which ranges from 50 to 150 cm, dipping south from 35 to 80°. The lower part of the section is dolomitized and covered

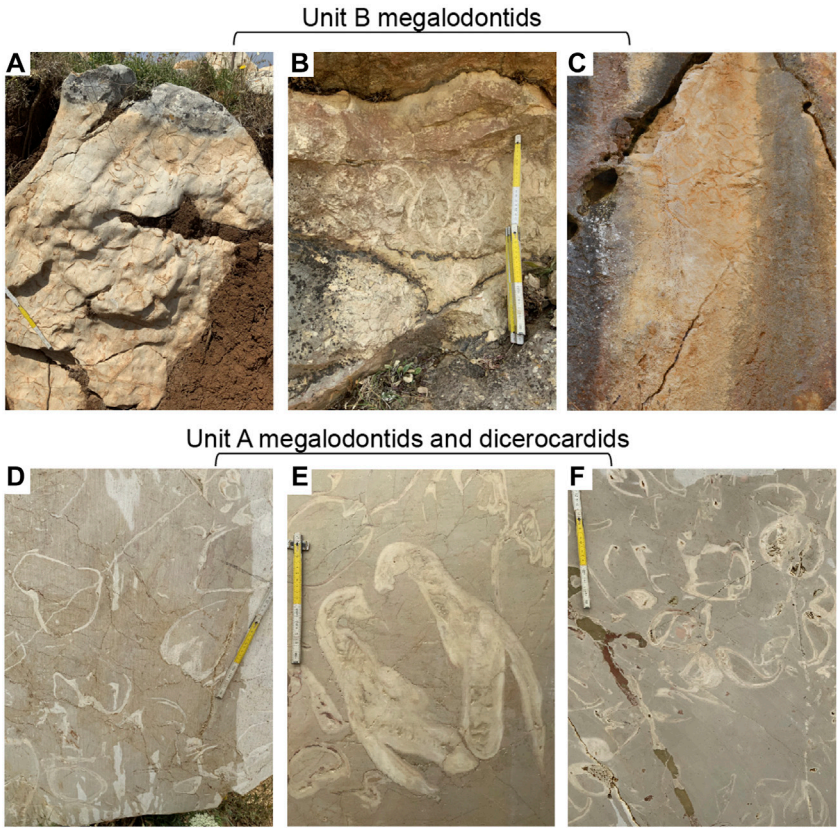

FIGURE 2 | Megalodontoids association in the Mt Sparagio section. **(A)**, **(B)** and **(C)** small megalodontids association in Unit B. **(D–F)** common presence of large megalodontids and dicerocardids shells in Unit A.

by eluvial-colluvial deposits and it is assumed to be Norian in age by the stratigraphic position. Upward, the studied section consists of 430 m thick, parallel-bedded, greyish to whitish limestones spanning the Rhaetian–Hettangian interval.

The macrofacies observations recognized peritidal carbonates formed by subtidal, intertidal and supratidal facies. Up to 13 facies-types were differentiated along the studied section (**Supplementary Table S1**). Most of the described facies are organized in shallowing-upward cycles (for a comprehensive description of facies-types and cycle stacking see Todaro et al., 2017).

On the basis of the palaeontological content in the subtidal facies, the Mt Sparagio section was divided into three informal units (**Figure 1**):

Unit A shows the common presence of large megalodontids and dicerocardids shells (**Figure 2D, E, F**), either in growth position or with disarticulated valves, in association with corals, benthic foraminifera and calcareous algae (**Figure 3A, B**). The estimated thickness of this unit is 111 m from the base of the measured section and it is well exposed along several quarries. The intertidal facies consists of stromatolite and loferite horizons that are capped by supratidal facies exhibiting black- and flat-pebble conglomerates and thick reddish-yellowish paleosoils.

Unit B shows a marked reduction in diversity and size of megalodontids whereas the dicerocardids disappear and only a few species of small megalodontids persist (**Figure 2A, B, C**). Despite this drastic biotic turnover, there are not significant variations in the benthic foraminifer assemblages and calcareous algae as observed in Unit A (**Figure 3C**). The top of Unit B is signed by an oolitic level intercalated in the subtidal facies (**Figure 3D**). Unit B reaches a thickness of 179 m. The intertidal-supratidal facies are similar to those of Unit A.

Unit C consists of shallowing-upward peritidal cycles lacking the typical fossil associations of Units A and B in the subtidal members. Only an oligotypic assemblage of encrusting algae characterizes the fossils content of the subtidal facies (**Figure 3F**). The stromatolitic facies are thicker than in the lower units representing two thirds of the total cycle thickness. Palaeosoils are thinner and less common and are represented by green-marly horizons. The total thickness of Unit C is 140 m. Between Unit B and Unit C a 10 m thick barren interval occurs consisting exclusively by calcitic spherules (up to 200 μm) (**Figure 3E**).

BIOSTRATIGRAPHY

The biostratigraphic record in the subtidal facies across all the studied section is very complete. Unit A and B, show the common

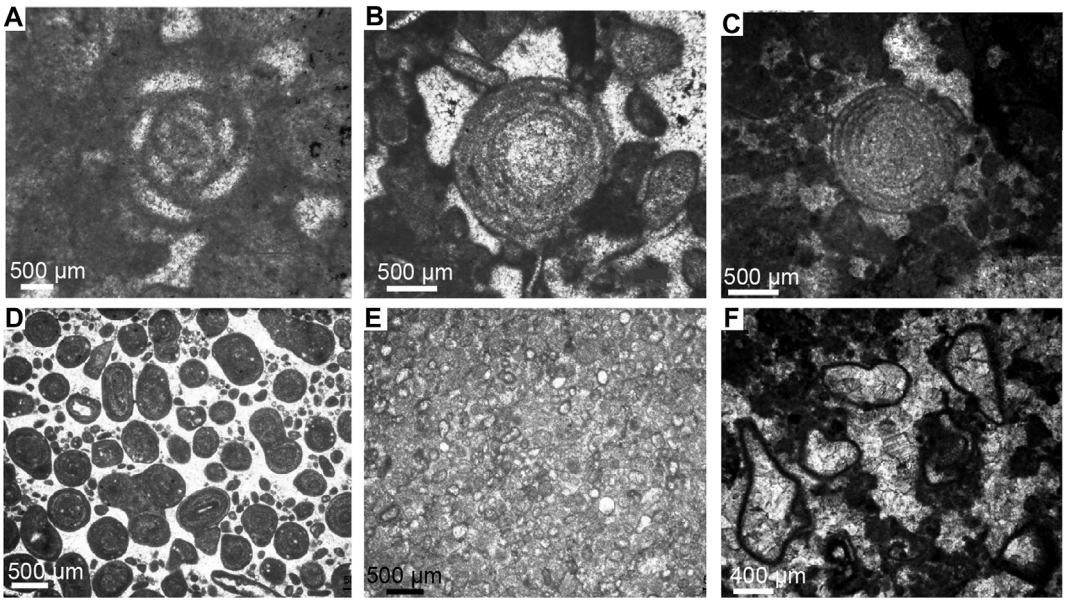

FIGURE 3 | Microfacies types in units A, B and C. **(A)** *Glomospirella* friedli in sp in Unit A; **(B)** grainstone with *Triasina hantkeni* belonging to Unit A; **(C)** grainstone with *Triasina hantkeni* of Unit B; **(D)** ooidal grainstone at the top of Unit B; **(E)** calcitic sphaerule belonging to the barren interval between Unit B and Unit C; **(F)** grainstone with *Thaumatoporella parvovesiculifera* belonging to Unit C.

presence of a benthic foraminifera association that comprises *Triasina hantkeni* (Majzon), *Auloconus permodiscoides* (Oberhauser), *Duotaxis birmanica* (Zaninetti & Bronnimann), *Tetrataxis inflata* (Kristan), *Aulotortus sinuosus* (Weynschenk), *Aulotuortus* sp., *Glomospira* sp., *Glomospirella* sp., *Trochammina* sp., *Frondicularia* sp., *Nodosaria*, sp. and *Textularia* sp. Nodular thalli of porostromata (*Cayeuxia* sp., *Orthonella* sp.) are concentrated in a few levels, whereas *Thaumatoporella parvovesiculifera* and fragments of dasycladales, such as *Griphoporella curvata*, are very rare (Todaro et al., 2017) (**Figure 3A, B, C**).

The occurrence of *Triasina hantkeni* with its large size test (up to 1 mm) allow to assign a Rhaetian age for Unit A and B (Gazdzicki, 1983; Di Bari and Rettori, 1996). The thickness of the *T. hantkeni* biozone (Unit A and B) is about 290 m, however, the base of this biozone could not be defined as the downward prosecution of the section is not exposed.

In Unit A, abundant and well preserved *Dicerocardium* spp. along with *Neomegalodon* spp. characterize the bivalve associations (**Figure 2D**). The size of the shells reaches giant dimensions up to 40 cm for dicerocardids (**Figure 2E**) and 25 cm for megalodontids (Todaro et al., 2017, 2018). Scleractinian corals carpets (*Retiophillia* sp.) also occur in this unit (Todaro et al., 2017).

In Unit B the scleractinian corals and the dicerocardids disappear and the bivalve community is represented only by small specimens of *Neomegalodon* and *Triadomegalodon* sp., the size of which does not exceed 10–15 cm (Todaro et al., 2018) (**Figure 2A, B, C**). The top of Unit B corresponds to the last occurrence (LO) of *T. hantkeni* and megalodontoids and to the presence of a discontinuous level up to 20 cm thick consisting of oolitic grainstone and interpreted as a storm layer (**Figure 3D**). A 10 m thick barren zone dominated by calcitic sphaerules (up to 200 µm in diameter) separates Unit B from Unit C (**Figure 3E**). In the subtidal facies of Unit C the fossil content consists almost exclusively by the encrusting alga *Thaumatoporella parvovesiculifera* associated with rare *Aeolisaccus dunningtoni* (**Figure 3F**). Upsection, the first benthic foraminifer *Siphovalvulina* sp. occurs about 10 m above the base of Unit C.

ISOTOPIC DATA

CAMP Influence (Sr, Zn, Pb)

The newly determined $^{87}Sr/^{86}Sr$ values of the Mt Sparagio section range between ~0.7075 and ~0.7087 (**Figure 4**), with the greatest majority of them overlapping the end-Triassic seawater composition ~0.70771-0.70776 (McArthur et al., 2001). Only six samples deviate significantly from the end-Triassic seawater composition (**Figure 4**). Two samples at the base of Unit B (Z15 and Z23) have less radiogenic Sr isotope compositions than seawater, overlapping with the compositional field of CAMP. The sample (Z18) that is stratigraphically comprised between these two samples shows an end-Triassic seawater Sr composition. In Unit C three samples have significantly more radiogenic $^{87}Sr/^{86}Sr$ values than end-Triassic seawater (TJ45, TJ48, TJ56), and are intercalated in the stratigraphic section by a sample (TJ54) with a $^{87}Sr/^{86}Sr$ value less radiogenic than end-Triassic seawater, shifted towards the CAMP isotope composition. The topmost sample of the investigated section (TJ58) is also slightly less radiogenic than end-Triassic seawater.

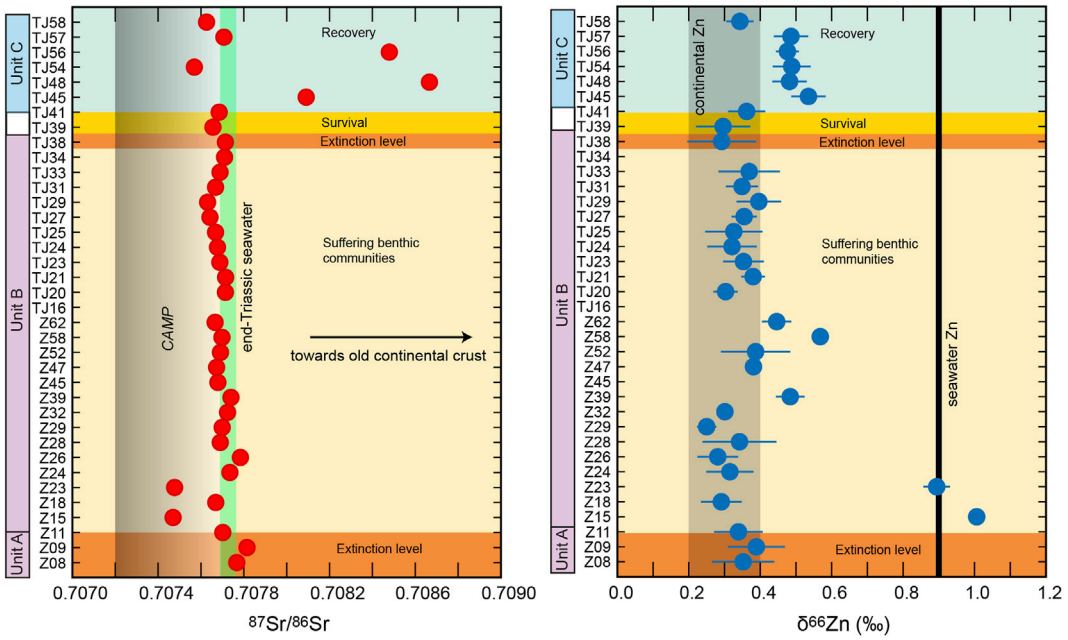

FIGURE 4 | $^{87}Sr/^{86}Sr$ values and $\delta^{66}Zn$ values of the Mt Sparagio section correlated to the three Units and to the extinction events (not in scale).

The $\delta^{66}Zn$ values of the Mt Sparagio section range between +0.25 and +1.00‰ (**Figure 4**). The greatest majority of them fall in the isotopic compositional range (~+0.3 to +0.4‰) of continental rocks and riverine input (Chen et al., 2013; Little et al., 2014). At the base of Unit B, two samples (Z15 and Z23) with CAMP-like Sr isotope compositions are characterized by $\delta^{66}Zn$ values between +0.9 and +1.0‰, similar to modern surface seawater (Maréchal et al., 2000; Little et al., 2014). Sample Z18, stratigraphically comprised between Z15 and Z23, which is characterized by an end-Triassic seawater Sr composition, has a continental Zn isotope signature. Therefore, the three samples in this part of the section show an anti-correlation between Sr and Zn isotope compositions. Three samples (Z39, Z58, Z62) in the middle part of the Unit B display erratic spikes marginally ($\delta^{66}Zn$ values of +0.45 and +0.48‰) to significantly heavier ($\delta^{66}Zn$ ~+0.58‰) than the dominant continental Zn recorded by the bulk of the section. The Unit C is characterized by a package of five stratigraphically sequential samples that show slightly but consistently higher $\delta^{66}Zn$ values (~+0.48 to +0.54‰) with respect to the continental Zn isotope range. This interval of the section corresponds to the samples that have either significantly more or slightly less radiogenic Sr than end-Triassic seawater. The topmost levels of Unit C returns to a continental Zn isotope signature.

Because of the very low concentrations of Pb in the investigated samples, only six of them returned reliable results (i.e., not affected by poor uncertainty and large uncontrolled instrumental mass fractionation due to low counting statistics). Two samples are those from the base of the section which returned CAMP-like Sr isotope compositions, two are from the middle part of the section with an end-Triassic seawater Sr isotope composition, and two are from the upper part of the section with a highly radiogenic Sr isotope composition (**Figure 5**). Initial isotope ratios of $^{206}Pb/^{204}Pb$, $^{207}Pb/^{204}Pb$ and $^{208}Pb/^{204}Pb$, corrected for time-integrated decay of U (and Th) at 200 Ma using U/Pb (and Th/Pb) ratios of Mesozoic Sicilian carbonates of comparable environment, are comprised between 18.27-23.21, 15.62-15.86, 38.15-38.82, respectively. The samples with CAMP-like Sr isotope compositions from the base of the section and those from the middle part of the section returned Pb isotope compositions consistent with CAMP (**Figure 5**). The samples from the upper part of the section, which have the most radiogenic $^{87}Sr/^{86}Sr$ values, have also the most radiogenic Pb isotope composition (outside CAMP), with high $^{207}Pb/^{204}Pb$ values that are indicative of derivation from relatively old continental rocks with high μ ($^{238}U/^{204}Pb$) values (**Figure 5**).

C,O and S

The new Sr and Zn isotope results are integrated with previously obtained C, O (Todaro et al., 2018) and S (He et al., 2020) isotope curves in **Figure 6**. The $\delta^{13}C_{carb}$ curve shows two main negative excursions separated by a positive peak with values ranging from -2.58‰ to 3.03‰ close to the base of the studied section (Todaro et al., 2018). The first negative trend shows a rapid decrease from ca. +1‰ to −2‰ at the top of Unit A followed by a return to more positive values up to +3‰. The second negative trend shows a decrease to more negative values of about −2.5‰ along the Unit B. After the second negative excursion, the carbon curve shows a gradual return to more positive values up to ca. +2.5‰ along Unit C (**Figure 6**).

The $\delta^{18}O_{carb}$ values were used to assess a possible climate change around the TJB (Todaro et al., 2018). At the top of Unit A,

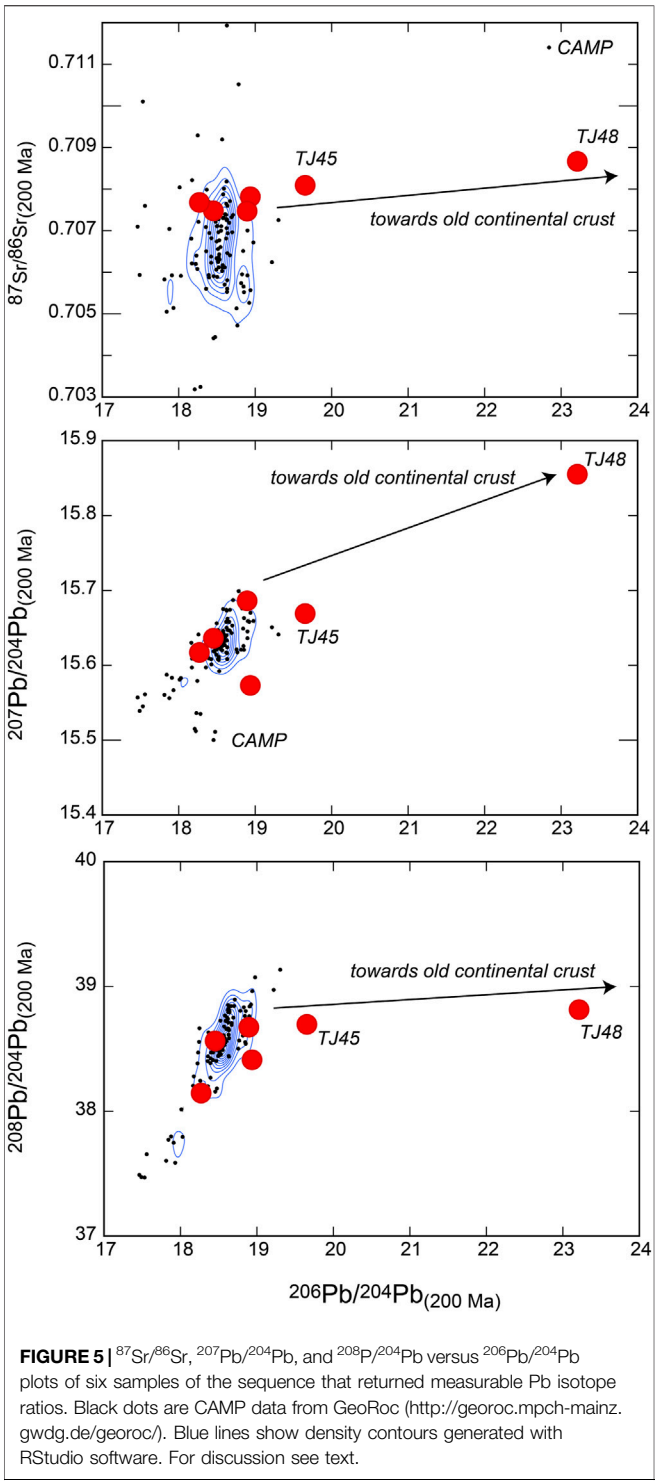

FIGURE 5 | $^{87}Sr/^{86}Sr$, $^{207}Pb/^{204}Pb$, and $^{208}P/^{204}Pb$ versus $^{206}Pb/^{204}Pb$ plots of six samples of the sequence that returned measurable Pb isotope ratios. Black dots are CAMP data from GeoRoc (http://georoc.mpch-mainz.gwdg.de/georoc/). Blue lines show density contours generated with RStudio software. For discussion see text.

the first warming trend (low $\delta^{18}O_{carb}$ values) is followed by a short cooling interval and then by a second more prolonged warming trend along the Unit B. A positive $\delta^{18}O_{carb}$ shift, at the TJB, crossing the interval between Unit B and Unit C, suggests instead the end of the warming phase (**Figure 6**).

The $\delta^{34}S_{CAS}$ curve shows a stable trend except for a large positive shift with a magnitude of >10‰ recorded at the top of Unit B (He et al., 2020) and coincident with the extinction of the Triassic benthic community (**Figure 6**).

DISCUSSION

The Mt Sparagio section offers at present the most complete record of the biostratigraphic and chemostratigraphic variations across the TJB in a continuous shallow water setting. Biostratigraphically, the Mt. Sparagio is easily comparable to other shallow water section described from the western Tethys, such as Croci di Acierno (Southern Apennines, De Castro 1990), Mt Messapion (Greece, Romano et al., 2008), Tahtaiskele (Karaburun Peninsula Turkey, Tunaboylu et al., 2014) and Mt Cefalo (Southern Apennines, Bachan et al., 2012), where similar extinction and recovery patterns of microfossil associations are described. As far as concern the macrofossil associations, in many of the Tethyan sections the presence of gigantic specimens of megalodontoids in the Rhaetian beds is reported by several authors (Végh-Neubrandt, 1982; Allasinaz, 1992, among others). The huge shell size reached by these pelecypods is attributed to the presence of photosymbionts (Végh-Neubrandt, 1982; De Freitas et al., 1993) as occurred in the Wallowaconchidae during the Upper Triassic of western North America (Yancey and Stanley, 1999), and their reduction in size has been attributed to the cessation of this symbiotic partnership (van de Schootbrugge and Wignall, 2016). At Mt Sparagio, the megalodontoids extinction trend shows two main pulses during the Rhaetian as high-diverse and giant species are confined to Unit A, while only few and small species are present in overlying Unit B, before the total extinction recorded in Unit C. The factors that controlled the reduction in biodiversity and size seem to have played a little role on the Rhaetian foraminifer association, except for the foraminifer *Triasina hantkeni* that recorded a diameter reduction between Unit A and B (Todaro et al., 2017).

The two extinction pulses recorded by the bivalve community are strictly correlated with the environmental perturbations documented as variation trends of the isotopic curves. In particular, the two pulses match well with the two $\delta^{13}C_{carb}$ negative excursions (**Figure 6**). The link between carbon isotope variations in the sedimentary record (Schobben et al., 2019) and mass extinction events (Raup and Sepkoski Jr, 1982) has typically been interpreted as caused by perturbations in the geological carbon cycle (Suarez et al., 2019) due to massive injection of isotopically light C, the ultimate effects of which would be global warming, oceanic acidification and a decrease of available carbonate in marine waters. Although the origin of this C is still debated (Suarez et al., 2019), there is now documented evidence (Wignall, 2001) for a likely role played by a surge of volcanic gas emissions during the emplacement of Large Igneous Provinces (LIP), including the CAMP that occurred right at the TJB (Hautmann et al., 2008; Greene et al., 2012; McRoberts et al., 2012; Al-Suwaidi et al., 2016). This interpretation of a LIP trigger has traditionally been hampered by the lack of sufficient information on the CO_2 abundance in these magmas (Black and Gibson, 2019). However, there is growing evidence that CAMP magmas may have been CO_2-rich (Capriolo et al.,

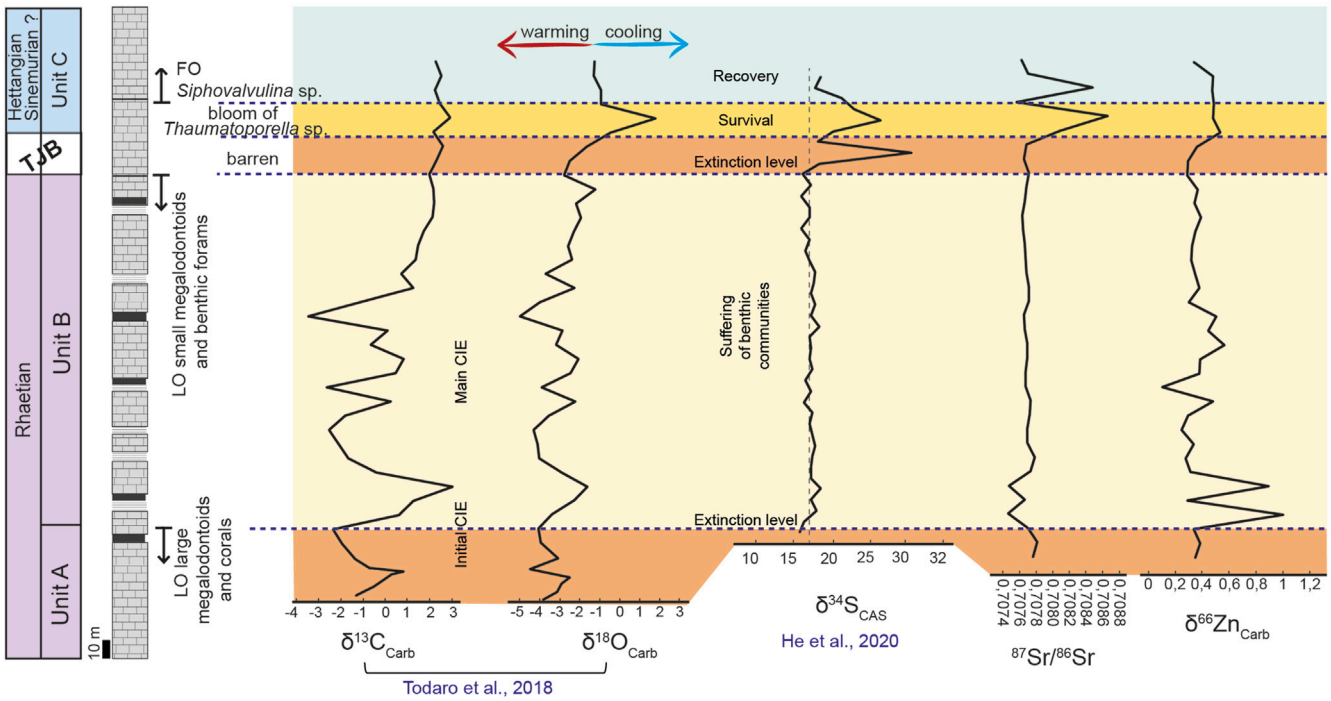

FIGURE 6 | Isotopic curves obtained in the Mt Sparagio section. The trends of the curves indicate environmental perturbations (acidification, climatic changes, marine anoxia, CAMP-influence) correlated with the two extinction pulses of the benthic community in the Rhaetian horizons. Black intervals represent the supratidal members of the peritidal cycles. The $\delta^{13}C_{carb}$ and $\delta^{18}O_{carb}$ are illustrated in Todaro et al. (2018), the $\delta^{34}S_{CAS}$ curve is after He et al. (2020).

2021), and modern volcano analogues (Aiuppa et al., 2021) indicate that magmas in rift and ocean island environments, can transport potentially large quantities of carbon to potentially trigger environmental change upon atmospheric injection if sourced deep in the upper mantle. In addition to perturbation of the carbon cycle, a temperature increase was also attributed to the CAMP activity (McElwain et al., 1999; Lindström et al., 2017). This is also well observable in the Mt Sparagio section by the trend of the $\delta^{18}O_{carb}$ curve (**Figure 6**). In particular, the biocalcification crisis characterized by a reduction of megalodontoids biodiversity seems strongly related to warmer temperatures recorded by low $\delta^{18}O_{carb}$ values while the end of this warming phase is marked by a positive $\delta^{18}O_{carb}$ shift and correlated to the extinction of the Rhaetian benthic community (Todaro et al., 2018). Warming and CO_2-induced ocean acidification are likely to have resulted eventually in oceanic anoxia, as fully supported by $\delta^{34}S_{CAS}$ curve (**Figure 6**). This exhibits a stable trend that is interrupted by a positive peak in correspondence of the extinction of Rhaetian benthic community, suggestive of the onset of anoxic conditions. The persistence of the positive trend throughout the barren interval suggests that anoxic conditions prevailed over the entire TJB interval (He et al., 2020).

Clues From Zn, Sr and Pb Isotopes

Zn isotopes are increasingly used to better understand processes related with mass extinctions and following biological recovery (Kunzmann et al., 2013; Liu et al., 2017). This opportunity is favoured by the Zn isotope compositions of seawater being significantly heavier than those of magmatic rocks and riverine input into oceans ($\delta^{66}Zn$ ~0.2–0.4‰: Chen et al., 2013; Little et al., 2014; **Figure 4**). The heavier Zn isotope composition of seawater is due to the preferential uptake of light Zn (^{64}Zn) by phytoplankton (using Zn as a micronutrient), resulting in a relative increase of the heavier Zn isotopes (e.g., ^{66}Zn) and therefore in higher $\delta^{66}Zn$ values in seawater (Marechal et al., 2000).

Similarly to Sr (Veizer, 1989), Zn in carbonates can derive either from dissolved Zn in seawater (from which carbonates chemically precipitate) or from continental Zn (if carbonates contain a detrital clay component) (Liu et al., 2017). The combined use of Sr and Zn isotopes in the same rock sample can therefore help better resolving seawater vs detrital origins for elements (**Figure 7**). Most of the samples in the investigated section show Sr isotope compositions consistent with that of end-Triassic seawater (**Figure 7**). This observation argues against a major detrital contribution from the continents, suggesting that the Zn isotope composition of the samples should also reflect the composition of seawater. However, the Zn isotopic signature of the largest part of the sequence is typical of riverine input and magmatic rocks, especially in the median-upper part of Unit B and in the barren interval (**Figures 4**, **6**), suggesting that the biological activity was strongly to completely suppressed in the greatest part of the investigated section. In fact, biological activity should drive the dissolved Zn introduced into seawater by riverine input magmatic activity with initial

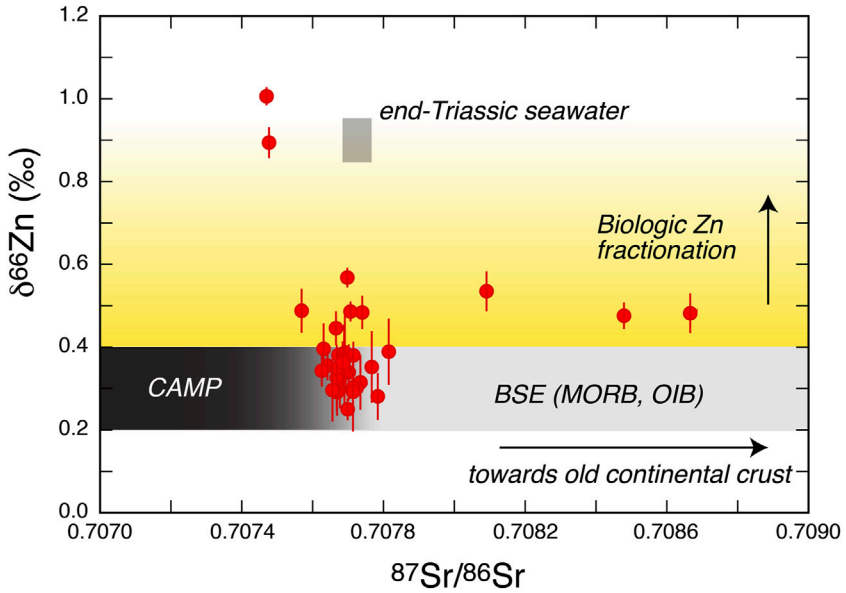

FIGURE 7 | Combined graph of Sr and Zn for the Mt Sparagio section used to resolve seawater vs detrital origins for elements. The end-Triassic (201–201.5 Ma) Sr seawater composition is from McArthur et al. (2001).

δ^{66}Zn ~0.2–0.4‰ to heavier isotope composition because of preferential uptake of light Zn by phytoplankton. Our data therefore support the use of Zn isotopes to track biological crises in the sedimentary record during pre- and syn-extinction levels, as also documented in the end-Permian mass extinction (Liu et al., 2017).

In contrast to this behaviour, at the base of Unit B (samples Z15 and Z23), Sr and Zn isotopes exhibit some peculiar signature (**Figures 4**, **6**). In this part of the section, the least radiogenic Sr isotope compositions are observed, and are associated with the most positive δ^{66}Zn compositions in our dataset (**Figures 4**, **6**, **7**). We stress that, as no petrographic evidence has been found for secondary/diagenetic processes, these Sr-Zn isotope signature must reflect sin-depositional processes. Moreover, the unusually low radiogenic ^{87}Sr/^{86}Sr signatures combined with Pb isotopes (**Figure 5**) overlap with the compositional field of CAMP volcanism. We thus propose that these isotopic compositions likely reflect a dominant and local input of "detrital" Sr derived from CAMP, either in the form of eroded particulate materials or volcanic fallout. The proximity of this CAMP-related Sr input is supported by the fact that seawater Sr isotope compositions are thought to be rapidly (within the timescales of the sedimentary record) homogenized throughout all oceans (Veizer, 1989). A local input also fits with the low Pb residence time in seawater.

The corresponding heavy (**Figure 7**) Zn isotope compositions (δ^{66}Zn of +0.9 and +1.0‰) are more puzzling to interpret. One possibility is that they reflect episodic and short events of increased biological activity, perhaps related to transient increased ocean productivity caused by micro-nutrient input during CAMP volcanism. Elevated volcanic nutrient supplies, perhaps related to oceanic deposition of volcanic ash (Jones and Gislason, 2008), have been recently suggested as drivers for the late Ordovician extinctions (Longman et al., 2021). However, this interpretation clashes with the evidence of detrital Sr at the base Unit B (samples Z15 and Z23). Since CAMP material contains several tens of ppm Zn, whereas seawater Zn concentrations are <1 ppb, it seems unlikely that the incorporation of "detrital" CAMP material (suggested by Sr isotopes) would have not resulted into a continental Zn isotopic signature (i.e., δ^{66}Zn +0.2–0.4‰) for these samples. A possible explanation is that there is a decoupling between Sr and Zn during the precipitation of carbonate rocks, in which the Zn would be more sensible to biological (rather than detrital) drivers. We finally note that the unusual composition of these two samples does not affect the general interpretation, discussed above, of the bulk sequence representing conditions of suppressed biological activity.

The top part of the sequence also shows some peculiar isotope compositions in Unit C, where an unusually radiogenic Sr (Figs., 4, 5, 6) and Pb (**Figure 5**) signature is observed. These compositions reveal a clear input of non-seawater, detrital Sr (and Pb) at the top of the sequence, with the radiogenic Sr and Pb signatures implying an old continental crustal source. We propose that this crustal contribution was derived from weathering of Variscan Calabrian-Peloritan Orogen (Fiannacca et al., 2019).

Interestingly, the samples belonging to Unit C exhibit a consistent Zn isotope signature that is slightly heavier than that of continental zinc (**Figures 6**, **7**), suggesting that the input from a more proximal continental crust basement was associated with the onset of a renewed biological activity and

consistent with the recovery phase of the Lower Jurassic carbonate factory.

CONCLUSION

The present study aimed to highlight a tight relationship between the environmental variations inferred by the isotopic records and the ETE pulses recorded by the Mt Sparagio section.

In the studied section, the isotope data of C, O, and S are indicative of serious environmental variations as recorded worldwide and related to the CAMP activity. The two negative excursions documented by the C-curve (Initial-CIE and Main-CIE) confirm the acidification processes that involved the benthic community. Moreover, the climate variations estimated from the oxygen isotopes indicate a warming-trend that corresponds to the reduction in biodiversity and size of the megalodontoids in the upper part of the Rhaetian beds. This warming trend could have deteriorated the photosymbiotic relationships of these pelecypods as inferred by several authors to explain their gigantism.

In the studied section, the total extinction of the Rhaetian benthic association is clearly related to a long-lasting carbon negative excursion (Main-CIE) coupled to a further warming trend.

Although the influence of CAMP on the ETE is well described in many TJB sections, the new isotope data (Zn, Pb, Sr) from Mt Sparagio section offer substantial documentation of a tight control of the Large Igneous Provinces on mass extinction events.

DATA AVAILABILITY STATEMENT

The original contributions presented in the study are included in the article/**Supplementary Material**, further inquiries can be directed to the corresponding author.

AUTHOR CONTRIBUTIONS

Field survey and data acquisition (ST; MR; PDS). Data interpretations (ST; MR; PDS; MC, AA). Writing- original draft (ST; MR; MC). Writing editing (ST; MR; PDS; MC; AA). Writing review (ST; MR; PDS; MC; AA). Illustrations (ST; MC).

FUNDING

This work was carried out with the financial support of the University of Palermo (2019_AIM_CTC_DISTEM_CI_1) by ST, (R4D14-P5F5RISS-MARGINE) by PDS and University of Padova (DOR1978195/19) by MR. AA acknowledges funding from the Italian Ministero Istruzione Università e Ricerca (Miur, Grant No. 2017LMNLAW).

SUPPLEMENTARY MATERIAL

The Supplementary Material for this article can be found online at: https://www.frontiersin.org/articles/10.3389/feart.2022.875466/full#supplementary-material

Supplementary Table S1 | Facies types and environmental interpretation described in the Mt Sparagio section (modified after Todaro et al., 2017).

REFERENCES

Abate, B., Di Maggio, C., Incandela, A., and Renda, P. (1991). Nuovi dati sulla geologia della Penisola di Capo San Vito (Sicilia nord-occidentale). *Mem. Della Soc. Geol. Ital.* 47, 15–25.

Aiuppa, A., Casetta, F., Coltorti, M., Stagno, V., and Tamburello, G. (2021). Carbon Concentration Increases with Depth of Melting in Earth's Upper Mantle. *Nat. Geosci.* 14, 697–703. doi:10.1038/s41561-021-00797-y

Al-Suwaidi, A. H., Steuber, T., and Suarez, M. B. (2016). The Triassic-Jurassic Boundary Event from an Equatorial Carbonate Platform (Ghalilah Formation, United Arab Emirates). *J. Geol. Soc.* 173, 949–953. doi:10.1144/jgs2015-102

Allasinaz, A. (1992). The Late Triassic-Hettangian Bivalves Turnover in Lombardy (Southern Alps) Verlag Nicht Ermittelbar. *Riv. It. Paleont. Strat.* 97, 431–454.

Antonelli, M., Franciosi, R., Pezzi, G., Querci, A., Ronco, G. P., and Vezzani, F. (1988). Paleogeographic Evolution and Structural Setting of the Northern Side of the Sicily Channel. *Mem. Della Soc. Geol. Ital.* 41, 141–157. doi:10.1016/0304-3800(88)90029-4

Bachan, A., Van De Schootbrugge, B., Fiebig, J., McRoberts, C. A., Ciarapica, G., and Payne, J. L. (2012). Carbon Cycle Dynamics Following the End-Triassic Mass Extinction: Constraints from pairedδ13Ccarbandδ13Corgrecords. *Geochem. Geophys. Geosyst.* 13, 415. doi:10.1029/2012GC004150

Barattolo, F., and Romano, R. (2005). Shallow Carbonate Platform Bioevents during the Upper Triassic-Lower Jurassic: an Evolutive Interpretation. *Boll. Della Soc. Geol. Ital.* 124, 123–142.

Beerling, D. J., and Berner, R. A. (2002). Biogeochemical Constraints on the Triassic-Jurassic Boundary Carbon Cycle Event. *Glob. Biogeochem. Cycles* 16, 10–13. doi:10.1029/2001GB001637

Black, B. A., and Gibson, S. A. (2019). Deep Carbon and the Life Cycle of Large Igneous Provinces. *Elements* 15, 319–324. doi:10.2138/gselements.15.5.319

Blackburn, T. J., Olsen, P. E., Bowring, S. A., McLean, N. M., Kent, D. V., Puffer, J., et al. (2013). Zircon U-Pb Geochronology Links the End-Triassic Extinction with the Central Atlantic Magmatic Province. *Science* 340, 941–945. doi:10.1126/science.1234204

Cacciatore, M. S., Todaro, S., Zarcone, G., and Di Stefano, P. (2010). Triasina Hantkeni Limestones from Western SicilyNew Developments on Triassic Integrated Stratigraphy. *Albertiana* 39, 87.

Callegaro, S., Rapaille, C., Marzoli, A., Bertrand, H., Chiaradia, M., Reisberg, L., et al. (2014). Enriched Mantle Source for the Central Atlantic Magmatic Province: New Supporting Evidence from Southwestern Europe. *Lithos* 188, 15–32. doi:10.1016/j.lithos.2013.10.021

Capriolo, M., Mills, B. J. W., Newton, R. J., Dal Corso, J., Dunhill, A. M., Wignall, P. B., et al. (202210373). Anthropogenic-scale CO2 Degassing from the Central Atlantic Magmatic Province as a Driver of the End-Triassic Mass Extinction. *Glob. Planet. Change* 209, 103731. doi:10.1016/j.gloplacha.2021.103731

Catalano, R., Doglioni, C., and Merlini, S. (2001). On the Mesozoic Ionian basin. *Geophys. J. Int.* 144, 49–64. doi:10.1046/j.0956-540x.2000.01287.x

Chen, H., Savage, P. S., Teng, F.-Z., Helz, R. T., and Moynier, F. (2013). Zinc Isotope Fractionation during Magmatic Differentiation and the Isotopic Composition of the Bulk Earth. *Earth Planet. Sci. Lett.* 369-370, 34–42. doi:10.1016/j.epsl.2013.02.037

Chiaradia, M., Müntener, O., and Beate, B. (2020). Effects of Aseismic ridge Subduction on the Geochemistry of Frontal Arc Magmas. *Earth Planet. Sci. Lett.* 531, 115984. doi:10.1016/j.epsl.2019.115984

Chiaradia, M., Pujol-Solà, N., Farré-de-Pablo, J., Aiuppa, A., Paonita, A., Rizzo, A. L., et al. (2018). Geochemistry and Isotope Composition (Sr, Pb, δ66Zn) of

Vulcano Fumaroles (Aeolian Islands, Italy). *Chem. Geology.* 493, 153–171. doi:10.1016/j.chemgeo.2018.05.038

Chiocchini, M., Farinacci, A., Mancinelli, A., Molinari, V., and Potetti, M. (1994). Biostratigrafia a foraminiferi, dasicladali e calpionelle delle successioni carbonatiche mesozoiche dell'Appennino centrale (Italia). *Biostratigrafia dell'Italia Centrale.* 9–129. doi:10.15165/studgeocam-1128

Ciarapica, G. (2007). Regional and Global Changes Around the Triassic-Jurassic Boundary Reflected in the Late Norian-Hettangian History of the Apennine Basins. *Palaeogeogr. Palaeoclimatol. Palaeoecol.* 244, 34–51. doi:10.1016/j.palaeo.2006.06.022

Coskun Tunaboylu, B., Altiner, D., İsintek, İ., and Demirci, D. (2014). Foraminiferal Biostratigraphy and Sequence Stratigraphy of Peritidal Carbonates at the Triassic-Jurassic Boundary (Karaburun Peninsula, Western Turkey). *J. Asian Earth Sci.* 90, 61–76. doi:10.1016/j.jseaes.2014.04.015

Davies, J. H. F. L., Marzoli, A., Bertrand, H., Youbi, N., Ernesto, M., and Schaltegger, U. (2017). End-Triassic Mass Extinction Started by Intrusive CAMP Activity. *Nat. Commun.* 8, 1–8. doi:10.1038/ncomms15596

De Castro, P. (1990). Studies on the Triassic Carbonates of the Salerno Province (Southern Italy): the Croci d'Acerno Sequence. *Boll. Della Soc. Geol. Ital.* 109, 187–217.

De Freitas, T. A., Brunton, F., and Bernecker, T. (1993). Silurian Megalodont Bivalves of the Canadian Arctic and Australia: Paleoecology and Evolutionary Significance. *Palaios* 8, 450–464. doi:10.2307/3515019

Deenen, M. H. L., Ruhl, M., Bonis, N. R., Krijgsman, W., Kuerschner, W. M., Reitsma, M., et al. (2010). A New Chronology for the End-Triassic Mass Extinction. *Earth Planet. Sci. Lett.* 291, 113–125. doi:10.1016/j.epsl.2010.01.003

Di Bari, D., and Rettori, R. (1996). Morphological Features of Triasina Hantkeni Majzon, 1954 (Foraminiferida, Aulotortidae) and Remarks on the Test wall Structure. *Revue de Micropaléontologie* 39, 305–313. doi:10.1016/S0035-1598(96)90146-4

Di Stefano, P., Favara, R., Luzio, D., Renda, P., Cacciatore, M. S., Calò, M., et al. (2015). A Regional-Scale Discontinuity in Western Sicily Revealed by a Multidisciplinary Approach: A New Piece for Understanding the Geodynamic Puzzle of the Southern Mediterranean. *Tectonics* 34, 2067–2085. doi:10.1002/2014TC003759

Fiannacca, P., Williams, I. S., Cirrincione, R., and Pezzino, A. (2019). Poly-orogenic Melting of Metasedimentary Crust from a Granite Geochemistry and Inherited Zircon Perspective (Southern Calabria-Peloritani Orogen, Italy). *Front. Earth Sci.* 7, 119. doi:10.3389/feart.2019.00119

Finetti, I. R., Del Ben, A., Fais, S., Forlin, E., Klingelé, E., Lecca, L., et al. (2005). "Crustal Tectono-Stratigraphic Setting of the Pelagian Foreland from the New CROP Seismic Data," in *CROP Project - Deep Seismic Explanation of the Central Mediterranean and Italy*, 413–446.

Galli, M. T., Jadoul, F., Bernasconi, S. M., Cirilli, S., and Weissert, H. (2007). Stratigraphy and Palaeoenvironmental Analysis of the Triassic-Jurassic Transition in the Western Southern Alps (Northern Italy). *Palaeogeogr. Palaeoclimatol. Palaeoecol.* 244, 52–70. doi:10.1016/j.palaeo.2006.06.023

Gazdzicki, A. (1983). Foraminifers and Biostratigraphy of Upper Triassic and Lower Jurassic of the Slovakian and Polish Carpathians. *Palaeontol. Pol.* 44, 109–169.

Giunta, G., and Liguori, V. (1972). La Geologia Dell'estremità Nord-Occidentale Della Sicilia. *Riv. Min. Sic.* 23 , 136–138, 165–226.

Greene, S. E., Martindale, R. C., Ritterbush, K. A., Bottjer, D. J., Corsetti, F. A., and Berelson, W. M. (2012). Recognising Ocean Acidification in Deep Time: An Evaluation of the Evidence for Acidification across the Triassic-Jurassic Boundary. *Earth-Science Rev.* 113, 72–93. doi:10.1016/j.earscirev.2012.03.009

Guex, J., Bartolini, A., Atudorei, V., and Taylor, D. (2004). High-resolution Ammonite and Carbon Isotope Stratigraphy across the Triassic-Jurassic Boundary at New York Canyon (Nevada). *Earth Planet. Sci. Lett.* 225, 29–41. doi:10.1016/j.epsl.2004.06.006

Hallam, A. (1997). Estimates of the Amount and Rate of Sea-Level Change across the Rhaetian-Hettangian and Pliensbachian-Toarcian Boundaries (Latest Triassic to Early Jurassic). *J. Geol. Soc.* 154, 773–779. doi:10.1144/gsjgs.154.5.077310.1144/gsjgs.154.5.0773

Hautmann, M., Benton, M. J., and Tomašových, A. (2008). Catastrophic Ocean Acidification at the Triassic-Jurassic Boundary. *njgpa* 249, 119–127. doi:10.1127/0077-7749/2008/0249-0119

He, T., Dal Corso, J., Newton, R. J., Wignall, P. B., Mills, B. J. W., Todaro, S., et al. (2020). An Enormous Sulfur Isotope Excursion Indicates marine Anoxia during the End-Triassic Mass Extinction. *Sci. Adv.* 6, eabb6704. doi:10.1126/sciadv.abb6704

He, T., Newton, R. J., Wignall, P. B., Reid, S., Dal Corso, J., Takahashi, S., et al. (2022). Shallow Ocean Oxygen Decline during the End-Triassic Mass Extinction. *Glob. Planet. Change* 210, 103770. doi:10.1016/j.gloplacha.2022.103770

Hesselbo, S. P., Robinson, S. A., Surlyk, F., and Piasecki, S. (2002). Terrestrial and marine Extinction at the Triassic-Jurassic Boundary Synchronized with Major Carbon-Cycle Perturbation: A Link to Initiation of Massive Volcanism? *Geol* 30, 251–254. doi:10.1130/0091-7613(2002)030<0251:tameat>2.0.co;2

Huynh, T. T., and Poulsen, C. J. (2005). Rising Atmospheric CO2 as a Possible Trigger for the End-Triassic Mass Extinction. *Palaeogeogr. Palaeoclimatol. Palaeoecol.* 217, 223–242. doi:10.1016/j.palaeo.2004.12.004

Jones, M. T., and Gislason, S. R. (2008). Rapid Releases of Metal Salts and Nutrients Following the Deposition of Volcanic Ash into Aqueous Environments. *Geochimica et Cosmochimica Acta* 72, 3661–3680. doi:10.1016/j.gca.2008.05.030

Jost, A. B., Bachan, A., van De Schootbrugge, B., Lau, K. V., Weaver, K. L., Maher, K., et al. (2017). Uranium Isotope Evidence for an Expansion of marine Anoxia during the End- T Riassic Extinction. *Geochem. Geophys. Geosyst.* 18, 3093–3108. doi:10.1002/2017GC006941

Kamoun, F., Peybernès, B., Ciszak, R., and Calzada, S. (2001). Triassic Palaeogeography of Tunisia. *Palaeogeogr. Palaeoclimatol. Palaeoecol.* 172, 223–242. doi:10.1016/S0031-0182(01)00283-8

Kiessling, W., Aberhan, M., Brenneis, B., and Wagner, P. J. (2007). Extinction Trajectories of Benthic Organisms across the Triassic-Jurassic Boundary. *Palaeogeogr. Palaeoclimatol. Palaeoecol.* 244, 201–222. doi:10.1016/j.palaeo.2006.06.029

Kunzmann, M., Halverson, G. P., Sossi, P. A., Raub, T. D., Payne, J. L., and Kirby, J. (2013). Zn Isotope Evidence for Immediate Resumption of Primary Productivity after Snowball Earth. *Geology* 41, 27–30. doi:10.1130/G33422.1

Larina, E., Bottjer, D. J., Corsetti, F. A., Thibodeau, A. M., Berelson, W. M., West, A. J., et al. (2021). Ecosystem Change and Carbon Cycle Perturbation Preceded the End-Triassic Mass Extinction. *Earth Planet. Sci. Lett.* 576, 117180. doi:10.1016/j.epsl.2021.117180

Lindström, S. (2016). Palynofloral Patterns of Terrestrial Ecosystem Change during the End-Triassic Event - A Review. *Geol. Mag.* 153, 223–251. doi:10.1017/S0016756815000552

Lindström, S. (2021). Two-phased Mass Rarity and Extinction in Land Plants during the End-Triassic Climate Crisis. *Front. Earth Sci.* 9, 343. doi:10.3389/feart.2021.780343

Lindström, S., van de Schootbrugge, B., Hansen, K. H., Pedersen, G. K., Alsen, P., Thibault, N., et al. (2017). A New Correlation of Triassic-Jurassic Boundary Successions in NW Europe, Nevada and Peru, and the Central Atlantic Magmatic Province: A Time-Line for the End-Triassic Mass Extinction. *Palaeogeogr. Palaeoclimatol. Palaeoecol.* 478, 80–102. doi:10.1016/j.palaeo.2016.12.025

Little, S. H., Vance, D., Walker-Brown, C., and Landing, W. M. (2014). The Oceanic Mass Balance of Copper and Zinc Isotopes, Investigated by Analysis of Their Inputs, and Outputs to Ferromanganese Oxide Sediments. *Geochimica et Cosmochimica Acta* 125, 673–693. doi:10.1016/j.gca.2013.07.046

Liu, S.-A., Wu, H., Shen, S.-z., Jiang, G., Zhang, S., Lv, Y., et al. (2017). Zinc Isotope Evidence for Intensive Magmatism Immediately before the End-Permian Mass Extinction. *Geology* 45, 343–346. doi:10.1130/G38644.1

Lo Cicero, G. (1986). Carbon and Oxygen Isotopic Composition of Norian Sediments. Panormide Carbonate Platform, Palermo. *Rend. Soc. Geol. It.* 9, 209–218.

Longman, J., Mills, B. J. W., Manners, H. R., Gernon, T. M., and Palmer, M. R. (2021). Late Ordovician Climate Change and Extinctions Driven by Elevated Volcanic Nutrient Supply. *Nat. Geosci.* 14, 924–929. doi:10.1038/s41561-021-00855-5

Luo, G., Richoz, S., van de Schootbrugge, B., Algeo, T. J., Xie, S., Ono, S., et al. (2018). Multiple Sulfur-Isotopic Evidence for a Shallowly Stratified Ocean Following the Triassic-Jurassic Boundary Mass Extinction. *Geochimica et Cosmochimica Acta* 231, 73–87. doi:10.1016/j.gca.2018.04.015

Mancinelli, A., Chiocchini, M., Chiocchini, R. A., and Romano, A. (2005). Biostratigraphy of Upper Triassic-Lower Jurassic Carbonate Platform Sediments of the central-southern Apennines (Italy). *Riv. Ital. di Paleontol. e Stratigr.* 111, 314. doi:10.13130/2039-4942/6314

Maréchal, C. N., Nicolas, E., Douchet, C., and Albarède, F. (2000). Abundance of Zinc Isotopes as a marine Biogeochemical Tracer. *Geochem. Geophys. Geosyst.* 1, 29. doi:10.1029/1999GC000029

Martini, R., Cirilli, S., Saurer, C., Abate, B., Ferruzza, G., and Lo Cicero, G. (2007). Depositional Environment and Biofacies Characterisation of the Triassic (Carnian to Rhaetian) Carbonate Succession of Punta Bassano (Marettimo Island, Sicily). *Facies* 53, 389–400. doi:10.1007/s10347-007-0115-3

Marzoli, A., Bertrand, H., Knight, K. B., Cirilli, S., Buratti, N., Vérati, C., et al. (2004). Synchrony of the Central Atlantic Magmatic Province and the Triassic-Jurassic Boundary Climatic and Biotic Crisis. *Geol* 32, 973–976. doi:10.1130/G20652.1

Marzoli, A., Renne, P. R., Piccirillo, E. M., Ernesto, M., Bellieni, G., and Min, A. D. (1999). Extensive 200-Million-Year-Old continental Flood Basalts of the Central Atlantic Magmatic Province. *Science* 284, 616–618. doi:10.1126/science.284.5414.616

McArthur, J. M., Howarth, R. J., and Bailey, T. R. (2001). Strontium Isotope Stratigraphy: LOWESS Version 3: Best Fit to the Marine Sr-Isotope Curve for 0-509 Ma and Accompanying Look-up Table for Deriving Numerical Age. *J. Geology.* 109, 155–170. doi:10.1086/319243

McElwain, J. C., Beerling, D. J., and Woodward, F. I. (1999). Fossil Plants and Global Warming at the Triassic-Jurassic Boundary. *Science* 285, 1386–1390. doi:10.1126/science.285.5432.1386

McRoberts, C. A., Krystyn, L., and Hautmann, M. (2012). Macrofaunal Response to the End-Triassic Mass Extinction in the West-Tethyan Kossen Basin, Austria. *Palaios* 27, 607–616. doi:10.2110/palo.2012.p12-043r

Nigro, F., and Renda, P. (2002). From Mesozoic Extension to Tertiary Collision: Deformation Patterns in the Units of the North-Western Sicilian Chain. *Bolletino Della Soc. Geol. Ital.* 121, 87–97.

Patacca, E., Scandone, P., Giunta, G., and Liguori, V. (1979). Mesozoic Paleo-Tectonic Evolution of the Ragusa Zone (southeastern Sicily). *Geol. Rom.* 18, 331–369.

Randazzo, V., Di Stefano, P., Todaro, S., and Cacciatore, M. S. (2020a). A Cretaceous Carbonate Escarpment from Western Sicily (Italy): Biostratigraphy and Tectono-Sedimentary Evolution. *Cretaceous Res.* 110, 104423. doi:10.1016/j.cretres.2020.104423

Randazzo, V., Le Goff, J., Di Stefano, P., Reijmer, J., Todaro, S., and Cacciatore, M. S. (2020b). Carbonate Slope Re-sedimentation in a Tectonically-active Setting (Western Sicily Cretaceous Escarpment, Italy). *Sedimentology* 67, 2360–2391. doi:10.1111/sed.12705

Raup, D. M., and Sepkoski, J. J., Jr (1982). Mass Extinctions in the marine Fossil Record. *Science* 215, 1501–1503. doi:10.1126/science.215.4539.1501

Romano, R., Masett, D., Carras, N., Barattolo, F., and Roghi, G. (2008). The Triassic/Jurassic Boundary in a Peritidal Carbonate Platform of the Pelagonian Domain: The Mount Messapion Section (Chalkida, Greece). *Riv. Ital. di Paleontol. e Stratigr.* 114, 431–452. doi:10.13130/2039-4942/5910

Ruhl, M., Bonis, N. R., Reichart, G.-J., Damsté, J. S. S., and Kürschner, W. M. (2011). Atmospheric Carbon Injection Linked to End-Triassic Mass Extinction. *Science* 333, 430–434. doi:10.1126/science.1204255

Ruhl, M., Kürschner, W. M., and Krystyn, L. (2009). Triassic-Jurassic Organic Carbon Isotope Stratigraphy of Key Sections in the Western Tethys Realm (Austria). *Earth Planet. Sci. Lett.* 281, 169–187. doi:10.1016/j.epsl.2009.02.020

Ruhl, M., and Kürschner, W. M. (2011). Multiple Phases of Carbon Cycle Disturbance from Large Igneous Province Formation at the Triassic-Jurassic Transition. *Geology* 39, 431–434. doi:10.1130/G31680.1

Schaller, M. F., Wright, J. D., and Kent, D. V. (2011). Atmospheric P Co 2 Perturbations Associated with the Central Atlantic Magmatic Province. *Science* 331, 1404–1409. doi:10.1126/science.1199011

Schobben, M., Van De Schootbrugge, B., and Wignall, P. B. (2019). Interpreting the Carbon Isotope Record of Mass Extinctions. *Elem. Int. Mag. Mineral. Geochemistry, Petrol.* 15, 331–337. doi:10.2138/gselements.15.5.331

Senowbari Daryan, B., Di Stefano, P., and Abate, B. (2015). Hypercalcified Sponges from the Upper Triassic (Norian-Rhaetian) Reefs of Sicily. *Quaderni Del. Museo Geologici G.G. Gemmellaro* 10, 1–300.

Sepkoski, J. J., Jr (1994). Extinction and the Fossil Record. *Geotimes* 39, 15–17.

Song, H., Kemp, D. B., Tian, L., Chu, D., Song, H., and Dai, X. (2021). Thresholds of Temperature Change for Mass Extinctions. *Nat. Commun.* 12, 4694. doi:10.1038/s41467-021-25019-2

Suarez, C. A., Edmonds, M., and Jones, A. P. (2019). Earth Catastrophes and Their Impact on the Carbon Cycle. *Elem. Int. Mag. Mineral. Geochemistry, Petrol.* 15, 301–306. doi:10.2138/gselements.15.5.301

Todaro, S., Agosta, F., Parrino, N., Cavalcante, F., Di Stefano, P., Giarrusso, R., et al. (2022). Fracture Stratigraphy and Oil First Migration in Triassic Shales, Favignana Island, Western Sicily, Italy. *Mar. Pet. Geology.* 135, 105400. doi:10.1016/j.marpetgeo.2021.105400

Todaro, S., Di Stefano, P., Zarcone, G., and Randazzo, V. (2017). Facies Stacking and Extinctions across the Triassic-Jurassic Boundary in a Peritidal Succession from Western Sicily. *Facies* 63, 20. doi:10.1007/s10347-017-0500-5

Todaro, S., Rigo, M., Randazzo, V., and Di Stefano, P. (2018). The End-Triassic Mass Extinction: A New Correlation between Extinction Events and δ13C Fluctuations from a Triassic-Jurassic Peritidal Succession in Western Sicily. *Sediment. Geology.* 368, 105–113. doi:10.1016/j.sedgeo.2018.03.008

Todaro, S., Sulli, A., Spatola, D., Micallef, A., Di Stefano, P., and Basilone, G. (2021). Depositional Mechanism of the Upper Pliocene-Pleistocene Shelf-Slope System of the Western Malta Plateau (Sicily Channel). *Sediment. Geology.* 417, 105882. doi:10.1016/j.sedgeo.2021.105882

Van De Schootbrugge, B., Payne, J. L., Tomasovych, A., Pross, J., Fiebig, J., Benbrahim, M., et al. (2008). Carbon Cycle Perturbation and Stabilization in the Wake of the Triassic-Jurassic Boundary Mass-Extinction Event. *Geochem. Geophys. Geosyst.* 9, a–n. doi:10.1029/2007GC001914

van de Schootbrugge, B., and Wignall, P. B. (2016). A Tale of Two Extinctions: Converging End-Permian and End-Triassic Scenarios. *Geol. Mag.* 153, 332–354. doi:10.1017/S0016756815000643

Végh-Neubrandt, E. (1982). *Triassische Megalodontaceae*: Entwicklung, Stratigraphie und Paläontologie. Budapest: Akadémiai kiadó, 1–526.

Veizer, J. (1989). Strontium Isotopes in Seawater through Time. *Annu. Rev. Earth Planet. Sci.* 17, 141–167. doi:10.1146/annurev.ea.17.050189.001041

Wignall, P. B., and Atkinson, J. W. (2020). A Two-phase End-Triassic Mass Extinction. *Earth-Science Rev.* 208, 103282. doi:10.1016/j.earscirev.2020.103282

Wignall, P. B. (2001). Large Igneous Provinces and Mass Extinctions. *Earth-Science Rev.* 53, 1–33. doi:10.1016/S0012-8252(00)00037-4

Wignall, P. B., Zonneveld, J.-P., Newton, R. J., Amor, K., Sephton, M. A., and Hartley, S. (2007). The End Triassic Mass Extinction Record of Williston Lake, British Columbia. *Palaeogeogr. Palaeoclimatol. Palaeoecol.* 253, 385–406. doi:10.1016/j.palaeo.2007.06.020

Yancey, T. E., and Stanley, Jr, G. D. (1999). Giant Alatoform Bivalves in the Upper Triassic of Western North America. *Palaeontology* 42, 1–23. doi:10.1111/1475-4983.00060

Zaffani, M., Jadoul, F., and Rigo, M. (2018). A New Rhaetian δ13Corg Record: Carbon Cycle Disturbances, Volcanism, End-Triassic Mass Extinction (ETE). *Earth-Science Rev.* 178, 92–104. doi:10.1016/j.earscirev.2018.01.004

Zarcone, G., and Di Stefano, P. (2010). La Piattaforma Carbonatica Panormide:un caso anomalo nell'evoluzione dei bacini della Tetide giurassica. *Ital. J. Geosci.* 129, 188–194. doi:10.3301/IJG.2010.01

Zarcone, G., Petti, F. M., Cillari, A., Di Stefano, P., Guzzetta, D., and Nicosia, U. (2010). A Possible Bridge between Adria and Africa: New Palaeobiogeographic and Stratigraphic Constraints on the Mesozoic Palaeogeography of the Central Mediterranean Area. *Earth-Science Rev.* 103, 154–162. doi:10.1016/j.earscirev.2010.09.005

Conflict of Interest: The authors declare that the research was conducted in the absence of any commercial or financial relationships that could be construed as a potential conflict of interest.

Publisher's Note: All claims expressed in this article are solely those of the authors and do not necessarily represent those of their affiliated organizations, or those of the publisher, the editors, and the reviewers. Any product that may be evaluated in this article, or claim that may be made by its manufacturer, is not guaranteed or endorsed by the publisher.

frontiers | Frontiers in Earth Science

ORIGINAL RESEARCH
published: 02 June 2022
doi: 10.3389/feart.2022.899562

So Volcanoes Created the Dinosaurs? A Quantitative Characterization of the Early Evolution of Terrestrial Pan-Aves

Max Cardoso Langer[1]*† *and Pedro L. Godoy*[1,2,3]†

[1]*Department of Biology, Universidade de São Paulo, Ribeirão Preto, Brazil,* [2]*Department of Anatomical Sciences, Stony Brook University, New York, NY, United States,* [3]*Department of Zoology, Universidade Federal do Paraná, Curitiba, Brazil*

The early Mesozoic is marked by several global-scale environmental events, including the emplacement of large igneous provinces, such as the Siberian Traps, Wrangellia, and Central Atlantic Magmatic Province (CAMP). These have been hypothesised as drivers of the successful diversification of Pan-Aves, the lineage of archosaurs closer to birds than to crocodiles. We characterize here the diversification and body size evolution of terrestrial pan-avians (excluding pterosaurs) along the Triassic and Early Jurassic, using phylogenetic- and occurrence-based approaches, in an attempt to test the influence of such drivers. As diversity metrics, we quantified raw species richness and phylogenetic diversity (using time-calibrated phylogenetic trees), and net diversification rates were estimated with PyRate and the episodic fossilized-birth-death model. We have also characterised through-time patterns of body size (femoral length) and estimated body size evolutionary rates. Our results indicate that macroevolutionary shifts estimated from occurrence data are placed more recently in time than those from phylogenetic-based approaches, as shown by the higher diversity increase, diversification rates, and body size disparity of terrestrial Pan-Aves in the Carnian. This is consistent with hypotheses suggesting that the Carnian Pluvial Episode (CPE) was crucial for the early radiation of the group. Yet, phylogeny-based results show higher diversity/diversification rates for the Ladinian and Norian, suggesting a minor effect for the Carnian Pluvial Episode (CPE). We also found no meaningful shifts in diversity, diversification, or size-related metrics across the Triassic-Jurassic boundary. Even if the end-Triassic mass extinction possibly emptied ecospace, allowing dinosaur diversity to increase during the Jurassic, our results suggest that this expansion did not occur fast and homogeneously for the entire group. In fact, a sustained reduction in diversity and sub-zero net diversification rates are seen after the extinction, but macroevolutionary patterns here should be interpreted with care towards the end of the Early Jurassic, as they may be biased by an "edge effect." Overall, few macroevolutionary shifts were consistently identified across all results, suggesting that the early diversification of terrestrial pan-avians was more nuanced and complex than anticipated.

Keywords: Pan-Aves, dinosaurs, body size evolution, PyRate, taxic richness, phylogenetic diversity, fossilized-birth-death, variable rates model

OPEN ACCESS

Edited by:
Haijun Song,
China University of Geosciences, China

Reviewed by:
Michael D'Emic,
Adelphi University, United States
David Button,
University of Bristol, United Kingdom
Randall Irmis,
The University of Utah, United States

***Correspondence:**
Max Cardoso Langer
mclanger@ffclrp.usp.br

†*These authors have contributed equally to this work*

Specialty section:
This article was submitted to Paleontology, a section of the journal Frontiers in Earth Science

Received: *18 March 2022*
Accepted: *09 May 2022*
Published: *02 June 2022*

Citation:
Langer MC and Godoy PL (2022) So Volcanoes Created the Dinosaurs? A Quantitative Characterization of the Early Evolution of Terrestrial Pan-Aves. Front. Earth Sci. 10:899562. doi: 10.3389/feart.2022.899562

INTRODUCTION

With about ten thousand catalogued species, crown-clade Aves corresponds to the most diverse group of living tetrapods (Clarke et al., 2020), with its origin buried deep into the Cretaceous Period (Lee et al., 2014). In fact, such diversity has been mostly shaped by the mass extinction at the end of that time interval (Field et al., 2018), after which most modern avian groups radiated (Kuhl et al., 2021). Yet, the evolutionary history of the entire avian lineage (Pan-Aves) is far more ancient, also encompassing most of the Mesozoic Era. During that time, it produced one of the most notable, long-scale radiations known in the history of life, the dinosaurs. Previous studies based on body fossils have made a compelling case that the bird-crocodile divergence occurred early in the Triassic (Ezcurra and Butler, 2018), matching the lowest range—249 million years ago (Ma)—of molecular-clock estimates (Chiari et al., 2012) and the footprint record of ornithodirans (a clade including the bulk of Pan-Aves) in Olenekian (ca. 251-247 Ma) rocks of Poland (Brusatte et al., 2011).

In fact, the early pan-avian radiation is considered to have occurred after the easing of the harsh environmental conditions associated to the Permo-Triassic mass extinction (Sun et al., 2012; Ezcurra and Butler, 2018), henceforth influenced by the emplacement of the Siberian Traps LIP (Large Igneous Province) at ca. 252 Ma (Burgess et al., 2017). Yet, the age of the oldest pan-avian body-fossils is controversial, due to the uncertainty in cross-continental correlation of tetrapod faunas based on which their bearing deposits are pinned in the Triassic timescale (Irmis, 2011; Marsicano et al., 2016). These include aphanosaurs from Russia and India (Benton et al., 2017; Liu et al., 2018; Ezcurra et al., 2021) and possibly younger ornithodirans from southern Africa (Nesbitt et al., 2010; Nesbitt et al., 2013; Peecook et al., 2013). However, there is consensus that those likely Middle Triassic pan-avians are older than all other recognised members of the lineage (Novas et al., 2021).

Although pan-avians were part of the biotic recovery from the Permo-Trassic extinction, their Early-Middle Triassic fossil record is meagre. This pattern drastically changes in the Carnian (ca. 237-227 Ma), when sedimentary deposits with a significant content of dinosaurs (e.g., Ischigualasto and Santa Maria formations) or non-dinosaur Pan-Aves (Chañares Formation) have been recorded especially across south Pangaea (Langer et al., 2018). The Late Triassic rise of dinosaurs was variously related to environmental shifts that took place during that period (Langer et al., 2010; Brusatte et al., 2011), nicknamed their "lucky break" by Benton (1984). More recently, data accumulated suggesting a pivotal role for the Carnian Pluvial Episode (CPE) in such environmental changes (Dal Corso et al., 2020), leading to the radiation of several groups, including the dinosaurs (Bernardi et al., 2018; Benton et al., 2018; Irmis 2011).

Starting at ca. 234 Ma and lasting for a maximum of two million years (Dal Corso et al., 2020; Mancuso et al., 2020), CPE was synchronous to, or slightly preceded, the oldest tetrapod faunas with uncontroversial dinosaur body-fossils in South America (Langer et al., 2018; Desojo et al., 2020), as well as the oldest dinosauromorph-dominated ichnofaunas of the Southern Alps (Bernardi et al., 2018) and other parts of the world (Mancuso et al., 2020). Hence, it has been considered as a potential trigger of such early rise/dominance (Benton et al., 2018), perhaps linked to the emplacement the Wrangellia LIP volcanism (Dal Corso et al., 2020). It is important to note, however, that it is not until somewhat later in the Triassic that dinosaurs actually became not only more diverse, but also dominant and widespread in terrestrial ecosystems (Brusatte et al., 2008; Irmis, 2011; Benton et al., 2018; Mancuso et al., 2020), with "prosauropods" representing a major component of several Norian tetrapod faunas in Europe, Greenland, South America, and South Africa. According to Kent and Clemmensen (2021), this might have been influenced by a dip in atmospheric $pCO2$ at ca. 215–212 Ma of uncertain origins, but close in time to the Manicouagan impact.

The end-Triassic mass extinction was one of the largest in Earth history and has been usually correlated to the emplacement of the Central Atlantic Magmatic Province (CAMP) at ca. 201 Mya (Whiteside et al., 2010; Blackburn et al., 2013; Davies et al., 2017). It has long been suggested (Colbert, 1958) that the emptying of ecospace caused by that extinction, especially of crocodile-line archosaurs, provided the opportunity for the first major radiation across all dinosaur groups (Olsen et al., 2002; Brusatte et al., 2008). In fact, a general increase in dinosaur diversity was recorded/estimated for the entire Late Triassic-Early Jurassic interval (Wang and Dodson, 2006; Brusatte et al., 2008; Sakamoto et al., 2016; Tennant et al., 2018). Yet, partially because of sampling biases (Barrett et al., 2009; Butler et al., 2011; Upchurch et al., 2011), the behaviour of diversity curves across the Triassic-Jurassic boundary is more dubious. Most authors identified a diversity rise, so that dinosaurs emerged from the extinction more diverse than they were before (Barrett et al., 2009; Butler et al., 2011; Irmis, 2011; Upchurch et al., 2011; Starrfelt and Liow, 2016). Instead, some studies found that, along with other groups, dinosaurs suffered the consequences of the mass extinction, reducing their raw diversity and diversification rates between the latest Triassic and the earliest Jurassic (Lloyd et al., 2008; Tennant et al., 2018).

In this study, we assess the impact of the Siberian Traps, Wrangellia, and CAMP volcanisms on the early evolution of terrestrial Pan-Aves. For that, we compiled a new set of phylogenetic and occurrence data of Triassic and Early Jurassic members of that group, which was used to estimate taxic (i.e., richness) and phylogenetic diversity, as well as diversification rates, through time. We also collected body size data to characterise patterns of body size change and calculate morphological evolution rates over the same time span. These analyses aimed to identify shifts in macroevolutionary patterns that may match the timing and intensity of the tree LIPs mentioned above. In doing so, we were able to more comprehensively characterise various aspects of early pan-avian evolution, especially those related to the rise of dinosaurs during the Late Triassic.

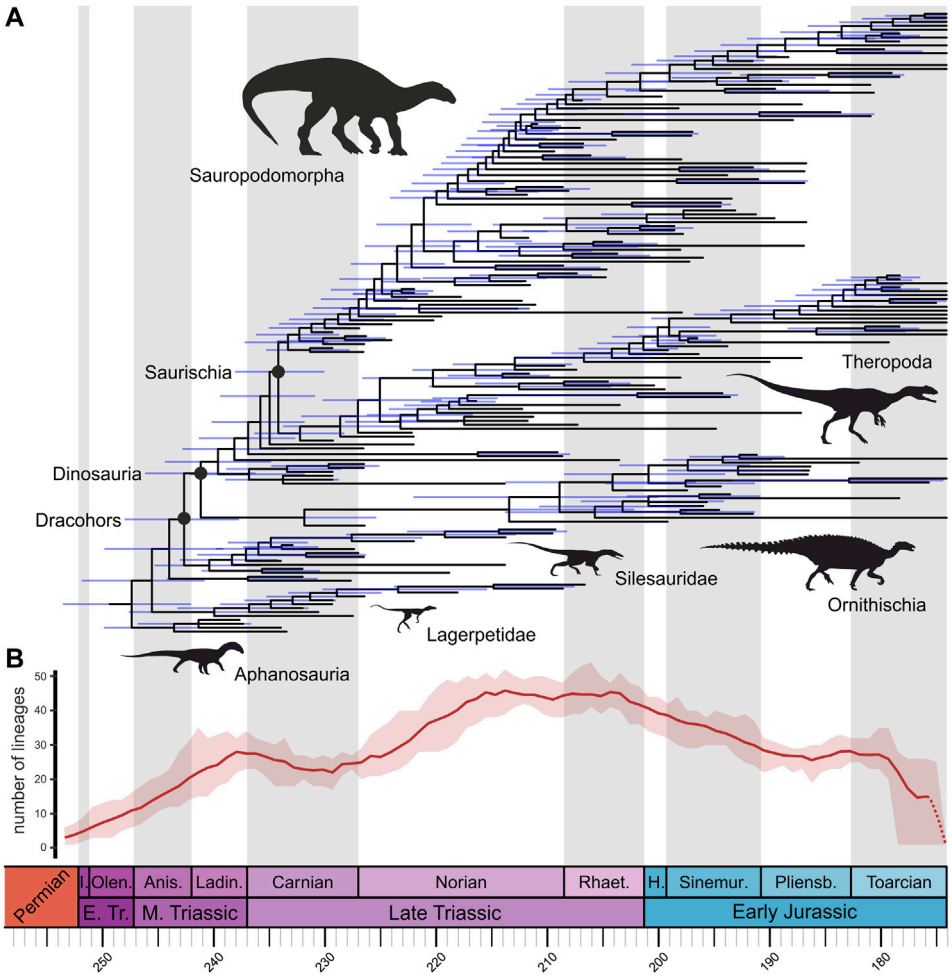

FIGURE 1 | (A) Time-calibrated phylogeny (majority rule consensus tree) of Triassic to Early Jurassic pan-avians (excluding pterosaurs), obtained from Bayesian analysis using the fossilized birth–death model. Phylogenetic relationships as in our supertree ST 1 (silesaurids external to Dinosauria, theropods forming Saurischia with sauropodomorphs, and herrerasaurs external to Eusaurischia). Blue bars indicate 95% highest posterior density age ranges of nodes. **(B)** Through-time phylogenetic diversity (lineage-through-time) of terrestrial Pan-Aves. Dark red solid line represents mean values for the ten trees from topology ST 1 with "ghost lineages," whereas light red shade represents maximum and minimum values for those same ten trees. Dashed red line represents the uncertainty of patterns through the Toarcian, from a possible "edge effect." Timescale abbreviations: Anis. = Anisian; H. Hettangian; I. = Induan; Ladin. = Ladinian; Olen. = Olenekian; Pliens. = Pliensbachian; Rhaet. = Rhaetian; Sinemur. = Sinemurian.

MATERIALS AND METHODS

Supertree Construction and Time-Calibration

Some of the analyses employed here require phylogenetic information. Therefore, using Mesquite 3.61 (Maddison and Maddison, 2019), we manually assembled an informal supertree of Triassic to Early Jurassic (Tr-EJ) terrestrial Pan-Aves. Although our focus was on Late Triassic patterns, we also included Early Jurassic taxa in order to minimise a possible "edge effect" (i.e., spurious results at the edges of our interval of interest derived from poor sampling or methodological limitations). The pterosaurs were not included in the supertree, as we understand that they occupy an entirely distinct morphofunctional space (i.e., flying animals) from that of other early pan-avians, which would add confounding factors to our study. The supertree included as many nominal species of Tr-EJ terrestrial pan-avians as possible, using the literature and the Paleobiology Database (PBDB) as sources of information. We did not add proposed junior synonyms of already included species, as well as taxa with very dubious phylogenetic/taxonomic affinities, as the putative Middle Triassic dinosaur *Nyasasaurus parringtoni* and the putative Early Jurassic segnosaur *Eshanosaurus deguchiianus*. Even though we acknowledge that some of these taxa could have an influence on our results, we explicitly decided that their inclusion would be potentially more problematic, as we would have to add them to arbitrary positions in the tree.

The supertree also includes eight Tr-EJ specimens with phylogenetic positions within Pan-Aves drawn from the literature, but with no species-level assignation. Finally, given that the supertree would be further used as input data to estimate diversification rates, we attempted to account for possible

cladogenetic events that occurred during the Tr-EJ, but were not represented in our supertree. For that, we created a version of the supertree added of terminals representing sister "ghost lineages" of branches with Tr-EJ species. The versions of the supertree with and without "ghost lineages" respectively include 187 and 164 terminals.

To account for the most notable diverging views of early pan-avian phylogeny, we built four alternative versions of the supertree (ST 1–4). Following several sources (e.g., Ezcurra, 2006; Irmis et al., 2007; Müler et al., 2018; Pacheco et al., 2019; Novas et al., 2021), ST 1 has silesaurids external to Dinosauria, theropods forming Saurischia with sauropodomorphs (rather than Ornithoscelida, with ornithischians), and herrerasaurs external to Eusaurischia (**Figure 1A**). The other versions of the supertree (**Supplementary Figures S1–S3**) differ from ST 1 in specific points: ST 2 has Theropoda and Ornithischia forming Ornithoscelida (Baron et al., 2017), ST 3 has silesaurids within Ornithischia (Langer and Ferigolo, 2013; Müller and Garcia, 2020), and ST 4 has sauropodomorphs at the earliest saurischian dichotomy, so that many Triassic taxa, including herrerasaurs, are placed along the theropod line (Sereno, 1990; Nesbitt et al., 2009). Although other phylogenetic arrangements for early dinosaurs were proposed in the literature, it was not feasible to accommodate them all here in further supertree versions. Except for the differences mentioned above, ST1–4 have all the same topological configuration, which was drawn from a vast array of sources (**Supplementary Table S1**). Accordingly, also taking into account the topologies with and without "ghost lineages," eight different versions of the supertree were used in our study. Because pterosaurs were not included in our analyses, the recent proposal that lagerpetids form its sister-group (Ezcurra et al., 2021) does not alter the pan-avian topologies evaluated here.

The eight supertree versions were then time-calibrated using Bayesian inference under a fossilized birth-death (FBD) process (Stadler, 2010; Ronquist et al., 2012a; Heath et al., 2014). We used R (version 4.1; R Core Team, 2021) package *paleotree* (Bapst, 2012) to create a MrBayes command, with an "empty" morphological matrix, to perform Bayesian Markov chain Monte Carlo (MCMC) tip-dating analyses in MrBayes version 3.2.6 (Ronquist et al., 2012b). The supertree versions were used as topological constraints, with the addition of three non-pan-avian archosauromorphs (*Ctenosauriscus koeneni*, *Jaxtasuchus salomoni*, *Euparkeria capensis*) as successive outgroups to Pan-Aves, which were then removed before subsequent macroevolutionary analyses. A uniform prior was used for the root of all versions of the supertree, constrained between 264.28 and 247.2 Ma (Turner et al., 2017; Ezcurra and Butler, 2018). Uniform priors were also used for the tip ages, which were set based on occurrence date information. These were taken from the most recent literature, using radioisotopic ages when available and looser age intervals for taxa from stratigraphic units lacking absolute ages (**Supplementary Table S2**). A fixed age of 174.1 Ma was assigned to all "ghost lineages" treated as terminals.

For each of the eight supertree versions, we performed two MCMC runs of 20,000,000 generations, with four chains each and a burn-in factor of 30%. Convergence was assessed using potential scale reduction factors (values approaching 1.0) and average standard deviation of split frequencies (values below 0.01). For each version of the supertree, we saved ten trees randomly sampled from the posterior distribution for subsequent analyses, as well as the maximum clade credibility (MCC) tree.

Diversification Rates From Time-Calibrated Phylogenetic Trees

For estimating through-time net diversification rates, we implemented a piecewise-constant (episodic) fossilized-birth-death (EFBD) model (Magee and Höhna, 2021) in a Bayesian framework. The model EFBD is an extension of previous fossilized-birth-death models (Stadler, 2010; Gavryushkina et al., 2014; Heath et al., 2014), which uses Horseshoe Markov random field (HSMRF) prior distributions (Magee et al., 2020) to keep rates of speciation (λ), extinction (μ) and fossilization (ϕ) constant within time intervals, but allowing them vary across intervals. This model enables to estimate variation in net diversification rates (λ-μ) using phylogenies (with extant and/or extinct taxa) as input data (Magee and Höhna, 2021). For our EFBD analyses, we used ten randomly-sampled trees for each of the eight different time-calibrated topologies (four with and four without "ghost lineages").

We used a Half-Cauchy distribution as prior for the global scale parameters of λ, μ, and ϕ. The global scale hyperpriors of the rates variation are dependent on the number of time bins used in the analyses. A time-interval scheme of approximately equal-length (ca. five million years) time bins was defined by subdividing longer Tr-EJ stages (i.e., Carnian, Norian, Sinemurian, Pliensbachian, and Toarcian), so that stages and time bins have matching boundaries. This resulted in sixteen time bins for the topologies with "ghost lineages" and fifteen for those without "ghost lineages" (given that the second group of trees had consistently younger root ages). For calculating hyperpriors, we used R function *setMRFGlobalScaleHyperpriorNShifts*() from package *RevGadgets* (Tribble et al., 2021).

Given that in the EFBD model the rate-changes are modelled backwards in time, it is usually necessary to estimate λ, μ, and ϕ at present. However, as we do not have extant taxa in our trees, this estimation used the most recent point in time of our study (i.e., end of the Early Jurassic), for each tree. This was done using empirical Bayes strategy, by setting a constant-rate fossilized-birth-death model and using their posterior distribution to determine the prior on the rates at the most recent point in time. For that, we adapted the RevBayes script available at https://revbayes.github.io/tutorials/divrate/efbdp_me.html and used the R function *posteriorSamplesToParametricPrior*() from *RevGadgets* to obtain the Gamma priors of each rate for all the 80 trees.

Another important aspect of the EFBD analyses is the sampling parameter ($\Phi 0$ or ρ; Magee et al., 2020), which is the probability of sampling extant species at the present. Again, as we

do not have living species in our trees, we used the most recent point in time. Estimating Φ0 is challenging, given that there is no unambiguous way to infer dinosaur diversity during the Mesozoic (Benson, 2018). Therefore, we ran two sets of EFBD analyses, one with Φ0 set to 0.08, in which we assume that the sampled species in our tree represent 8% of the total dinosaur diversity during the latest Early Jurassic, and another with Φ0 set to 0.3, which assumes that we sampled 30% of the real diversity. Although these values are arbitrary, we believe this procedure allowed us to test if changes in this parameter significantly affected the overall patterns of though-time net diversification rates.

We performed sixteen sets of EFBD analyses in RevBayes v1.1.0 (Höhna et al., 2016), with eight topologies (four with "ghost lineages" and four without) and two different values of Φ0, resulting in 160 analyses in total. Each analysis comprised two MCMC runs of 200,000 iterations (each iteration consisted of 685 moves), sampling every 200 generations. Convergence was inspected using the software Tracer (Rambaut et al., 2018), by confirming that the effective sample sizes (ESS) of all parameters were above 200. After discarding the first 10% of samples as burn-in, we used R package RevGadgets (Tribble et al., 2021) to summarize the results of all sixteen sets of analyses and visualize them using rates-through-time (RTT) plots.

Diversification Rates From Occurrence Data

We also estimated through-time net diversification rates from fossil occurrence data, by using the hierarchical Bayesian framework implemented in PyRate v3.0 (Silvestro et al., 2014a; Silvestro et al., 2014b; Silvestro et al., 2019). PyRate jointly models the preservation and diversification processes, using a birth-death model to estimate speciation and extinction rates (λ and μ, respectively) from estimated lifespans of taxa (Silvestro et al., 2015).

We downloaded Tr-EJ occurrence data for three main groups (Aphanosauria, Lagerpetidae, and Dinosauromorpha) from the Paleobiology Database (PBDB) on 24 December 2021, under the following settings: taxon = Aphanosauria/Lagerpetidae/Dinosauromorpha, taxonomic resolution = species, preservation = regular taxa only, taxon status = all, identification = latest, time rule = major. The dataset was then curated, with the inclusion of thirteen occurrences (i.e., newly named species and unnamed specimens with phylogenetic information available that were included in our supertree) and the exclusion of fifteen occurrences (mainly ichnotaxa). The final occurrence dataset included 410 occurrences from 176 species (and seven unnamed specimens, which probably represent new taxa), 65% of which are singletons.

From this occurrence dataset, we followed recent recommendations within Černý et al. (2021) and created two types of datasets: one in which the age of every occurrence was independently drawn from the corresponding range and one "site-linked" dataset. In the "site-linked" dataset, a single age is drawn from the temporal range of every site/collection and assigned to all the occurrences from the same PBDB collection number. This simultaneously accounts for age uncertainty and for the fact that the ages of all fossils from the same site are approximately equal. We further accounted for occurrence age uncertainty by replicating ten times the procedures to create site-linked and site-unlinked occurrence datasets, resulting in twenty datasets, which served as input data for the PyRate analyses.

For the PyRate analyses performed in this study, we broke down the birth-death process into time intervals, using the same time bins used for the EFBD analyses (i.e., 16 time bins of approximately five million years, delimited by stratigraphic stages). This was done to ease comparisons with the results of the EFBD analyses and was achieved by using the *-fixShift* option within PyRate, to estimate λ and μ within the time intervals. To avoid overparameterization, this option assumes Half-Cauchy prior distributions for λ and μ between shifts, with a hyperpriors on the scale parameters (Silvestro et al., 2015).

Instead of using a single preservation model for our PyRate analyses, we compared the results of three different models. The default model is the non-homogeneous Poisson process of preservation (NHPP), in which preservation rates (q) change during the lifespan of each lineage, following a bell-shaped distribution (Silvestro et al., 2014a). We also used a homogeneous Poisson process (HPP), in which q is constant through time (Silvestro et al., 2015), and a time-variable Poisson process (TPP), which assumes that q is constant within time intervals, but can vary across them (Silvestro et al., 2019). For the TPP models, we used the same time bins of approximately five million years. Also, to incorporate rate heterogeneity across lineages, a Gamma model of rate heterogeneity with five categories was used.

We performed six sets of PyRate analyses, with three preservation models and two types of occurrence datasets (site-linked and site-unliked), resulting in 60 analyses in total. Each analysis consisted of 1,000,000 MCMC iterations, sampling every 1,000 iterations. Convergence was inspected using the software Tracer (Rambaut et al., 2018), by confirming that the effective sample sizes (ESS) of most parameters were above 200. We excluded the first 10% of the samples as burn-in and combined the posterior estimates of each set of analyses to visualize the results using RTT plots. PyRate analyses performed here used adapted versions of the codes made available by Černý et al. (2021).

Taxic Richness and Phylogenetic Diversity

We also quantified diversity of Tr-EJ terrestrial pan-avians using two additional metrics: raw taxic richness (or taxonomic diversity) and phylogenetic diversity (also known as lineage richness or lineage-through-time plots). To quantify taxic richness, we used the same occurrence data and time bins from the PyRate analyses and subdivided pan-avian taxa using R function *taxicDivDisc*() from package *paleotree* (Bapst, 2012). Given that previous works demonstrated that the geological record affects the observed diversity (Barrett et al., 2009; Butler et al., 2011; Irmis, 2011; Upchurch et al., 2011), we also quantified the number of PBDB collections as a proxy for fossil localities, in order to better understand possible biases in the estimated taxic richness. In comparison to rock (i.e., geologic) units, the number of collections is also affected by anthropogenic

variables such as sampling effort, but both metrics are strongly correlated (Černý et al., 2021). We quantified the number of PBDB collections with aphanosaur, lagerpetid, and dinosauromorph body fossils, and also compared to those of continental origins with tetrapods in general. Finally, we also estimated phylogenetic diversity from the eight alternative topologies (four with "ghost lineages" and four without), using a set of ten trees randomly sampled from our time-calibration FBD analyses for each topology and the R function *ltt95*() from package *phytools* (Revell, 2012).

Body Size Data Collection and Rates of Morphological Evolution

We collected maximum femoral length from 161 species/specimens of Tr-EJ terrestrial pan-avians as proxy for total body size (**Supplementary Table S3**). Femoral length was selected because it has been demonstrated that this measurement scales isometrically with body length/mass during archosaur ontogeny (Anderson et al., 1985) and has therefore been vastly used in previous studies (e.g., Irmis 2011; Sookias et al., 2012a; Sookias et al., 2012b; Turner and Nesbitt, 2013; Sengupta et al., 2017; Pradelli et al., 2022). Approximately 75% of the femoral length data were made available by Pradelli et al. (2022), whereas the remaining data were collected from the literature. For consistency, we followed the protocol of Pradelli et al. (2022), using the largest available specimen for taxa with more than one preserved femur. For taxa lacking femora (or the complete bone), simple linear lengths of preserved skeletal parts were measured and used to estimate total femoral length from the closest taxon with both elements preserved. This resulted in ca. 39% of the femoral length dataset being estimated, either by us or Pradelli et al. (2022). All subsequent analyses and plots used log-transformed femoral length in millimetres (Benson et al., 2022). For analyses that require information from phylogenetic trees, we pruned the trees (derived from the original topologies) to keep only terminals for which we did have body size/femoral data.

Using the same sixteen time bins used for diversity/diversification analyses, we generated through-time plots of minimum, maximum, and mean pan-avian body size. Body size disparity was also estimated, using the standard deviation as a metric of disparity and calculating 95% confidence intervals from bootstrapped data (500 times) with R package *dispRity* (Guillerme, 2018). We also constructed four additional through-time plots that incorporated ancestral femoral length, which were estimated from the MCC trees of the four topologies with "ghost lineages" and using the R function *fastAnc*() from package *phytools* (Revell, 2012).

We also estimated morphological (=body size) evolutionary rates in a Bayesian framework using BayesTraits v3.0 (Pagel and Meade, 2006; Venditti et al., 2011; Baker et al., 2016; Meade and Pagel, 2017). We detected evolutionary rate shifts by using the variable rates model, which rescales branches that show trait variance incompatible with a homogenous (=Brownian motion) model (Baker et al., 2016). For ten trees of each of the eight original topologies, we run MCMC reversible-jump analyses for 2,000,000,000 generations, sampling parameters 80,000 and discarding the first 400,000,000 as burn-in. Using stepping-stone sampling (1,000 stones and 100,000 iterations per stone), we compared the fit of two models (homogeneous and heterogeneous rates) using Bayes factor, which revealed higher support for the heterogeneous/variable rates model. Convergence of MCMC runs was assessed with R package *coda* (Plummer et al., 2006), by confirming that the effective sample sizes (ESS) of all parameters were above 200. We then used the Variable Rates Post Processor (Baker et al., 2016) to extract values of rate through time (i.e., log-transformed relative evolutionary rate scalar) for each tree, divided by 90 equally spaced time bins of approximately one million years. We used an adapted version of the R code made available by Stubbs et al. (2021) to generate BayesTraits scripts for our analyses.

RESULTS AND DISCUSSION

Overall Patterns of Diversity and Diversification Rates

Similar overall patterns of phylogenetic diversity are observed across curves obtained from the four alternative topologies used in this study (**Figure 1B**, **Supplementary Figure S4**). In contrast, more differences are observed when trees that incorporate "ghost lineages" are compared to those without them (**Supplementary Figure S5**), with the latter usually showing slightly delayed increases in diversity. Another major difference is that trees with "ghost lineages" show an increase in phylogenetic diversity towards the end of the Early Jurassic (i.e., during the Pliensbachian) which is not recovered from trees without "ghost lineages."

Comparisons between raw taxic richness and phylogenetic diversity of Tr-EJ terrestrial pan-avians show marked differences in the timing and magnitude of most significant peaks. Whereas raw richness peaks during the Carnian (**Figure 2A**), the highest phylogenetic diversity values are usually observed in the Norian. Also, the second largest peak in taxic richness is seen in the Rhaetian. This is not reproduced in most of the phylogenetic diversity plots, for which the Rhaetian shows similar or lowers values to those of the Norian. These inconsistencies might be due to differences in datasets used to obtain both diversity metrics, given that we used occurrence data for quantifying raw richness and time-calibrated trees to estimate phylogenetic diversity. Yet, this might also result from real diversity hidden by ghost lineages, which cannot be captured by raw taxic richness. This is mostly demonstrated by the lineage-through-time plots constructed with the trees with explicitly included "ghost lineages," in which some increases in phylogenetic diversity predate rises in taxic richness, such as those in the Ladinian vs. Carnian and in the Norian vs. Rhaetian.

In terms of diversification rates, EFBD results (**Figure 3**, **Supplementary Figures S6–S21**) show relatively similar patterns across all topologies, with or without "ghost lineages," whereas changes in the value used for the sampling parameter (Φ0) seemed to only affect the rates for the last (i.e., most recent) time bin. PyRate results (**Figure 2B**, **Supplementary Figures S22–S27**) also show consistent patterns between site-linked and

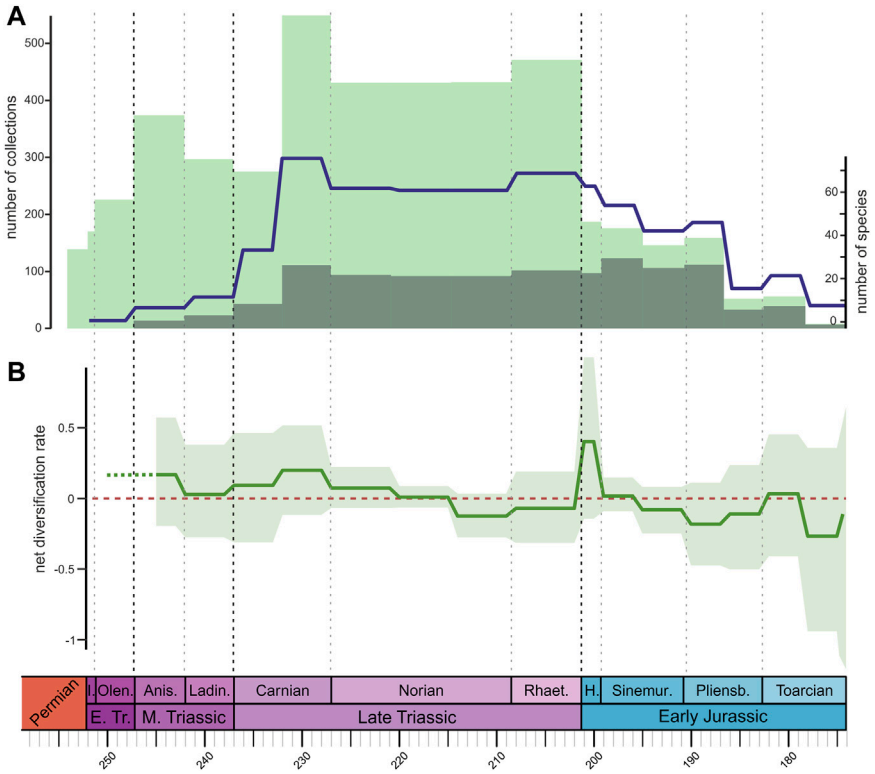

FIGURE 2 | (A) Through-time taxic richness of Triassic to Early Jurassic terrestrial Pan-Aves (solid blue line). Light green bars represent the number of PBDB collections bearing terrestrial tetrapods, whereas dark green bars represent PBDB collections with Pan-Aves (excluding pterosaurs). **(B)** Net diversification rates estimated from occurrence data using PyRate. Solid green line represents mean values; light green shade represents maximum and minimum rate values considering all ten replicates of the dataset. Results for the time-variable Poisson process (TPP) preservation model, using the "site-unlinked" occurrence dataset. Timescale abbreviations: as in **Figure 1**.

site-unliked analyses. In terms of preservation model, the TPP model received higher support and shows similar results to the HPP model (the second best supported), whereas the NHPP model yielded slightly lower rates in comparison to the other models (a pattern also observed by Černý et al., 2021). PyRate and EFBD results do share some similarities, such as below-zero net diversification rates during most of the Early Jurassic, but also exhibit significant differences. For example, EFBD results show much higher rates in the Middle Triassic than the PyRate results, whereas the latter display a peak in the Hettangian not seen in our EFBD results. These inconsistencies are likely due to the inherently different nature of the employed types of data (occurrence data vs. phylogenetic trees) and, consequently, of the two methods.

In the following paragraphs, we further report and discuss these results in a chronological order, from the Middle Triassic to the Early Jurassic, also comparing them to previously published studies that focused on similar questions, e.g., Barrett et al. (2009), Butler et al. (2011), Irmis (2011), Upchurch et al. (2011), Starrfelt and Liow (2016), Tennant et al. (2018). It is important to stress again that our prime aim was to analyze macroevolutionary patterns within the time frame of the tree main Triassic LIPs. For that, in an attempt to prevent an "edge effect" of masquerading such patterns along the Triassic-Jurassic boundary, we extended our data sampling into the entire Early Jurassic. In doing so, we were able to more comprehensively evaluate the Triassic-Jurassic event, but we moved the potential "edge effect" to the Early-Middle Jurassic boundary. Hence, we suggest caution in interpreting the Early Jurassic patterns reported here, especially those near the end of that time interval.

Pan-Avian Diversity Patterns in the Middle Triassic

Taxic diversity or richness of Pan-Aves was relatively low in the Middle Triassic (**Figure 2A**). This is consistent with patterns of dinosauromorph taxic diversity (Irmis, 2011, **Figure 3**) and pan-avian (=avemetatarsalian) morphological disparity (Brusatte et al., 2008) previously reported for that time interval. Across the Middle-Late Triassic boundary, we see a higher increase in taxic richness than Irmis (2011) reported for dinosauromorphs. This likely results from a reduction of Ladinian richness values due to the recent dating of the Chanares Formation of Argentina as Carnian in age (Ezcurra et al., 2017), which could also explain the Ladinian to Carnian maintenance of species richness found by Irmis (2011, fig. 4), when taxic diversity is normalised by the number of stratigraphic units with dinosauromorphs records. This overall pattern of taxic richness is consistent with our PyRate

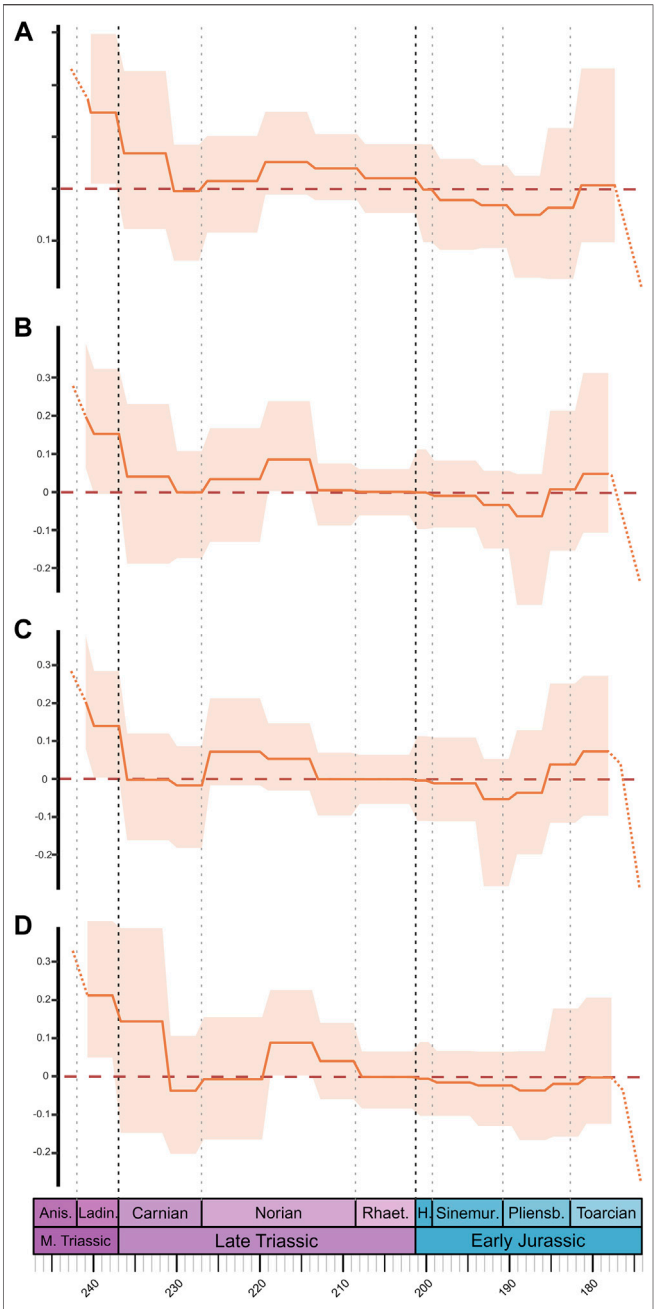

FIGURE 3 | Net diversification rates of Triassic to Early Jurassic terrestrial Pan-Aves, estimated from phylogenetic trees using the episodic fossilized-birth-death (EFBD) model from RevBayes. Solid orange line represents the mean values (posterior estimates) across all ten trees, whereas light orange shade represents 95% credible intervals. Dashed orange line represents the uncertainty of patterns through the Toarcian, from a possible "edge effect." Results shown for the four topologies with "ghost lineages" and sampling parameter (Φ0) of 0.08. Topologies **(A)** ST 1, **(B)** ST 2, **(C)** ST 3, and **(D)** ST 4. Timescale abbreviations: as in **Figure 1**.

results (i.e., diversification rates estimated from occurrence data), for which positive, but low rates are seen for the Ladinian (**Figure 2B**). However, in contrast to raw richness, PyRate results show relatively higher values for the Anisian, a pattern that might be explained by the inclusion of non-dinosaur early pan-avians in our analyses (e.g., aphanosaurs, silesaurids), which were accounted for the first time in quantitative studies investigating diversification patterns of the group.

The scenario changes when phylogenetic information is employed. In terms of phylogenetic diversity (i.e., accounting for "ghost-lineages"), relatively higher values are seen during the Middle Triassic, with a steady increase across the Anisian and Ladinian, peaking near the Middle-Late Triassic boundary (**Figure 1B**, **Supplementary Figure S4**). This matches overall patterns of dinosauromorph phylogenetic diversity found by Irmis (2011, fig. 3), but the new Carnian dating of the Chanares Formation mentioned above can explain our higher values for the Ladinian, compared to those found based on his strict temporally-calibrated phylogenies. Additionally, in our EFBD results (i.e., diversification rates estimated from time-calibrated phylogenetic trees), diversification rates are higher in the Middle Triassic than in any other time interval analysed here (**Figure 3**). Therefore, the overall patterns of diversity and diversification rates seem affected by the incorporation of phylogenetic information and, consequently, of divergence times (i.e., node ages) data. This is noticeable during the Middle Triassic, for which we see higher diversity and diversification rates when phylogenetic information is accounted for.

Given the meagre fossil record of Middle Triassic pan-avians, the analyses performed here are not suitable to elucidate much about patterns possibly influenced by the Permo-Triassic mass extinction. It may be asserted that pan-avians experienced important diversification events (**Figures 2B**, **3**) and a sustained rise in diversity (especially in phylogenetic diversity; **Figure 1B**, **Supplementary Figure S4**) along the Middle Triassic. This was previously hinted by the record of some dinosauriform-dominated ichnofaunas that predate the Ladinian-Carnian boundary (Olsen et al., 1998; Carrano and Wilson, 2001; Marsicano et al., 2007; Farlow et al., 2014; Benton et al., 2018; Mancuso et al., 2020). Thus, the Middle Triassic seems to have witnessed important pulses of pan-avian diversification, but these probably were not sufficient to result in significant impacts in taxic richness (**Figure 2A**). Indeed, the body-fossil record of lineages may only consistently increase when these are already well established, what will commonly postdate increases in diversification rates. Also, given that rates are estimated comparatively to previous time intervals, when the rising lineages are naturally less diverse, diversification rates will tend to be relatively higher in older time bins.

One may question how much of the Middle Triassic patterns of pan-avian diversity is dictated by the rock record. Indeed, raw richness curves for the Triassic greatly mirror those depicting the number of fossil localities with records of the group (using PBDB collections as a proxy for localities; **Figure 2A**). Yet, it is also correct that, unlike later in the Triassic (ca. 25%), and surely in the Jurassic (ca. 70%), few Middle Triassic continental fossil sites with tetrapod remains (ca. 10%) have pan-avian records (**Figure 2A**), indicating that the Triassic expansion of the group is not merely a sampling artefact. These results for the Middle Triassic indicate that, even if somehow delayed, pan-avian

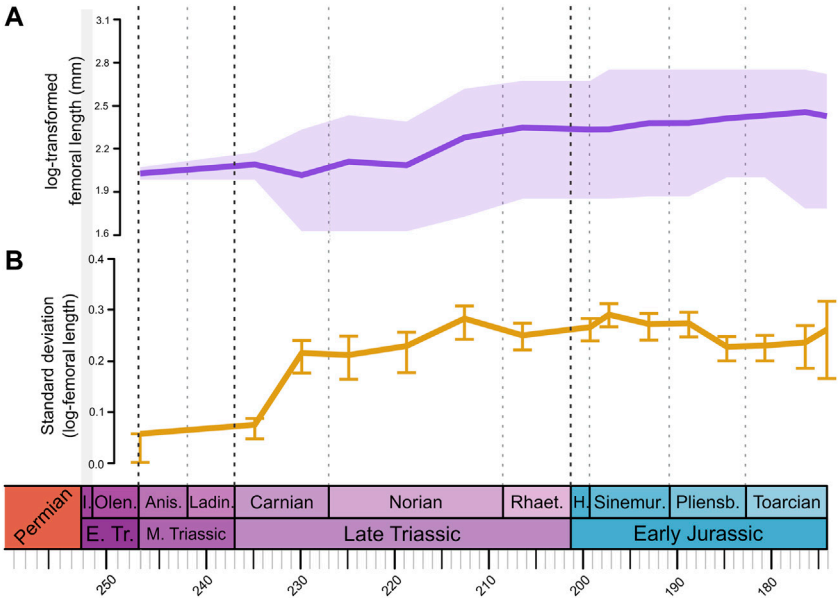

FIGURE 4 | Body size patterns of Triassic to Early Jurassic terrestrial Pan-Aves. **(A)** Body size represented by log-transformed femoral length in millimeters. Solid purple line represents mean body size, light purple shade indicates maximum and minimum sizes. **(B)** Solid yellow line represents body size disparity, estimated by calculating the standard deviation for each time bin. Error bars estimated by bootstrapping the data 500 times. Timescale abbreviations: as in **Figure 1**.

rise was part of the faunal recovery that followed the Permo-Triassic mass extinction. Accordingly, there is evidence that some of the main early pan-avian increases in diversity (**Figure 1B**, **Supplementary Figure S4**) and diversification rates (**Figures 2B**, **3**) preceded the Late Triassic.

Finally, *N. parringtoni* was not included in our analysis, but has been previously positioned as the sister-taxon to Dinosauria (Nesbitt et al., 2013), as well as within each of the three main dinosaur groups (Nesbitt et al., 2013; Baron et al., 2017). The inclusion of this taxon in the former position would probably not change much the results of the phylogeny-intermediated analyses presented here. On the contrary, the record of a Middle Triassic theropod, ornithischian, or sauropodomorph, as unlikely as it may be (Novas et al., 2021), would extend a number of ghost-lineages into that time interval, so that phylogenetic diversity and EFBD values in the Anisian-Ladinian would probably be much higher than estimated here (**Figures 1**, **3**).

What Really Happened in the Carnian?

The Carnian was divided in two time bins in our analyses, with terrestrial pan-avian taxic richness rising at "Carnian 1" (in comparison to the Ladinian) and reaching its peak by "Carnian 2" (**Figure 2A**). The increase at "Carnian 1" happens with only minor changes in the number of PBDB collections for both continental Tetrapoda and terrestrial Pan-Aves, whereas that of "Carnian 2" is synchronous to equivalent rises (**Figure 2A**). A similar taxic richness increase was found by Irmis (2011, fig. 3) for dinosauromorphs in the Carnian (although not when normalized by the record of geologic units, see above). This is consistent with previously proposed scenarios, in which a higher Carnian diversity, recently termed "dinosaur diversification event" (Bernardi et al., 2018), matches the oldest uncontroversial dinosaur records (Ezcurra 2010). Such diversification event was suggested to be synchronous (Bernardi et al., 2018) or to slightly postdate (Benton et al., 2018) the CPE, the proposed age of which, at 234–232 Ma (Dal Corso et al., 2020; Mancuso et al., 2020), places the event at the end of our "Carnian 1" time bin. Yet, it is important to notice that the maximal duration of the CPA (2 Ma) is significantly shorter than the ca. 5 Ma time bins employed here. In fact, the effects of such a short event will possibly appear downweighed in the time-bin it belongs to, and variations within that time bin will be unaccounted for. In any case, a steady increase in diversification rates (from PyRate analyses) is seen for our two Carnian time bins (**Figure 2B**), with a Late Triassic peak at "Carnian 2," showing that diversification rates estimated from occurrence data track the patterns of raw richness for this Stage. Yet, the increase in number of collections at "Carnian 2" cannot be ignored as a possible source of biases to these metrics.

Unlike taxonomic richness, phylogenetic diversity of terrestrial Pan-Aves in the Carnian is broadly similar to that seen in the Ladinian (**Figure 1B**, **Supplementary Figure S4**), although an increase trend is seen in the former Stage and the inverse is the case for the later, with a clear reduction from "Carnian 1" to "Carnian 2." A decline/maintenance in phylogenetic diversity from the Ladinian to the Carnian was also reported by Irmis (2011) when the data are normalized by the number of dinosauromorphs-bearing geological units (the same pattern was found for taxic diversity). Our EFBD results (**Figure 3**) show lower diversification rates in the Carnian than in the Middle Triassic, broadly tracking the phylogenetic diversity curve (**Figure 1B**, **Supplementary Figure S4**). Even

though the overall pattern remains the same, some differences are recognized in the EFBD results depending on the topology. For example, ST 3 topology (with silesaurids within Ornithischia) has comparatively lower Carnian rates, possibly due to an estimated Ladinian origin of Dinosauria, following the record of Middle Triassic ornithischians (**Figure 3C**). Likewise, ST 4 (with sauropodomorphs rising from the earliest saurischian dichotomy) shows notably higher rates for "Carnian 1," which could be explained by the placement of several Carnian taxa within Theropoda, resulting in an estimated "Carnian 1" origin of Eusaurischia (**Figure 3D**). A similar explanation can be used to explain the slightly delayed increase in phylogenetic diversity seen for ST 4, which occurs only after the Ladinian-Carnian boundary, contrasting with the three other topologies (**Supplementary Figure S4**).

As also seen in the Middle Triassic, our results for the Carnian are influenced by the use of phylogenetic information (i.e., the incorporation of temporal information from the time-calibration of the trees). Depending on the approach used, the Carnian is a stage in which terrestrial pan-avian richness/diversification is either higher or lower than/equal to that of the Middle Triassic. This is vital to consider, because previous studies suggested that the CPE, at the end of "Carnian 1," is linked to the "dinosaur diversification event," which is usually given a Carnian age (Ezcurra 2010; Benton et al., 2018; Bernardi et al., 2018). Thus, both taxonomic richness and PyRate results, which lack phylogenetic data, corroborate the hypothesis that the Carnian was a period of major diversity shifts for pan-avians, with high diversification rates and significant increases of richness. On the contrary, phylogenetic diversity and diversification rates estimated from EFBD analyses indicate that the main diversification pulses and increases in species richness among terrestrial Pan-Aves happened before the Carnian, with terrestrial pan-avian faunas of this stage remaining at similar levels of richness and having lower diversification rates than in the Middle Triassic. In this case, CPE cannot be considered a driver of pan-avian diversification, although it can still be regarded as favouring the establishment of terrestrial pan-avian faunas that diversified previous to that. Indeed, the oldest fossil assemblages with an expressive pan-avian record are from the Carnian, which also witnessed the first records of the group in northern Pangaea. So, it is clear that the Carnian was a critical moment for the establishment of pan-avians. However, the incorporation of phylogenetic information suggests that it is more likely that the diversification and rise in richness leading to this scenario happened before, towards the end of the Middle Triassic.

The Long Norian and the Peculiar Rhaetian

The Norian was divided into three time bins in our analyses, with terrestrial pan-avians keeping a relatively high and constant taxic richness, although lower than that of "Carnian 2" (**Figure 2A**). Irmis (2011, fig. 3) also found an initial drop in taxic richness during the Norian, but followed by a rise in the second half of the Stage. Such an increase is also reported by some other studies focusing only on dinosaurs (e.g., Butler et al., 2011; Upchurch et al., 2011; Starrfelt and Liow, 2016). However, Irmis (2011) suggests that the Norian rise of dinosauromorph diversity is heavily influenced by the richer rock record of the Stage, as also noticed by other counts of raw richness (Barrett et al., 2009; Butler et al., 2011; Upchurch et al., 2011). Indeed, when normalized by dinosauromorph-bearing geological units (Irmis, 2011, fig. 4), results for that group are comparable to ours of taxic richness, with a decrease in the first half of the Norian and maintaining similar values in the second half. In fact, our taxic richness results for the Norian seem influenced by the rock records, as they strongly correlate with the number of PBDB collections (**Figure 2A**). Also, the relatively low richness during the Norian reported here can be explained by two extra factors: the division of the Stage in more time bins (generally lowering TR in each one of them) and the inclusion of non-dinosaur terrestrial Pan-Aves, which may not have increased diversity from Carnian to Norian as much as dinosaurs alone. In addition, our PyRate results are consistent with the taxic richness curve, with a decrease in net diversification rates throughout the Norian (**Figure 2B**), reaching sub-zero values "Norian 3."

When phylogenetic data are accounted for, a different picture again emerges. The phylogenetic diversity of terrestrial Pan-Aves rises abruptly along the first two-thirds of the Norian, reaching the highest peak seen during the entire Tr-EJ time span, followed by a slight decrease in the last third of the Stage (**Figure 1B**, **Supplementary Figure S4**). This generally matches previous phylogeny-based estimates, which agree on a Norian rise of phylogenetic richness (Barrett et al., 2009; Irmis, 2011). Yet, when normalized by the rock record, Irmis (2011) found a reduction in dinosauromorph phylogenetic richness along that Stage, with an increase only for sauropodomorphs (Barrett et al., 2009). Our EFBD results (**Figure 3**) broadly match the phylogenetic diversity estimated for the Norian, with net diversification values mostly above zero and constantly higher than those of the Rhaetian and "Carnian 2."

As also seen for older time bins, our phylogeny-dependent analyses account for ghost-lineages extending back in time towards the Norian, in this case from Rhaetian-Jurassic taxa, so that estimated richness and diversification rates for that Stage are lower when a taxic/occurrence approach is employed. Hence, we agree with prior suggestions that the high Norian raw richness found in some studies are biased by the availability of further sites/deposits of that age. Yet, the phylogenetic data cannot be totally ignored, and our results indicate that the Norian hosted a diversity of terrestrial Pan-Aves that is still to be fully accounted, possibly related to taxa that diversified along that Stage to stablish themselves— more conspicuously impacting taxic counts—only latter in time. A possible candidate group to fill that gap are the ornithischian dinosaurs that, depending on the chosen topology, bear ghost-lineages encompassing almost the entire Late Triassic.

The Norian is traditionally considered a key-period for dinosaur evolution, when the group attained higher faunal dominance (McPhee et al., 2017; Benton et al., 2018), larger sizes (Benson et al., 2014; Apaldetti et al., 2018; Pradelli et al., 2022), greater disparity (Brusatte et al., 2008; Apaldetti et al., 2021), and a broader geographical distribution (Kent and Clemmensen 2021), although some of these patterns are clearly clade- and region-specific (Whiteside et al., 2015).

Indeed, the rise in terrestrial pan-avian body size (see below) and diversity seems biased towards sauropodomorphs. On the other hand, this group expanded their range to northern Pangaea in the Norian, together with other pan-avians, such as theropods and lagerpetids, although sauropodomorphs remain unrecorded in continental North America. This "northward dispersal" has been correlated with a greenhouse dip in atmospheric pCO_2 at ca. 215–212 Ma, which attenuated climate barriers (Kent and Clemmensen, 2021). Its timing broadly coincides with our "Norian 3" time bin, which records similar values of diversity (considering both taxic and phylogenetic diversity) and lower diversification rates (from both PyRate and EFBD results) compared to previous Norian time bins. Hence, if these climate changes affected terrestrial pan-avian diversity at all it was towards a reduction of such metrics. In any case, even if our data does not indicate that an important rise in the diversity of terrestrial Pan-Aves occurred in the Norian, this has been recognized for sauropodomorphs (Barrett et al., 2009; Irmis, 2011; Mannion et al., 2011) and seems to be an unbiased pattern for this group in particular. As discussed by Apaldetti et al. (2021), the Norian rise of Sauropodomorpha may be associated with a reduction in the diversity (although not extinction) of other herbivorous groups, such as rhynchosaurs, traversodontid cynodonts, and dicynodonts (Benton et al., 2018).

Consistent with our results for terrestrial Pan-Aves (**Figure 2A**), a Rhaetian increase in dinosaur estimated diversity/richness was reported by Starrfelt and Liow (2016) and Tennant et al. (2018), although with broad confidence intervals in the former. Our division of the Norian in three time bins likely explains the low richness in each of them (see above), relative to the single Rhaetian time bin, given that the reverse—a richer Norian—has been more commonly reported (Barrett et al., 2009; Butler et al., 2011; Upchurch et al., 2011; Starrfelt and Liow, 2016). This was found by Irmis (2011) for dinosauromorphs as well, although taxic richness was slightly higher in the Rhaetian when normalized by the number of bearing stratigraphic units. On the contrary, Barrett et al. (2009) found taxic richness to remain stable across the Norian-Rhaetian boundary for theropods, and to drop for sauropodomorphs, when the rock record is accounted for. Matching our taxic richness results, our PyRate results show an increase in diversification rates over the Norian-Rhaetian boundary, but keeping sub-zero values (**Figure 2B**). Again, those values match a Rhaetian rise in PBDB collections, which might bear some influence on our results.

Lineage-through-time plots show that the Rhaetian follows trends already present by the end-Norian, with phylogenetic diversity either persisting to decrease or maintaining stable values (**Figure 1B**, **Supplementary Figure S4**). Irmis (2011) found dinosauromorph phylogenetic diversity to reduce in the Rhaetian, but to slightly increase when normalized by the number of stratigraphic units. Likewise, Barrett et al. (2009) found Rhaetian lineage richness to decrease for all major dinosaur groups. Somehow mirroring phylogenetic diversity, the near-zero diversification rates for the Rhaetian found by our EFBD results are either equal or lower than those of the end-Norian (**Figure 3**).

Our phylogeny-intermediated results (i.e., phylogenetic diversity and EFBD results) for the Rhaetian consistently reveal lower values (**Figures 1B**, **3**), compared to those of the taxic/occurrence analyses (**Figure 2**). This matches higher values for the Norian, showing that the Rhaetian high taxic richness may be the result of a prior diversification event. Even if higher than in "Norian 3," the sub-zero rates from occurrence data reveals no meaningful diversification in the Rhaetian. Hence, taken as a whole, our results seem to indicate that the Rhaetian has not witnessed any major diversification event for terrestrial Pan-Aves; what is mostly in agreement with previous studies, except for Starrfelt and Liow (2016) and Tennant et al. (2018).

Patterns Across the Triassic-Jurassic Boundary

Our results show that a drop in terrestrial Pan-Aves taxic richness takes place across the Triassic-Jurassic boundary, matching that of PBDB collections with records of the group, which is much weaker than that for continental tetrapods in general (**Figure 2A**). This agrees with the dinosaur richness estimates of Starrfelt and Liow (2016) and Tennant et al. (2018), but most prior studies inferred instead a rise in dinosauromorph/dinosaur taxic richness from the Rhaetian to the Hettangian (Barrett et al., 2009; Butler et al., 2011; Upchurch et al., 2011; Irmis, 2011; Starrfelt and Liow, 2016). Yet, Barrett et al. (2009) found that this is the case only for ornithischians, when data are normalised by the rock record. Our results show a similar pattern of decrease in phylogenetic diversity (**Figure 1B**, **Supplementary Figure S4**), but mostly following a reduction trend already present in the Rhaetian. Again, this differs from most previous estimates of lineage richness, which increases in the Hettangian for Dinosauromorpha (most results of Irmis, 2011), as well as for all major dinosaur groups (Barrett et al., 2009). Such differences may be explained by the increased sampling of our dataset, as well as by not accounting for the diversity of non-dinosaurian taxa, in the case of Barrett et al. (2009), and by the employed methods of time-calibration and normalisation, in the case of Irmis (2011).

Perhaps the most striking of our results is the Hettangian peak in diversification rates from occurrence data (PyRate results; **Figure 2B**). However, as discussed by Černý et al. (2021), some diversification shifts by PyRate might not be real, but artificially generated by high rates of fossil preservation instead of net diversification rates. Thus, this Hettangian peak could simply be the product of a preservational bias, possibly linked to the higher number of PBDB collections—used here as a proxy for fossil localities—in the Sinemurian (**Figure 2A**), which could have generated the earlier diversification peak recorded here. Indeed, when the EFBD model is instead used for estimating net diversification rates, the Hettangian exhibits near-zero values, equal or slight lower than those for the Rhaetian (**Figure 3**). Although using time bins not strictly comparable to ours, Lloyd et al. (2008) found much lower diversification rates towards the Early Jurassic than for most of the Late Triassic, unlike the results presented here (see next section).

In sum, except for the probably spurious PyRate result for the Hettangian, all the metrics used here inform that no increase in richness nor higher diversification rates are seen right after the

Triassic-Jurassic boundary. These results differ from the general notion that dinosaurs further radiated following the end-Triassic extinction of several tetrapod groups (Olsen et al., 1987; Olsen et al., 2002). Our results may be simply an outcome of employing an updated dataset, compared to those of about one decade ago, as to better approach the results of more recent studies (Tennant et al., 2018). Yet, although analyses focusing on subgroups were not conducted here, a group-by-group look at Triassic-Jurassic pan-avian diversity patterns may provide important hints. Firstly, dinosaurs are the only terrestrial members of the group to enter the Jurassic, so that analyses focusing on this clade will necessarily produce relatively higher richness values for that Period, because they do not account for the Triassic record of other terrestrial pan-avians. As for the three major dinosaur groups, most prior studies (Barrett et al., 2009; Irmis, 2011; Upchurch et al., 2011; Starrfelt and Liow, 2016) found that ornithischians clearly increased richness across the boundary, whereas the contrary is the case for sauropodomorphs (Apaldetti et al., 2021), with theropods getting intermediate results. Hence, the fact that sauropodomorphs account for more than half of our sample across the Triassic-Jurassic boundary (**Figure 1A**) may explain why we retrieved lower Hettangian richness values.

Indeed, the end-Triassic extinction of pseudosuchian and therapsid groups most likely emptied ecospace for dinosaurs to expand into during the Jurassic. This is shown here by the major drop in continental PBDB collections with tetrapods, relative to those with terrestrial pan-avians (**Figure 2A**); meaning that the poorer record of Early Jurassic tetrapod-bearing sites did not affect much the taxic richness of terrestrial Pan-Aves, because the group became concomitantly more prevalent. Yet, our study indicates that the Early Jurassic rise of dinosaurs did not occur quickly and homogeneously for the entire group. Higher richness/diversification rates appear later in the Early Jurassic (see below), so that dinosaur upsurge after the extinction was more gradual than previously hinted. Nonetheless, theropods and especially ornithischians appear to have more rapidly expanded into ecospaces following the mass extinction. This may be because these groups had more equivalent ecological roles—i.e., small to medium herbivores and medium to large carnivores—to those of the extinct forms. Sauropodomorphs, on the other hand, were already quite dominant by the end of the Triassic, so that the extinction of other taxa seems to have not driven the group to major macroevolutionary shifts (Apaldetti et al., 2018; Apaldetti et al., 2021; Pol et al., 2020).

Early Jurassic Dinosaur Diversity

Although we are confident about the patterns described for the earliest Early Jurassic, those of later time bins should be taken with care due to possible "edge effect," in particular those of the two Toarcian time bins. Taxic diversity generally tends to reduce along the Early Jurassic, although the strong drop within the Pliensbachian may be biased by fewer PBDB collections (**Figure 2A**). Minor instances of increase are seen in the first halves of both Pliensbachian and Toarcian (**Figure 2A**), whereas lineage-through-time plots record a rise near the boundary between the two stages (**Figure 1B**, **Supplementary Figure S4**), which is however not seen if "ghost lineages" are not included in the phylogenetic trees (**Supplementary Figure S5**). This matches the net diversification values from occurrence data (**Figure 2B**), which show overall negative rates along most of the Early Jurassic, with a small increase early in the Toarcian. The EFBD results show a similar pattern, with overall sub-zero diversification rates, but higher near the Pliensbachian-Toarcian boundary (**Figure 3**). The strong decreases of diversification rates estimated from the EFBD model seen in "Toarcian 2" are possibly an "edge effect" artefact driven from the difficulty of estimating realistic values of the sampling parameter (Φ0) for extinct-only datasets. In general, it seems that the extension of ghost-lineages of Tr-EJ taxa in the phylogeny-intermediated analyses pulls the early Toarcian increase in diversification and richness slightly backwards in time, but this has to be evaluated with care because of potential "edge effect" biases.

For both for taxic richness and phylogenetic diversity, Irmis (2011) found a marked Early Jurassic decrease, with a small rise either in the Pliensbachian (for phylogenetic diversity when the rock record is taken into account) or in the Toarcian; what is in general agreement with the results found here. On the contrary, other studies found an increase in taxic richness in the Sinemurian, followed by a general decrease, in cases with a small Toarcian rise (Butler et al., 2011; Upchurch et al., 2011; Starrfelt and Liow, 2016; Tennant et al., 2018). Barrett et al. (2009) found a general Early Jurassic reduction trend in richness for all the tree major dinosaur groups independently, with a small Pliensbachian increase of theropod and sauropodomorph phylogenetic diversity. Instead, Pol et al. (2020) found a marked decrease in sauropodomorph phylogenetic diversity in the Pliensbachian, followed by a rise along the Toarcian. Accordingly, the emerging pattern for both ours and previous results is that dinosaur richness starts relatively high in the Early Jurassic, but decreases afterwards, with a small rise around the Toarcian. That is an interesting scenario, indicating that dinosaur diversified and already experienced an augmented diversity by the end of the Early Jurassic, which will characterize younger stages of the Mesozoic (Wang and Dodson, 2006). Again, this differs from the results of Lloyd et al. (2008), which found dinosaur diversification rates to be generally lower towards the end of the Early Jurassic; although the selection of time bins makes those studies difficult to compare. Irmis (2011) considered the Early Jurassic drop in dinosaur diversity to result from sampling biases, but the decoupling between taxic richness patterns and the number of PBDB collections found here, except for the passage between "Pliensbachian 1" and "Pliensbachian 2" (**Figure 2A**), indicates otherwise.

Body-Size Changes Along the Early Evolution of Terrestrial Pan-Aves

The mean body size of terrestrial Pan-Aves shows no abrupt changes across the Tr-EJ; instead, a steady general increase trend is seen along that time interval, somewhat stronger in the Triassic than in the Jurassic (**Figure 4A**). Slightly more pronounced inflections are seen in the reduction from "Carnian 1" to "Carnian 2" and the increase

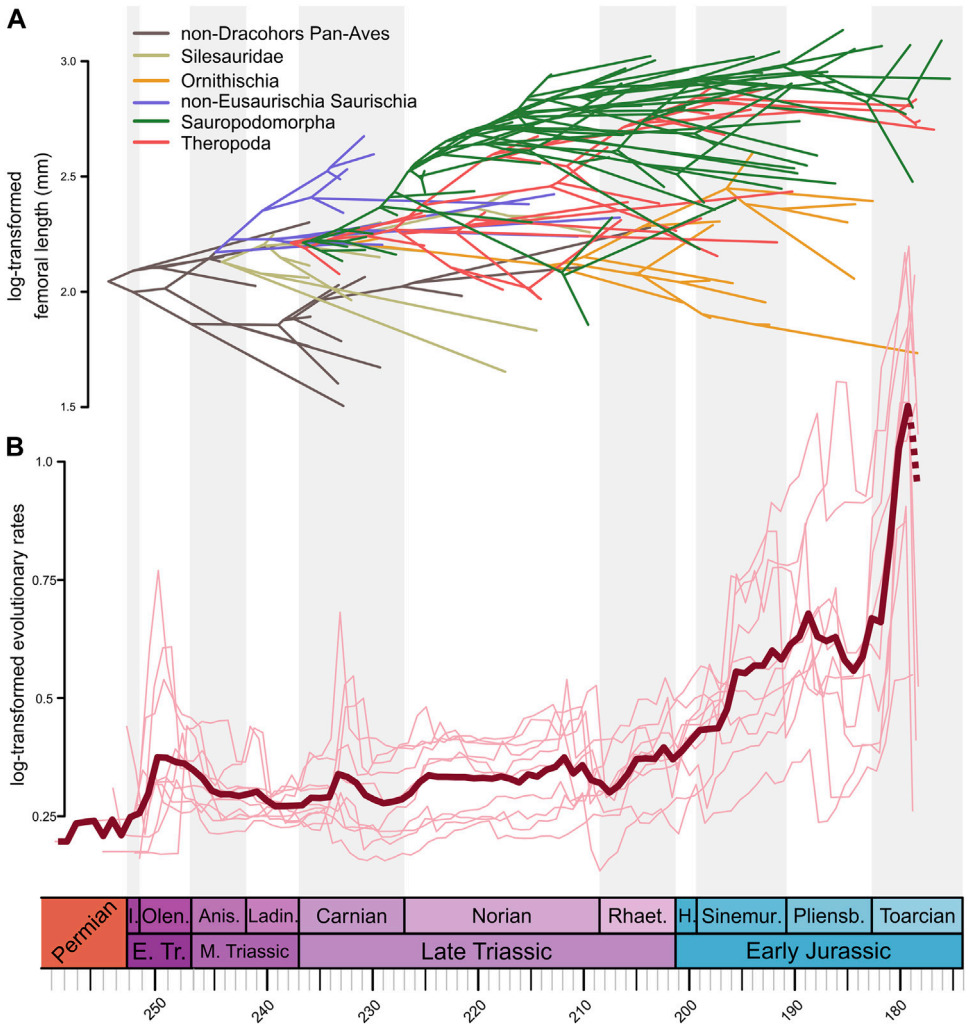

FIGURE 5 | (A) Phenogram of Triassic to Early Jurassic Pan-Aves (excluding pterosaurs) with body size incorporated (i.e., log-transformed femoral length in millimeters). Phylogenetic relationships displayed as in our supertree ST 1 (silesaurids external to Dinosauria, theropods forming Saurischia with sauropodomorphs, and herrerasaurs external to Eusaurischia). **(B)** Through-time rates of body size evolution (log-transformed relative evolutionary rate scalar) of terrestrial Pan-Aves estimated using a heterogeneous rates (or variable rates) model in BayesTraits. Light red lines represent values for each of the ten trees from the ST 1 with "ghost lineages." Dark red line represents mean rate values (mean scalar) from all ten trees. Dashed red line represents the uncertainty of patterns through the Toarcian from a possible "edge effect." Timescale abbreviations: as in **Figure 1**.

from "Norian 2" to "Norian 3." On the contrary, body size disparity shows a marked increase from "Carnian 1" to "Carnian 2" (**Figure 4B**), resulting from an increase in maximum size and, especially, a decrease in minimum size (**Figure 4A**). Indeed, relative to the small-to medium-sized Middle Triassic pan-avians, the Carnian witnessed a major rise in body size disparity within the group, with the appearance of tiny forms, like the ca. 10 cm long *Kongonaphon kely* (Kammerer et al., 2020), along with the first large-bodied dinosaurs, such as the up to 6 m long "*Frenguellisaurus sanjuanensis*" (Novas et al., 2021). For the rest of the Tr-EJ, body size disparity increases slightly at "Norian 3" and "Simemurian 1"—mainly due to increases in maximum size—and decreases near the Pliensbachian-Toarcian boundary—which is related to a reduction in minimum size.

When phylogenetic information is considered (i.e., through-time plots with ancestral body sizes; **Supplementary Figure S28**), the extension of ghost lineages significantly increases Middle Triassic size disparity, so that the "Carnian 2" increase is not so strong. Likewise, the extension of sauropodomorph, ornithischian, and theropod ghost lineages—respectively in ST2, ST3, and ST4 (**Supplementary Figure S29**)—increases the maximum size in "Carnian 1", so that only for ST1 mean body size does not reduce along the Carnian (**Supplementary Figure S28**). Also, the "Norian 3" increase in mean size is less marked for ST2 and ST3 (**Supplementary Figure S28**), probably because maximum sizes are already higher in "Norian 2" for those topologies (**Supplementary Figure S29**). A small decrease in mean body size is seen across the Triassic-Jurassic boundary for all topologies, as well as for the results without ancestral states (**Figure 4**, **Supplementary Figure S28**). The "Norian 3" peak in

body size disparity is generally less marked for all topologies, compared to when ancestral states are not estimated. On the other hand, the "Simemurian 1" peak is maintained, but reduced for ST3 (**Supplementary Figure S28**), probably because accounting for silesaurid sizes within the ornithischian lineage results in higher Hettangian disparity. Finally, the low Pliensbachian disparity seen in the results without ancestral body sizes is kept across all topologies when phylogenetic information is accounted for.

Pradelli et al. (2022) found a general reduction in body size of "non-Dinosauria Pan-Aves" from the Anisian to the Ladinian-Carnian. Because it excludes dinosaurs, these results are not strictly comparable to ours. Yet, that shift may be correlated with the slight reduction in mean body size we found for the whole Pan-Aves in "Carnian 2," which is probably driven by the record of smaller-sized non-dinosaurian members of the group in that time bin (**Figure 5A**). Marked increases in both mean and maximum body size were identified in the Carnian for dinosauromorphs (Irmis, 2011) and ornithodirans (Turner and Nesbitt, 2013). We did recognize an equivalent maximum size increase around that time frame, mainly lead by the appearance of large herrerasaurs (**Figures 4A**, **5A**), but because there is a concomitant decrease in minimum size, the mean body size shows no expressive changes. These shifts right follow the emplacement of the Wrangellia LIP and the correlated CPE, so that the environmental conditions following that event may have favoured the establishment of variable body sizes among terrestrial pan-avians.

Ornithodiran/dinosauromorph maximum and mean body size continue to increase after the Carnian. Yet, whereas previous estimates show changes to cluster in the first half of the Norian (Irmis, 2011; Turner and Nesbitt, 2013), we found stronger increases towards the end of that Stage. Either earlier or later in the Norian, that fluctuation is most probably driven by an increase in sauropodomorph body size, as previously recognized by several authors (Benson et al., 2014; Apaldetti et al., 2018; Apaldetti et al., 2021; Pol et al., 2020; Pradelli et al., 2022), but larger theropods also appear at that time (**Figure 5A**). The much stronger Late Triassic shifts in body size parameters, found by some previous studies (Carrano, 2006; Benson et al., 2014), usually towards higher disparity and larger body sizes, are likely related to their less comprehensive sampling, restricted to dinosaurs, and are not strictly comparable to our results for the entire realm of terrestrial Pan-Aves.

Olsen et al. (2002) proposed that the end-Triassic mass extinction (i.e., CAMP emplacement) led dinosaurs, particularly theropods, to attain larger sizes early in the Jurassic. This idea has been questioned by various authors (Irmis, 2011; Griffin, 2019; Griffin and Nesbitt, 2019; Spiekman et al., 2021), who claimed that large theropods were already present in the Triassic. Yet, because these were likely rare (Griffin, 2019) and still comparatively smaller than Early Jurassic taxa, studies keep finding a theropod size increase after the Triassic (Turner and Nesbitt, 2013); even if not statistically significant (e.g., Pradelli et al., 2022). This broadly agrees with our results (**Figures 4A**, **5A**), which show slightly larger theropods early in the Jurassic. In addition, our results also agree with recent finds that reveal no sauropodomorph maximum size increase after end-Triassic extinction (Apaldetti et al., 2018; Apaldetti et al., 2021; Pol et al., 2020; Pradelli et al., 2022). At the same time however, our results did not reveal any influence of the minimal size increase of sauropodomorphs inferred for that boundary (Apaldetti et al., 2021). The lack of meaningful body size changes in terrestrial Pan-Aves across the Triassic-Jurassic boundary in our analyses (**Figure 4**, **Supplementary Figure S28**) also agrees with the results of Brusatte et al. (2008), which shows no significant shifts in pan-avian morphological disparity at the time. Finally, as our results seem strongly driven by patterns seen in sauropodomorphs, which form the bulk of the pan-avian records at the Triassic-Jurassic boundary, they do not strictly refute the idea that theropods increased their size after the mass extinction.

In agreement with some previous studies (Turner and Nesbitt, 2013; Benson et al., 2014), we recovered a very general trend towards larger terrestrial Pan-Aves along the Early Jurassic (**Figure 4**). More specifically, Irmis (2011) recognised an increase in mean body size during the Pliensbachian-Toarcian, inferred as mainly driven by a reduction in minimum size. A Pliensbachian-Toarcian increase in both mean and minimum body size was also recovered for sauropodomorphs by Pradelli et al. (2022), corroborating a study of Pol et al. (2020), which associated a severe minimum size reduction in those dinosaurs to climatic changes related to the emplacement of the large Gondwanan igneous provinces of Chon Aike and Karoo-Ferrar. Similar results were found here (although these results should be taken with care due to possible "edge effect"), with an increase in the minimum size and a decrease in size disparity of terrestrial Pan-Aves at "Pliensbachian 2" and "Toarcian 1" (**Figure 4**), likely reflecting sauropodomorph patterns and maybe driven by those environmental shifts. Meanwhile, a slight general body size decrease was recognised for tetanuran theropods along the Early Jurassic (**Figure 5A**, **Supplementary Figure S28**), as already inferred by other studies (Turner and Nesbitt, 2013; Benson et al., 2014; Pradelli et al., 2022).

Finally, we found relatively low rates of body size evolution for terrestrial Pan-Aves during the entire Triassic, markedly rising in the Early Jurassic (**Figure 5B**; **Supplementary Figures S30–31**). This is consistent with the results of Turner and Nesbitt (2013), in which higher rates are also seen during the Early Jurassic, whereas Benson et al. (2014) found low rates for the entire time interval sampled here. Yet, a more detailed reading of our results shows important variations along the Triassic. Initial high rates are seen in early in the Olenekian, possibly related to the occupation of ecospace after the Permo-Triassic extinction, followed by a steady decrease until a second rise in the Carnian. Rates get low again, but rise in a two-fold scheme in the early and late Norian, to fall again early in the Rhaetian, only to start rising towards the higher Jurassic rates late in that Stage. Turner and Nesbitt (2013) also found relatively higher rates in the Carnian and late Norian, depending on the employed calibration, somewhat mirroring the results found here. Further, the higher Carnian rates match the increases in taxic richness (**Figure 2A**), net diversification values from occurrence data (**Figure 2B**), and body size disparity (**Figure 4B**), which might be somehow correlated with the environmental changes linked to the CPE. The Norian shifts in body size rates are harder to compare to those of other diversity metrics, but higher phylogenetic diversity (**Figure 1B**) and size disparity (**Figure 4B**) have been recorded late in that Stage, fitting the environmental changes discussed by Kent and Clemmensen (2021). Finally, the general Rhaetian-Jurassic increase in body size rates broadly matches some other diversity metrics analysed here

(**Figures 1B**, **2**, **3**, **4B**), with a Toarcian rise preceded by a Pliesnbachian drop of possible environmental causes (Pol et al., 2020). Indeed, if not biased by "edge effect," the high rates recorded in the Toarcian may be related to the appearance of the large-bodied eusauropods, which will dominate younger Jurassic ecosystems (Pol et al., 2020).

CONCLUSION

- The Early Triassic lacks body-fossil records of Pan-Aves, but a steady increase in the phylogenetic diversity of the group, along with high rates of body size evolution in the Olenekian, was estimated from phylogeny-based analyses and might fit as part of the biotic recovery from the Permo-Trassic extinction.
- Controversial records of aphanosaurs and silesaurids lead to a minor increase in taxic richness of terrestrial Pan-Aves in the Middle Triassic, along with no major changes in mean body size and body size disparity. Instead, phylogeny-based analyses reveal an increasing phylogenetic diversity, with high net diversification rates (estimated from EFBD), and decreasing rates of body size evolution.
- The Carnian witnessed major macroevolutionary shifts for terrestrial Pan-Aves, with significant increases in taxic richness and body size disparity, and high rates of body size evolution and net diversification (estimated from occurrence data). These patterns might have been driven by the environmental changes related to the CPE. On the other hand, both phylogenetic diversity and net diversification rates (estimated from EFBD) decreases along the Stage.
- Terrestrial Pan-Aves taxic richness remains stable along the Norian, slightly increasing in the Rhaetian. Instead, phylogenetic diversity steadily rises during the former Stage, reducing/stabilizing in the latter. Net diversification rates are higher in the Norian when estimated from EFBD, the opposite happening if based on occurrence data. Mean size and body size disparity steadily increase along the Norian-Rhaetian, but an indicial drop in body size evolutionary rates was estimated for the latter Stage.
- The Triassic-Jurassic boundary is not marked by any major macroevolutionary shift, with trends seen in the Rhaetian generally kept during the earliest Jurassic. The only exception is the high net diversification rates (estimated from occurrence data) in the Hettangian, which might be the by-product of preservational biases. Hence, although the end-Triassic mass extinction surely affected pan-avian evolution, its outcomes result more diffuse and not promptly seen across the boundary.
- Dinosaurs are the only terrestrial Pan-Aves recorded in the Early Jurassic, which starts with a sustained reduction in diversity, overall near-to- or sub-zero diversification rates, and stable body size disparity and mean size values. Further drops in taxic richness, net diversification rates, and body size disparity, as well as low rates of body size evolution, are seen near the Pliensbachian. This may be related to climatic changes akin to igneous activities in Gondwanan areas, whereas more recent patterns recorded here should be interpreted with caution, as possibly biased by an "edge effect."
- Few major macroevolutionary shifts were consistently identified across all analysed parameters or methods employed, suggesting that the early diversification of terrestrial pan-avians during the Triassic and Early Jurassic was more nuanced and complex than anticipated.

DATA AVAILABILITY STATEMENT

The original contributions presented in the study are included in the article/**Supplementary Material**. Additional supplementary can be found in a dedicated Zenodo repository (https://zenodo.org/record/6505159), doi: 10.5281/zenodo.6505159. This includes the datasets used in this study, together with scripts used to run macroevolutionary analyses (i.e., RevBayes, PyRate and BayesTraits) and the outputs of these analyses.

AUTHOR CONTRIBUTIONS

MCL collected the data and PLG conducted analyses. Both authors contributed equally to the conceptualization and writing of the manuscript.

FUNDING

MCL was supported by Fundação de Amparo à Pesquisa do Estado de São Paulo (FAPESP grant number: 2020/07997-4). PLG was supported by the National Science Foundation (NSF DEB grant number: 1754596) and Coordenação de Aperfeiçoamento de Pessoal de Nivel Superior (CAPES grant number: 88887.583087/2020-00).

ACKNOWLEDGMENTS

We thank all contributors to the Paleobiology Database. This is Paleobiology Database official publication 428. We thank Sebastian Höhna, Tom Stubbs, Armin Elsler, and Andrew Meade for help with rates analyses *software* (RevBayes and BayesTraits). We further thank Černý et al. (2021) and Stubbs et al. (2021) for making detailed scripts accessible (for PyRate and BayesTraits analyses), as well as the RevBayes Team for making many tutorials available in their website (https://revbayes.github.io/tutorials/). We also thank Jacopo Dal Corso, Sara Callegaro, and Haijun Song for inviting us to contribute into this article collection, as well as Randall Irmis and two anonymous reviewers, whose constructive comments significantly improved our paper.

SUPPLEMENTARY MATERIAL

The Supplementary Material for this article can be found online at: https://www.frontiersin.org/articles/10.3389/feart.2022.899562/full#supplementary-material

REFERENCES

Anderson, J. F., Hall-Martin, A., and Russell, D. A. (1985). Long-Bone Circumference and Weight in Mammals, Birds and Dinosaurs. *J. Zoology* 207, 53–61. doi:10.1111/j.1469-7998.1985.tb04915.x

Apaldetti, C., Martínez, R. N., Cerda, I. A., Pol, D., and Alcober, O. (2018). An Early Trend Towards Gigantism in Triassic Sauropodomorph Dinosaurs. *Nat. Ecol. Evol.* 2, 1227–1232. doi:10.1038/s41559-018-0599-y

Apaldetti, C., Pol, D., Ezcurra, M. D., and Martínez, R. N. (2021). Sauropodomorph Evolution Across the Triassic-Jurassic Boundary: Body Size, Locomotion, and Their Influence on Morphological Disparity. *Sci. Rep.* 11, 22534. doi:10.1038/s41598-021-01120-w

Baker, J., Meade, A., Pagel, M., and Venditti, C. (2016). Positive Phenotypic Selection Inferred from Phylogenies. *Biol. J. Linn. Soc.* 118, 95–115. doi:10.1111/bij.12649

Bapst, D. W. (2012). Paleotree : An R Package for Paleontological and Phylogenetic Analyses of Evolution. *Methods Ecol. Evol.* 3, 803–807. doi:10.1111/j.2041-210x.2012.00223.x

Baron, M. G., Norman, D. B., and Barrett, P. M. (2017). A New Hypothesis of Dinosaur Relationships and Early Dinosaur Evolution. *Nature* 543, 501–506. doi:10.1038/nature21700

Barrett, P. M., McGowan, A. J., and Page, V. (2009). Dinosaur Diversity and the Rock Record. *Proc. R. Soc. B* 276, 2667–2674. doi:10.1098/rspb.2009.0352

Benson, R. B. J., Campione, N. E., Carrano, M. T., Mannion, P. D., Sullivan, C., Upchurch, P., et al. (2014). Rates of Dinosaur Body Mass Evolution Indicate 170 Million Years of Sustained Ecological Innovation on the Avian Stem Lineage. *PLoS Biol.* 12, e1001853. doi:10.1371/journal.pbio.1001853

Benson, R. B. J. (2018). Dinosaur Macroevolution and Macroecology. *Annu. Rev. Ecol. Evol. Syst.* 49, 379–408. doi:10.1146/annurev-ecolsys-110617-062231

Benson, R. B. J., Godoy, P., Bronzati, M., Butler, R. J., and Gearty, W. (2022). Reconstructed Evolutionary Patterns for Crocodile-Line Archosaurs Demonstrate Impact of Failure to Log-Transform Body Size Data. *Commun. Biol.* 5, 171. doi:10.1038/s42003-022-03071-y

Benton, M. J., Briggs, D. E. G., Clack, J. A., Edwards, D., Galway-Witham, J., Stringer, C. B., et al. (2017). Russia-UK Collaboration in Paleontology: Past, Present, and Future. *Paleontol. J.* 51, 576–599. doi:10.1134/s0031030117060028

Benton, M. J. (1984). Dinosaurs' Lucky Break. *Nat. Hist.* 93, 54–59.

Bernardi, M., Gianolla, P., Petti, F. M., Mietto, P., and Benton, M. J. (2018). Dinosaur Diversification Linked with the Carnian Pluvial Episode. *Nat. Commun.* 9, 1499–1026. doi:10.1038/s41467-018-03996-1

Bernardi, M., Gianolla, P., Petti, F. M., Mietto, P., and Benton, M. J. (2018). Dinosaur Diversification Linked with the Carnian Pluvial Episode. *Nat. Commun.* 9, 1499. doi:10.1038/s41467-018-03996-1

Blackburn, T. J., Olsen, P. E., Bowring, S. A., McLean, N. M., Kent, D. V., Puffer, J., et al. (2013). Zircon U-Pb Geochronology Links the End-Triassic Extinction with the Central Atlantic Magmatic Province. *Science* 340, 941–945. doi:10.1126/science.1234204

Brusatte, S. L., Benton, M. J., Ruta, M., and Lloyd, G. T. (2008). The First 50 Myr of Dinosaur Evolution: Macroevolutionary Pattern and Morphological Disparity. *Biol. Lett.* 4, 733–736. doi:10.1098/rsbl.2008.0441

Brusatte, S. L., Niedźwiedzki, G., and Butler, R. J. (2011). Footprints Pull Origin and Diversification of Dinosaur Stem Lineage Deep into Early Triassic. *Proc. R. Soc. B* 278, 1107–1113. doi:10.1098/rspb.2010.1746

Burgess, S. D., Muirhead, J. D., and Bowring, S. A. (2017). Initial Pulse of Siberian Traps Sills as the Trigger of the End-Permian Mass Extinction. *Nat. Commun.* 8, 164. doi:10.1038/s41467-017-00083-9

Butler, R. J., Benson, R. B. J., Carrano, M. T., Mannion, P. D., and Upchurch, P. (2011). Sea Level, Dinosaur Diversity and Sampling Biases: Investigating the 'common Cause' Hypothesis in the Terrestrial Realm. *Proc. R. Soc. B* 278, 1165–1170. doi:10.1098/rspb.2010.1754

Carrano, M. (2006). "Body-size Evolution in the Dinosauria," in *Amniote Paleobiology: Perspectives on the Evolution of Mammals, Birds, and Reptiles*. Editors M. T. Carrano, R. W. Blob, T. J. Gaudin, and J. R. Wible (Chicago, IL: University of Chicago Press), 225–268.

Carrano, M. T., and Wilson, J. A. (2001). Taxon Distributions and the Tetrapod Track Record. *Paleobiology* 27, 564–582. doi:10.1666/0094-8373(2001)027<0564:tdattt>2.0.co;2

Černý, D., Madzia, D., and Slater, G. J. (2021). Empirical and Methodological Challenges to the Model-Based Inference of Diversification Rates in Extinct Clades. *Syst. Biol.* 71, 153–171.

Chiari, Y., Cahais, V., Galtier, N., and Delsuc, F. (2012). Phylogenomic Analyses Support the Position of Turtles as the Sister Group of Birds and Crocodiles (Archosauria). *BMC Biol.* 10, 65. doi:10.1186/1741-7007-10-65

Clarke, J. A., Mindell, D. P., de Queiroz, K., Hanson, M., Norell, M. A., and Gauthier, J. A. (2020). "Aves C. Linnaeus 1758 [J. A. Clarke, D. P. Mindell, K. de Queiroz, M. Hanson, M. A. Norell, and J. A. Gauthier], Converted Clade Name," in *Phylonyms*. Editors K. de Queiroz, P. D. Cantino, and J. A. Gauthier (Boca Raton, FL: CRC Press), 1247–1254.

Colbert, E. H. (1958). Tetrapod Extinctions at the End of the Triassic Period. *Proc. Natl. Acad. Sci. U.S.A.* 44, 973–977. doi:10.1073/pnas.44.9.973

Dal Corso, J., Bernardi, M., Sun, Y., Song, H., Seyfullah, L. J., Preto, N., et al. (2020). Extinction and Dawn of the Modern World in the Carnian (Late Triassic). *Sci. Adv.* 6, eaba0099. doi:10.1126/sciadv.aba0099

Davies, J. H. F. L., Marzoli, A., Bertrand, H., Youbi, N., Ernesto, M., and Schaltegger, U. (2017). End-Triassic Mass Extinction Started by Intrusive CAMP Activity. *Nat. Commun.* 8, 15596. doi:10.1038/ncomms15596

Desojo, J. B., Fiorelli, L. E., Ezcurra, M. D., Martinelli, A. G., Ramezani, J., Da Rosa, Á. A. S., et al. (2020). The Late Triassic Ischigualasto Formation at Cerro Las Lajas (La Rioja, Argentina): Fossil Tetrapods, High-Resolution Chronostratigraphy, and Faunal Correlations. *Sci. Rep.* 10, 12782. doi:10.1038/s41598-020-67854-1

Ezcurra, M. D. (2010). A New Early Dinosaur (Saurischia: Sauropodomorpha) from the Late Triassic of Argentina: A Reassessment of Dinosaur Origin and Phylogeny. *J. Syst. Palaeontol.* 8, 371–425. doi:10.1080/14772019.2010.484650

Ezcurra, M. D. (2006). A Review of the Systematic Position of the Dinosauriform Archosaur *Eucoelophysis Baldwini* from the Upper Triassic of New Mexico, USA. *Geodiversitas* 28, 649–684.

Ezcurra, M. D., Bandyopadhyay, S., and Gower, D. J. (2021). A New Erythrosuchid Archosauriform from the Middle Triassic Yerrapalli Formation of South-Central India. *Ameghiniana* 58, 132–168. doi:10.5710/amgh.18.01.2021.3416

Ezcurra, M. D., and Butler, R. J. (2018). The Rise of the Ruling Reptiles and Ecosystem Recovery from the Permo-Triassic Mass Extinction. *Proc. R. Soc. B* 285, 20180361. doi:10.1098/rspb.2018.0361

Ezcurra, M. D., Fiorelli, L. E., Martinelli, A. G., Rocher, S., von Baczko, M. B., Ezpeleta, M., et al. (2017). Deep Faunistic Turnovers Preceded the Rise of Dinosaurs in Southwestern Pangaea. *Nat. Ecol. Evol.* 1, 1477–1483. doi:10.1038/s41559-017-0305-5

Farlow, J. O., Schachner, E. R., Sarrazin, J. C., Klein, H., and Currie, P. J. (2014). Pedal Proportions of Poposaurus Gracilis: Convergence and Divergence in the Feet of Archosaurs. *Anat. Rec.* 297, 1022–1046. doi:10.1002/ar.22863

Field, D. J., Bercovici, A., Berv, J. S., Dunn, R., Fastovsky, D. E., Lyson, T. R., et al. (2018). Early Evolution of Modern Birds Structured by Global Forest Collapse at the End-Cretaceous Mass Extinction. *Curr. Biol.* 28, 1825–1831. doi:10.1016/j.cub.2018.04.062

Gavryushkina, A., Welch, D., Stadler, T., and Drummond, A. J. (2014). Bayesian Inference of Sampled Ancestor Trees for Epidemiology and Fossil Calibration. *PLoS Comput. Biol.* 10, e1003919. doi:10.1371/journal.pcbi.1003919

Griffin, C. T. (2019). Large Neotheropods from the Upper Triassic of North America and the Early Evolution of Large Theropod Body Sizes. *J. Paleontology* 93, 1010–1030.

Griffin, C. T., and Nesbitt, S. J. (2019). Does the Maximum Body Size of Theropods Increase across the Triassic-Jurassic Boundary? Integrating Ontogeny, Phylogeny, and Body Size. *Anat. Rec.* 303, 1158–1169. doi:10.1002/ar.24130

Guillerme, T. (2018). dispRity: A Modular R Package for Measuring Disparity. *Methods Ecol. Evol.* 9, 1755–1763. doi:10.1111/2041-210x.13022

Heath, T. A., Huelsenbeck, J. P., and Stadler, T. (2014). The Fossilized Birth-Death Process for Coherent Calibration of Divergence-Time Estimates. *Proc. Natl. Acad. Sci. U. S. A.* 111, E2957–E2966. doi:10.1073/pnas.1319091111

Höhna, S., Landis, M. J., Heath, T. A., Boussau, B., Lartillot, N., Moore, B. R., et al. (2016). RevBayes: Bayesian Phylogenetic Inference Using Graphical Models and an Interactive Model-Specification Language. *Syst. Biol.* 65, 726–736. doi:10.1093/sysbio/syw021

Irmis, R. B., Nesbitt, S. J., Padian, K., Smith, N. D., Turner, A. H., Woody, D., et al. (2007). A Late Triassic Dinosauromorph Assemblage from New Mexico and the Rise of Dinosaurs. *Science* 317 (5836), 358–361.

Irmis, R. B. (2011). Evaluating Hypotheses for the Early Diversification of Dinosaurs. *Earth Environ. Sci. Trans. R. Soc. Edinb.* 101, 397–426. doi:10.1017/s1755691011020068

Kammerer, C. F., Nesbitt, S. J., Flynn, J. J., Ranivoharimanana, L., and Wyss, A. R. (2020). A Tiny Ornithodiran Archosaur from the Triassic of Madagascar and the Role of Miniaturization in Dinosaur and Pterosaur Ancestry. *Proc. Natl. Acad. Sci. U.S.A.* 117, 17932–17936. doi:10.1073/pnas.1916631117

Kent, D. V., and Clemmensen, L. B. (2021). Northward Dispersal of Dinosaurs from Gondwana to Greenland at the Mid-Norian (215–212 Ma, Late Triassic) Dip in Atmospheric pCO2. *Proc. Natl. Acad. Sci. U. S. A.* 118, e2020778118. doi:10.1073/pnas.2020778118

Kuhl, H., Frankl-Vilches, C., Bakker, A., Mayr, G., Nikolaus, G., Boerno, S. T., et al. (2021). An Unbiased Molecular Approach Using 3′-UTRs Resolves the Avian Family-Level Tree of Life. *Mol. Biol. Evol.* 38, 108–127. doi:10.1093/molbev/msaa191

Langer, M. C., Ezcurra, M. D., Bittencourt, J. S., and Novas, F. E. (2010). The Origin and Early Evolution of Dinosaurs. *Biol. Rev.* 85, 55–110. doi:10.1111/j.1469-185x.2009.00094.x

Langer, M. C., and Ferigolo, J. (2013). The Late Triassic Dinosauromorph *Sacisaurus Agudoensis* (Caturrita Formation; Rio Grande Do Sul, Brazil): Anatomy and Affinities. *Geol. Soc. Lond. Spec. Publ.* 379, 353–392. doi:10.1144/sp379.16

Langer, M. C., Ramezani, J., and Da Rosa, Á. A. S. (2018). U-pb Age Constraints on Dinosaur Rise from South Brazil. *Gondwana Res.* 57, 133–140. doi:10.1016/j.gr.2018.01.005

Lee, M. S. Y., Cau, A., Naish, D., and Dyke, G. J. (2014). Morphological Clocks in Paleontology, and a Mid-Cretaceous Origin of Crown Aves. *Syst. Biol.* 63, 442–449. doi:10.1093/sysbio/syt110

Liu, J., Ramezani, J., Li, L., Shang, Q. H., Xu, G. H., Wang, Y. Y., et al. (2018). High-Precision Temporal Calibration of Middle Triassic Vertebrate Biostratigraphy: U-Pb Zircon Constraints for the *Sinokannemeyeria* Fauna and *Yonghesuchus*. *Vertebr. Palasiat.* 56, 16–24.

Lloyd, G. T., Davis, K. E., Pisani, D., Tarver, J. E., Ruta, M., Sakamoto, M., et al. (2008). Dinosaurs and the Cretaceous Terrestrial Revolution. *Proc. R. Soc. B* 275, 2483–2490. doi:10.1098/rspb.2008.0715

Maddison, W. P., and Maddison, D. R. (2019). Mesquite: A Modular System for Evolutionary Analysis. Version 3.61. Available at: http://www.mesquiteproject.org.

Magee, A. F., and Höhna, S. (2021). *Impact of K-Pg Mass Extinction Event on Crocodylomorpha Inferred from Phylogeny of Extinct and Extant Taxa*. bioRxiv, 426715. doi:10.1101/2021.01.14.426715

Magee, A. F., Höhna, S., Vasylyeva, T. I., Leaché, A. D., and Minin, V. N. (2020). Locally Adaptive Bayesian Birth-Death Model Successfully Detects Slow and Rapid Rate Shifts. *PLoS Comput. Biol.* 16, e1007999. doi:10.1371/journal.pcbi.1007999

Mancuso, A. C., Benavente, C. A., Irmis, R. B., and Mundil, R. (2020). Evidence for the Carnian Pluvial Episode in Gondwana: New Multiproxy Climate Records and Their Bearing on Early Dinosaur Diversification. *Gondwana Res.* 86, 104–125. doi:10.1016/j.gr.2020.05.009

Mannion, P. D., Upchurch, P., Carrano, M. T., and Barrett, P. M. (2011). Testing the Effect of the Rock Record on Diversity: A Multidisciplinary Approach to Elucidating the Generic Richness of Sauropodomorph Dinosaurs through Time. *Biol. Rev.* 86, 157–181. doi:10.1111/j.1469-185x.2010.00139.x

Marsicano, C. A., Domnanovich, N. S., and Mancuso, A. C. (2007). Dinosaur Origins: Evidence from the Footprint Record. *Hist. Biol.* 19, 83–91. doi:10.1080/08912960600866920

Marsicano, C. A., Irmis, R. B., Mancuso, A. C., Mundil, R., and Chemale, F. (2016). The Precise Temporal Calibration of Dinosaur Origins. *Proc. Natl. Acad. Sci. U.S.A.* 113, 509–513. doi:10.1073/pnas.1512541112

McPhee, B. W., Bordy, E. M., Sciscio, L., and Choiniere, J. N. (2017). The Sauropodomorph Biostratigraphy of the Elliot Formation of Southern Africa: Tracking the Evolution of Sauropodomorpha Across the Triassic–Jurassic Boundary. *Acta Palaeontol. Pol.* 62, 441–465. doi:10.4202/app.00377.2017

Meade, A., and Pagel, M. (2017). BayesTraits V3.0. Available at: http://www.evolution.reading.ac.uk/BayesTraitsV3/BayesTraitsV3.html.

Müler, R. T., Langer, M. C., Bronzati, M., Pacheco, C. P., Cabreira, S. F., and Dias-da-Silva, S. (2018). Early Evolution of Sauropodomorphs: Anatomy and Phylogenetic Relationships of a Remarkably Wellpreserved Dinosaur from the Upper Triassic of Southern Brazil. *Zoological J. Linn. Soc.* 184, 1187–1248.

Müller, R. T., and Garcia, M. S. (2020). A Paraphyletic 'Silesauridae' as an Alternative Hypothesis for the Initial Radiation of Ornithischian Dinosaurs. *Biol. Lett.* 16, 20200417. doi:10.1098/rsbl.2020.0417

Nesbitt, S. J., Barrett, P. M., Werning, S., Sidor, C. A., and Charig, A. J. (2013). The Oldest Dinosaur? A Middle Triassic Dinosauriform from Tanzania. *Biol. Lett.* 9, 20120949. doi:10.1098/rsbl.2012.0949

Nesbitt, S. J., Sidor, C. A., Irmis, R. B., Angielczyk, K. D., Smith, R. M. H., and Tsuji, L. A. (2010). Ecologically Distinct Dinosaurian Sister Group Shows Early Diversification of Ornithodira. *Nature* 464, 95–98. doi:10.1038/nature08718

Nesbitt, S. J., Smith, N. D., Irmis, R. B., Turner, A. H., Downs, A., and Norell, M. A. (2009). A Complete Skeleton of a Late Triassic Saurischian and the Early Evolution of Dinosaurs. *Science* 326, 1530–1533. doi:10.1126/science.1180350

Novas, F. E., Agnolin, F. L., Ezcurra, M. D., Temp Müller, R., Martinelli, A. G., and Langer, M. C. (2021). Review of the Fossil Record of Early Dinosaurs from South America, and its Phylogenetic Implications. *J. S. Am. Earth Sci.* 110, 103341. doi:10.1016/j.jsames.2021.103341

Olsen, P. E., Kent, D. V., Sues, H.-D., Koeberl, C., Huber, H., Montanari, A., et al. (2002). Ascent of Dinosaurs Linked to an Iridium Anomaly at the Triassic-Jurassic Boundary. *Science* 296, 1305–1307. doi:10.1126/science.1065522

Olsen, P. E., Shubin, N. H., and Anders, M. H. (1987). New Early Jurassic Tetrapod Assemblages Constrain Triassic-Jurassic Tetrapod Extinction Event. *Science* 237, 1025–1029. doi:10.1126/science.3616622

Olsen, P. E., Smith, J. B., and McDonald, N. G. (1998). Type Material of the Type Species of the Classic Theropod Footprint generaEubrontes, Anchisauripus, and Grallator (Early Jurassic, Hartford and Deerfield Basins, Connecticut and Massachusetts, U.S.A.). *J. Vertebrate Paleontology* 18, 586–601. doi:10.1080/02724634.1998.10011086

Pacheco, C., Müller, R. T., Langer, M., Pretto, F. A., Kerber, L., and Dias da Silva, S. (2019). *Gnathovorax Cabreirai*: A New Early Dinosaur and the Origin and Initial Radiation of Predatory Dinosaurs. *PeerJ* 7, e7963. doi:10.7717/peerj.7963

Pagel, M., and Meade, A. (2006). Bayesian Analysis of Correlated Evolution of Discrete Characters by Reversible-Jump Markov Chain Monte Carlo. *Am. Nat.* 167, 808–825. doi:10.1086/503444

Peecook, B. R., Sidor, C. A., Nesbitt, S. J., Smith, R. M. H., Steyer, J. S., and Angielczyk, K. D. (2013). A New Silesaurid from the Upper Ntawere Formation of Zambia (Middle Triassic) Demonstrates the Rapid Diversification of Silesauridae (Avemetatarsalia, Dinosauriformes). *J. Vertebrate Paleontology* 33, 1127–1137. doi:10.1080/02724634.2013.755991

Plummer, M., Best, N., Cowles, K., and Vines, K. (2006). CODA: Convergence Diagnosis and Output Analysis for MCMC. *R. News* 6, 7–11.

Pol, D., Ramezani, J., Gomez, K., Carballido, J. L., Carabajal, A. P., Rauhut, O. W. M., et al. (2020). Extinction of Herbivorous Dinosaurs Linked to Early Jurassic Global Warming Event. *Proc. R. Soc. B* 287, 20202310. doi:10.1098/rspb.2020.2310

Pradelli, L. A., Leardi, J. M., and Ezcurra, M. D. (2022). Body Size Disparity of the Archosauromorph Reptiles During the First 90 Million Years of Their Evolution. *Ameghiniana* 59, 47–77. doi:10.5710/amgh.16.09.2021.3441

Rambaut, A., Drummond, A. J., Xie, D., Baele, G., and Suchard, M. A. (2018). Posterior Summarization in Bayesian Phylogenetics Using Tracer 1.7. *Syst. Biol.* 67, 901–904. doi:10.1093/sysbio/syy032

Revell, L. J. (2012). Phytools: An R Package for Phylogenetic Comparative Biology (And Other Things). *Methods Ecol. Evol.* 2, 217–223.

Ronquist, F., Klopfstein, S., Vilhelmsen, L., Schulmeister, S., Murray, D. L., and Rasnitsyn, A. P. (2012a). A Total-Evidence Approach to Dating with Fossils, Applied to the Early Radiation of the Hymenoptera. *Syst. Biol.* 61, 973–999. doi:10.1093/sysbio/sys058

Ronquist, F., Teslenko, M., Van Der Mark, P., Ayres, D. L., Darling, A., Höhna, S., et al. (2012b). MrBayes 3.2: Efficient Bayesian Phylogenetic Inference and Model Choice across a Large Model Space. *Syst. Biol.* 61, 539–542. doi:10.1093/sysbio/sys029

Sakamoto, M., Benton, M. J., and Venditti, C. (2016). Dinosaurs in Decline Tens of Millions of Years Before Their Final Extinction. *Proc. Natl. Acad. Sci. U.S.A.* 113, 5036–5040. doi:10.1073/pnas.1521478113

Sengupta, S., Ezcurra, M. D., and Bandyopadhyay, S. (2017). A New Horned and Long-Necked Herbivorous Stem-Archosaur from the Middle Triassic of India. *Sci. Rep.* 7, 8366. doi:10.1038/s41598-017-08658-8

Sereno, P. C. (1990). The Evolution of Dinosaurs. *Science* 5423, 2137–2147.
Silvestro, D., Cascales-Miñana, B., Bacon, C. D., and Antonelli, A. (2015). Revisiting the Origin and Diversification of Vascular Plants Through a Comprehensive Bayesian Analysis of the Fossil Record. *New Phytol.* 207, 425–436. doi:10.1111/nph.13247
Silvestro, D., Salamin, N., Antonelli, A., and Meyer, X. (2019). Improved Estimation of Macroevolutionary Rates from Fossil Data Using a Bayesian Framework. *Paleobiology* 45, 546–570.
Silvestro, D., Salamin, N., and Schnitzler, J. (2014b). PyRate: A New Program to Estimate Speciation and Extinction Rates from Incomplete Fossil Data. *Methods Ecol. Evol.* 5, 1126–1131.
Silvestro, D., Schnitzler, J., Liow, L. H., Antonelli, A., and Salamin, N. (2014a). Bayesian Estimation of Speciation and Extinction from Incomplete Fossil Occurrence Data. *Syst. Biol.* 63, 349–367. doi:10.1093/sysbio/syu006
Sookias, R. B., Butler, R. J., and Benson, R. B. (2012b). Rise of Dinosaurs Reveals Major Body-Size Transitions Are Driven by Passive Processes of Trait Evolution. *Proc. Biol. Sci.* 279, 2180–2187. doi:10.1098/rspb.2011.2441
Sookias, R. B., Benson, R. B. J., and Butler, R. J. (2012a). Biology, Not Environment, Drives Major Patterns in Maximum Tetrapod Body Size Through Time. *Biol. Lett.* 8, 674–677. doi:10.1098/rsbl.2012.0060
Spiekman, S. N. F., Ezcurra, M. D., Butler, R. J., Fraser, N. C., and Maidment, S. C. R. (2021). Pendraig Milnerae, a New Small-Sized Coelophysoid Theropod from the Late Triassic of Wales. *R. Soc. open Sci.* 8, 210915. doi:10.1098/rsos.210915
Stadler, T. (2010). Sampling-Through-Time in Birth-Death Trees. *J. Theor. Biol.* 267, 396–404. doi:10.1016/j.jtbi.2010.09.010
Starrfelt, J., and Liow, L. H. (2016). How Many Dinosaur Species Were There? Fossil Bias and True Richness Estimated Using a Poisson Sampling Model. *Phil. Trans. R. Soc. B* 371, 20150219. doi:10.1098/rstb.2015.0219
Stubbs, T. L., Pierce, S. E., Elsler, A., Anderson, P. S., Rayfield, E. J., and Benton, M. J. (2021). Ecological Opportunity and the Rise and Fall of Crocodylomorph Evolutionary Innovation. *Proc. Royal Soc. B* 288 (1947), 20210069.
Sun, Y., Joachimski, M. M., Wignall, P. B., Yan, C., Chen, Y., Jiang, H., et al. (2012). Lethally Hot Temperatures During the Early Triassic Greenhouse. *Science* 338, 366–370. doi:10.1126/science.1224126
Tennant, J. P., Chiarenza, A. A., and Baron, M. (2018). How Has Our Knowledge of Dinosaur Diversity Through Geologic Time Changed Through Research History? *PeerJ* 6, e4417. doi:10.7717/peerj.4417
Tribble, C. M., Freyman, W. A., Landis, M. J., Lim, J. Y., Barido-Sottani, J., Kopperud, B. T., et al. (2021). RevGadgets: An R Package for Visualizing Bayesian Phylogenetic Analyses from RevBayes. *Methods Ecol. Evol.* 13, 314–323. doi:10.1111/2041-210x.13750
Turner, A. H., and Nesbitt, S. J. (2013). Body Size Evolution During the Triassic Archosauriform Radiation. *Geol. Soc. Lond. Spec. Publ.* 379, 573–597. doi:10.1144/sp379.15
Turner, A. H., Pritchard, A. C., and Matzke, N. J. (2017). Empirical and Bayesian Approaches to Fossil-Only Divergence Times: A Study Across Three Reptile Clades. *PLoS One* 12, e0169885. doi:10.1371/journal.pone.0169885
Upchurch, P., Mannion, P. D., Benson, R. B. J., Butler, R. J., and Carrano, M. T. (2011). "Geological and Anthropogenic Controls on the Sampling of the Terrestrial Fossil Record: A Case Study from the Dinosauria," in *Comparing the Geological and Fossil Records: Implications for Biodiversity Studies*. Editors A. J. McGowan and A. B. Smith (London: Geological Society of London), 209–240. doi:10.1144/sp358.14
Venditti, C., Meade, A., and Pagel, M. (2011). Multiple Routes to Mammalian Diversity. *Nature* 479, 393–396. doi:10.1038/nature10516
Wang, S. C., and Dodson, P. (2006). Estimating the Diversity of Dinosaurs. *Proc. Natl. Acad. Sci. U.S.A.* 103, 13601–13605. doi:10.1073/pnas.0606028103
Whiteside, J. H., Lindström, S., Irmis, R. B., Glasspool, I. J., Schaller, M. F., Dunlavey, M., et al. (2015). Extreme Ecosystem Instability Suppressed Tropical Dinosaur Dominance for 30 Million Years. *Proc. Natl. Acad. Sci. U.S.A.* 112, 7909–7913. doi:10.1073/pnas.1505252112
Whiteside, J. H., Olsen, P. E., Eglinton, T., Brookfield, M. E., and Sambrotto, R. N. (2010). Compound-Specific Carbon Isotopes from Earth's Largest Flood Basalt Eruptions Directly Linked to the End-Triassic Mass Extinction. *Proc. Natl. Acad. Sci. U.S.A.* 107, 6721–6725. doi:10.1073/pnas.1001706107

Conflict of Interest: The authors declare that the research was conducted in the absence of any commercial or financial relationships that could be construed as a potential conflict of interest.

frontiers | Frontiers in Earth Science

ORIGINAL RESEARCH
published: 13 June 2022
doi: 10.3389/feart.2022.883788

Paleoenvironmental and Biotic Changes in the Late Triassic of Argentina: Testing Hypotheses of Abiotic Forcing at the Basin Scale

Adriana C. Mancuso[1], Randall B. Irmis[2,3], Tomás E. Pedernera[1], Leandro C. Gaetano[4,5], Cecilia A. Benavente[1,6] and Benjamin T. Breeden III[2,3]*

[1]Instituto Argentino de Nivología, Glaciología y Ciencias Ambientales (IANIGLA), CCT-Mendoza, CONICET, Parque General San Martín, Mendoza, Argentina, [2]Natural History Museum of Utah, University of Utah, Salt Lake City, UT, United States, [3]Department of Geology & Geophysics, University of Utah, Salt Lake City, UT, United States, [4]Instituto de Estudios Andinos "Don Pablo Groeber" (IDEAN, UBA-CONICET), Departamento de Ciencias Geológicas, Facultad de Ciencias Exactas y Naturales, Universidad de Buenos Aires, Ciudad Universitaria C1428EHA, Buenos Aires, Argentina, [5]Evolutionary Studies Institute, University of the Witwatersrand, Johannesburg, South Africa, [6]Geology, Facultad de Ciencias Exactas y Naturales (FCEN), Universidad Nacional de Cuyo (UNCuyo), Mendoza, Argentina

OPEN ACCESS

Edited by:
Jacopo Dal Corso,
China University of Geosciences Wuhan, China

Reviewed by:
Piero Gianolla,
Department of Physics and Earth Science, Italy
Alastair Ruffell,
Queen's University Belfast, United Kingdom

***Correspondence:**
Adriana C. Mancuso
amancu@mendoza-conicet.gob.ar

Specialty section:
This article was submitted to Paleontology, a section of the journal Frontiers in Earth Science

Received: 25 February 2022
Accepted: 03 May 2022
Published: 13 June 2022

Citation:
Mancuso AC, Irmis RB, Pedernera TE, Gaetano LC, Benavente CA and Breeden III BT (2022) Paleoenvironmental and Biotic Changes in the Late Triassic of Argentina: Testing Hypotheses of Abiotic Forcing at the Basin Scale. Front. Earth Sci. 10:883788. doi: 10.3389/feart.2022.883788

Paleoenvironmental factors such as climate change are often hypothesized as critical for ecosystem changes over evolutionary time scales. Theoretically, these changes should be observable in the fossil record, but the robust linkage of biotic shifts to climate events remains difficult. The Late Triassic Period is an ideal interval for testing such hypotheses within terrestrial ecosystems because of a number of large-scale climate events, such as the Carnian Pluvial Episode (CPE), and a rich, well-studied fossil record. Nonetheless, at regional to global scales, few linkages have been identified during most of the Late Triassic. Here, we synthesize a multi-proxy basin-scale dataset of paleoenvironmental data, including new information from clay mineralogy and paleosol major- and trace-element geochemistry, to understand paleoclimate changes in the Ischigualasto-Villa Unión Basin of northwestern Argentina. In combination with diversity and relative abundance information from the well-sampled plant and tetrapod fossil record in the basin, we then use accepted evolutionary models of abiotic forcing of changes in ecosystems to test previously proposed hypotheses of floral and faunal variations at a basin scale. We find that although many patterns are best explained by sampling issues and taphonomy, pseudosuchian archosaur diversity and rhynchosaur relative abundance conform to predictions of paleoenvironmental forcing as the climate changed from warmer, drier conditions to more temperate humid conditions. These data demonstrate how high-resolution multi-proxy data and a well-sampled fossil record at a basin-scale can be used to test hypotheses of abiotic forcing of ecosystems in deep time, and highlights where future efforts should be directed in terms of filling data gaps and testing new hypotheses.

Keywords: Carnian Pluvial Episode, Gondwana, Ischigualasto Formation, Ischigualasto-Villa Unión Basin, multiproxy climate dataset

1 INTRODUCTION

Biotic systems are constantly interacting and changing, so they are in dynamic equilibrium (e.g., Vrba, 1995; Faith et al., 2021). Both intrinsic (biotic) and extrinsic (abiotic) factors are proposed as drivers of evolutionary events such as speciation, extinction, and migration (e.g., Vrba, 1995; Benton et al., 2021; Dunne et al., 2021). One of the challenges in the deep-time paleobiologic record is to understand the relative contributions of biotic and abiotic forcing on the assembly and evolution of ecosystems. Given that there is abundant observational evidence for climate change affecting extant ecosystems (e.g., Moritz et al., 2008; Tingley et al., 2009; Rowe et al., 2015), and strong inferential evidence for climate-caused mass extinction events in the geologic past (e.g., see summary in Whiteside and Grice, 2016), a key question is to what extent do abiotic factors such as climate change drive evolution through Earth's history?

The Triassic Period is an ideal study system to help answer this question in deep time, because its record of climate and ecosystem evolution is a particularly dynamic ~50 million year interval. The Triassic was a critical time for the origin and early diversification of Mesozoic ecosystems. On land, during the Triassic, several modern vertebrate clades originated and diversified, such as neopterygian fishes, lissamphibians, lepidosaurs, turtles, dinosaurs, and mammaliaforms (e.g., Fraser and Sues, 2011; Jones et al., 2013; Friedman, 2015; Schoch and Sues, 2015; Giles et al., 2017; Stocker et al., 2019). In Gondwana, which has a particularly rich non-marine fossil record of this time, the tetrapod assemblage is dominated by synapsid and archosauromorph lineages (e.g., Romer, 1970; Ezcurra, 2010; Abdala et al., 2020; Bordy et al., 2020; Schultz et al., 2020). The Late Triassic is also the time of dinosaur origin and diversification, the origin of turtles, the diversification of non-mammaliaform cynodonts that are closely related to the first mammaliaforms, and the decline of basal archosauromophs and early synapsids (see **Supplementary Material**) (Irmis, 2011; Irmis et al., 2011; Whiteside et al., 2011, 2015; Abdala et al., 2020; Dunne et al., 2021). Among terrestrial plants, this period is characterized by the dominance of seed- over spore-based lineages, with gymnosperms typically having greater relative abundance in fossil assemblages than pteridophytes (McElwain, 2018). In Gondwana, the most significant floral change is the replacement of the late Paleozoic *Glossopteris* flora by the Triassic *Dicroidium* flora (Balme and Helby, 1973; Zamunner et al., 2001; Abu Hamad et al., 2008; Chandra et al., 2008; Mays and Mcloughlin, 2019). Thus, recovery after the end-Permian extinction led to the diversification of the *Dicroidium* flora during the Early Triassic (Bodnar et al., 2021), and the Late Triassic is the climax of this floral assemblage in Gondwana (McLoughlin, 2001, 2011; Kustatscher et al., 2018).

From a climate perspective, the Triassic experienced enhanced monsoonal circulation because of the large exposed land area of Pangea across the equator (Kutzbach and Gallimore, 1989; Parrish, 1993; Wilson et al., 1994; Péron et al., 2005; Sellwood and Valdes, 2006; Holz, 2015; Harris et al., 2017). However, there is a common perception of a globally hot, dry, and seasonal climate globally (e.g., Retallack, 2009; Holz, 2015), despite evidence of much more varied climate regimes. In Gondwana, fluctuating climate conditions dominated with arid to semiarid conditions during the Early Triassic (Sellwood and Valdes, 2006; Boucot et al., 2013; Harris et al., 2017; Dunne et al., 2021), and more humid seasonality conditions during the Middle Triassic (Sellwood and Valdes, 2006; Mancuso et al., 2021). The Late Triassic was dominated by seasonal sub-humid conditions with one or more semi-arid intervals, particularly in the interior of the landmass (Sellwood and Valdes, 2006; Dunne et al., 2021; Mancuso et al., 2021). In particular, the "Carnian Pluvial Episode" (CPE) (Simms and Ruffell, 1989, 1990), which recorded an extensive rise in humidity and temperature in many depositional environments, has been documented in Gondwana and in the Tethys and Panthalassa oceans (e.g., Dal Corso et al., 2012, 2015, 2018; Ogg, 2015; Ruffell et al., 2016; Sun et al., 2016; Miller et al., 2017; Mancuso et al., 2020a; Tomimatsu et al., 2021). The CPE is particularly interesting due to the fact that it has been linked with major changes in terrestrial ecosystems (e.g., Goddéris et al., 2008; Benton et al., 2018; Bernardi et al., 2018; Dal Corso et al., 2020).

1.1 Climate and Evolution in the Triassic of Gondwana

A long-standing question has been how spatial and temporal differences in paleoclimate have influenced the distribution and diversity of Triassic biota, and data from the Ischigualasto-Villa Unión Basin have been key parts of these discussions for over 50 years (e.g., Romer, 1970; Colbert, 1971; Robinson, 1971, 1973; Dolby and Balme, 1976; Shubin and Sues, 1991; Foster et al., 1994; Zavattieri and Batten, 1996; Cirilli, 2010; Ezcurra, 2010; César and Colombi, 2013; Whiteside et al., 2015; Kustatscher et al., 2018; Dunne et al., 2021; Liu et al., 2021; Mancuso et al., 2021). The literature contains a variety of hypotheses that relate non-marine Triassic flora and fauna to various paleoclimate conditions; these typically focus on the richness and/or relative abundance of certain taxa to general climate variables such as warmer/colder or wetter/drier. Many of these hypotheses were developed from global datasets and/or other regions, but are important to evaluate because they apply to plant and animal groups preserved within the Ischigualasto-Villa Unión Basin.

More specifically, some groups of plants have been associated with specific climatic conditions, for example, Equisetopsida and Polypodiopsida have been linked to wet episodes of the seasonal subtropical climate during the Triassic (e.g., Channing et al., 2011; Husby, 2013; Bodnar et al., 2018; Coturel et al., 2018). The clade Gymnospermopsida is the most diverse group of plants during the Triassic. The different taxa referred to in this group have been conserved in different environments and exhibit a great variety of forms, which is why they would have developed successfully in a variety of subtropical zone environments with hot and seasonally humid climates (Fritts, 1976; Retallack, 1977; Anderson and Anderson, 1983, 1985, 1989; Holmes, 1985; He et al., 1997; Artabe et al., 2001, 2003; Kerp et al., 2001; Spalletti et al., 2003; Bomfleur et al., 2014). With respect to the recognized microflorisic sub-provinces in Gondwana, the Onslow microflora is suggested to indicate hot and humid climatic conditions, while

the Ipswich microflora is an hypothesized to be indicative of relatively colder temperature zones (Dolby and Blame 1976). Changes in plant richness are also associated with changes in environmental and climatic parameters. These events are interpreted as successive ecological disturbances, rather than as abrupt changes in biodiversity (Sun et al., 2012; Hochuli et al., 2016; Mishra et al., 2017; Fielding et al., 2019; Nowak et al., 2019, 2020; Vajda et al., 2020).

To summarize, the literature contains the following hypotheses that propose a relationship between Triassic plant and non-marine tetrapod assemblage composition and climate:
Hypothesis 1. Plant species richness correlated with humid/arid conditions.

1a. High species richness was associated with higher humidity intervals and lower species richness with seasonally arid periods (Berry and Raison, 1981; Sun et al., 2012; Nowak et al., 2020).

1b. Taxa such as Equisetopsida, Polypodiopsida, and Voltziales preferred humid conditions (Bomfleur et al., 2013; Bodnar et al., 2018; Coturel et al., 2018).

1c. Umkomasiales increased relative abundance in different climatic conditions (Retallack, 1977; Bomfleur and Kerp, 2010; Bomfleur et al., 2014; D'Angelo, 2019).

1d. Others Pteridospermales such as Peltaspermales (Doubinger et al., 1995; Lausberg and Kerp, 2000; Kerp et al., 2001; Di Michele, 2013), Ginkgoales (He et al., 1997; Barboni and Dutra, 2015), Coniferales (Fritts, 1976; Holmes, 1985), and Gnetales (Wang and Zheng, 2010) increased relative abundance during intervals with marked seasonality.

1e. Cycadales and Benettitales were more abundant in hot and dry climatic conditions (Taylor et al., 2009).

Hypothesis 2. Synapsids, particularly traversodontid cynodonts, were more diverse (higher richness) in wetter areas (Whiteside et al., 2011).

2a. Dicynodonts preferred wetter intervals (Liu et al., 2021).

Hypothesis 3. Cynodont richness increased during warm conditions (Liu et al., 2021).

Hypothesis 4. Pseudosuchian richness was highest in warmer, less seasonal conditions (Dunne et al., 2021).

Hypothesis 5. Rhynchosaur abundance increased during more arid intervals (Azevedo et al., 1990).

1.2 Testing for a Climate-Biota Relationship

Despite an abundance of hypotheses linking changes in the Triassic fossil record to climate, there are significant challenges to observing and interpreting a robust correlation between richness or abundance and climate variables. Taphonomic filters and differences in sampling are well-recognized as having the potential to bias observed diversity (Behrensmeyer and Chapman, 1993; Kidwell and Flessa, 1996; Kidwell and Holland, 2002; Falcon-Lang et al., 2009), and equally problematic is the potential mismatch between the spatiotemporal scale/resolution of fossil data, paleoclimatic data, and hypotheses linking the two (e.g., Faith et al., 2021: Fig 3). Although there is a long history of pattern matching approaches, whereby paleontologists try to identify simultaneous changes in the fossil record and paleoenvironmental proxy data, these studies generally have low power and have met with limited success, because they often rely on a posteriori hypotheses from these correlations rather than attempting to test explicitly a priori hypotheses based on our understanding of Earth-life systems (Faith et al., 2021). In contrast, there is an abundance of evolutionary models for biotic response to climate change on geologic timescales (e.g., table 1 in Barnosky, 2001, and references therein). The application of these models to the fossil record provides a stronger way to test for climate-caused biotic change because they make specific predictions about changes in richness and relative abundance, and their timing relative to climate change, that can be tested in the geologic record (Faith et al., 2021). These predictions can also be further refined when ecological preferences and physiological constraints for specific lineages are known from independent evidence (e.g., observations from extant relatives).

Before examining causal models linking climatic and biotic change, it is important to establish the null model. The most basic null hypothesis is that species/lineages/clades do not respond to climate change, but this seems biologically unrealistic given an abundance of modern observational evidence to the contrary (e.g., Huntley, 1991; Thuiller et al., 2005; Moritz et al., 2008; Tingley et al., 2009; Minin and Voskova, 2014; Rowe et al., 2015). A null hypothesis that better matches our understanding of ecological systems is essentially an extension of Hubbell's neutral theory (e.g., Hubbell, 2001; Rosindell et al., 2011, 2012), predicting that each species responds individually to climate change, and therefore net origination and extinction at any particular time interval is at equilibrium. In both cases, there should be no elevated turnover correlated with climate change events, and the pattern would be indistinguishable from normal background origination and extinction.

Models of evolution driven by changes in the physical environment were termed 'Court Jester' hypotheses by Barnosky (2001), to distinguish them from Red Queen hypotheses of evolution driven by biotic interactions. He concluded that Court Jester processes occurred at larger spatiotemporal scales (Barnosky, 2001: Fig 7), making them possibly easier to detect in the fossil record. The most relevant models for this study are the 'relay' and 'turnover pulse' hypotheses proposed by Vrba (1985, 1992, 1993, 1995). She proposed that because species are adapted to both the physical and biologic aspects of their habitat, the primary driver of species turnover is climate change (Vrba, 1985, 1992, 1993). Therefore, during times of stable climate, this should result in relatively little speciation and extinction, but during climate change intervals, there should be elevated "pulses" of origination and extinction observed (Vrba, 1985, 1993, 1995). This is similar to the mathematically-derived 'stationary model' of Stenseth and Maynard Smith (1984), but whereas Vrba's hypothesis focused on turnover within the clade(s), Stenseth and Maynard Smith explicitly modeled communities, and did not distinguish between actual phyletic speciation/extinction, local extirpation, and immigration/emigration (Vrba, 1993).

Vrba (1995) refined the turnover pulse hypothesis with the relay model, which made detailed predictions about the order in which lineages should speciate and go extinct in relation to a climate event. Given a theoretical climate variable that changed

from X to Y, Vrba (1995) predicted the following sequence of events: 1) extinction of species adapted to X; 2) minor speciation of remaining species adapted to X; 3) minor extinctions of species adapted to Y; and 4) speciation of species adapted to Y. So, to use Vrba's (1995: Fig. 3.3) example of a warming trend, there should be an initial pulse of extinction of lineages adapted to cooler conditions (though some speciation of these lineages may still occur), followed by a pulse of speciation of lineages adapted to warmer conditions (though a few warm-adapted species will still go extinct in this interval). In the same contribution, Vrba (1995) proposed the traffic light model, which examined climate forcing of immigration/emigration. This model is less relevant to the current study because we are examining biotic change within a single basin, and do not have equivalent extrabasinal records with which to compare to.

It is important to emphasize that Vrba's (1985, 1992, 1993, 1995) predictions for the turnover pulse and relay models were restricted to speciation (origination) and extinction of species (i.e., changes in species richness); she did not discuss changes in abundance. Despite this, some subsequent studies have applied these models to changes in species' relative abundance through time, without explicitly justifying why this should be the case (e.g., Barnosky, 2001; Bobe et al., 2002). Nonetheless, some logical predictions for abundance can be made as long as the climate event is not so sudden that it appears "instantaneous" in the geologic record. As a climate variable changes over geologic timescales, one might predict an observation of a species declining in abundance prior to its ultimate extinction, or conversely increasing in abundance after its initial origination. In contrast, some studies have observed remarkable stability in species abundance over geologic timescales (dubbed "community inertia") despite experiencing major climatic changes (e.g., McGill et al., 2005). If this is the case more generally, species abundances may be stable until they reach a climate threshold or 'tipping point', after which they suddenly go extinct. In this model, the climate threshold would also instigate speciation and an increase in abundance rapid enough that it is not observed in the fossil record.

Although these evolutionary models provide explicit and testable a priori hypotheses to infer climate-caused biotic change, patterns in the fossil record cannot simply be taken at face value. First, it is important to ask whether the spatial and temporal resolution of available data match that of the hypothesis being tested (Vrba, 1995; Faith et al., 2021: Fig. 3). Time and spatial averaging of fossil assemblages are pervasive (Behrensmeyer et al., 1992; Behrensmeyer and Chapman, 1993; Kidwell and Holland, 2002), so it is critical to recognize whether the effects of these processes has caused any biotic change to be averaged over a larger scale than that of the climate change itself. This consideration also applies to paleoclimate proxy data; do these proxies reflect changes just within a few meters, at the local landscape, regional, or continental to global scales? Similarly, taphonomic and sampling filters can easily distort observed patterns in the fossil record, leading to erroneous inferences about how these data compare to model predictions (e.g., Vrba, 1995: Figs. 3.3–3.4). As one basic example, richness scales with number of fossil specimens and sites, so if we observe a pulsed change in richness in a dataset it may simply reflect change in sample size rather than a paleobiologic signal. Therefore, taphonomic and sampling control of richness and abundance patterns must be evaluated before using these data to test for climate response.

1.3 Hypothesis Predictions

With the above caveats, the turnover pulse and relay models make the following predictions for previously proposed hypotheses that link Triassic floral and tetrapod clades to paleoclimate conditions:

Hypothesis1a: More humid conditions will be associated with a pulse of plant species first appearances (FAs), and more arid conditions will be associated with a pulse of plant species last appearances (LAs).

Hypothesis1b: During more humid conditions there will be a pulse of hydrophytic and hygrophytic plant species FAs and xerophytic plant species LAs; and during more arid conditions, there will be a pulse of mesophytic and xerophytic plant species FAs and hydrophytic/hygrophytic plant species LAs.

Hypothesis 2: The onset of wetter conditions will be associated with a pulse of synapsid FAs, particularly among traversodontids and dicynodonts, and conversely a pulse of LAs with drier conditions.

Hypothesis 3: The onset of warmer conditions will be associated with a pulse of cynodont FAs, and conversely a pulse of LAs with cooler conditions.

Hypothesis 4: Warmer conditions correlate with a pulse of pseudosuchian archosaur FAs, whereas cooler or more seasonal conditions correlate with a pulse of pseudosuchian LAs.

Hypothesis 5: Rhynchosaur relative abundance increases with the onset of more arid conditions, and decreases with the onset of wetter conditions.

2 GEOLOGICAL SETTING

Throughout the Late Permian-Triassic, subduction along the southwestern margin of Gondwana produced the Bermejo half-graben systems along northwest-trending pre-existing Paleozoic sutures (**Figure 1**) (e.g., Uliana and Biddle, 1988; Uliana et al., 1989; Lovecchio et al., 2020). The extensional Ischigualasto-Villa Unión Basin (IVUB), part of this extensional system, developed as an elongated half-graben rift with NW-SE orientation associated with the Valle Fértil Fault (**Figure 1**), which is interpreted to be a Triassic normal fault. The IVUB had a half-graben geometry with a deeper area located toward the northwest, at least during the synrift phase(s) as show the architectural and stacking patterns, and paleogeographic distribution of deposits and source areas (Currie et al., 2009; Mancuso and Caselli, 2012; Benavente et al., 2022). The IVUB records the most extensive Triassic Gondwana succession with 2,000–6,000 m of alluvial, fluvial, and lacustrine sediments preserving an exceptionally diverse and abundant floral and

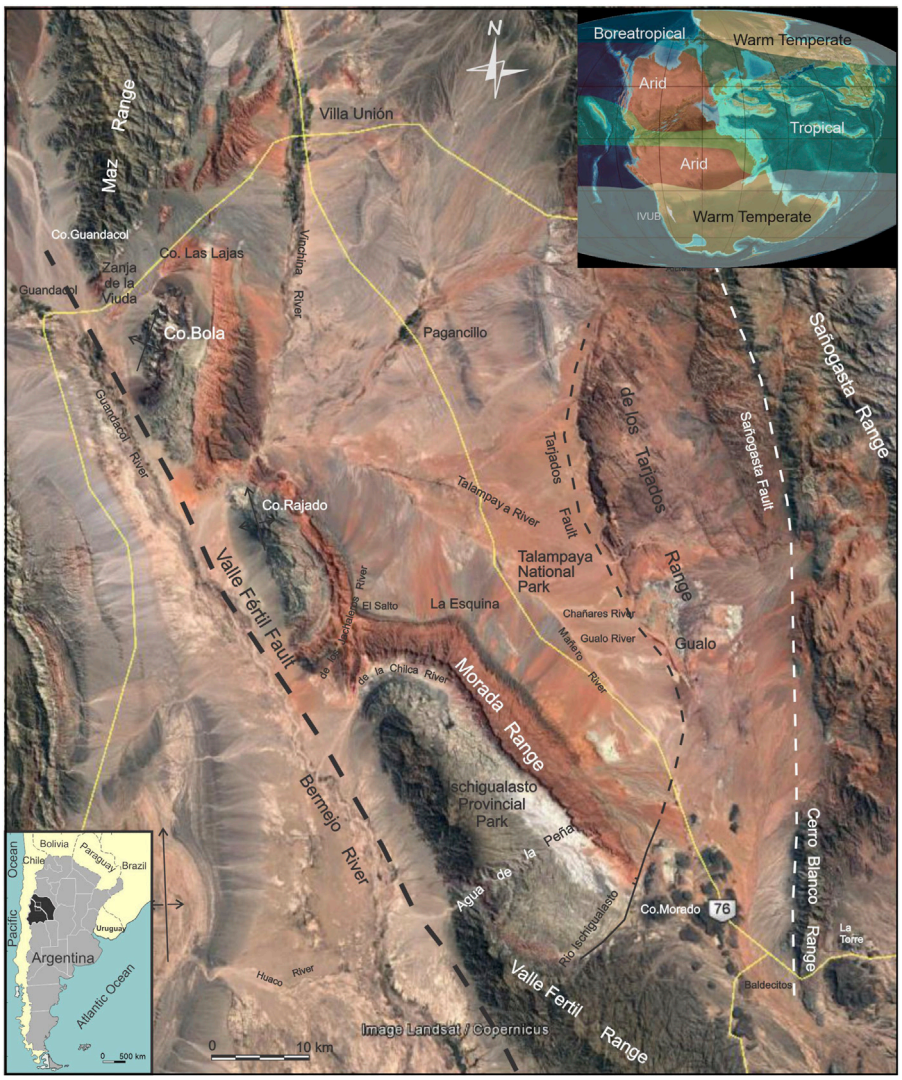

FIGURE 1 | Satellite image of the Ischigualasto-Villa Unión Basin with localities relevant to this study labeled. The satellite image is taken from Google Earth. Paleogeographic map for the Late Triassic Period (modified from https://deeptimemaps.com/) with paleoclimate inferred zones from lithological indicators (modified from Boucot et al., 2013).

faunal fossil assemblage (Stipanicic and Marsicano, 2002). The Triassic infill of the IVUB has not been affected by deep burial (Ruiz and Introcaso, 1999), similar to the adjacent Cuyana rift Basin. The deposits of the two basins have only been affected by the Andes uplift and buried by a relatively thin Cenozoic sedimentary column with no exhumation processes involved (Abarzúa, 2016; Benavente et al., 2019).

The Agua de la Peña Group, which includes the Chañares, Los Rastros, Ischigualasto, and Los Colorados formations (Mancuso 2005), unconformably overlies the Tarjados Formation redbeds (López-Gamundí et al., 1989; Caselli, 1998). The four units have conformable gradational boundaries. Between each formation there is a clear change in the depositional system, which makes lithostratigraphic recognition possible, but without marked discontinuity. The lower Carnian Chañares Formation consists of tuffaceous sandstone, siltstone, orthoconglomerate, and paraconglomerate deposited in fluvial and lacustrine-margin settings, and alluvial fans environments, respectively (Rogers et al., 2001; Mancuso et al., 2014; Marsicano et al., 2016), and transitions into the Los Rastros Formation, characterized by a deep lacustrine black shale and deltaic sandstone (Mancuso and Caselli, 2012; Mancuso et al., 2020a; Benavente et al., 2022). Recent radioisotopic ages for the Chañares and Los Rastros formations reveal that they span the latest Ladinian/early Carnian through mid-Carnian (Marsicano et al., 2016; Mancuso et al., 2020a; Irmis et al., 2022). Therefore, both units are considered a lateral variation of the same sedimentary succession (Mancuso and Caselli, 2012; Mancuso et al., 2014, 2020a). The Chañares-Los Rastros succession preserves warmer and more humid conditions than before or after, representing the first detailed paleoclimate data for the CPE in Gondwana based on a multiproxy paleoclimate interpretation

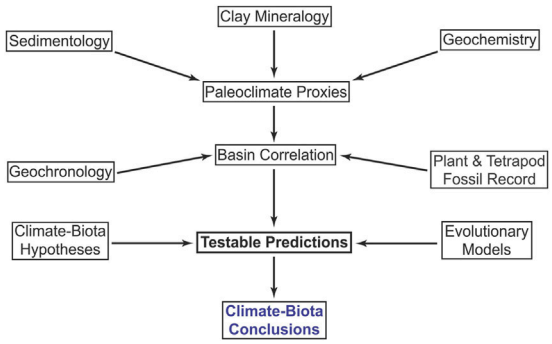

FIGURE 2 | Conceptual flow diagram explaining how we synthesized data to test hypotheses for biotic response to climate change in Triassic sediments of the Ischigualasto-Villa Unión Basin, Argentina. Multiple types of geologic data (**Sections 3**–**3.1**) were used to infer paleoclimatic proxies (**Sections 4.1**–**4.4**), which were combined with data from the fossil record (**Sections 3.2**, **4.5**–**4.6**) and geochronologic age constraints through basin correlation. These integrated data were then used to test predictions (**Sections 1.3**, **3.3**, **4.7**) derived from applying explicit evolutionary models (**Section 1.2**) to previously-proposed hypotheses (**Section 1.1**).

(sedimentology, mineralogy, paleontology, and C and O stable isotope data) from the same strata (Mancuso et al., 2020a; Benavente et al., 2022).

The lacustrine-deltaic Los Rastros Formation is conformably overlain by upper Carnian-lower Norian sandstone, mudstone, and tuff deposited in the moderate sinuosity fluvial system of the Ischigualasto Formation (Currie et al., 2009; Martínez et al., 2011; Colombi et al., 2017, 2021). This unit is well-dated by radioisotopic ages (Rogers et al., 1993; Martínez et al., 2011; Desojo et al., 2020; Colombi et al., 2021), and preliminary age modeling indicates it spans from ~232.5 to ~224.5 Ma or younger (Irmis et al., 2022). This fluvial system records the wide development of a floodplain, including extensive paleosols (Tabor et al., 2006; Currie et al., 2009). The paleontological content, and their taphonomic features, sedimentological, and pedologic (type of paleosols) evidence suggest seasonal semi-arid conditions, with evidence of semi-humid conditions recorded in the Valle de la Luna Member (Tabor et al., 2004, 2006; Colombi and Parish, 2008; César and Colombi, 2013).

Finally, the Ischigualasto Formation is conformably overlain by Norian sandstone and mudstone moderate-sinuosity fluvial red beds of the Los Colorados Formation (Caselli et al., 2001; Santi Malnis et al., 2020). Paleomagnetic dating suggests an age range 227 to 213 Ma, indicating that the Los Colorados Formation was deposited during the early-middle Norian Stage (Kent et al., 2014). The climate condition of the Los Colorados succession is controversial; some authors propose arid conditions mainly based on the red color of the sediments (López-Gamundí et al., 1989; Milana and Alcober, 1994; Cladera et al., 1998), whereas more detailed sedimentological analysis supported the interpretation of moderately sinuous fluvial systems that lack evidence of aridity such as intraclast breccias, desiccation cracks, and eolian or evaporite lenses (Bossi, 1971; Caselli et al., 2001; Arcucci et al., 2004).

3 MATERIALS AND METHODS

The Flow diagram (**Figure 2**) summarizes the sedimentological, chronostratigraphic, paleoclimate, and paleontological dataset analyzed in this contribution.

We measured and sampled a detailed stratigraphic section of the Ischigualasto Formation at centimeter scale in the NW area of the basin at the Cerro Bola locality (**Figure 1**). The Rock Color Chart of the Geological Society of America (GSA 1948) was used for Munsell color descriptions. Fresh, unweathered hand samples were collected for clay mineralogical and XRF elemental analysis. The sedimentological analysis consisted of determining facies defined by sedimentary structures and textures and recorded using the acronyms of the lithofacies code proposed by Miall (1996). Facies associations were identified to interpret the depositional environments and sub-environments (**Supplementary Table S1**).

Paleosol profiles were recognized and described using established criteria (Retallack, 1988; Kraus and Aslan, 1993; Kraus, 1999; Tabor et al., 2006). The top of paleosol was identified where a marked change in grain size, color, and/or sedimentary structures occur, whereas the based was identified where unaltered parent material occurs (Tabor et al., 2006). Thus, the paleosols were classified based on the occurrence of morphological features observable in outcrop and hand sample (e.g., thickness, color, type, and distribution of mottling, soil structure), following previously established by Tabor et al. (2006) for the Ischigualasto Formation.

The mineralogical composition of samples was analyzed with X-ray diffraction (XRD) of the <2 μm sample fraction using a PANalytical X'Pert PRO diffractometer; each sample was prepared with three methods (air-dried, glycolated, and calcined) (see **Supplementary Material**). For mixed-layer illite/smectite, the contribution of illite was determined by the Reichweite value (R) calculated following Moore and Reynolds (1997). Representative mudstone and silty mudstone samples were analyzed for major and trace element abundances using a Bruker AXS TRACER III-V energy-dispersive hand-held X-ray fluorescence (XRF) unit (see **Supplementary Material**). Raw data were collected as a spectrogram and converted to weight percent for major elements and ppm for trace elements using a matrix-specific mudstone calibration (Rowe et al., 2012).

3.1 Paleoclimate Proxies

We use multiple proxies including the clay mineral assemblages, kaolinite/illite, smectite/illite, and smectite/kaolinite ratios, molar chemical index of alteration (CIA molar), K/Al, Ba/Sr (**Supplementary Tables S3, S4**) to reconstruct physical and chemical weathering intensity and seasonality through time (Chamley, 1989; Liu et al., 2005; Clift et al., 2014). The ratios of kaolinite/illite and smectite/illite are proxies for the intensity of chemical weathering, but the latter ratio also includes seasonality as a variable. The smectite/kaolinite ratio reveals a history of chemical vs. physical weathering rates, where the relatively higher ratios suggest a strengthened chemical weathering and weak physical erosion; by contrast, the lower ratios indicate intensified physical erosion and weakened chemical weathering

(Chamley, 1989; Weaver, 1989; Ruffell et al., 2002; Fürsich et al., 2005).

The Chemical Index of Alteration (CIA), proposed by Nesbitt and Young (1982), is calculated based on the major element chemistry of mudrocks. We used the convention of converting the raw abundances into moles by dividing the weight percent by molecular weight, which gives the relative abundance on an atomic stoichiometric basis (Retallack, 2001; Sheldon and Tabor, 2009). The CIA (molar) results in a proportion between alumina and alkalis plus calcium:

$$\mathrm{CIA_{molar}} = \mathrm{Al_2O_3\,(molar)} / (\mathrm{CaO\,(molar)} + \mathrm{Na_2O\,(molar)} + \mathrm{K_2O\,(molar)})$$

and was proposed as a more sensitive measure of the degree of chemical weathering (Goldberg and Humayun, 2010; Retallack et al., 2011; Horn et al., 2018b). The CIA, K/Al, and kaolinite/illite proxies are based on the principle that larger cations (Al) remain fixed in the weathering profile. In contrast, smaller cations (Ca, Na, K) are selectively leached during alteration. Further, the chemical weathering intensity can be estimated based on the ratio for a single element (i.e., K) mobilized during weathering of silicates in comparison to that of a non-mobile element (e.g., Al) (Gaillardet et al., 1999; Garzanti et al., 2014).

Variation of the Ba/Sr ratio has also been considered a proxy for leaching intensity (Gallet et al., 1996; Sheldon and Tabor, 2009), because an increase in chemical weathering intensity rapidly leaches out Sr compared to Ba (Nesbitt and Young, 1982). However, it is necessary to consider that different parent materials have variable initial concentrations and can reduce the leaching elements in high water table soils.

Based on the comprehensive discussion in Sheldon and Tabor (2009) and Tabor and Myers (2015), we selected the following paleotemperature and paleoprecipitation equations. Sheldon et al. (2002) proposed the following based on ΣBases/Al for the Bw or Bt horizons for precipitation:

$$P\left(\frac{mm}{yr}\right) = -259.3\,Ln\left(\frac{\sum Bases}{Al}\right) + 759$$
$$\left(\mathrm{SE} = \pm\ 235\ \mathrm{mm/y},\ \mathrm{R^2} = 0.66\right)$$

This equation was used on the Ischigualasto horizons interpreted as protosols. On the other hand, the calcium-magnesium weathering index (CALMAG) in relation to MAP developed for vertisols (Nordt and Driese, 2010) was applied to the Ischigualasto levels interpreted as vertisol and calcisols:

$$P\left(\frac{mm}{yr}\right) = 22.69\left(100\left[\frac{Al_2O_3}{Al_2O_3 + CaO + MgO}\right]\right) - 435.8$$
$$\left(\mathrm{SE} = \pm\ 108\ \mathrm{mm},\ \mathrm{R^2} = 0.90\right)$$

In this study, the CIA-K equation (Sheldon et al., 2002) was not used because it is inappropriate for calcisols and gleyed soils (Sheldon and Tabor, 2009; Tabor and Myers, 2015). For our Ischigualasto data, MAP estimates from the CIA-K equation overestimates the paleoprecipitation compared to other weathering and humidity indexes.

The relationship between MAT and "clayeyness" (Al/Si) of the Bw or Bt horizon was proposed by Sheldon (2006) for poorly-developed paleosols:

$$T(^\circ C) = 46.9\,(Al/Si) + 4$$
$$\left(\mathrm{SE} = \pm\ 0.6\ ^\circ\mathrm{C},\ \mathrm{R^2} = 0.96\right)$$

This regression was used for Ischigualasto levels that show incipient paleosol features such as poor mottling and poorly defined soil horizons (horizonation). The paleosol weathering index (PWI) to estimate MAT proposed by Gallagher and Sheldon (2013) take on Na and K are more easily weathered and leached from soils than are Mg and Ca:

$$T(^\circ C) = -2.74\,Ln(100\,(4.20Na + 1.66Mg + 5.54K + 2.05Ca))21.39$$
$$\left(\mathrm{SE} = \pm\ 2.1^\circ\mathrm{C},\ \mathrm{R^2} = 0.57\right)$$

were used for mottled paleosols with well-developed Bt horizons. The salinization estimation equation ($(K_2O + Na_2O)/Al_2O_3$; Sheldon et al., 2002) was not used for warmer Mesozoic climates, because that equation underestimates MAT in environments with seasonal precipitation (Sheldon and Tabor, 2009; Tabor and Myers, 2015). The use of several equations to estimate MAP and MAT was previously proposed (Sheldon and Tabor, 2009; Tabor and Myers, 2015), and is appropriate for the Ischigualasto succession because of the different kinds of paleosols recorded. These equations provide complimentary data based on the characteristic of each equation reducing the over- and under-estimation of paleoprecipitation and paleotemperature from using a single relationship (**Supplementary Table S5**). However, the use of more than one equation shows an artificial discontinuity in the dispersion graph (**Supplementary Figure S1**).

3.2 Paleontological Data

A literature review allowed us to generate a database that includes the plant (micro and macro-fossil) and tetrapod taxa known from each unit of the Agua de la Peña Group, as of November 2021. The tables with the taxa registered in each unit are available in (**Supplementary Tables S6–S8**). The complete list of the references consulted can be found also in the (**Supplementary Table S9**).

The plant macrofossil occurrences from the Los Rastros, Ischigualasto, and Los Colorados formations were organized by more inclusive taxonomic groups. This was carried out following the systematic schemes proposed by Stewart and Rothwell (1993) for gymnosperms, Smith et al. (2006), and PPG (2016) for ferns (**Supplementary Table S10**). For palynomorphs recorded from the same formations, an attempt was made to establish the botanical affinity of the miospores with the plant group interpreted as the most likely producer based on Ruffo Rey (2021) and references therein (**Supplementary Table S11**). Lastly, the hypothesized temperature preference and humidity requirement of the taxa were assigned according to Zhang et al. (2020) and Ruffo Rey (2021) (**Supplementary Table S12**).

For tetrapod fossils, we assembled a database of taxa and specimens using Martínez et al. (2011) as a foundation, augmenting it with data from Desojo et al. (2020) and other more recent publications (**Supplementary Table S13**). The Chañares tetrapod data are derived from Mancuso et al. (2014) and Ordoñes et al. (2020), whereas the Los Rastros tetrapod data are assembled from Marsicano et al. (2004, 2007, 2010) and Mancuso and Marsicano (2008). Given the thermal tolerance of modern groups (Bennett, 2018), Liu et al. (2021) proposed preferred temperatures for Permo-Triassic tetrapod groups. Additionally, Dunne et al. (2021) explored the paleolatitudinal distribution of the major Late Triassic tetrapod groups, defined the paleoclimatic ranges that they occupied, and proposed a range of climate preferences for each major Late Triassic tetrapod group (see **Figure 6** in Dunne et al., 2021). Based on the inferences of this previous work, we grouped the major tetrapod clades recorded in the Late Triassic Agua de la Peña Group into relative temperature and precipitation preferences (**Supplementary Table S14**).

3.3 Hypothesis Testing

To test the previously proposed hypotheses for climate forcing of the fossil biota preserved in the Ischigualasto Formation, we used the stratigraphic bins of Martínez et al. (2011) to examine changes in FAs, LAs, and relative abundance of taxa through the section. Because there is always going to be a 'background' rate of FAs and LAs, we focused on outlier datapoints where these rates are elevated; i.e., possible evidence of Vrba's pulses. This record of FAs/LAs was also compared to specimen sample size for each bin to examine how sampling might be driving the observed appearance and disappearance of taxa. To further test the effect of sampling on observed diversity at a larger scale, we used rarefaction (Raup, 1975; Tipper, 1979), implemented in the software package Analytic Rarefaction v. 1.3 (Holland, 2003), to examine whether different sample sizes might explain the different species richness of the *Scaphonyx-Exaeretodon-Herrerasaurus* biozone vs. the *Exaeretodon* biozone. Finally, to examine whether observed differences in relative abundance relate to sample size changes across bins, we used PAST v. 4.03 (Hammer et al., 2001) to calculate adjusted residuals for each bin and conduct a composite Chi-squared test for the taxon of interest vs. the rest of the dataset (Grayson and Delpech, 2003; Faith and Lyman, 2019).

4 RESULTS

The fluvial paleoenvironment recorded in the Ischigualasto Formation is well-described in numerous studies from the past 75+ years (Frenguelli, 1944, 1948; Bossi, 1971; Rogers et al., 1993; Currie et al., 2009; Colombi et al., 2021). The Ischigualasto Formation sequence we measured and described at the Cerro Bola locality (**Figures 1**, **3**) preserves similar sedimentological characteristics to previously studied localities (**Supplementary Table S1**). The fluvial system is dominated by multi-story channels and single-story channels associated with levee facies in some cases and floodplain facies in others. The crevasse channel and crevasse splay facies are interbedded with floodplain facies. These floodplain facies are dominated by paleosols (protosol, vertisol, gleyed vertisol, argilllic vertisol, argillic calcisol, and calcisol). In agreement with previous work, the system at this locality shows a general flow to the north (NE-NW) (Currie et al., 2009). The correlation though basin for the Ischigualasto Formation was based on a distinctive thick volcaniclastic horizon used as the datum among the Ischigualasto Provincial Park, Cerro Bola, and Las Lajas sections (see **Supplementary Figure S3**).

4.1 Clay Mineralogy

Ischigualasto Formation clay mineralogy at the Cerro Bola locality is characterized by assemblages that include smectite, illite, mixed-layer illite/smectite, kaolinite, and chlorite (**Figure 3**, **Supplementary Table S2**). This compares well with previously published clay mineralogy records from other localities (Agua de la Peña, Río Ischigualasto, and Zanja de la Viuda) in the basin, which also show variable dominance of smectite, illite, kaolinite, chlorite, and mixed-layer illite/smectite (Bossi, 1970; Ovejero and Bossi, 1984).

Abundant illite might suggest four possible processes: the leaching of smectite (Chamley, 1989); leaching of acidic rock such as volcanic (Singer, 1980); burial diagenesis (Fursich et al., 2005); and/or enhanced weathering under an increasing hydrolysis index (Fürsich et al., 2005; Do Campo et al., 2010). The illite abundance is variable up-section and its crystallinity is low, which rules out leaching and diagenesis processes (Fürsich et al., 2005; Barrenechea et al., 2018). Therefore, the most likely explanation for abundant illite is an enhanced hydrolysis index (HI) due to increased erosion at the catchment of the basins (Fürsich et al., 2005; Do Campo et al., 2010; Rostási et al., 2011; Mancuso et al., 2020b). In the cases where these assemblages include smectite, this suggests seasonal conditions that point to enhanced erosion during the wet season (Chamley, 1989). Mixed-layer illite/smectite with a value of R3 is interpreted as an indicator of leaching (Bossi, 1970; Moore and Reynolds, 1997). Chlorite is commonly found in soils as a primary (authigenic) product, but it can also be a detrital source (Moore and Reynolds, 1997). The few levels that recorded low proportions of chlorite have subtle pedogenic features; therefore, we interpret that the presence of chlorite in these samples might be due to transport from a different source for sediment supply, possibly granitic bedrock (Chamley, 1989). Thus, the second assemblage group (illite, mixed-layer illite/smectite, smectite, and trace chlorite) can be interpreted as formed in high erosion rates under seasonal climate conditions. In the assemblages of the third and fourth groups, the presence of kaolinite might point to reworked felsic volcanic deposits; and/or to more warm and humid conditions (Singer, 1984; Kalm et al., 1996). The assemblages of illite and kaolinite, including detrital illite, most likely indicate enhanced leaching from a high water regime under warm and humid conditions. Therefore, these assemblages can be interpreted as produced by an enhanced HI under warm, humid conditions (Chamley, 1989; Milroy et al., 2019). Finally, in different proportions, the fourth category of assemblages containing illite, mixed-layer illite/smectite, smectite, and kaolinite can also be interpreted as formed by enhanced HI in relatively more humid and seasonal conditions (Chamley, 1989; Do Campo et al., 2010).

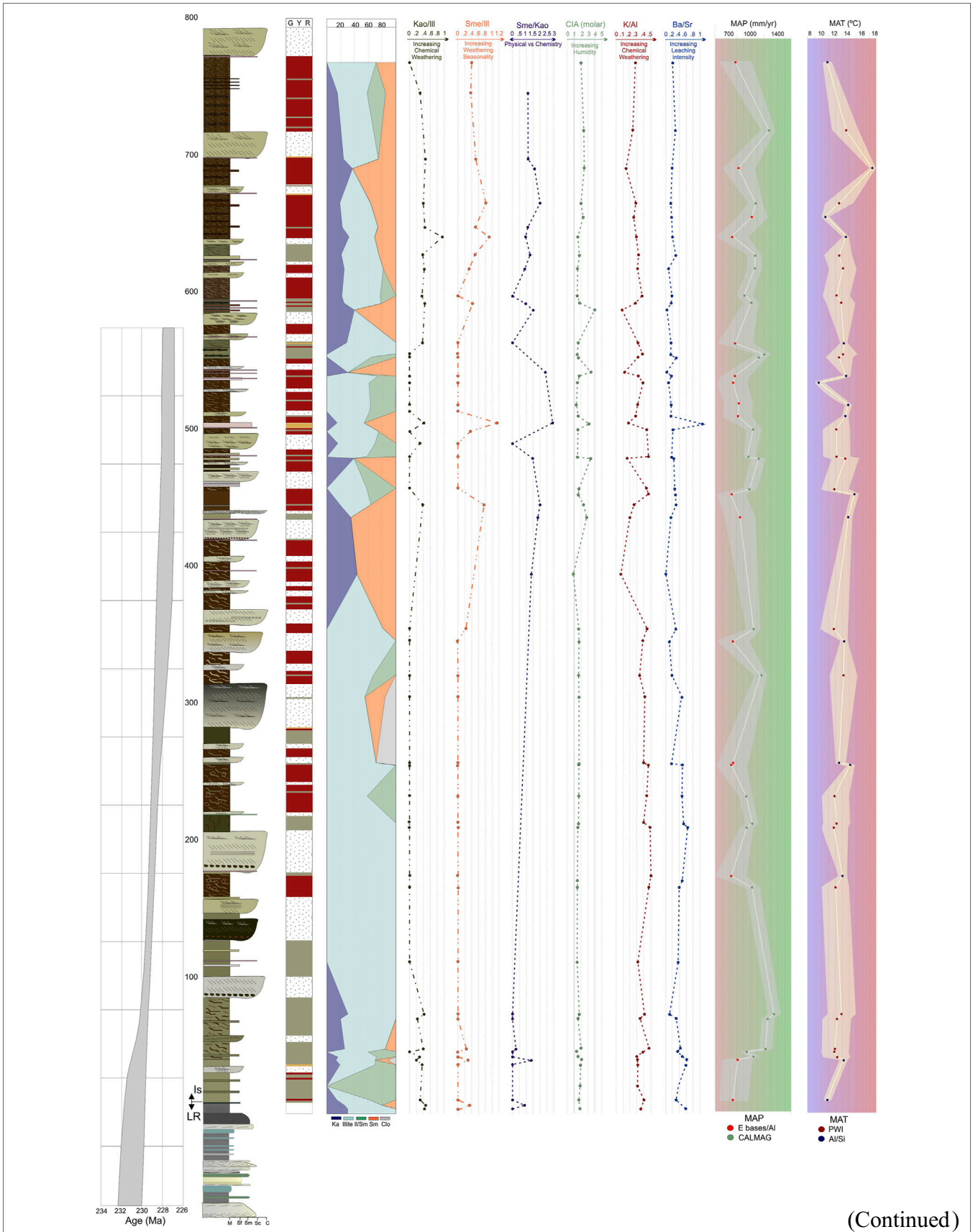
800
700
600
500
400
300
200
100
Is
LR
234 232 230 228 226
Age (Ma)
M Sf Sm Sc C
G Y R
20 40 60 80
Ka Illite Il/Sm Sm Clo
Kao/Ill
0 .2 .4 .6 .8 1
Increasing Chemical Weathering
Sme/Ill
0 .2 .4 .6 .8 1 1.2
Increasing Weathering Seasonality
Sme/Kao
0 .5 1 1.5 2 2.5 3
Physical vs Chemistry
CIA (molar)
0 1 2 3 4 5
Increasing Humidity
K/Al
0 .1 .2 .3 .4 .5
Increasing Chemical Weathering
Ba/Sr
0 .2 .4 .6 .8 1
Increasing Leaching intensity
MAP (mm/yr)
700 1000 1400
MAT (°C)
8 10 12 14 16 18
MAP
E bases/Al
CALMAG
MAT
PWI
Al/Si

(Continued)

FIGURE 3 | (Continued) Detailed stratigraphic section measured of the Ischigualasto Formation at the Cerro Bola area with the plot of the paleoclimate proxies. Geochronologic age constraints for the Ischigualasto Formation are from the preliminary Bayesian age model with uncertainty envelope (gray shading) for the unit based on radioisotopic ages (Irmis et al., 2022).

Overall, the general clay mineralogy trend suggests a fluctuation between humid and warm conditions (Los Rastros Fm) (Mancuso et al., 2020a; Benavente et al., 2022) and more seasonal and less humid conditions represented by the abundance of smectite and relatively less kaolinite up-section (Ischigualasto Fm). The overall more seasonal and less humid conditions in the Ischigualasto Formation begin with warm and humid seasonal conditions in the first ~100 m, with a variable combination of kaolinite, smectite, illite, and mix-layer illite/smectite, followed by less humid seasonal conditions with enhanced HI, characterized by the dominance of illite. Finally, above the ~380 m level there is a return to more humid seasonal conditions, with a variable combination of kaolinite, smectite, illite, and mix-layer illite/smectite. The high variability found in the mineralogical assemblages of the studied unit reflects variable sources of minerals for the fluvial system (Bossi, 1970).

4.2 Mineralogical Proxies

Clay mineralogical proxies (kaolinite/illite, smectite/illite, and smectite/kaolinite ratios) display temporal trends in both physical erosion and chemical weathering (see **Supplementary Material**). The kaolinite/illite ratio trend suggests moderate to high chemical weathering in the first ~100 m and upper ~380 m of the section, and low chemical weathering between ~100 and 380 m. The smectite/illite ratio trend suggests moderate weathering seasonality in the lowermost ~100 m, low weathering seasonality between ~100 and 380 m, and high weathering seasonality above ~380 m. The smectite/kaolinite ratio suggests predominantly physical weathering in the first ~100 m, and fluctuation between physical and chemical weathering above the ~380 m level in the section.

4.3 Major and Trace Element Proxies

The trend in CIA molar estimates supports a sub-humid interpretation for the first ~380 m of section and above ~600 m in section, and more variable humid conditions between ~380 and 600 m. The K/Al ratio reflects high chemical weathering below ~380 m, and variable chemical weathering above this horizon. Finally, the Ba/Sr ratio suggests extensive leaching conditions below ~380 m, and less leaching above (see **Supplementary Material**).

4.4 Paleoprecipitation and Paleotemperature Estimates

Our MAP estimates vary between 721 and 1,343.5 mm/yr, and our MAT estimates vary between 9.41 and 17.52°C (**Figure 2**; **Supplementary Table S5**). Despite this variability, the general trends through the section appear to vary around a mean MAP of 950 mm/yr, and display a subtle directional change in MAT from 12.5 to 13.5°C. Particularly notable is that lower dispersion of MAT values is observed in between the base of the section and ~380 m level, in contrast with the higher dispersion recorded above this interval. However, of the seven data points with the lowest MAP and highest MAT values, three occur in the lower part of the section (**Figure 3**; **Supplementary Table S5**).

Therefore, despite some small discrepancies, these multiple proxies are in general agreement with the stratigraphic trend in paleoenvironmental conditions. Evidence of warm and humid conditions with moderate seasonality and chemical weathering dominate the lower part section (basal 100 m). Towards the middle part of the section (from 100 to 380 m) there is evidence for predominantly sub-humid to semi-arid conditions with variable chemical weathering and moderate to low seasonality. Finally, above the 380 m level, these data suggest more humid seasonal conditions with variation in seasonality and chemical weathering.

4.5 Plant Fossil Record

The Upper Triassic, particularly the Stage Carnian, is the interval where the *Dicroidium* flora is hypothesized to have diversified and spread across Gondwana (McLoughlin, 2001, 2011; Kustatscher et al., 2018; Bodnar et al., 2021). The formations of the Agua de la Peña Group preserve the typical *Dicroidium* floral assemblage; the main differences are in the specific richness of each unit (see **Supplementary Tables S6, S7**).

The Los Rastros Formation preserves the highest species richness with 72 taxa, followed by the Ischigualasto Formation with 24 taxa, and finally, the Los Colorados Formation with only three taxa (**Figure 4A**; **Supplementary Table S6**). Members of Lycopodiopsida and Czekanowskiales are only recorded in the Los Rastros Formation (**Figure 4A**; **Supplementary Table S6**). Moreover, the Los Rastros Formation preserves a higher number of taxa belonging to the groups Equisetopsida, Polypodiopsida, Umkomasiales, Peltaspermales, Ginkgoales, Voltziales, and gymnosperms with uncertain affinity, in comparison with the Ischigualasto and Los Colorados formations (**Figure 4A**; **Supplementary Table S6**). In contrast, Cycadales and Bennettitales are better represented in the Ischigualasto Formation, while the number of Gnetales is equal in the Los Rastros and Ischigualasto formations (**Figure 4A**; **Supplementary Table S6**).

This trend in species richness, particularly the number of taxa per group, shows the predominance of Umkomasiales followed by Ginkgoales, Voltziales, and gymnosperms with uncertain affinity in the Los Rastros Formation, whereas in the Ischigualasto Formation the Umkomasiales continue to dominate but Cycadales, Bennettitales, and Coniferales represent a higher percentage of diversity, and Equisetopsida, Ginkgoales, Voltziales, and gymnosperms with uncertain affinity are more species-poor (**Figure 4B**; **Supplementary Table S6**).

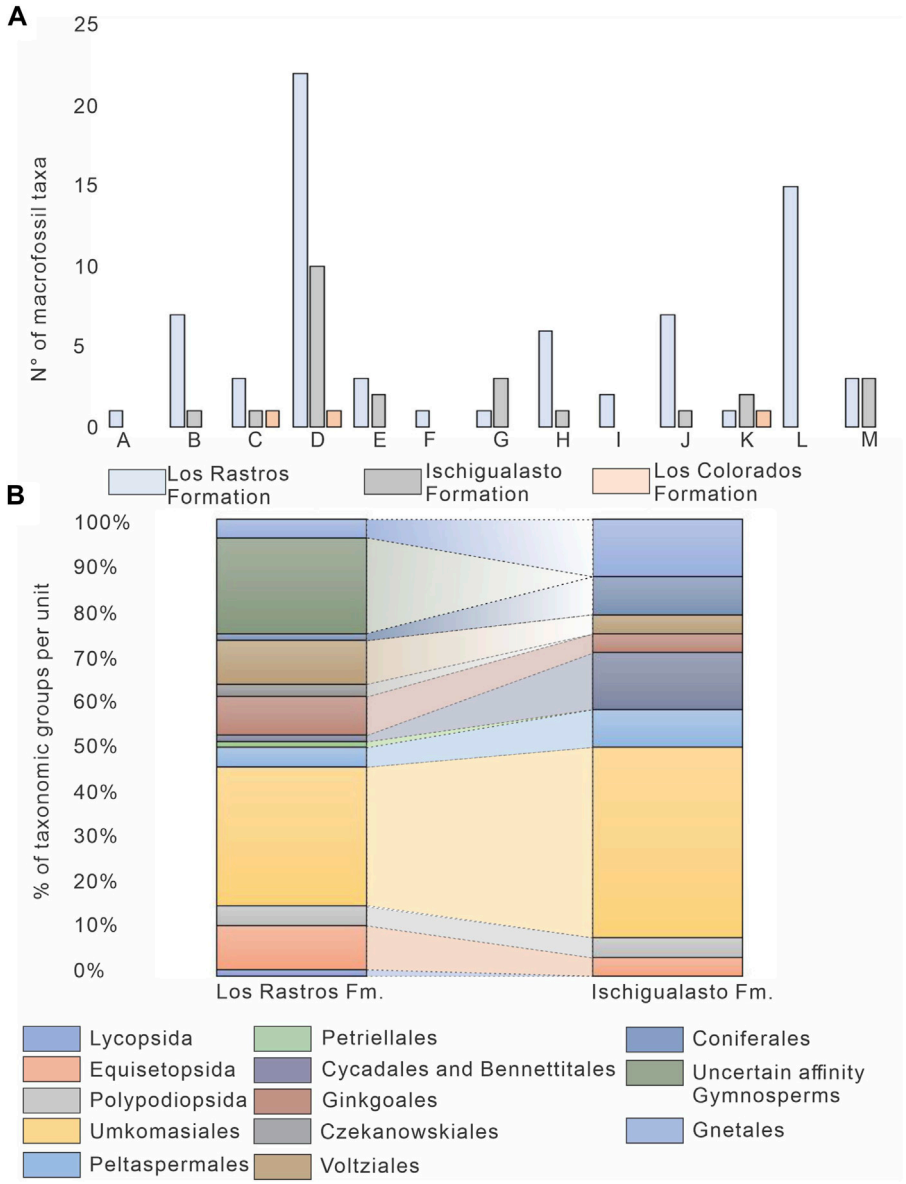

FIGURE 4 | Paleobotanical record of the Los Rastros, Ischigualasto, and Los Colorados formations. **(A)**. Number of macrofossil taxa per taxonomic group in each unit. A. Lycopsida, B. Equisetopsida, C. Polypodiopsida, D. Umkomasiales, E. Peltaspermales, F. Petriellales, G. Cycadales and Bennettitales, H. Ginkgoales, I. Czekanowskiales, J. Voltziales, K. Coniferales, L. Uncertain affinity Gymnosperms, M, Gnetales. **(B)**. Percentage of taxa of each taxonomic group registered in the Los Rastros and Ischigualasto formations.

Groups such as the Petriellales and Czekanowskiales are only recorded in the Los Rastros Formation, and taxa such as Polypodiopsida (ferns) represent a similar percentage of the vegetation in the Los Rastros and the Ischigualasto formations (**Figure 4B**; **Supplementary Table S6**). The scarcity of plant macrofossils in the Chañares and Los Colorados formations means their assemblages cannot be used to assess changes in richness (see **Supplementary Material**).

The palynomorph record is more diverse, with 42 taxa recorded for the Chañares Formation, 212 taxa from the Los Rastros Formation, and 90 taxa for the Ischigualasto Formation (**Supplementary Table S7**). Miospores in the Chañares Formation indicate the presence of Lycopodiopsida, Polypodiopsida, Peltaspermales, Umkomasiales (Perez Lonaize et al., 2018). In the Los Rastros Formation, palynological data indicate the presence of taxa not represented by macrofossil remains, such as Caytoniales, and different groups of Coniferales such as Podocarpaceae and Araucariaceae (**Supplementary Table S7**). The same trend is observed with spores indicating the presence of Lycopodiopsida in the Ischigualasto Formation (**Supplementary Table S7**).

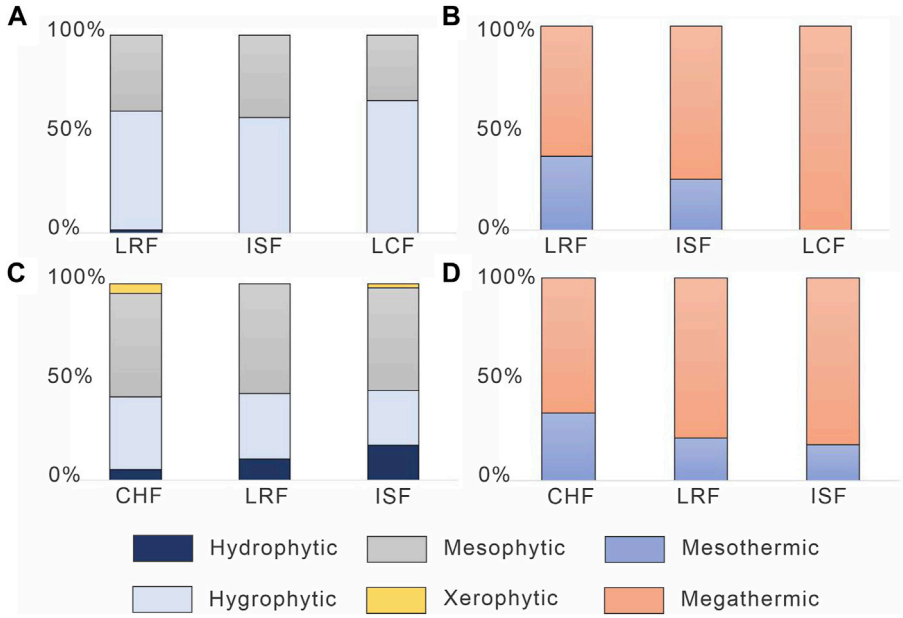

FIGURE 5 | Inferred plant temperature and humidity preference based on previous authors. **(A)**. Percentages of hydrophytic, hygrophytic, and mesophytic macrofossil taxa. **(B)**. Percentage of mesothermic and megathermic macrofossil taxa. **(C)**. Percentages of hydrophytic, hygrophytic, mesophytic, and xerophytic microfossil taxa. **(D)**. Percentage of mesothermic and megathermic microfossil taxa. CHF, Chañares Formation; ISF, Ischigualasto Foramtion; LCF, Los Colorados Formation; LRF, Los Rastros Formation.

4.5.1 Plant Paleoecology

The plant macrofossil record in the Los Rastros Formation is dominated by taxa that previous authors have inferred to be hygrophytic (60%), followed by mesophytic taxa (38%), and hydrophytic taxa (2%). In the Ischigualasto Formation, inferred hydrophytic taxa dominate (58%) followed by mesophytic (42%) taxa. Finally, the overlying Los Colorados Formation is also dominated by taxa inferred to be hygrophytic (67%) and mesophytic (33%), but this comprises only three taxa (**Figure 5A**; **Supplementary Table S10**). Although the number of taxa interpreted as megathermic taxa in the Los Rastros Formation was represented by 64% and 36% were mesothermic taxa (**Supplementary Table S10**). In the Ischigualasto Formation 75% were megathermic and 25% mesothermic taxa. Finally, the three taxa mentioned in the Los Colorados Formation are interpreted as megathermic taxa (**Figure 5B**; **Supplementary Table S10**).

Interestingly, there appear to be no substantial changes in the floral composition, at least with respect to moisture requirement, among the three units (**Figure 5A**). However, inferred temperature tolerance shows a progressive increase from the Los Rastros Formation to the Los Colorados Formation based on the proportion of megathermic taxa compared to mesothermic elements (**Figure 5B**). But, this trend should be interpreted with caution given that the Los Colorados assemblage contains only three taxa.

In the Chañares palynomorph assemblage, inferred mesophytic taxa dominate (53%), with 37% inferred hygrophytic taxa, and ~5% hydrophytic and xerophytic taxa (**Figure 5C**; **Supplementary Table S11**). In the Los Rastros Formation, 56% of the palynomorph taxa are interpreted as mesophytic, 33% as hygrophytic, and 11% hydrophytic (**Figure 5C**; **Supplementary Table S11**). In the Ischigualasto Formation, 52% are inferred to be mesophytic taxa, 28% hygrophytic, 18% hydrophytic, and 2% xerophytic (**Figure 5C**; **Supplementary Table S11**). In terms of temperature tolerance, 67% of Chañares Formation taxa are interpreted as megathermic taxa and 33% mesothermic (**Figure 5D**; **Supplementary Table S11**), whereas 79% of Los Rastros Formation taxa are interpreted as megathermic and 21% as mesothermic (**Figure 5D**; **Supplementary Table S11**). Finally, in the Ischigualasto Formation 83% of taxa are interpreted as megathermic and 17% are interpreted as mesothermic (**Figure 5D**; **Supplementary Table S11**).

The general trend suggests that the Chañares and Ischigualasto formations are similar in containing a small number of inferred xerophytic taxa, but the latter unit has a higher proportion of hydrophytic taxa (**Figure 5C**). In general, the proportion of hydrophytic elements increases up-section from the Chañares through Ischigualasto formations (**Figure 5C**). The lack of inferred xerophytic taxa in the Los Rastros Formation could be evidence that the pulse of warm and humid conditions during the CPE displaced species with drier habitat preferences. Finally, through the section there is a decrease in inferred mesothermal taxa with a relative increase in megathermal taxa (**Figure 5D**).

4.6 Tetrapod Fossil Record

In terms of species richness, the Chañares Formation is dominated by synapsids (dicynodonts and cynodonts)

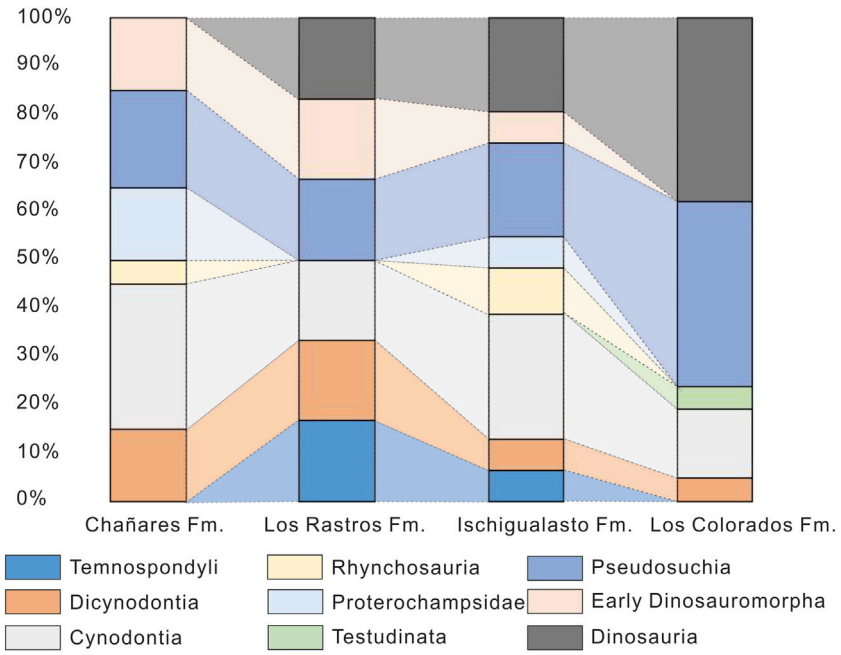

FIGURE 6 | Paleovertebrate record in the units of the Agua de la Peña Group. Percentage of taxa of each taxonomic group registered in each formation.

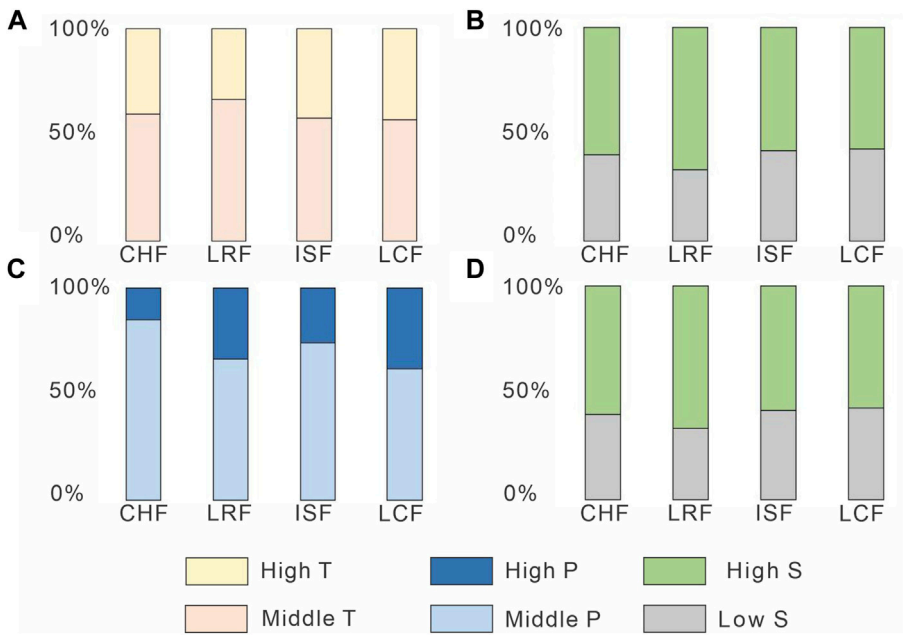

FIGURE 7 | Inferred tetrapod habit preference (based on previous authors) for the Upper Triassic Agua de la Peña Group. **(A)**. Percentage of prefered range temperature tetrapod taxa. **(B)**. Percentage of tolerance to seasonal variation in temperature. **(C)**. Percentage of prefered range precipitation tetrapod taxa. **(D)**. Percentage of tolerance to seasonal variation in precipitation. CHF, Chañares Formation; ISF, Ischigualasto Foramtion; LCF, Los Colorados Formation; LRF, Los Rastros Formation.

followed by archosauriforms (proterochampsids, pseudosuchians, and dinosauromorphs) (**Figure 6**; **Supplementary Table S8**). The body fossil and ichnological record of the Los Rastros suggest at least the presence of these same groups plus temnospondyls, but ichnotaxonomic richness is not comparable to the body fossil record (**Figure 6**;

Supplementary Table S8). Therapsids (dicynodont and cynodont) continue to dominate in the Ischigualasto assemblage, but are proportionally less species-rich due to the rise in species richness of pseudosuchians, rhynchosaurs, and dinosaurs (**Figure 6**; **Supplementary Table S8**). Finally, in the Los Colorados Formation, the tetrapod assemblage is dominated by dinosaurs and pseudosuchians, with a lower proportion of therapsids (dicynodont and cynodont) and testudinatans (**Figure 6**; **Supplementary Table S8**). Thus, through the Late Triassic Agua de la Peña Group, dinosaurs and pseudosuchians taxa become more species-rich, coincided with a decrease in early archosauromorph and synapsid richness (**Figure 6**; **Supplementary Table S8**), as discussed by previous authors (Irmis, 2011; Marsicano et al., 2016). However, it is important to note that the quality of the body fossil record, as well as the ichnological record, is driven by preservational conditions in the basin (see **Supplementary Material**).

4.6.1 Tetrapod Paleoecology

The habitat preferences inferred for fossil tetrapods by previous authors are relatively consistent through the Agua de la Peña Group (**Figure 7A**; **Supplementary Table S15**). All the Agua de la Peña units are dominated by taxa (60%) that are thought to prefer temperate conditions (between 20 and 30 C) followed by taxa (40%) that are thought to prefer high temperature (>30°C). A similar split is observed for inferred seasonality preferences, with 60% of taxa tolerant of high seasonal variation, and 40% of taxa tolerant low seasonal variation (**Figure 7B**; **Supplementary Table S15**). In contrast, there appears to be a trend of increasing species richness among taxa that are inferred to prefer wetter conditions (>2 mm/day), from 15% in the Chañares to 40% in the Los Colorados Formation, whereas taxa that might prefer mid-range precipitation values (between 1.5 and 2 mm/day) decrease (**Figure 7C**; **Supplementary Table S15**). The tolerance to seasonal variation in precipitation displays a similar pattern to temperature (**Figure 7D**; **Supplementary Table S15**).

4.7 Hypothesis Testing

The bulk of fossil assemblages from the Chañares, Los Rastros, and Los Colorados formations are restricted to narrow intervals that are stratigraphically disjunct from each other and from the more continuous record of the Ischigualasto Formation. Therefore, only the Ischigualasto Formation is densely sampled enough to test the hypothesis predictions we outline at the beginning of this contribution. However, because the Ischigualasto Formation is unevenly sampled for plant fossils, with diagnostic specimens largely restricted to a few levels in the middle part of the formation (**Figure 8**), there are not enough data points to evaluate changes in diversity, relative abundance, or FA/LA pulses. As such, we cannot directly test the aforementioned floral predictions (hypotheses 1a-1e in **Section 1.3**) in the context of changes within the Ischigualasto Formation. Therefore, the rest of this section focuses on the tetrapod body fossil record, which is well-sampled and spans nearly the entire formation.

4.7.1 Species Richness

As noted by previous authors (e.g., Martínez et al., 2011; Colombi et al., 2021), one of the most striking patterns in the Ischigualasto Formation tetrapod fossil record is the long-term decline in species richness up-section. The lowest 50 m (bins 1 & 2) of the formation are most diverse, both in total richness and for most individual clades (e.g., Cynodontia, Proterochampsidae, Dinosauromorpha). In fact, the absence of some taxa higher in the section has been used to define biozones in the formation, with the lowest 300 m of the formation grouped into the *Scaphonyx-Exaeretodon-Herrerasaurus* biozone, and the overlying ~350 m separated into the *Exaeretodon* biozone (Martínez et al., 2011). The boundary between the two biozones is defined by the LA of the rhynchosaur *Scaphonyx* and dinosaur *Herrerasaurus*, rather than the FA of any taxon.

Given that species richness scales directly with sampling (i.e., the more specimens you find, the more species you are likely to find) (e.g., Raup, 1972, 1975), a natural question is whether the declining species richness of the Ischigualasto Formation reflects original assemblage composition or is at least in part an artifact of sample size, given that the number of specimens for each stratigraphic bin also declines up-section (**Figure 8**). In fact, a simple bivariate regression reveals a strong linear relationship (R^2 = 0.8179) between the number of specimens and species richness of each bin (**Supplementary Figure S4**). Similarly, when compared at the same number of specimens, the 95% confidence bounds greatly overlap for rarefaction curves of the *Scaphonyx-Exaeretodon-Herrerasaurus* and *Exaeretodon* biozones (**Supplementary Figure S4**). Both of these analyses suggest that sampling (i.e., number of collected specimens) is a significant control on observed tetrapod species richness in the Ischigualasto Formation. Therefore, absolute species richness of the Ischigualasto Formation cannot be taken at face value for paleoecological interpretation, and must take sampling into account.

4.7.2 First and last Appearances

Given the patterns of tetrapod species richness observed in the Ischigualasto Formation, it is unsurprising that FAs and LAs follow a similar trend, with the bulk of these events concentrated in the lower part of the formation, though there appear to be two LA pulses in the middle part of the formation (**Figure 8**). It is important to note that the FAs/LAs of the first and last stratigraphic bin are almost certainly artifacts. With the exception of the dicynodont *Jachaleria*, all other taxa are restricted to the Ischigualasto Formation (i.e., they do not occur in the underlying Los Rastros Formation or overlying Los Colorados Formation). As such, there is necessarily a pulse of FAs in the lowest bin of the Ischigualasto Formation, and any taxa present in the highest bin also have their LA in that bin. Because the Los Rastros and lower Los Colorados Formation have a very poor body fossil record, with present data it is impossible to evaluate whether any Ischigualasto Formation taxa might have had longer stratigraphic ranges that extended into these formations. As such, the FAs of the oldest stratigraphic

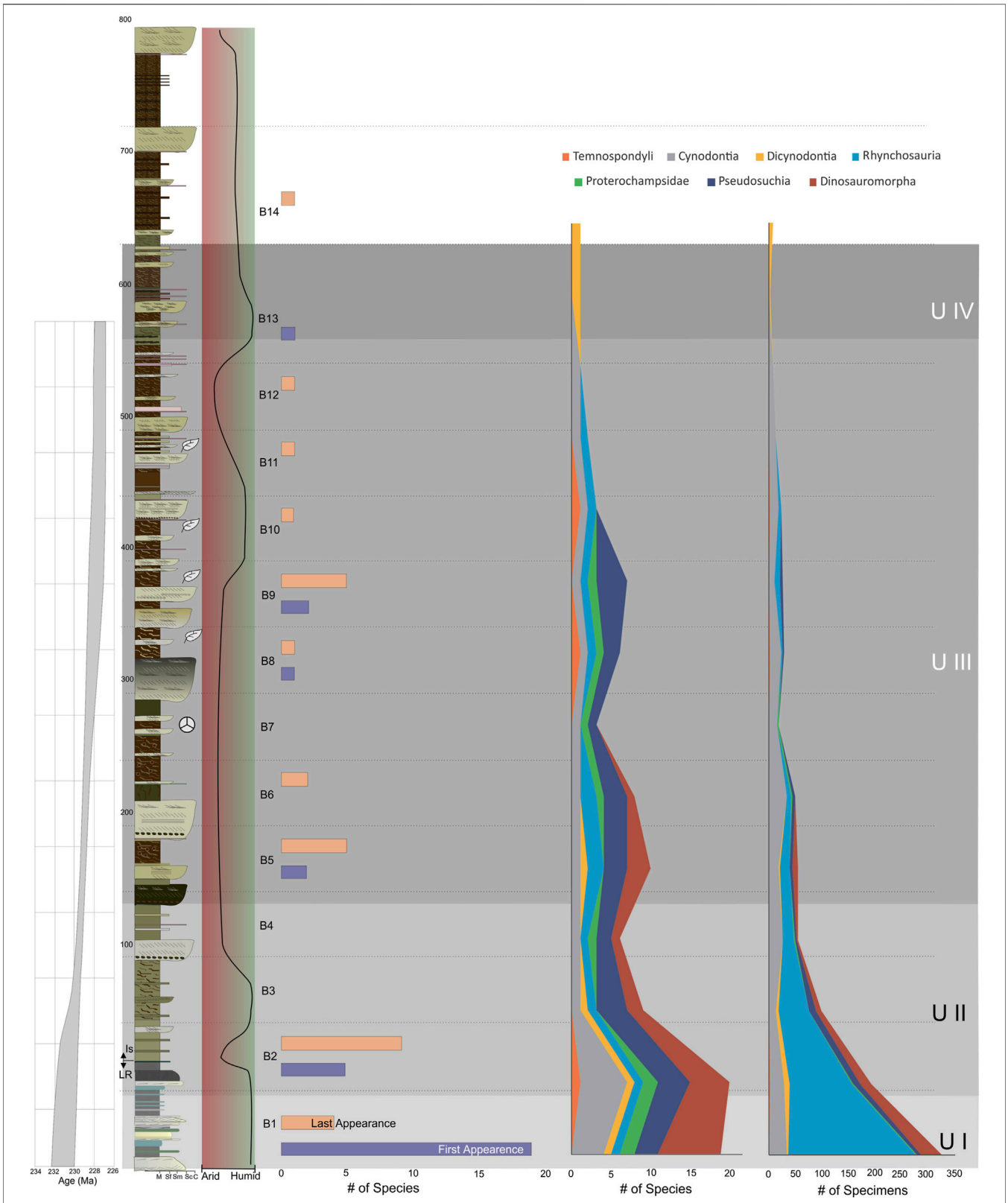

FIGURE 8 | Ischigualasto Formation stratigraphic section including paleobotany levels distribution, first and last appearance of tetrapod record, and tetrapod diversity (number of species) and abundance (number of specimens) in the different Ischigualasto time bins as defined by Martínez et al. (2011). Data modified from Colombi and Parrish (2008), Colombi et al. (2011), Cesari and Colombi (2013), Martínez et al. (2011), Desojo et al. (2020), and Drovandi et al. (2021). Age model same as **Figure 2**.

bin and LAs of the youngest stratigraphic bin are excluded from further analysis and interpretation.

Before using these data to test hypotheses of climate forcing (**Section 1.1**), it is important to evaluate the effect of sampling on observed FAs and LAs, given that it appears to be a primary control of tetrapod richness in the Ischigualasto fossil record. The number of first appearances in a bin is correlated with the number of specimens in each bin ($R^2 = 0.5296$) suggesting some sampling control, but the number of last appearances per bin is less so, with only a weak correlation ($R^2 = 0.2790$) (**Supplementary Figure S5**). This suggests that observed FA pulses are difficult to interpret (with no bins where number of FAs is much greater than expected given sample size), LA pulses might be more informative. Three LA pulses are observed in the Formation: bin 2, bin 4, and bin 9 (**Figure 8**), all of which have more LAs than expected given their specimen sample size (**Supplementary Figure S5**). The pulse in bin 2 (LAs of 1 temnospondyl, 5 synapsid, 1 proterochampsid, and 2 dinosauromorph species) is difficult to interpret; although it is the second best sampled bin, this interval still contains ~40% fewer specimens than the underlying bin 1, so one might expect a large number of rare taxa to disappear from the record in bin 2 as sampling decreases. That said, this interval does preserve a short-term change towards more arid conditions (**Figures 3**, **8**). Bin 5 (LAs of 1 synapsid, 1 pseudosuchian, and 3 dinosauromorph species) does not appear to correlate with any clear changes in available paleoclimate proxies. Bin 9 is the most intriguing LA pulse, because it is associated with a significant change to more humid seasonal conditions inferred from our paleoclimate proxies at the ~380 m level (**Figures 3**, **8**). All of the LAs in bin 9 are archosauriform reptile species (1 proterochampsid, 4 pseudosuchians).

How do these results compare with our predictions for paleoclimate forcing of species FAs and LAs? None can be fully tested, mostly because Ischigualasto tetrapod FAs appear to be controlled by sampling. Therefore, we cannot confidently use the record of FA pulses to interrogate our hypotheses. Nonetheless, to the extent possible, below we evaluate the extent to which our results conform to or contradict predictions, with a focus on the LA record.

Hypothesis 2: The only significant pulse for synapsids is in bin 2, with three FAs and four LAs. This bin is associated with a short-term pulse in arid conditions, which is consistent with the prediction for a pulse in synapsid LAs. Alternatively, most of these LAs are relatively rare taxa, and their disappearance could just as well be explained by declining sample size up-section.

Hypothesis 3: The only observed cynodont FA and LA pulse is the aforementioned event in bin 2, but there is no clear paleotemperature proxy change in this interval. Indeed, paleotemperature estimates are relatively stable for the lower half of the Formation (bins 1–10) (**Figure 3**). Therefore, this hypothesis is not supported by the available data.

Hypothesis 4: A significant pulse (4 species) in pseudosuchian archosaur LAs is observed in bin 9, which is associated with a shift to more humid seasonal conditions (~380 m). However, this hypothesis specifically links a pseudosuchian LA pulse to cooler, more seasonal conditions, rather than changes in aridity/humidity. Available paleoclimate proxies do not show clear evidence for cooler conditions at this time, but all proxies display increasing variability and clay mineralogy (smectite/illite ratio) suggests evidence for increasing seasonality (**Figure 3**). Thus, our data could be consistent with this hypothesis, but the lack of a strong association with paleotemperature changes makes it equivocal.

A final important observation is that the number of FAs in a bin is strongly correlated with the number of LAs in the same bin ($R^2 = 0.8571$) (**Supplementary Figure S5**). This contrasts with the predictions of Vrba's relay model, where FA and LA pulses should be separated in time (e.g., Vrba, 1995: Fig. 3.3). There could be several explanations for this. One possibility is that empirical reality (at least in the case of the Ischigualasto Formation) does not match the theoretical model, suggesting other processes are affecting the first and last appearances of taxa, or that the model needs revision. An alternative, and perhaps more likely explanation, is that this result is an artifact of the resolution of our data. As Vrba (1995) discussed, taphonomic and sampling biases can appear to compress the record so that chronologically separate events appear to occur at the same time in the fossil record. Specifically in our case, bin size and duration seems a likely culprit. According to the age model (**Figures 3**, **8**), each of these bins represent anywhere from ~20,000 to ~780,000 years (mean duration 290,000 years; median duration 300,000 years). Thus, in a single data point (i.e. bin) we are time-averaging first and last appearances over 10^3–10^6 years, and it is exactly at this timescale that Vrba (1992, 1995) hypothesized the relay model should play out. So it seems reasonable that our bins are simply too large in duration to distinguish in time between associated but temporally separate FA and LA pulses.

4.7.3 Relative Abundance

One of the most striking patterns in tetrapod relative abundance in the Ischigualasto Formation is that rhynchosaurs (specifically *Scaphonyx*) are exceedingly common near the base of the formation, but quickly decline and disappear by the middle third of the Formation (bin 8) (**Figure 8**), so much so that the lowest biozone in the Formation is named in part for *Scaphonyx* (Martínez et al., 2011). But this trend could be driven by sampling, given that the decline in *Scaphonyx* relative abundance mirrors the up-section decline in overall specimen sample size. The adjusted residuals (ARs) (**Supplementary Table S16**) indicate this is not the case; the positive ARs for bins 1 and 2 indicate *Scaphonyx* is over-represented relative to what is expected given sample size, and the negative ARs for bins 5–12 indicate it is under-represented relative to what is expected. Furthermore, the Chi-squared test indicates this difference is significant ($p < 1.77E\text{-}38$). These data suggest that the abundance of *Scaphonyx* in bins 1 and 2, and its subsequent decline, are at least in part an actual paleoecological signal. As such, how do these data compare to predictions for rhynchosaur relative abundance changes in relation to paleoclimate?

Hypothesis 5: The rapid decline in *Scaphonyx* abundance is associated with the onset of more arid, slightly warmer, and less seasonal conditions (~100 m level). This directly contradicts the

predictions for this hypothesis, which suggests that rhynchosaur relative abundance should increase with more arid conditions. In fact, rhynchosaurs (*Teyumbaita* n. sp.) become slightly more abundant higher in the section (bins 9 and 10) with a pulse of more humid conditions. Therefore, our data appear to falsify this hypothesis, at least as it applies to the Ischigualasto Formation.

It could be that this hypothesis is simply wrong, and rhynchosaur relative abundance is unrelated to aridity. Alternatively, the original formulators of the hypothesis may have been caught-out by the subtleties of the paleoclimate record. This hypothesis was based on relative abundance data from the Middle-Upper Triassic fossil assemblage of the Paraná Basin, southern Brazil (Azevedo et al., 1990). Here, rhynchosaurs are most abundant in the Santa Maria and Caturrita formations (Azevedo et al., 1990), a sequence with an overall semi-arid inferred climate regime (see review in Mancuso et al., 2021). But, more recent paleoclimate studies indicate that the upper Santa Maria and lower Caturrita formations (lower Candelaria sequence) were relatively wetter than underlying and overlying strata (Horn et al., 2018a,b; Mancuso et al., 2021), and these are precisely the intervals with the most abundant rhynchosaurs (Azevedo et al., 1990: Figs. 5, 6). This is also consistent with the rarity/absence of rhynchosaurs in the more arid Upper Triassic deposits of western North America (Irmis, 2011; Whiteside et al., 2011, 2015). Thus, it may be that rhynchosaur abundance is instead correlated with more humid conditions.

5 DISCUSSION

5.1 Geographic and Chronologic Scale of Climate Proxies

During the early Late Triassic (Carnian to early Norian), the IVUB was deposited between 44.6°S and 49.6°S paleolatitude, including 95% confidence intervals (230 Ma paleopole of van Hinsbergen et al., 2015; see Mancuso et al., 2021: Fig. 3). The most recent Carnian Global Circulation Model (GCM) predicts a MAT of 0.85°C and MAP of 1,161 mm/year for the IVUB, with warmest and coldest monthly means of 37.6°C to −35.9°C, and wettest and driest monthly means of 1,238 mm/year to 1,083 mm/year (Dunne et al., 2021).

Our new proxy data estimates of MAP from the Ischigualasto Formation match well with the GCM predictions (Dunne et al., 2021), with a range of values from 721–1,343 mm/year (mean of 959 mm, median of 969 mm, standard deviation of ±176 mm) that overlaps with the GCM estimate of 1,161 mm/year (Dunne et al., 2021). In contrast, the GCM MAT estimate of 0.85°C (Dunne et al., 2021) is considerably lower than our proxy estimates of 9.4–17.5°C (mean of 12.7°C, median of 12.6°C, standard deviation of ±3.6°C). This discrepancy in MAT estimates is stark but may have a relatively simple explanation. The Ischigualasto Formation climate values were extracted from the GCM results using an inferred paleolatitude of 52°S, as reconstructed using the plate kinematic model in the Paleobiology Database. However, if a paleolatitude of 44.6°S-49.6°S is used (van Hinsbergen et al., 2015), this results in MAT values between 6–14°C, much closer to our proxy estimates. Because the latitudinal gradient in this area of Gondwana is less severe for MAP, these lower paleolatitudes would result in values between 700–1,400 mm/year, still consistent with our proxy estimates. From a clay mineralogy standpoint, the high smectite/illite ratios in the upper part of the Ischigualasto Formation are consistent with the aforementioned high temperature seasonality predicted by GCM results (Dunne et al., 2021).

The Chañares-Los Rastros-Ischigualasto succession preserves a nearly continuous record of the Late Triassic from the early Carnian through early Norian (~236.5–224.5 Ma). Recently published multi-proxy data (Mancuso et al., 2020a; Benavente et al., 2022) support a general trend from seasonal semi-arid to sub-humid conditions during the early Carnian (~236.5–235 Ma, Chañares Formation) to humid and warm conditions during middle Carnian (~235–231.3 Ma, Los Rastros Formation) (**Figure 9**). The warmer and wetter phase was proposed as possible evidence of the Carnian Pluvial Episode in Gondwana (Mancuso et al., 2020a; Benavente et al., 2022). The new multi-proxy data presented here for the Ischigualasto Formation supply evidence of a fluctuating climate trend for the late Carnian to early Norian (~231.3–224.5 Ma) at the Cerro Bola locality (**Figure 9**). The first ~100 m during the late Carnian (~231–229.5 Ma) record seasonal warm, humid conditions with a short episode of sub-humid to semi-arid conditions (**Figure 9**). Subsequently, during the latest Carnian (~229.5–227.8 Ma) between ~100–380 m, the Ischigualasto Formation was deposited under seasonal sub-humid to semi-arid conditions, followed by more variable, humid, more seasonal conditions at the very end of the Carnian and during the earliest Norian (~227.8–224.5 Ma) (**Figure 9**). The estimates of MAT and MAP for the Ischigualasto paleosols show a similar trend, with a mean around 950 mm/yr for MAP but with higher values in the lowermost and upper parts of the section, and a subtle change in MAT from 12.5 to 13.5°C, but lower than estimated for the Los Rastros (Mancuso et al., 2020a; Benavente et al., 2022). Our new multi-proxy data agrees well with paleosol data from the Ischigualasto Provincial Park (Tabor et al., 2004, 2006). These data from further southeast in the basin also suggested a complex pattern (see **Supplementary Material** Correlation through basin and **Supplementary Figure S3** for more detailed information about the correlation between Ischigualasto Provincial Park and Cerro Bola area), beginning with a humid episode (the lower quarter of the unit), followed by relatively dry conditions (the middle half of the unit), finishing with more humid conditions again (the upper quarter) with cool temperatures between ~0–10°C (estimating using $\delta^{18}O_{carb}$ values from pedogenic carbonate nodules). In contrast, paleobotanical and sedimentological data from this same area suggest generally seasonal arid to semi-arid conditions with a semi-humid episode in the middle of the unit (Colombi and Parrish, 2008; César and Colombi, 2013; Colombi et al., 2013).

These differences likely reflect the spatial and temporal scale at which the proxies record paleoenvironment. The proxies for MAP and MAT are dependent upon local geochemical conditions and thus could easily vary across the basin. At the

same time, they are somewhat time-averaged given how long it takes paleosols to develop. Sedimentological indicators can also be quite localized with significant lateral variation, and paleosol morphology (e.g., pedotype) is driven in part by changes in the local water table. Therefore, it is not surprising that studies using different proxies from different parts of the basin may observe variation in inferred paleoclimate conditions. From a palaeontological perspective, using fossils to interpret climate conditions is circular if one is then comparing that climate record with the fossil record. Regardless, the differences between the climate reconstruction from geochemical, clay mineralogy, and paleosol morphology data compared to the paleontological interpretations (macro and microflora, vertebrate) (Colombi and Parrish, 2008; Césari and Colombi, 2013; Colombi et al., 2013) can be explained due to the strong dependence of fossil preservation with local sedimentological conditions (see **Supplementary Material**). The floral record is essentially preserved under high water-table conditions (Agua de la Peña locality and around the site), independent of larger-scale changes in climate (Colombi and Parrish, 2008; Césari and Colombi, 2013). In addition, vertebrate fossil assemblages are mainly preserved on well-drained low water-table deposits (Colombi et al., 2013). Therefore, the paleontological record largely reflects local taphonomic and sedimentological conditions instead of basin-wide or regional climate.

Clay mineralogy data for the Chañares, Los Rastros, and Ischigualasto formations has also been documented for other parts of the IVUB (Bossi, 1970; Ovejero and Bossi, 1984; Tabor et al., 2006; Mancuso et al., 2020a). The mineralogical assemblages found at the Cerro Bola locality agree with previous Ischigualasto Formation mineralogical data from Agua de la Peña and Zanja de la Viuda localities (Bossi, 1970; Ovejero and Bossi, 1984; Tabor et al., 2006). These clay assemblages record varying proportions of smectite, illite, kaolinite, chlorite, and mixed-layer illite/smectite. Smectite is the dominant clay mineral, followed by kaolinite and illite, at Ischigualasto Provincial Park (Bossi, 1970; Tabor et al., 2006); in contrast, at the Cerro Bola and Zanja de la Viuda localities (**Figure 1**), illite is the dominant component followed by a similar contribution of kaolinite and smectite (**Figure 2**; see **Figure 5** in Ovejero and Bossi, 1984). Nevertheless, within the Ischigualasto Formation, there are consistent assemblages across the basin that highlight the general pattern of an enhanced hydrolysis index due to increased leaching. Those intervals are characterized by a higher contribution of kaolinite and smectite and might record geologically brief episodes of discrete enhanced humidity (380–420, 465, 550, 580, and 680 m levels at Cerro Bola). Similarly, the mineralogical assemblages found at the Gualo locality and Cerro Bola for the Chañares and Los Rastros formations (Mancuso et al., 2020a) agree with the mineralogy previously documented at the Río Ischigualasto, Zanja de la Viuda localities (Bossi, 1970; Ovejero and Bossi, 1984). In general, illitization processes have been more pervasive in the Ischigualasto deposits than in the Chañares and Los Rastros assemblages (Mancuso et al., 2020a).

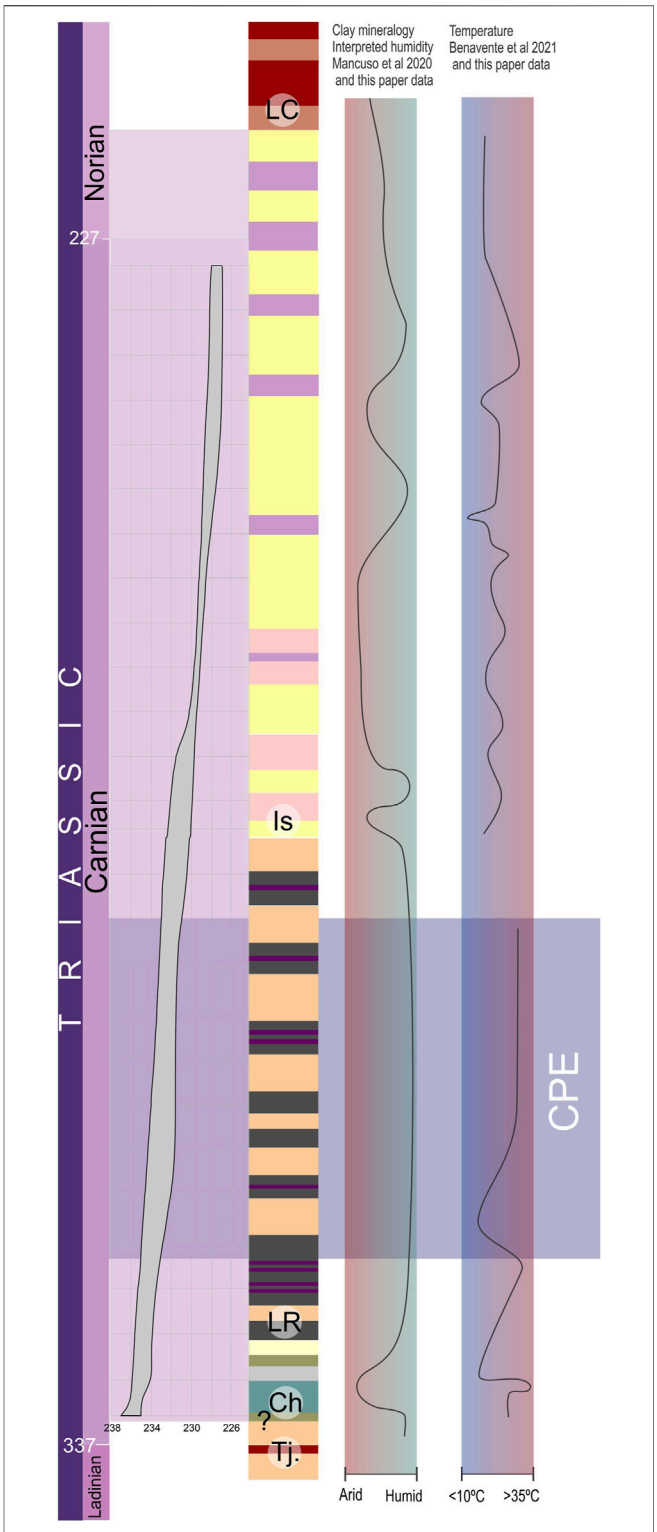

FIGURE 9 | Summary of Agua de la Peña Group paleoclimate interpretations. Geochronologic age constraints for the Chañares, Los Rastros, and Ischigualasto formations modified from the preliminary age model with uncertainty envelope (gray shading) for the unit based on radioisotopic ages (Irmis et al., 2022). Ch, Chañares Formation; Is, Ischigualasto Formation; LC, Los Colorados Formation; LR, Los Rastros Formation; Tj, Tarjados Formation.

Interestingly, Bossi (1970) suggested that clay mineral assemblages are relatively consistent within their depositional subenvironments. For example, illite dominates lateral accretion fluvial elements and kaolinite and to a less extent smectite are predominant in fluvial lateral suspension and vertical accretion deposits. These are the natural authigenic subenvironments for those clay minerals and support the primary composition of the mineralogical assemblages that are most likely reflecting a paleoclimate signal. In our analysis, we have found that the lake center deposits (Los Rastros Formation - Bossi´s vertical accretion deposits) are dominated by kaolinite and less common smectite; and the fluvial floodplains with occasional ponds (Ischigualasto Formation - Bossi´s fluvial lateral suspension) are dominated by variable proportions of kaolinite-illite- smectite-illite/smectite.

Analyzing the mineralogical proxies (kaolinite/illite, smectite/illite, and smectite/kaolinite ratios), the general trend of highly dispersed values in lower and upper levels of the Ischigualasto is also recorded in the sections from Agua de la Peña and Zanja de la Viuda (Bossi, 1970; Ovejero and Bossi, 1984). Therefore, the clay mineralogy proxy evidence suggests basin-wide seasonal semi-arid to sub-humid paleoclimate trend during deposition of the early Carnian Chañares Formation, humid and warm conditions for the middle Carnian Los Rastros Formation, followed by variable seasonal less humid conditions for the late Carnian-early Norian Ischigualasto Formation. This consistency across the basin thus provides some confidence in using our results to compare with the basin-wide fossil record. Unfortunately, other proxies included in this contribution can not be compared directly with other localities of the IVUB; however, as mentioned previously, the general climate trend we observed compares well with paleosol data from the Ischigualasto Provincial Park (Tabor et al., 2004, 2006).

5.2 Paleobotanical Record and Links With Climatic Proxies

Although limitations in sampling mean that we cannot compare the paleobotanical and climate record using our hypothesis testing framework, the plant fossil record suggests that changes in vegetation accompanied broad changes in climatic conditions across the formations. In the Los Rastro Formation, vegetation was stable both in time and space (Pedernera et al., 2020). This stability could be related to the more humid and stable climatic conditions proposed for the unit (Mancuso et al., 2020a). On the other hand, the lower number of plant macrofossil taxa recorded in the Ischigualasto Formation (**Figure 4**), and lower number of taxa per taxonomic group (see **Supplementary Material**) could be related to the high variability of the MAP and MAT, though we caution that a more direct comparison would require sample standardization techniques (e.g., rarefaction or quorum sub-sampling). These plant fossils come from specific fossiliferous levels restricted temporally and spatially (Colombi and Parrish, 2008; Drovandi et al., 2021). Indeed, the taphofacies described by Colombi and Parrish (2008) are both temporally and spatially restricted; these authors indicate that the observed patterns are due to the fluvial architecture and paleosols related to the evolution of the climate during the deposition of the Ischigualasto Formation. An extensive systematic sampling of the unit to reduce sampling gaps could help clarify changes in the plant fossil record allowing one to more directly test the hypothesis predictions outlined in **Section 1.3**.

The palynomorph assemblages of the Chañares and Ischigualasto formations have been considered part of a 'transitional zone' between the Ipswich and the Onslow subprovinces (César and Colombi, 2013; Perez Lonaize et al., 2018). In contrast, the Los Rastros microfloral assemblage is typical of the Ipswich sub-province (Ottone et al., 2005; Ottone and Mancuso, 2006; César and Colombi, 2016). Traditionally, the Onslow microflora has been used as an indicator of hot and humid climatic conditions, whereas the Ipswich microflora has been considered an indicator of relatively cooler temperature zones (Dolby and Blame, 1976). However, the microfloristic assemblages described in the formations of the Agua de la Peña Group do not agree with MAT and MAP estimates proposed for the same units. The Chañares Formation has been interpreted as seasonal semi-arid to sub-humid (Mancuso et al., 2020a), the Los Rastros Formation humid and warm (Mancuso et al., 2020a), and the Ischigualasto Formation data indicate variable semi-arid to humid variable conditions for the unit (**Figure 3**). As such, one might predict that the Chañares and Ischigualasto microfloral assemblages would be most similar to the Ipswich microflora, whereas the microflora of the Los Rastros Formation would have a greater presence of Onslow characteristic elements; this is the opposite of what is preserved. Therefore, the differences in the palynological assemblages among the Chañares, Los Rastros, and Ischigualasto formations may not be associated with climatic variations and these differences could be linked with the intrabasin spatial distribution of habitats for plant microspores producers. It is very possible that the Los Rastros Formation was also located in this microfloral province transition zone (cf. César and Colombi, 2013), and the more humid conditions during the CPE restricted typical Onslow miospore plant producers to distal upland areas that are not preserved in this unit. These complexities reinforce the need for independent paleoclimate proxies (such as those in this contribution) for properly interpreting possible climate influence on floras in deep time.

Ultimately, systematic sampling for palynomorphs and plant macrofossils throughout this sequence, particularly the Ischigualasto Formation, is necessary to develop a well-sampled record at many different stratigraphic levels. Only with this improved high-resolution record will there be enough data points to properly test proposed hypotheses linking plant diversity and relative abundance with climate (Pardoe et al., 2021).

5.3 Tetrapod Record and Links With Climatic Proxies

Assessing changes in tetrapod composition in relation to paleoclimate across the different formations of the Agua de la Peña Group is very difficult given that there are large stratigraphic

gaps between samples (e.g., upper Los Rastros and lower Los Colorados formations), and different styles of preservation that are not directly comparable (i.e., predominantly ichnofossils from the Los Rastros compared to body fossils from all other formations). Indeed, whether one examines changes in clade species richness (**Figure 6**) or inferred habitat preference (**Figure 7**), there are no changes that seem clearly related to climate differences between the formations. This highlights the challenges of the traditional pattern-matching approach; namely, that other factors (e.g., preservation, sampling) can mask any original direct correlation with climate variables. In any case, it is not necessarily clear that one should expect such simple correlations, given that it does not reflect known evolutionary models (e.g., Faith et al., 2021).

The synapsid fossil record from the IVUB exemplifies these difficulties. The decrease in dicynodont diversity from the Chañares to Ischigualasto Formation, and their absence in the upper levels of the Norian Los Colorados Formation, follows global trends, so it seems imprudent to try to ascribe it to regional/basin-scale climate change. In contrast, cynodonts, in particular probainognathians, proliferated on many continents during the Carnian and into the Norian and Rhaetian, even in relatively nearby regions (see Abdala et al., 2020 for a review). Therefore, their absence above bin 2 in the Ischigualasto Formation (with the exception of *Exaeretodon*) does seem to be a more local pattern. One might hypothesize this change reflects the more arid seasonal conditions above the 100 m level, but it also could simply be a result of declining sample size not picking up rare taxa that are only known from a handful of specimens. As another example, higher in section, in the uppermost portion of the Ischigualasto Formation, fossils in Unit IV are scarce (**Figure 8**, **Supplementary Figures S6, S7**). They are only represented by 1 specimen (a single bone) of the dicynodont *Jachaleria* and a few isolated indeterminate archosaur elements (Martínez et al., 2011). In the lowermost Los Colorados Formation, vertebrate representation is also poor, with only 8 specimens of *Jachaleria* reported (Martínez et al., 2011), although recently a bonebed including a minimum of 200 bones (mostly *Jachaleria*) has been reported (Colombi et al., 2018). The top of the Ischigualasto Formation and the lower levels of the Los Colorados Formation appear to represent an interval in which fossils are scarce. Martínez et al. (2011) proposed that this extremely low abundance of vertebrates cannot be explained by poor sampling or poorly exposed outcrops, and suggested that this situation could be correlated with more arid conditions and better explained by a true absence of fauna or by a taphonomic bias (Martínez et al., 2011). In contrast, our results regarding the interpretation of aridity point to the opposite (**Figure 8**), with a change to more humid (bin 13) conditions near the top of the Ischigualasto Formation. So does the low diversity and abundance of tetrapods at this boundary interval reflect actual rarity on the paleolandscape, preservational/sampling bias, or a combination of the two? Examination of the more detailed tetrapod record of the Ischigualasto Formation is equally ambiguous to interpret from a pattern-matching perspective, with few obvious changes in species richness, relative abundance, or stratigraphic ranges (**Figure 8**; **Supplementary Figure S13**) coinciding with the main paleoclimate changes inferred from the proxy datasets in this study.

For this reason, building on recent work from other authors (Faith et al., 2021), we instead proposed an approach for evaluating explicit predictions from existing hypotheses using known evolutionary models for vertebrate response to climate change in deep time. The advantage of this approach is that it makes specific a priori predictions based on what we know about evolution that can then be tested using the fossil record, rather than a posteriori trying to match changes in paleoclimate proxies with those from fossil assemblages. Nonetheless, our study demonstrates how difficult this can be even with a rich climate proxy record and abundant fossil dataset. This Ischigualasto case study highlighted how sampling and taphonomy can strongly control patterns in the fossil record even when many specimens are known from many different stratigraphic levels. As a result we were unable to fully test the predictions for each hypothesis, particularly when it came to evaluating pulses of first occurrences. Though we observed a few subtle changes that do not appear to be tied to sampling, one might query why there is not a stronger correlation with paleoclimatic changes. One or more processes may be at play. First, it might be that the magnitude and/or pace of climate change observed simply was not great enough to force major changes in ecosystem structure. Alternatively, despite our abundant fossil record, it might be that other changes are subtle enough that they require even greater stratigraphic resolution (e.g., meter scale as opposed to 50 m bins) with even denser specimen sampling.

Even so, there are definitely reasons for optimism. First, we were able to find partial support for one hypothesis, with a pulse of pseudosuchian archosaur LAs associated with a shift to more humid conditions, which was consistent with the predictions for Hypothesis 4. Second, we were able to provide fairly strong evidence to help falsify Hypothesis 5, where we observed the opposite trend in rhynchosaur relative abundance (compared to the climate trend) than predicted. In this case, we can formulate a new hypothesis; namely, that rhynchosaur abundance increased during more humid intervals. Notably, this tetrapod clade is perhaps the best sampled in the formation in terms of number of specimens, exemplifying the predictive power of large sample sizes. And even where we were unable to find evidence for/against hypotheses, lacked the sampling to make evaluations, or found a strong sampling control on diversity and abundance patterns, it highlights where more work should be concentrated in the basin to build datasets that are sufficient for hypothesis testing. Finally, and perhaps most importantly, regardless of specific results for the Ischigualasto Formation or IVUB, our study is an example of how one can use this predictive framework in future studies to evaluate biotic response to climate change in deep time.

6 CONCLUSION

Our new multiproxy dataset for the Ischigualasto Formation provides insights into key changes in paleoenvironment and paleoclimate during the late Carnian and early Norian. Combined with previous work in other parts of the basin and other formations, we are able to identify and elucidate basin-scale trends in paleoclimate, and compare them to the extensive floral and vertebrate fossil records. Although sampling is a primary control of patterns observed in these fossil assemblages, we observe a small number of changes in species richness and relative abundance that are consistent with predictions from evolutionary models for climate forcing of biotic change. Moreover, our approach to testing for associations highlights data gaps that must be filled by additional sampling, and makes new testable predictions that can be tested by future work.

DATA AVAILABILITY STATEMENT

The original contributions presented in the study are included in the article/**Supplementary Material**, further inquiries can be directed to the corresponding author.

AUTHOR CONTRIBUTIONS

ACM and RBI designed the project. ACM and RBI conducted geological sections and palaeoenvironmental interpretation. BTB conducted XRF analyses. ACM and CAB conducted climate studies. ACM, RBI, TEP, and LCG conducted paleontological studies. ACM, RBI, and TEP designed and prepared the figures. RBI and TEP conducted the statistical analysis. ACM, RBI, TEP, and LCG wrote the **Supplementary Material**. ACM and RBI wrote the manuscript with input from all authors.

FUNDING

Field and laboratory research were supported by the PIP CONICET 11420090100209/10 and PICT 2013-0805 (ACM). Additional financial support was provided by the Consejo Nacional de Investigaciones Científicas y Técnicas (CONICET), and University of Utah.

ACKNOWLEDGMENTS

We thank E. Previtera, M. Bourguet, and C. Sancho (IANIGLA-CONICET) for their support during fieldwork. For access permission, we thank Carlos Ariel Ormeño and Ana Mercado Luna (Dirección de Patrimonio Arqueológico y Paleontológico, Secretaría de Cultura de La Rioja) and Administración de Parques Nacionales. We are deeply indebted to the staff of Parque Nacional Talampaya for their constant assistance in the field. Andrea Brunelle, Brenda Bowen, and Isaac Hart (University of Utah) kindly provided XRF access. We thank Tyler Faith for discussions on testing the relationship between paleoclimate and the fossil record, and for assistance with calculating adjusted residuals. Emma Dunne generously shared the individual GCM paleoclimate values for the Ischigualasto Formation from her 2021 study. This is LCG´s R-419 contribution to the IDEAN. We thank the editor and two referees for comments that improved the manuscript.

SUPPLEMENTARY MATERIAL

The Supplementary Material for this article can be found online at: https://www.frontiersin.org/articles/10.3389/feart.2022.883788/full#supplementary-material

REFERENCES

Abarzúa, F. (2016). *Estratigrafía, análisis de cuenca y aspectos exploratorios en el extremo norte de Cuenca Cuyana, in Precordillera Occidental y Valle de Calingasta*. PhD dissertation. Facultad de Ciencias Exactas, Físicas y Naturales (Universidad Nacional de San Juan), 188.

Abdala, F., Gaetano, L. C., Martinelli, A. G., Soares, M. B., Hancox, P. J., and Rubidge, B. S. (2020). Non-mammaliaform Cynodonts from Western Gondwana and the Significance of Argentinean Forms in Enhancing Understanding of the Group. *J. S. Am. Earth Sci.* 104, 1028841–1028932. doi:10.1016/j.jsames.2020.102884

Abu Hamad, A., Kerp, H., Vörding, B., and Bandel, K. (2008). A Late Permian Flora with *Dicroidium* from the Dead Sea Region, Jordan. *Rev. Palaeobot. Palynology* 149, 85–130. doi:10.1016/j.revpalbo.2007.10.006

Anderson, J. M., and Anderson, H. M. (1983). *Palaeoflora of Southern Africa: Molteno Formation (Triassic) 1, Introduction*. Rotterdam: Dicroidium. A.A. Balkema.

Anderson, J. M., and Anderson, H. M. (1985). *Palaeoflora of Southern Africa: Prodromus of South African Megafloras*. Rotterdam: Devonian to Lower Cretaceous. Balkema.

Anderson, J. M., and Anderson, H. M. (1989). *Palaeoflora of Southern Africa: Molteno Formation (Triassic). 2. Gymnosperms (Excluding Dicroidium)*. Rotterdam: A.A. Balkema.

Arcucci, A. B., Marsicano, C. A., and Caselli, A. T. (2004). Tetrapod Association and Paleoenvironment of Los Colorados Formation (Argentina): A Significant Sample from Western Gondwana at the End of the Triassic. *Geobios* 37, 555–568. doi:10.1016/j.geobios.2003.04.008

Artabe, A. E., Morel, E. M., and Spalletti, L. A. (2001). "Paleoecología de las floras Triásicas Argentinas," in *El Sistema Triásico en la Argentina*. Editors A. E. Artabe, E. M. Morel, and A. B. Zamuner (La Plata: Fundación Museo de La Plata "Francisco Pascasio Moreno), 199–225.

Artabe, E. A., Morel, E. M., and Spalletti, L. A. (2003). Caracterización de las provincias fitogeográficas Triásicas del Gondwana extratropical. *Ameghiniana* 40 (3), 1–19.

Azevedo, S. A., Schultz, C. L., and Barberena, M. C. (1990). Novas evidéncias bioestratigráficas e paleoecológicas na análise da evolução explosiva dos rincossauros do Triássico. *Paula-Coutiana* 4, 23–33.

Balme, B. E., and Helby, R. J. (1973). "Floral Modifications at the Permian-Triassic Boundary in Australia," in *Permian Triassic Systems and Their Mutual Boundary*. Editor V. I. Ustritsky (CSPG Special Publications, Memoir), 2, 433–444.

Barboni, R., and Dutra, T. L. (2015). First Record of Ginkgo-Related Fertile Organs (*Hamshawvia, Stachyopitys*) and Leaves (*Baiera, Sphenobaiera*) in the Triassic of Brazil, Santa Maria Formation. *J. S. Am. Earth Sci.* 63, 417–435. doi:10.1016/j.jsames.2015.08.001

Barnosky, A. D. (2001). Distinguishing the Effects of the Red Queen and Court Jester on Miocene Mammal Evolution in the Northern Rocky Mountains. *J.*

Vertebrate Paleontology 21, 172–185. doi:10.1671/0272-4634(2001)021[0172:dteotr]2.0.co;2

Barrenechea, J. F., López-Gómez, J., and De La Horra, R. (2018). Sedimentology, Clay Mineralogy and Palaeosols of the Mid-carnian Pluvial Episode in Eastern Spain: Insights into Humidity and Sea-Level Variations. *J. Geol. Soc.* 175, 993–1003. doi:10.1144/jgs2018-024

Behrensmeyer, A. K., and Chapman, R. E. (1993). Models and Simulations of Time-Averaging in Terrestrial Vertebrate Accumulations. *Short. Courses Paleontol.* 6, 125–149. doi:10.1017/s2475263000001082

Behrensmeyer, A. K., Hook, R. W., Badgley, C. E., Boy, J. A., Chapman, R. E., Dodson, P., et al. (1992). "Paleoenvironmental Contexts and Taphonomic Modes," in *Terrestrial Ecosystems through Time: Evolutionary Paleoecology of Terrestrial Plants and Animals*. Editors A. K. Behrensmeyer, J. D. Damuth, W. A. Dimichele, R. Potts, H.-D. Sues, and S. L. Wing (Chicago: University of Chicago Press), 15–136.

Benavente, C. A., Mancuso, A. C., and Bohacs, K. M. (2019). Paleohydrogeologic Reconstruction of Triassic Carbonate Paleolakes from Stable Isotopes: Encompassing Two Lacustrine Models. *J. S. Am. Earth Sci.* 95, 102292. doi:10.1016/j.jsames.2019.102292

Benavente, C. A., Mancuso, A. C., Irmis, R. B., Bohacs, K. M., and Matheos, S. (2022). Tectonically Conditioned Record of Continental Interior Paleoclimate during the Carnian Pluvial Episode: The Upper Triassic Los Rastros Formation, Argentina. *Geol. Soc. Am. Bull.* 134 (1-2), 60–80. doi:10.1130/B35847.1

Bennett, J. M. (2018). GlobTherm, a Global Database on Thermal Tolerances for Aquatic and Terrestrial Organisms. *Sci. Data* 5 (1), 180022. doi:10.1038/sdata.2018.22

Benton, M. J., Bernardi, M., and Kinsella, C. (2018). The Carnian Pluvial Episode and the Origin of Dinosaurs. *J. Geol. Soc.* 175, 1019–1026. doi:10.1144/jgs2018-049

Benton, R. B. J., Butler, R., Close, R. A., Saupe, E., and Rabosky, D. L. (2021). Biodiversity across Space and Time in the Fossil Record. *Curr. Biol.* 31, R1225–R1236. doi:10.1016/j.cub.2021.07.071

Bernardi, M., Gianolla, P., Petti, F. M., Mietto, P., and Benton, M. J. (2018). Dinosaur Diversification Linked with the Carnian Pluvial Episode. *Nat. Commun.* 9, 1–10. doi:10.1038/s41467-018-03996-1

Berry, J. A., and Raison, J. K. (1981). "Responses of Macrophytes to Temperature," in *Physiological Plant Ecology I*. Editors O. L. Lange, P. S. Nobel, C. B. Osmond, and H. Ziegler (Berlin, Heidelberg: Springer), 277–338. doi:10.1007/978-3-642-68090-8_11

Bobe, R., Behrensmeyer, A. K., and Chapman, R. E. (2002). Faunal Change, Environmental Variability and Late Pliocene Hominin Evolution. *J. Hum. Evol.* 42, 475–497. doi:10.1006/jhev.2001.0535

Bodnar, J., Coturel, E. P., Falco, J. I., and Beltrán, M. (2021). An Updated Scenario for the End-Permian Crisis and the Recovery of Triassic Land Flora in Argentina. *Hist. Biol.* 33 (12), 3654–3672. doi:10.1080/08912963.2021.1884245

Bodnar, J., Drovandi, J. M., Morel, E. M., and Ganuza, D. G. (2018). Middle Triassic Dipterid Ferns from West-Central Argentina and Their Relationship to Palaeoclimatic Changes. *Acta Palaeontol. Pol.* 63 (2), 397–416. doi:10.4202/app.00459.2018

Bomfleur, B., and Kerp, H. (2010). *Dicroidium* Diversity in the Upper Triassic of North Victoria Land, East Antarctica. *Rev. Palaeobot. Palynology* 160 (3-4), 67–101. doi:10.1016/j.revpalbo.2010.02.006

Bomfleur, B., Decombeix, A. L., Escapa, I. H., Schwendemann, A. B., and Axsmith, B. (2013). Whole–plant Concept and Environment Reconstruction of a *Telemachus* Conifer (Voltziales) from the Triassic of Antarctica. *Int. J. Plant Sci.* 174 (3), 425–444. doi:10.1086/668686

Bomfleur, B., Decombeix, A. L., Schwendemann, A. B., Escapa, I. H., Taylor, E. L., Taylor, T. N., et al. (2014). Habit and Ecology of the Petriellales, an Unusual Group of Seed Plants from the Triassic of Gondwana. *Int. J. Plant Sci.* 175 (9), 1062–1075. doi:10.1086/678087

Bordy, E. M., Abrahams, M., Sharman, G. R., Viglietti, P. A., Benson, R. B. J., McPhee, B. W., et al. (2020). A Chronostratigraphic Framework for the Upper Stormberg Group: Implications for the Triassic-Jurassic Boundary in Southern Africa. *Earth-Science Rev.* 203, 1031201–1031224. doi:10.1016/j.earscirev.2020.103120

Bossi, G. E. (1970). Asociaciones mineralógicas de las arcillas en la cuenca de Ischigualasto – Ischichuca. Parte II: Perfiles de la Hoyada de Ischigualasto. *Acta Geol. Lilloana* 11 (4), 73–100.

Bossi, G. E. (1971). Análisis de la Cuenca de Ischigualasto-Ischichuca. *I Congreso Hispano-Luso-Americano de Geologia Economica*. Madrid: Ibérica, 611–626.

Boucot, A. J., Xu, C., Scotese, C. R., and Morley, R. J. (2013). Phanerozoic Climate: an Atlas of Lithologic Indicators of Climate. *SEPM Concepts Sedimentol. Paleontol.* 11.

Caselli, A. T. (1998). *Estratigrafía y sedimentología de las formaciones Patquía (Pérmico) y Talampaya (Triásico inferior) en las Sierras Pampeanas Noroccidentales y Precordillera Central (provincias de La Rioja y San Juan)*. Buenos Aires, Argentina: Universidad de Buenos Aires, 437.

Caselli, A. T., Marsicano, C. A., and Arcucci, A. B. (2001). Sedimentología y paleontología de la Formación Los Colorados, Triásico Superior (provincias de La Rioja y San Juan, Argentina). *Rev. Asoc. Geol. Argent.* 56, 173–188.

Césari, S. N., and Colombi, C. E. (2013). A New Late Triassic Phytogeographical Scenario in Westernmost Gondwana. *Nat. Commun.* 4, 18891–18896.

Césari, S. N., and Colombi, C. E. (2016). Palynology of the Late Triassic Ischigualasto Formation, Argentina: Paleoecological and Paleogeographic Implications. *Palaeogeogr. Palaeoclimatol. Palaeoecol.* 449, 365–384.

Chamley, H. (1989). *Clay Sedimentology*. Berlin: Springer-Verlag.

Chandra, S., Singh, K. J., and Jha, N. (2008). First Report of the Fertile Plant Genus Umkomasia from Late Permian Beds in India and its Biostratigraphic Significance. *Palaeontology* 51, 817–826. doi:10.1111/j.1475-4983.2008.00767.x

Channing, A., Zamuner, A., Edwards, D., and Guido, D. (2011). *Equisetum thermale* Sp. Nov. (Equisetales) from the Jurassic San Agustín Hot Spring Deposit, Patagonia: Anatomy, Paleoecology, and Inferred Paleoecophysiology. *Am. J. Bot.* 98 (4), 680–697. doi:10.3732/ajb.1000211

Cirilli, S. (2010). Upper Triassic-Lowermost Jurassic Palynology and Palynostratigraphy: A Review. *Geological Society of London Special Publication* 334, 285–314. doi:10.1144/sp334.12

Cladera, G., Rougier, G., de la Fuente, M., and Arcucci, A. B. (1998). Niveles fosilíferos del sector superior de la Formación Los Colorados (Triásico Tardio) en las proximidades de «La Esquina», Provincia de La Rioja, Argentina. *Acta Geol. Lilloana* 18, 159.

Clift, P. D., Wan, S., and Blusztajn, J. (2014). Reconstructing Chemical Weathering, Physical Erosion and Monsoon Intensity since 25 Ma in the Northern South China Sea: A Review of Competing Proxies. *Earth-Science Rev.* 10, 86–102. doi:10.1016/j.earscirev.2014.01.002

Colbert, E. H. (1971). Tetrapods and Continents. *Q. Rev. Biol.* 46, 250–269. doi:10.1086/406898

Colombi, C. E., and Parrish, J. T. (2008). Late Triassic Environmental Evolution in Southwestern Pangea: Plant Taphonomy of the Ischigualasto Formation. *Palaios* 23, 778–795. doi:10.2110/palo.2007.p07-101r

Colombi, C. E., Montañez, I. P., and Parrish, J. T. (2011). Registro de la relación isotópica de carbono en la paleoflora de la Formación Ischigualasto (Triásico Superior), noroeste argentino: implicaciones paleoatmosféricas. *Rev. Bras. Paleontol.* 14, 39–50. doi:10.4072/rbp.2011.1.04

Colombi, C. E., Rogers, R. R., and Alcober, O. A. (2013). Vertebrate Taphonomy of the Ischigualasto Formation. *Society of Vertebrate Paleontology Memoir* 12, 31–50. doi:10.1080/02724634.2013.809285

Colombi, C. E., Limarino, C. O., and Alcober, O. A. (2017). Allogenic Controls on the Fluvial Architecture and Fossil Preservation of the Upper Triassic Ischigualasto Formation, NW Argentina. *Sediment. Geol.* 362, 1–16. doi:10.1016/j.sedgeo.2017.10.003

Colombi, C. E., Martínez, R. N., Césari, S. N., Alcober, O. A., Limarino, C. O., and Montañez, I. P. (2021). A High-Precision U–Pb Zircon Age Constraints the Timing of the Faunistic and Palynofloristic Events of the Carnian Ischigualasto Formation, San Juan, Argentina. *J. S. Am. Earth Sci.* 111, 103433. doi:10.1016/j.jsames.2021.103433

Colombi, C., Martínez, R., Santi Malnis, P., Apaldetti, C., Yañez, I., Abelín, D., et al. (2018). Bonebed en las facies basales de la Formación Los Colorados (Noriano), Cuenca de Ischigualasto-Villa Unión, San Juan, Argentina. *Actas Reunión de Comunicaciones de la Asociación Paleontológica Argentina*, 54.

Coturel, E. P., Bodnar, J., Morel, E. M., Ganuza, D., Sagasti, A. J., and Beltrán, M. (2018). New Species of Osmundaceous Fertile Leaves from the Upper Triassic of Argentina. *Acta Palaeobot.* 58 (2), 107–119.

Currie, B. S., Colombi, C. E., Tabor, N. J., Shipman, T. C., and Montañez, I. P. (2009). Stratigraphy and Architecture of the Upper Triassic Ischigualasto Formation, Ischigualasto Provincial Park, San Juan, Argentina. *J. S. Am. Earth Sci.* 27, 74–87. doi:10.1016/j.jsames.2008.10.004

D'Angelo, J. A. (2019). Molecular Structure of the Cuticles of *Dicroidium* and *Johnstonia* (Corystospermaceae, Triassic, Argentina). Ecophysiological Adaptations of Two Chemically Indistinguishable, Morphology-Based Taxa. *Rev. Palaeobot. Palynology* 268, 109–124. doi:10.1016/j.revpalbo.2019.05.007

Dal Corso, J., Ruffell, A., and Preto, N. (2018). The Carnian Pluvial Episode (Late Triassic): New Insights into This Important Time of Global Environmental and Biological Change. *J. Geol. Soc.* 175, 986–988. doi:10.1144/jgs2018-185

Dal Corso, J., Bernardi, M., Sun, Y., Song, H., Seyfullah, L. J., Preto, N., et al. (2020). Extinction and Dawn of the Modern World in the Carnian (Late Triassic). *Sci. Adv.* 6, 1–12, eaba0099. doi:10.1126/sciadv.aba0099

Dal Corso, J., Gianolla, P., Newton, R. J., Franceschi, M., Roghi, G., Caggiati, M., et al. (2015). Carbon Isotope Records Reveal Synchronicity between Carbon Cycle Perturbation and the "Carnian Pluvial Event" in the Tethys Realm (Late Triassic). *Glob. Planet. Change* 127, 79–90. doi:10.1016/j.gloplacha.2015.01.013

Dal Corso, J., Mietto, P., Newton, R. J., Pancost, R. D., Preto, N., Roghi, G., et al. (2012). Discovery of a Major Negative $\delta^{13}C$ Spike in the Carnian (Late Triassic) Linked to the Eruption of Wrangellia Flood Basalts. *Geology* 40, 79–82. doi:10.1130/g32473.1

Di Michele, W. A. (2013). Wetland-dryland Vegetational Dynamics in the Pennsylvanian Ice Age Tropics. *Int. J. Plant Sci.* 175 (2), 123–164.

Do Campo, M., del Papa, C., Nieto, F., Hongn, F., and Petrinovic, I. (2010). Integrated Analysis for Constraining Palaeoclimatic and Volcanic Influences on Clay–Mineral Assemblages in Orogenic Basins (Palaeogene Andean Foreland, Northwestern Argentina). *Sediment. Geol.* 228, 98–112. doi:10.1016/j.sedgeo.2010.04.002

Dolby, J. H., and Balme, B. E. (1976). Triassic Palynology of the Carnarvon Basin, Western Australia. *Rev. Palaeobot. Palynology* 22, 105–168. doi:10.1016/0034-6667(76)90053-1

Doubinger, J., Vetter, P., Langiaux, J., Galtier, J., and Broutin, J. (1995). La flore fossile du bassin houiller de Saint-Étienne. *Muséum National d'Histoire Naturelle*, Paris 164.

Drovandi, J. M., Correa, G. A., Colombi, C. E., and Césari, S. N. (2021). *Dicroidium* (*Zuberia*) *zuberi* (Szajnocha) Archangelsky from Exceptional Carnian Leaf Litters of the Ischigualasto Formation, Westernmost Gondwana. *Hist. Biol.*, 1–14. doi:10.1080/08912963.2021.1974017

Dunne, E. M., Farnsworth, A., Greene, S. E., Lunt, D. J., and Butler, R. J. (2021). Climatic Drivers of Latitudinal Variation in Late Triassic Tetrapod Diversity. *Palaeontology* 64, 101–117. doi:10.1111/pala.12514

Ezcurra, M. D. (2010). Biogeography of Triassic Tetrapods: Evidence for Provincialism and Driven Sympatric Cladogenesis in the Early Evolution of Modern Tetrapod Lineages. *Proc. R. Soc. Lond. Biol. Sci.* 277, 2547–2552. doi:10.1098/rspb.2010.0508

Faith, J. T., and Lyman, R. L. (2019). *Paleozoology and Paleoenvironments: Fundamentals, Assumptions, Techniques*. Cambridge: Cambridge University Press.

Faith, J. T., Du, A., Behrensmeyer, A. K., Davies, B., Patterson, D. B., Rowan, J., et al. (2021). Rethinking the Ecological Drivers of Hominin Evolution. *Trends Ecol. Evol.* 36, 797–807. doi:10.1016/j.tree.2021.04.011

Falcon-Lang, H. J., Nelson, W. J., Elrick, S., Looy, C. V., Ames, P. R., and Dimichele, W. A. (2009). Incised Channel Fills Containing Conifers Indicate that Seasonally Dry Vegetation Dominated Pennsylvanian Tropical Lowlands. *Geology* 37, 923–926. doi:10.1130/g30117a.1

Fielding, C. R., Frank, T. D., McLoughlin, S., Vajda, V., Mays, C., Tevyaw, A. P., et al. (2019). Age and Pattern of the Southern High-Latitude Continental End-Permian Extinction Constrained by Multiproxy Analysis. *Nat. Commun.* 10, 1–12. doi:10.1038/s41467-018-07934-z

Foster, C. B., Balme, B. E., and Helby, R. (1994). First Record of Tethyan Palynomorphs from the Late Triassic of East Antarctica. *J. Aust. Geol. Geophys.* 15, 239–246.

Fraser, N. C., and Sues, H.-D. (2011). The Beginning of the 'Age of Dinosaurs': A Brief Overview of Terrestrial Biotic Changes during the Triassic. *Earth Environ. Sci. Trans. R. Soc. Edinb.* 101, 189–200. doi:10.1017/s1755691011020019

Freguelli, J. (1944). La serie del llamado "Rético" en el oeste Argentino (Nota preliminar). *Notas del Museo de La Plata. Geología* 30, 261–279.

Freguelli, J. (1948). Estratigrafía y edad del llamado "Rético" en la Argentina. *An. Soc. Argent. Estud. Geográficos, GAEA* 8, 159–309.

Friedman, M. (2015). The Early Evolution of Ray-Finned Fishes. *Palaeontology* 58, 213–228.

Fritts, H. C. (1976). *Tree Rings and Climate*. London: Academic Press.

Fürsich, F. T., Singh, I. B., Joachimski, M., Krumm, S., Schlirf, M., and Schlirf, S. (2005). Palaeoclimate Reconstructions of the Middle Jurassic of Kachchh (Western India): an Integrated Approach Based on Palaeoecological, Oxygen Isotopic, and Clay Mineralogical Data. *Palaeogeogr. Palaeoclimatol. Palaeoecol.* 217, 289–309.

Gaillardet, J., Dupre, B., and Allegre, C. J. (1999). Geochemistry of Large River Suspended Sediments: Silicate Weathering or Recycling Tracer? *Geochim. Cosmochim. Acta* 63, 4037–4051. doi:10.1016/s0016-7037(99)00307-5

Gallagher, T. M., and Sheldon, N. D. (2013). A New Paleothermometer for Forest Paleosols and its Implications for Cenozoic Climate. *Geology* 41, 647–650. doi:10.1130/g34074.1

Gallet, S., Jahn, B., and Torii, M. (1996). Geochemical Characterization of the Luochuan Loess-Paleosol Sequence, China, and Paleoclimatic Implications. *Chem. Geol.* 133, 67–88. doi:10.1016/s0009-2541(96)00070-8

Garzanti, E., Padoan, M., Setti, M., Lopez-Galindo, A., and Villa, I. M. (2014). Provenance versus Weathering Control on the Composition of Tropical River Mud (Southern Africa). *Chem. Geol.* 366, 61–74. doi:10.1016/j.chemgeo.2013.12.016

Giles, S., Xu, G.-H., Near, T. J., and Friedman, M. (2017). Early Members of 'living Fossil' Lineage Imply Later Origin of Modern Ray-Finned Fishes. *Nature* 549, 265–268. doi:10.1038/nature23654

Goddéris, Y., Donnadieu, Y., de Vargas, C., Pierrehumbert, R. T., Dromart, G., and van de Schootbrugge, B. (2008). Causal or Casual Link between the Rise of Nannoplankton Calcification and a Tectonically-Driven Massive Decrease in Late Triassic Atmospheric CO_2? *Earth Planet. Sci. Lett.* 267, 247–255.

Goldberg, K., and Humayun, M. (2010). The Applicability of the Chemical Index of Alteration as Paleoclimatic Indicator: An Example from the Permian of the Parana Basin, Brazil. *Palaeogeogr. Palaeoclimatol. Palaeoecol.* 293, 175–183. doi:10.1016/j.palaeo.2010.05.015

Grayson, D. K., and Delpech, F. (2003). Ungulates and the Middle-To-Upper Paleolithic Transition at Grotte XVI (Dordogne, France). *J. Archaeol. Sci.* 30, 1633–1648. doi:10.1016/s0305-4403(03)00064-5

Hammer, Ø., Harper, D. a. T., and Ryan, P. D. (2001). PAST: Paleontological Statistics Software Package for Education and Data Analysis. *Palaeontol. Electron.* 4 (1), 1–9.

Harris, R., McCall, R., Randall, O., Tawang, M. H. B., Williams, R., Fairman, J. G., Jr, et al. (2017). Climate Change during the Triassic and Jurassic. *Geol. Today* 33, 210–215. doi:10.1111/gto.12210

He, S.-A., Yin, G., and Pang, Z.-J. (1997). "Resources and Prospects of *Ginkgo biloba* in China," in *Ginkgo Biloba a Global Treasure*. Editor T. Hori (Tokyo): Springer), 373–383.

Hochuli, P. A., Sanson-Barrera, A., Schneebeli-Hermann, E., and Bucher, H. (2016). Severest Crisis Overlooked-Worst Disruption of Terrestrial Environments Postdates the Permian-Triassic Mass Extinction. *Sci. Rep.* 6 (1), 1–7. doi:10.1038/srep28372

Holland, S. M. (2003). *Analytic Rarefaction*. v1.3 ed.: Available at: https://strata.uga.edu/software/.

Holmes, R. L. (1985). *A Users Manual for Program COFECHA [Computer-Assisted Quality Control in Tree-Ring Dating and Measurement]*. Laboratory of Tree-Ring Research, 2–23.

Holz, M. (2015). Mesozoic Paleogeography and Paleoclimates – A Discussion of the Diverse Greenhouse and Hothouse Conditions of an Alien World. *J. S. Am. Earth Sci.* 61, 91–107. doi:10.1016/j.jsames.2015.01.001

Horn, B. L. D., Goldberg, K., and Schultz, C. L. (2018b). A Loess Deposit in the Late Triassic of Southern Gondwana, and its Significance to Global Paleoclimate. *J. S. Am. Earth Sci.* 81, 189–203. doi:10.1016/j.jsames.2017.11.017

Horn, B. L. D., Goldberg, K., and Schultz, C. L. (2018a). Interpretation of Massive Sandstones in Ephemeral Fluvial Settings: A Case Study from the Upper Candelária Sequence (Upper Triassic, Paraná Basin, Brazil). *J. S. Am. Earth Sci.* 81, 108–121. doi:10.1016/j.jsames.2017.10.009

Hubbell, S. P. (2001). *The Unified Theory of Biodiversity and Biogeography*. Princeton: Princeton University Press.

Huntley, B. (1991). How Plants Respond to Climate Change: Migration Rates, Individualism and the Consequences for Plant Communities. *Ann. Bot.* 67, 15–22. doi:10.1093/oxfordjournals.aob.a088205

Husby, C. (2013). Biology and Functional Ecology of Equisetum with Emphasis on the Giant Horsetails. *Botanical Rev.* 79 (2), 147–177. doi:10.1007/s12229-012-9113-4

Irmis, R. B. (2011). Evaluating Hypotheses for the Early Diversification of Dinosaurs. *Earth Environ. Sci. Trans. R. Soc. Edinb.* 101, 397–426. doi:10.1017/s1755691011020068

Irmis, R. B., Mundil, R., Martz, J. W., and Parker, W. G. (2011). High-Resolution U-Pb Ages from the Upper Triassic Chinle Formation (New Mexico, USA) Support a Diachronous Rise of Dinosaurs. *Earth Planet. Sci. Lett.* 309, 258–267. doi:10.1016/j.epsl.2011.07.015

Irmis, R. B., Mundil, R., Mancuso, A. C., Carrillo-Briceño, J. D., Ottone, E. G., and Marsicano, C. A. (2022). South American Triassic Geochronology: Constraints and Uncertainties for the Tempo of Gondwanan Non-marine Vertebrate Evolution. *J. S. Am. Earth Sci.* 103770. doi:10.1016/j.jsames.2022.103770

Jones, M. E. H., Anderson, C. L., Hipsley, C. A., Müller, J., Evans, S. E., and Schoch, R. R. (2013). Integration of Molecules and New Fossils Supports a Triassic Origin for Lepidosauria (Lizards, Snakes, and Tuatara). *BMC Evol. Biol.* 13 (208), 201–221. doi:10.1186/1471-2148-13-208

Kalm, V. E., Rutter, N. W., and Rokosh, C. D. (1996). Clay Minerals and Their Paleoenvironmental Interpretation in the Baoji Loess Section, Southern Loess Plateau, China. *Catena* 27, 49–61. doi:10.1016/0341-8162(96)00008-2

Kent, D. V., Santi Malnis, P., Colombi, C. E., Alcober, O. A., and Martínez, R. N. (2014). Age Constraints on the Dispersal of Dinosaurs in the Late Triassic from Magnetochronology of the Los Colorados Formation (Argentina). *Proc. Natl. Acad. Sci.* 111, 7958–7963. doi:10.1073/pnas.1402369111

Kerp, H., Hass, H., and Mosbrugger, V. (2001). "New data on *Nothia aphylla* Lyon 1964 ex El-Saadawy et Lacey 1979, a poorly known plant from the Lower Devonian Rhynie Chert," in *Plants Invade the Land: Evolutionary and Environmental Perspectives*. Editors P. G. Gensel and D. Edwards (New York: Columbia University Press), 52–82. doi:10.7312/gens11160-005

Kidwell, S. M., and Flessa, K. W. (1996). The Quality of the Fossil Record: Populations, Species, and Communities. *Annu. Rev. Earth Planet. Sci.* 24, 433–464. doi:10.1146/annurev.earth.24.1.433

Kidwell, S. M., and Holland, S. M. (2002). The Quality of the Fossil Record: Implications for Evolutionary Analyses. *Annu. Rev. Ecol. Syst.* 33, 561–588. doi:10.1146/annurev.ecolsys.33.030602.152151

Kraus, M. J. (1999). Paleosols in Clastic Sedimentary Rocks: Their Geologic Applications. *Earth Sci. Rev.* 47, 41–70. doi:10.1016/s0012-8252(99)00026-4

Kraus, M. J., and Aslan, A. (1993). Eocene Hydromorphic Paleosols: Significance for Interpreting Ancient Floodplain Processes. *J. Sediment. Pet.*. 63, 453–463. doi:10.1306/d4267b22-2b26-11d7-8648000102c1865d

Kustatscher, E., Ash, S. R., Karasev, E., Pott, C., Vajda, V., Yu, J., et al. (2018). "Flora of the Late Triassic," in *The Late Triassic World: Earth in a Time of Transition*. Editor L. H. Tanner (Cham, Switzerland: Springer International Publishing), 545–622. doi:10.1007/978-3-319-68009-5_13

Kutzbach, J. E., and Gallimore, R. G. (1989). Pangaean Climates: Megamonsoons of the Megacontinent. *J. Geophys. Res. D* 94, 3341–3357. doi:10.1029/jd094id03p03341

Lausberg, S., and Kerp, H. (2000). Conifer-dominated Flora from the Lower Rotliegend Near Alsenz, Saar-Nahe-Basin (Germany). *Feddes Repert.* 111 (7/8), 399–426. doi:10.1002/fedr.20001110706

Liu, J., Angielczyk, K. D., and Abdala, F. (2021). Permo-Triassic Tetrapods and Their Climate Implications. *Glob. Planet. Change* 205, 1036181–1036189. doi:10.1016/j.gloplacha.2021.103618

Liu, Z., Colin, C., Trentesaux, A., Siani, G., FrankBlamart, N. D., and Farid, S. (2005). Late Quaternary Climatic Control on Erosion and Weathering in the Eastern Tibetan Plateau and the Mekong Basin. *Quat. Res.* 63, 316–328. doi:10.1016/j.yqres.2005.02.005

López-Gamundí, O. R., Alvarez, L., Andreis, R., Bossi, G., Espejo, I., Fernandez-Seveso, F., et al. (1989). "Cuencas Intermontanas," in *Cuencas Sedimentarias Argentinas. Serie Correlación Geológica, No 6*. Editors G. Chebli and L. Spalletti (Instituto Superior de Correlación Geológica, Universidad Nacional de Tucumán), 123–167.

Lovecchio, J. P., Rohais, S., Joseph, P., Bolatti, N. D., and Ramos, V. A. (2020). Mesozoic Rifting Evolution of SW Gondwana: a Poly-Phased, Subduction-Related, Extensional History Responsible for Basin Formation along the Argentinean Atlantic Margin. *Earth-Science Rev.* 203, 1031381–1031427. doi:10.1016/j.earscirev.2020.103138

Mancuso, A. C. (2005). Revisión y aportes a la estratigrafía de la sección inferior del Grupo Agua de la Peña (Triásico Medio, Argentina). *XVI Congr. Geol. Argent. La Plata, Argent. Actas* 3, 415–422.

Mancuso, A. C., and Caselli, A. (2012). Paleolimnology Evolution in Rift Basins: the Ischigualasto-Villa Unión Basin (Central-western Argentina) during the Triassic. *Sediment. Geol.* 275-276, 38–54. doi:10.1016/j.sedgeo.2012.07.012

Mancuso, A. C., and Marsicano, C. A. (2008). Paleoenvironments and Taphonomy of a Triassic Lacustrine System (Los Rastros Formation, Central-Western Argentina). *Palaios* 23, 535–547. doi:10.2110/palo.2007.p07-064r

Mancuso, A. C., Benavente, C. A., Irmis, R. B., and Mundil, R. (2020a). Evidence for the Carnian Pluvial Episode in Gondwana: New Multiproxy Climate Records and Their Bearing on Early Dinosaur Diversification. *Gondwana Res.* 86, 104–125. doi:10.1016/j.gr.2020.05.009

Mancuso, A. C., Krapovickas, V., Benavente, C. A., and Marsicano, C. A. (2020b). An Integrative Physical, Mineralogical, and Ichnological Approach to Characterize Underfilled Lake-Basin. *Sedimentology* 67, 3088–3118.

Mancuso, A. C., Gaetano, L. C., Leardi, J. M., Abdala, F., and Arcucci, A. B. (2014). The Chañares Formation: a Window to the Palaeobiology of a Middle Triassic Vertebrate Fauna. *Lethaia* 47, 244–265. doi:10.1111/let.12055

Mancuso, A. C., Horn, B. L. D., Benavente, C. A., Schultz, C. L., and Irmis, R. B. (2021). The Paleoclimatic Context for South American Triassic Vertebrate Evolution. *J. S. Am. Earth Sci.* 110 (103321), 1–26. doi:10.1016/j.jsames.2021.103321

Marsicano, C., Domnanovich, N., and Mancuso, A. C. (2007). Dinosaur Origins: Evidence from the Footprint Record. *Hist. Biol.* 19, 83–91. doi:10.1080/08912960600866920

Marsicano, C. A., Arcucci, A. B., Mancuso, A., and Caselli, A. T. (2004). Middle Triassic Tetrapod Footprints of Southern South America. *Ameghiniana* 41, 171–184.

Marsicano, C. A., Mancuso, A. C., Palma, R. M., and Krapovickas, V. (2010). Tetrapod Tracks in a Marginal Lacustrine Setting (Middle Triassic, Argentina): Taphonomy and Significance. *Palaeoecol. Palaeogeogr. Palaeoclimatol.* 291, 388–399. doi:10.1016/j.palaeo.2010.03.009

Marsicano, C. A., Irmis, R. B., Mancuso, A. C., Mundil, R., and Chemale, F. (2016). The Precise Temporal Calibration of Dinosaur Origins. *Proc. Natl. Acad. Sci. U. S. A.* 113, 509–513. doi:10.1073/pnas.1512541112

Martínez, R. N., Sereno, P. C., Alcober, O. A., Colombi, C. E., Renne, P. R., Montañez, I. P., et al. (2011). A Basal Dinosaur from the Dawn of the Dinosaur Era in Southwestern Pangaea. *Science* 331, 206–210. doi:10.1126/science.1198467

Mays, C., and McLoughlin, S. (2019). Caught between Mass Extinctions—The Rise and Fall of *Dicroidium*. *Deposits Mag.* 59, 43–47.

McElwain, J. C. (2018). Paleobotany and Global Change: Important Lessons for Species to Biomes from Vegetation Responses to Past Global Change. *Annu. Rev. Plant Biol.* 69, 761–787. doi:10.1146/annurev-arplant-042817-040405

McGill, B. J., Hadly, E. A., and Maurer, B. A. (2005). Community Inertia of Quaternary Small Mammal Assemblages in North America. *Proc. Natl. Acad. Sci.* 102, 16701–16706. doi:10.1073/pnas.0504225102

McLoughlin, S. (2001). The Breakup History of Gondwana and its Impact on Pre-cenozoic Floristic Provincialism. *Aust. J. Bot.* 49 (3), 271–300. doi:10.1071/bt00023

McLoughlin, S. (2011). *Glossopteris*: Insights into the Architecture and Relationships of an Iconic Permian Gondwanan Plant. *J. Botanical Soc. Bengal* 65, 93–106.

Miall, A. D. (1996). *The Geology of Fluvial Deposits: Sedimentary Facies, Basin Analysis and Petroleum Geology*. Berlin: Springer-Verlag, 582.

Milana, J. P., and Alcober, O. (1994). Modelo tectosedimentario de la Cuenca Triásica de Ischigualasto (San Juan, Argentina). *Rev. Asoc. Geol. Argent.* 49, 217–235.

Miller, C. S., Peterse, F., da Silva, A. C., Baranyi, V., Reichart, G. J., and Kürschner, W. M. (2017). Astronomical Age Constraints and Extinction Mechanisms of the Late Triassic Carnian Crisis. *Nat. Sci. Rep.* 7, 1–7. doi:10.1038/s41598-017-02817-7

Milroy, P., Wright, V. P., and Simms, M. J. (2019). Dryland Continental Mudstones: Deciphering Environmental Changes in Problematic Mudstones from the Upper Triassic (Carnian to Norian) Mercia Mudstone Group, South-west Britain. *Sedimentology* 66, 2557–2589. doi:10.1111/sed.12626

Minin, A. A., and Voskova, A. V. (2014). Homeostatic Responses of Plants to Modern Climate Change: Spatial and Phenological Aspects. *Russ. J. Dev. Biol.* 45 (3), 127–133. doi:10.1134/s1062360414030023

Mishra, S., Aggarwal, N., and Jha, N. (2017). Palaeoenvironmental Change across the Permian-Triassic Boundary Inferred from Palynomorph Assemblages (Godavari Graben, South India). *Palaeobiodiversity Palaeoenvironments* 98, 177–204. doi:10.1007/s12549-017-0302-3

Moore, D. M., and Reynolds, R. C., Jr. (1997). *X-Ray Diffraction and the Identification and Analysis of Clay Minerals*. Oxford: Oxford University Press, 337.

Moritz, C., Patton, J. L., Conroy, C. J., Parra, J. L., White, G. C., and Beissinger, S. R. (2008). Impact of a Century of Climate Change on Small-Mammal Communities in Yosemite National Park, USA. *Science* 5899, 261–264. doi:10.1126/science.1163428

Nesbitt, H. W., and Young, G. M. (1982). Early Proterozoic Climates and Plate Motions Inferred from Major Element Chemistry of Lutites. *Nature* 299, 715–717. doi:10.1038/299715a0

Nordt, L. C., and Driese, S. D. (2010). New Weathering Index Improves Paleorainfall Estimates from Vertisols. *Geology* 38, 407–410. doi:10.1130/g30689.1

Nowak, H., Schneebeli-Hermann, E., and Kustatscher, E. (2019). No Mass Extinction for Land Plants at the Permian-Triassic Transition. *Nat. Commun.* 10, 1–8. doi:10.1038/s41467-018-07945-w

Nowak, H., Vérard, C., and Kustatscher, E. (2020). Palaeophytogeographical Patterns across the Permian-Triassic Boundary. *Front. Earth Sci.* 8, 609. doi:10.3389/feart.2020.613350

Ogg, J. G. (2015). The Mysterious Mid-Carnian "Wet Intermezzo" Global Event. *J. Earth Sci.* 26, 181–191. doi:10.1007/s12583-015-0527-x

Ordoñez, A., Marsicano, C. A., and Mancuso, A. C. (2020). New Material of *Dinodontosaurus* (Therapsida, Anomodontia) from West-Central Argentina and a Reassessment of the Triassic South American Dinodontosaurus Assemblage Zone. *J. S. Am. Earth Sci.*, 102597.

Ottone, E. G., and Mancuso, A. C. (2006). Algas Chlorococcales Como Indicadores Paleoambientales: Nuevos Datos De La Formación Los Rastros, Triásico Medio A Superior Del Centro–Oeste De Argentina. *Revista del Museo Argentino de Ciencias Naturales, Nueva Serie* 8, 209–220. doi:10.22179/revmacn.8.321

Ottone, E. G., Mancuso, A. C., and Resano, M. (2005). Miospores and Chlorococcalean Algae from the Los Rastros Formation, Middle to Upper Triassic of Central-Western Argentina. *Ameghiniana* 42, 347–362.

Ovejero, R., and Bossi, G. E. (1984). Asociaciones mineralogicas de lasarcillas de la Cuenca de Ischigualasto-Ischichuca. Parte III: Perfil Zanja de la Viuda. *Noveno Congreso Geologico Argentio Actas V*, 197–208.

Pardoe, H. S., Cleal, C. J., Berry, C. M., Cascales-Miñana, B., Davis, B. A., Diez, J. B., et al. (2021). Palaeobotanical Experiences of Plant Diversity in Deep Time. 2: How to Measure and Analyse Past Plant Biodiversity. *Palaeogeogr. Palaeoclimatol. Palaeoecol.* 580, 110618. doi:10.1016/j.palaeo.2021.110618

Parrish, J. T. (1993). Climate of the Supercontinent Pangaea. *J. Geol.* 101, 215–233. doi:10.1086/648217

Pedernera, T. E., Mancuso, A. C., Ottone, E. G., and Benavente, C. A. (2020). Paleobotany of the Upper Triassic Los Rastros Formation, Ischigualasto-Villa Unión Basin, La Rioja, Argentina. *J. S. Am. Earth Sci.* 102, 102660. doi:10.1016/j.jsames.2020.102660

Perez Loinaze, V. S., Vera, E. I., Fiorelli, L. E., and Desojo, J. B. (2018). Palaeobotany and Palynology of Coprolites from the Late Triassic Chañares Formation of Argentina: Implications for Vegetation Provinces and the Diet of Dicynodonts. *Palaeogeogr. Palaeoclimatol. Palaeoecol.* 502, 31–51. doi:10.1016/j.palaeo.2018.04.003

Péron, S., Bourquin, S., Fluteau, F., and Guillocheau, F. (2005). Paleoenvironment Reconstructions and Climate Simulations of the Early Triassic: Impact of the Water and Sediment Supply on the Preservation of Fluvial Systems. *Geodin. Acta* 18, 431–446.

Pteridophyte Phylogeny Group (2016). A Community-derived Classification for Extant Lycophytes and Ferns. *J. Syst. Evol.* 54 (6), 563–603.

Raup, D. M. (1972). Taxonomic Diversity during the Phanerozoic. *Science* 177, 1065–1071. doi:10.1126/science.177.4054.1065

Raup, D. M. (1975). Taxonomic Diversity Estimation Using Rarefaction. *Paleobiology* 1, 333–342. doi:10.1017/s0094837300002633

Retallack, G. J. (1977). Reconstructing Triassic Vegetation of Eastern Australasia: a New Approach for the Biostratigraphy of Gondwanaland. *Alcheringa* 1, 253–283. doi:10.1080/03115517708527763

Retallack, G. J. (1988). "Field Recognition of Paleosols," in Paleosols and Weathering through Geologic Time: Principles and Applications, Special Paper 216. Editors J. Reinhardt, and W. R. Sigleo (Geological Society of America), 1–20. doi:10.1130/spe216-p1

Retallack, G. J. (2001). *Soils of the Past: An Introduction to Paleopedology*. Oxford, UK: Blackwell Sci.

Retallack, G. J. (2009). Greenhouse Crises of the Past 300 Million Years. *Geol. Soc. Am. Bull.* 121, 1441–1455. doi:10.1130/b26341.1

Retallack, G. J., Sheldon, N. D., Carr, P. F., Fanning, M., Thompson, C. A., Williams, M. L., et al. (2011). Multiple Early Triassic Greenhouse Crises Impeded Recovery from Late Permian Mass Extinction. *Palaeogeogr. Palaeoclimatol. Palaeoecol.* 308, 233–251. doi:10.1016/j.palaeo.2010.09.022

Robinson, P. L. (1971). A Problem of Faunal Replacement on Permo-Triassic Continents. *Palaeontology* 14, 131–153.

Robinson, P. L. (1973). "Palaeoclimatology and Continental Drift," *Implications of Continental Drift to the Earth Sciences*. Editors D. H. Tarling and S. K. Runcorn (London: Academic Press), Vol. 1, 451–476.

Rogers, R. R., Arcucci, A. B., Abdala, F., Sereno, P. C., Forster, C. A., and May, C. L. (2001). Paleoenvironment and Taphonomy of the Chañares Formation Tetrapod Assemblage (Middle Triassic), Northwestern Argentina: Spectacular Preservation in Volcanogenic Concretions. *Palaios* 16, 461–481. doi:10.1669/0883-1351(2001)016<0461:patotc>2.0.co;2

Rogers, R., Swisher, C., III, Sereno, P., Monetta, A., Forster, C., and Martínez, R. (1993). The Ischigualasto Tetrapod Assemblage (Late Triassic, Argentina) and ^{40}Ar/^{39}Ar Dating of Dinosaur Origins. *Science* 260, 794–797. doi:10.1126/science.260.5109.794

Romer, A. S. (1970). "The Triassic Faunal Succession and the Gondwanaland Problem," in *Gondwana Stratigraphy, IUGS Symposium* (Paris: UNESCO), 375–400.

Rosindell, J., Hubbell, S. P., and Etienne, R. S. (2011). The Unified Neutral Theory of Biodiversity and Biogeography at Age Ten. *Trends Ecol. Evol.* 26, 340–348. doi:10.1016/j.tree.2011.03.024

Rosindell, J., Hubbell, S. P., He, F., Harmon, L. J., and Etienne, R. S. (2012). The Case for Ecological Neutral Theory. *Trends Ecol. Evol.* 27, 203–208. doi:10.1016/j.tree.2012.01.004

Rostási, Á., Raucsik, B., and Varga, A. (2011). Palaeoenvironmental Controls on the Clay Mineralogy of Carnian Sections from the Transdanubian Range (Hungary). *Palaeogeogr. Palaeoclimatol. Palaeoecol.* 300, 101–112.

Rowe, H., Hughes, N., and Robinson, K. (2012). The Quantification and Application of Handheld Energy-Dispersive X-Ray Fluorescence (ED-XRF) in Mudrock Chemostratigraphy and Geochemistry. *Chem. Geol.* 324-325, 122–131. doi:10.1016/j.chemgeo.2011.12.023

Rowe, K. C., Rowe, K. M. C., Tingley, M. W., Koo, M. S., Patton, J. L., Conroy, C. J., et al. (2015). Spatially Heterogeneous Impact of Climate Change on Small Mammals of Montane California. *Proc. R. Soc. Lond. Biol. Sci.* 282, 1–10. doi:10.1098/rspb.2014.1857

Ruffell, A., McKinley, J. M., and Worden, R. H. (2002). Comparison of Clay Mineral Stratigraphy to Other Proxy Palaeoclimate Indicators in the Mesozoic of NW Europe. *Philosophical Trans. R. Soc. Lond. A* 360, 675–693. doi:10.1098/rsta.2001.0961

Ruffell, A., Simms, M. J., and Wignall, P. B. (2016). The Carnian Humid Episode of the Late Triassic: a Review. *Geol. Mag.* 153, 271–284. doi:10.1017/s0016756815000424

Ruffo Rey, L. J. (2021). Vegetation dynamics of Cerro de Las Cabras Formation (Middle Triassic) from palynological assemblages and the Eco-Guild model: New paleoenvironmental and paleoclimatic interpretations. *J. S. Am. Earth Sci.* 112, 103629. doi:10.1016/j.jsames.2021.103629

Ruiz, F., and Introcaso, A. (1999). Un modelo gravimétrico 3D de la profunda cuenca sedimentaria de Ischigualasto-Villa Unión (San juan y La Rioja) Argentina. *Rev. Bras. Geof* 17, 3–11. doi:10.1590/s0102-261x1999000100001

Santi Malnis, P., Colombi, C. E., Rothis, L. M., and Alcober, O. (2020). Fluvial Architecture and Paleoenvironmental Evolution of the Los Colorados

Formation (Norian): Postrift Stage of the Ischigualasto–Villa Union Basin, NW Argentina. *J. Sediment. Res.* 90, 1436–1462. doi:10.2110/jsr.2020.65

Schoch, R. R., and Sues, H.-D. (2015). A Middle Triassic Stem-Turtle and the Evolution of the Turtle Body Plan. *Nature* 523, 584–587. doi:10.1038/nature14472

Schultz, C. L., Martinelli, A. G., Soares, M. B., Pinheiro, F. L., Kerber, L., Horn, B. L. D., et al. (2020). Triassic Faunal Successions of the Paraná Basin, Southern Brazil. *J. S. Am. Earth Sci.* 104, 102846. doi:10.1016/j.jsames.2020.102846

Sellwood, B. W., and Valdes, P. J. (2006). Mesozoic Climates: General Circulation Models and the Rock Record. *Sediment. Geol.* 190, 269–287. doi:10.1016/j.sedgeo.2006.05.013

Sheldon, N. D. (2006). Quaternary Glacial-Interglacial Climate Cycles in Hawaii. *J. Geol.* 114, 367–376. doi:10.1086/500993

Sheldon, N. D., and Tabor, N. J. (2009). Quantitative Paleoenvironmental and Paleoclimatic Reconstruction Using Paleosols. *Earth Sci. Rev.* 95, 1–52. doi:10.1016/j.earscirev.2009.03.004

Sheldon, N. D., Retallack, G. J., and Tanaka, S. (2002). Geochemical Climofunctions from North America Soils and Application to Paleosols across the Eocene–Oligocene Boundary in Oregon. *J. Geol.* 110, 687–696. doi:10.1086/342865

Shubin, N. H., and Sues, H.-D. (1991). Biogeography of Early Mesozoic Continental Tetrapods: Patterns and Implications. *Paleobiology* 17, 214–230. doi:10.1017/s0094837300010575

Simms, M. J., and Ruffell, A. H. (1989). Synchroneity of Climatic Change in the Late Triassic. *Geology* 17, 265–268. doi:10.1130/0091-7613(1989)017<0265:soccae>2.3.co;2

Simms, M. J., and Ruffell, A. H. (1990). Climatic and Biotic Change in the Late Triassic. *J. Geol. Soc., London* 147, 321–327. doi:10.1144/gsjgs.147.2.0321

Singer, A. (1980). The Paleoclimatic Interpretation of Clay Minerals in Soils and Weathering Profiles. *Earth-Sciences Rev.* 15, 303–326. doi:10.1016/0012-8252(80)90113-0

Singer, A. (1984). The Paleoclimatic Interpretation of Clay Minerals in Sediments—A Review. *Earth-Sciences Rev.* 21, 251–293. doi:10.1016/0012-8252(84)90055-2

Smith, A. R., Pryer, K. M., Schuettpelz, E., Korall, P., Schneider, H., and Wolf, P. G. (2006). A Classification for Extant Ferns. *Taxon* 55, 705–731. doi:10.2307/25065646

Spalletti, L. A., Artabe, A. E., and Morel, E. M. (2003). Geological Factors and Evolution of Southwestern Gondwana Triassic Plants. *Gondwana Res.* 6, 119–134. doi:10.1016/s1342-937x(05)70648-1

Stenseth, N. C., and Maynard Smith, J. (1984). Coevolution in Ecosystems: Red Queen Evolution or Stasis? *Evolution* 38, 870–880. doi:10.1111/j.1558-5646.1984.tb00358.x

Stewart, W. N., and Rothwell, G. W. (1993). *Paleobotany and the Evolution of Plants*. Cambridge: Cambridge University Press.

Stipanicic, P. N., and Marsicano, C. (2002). *Léxico Estratigráfico de la Argentina: TRIÁSICO*. Asociación Geológica Argentina.

Stocker, M. R., Nesbitt, S. J., Kligman, B. T., Paluh, D. J., Marsh, A. D., Blackburn, D. C., et al. (2019). The Earliest Equatorial Record of Frogs from the Late Triassic of Arizona. *Biol. Lett.* 15, 1–5. doi:10.1098/rsbl.2018.0922

Sun, Y., Joachimski, M. M., Wignall, P. B., Yan, C., Chen, Y., Jiang, H., et al. (2012). Lethally Hot Temperatures during the Early Triassic Greenhouse. *Science* 338, 366–370. doi:10.1126/science.1224126

Sun, Y. D., Wignall, P. B., Joachimski, M. M., Bond, D. P. G., Grasby, S. E., Laib, X. L., et al. (2016). Climate Warming, Euxinia and Carbon Isotope Perturbations during the Carnian (Triassic) Crisis in South China. *Earth Planet. Sci. Lett.* 444, 88–100. doi:10.1016/j.epsl.2016.03.037

Tabor, N. J., and Myers, T. S. (2015). Paleosols as Indicators of Paleoenvironment and Paleoclimate. *Annu. Rev. Earth Planet. Sci.* 43, 333–361. doi:10.1146/annurev-earth-060614-105355

Tabor, N. J., Montañez, I. P., Zierenberg, R., and Currie, B. S. (2004). Mineralogical and Geochemical Evolution of a Basalt-Hosted Fossil Soil (Late Triassic, Ischigualasto Formation, Northwest Argentina); Potential for Paleoenvironmental Reconstruction. *Geol. Soc. Am. Bull.* 116, 1280–1293. doi:10.1130/b25222.1

Tabor, N. J., Montañez, I. P., Kelso, K. A., Currie, B. S., Shipman, T. A., and Colombi, C. E. (2006). Late Triassic Soil Catena: Landscape and Climate Controls on Paleosol Morphology and Chemistry across the Carnian-Age Ischigualasto–Villa Union Basin, Northwestern Argentina. *Geological Society of America Special Paper* 416, 17–42.

Taylor, T. N., Taylor, E. L., and Krings, M. (2009). "Cycadophytes," in *Paleobotany, the Biology and Evolution of Fossil Plants*. Editors T. N. Taylor, E. L. Taylor, and M. Krings (Amsterdam): Academic Press), 703–741. doi:10.1016/b978-0-12-373972-8.00017-6

Thuiller, W., Lavorel, S., Araújo, M. B., Sykes, M. T., and Prentice, I. C. (2005). Climate Change Threats to Plant Diversity in Europe. *Proc. Natl. Acad. Sci.* 102 (23), 8245–8250. doi:10.1073/pnas.0409902102

Tingley, M. W., Monahan, W. B., Beissinger, S. R., and Moritz, C. (2009). Birds Track Their Grinnellian Niche through a Century of Climate Change. *Proc. Natl. Acad. Sci.* 106 (Suppl. 2), 19637–19643. doi:10.1073/pnas.0901562106

Tipper, J. C. (1979). Rarefaction and Rarefiction-The Use and Abuse of a Method in Paleoecology. *Paleobiology* 5, 423–434. doi:10.1017/s0094837300016924

Tomimatsu, Y., Nozaki, T., Sato, H., Takaya, Y., Kimura, J. I., Chang, Q., et al. (2021). Marine Osmium Isotope Record during the Carnian "Pluvial Episode" (Late Triassic) in the Pelagic Panthalassa Ocean. *Glob. Planet. Change* 197, 103387. doi:10.1016/j.gloplacha.2020.103387

Uliana, M. A., and Biddle, K. (1988). Mesozoic-Cenozoic Paleogeographic and Geodynamic Evolution of Southern South America. *Rev. Bras. Geociências* 18, 172–190. doi:10.25249/0375-7536.1988182172190

Uliana, M. A., Biddle, K. T., and Cerdan, J. (1989). Mesozoic Extension and the Formation of Argentine Sedimentary Basins. *Tulsa: American Association of Petroleum Geologists, Memoir* 46, 599–614.

Vajda, V., McLoughlin, S., Mays, C., Frank, T. D., Fielding, C. R., and Tevyaw, A. (2020). End-Permian (252 Mya) Deforestation, Wildfires and Flooding -An Ancient Biotic Crisis with Lessons for the Present. *Earth PlanetScience Lett.* 529, 115875. doi:10.1016/j.epsl.2019.115875

Van Hinsbergen, D. J. J., De Groot, L. V., Van Schaik, S. J., Spakman, W., Bijl, P. K., and Sluijs, A. (2015). A Paleolatitude Calculator for Paleoclimate Studies. *PLoS ONE* 10, 1–21. doi:10.1371/journal.pone.0126946

Vitt, L. J., and Caldwell, J. P. (2014). *Herpetology: An Introductory Biology of Amphibians and Reptiles*. Amsterdam: Academic Press, 757.

Vrba, E. S. (1985). Environment and Evolution: Alternative Causes of the Temporal Distribution of Evolutionary Events. *South Afr. J. Sci.* 81, 229–236.

Vrba, E. S. (1992). Mammals as a Key to Evolutionary Theory. *J. Mammal.* 73, 1–28. doi:10.2307/1381862

Vrba, E. S. (1993). Turnover-pulses, the Red Queen, and Related Topics. *Am. J. Sci.* 293-A, 418–452. doi:10.2475/ajs.293.a.418

Vrba, E. S. (1995). "On the Connections between Paleoclimate and Evolution," in *Paleoclimate and Evolution, with Emphasis on Human Origins*. Editors E. S. Vrba, G. H. Denton, T. C. Partridge, and L. H. Burckle (New Haven: Yale University Press), 24–45.

Wang, X., and Zheng, S. (2010). Whole Fossil Plants of *Ephedra* and Their Implications on the Morphology, Ecology and Evolution of Ephedraceae (Gnetales). *Chin. Sci. Bull.* 55 (15), 1511–1519. doi:10.1007/s11434-010-3069-8

Weaver, C. E. (1989). Clays, Muds, and Shales. *Dev. Sedimentology* 44, 1–819.

Whiteside, J. H., and Grice, K. (2016). Biomarker Records Associated with Mass Extinction Events. *Annu. Rev. Earth Planet. Sci.* 44, 581–612. doi:10.1146/annurev-earth-060115-012501

Whiteside, J. H., Grogan, D. S., Olsen, P. E., and Kent, D. V. (2011). Climatically Driven Biogeographic Provinces of Late Triassic Tropical Pangea. *Proc. Natl. Acad. Sci.* 108, 8972–8977. doi:10.1073/pnas.1102473108

Whiteside, J. H., Lindström, S., Irmis, R. B., Glasspool, I. J., Schaller, M. F., Dunlavey, M., et al. (2015). Extreme Ecosystem Instability Suppressed Tropical Dinosaur Dominance for 30 Million Years. *Proc. Natl. Acad. Sci.* 112, 7909–7913. doi:10.1073/pnas.1505252112

Wilson, K. M., Pollard, D., Hay, W. W., Thompson, S. l., and Wold, C. N. (1994). General Circulation Model Simulations of Triassic Climates: Preliminary Results. *Geological Society of America Special Paper* 288, 91–116. doi:10.1130/spe288-p91

Zamuner, A. B., Zavattieri, A. M., Artabe, A. E., and Morel, E. M. (2001). "Paleobotánica," in *El Sistema Triásico en la Argentina*. Editors A. E. Artabe, E. M. Morel, and A. B. Zamuner (La Plata): Fundación Museo de La Plata "Francisco Pascasio Moreno"), 143–184.

Zavattieri, A. M., and Batten, D. J. (1996). "Miospores from Argentinian Triassic Deposits and Their Potential for Intercontinental Correlation," In *Palynology: Principles and Applications*. Editors J. Jansonius and D. C. Mcgregor (Dallas: Association of Stratigraphic Palynologists Foundation), 2, 767–778.

Zhang, J., Lenz, O. K., Hornung, J., Wang, P., Ebert, M., and Hinderer, M. (2020). Palynology and the Eco-Plant Model of Peat-Forming Wetlands of the Upper Triassic

Haojiagou Formation in the Junggar Basin, Xinjiang, NW China. *Palaeogeogr. Palaeoclimatol. Palaeoecol.* 556, 109888. doi:10.1016/j.palaeo.2020.109888

Conflict of Interest: The authors declare that the research was conducted in the absence of any commercial or financial relationships that could be construed as a potential conflict of interest.

Publisher's Note: All claims expressed in this article are solely those of the authors and do not necessarily represent those of their affiliated organizations, or those of the publisher, the editors and the reviewers. Any product that may be evaluated in this article, or claim that may be made by its manufacturer, is not guaranteed or endorsed by the publisher.

frontiers | Frontiers in Earth Science

REVIEW
published: 17 June 2022
doi: 10.3389/feart.2022.899541

Triassic Revolution

Michael J. Benton[1]* *and Feixiang Wu*[2]

[1]School of Earth Sciences, University of Bristol, Bristol, United Kingdom, [2]Institute of Vertebrate Paleontology and Paleoanthropology, Chinese Academy of Sciences, Beijing, China

The Triassic has long been recognized as a time during which marine and terrestrial ecosystems modernized dramatically, and it seems to have been a two-step process. First, recovery from the Permian-Triassic mass extinction (PTME) was a time of extraordinary renewal and novelty, and these processes of change were enhanced, it seems, by the effects of the Carnian Pluvial Episode (CPE). After the CPE, in the oceans, not only did the carbonate factory begin to change towards its modern form, but also arguably the Mesozoic Marine Revolution (MMR) speeded up. When the MMR was proposed it was seen as a process that occurred in the Late Jurassic and Cretaceous, as modern crustaceans, gastropods, and fishes enhanced predator-prey arms races. New evidence from China and elsewhere suggests in fact the MMR was already underway in the Middle and Late Triassic, and so was coincident with Sepkoski's classic idea that Paleozoic faunas were replaced by Modern marine faunas from the beginning of the Triassic. On land, ongoing competition between synapsids and archosauromorphs through the Triassic was marked by a posture shift from sprawling to erect, and a shift in physiology to warm-bloodedness, with insulating skin coverings of hair and feathers. Dinosaurs, for example, originated in the Early or Middle Triassic, but did not diversify until after the CPE. These arms races, the MMR in the sea, and the endothermy shift in tetrapods, were triggered by the PTME, and then enhanced by the CPE.

Keywords: Carnian Pluvial Episode, Mesozoic Marine Revolution, modern marine fauna, archosaurs, synapsids

OPEN ACCESS

Edited by:
Sara Callegaro,
University of Oslo, Norway

Reviewed by:
Yadong Sun,
University of Erlangen Nuremberg, Germany
Martin Daniel Ezcurra,
Museo Argentino de Ciencias Naturales Bernardino Rivadavia, Argentina

***Correspondence:**
Michael J. Benton
mike.benton@bristol.ac.uk

Specialty section:
This article was submitted to Paleontology, a section of the journal Frontiers in Earth Science

Received: *18 March 2022*
Accepted: *20 May 2022*
Published: *17 June 2022*

Citation:
Benton MJ and Wu F (2022) Triassic Revolution. Front. Earth Sci. 10:899541. doi: 10.3389/feart.2022.899541

INTRODUCTION

When Phillips (1841) named the geological eras, the Palaeozoic, Mesozoic, and Kainozoic (now, Cenozoic), he noted that each was characterized by very different kinds of animals and plants, and that their boundaries marked major shifts in the faunas and floras. He intended these stratigraphic terms to be overtly biological, reflecting the nature of the fossils, and paleontologists have since understood that the boundaries between Paleozoic and Mesozoic and Mesozoic and Cenozoic mark the end-Permian and end-Cretaceous mass extinctions, dated respectively, at 252 and 66 Ma (million years ago). The times following these two mass extinctions represent notable episodes of the recovery of life, during the Triassic and Paleogene periods respectively. The succession from dinosaurs to mammals and birds in the Paleogene has been described many times, as well as the evolution of new ecosystems in the oceans after the extinctions of marine reptiles, ammonites, belemnites and rudists at the end of the Cretaceous. The recovery of life in the Triassic after the much more severe end-Permian event has long been seen as even more dramatic.

Van Valen (1984) identified the Permian-Triassic boundary (PTB) as a singularity in the evolution of Phanerozoic marine animals, marked by a shift in evolutionary dynamics. Similarly, Sepkoski (1984) argued the "Modern Evolutionary Fauna" emerged after the PTB, in succession to

his "Cambrian" and "Paleozoic" evolutionary faunas, but he saw very little evidence for a step-change across the Cretaceous-Paleogene boundary. Whereas the Paleozoic marine fauna had been dominated by brachiopods, rugose corals, tabulate corals, cephalopods, trilobites, graptolites, and crinoids, and lower actinopterygian fishes (e.g., "paleonisciform" or "paleopterygian" fishes; Romano et al., 2016) and non-neoselachian sharks, the Modern fauna, commencing in the Triassic, was characterized by bivalves, gastropods, malacostracan crustaceans (crabs, lobsters), echinoids, neoselachian sharks, neopterygian bony fishes (including basal holosteans and teleosts), and marine tetrapods (reptiles in the Mesozoic, whales in the Cenozoic). These changes also reflect sharp rises from Paleozoic to Mesozoic in the proportions of motile (free-swimming) animals to non-motile (bottom-dwelling) and in the proportions of predators to non-predators (Bambach et al., 2002). The major changes were set in train following the devastating effects of the Permian-Triassic mass extinction (PTME).

In considering the timing of major events in the Triassic, the Carnian Pluvial Episode (CPE), dated from 233 to 232 Ma, has also emerged as potentially very important in punctuating the rise of modern ecosystems on land and in the oceans (Simms and Ruffell, 1989; Roghi et al., 2010; Dal Corso et al., 2020). This episode was triggered by repeated eruptions of the Wrangellia Large Igneous Province, which led to a series of consequences similar to those that occurred during the PTME, including sharp global warming and especially in tropical latitudes, acid rain and mass wasting on land, and ocean acidification and seabed anoxia in the oceans. Through a million years, repeated eruptions drove temperatures up and generated excess rainfall on land, but after the eruptions ceased some 232 Ma, the CPE humid phase reverted to aridity, and it was the humid-to-arid switch that led to substantial extinctions and major changes in ecosystems (Roghi et al., 2010; Dal Corso et al., 2020). In the sea, the first scleractinian reefs and rock-forming calcareous nannofossils diversified, both reflecting and enabling substantial changes in ocean chemistry (Dal Corso et al., 2020). Some new predatory clades that had originated in the aftermath of the PTME (e.g., decapod crustaceans, coleoid cephalopods, asteroid and cidaroid echinoderms, neopterygian bony fishes, neoselachian sharks) diversified substantially at this point, marking a step-change in predatory attack (e.g., durophagy, hole-drilling) and defensive and escape strategies (e.g. cementation, deep burrowing, fast escape swimming). On land, there were major diversifications and originations of conifers, insects, dinosaurs, crocodiles, lepidosaurs, turtles, and mammals; most of these groups had originated much earlier, in the Early and Middle Triassic, but diversified and became ecologically significant after the CPE (Dal Corso et al., 2020). Thus emerged the roots of modern ecosystems.

In related, but parallel work, Vermeij (1977) identified the Mesozoic Marine Revolution as a key episode in the history of marine animals. He noted that typical Mesozoic and modern marine predators, such as malacostracan arthropods, gastropods, echinoids, and vertebrates (including neoselachian sharks, teleost fishes, and marine reptiles) were all faster and nastier than their Paleozoic precursors. As predators became faster to catch their prey, the prey evolved means of escape and defense, including a thicker shell or the ability to burrow deeper. Predatory modes also became more deadly, with many fishes and reptiles becoming durophages, capable of crushing thick-shelled oysters, and with gastropods perfecting their hole-piercing equipment to penetrate through shell to flesh, and sharks and teleosts with mobile mouth parts to enlarge their gapes. Vermeij pointed to the origins of many of these adaptations in the Cretaceous and suggested the MMR began in the Jurassic. Based on new evidence, Vermeij (2008) revised his original view, and noted an early burst of the MMR in the Late Triassic and Early Jurassic, and since then additional evidence has revealed origins of many key MMR predators in the Early and Middle Triassic (Hu et al., 2011; Benton et al., 2013; Tackett, 2016; Tackett and Bottjer, 2016; Brayard et al., 2017; Waller, 2006; Hautmann et al., 2017), and if this is true, it links the initial driver of the MMR to the recovery of life following the PTME and the origin of modern-style ecosystems in the oceans.

Among vertebrates in particular, the nature of their recovery also seems to mark something unusual. Certain clades such as fishes and tetrapods showed very rapid diversifications in the sea (Benton et al., 2013; Scheyer et al., 2014; Motani et al., 2015) and on land (Ezcurra, 2016; Ezcurra et al., 2020a, b; Benton, 2021). Indeed, the changes among ecologically dominant tetrapods on land, cutting across the major clades of archosaurs and synapsids, seem to mark a quickening of life in general. Both archosaurs (including the ancestors of dinosaurs and birds) and synapsids (including the ancestors of mammals) show evidence of a major shift in posture (sprawling to upright) and in thermal physiology (ectothermy to endothermy). These changes affected the nature of energy transfer through ecosystems, so they share more in common with modern than Paleozoic ecosystems. Importantly, changes initiated by the PTME appear to have been accelerated by the CPE, which triggered remarkable changes in plants, insects, and tetrapods, including the origins of dinosaurs and of mammals.

Here, we explore critical points about the Triassic, and with a key focus on the CPE and whether the combined "double hit" of the hugely devastating PTME, and then the smaller, but hugely influential, CPE 20 Myr later marked the origins of modern ecosystems in the sea and on land.

EARLY START OF THE MESOZOIC MARINE REVOLUTION

Definition of the Mesozoic Marine Revolution

In considering the recovery of life after the PTME, and when the MMR started, it is important to recall that there had been a long history of increasingly effective predatory and defensive strategies among marine animals throughout the Paleozoic, and especially with some escalation in the Devonian and Carboniferous (Brett and Walker, 2002), and with renewal of Paleozoic predatory modes in the new world of the Triassic as well as further escalation (Walker and Brett, 2002). A key question is when

the MMR began, and whether a case can be made plausibly that the MMR is a part of, or equivalent with, the Triassic recovery of life from the rigors of the PTME.

In his original works, Vermeij (1977) and Vermeij et al. (1981) made the case that the MMR began in the Cretaceous, based on several lines of evidence: 1) an increase in snail-shell sturdiness in response to the evolution of new shell-destroying predators such as teleosts, stomatopods, and decapod crustaceans, 2) an intensification of grazing, and 3) deeper burrowing than ever seen before in certain taxa, a classic means of escape from intense predation. He noted that these new behaviors coincided with the origin of several clades that dominate oceans today, including mesogastropods, neogastropods, stomatopod crustaceans, and shell-crushing rays and teleosts. Vermeij et al. (1981) tested the timing of the MMR by focusing on shell damage in gastropods through the Phanerozoic, and they identified a step-change in such damage at some point between the Late Triassic and Late Cretaceous but did not have sufficient sampling to say when this had occurred other than at some point in the Jurassic.

In his review of 46 innovations among marine animals throughout the Mesozoic, Vermeij (2008) noted a two-step model for the MMR, with bursts of innovation in the Late Triassic–Early Jurassic interval (0.42 innovations per million years) and in the mid–Late Cretaceous (0.60) separated by a time of only modest innovation from Middle Jurassic–Early Cretaceous (0.12). Marine innovations in the Carnian included origins of calcified phytoplankton (dinoflagellates, calcified nannoplankton), compound plates in echinoids, giant marine tetrapods, turtle form in tetrapods, articulating teeth in hinges of cementing bivalves, suckered arms in squid, diverse zooxanthellate reef-building corals, bioerosive herbivory, and obligately deep-boring bivalves.

Re-Dating the MMR

Vermeij's (2008) analysis accepted the idea of a Late Triassic start to the MMR, which we could now indicate was part of the aftermath of the CPE, but there is still a question around whether the MMR kicked off even earlier, in the Early and Middle Triassic. Vermeij (2008) enumerated a list of 46 predatory and defensive-escape innovations seen in Mesozoic organisms, including 31 marine and 15 terrestrial examples. We repeat this analysis in the sense of listing innovations relevant to the predator-prey escalation in the Triassic but excluding his terrestrial examples.

The numerical counts presented by Vermeij (2008) are arbitrary, and different authors might produce different listings, which makes the estimates of rates of change only indicative, as he acknowledged. We do not present any such statistical metrics. In any case, there would be more appropriate approaches in ecological terms, estimating for example the proportions of predatory interactions of the "new" type versus others; this would allow discrimination between the maximal point of origin of an innovation and the point at which it became prevalent in ecosystems.

In many examples noted below, a related issue is to separate origins based on phylogenetic inference from origins based on abundant fossils. For example, some fiendish predatory adaptations of Mesozoic hunters, such as the muscular tentacles of hunting cephalopods armed with suckers and hooklets, are largely soft-tissue and so hard to fossilize, and yet phylogenetic evidence indicates likely points of origin before fossils became abundant. Does this mean the adaptation was widespread but poorly fossilized, or in fact only rarely present and so of negligible ecological importance? In the summary to follow, we will keep these concerns about data and methods in mind, and look at the carbonate factory first, then the new predators, and finally the new defenses against these predators.

Carbonate Factory-Plankton Revolution

Carbonate factories are the combination of sedimentary environment, organisms and precipitation processes that lead to the formation of a carbonate platform, and they can be divided into multiple systems, including tropical, cool-water, and mud-mound types (Schlager, 2005; Reijmer, 2021). Key controlling factors on these systems include light, water temperature, nutrients, salinity, substrate, and carbonate saturation; local controls are also ocean currents, upwelling and non-upwelling systems, ocean-atmosphere systems, atmospheric systems, shallow-water dynamics, and terrestrial sediment and water inputs (Reijmer, 2021).

The nature and location of the dominant carbonate factories through time have been critical in the regulation of ocean chemistry and cycling of carbon. When calcifying organisms arose in the Cambrian, the products of weathering were captured, and this affected the carbon cycle permanently. Then there was a dramatic shift in the main locus of the carbonate factory from continental shelves to deep seas and this followed the rise of calcifying plankton in the Late Triassic and Jurassic (**Figure 1**). The changes in ocean chemistry and function were profound (Ridgwell, 2005). Before the switch, in Paleozoic seas, this kind of "neritic ocean" was subject to extreme fluctuations in carbonate content and pH according to topography and climate, reflecting variable weathering on land and halving and doubling of the area of the continental shelf. The consequences were that the ocean could become extremely saturated with carbonates washed in from weathering on land at times of low sea level when areas for deposition of carbonates were restricted. After the ocean revolution when carbonate factories moved towards deeper waters, as today, such variations in saturation do not occur; the deep-sea carbonate sink enables the oceanic saturation state to self-regulate. This also had impacts on the concentration of carbon dioxide in the atmosphere and the degree of acidification (pH level) of the ocean itself.

In their review of 1.5 billion years of eukaryotic planktonic evolution, Falkowski et al. (2004) identified a major ecological reset in the Triassic that marked a comprehensive overhaul in how the oceanic carbon cycle worked. Before the reset, Paleozoic marine phytoplankton were perhaps less diverse and abundant, and less important in nutrient cycling. The extinction of many groups in the PTME marked the beginning of a new marine world dominated by the modern groups of phytoplankton (e.g.,

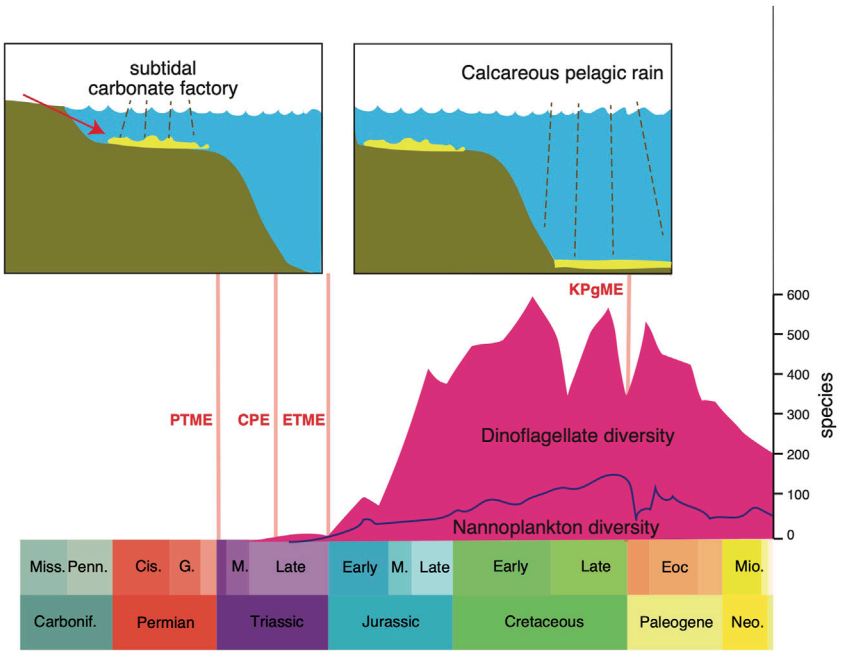

FIGURE 1 | The major shift in the marine carbonate factory from the shelf-based model through the Palaeozoic and most of the Triassic, and the modern-style deep-water carbonate factory of today, which began in the latest Triassic. Abbreviations: Carbonif, Carboniferous; Cis, Cisuralian; CPE, Carnian Pluvial Episode; Eoc, Eocene; ETME, end-Triassic mass extinction; KPgME, Cretaceous-Paleogene mass extinction; M, Middle; Mio, Miocene; Miss, Mississippian; Neo, Neogene; Penn, Pennsylvanian; PTME, Permian-Triassic mass extinction. Dinoflagellate diversity through time from Fensome et al. (1996), Nannoplankton diversity from Bown et al. (2005), and sketch carbonate factory models based on James (1984).

dinoflagellates, coccolithophores), which originated about the same time in the Middle and Late Triassic (**Figure 1**). The new eukaryotic plankton of the Triassic possessed plastids derived from an ancestral red alga that enabled them to develop a "dual fuel" metabolism, whereby they could retain fixed nitrogen within the cell, while simultaneously obtaining organic carbon via photosynthesis, and even assimilating dissolved and particulate organic matter (Falkowski et al., 2004). Initially, dinoflagellates and coccolithophores flourished in the relatively warm, quiescent Mesozoic seas, when wind speeds and oceanic thermohaline circulation were relatively sluggish. When the major polar icecaps emerged about 33 Ma in the early Oligocene (Zachos et al., 2001; Norris et al., 2013; Westerhold et al., 2020), climates cooled, winds freshened and ocean circulation speeded up, and diatoms began to replace dinoflagellates and coccolithophores as dominant eukaryotic phytoplankton in the oceans.

The transition from the neritic to deep-sea dominant ocean pattern was dated at the Triassic-Jurassic boundary by Ridgwell. (2005), and to the aftermath of the CPE by Dal Corso et al. (2020). Carbonate fluxes and nannoplankton diversity remained low through the Late Triassic and Early Jurassic, and production was restricted to epi-continental areas. The true colonization of the oceans occurred through a very long time, reaching an advanced stage in the Early Cretaceous, based on analysis of species diversity through time (**Figure 1**), but importantly also estimated accumulation rates on the ocean floor: rates of accumulation rose one-hundredfold, from 10^{9} $m^{2}yr^{-1}$ in the Early Jurassic to 10^{11} $m^{2}yr^{-1}$ in the Early Cretaceous (Suchéras-Marx et al., 2019).

The concurrent rise of calcifying plankton groups in the oceans as well as new reef-building corals (scleractinians) and other metazoan reef-builders, contributed to a major shift in the global carbon cycle. Today, the three eukaryotic phytoplankton groups are responsible for the great majority of the export of organic matter to the ocean interior and into deep-ocean sediments (Falkowski et al., 2004). Their huge contribution to carbon cycling is documented in the Italian Dolomites where the rise of coccolithophores and dinoflagellates in the Carnian is marked by a huge increase in calcispheres in the carbonate rocks; their frequency rose from essentially 0% in the Middle Triassic to 10% after the CPE, and >50% of rock volume in the Rhaetian. As Dal Corso et al. (2020, p. 6) note, "The rise of these calcispheres may represent a milestone in Earth history that could have fundamentally changed the global carbon cycle and certainly deserves more attention." At the same time, the "carbonate factory," the processes of conversion of carbon into calcium carbonate within organisms, had occurred mainly in microbial reefs in earlier parts of the Triassic, and switched to metazoan reefs (i.e., corals, sponges, bryozoans) during and immediately after the CPE (Dal Corso et al., 2020). These together shifted the main sites of carbonate accumulation from the continental shelf to offshore locations, as reef debris was washed offshore, but more importantly, calcareous nannoplankton lived over deep waters as well as shelf waters, and shed their skeletons into deeper waters. These deep-water carbonates helped stabilize the global carbon

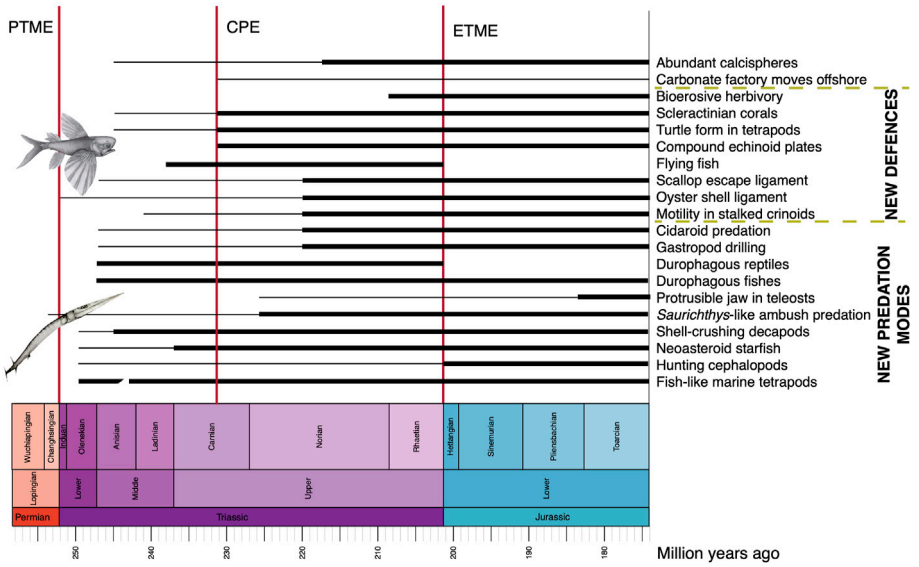

FIGURE 2 | Novel predatory and defensive modes in Triassic seas, showing approximate timings of known fossil records, or times when a phenomenon became established (thick line) and earlier occurrences, either inferred from phylogeny or based on rare fossils (thin line). The flying fish *Potanichthys* and the ambush-predatory *Saurichthys* are by Fei-xiang Wu.

cycle by improving the buffering capacity of the oceans (Ridgwell., 2005). This was a key switch in global ocean chemistry, marked by a shift of major carbonate reservoirs offshore and into deeper waters, which were less susceptible to fluctuating sea levels than the earlier carbonate accumulations on continental shelves.

New Predators

As noted earlier, the Triassic revolution in the oceans is marked not only by the beginning of the shift in the carbonate factory, but also by a great number of new predators and predatory modes, matched by many new defensive and escape strategies by the prey organisms (**Figure 2**).

Predatory crustaceans, primarily shrimp- and lobster-like decapods, were widespread in the Triassic, and these include stem penaeoid and caridean shrimps and polychelidan and astacidean lobsters (Hegna et al., 2020). It is likely that crown families, known from fossils in the Jurassic, such as the Anomura (hermit crabs, squat lobsters, false crabs, stone crabs) and Brachyura (true crabs), will also yield fossils back into the Triassic, as indicated by molecular estimates (e.g., Bai et al., 2018) that substantial diversifications followed the PTME, in the Early to Middle Triassic. Modern families identified so far in the Triassic include Penaeidae (prawns and shrimps), Palinuridae and Glypheidae (rock and glypheid lobsters), and Upogebiidae (mud shrimps). New fossil finds from the Middle Triassic (Anisian) of China show the Luoping fauna included five decapod species, capable of variously hunting and scavenging their prey (Feldmann et al., 2012). In their review of decapod hunting modes, Schweitzer and Feldmann (2010) noted that decapods had adaptations for shell-crushing since the Early Triassic.

Coleoid cephalopods, squid, cuttlefish, octopuses, and belemnoids, diversified substantially through the Mesozoic, and their fossils, especially those of the hunting forms with tentacles bearing suckers and hooks, such as phragmoteuthids and belemnites to a lesser extent, became common in the Late Triassic. These forms, modern and ancient, hunted by grasping immobile or slow-moving prey in their tentacles and snipping and crushing the shell with their beak. Combined molecular and fossil evidence (Tanner et al., 2017) confirms massive diversification of such hunting coleoids in the Early Jurassic, but there was slow diversification through the Triassic, with a reported squid-like coleoid from the Early Jurassic of Idaho, United States (Doguzhaeva et al., 2018).

New echinoderm predators emerged. The PTME witnessed the extinction of most echinoderm clades, and Early Triassic fossil records are poor, but they show a rapid re-diversification of ophiuroids and crinoids in the Middle Triassic, and significant expansions of all clades in the Late Triassic (Twitchett and Oji, 2005). Asteroidea (starfishes) are rare as fossils in the Triassic, but these voracious predators likely arose early in the Triassic according to phylogenomic analyses, with the PTME marking the trigger for origin of the most diverse living clade, Neoasteroidea, at that point (Mah and Blake, 2012). Their rarity as fossils may reflect the fact that they require special conditions to fossilize. Cidaroid echinoids diversified substantially from the Carnian onwards, and perhaps drove the evolution of motile crinoids (see below).

Marine predatory vertebrates show spectacular and rapid diversifications in the Early and Middle Triassic, and new discoveries from China have confirmed their early start in the Triassic, but not in the Late Permian (Benton et al., 2013; Scheyer et al., 2014; Motani et al., 2015). Among osteichthyans, the clade

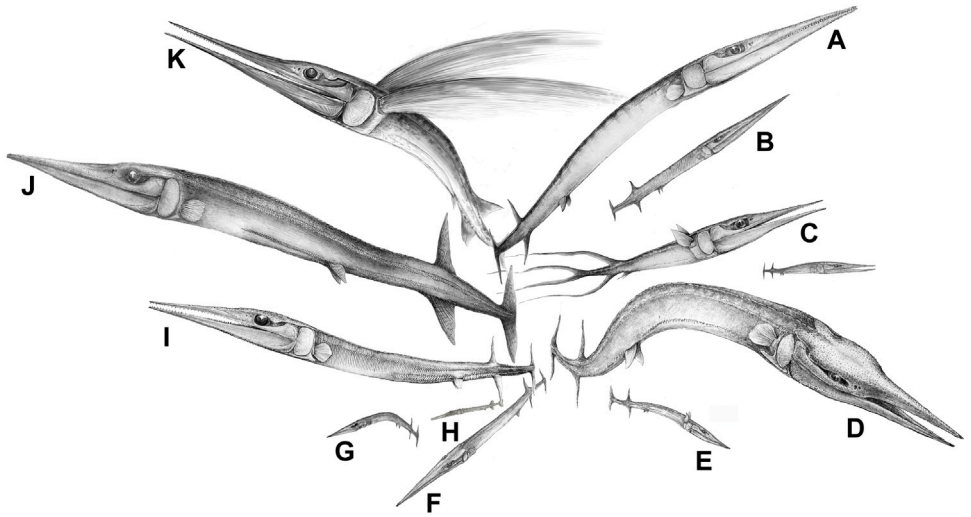

FIGURE 3 | The diversification of the saurichthyiform fishes ('lizard fish') in the Middle Triassic of South China (eastern paleo-Tethys), reflecting the establishment of a complexly tiered marine ecosystem (or marine fish communities) with intensive predator-prey interactions along the food chains. Species list: **(A)**, *Saurichthys dawaziensis*; **(B)**, *Saurichthys* sp. 1 (under description); **(C)**, *Sinosaurichthys longimedialis*; **(D)**, *Yelangichthys macrocephalus*; **(E)**, *Sinosaurichthys* sp. (under description); **(F)**, *Saurichthys* sp. 2; **(G)**, *Sinosaurichthys minuta*; **(H)**, *Saurichthys spinosa*; **(I)**, *Saurichthys yunnanensis*; **(J)**, *Saurichthys yangjuanensis*, which preyed on the coexisting Sinosaurichthys longipectoralis (see, Wu et al., 2015); **(K)**, Sinosaurichthys longipectoralis. **A,C,E–I** from the Anisian of the Luoping Biota; **D,J,K** from the Anisian of the Panxian Biota; B from the Ladinian of the Xingyi Biota. Artwork by Fei-xiang Wu.

Neopterygii expanded enormously in this time, comprising holosteans plus teleosts, and today representing 99% of living bony fishes (Benton et al., 2013; Romano et al., 2016; Xu, 2020; Romano, 2021). Romano (2021) makes a case that there is a hiatus in preservation during the crucial time between Olenekian and early Anisian, from 250 to 246 Ma, so perhaps artificially pushing apparent origins of some clades from Early to Middle Triassic. Similarly, the modern shark clade, Neoselachii, also diversified from the Early Triassic onwards, diversifying into several lineages, but apparently slowly (Cuny and Benton, 1999).

Ambush predation had evolved among fishes in the mid-Paleozoic, but the hugely abundant, elongate osteichthyan *Saurichthys* apparently adopted new, super sneaky strategies. Computational fluid dynamics studies of 3D models show that *Saurichthys* had adaptations to make its approach and final lunge undetectable by minimizing flow disturbance, as with modern needlefish and gars (Kogan et al., 2015). According to these authors, pike, which are also ambush hunters, generate more disturbance as they lunge for the kill, but they compensate for this by faster attack speed and their protrusible jaws. Saurichthyid fishes exploded on the scene in the Middle Triassic (**Figure 3**). They originated in the latest Permian (*Eosaurichthys* from Changxing, Zhejiang, China) and diversified to dozens of species in the Middle Triassic (Wu et al., 2011, Wu et al., 2015, Wu et al., 2018) and continued until the Middle Jurassic (Maxwell, 2016), hence surviving two major biotic crises. In addition, a lineage of saurichthyiform fishes from the Anisian of China had evolved a distinct crushing feeding mechanism, comprising massive jaws but small and blunt teeth (Wu et al., 2013). These Triassic fishes, however, did not have protrusible jaws, and this important feeding adaptation was absent in early teleosts such as *Pholidophorus* from the Late Triassic (Arratia, 2017), and is characteristic of the Acanthomorpha (Schaeffer and Rosen, 1961), originating in the Late Jurassic or Early Cretaceous (Chen et al., 2014).

Among marine reptiles, there was substantial diversification in the Early and Middle Triassic, documented especially well in the south of China (Chaohu, Panxian, Luoping, Xingyi, Guanling faunas) and in central Europe (Benton et al., 2013; Scheyer et al., 2014; Motani et al., 2015), including groups such as ichthyosaurs, sauropterygians (pachypleurosaurs, nothosaurs, placodonts), thalattosaurs, saurosphargids, hupehsuchians, archosauromorphs, and chelonians. The recent analysis of a giant ichthyosaur, *Cymbospondylus youngorum*, from the Anisian-aged Fossil Hill Member of the Favret Formation in Nevada, gives impressive evidence of the rapid diversification of these marine reptiles (Sander et al., 2021). This animal is estimated as 17.6 m long and weighing 45 tons, and the authors carry out detailed macroevolutionary analysis which shows enormously rapid achievement of huge diversity and great body size by ichthyosaurs in the Olenekian and Anisian, a prime example of an 'early burst' radiation. They identify 30 species of ichthyosaurs in the Olenekian–Ladinian interval, and explosive evolution of body size from initial sizes of <1 m to a broad range in the Anisian from 0.5 to 17 m, some 5 Myr later. The speed of diversification far outstrips that experienced by whales as they evolved towards large size in the Cenozoic.

The huge body sizes achieved by some ichthyosaur lineages in the Triassic is matched by the fact that many or most of the marine reptiles were probably warm-blooded (endothermic) to some extent, generating internal body heat as mammals and birds do today, in contrast to the largely ectothermic (cold-blooded) modern reptiles. For example, study of bone histology shows that

ichthyosaurs were likely homeothermic by virtue of large size and insulation or even regionally endothermic, enabling fast and sustained activity from their origin in the Early Triassic (Nakajima et al., 2014; Lindgren et al., 2018). On the other hand, whereas plesiosaurs from their origination in the Late Triassic may have been endothermic, the Triassic sauropterygians such as nothosaurs, pachypleurosaurs and placodonts, were almost certainly still ectothermic, as indicated by bone histology (Wintrich et al., 2017).

These ichthyosaurs, the other marine reptiles, as well as the sharks and some of the neopterygian bony fishes, were predators, and the larger ichthyosaurs, nothosaurs, thalattosaurs, and hupehsuchians were apex predators, themselves feeding on other marine reptiles. These all represent new predatory levels in the trophic systems of the Olenekian and Anisian, substantially different from the Permian when sharks were the sole top predators (Benton et al., 2013; Scheyer et al., 2014; Sander et al., 2021). The new groups of marine fishes and reptiles occupied other predatory niches too.

Durophagy, the predatory adaptation to crush hard shells, arose several times among Paleozoic predators, for example in placoderms and some sharks (Brett and Walker, 2002), but the habit had disappeared, before its re-emergence among different groups of fishes and newly in reptiles in the Early and Middle Triassic (Tackett, 2016; Tackett and Bottjer, 2016). Shell-crushing vertebrates emerged at the start of the Middle Triassic. Several groups of fishes (hybodontid sharks, colobodontids) and reptiles (placodonts, some ichthyosaurs, some thalattosaurs) had specialized shell-crushing dentitions, and some were relatively large such as 30-cm-long colobodontids (Xu, 2020). Note, however, that although colobontid fishes had blunt teeth on the buccal surface, they had pencil-like teeth on the jaws, which might indicate a predatory habit. Therefore, they were probably not obligate durophages, and may also have preyed on thick-scaled holostean fishes, using the sharp teeth to snatch and manipulate their prey, and the blunt buccal teeth to crush their scales. Importantly also, durophagous fishes and reptiles made up a rather small proportion of the taxic diversity of the Panxian and Luoping (Anisian) marine communities. Linked evidence that shell-crushing occurred in the Middle Triassic vertebrates are regurgitated masses of shell debris and crinoid remains ('bromalites') reported by Salamon et al. (2012) from the Middle Triassic of Poland. Several authors have interpreted such evidence as evidence that the MMR began explicitly as a part of the Early–Middle Triassic recovery from the PTME (e.g., Salamon et al., 2012; Benton et al., 2013; Xu, 2020).

Adaptations for durophagy occur also in Triassic hybodont sharks, with typical crushing teeth and body lengths over 2 m in some cases. There may have been some shell-crushing hybodonts in the Permian (Vermeij, 1977), but the Lonchidiidae, which originated in the Middle Triassic, were the first of several Mesozoic families of hybodonts to adopt durophagy. In Jurassic species, there are also cases of stomach contents and regurgitations of belemnites (Klug et al., 2021).

Durophagy in ichthyosaurs evolved 3–5 times during the Triassic, and indeed more than half the species of Early and Middle Triassic ichthyosaurs had at least some molariform teeth (Huang et al., 2020). Indeed, Huang et al. (2020) suggest that the prevalence of durophagy among these marine reptiles indicates that their specific adaptations to consuming hard-shelled prey and hard-scaled fishes explains much of their early success. Further, the nature of the crushing teeth varies, suggesting that different ichthyosaurs specialized on different kinds of hard-shelled prey. All the durophagous reptiles (placodonts, ichthyosaurs, thalattosaurs) died out at the end of the Triassic, or earlier, and the habit did not re-emerge in marine reptiles until the Late Jurassic, in plesiochelyid turtles, and Late Cretaceous, in some mosasauroids and turtles (Stubbs and Benton, 2016).

New Defenses and Evasions

The new predators and their cunning modes of attack in Triassic oceans stimulated new defensive adaptations in their prey (**Figure 2**). In an earlier review, McRoberts (2001) found that Mesozoic predatory adaptations such as durophagy, shell snipping, and shell boring were present, but not prevalent in the Triassic. He noted steadily rising diversity among bivalves through the Triassic but explained the series of innovations just noted driven by environmental changes associated with the recovery of life following the PTME, rather than evidence for an escalation of predator-prey interactions, a key element of the MMR, mainly because of the apparent rarity of the new predatory groups and evidence for their activities such as boreholes and snipped shell edges. This view was strengthened by reports of predatory attack on mollusks in the Early Jurassic and Late Triassic. Harper et al. (1998) suggested a Triassic start for the MMR based on evidence for high levels of boring predation marks on bivalve shells from the Lower Jurassic.

Shell drilling was not a Mesozoic innovation, having been reported through the Paleozoic, and attributed to platyceratid gastropods (Brett and Walker, 2002). However, the drilling predation habit was not continuous through geological time, with a gap from Late Carboniferous to Permian, and a gradual increase from the Middle Triassic to the present day (Walker and Brett, 2002; Klompmaker et al., 2016; Tackett and Tintori, 2019, **Figure 5**). Fürsich and Jablonski (1984) reported extensive findings of boreholes from the Triassic, evidence of the new gastropod predation modes. Strong external shell sculptures, interpreted as an antipredatory feature, and typical of the MMR (Vermeij, 1977), were also reported in Triassic gastropods and bivalves (Nützel, 2002). The relatively low levels of boreholes in the Triassic are indicative of the re-invention of this feeding strategy in the Early to Middle Triassic, and its slow expansion through the Jurassic and Early Cretaceous (0–5%), until it rose to modern levels (c. 20%) in the Late Cretaceous when there was a great increase in drilling by naticid and muricid gastropods (Harper, 2003).

Trace fossils provide additional evidence for an escalation in predator-prey behavior in the Triassic. Previous authors noted an increase in infaunalization in the Early Triassic (Stanley, 1968, 1977; Foster and Twitchett, 2014). What we cannot demonstrate is whether this behavior was new and was not already happening in the Late Permian. Buatois et al. (2016) report that trace fossils show evidence that seabed ecosystems had fully recovered by the Middle Triassic in equatorial carbonate settings, although these ichnoassemblages show

limited infaunalization and simple tiering structures. These authors note major changes in Jurassic ichnoassemblages that mark the rise to dominance of the Modern Evolutionary Fauna. In general, the intensity of bioturbation, trace fossil diversity, complexity of tiering, and maximum burrow depths, increased through the Early and Middle Triassic, indicating stepwise recovery of benthic biodiversity and range of feeding modes (Luo et al., 2020). Bioerosive herbivory, whereby mollusks, echinoids and other taxa feed actively across sea-shore services, consuming green algae, began in the Rhaetian and became common in the Jurassic (Radley, 2010), and it is unclear whether older examples are confidently known in the Triassic.

Cementing to rocks and clamping tight shut are mechanisms that oysters and other mollusks use to avoid the attentions of predators. Hautmann (2004) reported the origin of a major antipredatory adaptation in Triassic bivalves coupled with substantial diversification of the major clade Pteriomorpha, which includes mussels, scallops, and oysters. Pteriomorph bivalves are characterized by modified alivincular ligaments that substantially strengthen the hinge line and enable them to adopt one of two new defense strategies; oysters and mussels can clamp down and keep the shell shut against attempts to prize it open by starfishes, and scallops and other swimmers can close the shell fast under attack and escape by snapping shut and squirting water out. Hautmann (2004) noted that three modified alivincular ligament types emerged in parallel in different pteriomorph clades in the Late Triassic and Early Jurassic. Hautmann et al. (2017) reported Early and Middle Triassic cementing oysters, and their origin and diversification early in the Triassic has been explained as paralleling the diversification of durophagous crustaceans, fishes and reptiles.

The alivincular ligament, as noted, enables scallops and relatives to snap the valves shut and escape by rocket propulsion. Hautmann (2010) reported the first scallop from the early Ladinian of Europe. Further, phylogenetic analyses of the pecten families Pectinidae and Entolioididae show they originated in the Early Triassic, likely with their shell-clapping habit and strengthened alivincular ligament from the start (Waller, 2006).

Escape by fast swimming has also been suggested as evidence of new predation pressures on crinoids. Motility in stalked crinoids perhaps evolved for similar reasons. Baumiller et al. (2010) noted evidence for active predation by cidaroid echinoids on stalked crinoids from the Middle Triassic of Poland, as well as in later stratigraphic units, and suggested that this new mode of hunting promoted the evolution of motile crinoids as a means of escape from their fellow echinoderms. Cidaroid echinoids diversified through the Triassic and Early Jurassic (Kier, 1974), and their predation on crinoids perhaps drove this new mode of life.

An unexpected discovery was the first flying fish, from the late Ladinian of China (**Figure 2**) (Xu et al., 2013). This was a locomotory mode that had been identified in the Late Triassic thoracopterid bony fishes (Tintori and Sassi, 1992), and it is a convergent precursor of the Exocetidae (Beloniformes), the flying fishes of today. Fish fly, by launching themselves out of the water, as an escape strategy, but so far as we know, this mode of escape from predation did not exist in the Jurassic or Early Cretaceous, until *Exocoetoides* (?Aulopiformes, Chirothricidae) evolved in the Late Cretaceous (Davis, 1887).

Two Phases in the Triassic MMR

These studies of evolution among potential predators tend to show earlier-than-expected origins of many clades, and some of them, such as ichthyosaurs, apparently diversified explosively in the first 5–10 Myr of the Triassic. Others show an early origin of the clade or the innovation, but a slow expansion, and sometimes an uptick in the Carnian or Norian, in many cases following the CPE (**Figure 2**). There is a similar divergence of evidence for patterns of new modes of predation, as well as predation avoidance and escape strategies, with some modes occurring very early in the Triassic, and others expanding slowly and spreading more rapidly in the Late Triassic to Early Jurassic.

There are two reasons for a coincidence between the processes of recovery of life from the extreme levels of devastation wrought by the PTME, and the beginning of the MMR and origin of modern marine ecosystems. First is that the extinction cleared ecospace and allowed new taxa to dominate earliest Triassic ecosystems, and these new taxa established new, faster life modes and arms races than seen in the Paleozoic. Second are the more immediate aspects of the turmoil of post-PTME seas, when harsh environmental conditions interfered with the recovery and forced some strong ecological interactions. During the Early and Middle Triassic, new clades with their new adaptations emerged, both new antipredatory strategies such as thickened shells and cementation in oysters and mussels, snap escape swimming by scallops, motile crinoids, prominent sculpture by gastropods and bivalves, and deep burrowing by many taxa, as well as the new hunting modes, including shell snipping by malacostracans, hole boring using chemical and mechanical means by gastropods, and durophagy by hybodont sharks and reptiles.

The strong evidence for substantial expansion among invertebrate predatory clades, as well as neoselachian sharks, durophagous fishes and reptiles, and evidence of predatory activity and anti-predatory adaptations (motile crinoids; heavily ridged shells; cemented oysters; shell-clapping scallops) from the Carnian onwards could reflect bias in the fossil record, namely the availability of numerous extensively fossiliferous marine geological formations in Europe, North America, China and elsewhere that preserve more fossils and to higher quality. However, some of the apparent explosion of new clades and innovations, especially for example the diversification of scleractinian corals and coral reefs, and the plankton revolution, are likely real, and consequences of the impact of the CPE (Dal Corso et al., 2020). The plankton revolution of the Late Triassic (Falkowski et al., 2004) was the time when all modern marine plankton (calcareous nannoplankton, planktonic foraminifera, dinoflagellates, radiolaria) originated or diversified. These provided the basis for new trophic structures in the oceans and could have triggered the explosive diversification of consumers at all levels.

In summary, new evidence from marine ecosystems has shown that the initiation of the MMR has moved back in steps through the last decades. At first, Vermeij (1977) suggested that the major

escalation in predator-prey interaction began in the Late Jurassic, but then marshalled evidence that the first phase actually dated back to the Late Triassic-Early Jurassic (Vermeij, 2008). New evidence, as noted by many authors and summarized here, is that the initiation of the MMR coincides with the building of the 'Modern' marine ecosystem from the Early Triassic onwards (Sepkoski, 1984), and that there was a second escalation following the CPE some 232 Ma, marked by major revolutions in plankton, carbonate factory, predatory modes, and anti-predator defenses (Dal Corso et al., 2020).

Further evidence for escalation through the Triassic is that some of the new predatory and defensive adaptations disappeared at the end of the Triassic, including widespread durophagy in marine reptiles and flying adaptations in fishes; these adaptations re-emerged in other groups later in the Mesozoic.

THE TRIASSIC TERRESTRIAL REVOLUTION

Physiological Escalation

Biologists, and the general public, readily divide vertebrates into 'cold-blooded' fishes, amphibians and reptiles on the one hand, and 'warm-blooded' mammals and birds on the other. It is broadly assumed that these represent respectively low-energy and high-energy modes of life, or 'slow' and 'fast' organisms in terms of the speed with which they live their lives, but also the amount of energy, oxygen and carbon they consume. Mammals and birds are fast-moving, capable of sustained locomotion and nocturnality, whereas amphibians and reptiles are generally slower moving, not capable of sustained fast movement, and apparently motionless for much of the time. In fact, there may be a twenty-fold difference in energy consumption between the two physiological groups. Metabolic rate, measured as the rate of consumption of oxygen, depends on the size of the animal (it is relatively higher in small animals), but as an example a small bird may use up 10 ml of oxygen in 1.3 h, whereas a lizard of similar body mass would take 23.8 h to use the same amount of oxygen, a 20-fold difference (Bennett and Nagy, 1977; Gillooly et al., 2001).

This reflects fundamental differences between endothermy ('warm-bloodedness'; production of heat by physiological means) and ectothermy ('cold-bloodedness'; acquisition of heat from external environmental sources): endotherms consume oxygen and food in considerable quantities to fuel their inner furnaces, whereas ectotherms rely on sunlight directly or indirectly. At larger body sizes, differences in metabolic rate may become less because bulky ectotherms achieve insulation by being large and so retain heat passively when the external environment cools down (McNab, 1978; Paladino et al., 1990). This enables some large living reptiles such as sea turtles and some snakes to achieve a kind of warm-bloodedness, termed gigantothermy or inertial homeothermy, possibly also true for dinosaurs and other extinct reptiles including ichthyosaurs and plesiosaurs (Paladino et al., 1990; Seymour, 2013; Lindgren et al., 2018).

However, it is not clear that inertial endothermy is necessarily equivalent to endothermy in terms of metabolic rate and outputs: Seymour (2013) found that whereas a small crocodilian (1 kg) can produce up to 57% of the power output of a mammal of similar body mass, a large crocodile (200 kg) with relatively inertially constant body temperature nonetheless produced only 14% of the power of a mammal of similar body mass. The deficit relates to the relative aerobic capacity of endotherms and ectotherms, their ability to take in and use oxygen in a continuous manner.

This difference is made more marked by posture. Lizards and most ectothermic tetrapods are sprawlers that move by swinging the vertebral column from side to side as they take strides. As the right arm moves forward, the torso twists left and air is expelled from the left to the right lung, and vice versa as the left arm moves forward. Mammals and birds have erect, or parasagittal, posture with the limbs held beneath the body and moving back and forwards parallel to the backbone. Mammal backbones flex up and down and air is pumped in and out of the lungs by compression and relaxation of the diaphragm; birds have a one-way respiration system involving air sacs connected to the lungs. Both groups show high endurance when compared to ectothermic tetrapods; salamanders and lizards can either run or breathe, but not both (Carrier, 1987).

Benton (2021) argued that the Triassic was the crucial time in the independent origins of endothermy in the bird and mammal lineages. He pointed to the origin of parasagittal gait and insulating dermal coverings in the Early and Middle Triassic, 250 Ma, and speculated that this happened during the time when life was recovering from the PTME. Then all aspects of a higher-paced, endothermic lifestyle became established in archosaurs and synapsids as they engaged in competitive and predator-prey arms races throughout the Triassic. Can this case be sustained in the face of very different models for the origins of endothermy?

Origins of Endothermy

The origins of endothermy in mammals and birds have long been discussed, and current estimates of timing range widely, from Carboniferous to Jurassic. Grigg et al. (2022) argued that endothermy in both clades should be traced back to the origin of amniotes in the mid-Carboniferous, some 310 Ma, based on a combination of the close similarities of the fundamentals of avian and mammalian endothermy, as well as paleontological evidence. On the other hand, Rezende et al. (2020) argued that endothermy emerged in birds only with the extreme miniaturization that took place in the paravian lineage in the Middle and Late Jurassic, 175 Ma. Similarly, Newham et al. (2022) identify a late origin of endothermy in mammals also in the Middle Jurassic.

Grigg et al. (2022) argue for a single origin of endothermy in early amniotes from physiological and paleontological evidence. First, they note revisions to the standard assumption that non-shivering thermogenesis (NST), the fundamental source of tetrapod endothermy, originates from skeletal muscle in birds and brown adipose tissue in mammals; in fact, they note that brown adipose tissue is absent in monotremes, marsupials and many eutherian mammals, and that muscle-based NST in birds and mammals shares the same processes of calcium transfer at cellular level. Second, they marshal paleontological evidence for an early, shared origin of whole-body endothermy in all amniotes, and as seen today in birds and mammals: 1) evidence from bone histology for fibrolamellar bone and endothermy in Carboniferous and Permian amniotes including ophiacodontids, edaphosaurids,

sphenacodontians, dinocephalians, gorgonopsians, dicynodonts, and pareiasaurs; 2) erect or semi-erect posture and large body size in some Permian synapsids (*Dimetrodon*, *Inostrancevia*, *Moschops*) and sauropsids (*Scutosaurus*, *Moradisaurus*); 3) large nutrient foramina in long bones of caseids, edaphosaurids, sphenacodontids, dicynodonts, gorgonopsids, and cynodonts suggesting rapid growth and repair associated with high-speed locomotion; and 4) obligate bipedality in Triassic archosaurs. If whole-body endothermy arose soon after the origin of amniotes in the mid-Carboniferous and persisted in all clades including the bird and mammal lineages, the ancestors of turtles, lizards, snakes, and crocodilians must have reverted from endothermy to ectothermy independently at certain points in their histories. Indeed, it has often been suggested that crocodilians were ancestrally endothermic based on their 4-chambered hearts, bird-like lungs, and fibrolamellar bone in juveniles (Seymour et al., 2004). However, the proposal (Grigg et al., 2022) of reversion from endothermy to ectothermy in the ancestors of turtles and lepidosaurs (lizard snakes and relatives) is novel.

At the other end of the scale, as noted, some recent papers propose that avian and mammalian endothermy arose 135 Myr later, in the Middle Jurassic. Rezende et al. (2020) argued that endothermy arose in the bird lineage at the same time as miniaturization brought their body size down to a point where the costs of elevated energy requirements were mitigated. They argue that the cost of maintaining body temperature higher than ambient (= environmental) temperature is high in a large animal, so miniaturization brings the cost down. Their calculations suggest that the transition from ectothermy to endothermy happened between body masses of 100 and 1 kg, and especially at about 10 kg, so they suggest that many maniraptorans, and all paravians were endothermic. This transition occurred in the Early to Middle Jurassic, about 180–170 Ma, well before the origin of birds, and associated with the acquisition of diverse avian-like feather types by numerous maniraptoran dinosaurian lineages.

Similarly, Newham et al. (2022) point to the Middle Jurassic as the time of origin of endothermy in mammals, long after the emergence of indicators accepted by other authors (e.g., Botha-Brink et al., 2018; Benton, 2021) as evidence for earlier origins, whether in the Middle or Late Permian (separation of lumbar and thoracic regions and origin of diaphragm; differentiation of dentition; bony secondary palate; enlargement of brain), Early Triassic (parasagittal gait; nutrient foramina on snout suggesting muscular lips and hair; parental care; fibrolamellar bone; reduced red blood cell size), or Late Triassic (neurosensory evolution and hair; miniaturization on mammalian lineage; ossified nasal turbinates). Newham et al. (2022) acknowledge all these features and their relative timings of origin but argue that they indicate modifications to locomotory mode and enhanced aerobic activity, but not endothermy. They emphasize the importance of the acquisition of both a high basal metabolic rate (BMR) and a high maximum metabolic rate (MaMR), both of which are features of modern mammals. Their studies of the Early Jurassic mammal *Morganucodon* show that, although it had all these features, as well as the mammalian jaw joint, diphyodonty (tooth replacement limited to milk and adult sets), and determinate growth, growth increments

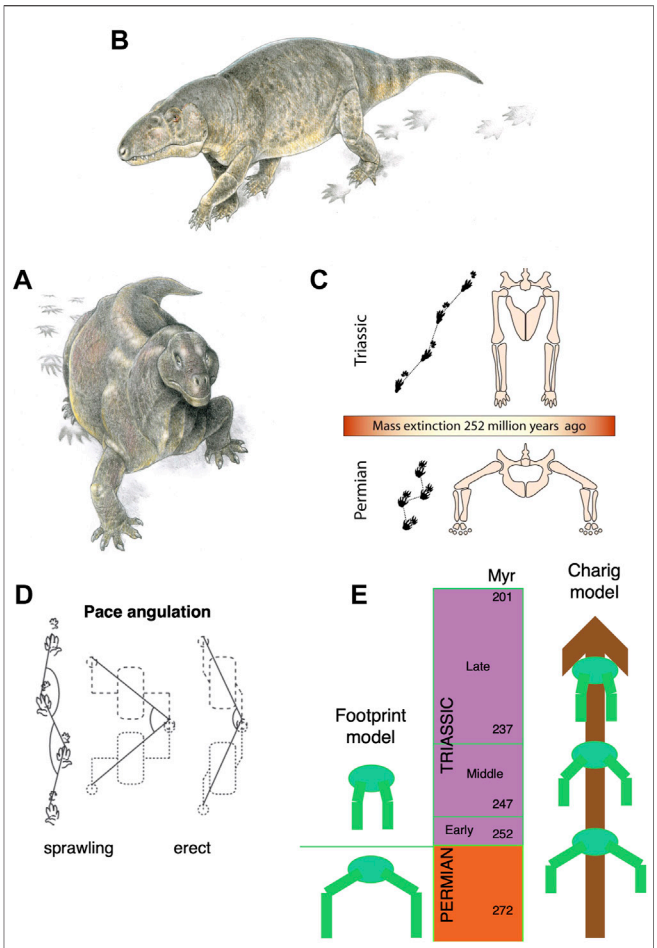

FIGURE 4 | Posture shift from sprawling to parasagittal, among synapsids and archosauromorphs. **(A)** A sprawling synapsid, *Moschops* from the Late Permian. **(B)** An erect-postured archosauriform, *Vjushkovia* from the Early and Middle Triassic, both with tracks. **(C)** The transition from sprawling to erect posture across the Permian-Triassic boundary. **(D)** Measurement of pace angulation of tracks, showing sprawling and erect tracks, with sketch body and limbs (values of pace angulation 138° indicate an erect posture). **(E)** Contrast of the instant switch from sprawling to erect posture across the Permian-Triassic boundary, 252 Ma (left) with the classic Charig (1972) model of a more prolonged postural shift, occurring through much of the Triassic. Panels A and B are by Jim Robins; C by Simon Powell; D is from Kubo and Benton (2009), and E is original; all from Benton (2021).

in the cement that fixed the teeth in their sockets indicated a life span of 14 years, and 9 years for another Early Jurassic mammal, *Kuehneotherium*. Such long life spans are more in line with ectotherms than endotherms of such small body sizes. Further, the sizes of nutrient foramina in the limb bones of *Morganucodon* indicate a MaMR value closer to that of modern reptiles than mammals.

In his overview of the evolution of endothermy, Lovegrove (2017) suggested a three-phase model in both birds and mammals, which each followed independently, through stages of 1) parental care and locomotion; 2) thermoregulation and miniaturization; and 3) locomotion and climate adaptation. In the bird lineage (Archosauria), these phases ran respectively from Late

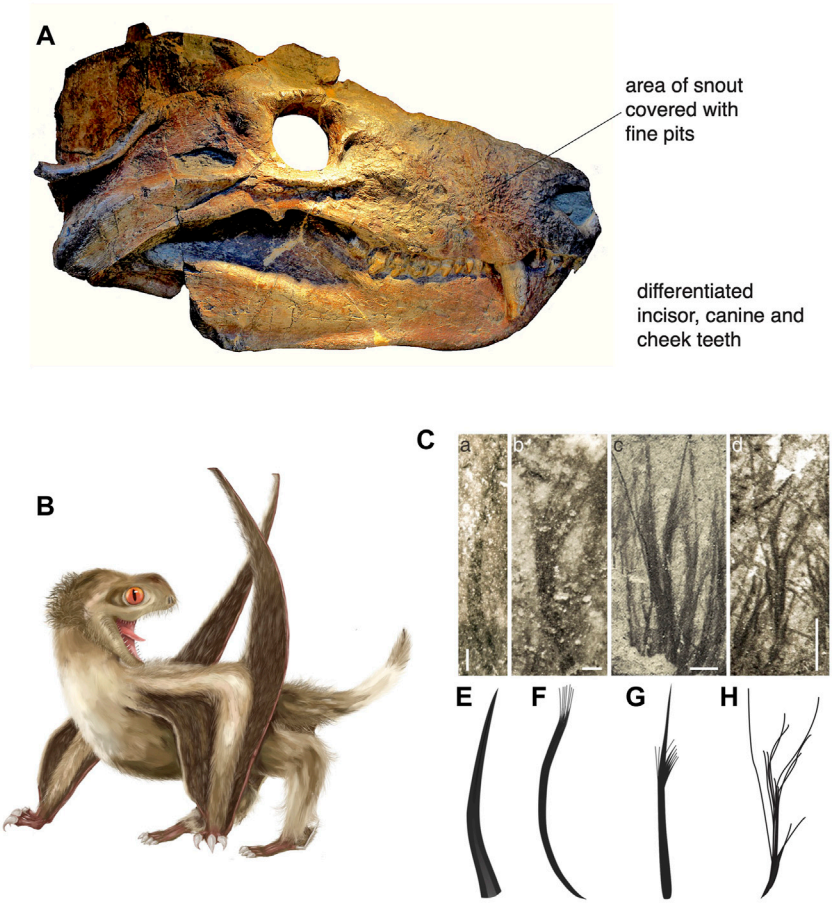

FIGURE 5 | Evidence for insulating pelage in synapsids **(A)** and archosauromorphs **(B,C)**. **(A)** Skull of the Middle Triassic cynodont *Cynognathus* in lateral view, showing pits on the snout suggesting vibrissae. **(B)** An anurognathid pterosaur from the Middle Jurassic of China, from which the four feather types were identified. **(C)** The four pterosaurian feather types: monofilaments (a, e), tufted monofilaments (b, f), bunched fibres (c, g), and down feathers (d, h). **(A)** Photo by Emöke Dénes, Wikimedia; **(B)** artwork by Yuan Zhang; **(C)** Image based on Yang et al. (2019).

Permian–Triassic; Jurassic–Early Cretaceous; and Early Cretaceous–Modern, and in the mammal lineage (Synapsida) from Middle Permian–Middle Triassic; Late Triassic–Paleogene; and Paleogene–Modern. Newham et al. (2022) present a similar sequence for mammals, with initial stages of increasing aerobic capacity (MMR) and improving thermoregulatory ability (BMR) through the Permian and Triassic, and the establishment of endothermy (acquisition of mammalian BMR and MaMR) in the Late Jurassic and Cretaceous, coincident with the origin of modern mammals.

Triassic Arms Races

Whether we accept origins of endothermy in the Carboniferous, Permian, Triassic or Jurassic, it is worth considering steps along the way and when they happened. In fact, much of the debate outlined above depends on definitions of endothermy, but despite quandaries around that issue, we can observe many definite changes in the fossils, including origins of erect posture, dermal insulation, and elevated metabolic rates as inferred from bone histology from the Early Triassic onwards. Importantly, the changes appear to occur in parallel in the two major clades of terrestrial tetrapods of the time, the archosauromorphs (including ancestors of crocodilians, dinosaurs and birds) and synapsids (including ancestors of mammals).

These two great clades passed at low diversity into the Triassic. Archosauromorphs had existed only at low diversity in the Late Permian, and synapsids were hit hard by the PTME, and perhaps only ten or twenty species survived (Benton et al., 2004; Irmis and Whiteside, 2011). The earliest Triassic archosauromorphs and synapsids diversified rapidly in the new world, and they appear to have embedded a series of new adaptations that spread through all Triassic survivors and their descendants.

First is Posture

It had long been noted that Late Permian synapsids showed substantial modifications in their posture with the limbs tucked

beneath the body and modified rib cages suggesting the presence of a diaphragm, and a vertebral column that flexed up and down rather than side to side (e.g., Jones et al., 2019). Among archosauromorphs, or archosaurs in particular, a different pattern of postural evolution had been suggested, passing stepwise from a sprawling posture to semi-erect, and then fully erect by Middle and Late Triassic (Charig, 1972). This idea of a gradual postural shift was challenged by Kubo and Benton (2009) who showed an apparently instant switch in the posture of medium-sized tetrapods that coincided with the Permian-Triassic boundary (**Figure 4**). Using a large sample of fossil trackways, they showed that all the Middle and Late Permian tracks suggested sprawling locomotion, whereas from the Early Triassic onwards, the postures were parasagittal. This can be determined readily from fossil trackways by measuring the pace angulation (the angle between successive right-left-right footprint sets): values were 88° in the Middle and Late Permian, but 140°, 149°, and 156° in the Early, Middle and Late Triassic. This documents a shift from very widely sprawling reptiles in the Permian to purely parasagittal forms in the Triassic, and showing some, but not much, evolution of parasagittality.

This simple switch from sprawling to erect posture across the PTB has been challenged by Sullivan (2015) who notes that the skeletons of Early Triassic archosaurs such as proterosuchids and erythrosuchids show they were almost certainly sprawlers. This apparent mismatch of footprint and skeletal evidence requires more study, but either way an erect posture was the norm for archosaurs and synapsids by the Middle Triassic.

Second is Dermal Insulation

A common assumption by physiologists is that the feathers of birds and hair of mammals are correlated with their endothermy and that they act as insulation. Therefore, if such insulating pelage were identified in the fossils, this might also suggest warm-bloodedness, if not endothermy of a modern kind. Such conditions had been suggested by Watson (1913, 1931) based on abundant pits around the

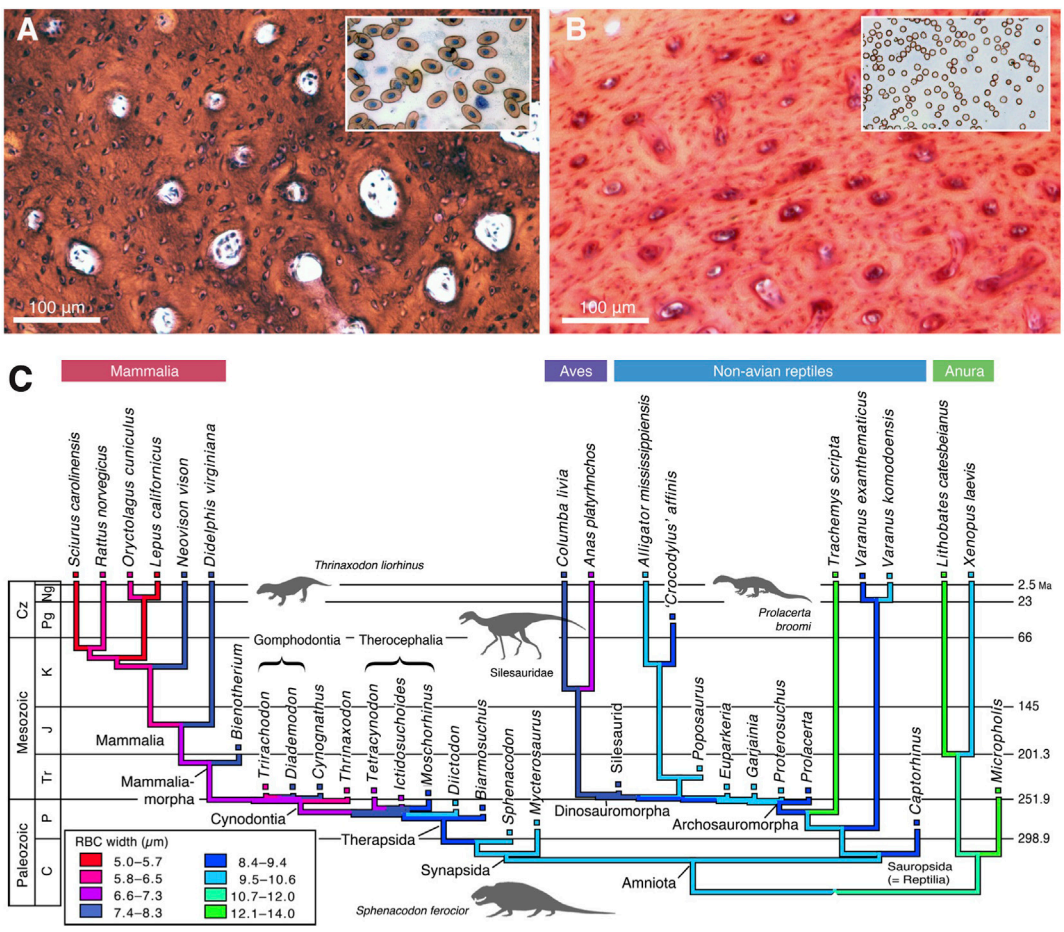

FIGURE 6 | Bone microvascularization and red blood diameter. **(A,B)** Microphotographs of histological sections of limb bones of American bullfrog **(A)** and rabbit (VB), with diagrammatic version to show larger vessels and fewer of them in the ectotherm **(A)** than in the endotherm **(B)**. **(C)** Phylogenetic tree showing optimisation of ancestral states reconstruction of red blood cell size (based on bone microvascularization) for tetrapods; among synapsids, therocephalians and cynodonts show mammal-like red blood cell sizes by the Permian-Triassic transition, whereas Triassic archosaurs show a mix of modern bird and crocodilian values in the Triassic. All images courtesy of Adam Huttenlocker.

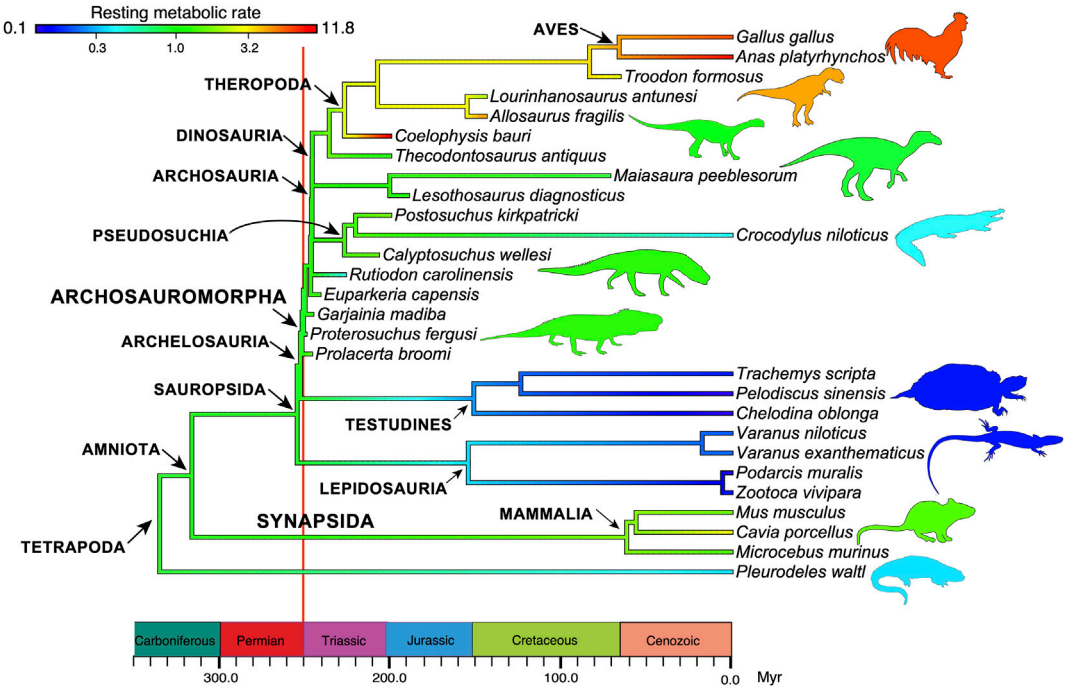

FIGURE 7 | The evolution of endothermy in archosauromorphs and synapsids from the Permian to the present day. In the analysis, ancestral states of resting metabolic rates, measured in mLO_2h^{-1} $g^{-0.67}$, are estimated at each branching point in the phylogeny and color-coded to indicate the level (note the logarithmic scale). Values for ectotherms are typically 1.0, with modern mammals having RMR values in the range 1.5–3.5, and modern birds, 8–12 mLO_2h^{-1} $g^{-0.67}$. Based on data in Legendre et al. (2016), with thanks to Lucas Legendre for the base image.

snout in cynodonts and therocephalians, carnivorous synapsids: he argued that the pits (**Figure 5A**) were presumably for nerves that invested the sensory whiskers, or vibrissae, and that these early meat-eaters also had muscular mammalian-like lips, as well as upright posture and enlarged brains, all indicative of endothermy. Fossil hairs have been identified in Late Permian coprolites from South Africa (Smith and Botha-Brink, 2011) and Russia (Bajdek et al., 2016). Nevertheless, Botha-Brink et al. (2018) suggest that hair evolved, or at least formed an insulating pelage, in synapsids in the early Late Triassic. It now seems evident that archosauromorphs also had feathers, especially short, fluffy insulating-type feathers, since the Early Triassic. The evidence is that theropod dinosaurs have very clearly avian-like feathers (Xu et al., 2014), as do some ornithischian dinosaurs such as *Kulindadromeus*. If dinosaurs all have feathers or the propensity for feathers, then feathers would date to the origin of dinosaurs (Benton et al., 2019; Yang et al., 2019). Pterosaurs, the sister group of dinosaurs, also have dermal insulating structures commonly called pycnofibres. New evidence (Yang et al., 2019; Cincotta et al., 2022) shows these pycnofibres take a variety of forms, including branching and tufting structures as seen among dinosaurs and birds (**Figures 5B,C**), so these are presumably also feathers. However, even if researchers balk at calling pycnofibres feathers, it does not change the fact that insulating dermal structures appeared in the first dinosaurs and the first pterosaurs, and the shared ancestry of these two clades is dated to the Early or early Middle Triassic. This realization of such early origins is a new discovery based on the occurrence of sister-group taxa such as silesaurids and aphanosaurians in the Anisian (Benton et al., 2014; Nesbitt et al., 2017; Benton, 2021).

According to an alternative view (Ezcurra et al., 2020a), the key Manda Formation of Tanzania is redated as late Ladinian to early Carnian rather than mid to late Anisian, so moving the dates of origin of some key early avemetatarsalians forward in time. However, even if the ages of these early avemetatarsalians are much younger than generally assumed, there are definitive members of the sister clade of Avemetatarsalia, the Pseudosuchia, in the Olenekian (Butler et al., 2011), so dating the origin of both clades as minimally Early Triassic (Olenekian). According to current phylogenies (e.g., Nesbitt et al., 2017; Ezcurra et al., 2020b), Pterosauria and sister clades and Dinosauria and sister clades each form unique lineages that diverged at the origin of Avemetatarsalia, so we assume an Early Triassic origin for both. One aphanosaurian, *Dongusuchus* from the Donguz Svita of Russia, is almost certainly Anisian in age, and if correctly identified as an aphanosaurian (Nesbitt et al., 2017), this brings the origins of the dinosaur and pterosaur lineages down to middle Anisian, if not late Olenekian, whatever the age of the Manda Formation.

Third is evidence of high metabolic rate in the bone histology of Triassic archosauromorphs and synapsids. Investigators have noted the widespread presence of fibrolamellar bone, often with extensive secondary remodeling through Haversian canals, both of which are features of the bone of living endotherms such as birds and mammals that exhibit fast growth (e.g., Ricqlès et al., 2008; Botha-Brink et al., 2018). Importantly, the sizes of canals through bone can indicate metabolic rate: birds and mammals today have small red blood cells (RBC) to enable the transport of increased amounts of oxygen when compared to ectotherms such as amphibians or reptiles which have

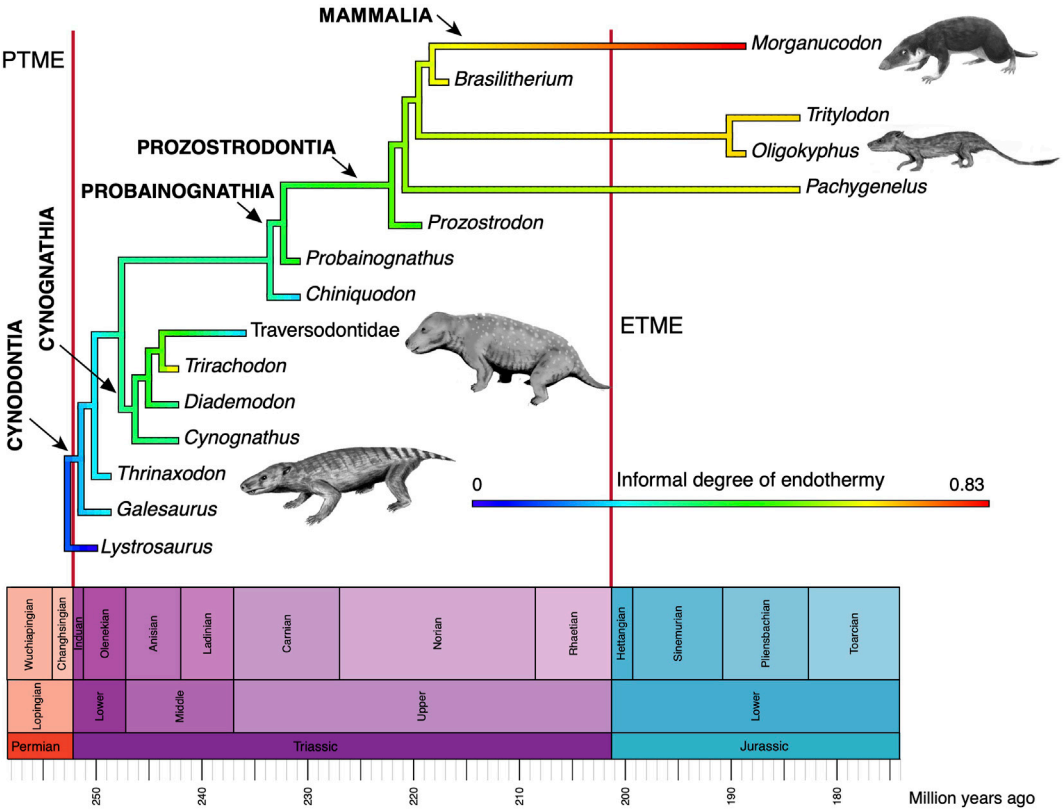

FIGURE 8 | Evolution of endothermy among synapsids, showing a range of values of an informal metric of endothermy (data in Benton, 2021, table 1). The small animal images are by Nobu Tamura (*Thrinaxodon*, *Oligokyphus*, *Exaeretodon*) and FunkMonk (*Morganucodon*), all Creative Commons (Wikimedia).

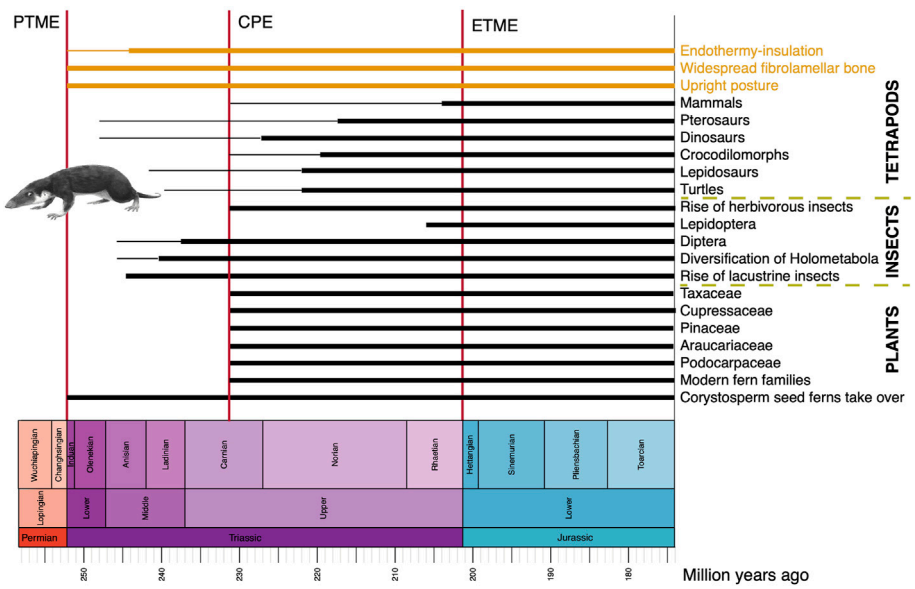

FIGURE 9 | Novel physiological and functional characteristics, new tetrapod, insect and plant groups in the Triassic on land. As in **Figure 2**, the image shows approximate timings of known fossil records, or times when a phenomenon became established (thick line) and earlier occurrences, either inferred from phylogeny or based on rare fossils (thin line). The early mammal *Morganucodon* is by FunkMunk (Wikimedia).

larger red blood cells. RBC size then is a measure of endothermy *vs.* ectothermy and, although the red blood cells are not preserved, the scaling of bone microvascularization provides a good measure. Huttenlocker and Farmer (2017) showed that Triassic synapsids and archosauromorphs generally had RBC sizes <10 μm and many were <7 μm, suggesting coincident evolution of endothermy in both lineages from the Early Triassic onwards (**Figure 6**). Microvessel size is only one direct anatomical indicator of thermal physiology in the bone of fossil tetrapods; other indicators include vascular density, osteocyte density, osteocyte shape, and osteocyte area, and these were used in combination by Legendre et al. (2016) to estimate resting metabolic rate (RMR) of a wide variety of Permian and Mesozoic animals (**Figure 6**). Their multi-factor histological metric is calibrated from modern reptiles, birds and mammals for which the RMR is known, and values are then determined for fossil forms. Their calibrated ancestral states reconstruction (**Figure 7**) indicates widespread endothermy (yellow-green, yellow, red colours) in both Triassic archosauromorphs and synapsids. A similar phylogenetic study, showing more detail of Synapsida and a broad array of traits (**Figure 8**) confirms stepwise acquisition of derived features through the Triassic (Botha-Brink et al., 2018).

The conclusion from studies of posture, insulatory structures and bone histology is that both archosauromorphs and synapsids were evolving a broad array of structures indicative of more active lifestyles, even endothermy throughout the Triassic (**Figure 9**). In their ecosystems, both lineages included a broad diversity of herbivores and carnivores of various sizes, and they were living side by side, presumably competing for food and engaging in predator-prey relationships, where sometimes the top predators were archosauromorphs, sometimes synapsids. Overall then these are the lines of evidence that led Benton (2021) to argue for side-by-side evolution of indicators of enhanced metabolic rates in both lineages and interpreted these ecologically as arms races through the Triassic that culminated in dinosaurs and pterosaurs on one hand, mammals on the other.

In all cases for terrestrial tetrapods, steps in their evolution from Paleozoic holdover taxa in the Early Triassic to modern-style animals by the end of the Triassic, were mediated by major events, most notably the CPE (Bernardi et al., 2018; Dal Corso et al., 2020). For dinosaurs and pterosaurs, it seems that both clades originated in the late Early or early Middle Triassic, but fossils of unequivocal examples are not known until the Late Triassic, after the CPE. By this time, with major changes in climates and floras, other 'modern' tetrapods are encountered at this time, including lizards, rhynchocephalians, turtles, crocodylomorphs, and mammals. Perhaps then the combination of global clear-out and reset by the PTME, followed by the CPE, triggered the birth of modern-style ecosystems on land as well as in the oceans (Dal Corso et al., 2020).

Plants and Insects

The fossil record of other terrestrial organisms has not been explored as thoroughly as that of tetrapods, but plants and insects also appear to show major steps towards modernization of ecosystems through the Triassic, and especially following the CPE (**Figure 9**). Plants suffered a major setback at the beginning of the Triassic because the PTME wiped out large sectors of the plant communities, most notably trees. The famous Early to Middle Triassic 'coal gap' marks a time of 10–20 Myr when trees and forests were absent. In Gondwana, corystosperm seed ferns dominated floras, and forests became diverse and productive during the humid conditions of the CPE, marking the return of substantial coal seams. Numerous plant groups that were to be important components of Mesozoic floras emerged and diversified at or after the CPE (Dal Corso et al., 2020; Lu et al., 2021), including the Bennettitales and several modern fern families (Hymenophyllaceae, Matoniaceae, Dipteridaceae). Probably more significant in the landscape were the diversifying new conifer groups, adapted to post-CPE arid conditions, including Podocarpaceae (podocarps), Araucariaceae (monkey puzzle trees), Pinaceae (pines, cedars, firs), Cupressaceae (cypresses), Taxaceae (yews), and the extinct Cheirolepidiaceae. The importance of this phase is also that these represent by far the majority of modern conifers, all of which trace their origins to this time in the Late Triassic.

The impact of the PTME on insects has been hard to determine because of patchy occurrences, but there were high rates of extinction at the end of the Permian and high rates of origination in the Early Triassic (Nicholson et al., 2014). Family-level richness of insects began to increase steadily towards the present from the Triassic onwards, and apparently with a marked increase in rates in the Carnian (Nicholson et al., 2015). New evidence from China (Zheng et al., 2018) confirms that lacustrine insects diversified substantially in the Middle Triassic, part of the 'Mesozoic Lacustrine Revolution', with the earliest caddisfly cases (Trichoptera), water boatmen (Hemiptera), diverse polyphagan beetles (Coleoptera), and scorpionflies (Mecoptera). The clade Holometabola, comprising 95% modern insect species, diversified substantially in the Middle to Late Triassic, perhaps because of their resilience and buffering from environmental variability through developmental and ecological adaptations, coupled with the diversification of new plant groups as life recovered from the impacts of the PTME (Wang et al., 2022). Among major new insect groups originating in the Triassic are Diptera (flies), first known from the early Middle Triassic (Lukashevich, 2021) and Lepidoptera (moths and butterflies), first known from the Late Triassic (van Eldijk et al., 2018). Modern herbivorous insects diversified substantially in the Late Triassic after the CPE, including aquatic insects, hydraphagans (water beetles), and staphylinids (rove beetles), and many modern feeding modes (piercing and sucking, galling, leaf mining, seed predation) seem to have diversified in the Carnian (Dal Corso et al., 2020).

CONCLUSION

When Van Valen (1984) identified the PTME as the pivotal turning point in the history of Phanerozoic life, and when Sepkoski (1984) noted the origin of the 'Modern' marine evolutionary fauna in the Triassic, both authors stressed the

revolutionary nature of the Triassic for the evolution of life in the sea. New work has confirmed their insights, in particular moving the MMR back in time to coincide with recovery from catastrophe through the Early and Middle Triassic. New work on Triassic dinosaurs and other terrestrial tetrapods has confirmed the critical role of the Triassic also in the origins of modern terrestrial ecosystems. Most notably, several lines of evidence (posture, insulation, bone histology) point to widespread elevated metabolic rates in both main tetrapod lineages, the archosauromorphs and synapsids. The endothermy of modern birds and mammals began to evolve in the Early to Middle Triassic. Likewise, plants and insects show dramatic changes. In many cases, we see a two-step process, with the initial stages occurring in the turmoil of perturbed ecosystems through the first 5–8 Myr of the Early and early Middle Triassic (252–246 Ma), followed by substantial reorganisations of marine and terrestrial ecosystems after the CPE (233–232 Ma). Thus were born the fundamentals of modern ecosystems.

AUTHOR CONTRIBUTIONS

All authors listed have made a substantial, direct, and intellectual contribution to the work and approved it for publication.

FUNDING

This work was supported by a Natural Environment Research Council (NERC) UK (grant NE/P013724/1) and European Research Council (ERC) Advanced Grant (number 788203) and the Strategic Priority Research Program of the Chinese Academy of Sciences (CAS) (grant XDA20070203).

ACKNOWLEDGMENTS

We thank ME and YS for their very helpful comments.

REFERENCES

Arratia, G. (2017). New Triassic Teleosts (Actinopterygii, Teleosteomorpha) from Northern Italy and Their Phylogenetic Relationships Among the Most Basal Teleosts. *J. Vert. Paleontol.* 37 (2), e1312690. doi:10.1080/02724634.2017.1312690

Bai, J., Xu, S., Nie, Z., Wang, Y., Zhu, C., Wang, Y., et al. (2018). The Complete Mitochondrial Genome of *Huananpotamon Lichuanense* (Decapoda: Brachyura) with Phylogenetic Implications for Freshwater Crabs. *Gene* 646, 217–226. doi:10.1016/j.gene.2018.01.015

Bajdek, P., Qvarnström, M., Owocki, K., Sulej, T., Sennikov, A. G., Golubev, V. K., et al. (2016). Microbiota and Food Residues Including Possible Evidence of Pre-mammalian Hair in Upper Permian Coprolites from Russia. *Lethaia* 49, 455–477. doi:10.1111/let.12156

Bambach, R. K., Knoll, A. H., and Sepkoski, J. J., Jr. (2002). Anatomical and Ecological Constraints on Phanerozoic Animal Diversity in the Marine Realm. *Proc. Natl. Acad. Sci. U.S.A.* 99, 6854–6859. doi:10.1073/pnas.092150999

Baumiller, T. K., Salamon, M. A., Gorzelak, P., Mooi, R., Messing, C. G., and Gahn, F. J. (2010). Post-paleozoic Crinoid Radiation in Response to Benthic Predation Preceded the Mesozoic Marine Revolution. *Proc. Natl. Acad. Sci. U.S.A.* 107, 5893–5896. doi:10.1073/pnas.0914199107

Bennett, A. F., and Nagy, K. A. (1977). Energy Expenditure in Free-Ranging Lizards. *Ecology* 58, 697–700. doi:10.2307/1939022

Benton, M. J., Dhouailly, D., Jiang, B., and McNamara, M. (2019). The Early Origin of Feathers. *Trends Ecol. Evol.* 34, 856–869. doi:10.1016/j.tree.2019.04.018

Benton, M. J., Forth, J., and Langer, M. C. (2014). Models for the Rise of the Dinosaurs. *Curr. Biol.* 24, R87–R95. doi:10.1016/j.cub.2013.11.063

Benton, M. J. (2021). The Origin of Endothermy in Synapsids and Archosaurs and Arms Races in the Triassic. *Gondwana Res.* 100, 261–289. doi:10.1016/j.gr.2020.08.003

Benton, M. J., Tverdokhlebov, V. P., and Surkov, M. V. (2004). Ecosystem Remodelling Among Vertebrates at the Permian-Triassic Boundary in Russia. *Nature* 432, 97–100. doi:10.1038/nature02950

Benton, M. J., Zhang, Q., Hu, S., Chen, Z.-Q., Wen, W., Liu, J., et al. (2013). Exceptional Vertebrate Biotas from the Triassic of China, and the Expansion of Marine Ecosystems after the Permo-Triassic Mass Extinction. *Earth-Science Rev.* 125, 199–243. doi:10.1016/j.earscirev.2013.05.014

Bernardi, M., Gianolla, P., Petti, F. M., Mietto, P., and Benton, M. J. (2018). Dinosaur Diversification Linked with the Carnian Pluvial Episode. *Nat. Commun.* 9, 1499. doi:10.1038/s41467-018-03996-1

Botha-Brink, J., Bento Soares, M., and Martinelli, A. G. (2018). Osteohistology of Late Triassic Prozostrodontian Cynodonts from Brazil. *PeerJ* 6, e5029. doi:10.7717/peerj.5029

Bown, P. R. (2005). Calcareous Nannoplankton Evolution: A Tale of Two Oceans. *Micropaleontology* 51, 299. doi:10.2113/gsmicropal.51.4.299

Brayard, A., Krumenacker, L. J., Botting, J. P., Jenks, J. F., Bylund, K. G., Fara, E., et al. (2017). Calcareous Nannoplankton Evolution: a Tale of Two Oceans. *Micropaleontology* 51, e1602159. doi:10.2113/gsmicropal.51.4.299

Brett, C. E., and Walker, S. E. (2002). Predators and Predation in Paleozoic Marine Environments. *Paleontol. Soc. Pap.* 8, 93–118. doi:10.1017/s1089332600001078

Buatois, L. A., Carmona, N. B., Curran, H. A., Netto, R. G., Mángano, N. G., and Wetzel, A. (2016). "The Mesozoic Marine Revolution," in *The Trace Fossil Record of Major Evolutionary Events, Volume 2*. Editors M. G. Mángano and L. A. Buatois (Dordrecht: Topics in Geobiology), 40, 18–134. doi:10.1007/978-94-017-9597-5_2

Butler, R. J., Brusatte, S. L., Reich, M., Nesbitt, S. J., Schoch, R. R., and Hornung, J. J. (2011). The Sail-Backed Reptile *Ctenosauriscus* from the Latest Early Triassic of Germany and the Timing and Biogeography of the Early Archosaur Radiation. *PLoS ONE* 6, e25693. doi:10.1371/journal.pone.0025693

Carrier, D. R. (1987). The Evolution of Locomotor Stamina in Tetrapods: Circumventing a Mechanical Constraint. *Paleobiology* 13, 326–341. doi:10.1017/s0094837300008903

Charig, A. J. (1972). "The Evolution of the Archosaur Pelvis and Hind-Limb: an Explanation in Functional Terms," in *Studies in Vertebrate Evolution*. Editors K. A. Joysey and T. S. Kemp (Edinburgh: Oliver & Boyd), 121–155.

Chen, W.-J., Santini, F., Carnevale, G., Chen, J.-N., Liu, S.-H., LavouÃ©, S. b., et al. (2014). New Insights on Early Evolution of Spiny-Rayed Fishes (Teleostei: Acanthomorpha). *Front. Mar. Sci.* 1, 53. doi:10.3389/fmars.2014.00053

Cincotta, A., Nicolaï, M., Campos, H. B. N., McNamara, M., D'Alba, L., Shawkey, M. D., et al. (2022). Pterosaur Melanosomes Support Signalling Functions for Early Feathers. *Nature* 604, 684–688. doi:10.1038/s41586-022-04622-3

Cuny, G., and Benton, M. J. (1999). Early Radiation of the Neoselachian Sharks in Western Europe. *Geobios* 32, 193–204. doi:10.1016/s0016-6995(99)80032-1

Dal Corso, J., Bernardi, M., Sun, Y., Song, H., Seyfullah, L. J., Preto, N., et al. (2020). Extinction and Dawn of the Modern World in the Carnian (Late Triassic). *Sci. Adv.* 6, eaba0099. doi:10.1126/sciadv.aba0099

Davis, J. W. (1887). The Fossil Fishes of the Chalk of Mount Lebanon in Syria. *Sci. Trans. R. Dublin Soc.* 3, 457

Doguzhaeva, L. A., Brayard, A., Goudemand, N., Krumenacker, L. J., Jenks, J. F., Bylund, K. G., et al. (2018). An Early Triassic Gladius Associated with Soft Tissue Remains from Idaho, USA—a Squid-like Coleoid Cephalopod at the Onset of Mesozoic Era. *Acta Palaeontol. Pol.* 63, 341–355. doi:10.4202/app.00393.2017

Ezcurra, M. D., Fiorelli, L. E., Trotteyn, M. J., Martinelli, A. G., and Desojo, J. B. (2020a). The Rhynchosaur Record, Including a New Stenaulorhynchine Taxon, from the Chañares Formation (Upper Ladinian–?lowermost Carnian Levels) of

La Rioja Province, North-Western Argentina. *J. Syst. Palaeontol.* 18, 205. doi:10.1080/14772019.2020.1856205

Ezcurra, M. D., Nesbitt, S. J., Bronzati, M., Dalla Vecchia, F. M., Agnolin, F. L., Benson, R. B. J., et al. (2020b). Enigmatic Dinosaur Precursors Bridge the Gap to the Origin of Pterosauria. *Nature* 588, 445–449. doi:10.1038/s41586-020-3011-4

Ezcurra, M. D. (2016). The Phylogenetic Relationships of Basal Archosauromorphs, with an Emphasis on the Systematics of Proterosuchian Archosauriforms. *PeerJ* 4, e1778. doi:10.7717/peerj.1778

Falkowski, P. G., Katz, M. E., Knoll, A. H., Quigg, A., Raven, J. A., Schofield, O., et al. (2004). The Evolution of Modern Eukaryotic Phytoplankton. *Science* 305, 354–360. doi:10.1126/science.1095964

Feldmann, R. M., Schweitzer, C. E., Hu, S., Zhang, Q., Zhou, C., Xie, T., et al. (2012). Macrurous Decapoda from the Luoping Biota (Middle Triassic) of China. *J. Paleontol.* 86, 425–441. doi:10.1666/11-113.1

Fensome, R. A., MacRae, R. A., Moldowan, J. M., Taylor, F. J. R., and Williams, G. L. (1996). The Early Mesozoic Radiation of Dinoflagellates. *Paleobiology* 22, 329–338. doi:10.1017/s0094837300016316

Foster, W. J., and Twitchett, R. J. (2014). Functional Diversity of Marine Ecosystems after the Late Permian Mass Extinction Event. *Nat. Geosci.* 7, 233–238. doi:10.1038/ngeo2079

Fürsich, F. T., and Jablonski, D. (1984). Late Triassic Naticid Drillholes: Carnivorous Gastropods Gain a Major Adaptation but Fail to Radiate. *Science* 224, 78

Gillooly, J. F., Brown, J. H., West, G. B., Savage, V. M., and Charnov, E. L. (2001). Effects of Size and Temperature on Metabolic Rate. *Science* 293, 2248–2251. doi:10.1126/science.1061967

Grigg, G., Nowack, J., Bicudo, J. E. P. W., Bal, N. C., Woodward, H. N., and Seymour, R. S. (2022). Whole-body Endothermy: Ancient, Homologous and Widespread Among the Ancestors of Mammals, Birds and Crocodylians. *Biol. Rev.* 97, 766–801. doi:10.1111/brv.12822

Harper, E. M. (2003). Assessing the Importance of Drilling Predation over the Palaeozoic and Mesozoic. *Palaeogeogr. Palaeoclimatol. Palaeoecol.* 201, 185–198. doi:10.1016/s0031-0182(03)00624-2

Harper, E. M., Forsythe, G. T. W., and Palmer, T. (1998). Taphonomy and the Mesozoic Marine Revolution: Preservation State Masks the Importance of Boring Predators. *Palaios* 13, 352–360. doi:10.2307/3515323

Hautmann, M. (2004). Early Mesozoic Evolution of Alivincular Bivalve Ligaments and its Implications for the Timing of the 'Mesozoic Marine Revolution'. *Lethaia* 37, 165–172. doi:10.1080/00241160410005835

Hautmann, M. (2010). The First Scallop. *Paläontol. Z.* 84, 317–322. doi:10.1007/s12542-009-0041-5

Hautmann, M., Ware, D., and Bucher, H. (2017). Geologically Oldest Oysters Were Epizoans on Early Triassic Ammonoids. *J. Molluscan Stud.* 83, 253–260. doi:10.1093/mollus/eyx018

Hegna, T. A., Luque, J., and Wolfe, J. M. (2020). "The Fossil Record of the Pancrustacea. 21–52," in *The Natural History of the Crustacea. Vol. 8. Evolution and Biogeography of the Crustacea*. Editors M. Thiel and G. C. B. Poore (New York: Oxford University Press).

Hu, S.-x., Zhang, Q.-y., Chen, Z.-Q., Zhou, C.-y., Lü, T., Xie, T., et al. (2011). The Luoping Biota: Exceptional Preservation, and New Evidence on the Triassic Recovery from End-Permian Mass Extinction. *Proc. R. Soc. B* 278, 2274–2282. doi:10.1098/rspb.2010.2235

Huang, J.-d., Motani, R., Jiang, D.-y., Ren, X.-x., Tintori, A., Rieppel, O., et al. (2020). Repeated Evolution of Durophagy during Ichthyosaur Radiation after Mass Extinction Indicated by Hidden Dentition. *Sci. Rep.* 10, 7798. doi:10.1038/s41598-020-64854-z

Huttenlocker, A. K., and Farmer, C. G. (2017). Bone Microvasculature Tracks Red Blood Cell Size Diminution in Triassic Mammal and Dinosaur Forerunners. *Curr. Biol.* 27, 48–54. doi:10.1016/j.cub.2016.10.012

Irmis, R. B., and Whiteside, J. H. (2011). Delayed Recovery of Non-marine Tetrapods after the End-Permian Mass Extinction Tracks Global Carbon Cycle. *Proc. R. Soc. B* 279, 1310–1318. doi:10.1098/rspb.2011.1895

James, N. P. (1984). "Shallowing-upward Sequences in Carbonates," in *Faciees Models*. Editor R. G. Walker. second edition (St John's, Nova Scotia: Geoscience Canada Reprint Series), 1, 213

Jones, K. E., Angielczyk, K. D., and Pierce, S. E. (2019). Stepwise Shifts Underlie Evolutionary Trends in Morphological Complexity of the Mammalian Vertebral Column. *Nat. Commun.* 10, 5071. doi:10.1038/s41467-019-13026-3

Kier, P. M. (1974). Evolutionary Trends and Their Functional Significance in the Post-Paleozoic Echinoids. *J. Paleontol.* 48, 1–95. doi:10.1017/s0022336000061321

Klompmaker, A. A., Nützel, A., and Kaim, A. (2016). Drill Hole Convergence and a Quantitative Analysis of Drill Holes in Mollusks and Brachiopods from the Triassic of Italy and Poland. *Palaeogeogr. Palaeoclimatol. Palaeoecol.* 457, 342–359. doi:10.1016/j.palaeo.2016.06.017

Klug, C., Schweigert, G., Hoffmann, R., Weis, R., and De Baets, K. (2021). Fossilized Leftover Falls as Sources of Palaeoecological Data: a 'pabulite' Comprising a Crustacean, a Belemnite and a Vertebrate from the Early Jurassic Posidonia Shale. *Swiss J. Palaeontol.* 140, 10. doi:10.1186/s13358-021-00225-z

Kogan, I., Pacholak, S., Licht, M., Schneider, J. W., Brücker, C., and Brandt, S. (2015). The Invisible Fish: Hydrodynamic Constraints for Predator-Prey Interaction in Fossil Fish *Saurichthys* Compared to Recent Actinopterygians. *Biol. Open* 4, 1715–1726. doi:10.1242/bio.014720

Kubo, T., and Benton, M. J. (2009). Tetrapod Postural Shift Estimated from Permian and Triassic Trackways. *Palaeontology* 52, 1029–1037. doi:10.1111/j.1475-4983.2009.00897.x

Legendre, L. J., Guénard, G., Botha-Brink, J., and Cubo, J. (2016). Palaeohistological Evidence for Ancestral High Metabolic Rate in Archosaurs. *Syst. Biol.* 65, 989–996. doi:10.1093/sysbio/syw033

Lindgren, J., Sjövall, P., Thiel, V., Zheng, W., Ito, S., Wakamatsu, K., et al. (2018). Soft-tissue Evidence for Homeothermy and Crypsis in a Jurassic Ichthyosaur. *Nature* 564, 359–365. doi:10.1038/s41586-018-0775-x

Lovegrove, B. G. (2017). A Phenology of the Evolution of Endothermy in Birds and Mammals. *Biol. Rev.* 92, 1213–1240. doi:10.1111/brv.12280

Lu, J., Zhang, P. X., Dal Corso, J., Yang, M. F., Wignall, P. B., Greene, S. E., et al. (2021). Volcanically Driven Lacustrine Ecosystem Changes during the Carnian Pluvial Episode (Late Triassic). *Proc. Natn. Acad. Sci. U. S. A.* 118, e2109895118 doi:10.1073/pnas.2109895118

Lukashevich, E. D. (2021). The Oldest Diptera (Insecta) from the Upper Buntsandstein (Early Middle Triassic) of Europe. *Zootaxa* 5067, 135–143. doi:10.11646/zootaxa.5067.1.10

Luo, M., Shi, G. R., Buatois, L. A., and Chen, Z.-Q. (2020). Trace Fossils as Proxy for Biotic Recovery after the End-Permian Mass Extinction: a Critical Review. *Earth-Science Rev.* 203, 103059. doi:10.1016/j.earscirev.2019.103059

Mah, C. L., and Blake, D. B. (2012). Global Diversity and Phylogeny of the Asteroidea (Echinodermata). *PLoS ONE* 7 (4), e35644. doi:10.1371/journal.pone.0035644

Maxwell, E. E. (2016). First Middle Jurassic Record of Saurichthyidae (Actinopterygii). *PalZ* 90, 287–291. doi:10.1007/s12542-015-0281-5

McNab, B. K. (1978). The Evolution of Endothermy in the Phylogeny of Mammals. *Am. Nat.* 112, 1–21. doi:10.1086/283249

McRoberts, C. A. (2001). Triassic Bivalves and the Initial Marine Mesozoic Revolution: A Role for Predators? *Geol.* 29, 359–362. doi:10.1130/0091-7613(2001)029<0359:tbatim>2.0.co;2

Motani, R., Jiang, D.-Y., Chen, G.-B., Tintori, A., Rieppel, O., Ji, C., et al. (2015). A Basal Ichthyosauriform with a Short Snout from the Lower Triassic of China. *Nature* 517, 485–488. doi:10.1038/nature13866

Nakajima, Y., Houssaye, A., and Endo, H. (2014). Osteohistology of the Early Triassic Ichthyopterygian Reptile *Utatsusaurus Hataii*: Implications for Early Ichthyosaur Biology. *Acta Palaeontol. Pol.* 59, 343. doi:10.4202/app.2012.0045

Nesbitt, S. J., Butler, R. J., Ezcurra, M. D., Barrett, P. M., Stocker, M. R., Angielczyk, K. D., et al. (2017). The Earliest Bird-Line Archosaurs and the Assembly of the Dinosaur Body Plan. *Nature* 544, 484–487. doi:10.1038/nature22037

Newham, E., Gill, P. G., and Corfe, I. J. (2022). New Tools Suggest a Middle Jurassic Origin for Mammalian Endothermy. *BioEssays* 44, 2100060. doi:10.1002/bies.202100060

Nicholson, D. B., Mayhew, P. J., and Ross, A. J. (2015). Changes to the Fossil Record of Insects through Fifteen Years of Discovery. *PLoS ONE* 10 (7), e0128554. doi:10.1371/journal.pone.0128554

Nicholson, D. B., Ross, A. J., and Mayhew, P. J. (2014). Fossil Evidence for Key Innovations in the Evolution of Insect Diversity. *Proc. R. Soc. B* 281, 20141823. doi:10.1098/rspb.2014.1823

Norris, R. D., Turner, S. K., Hull, P. M., and Ridgwell, A. (2013). Marine Ecosystem Responses to Cenozoic Global Change. *Science* 341, 492–498. doi:10.1126/science.1240543

Nützel, A. (2002). The Late Triassic Species *Cryptaulax? Bittneri* (Mollusca: Gastropoda: Procerithiidae) and Remarks on Early Aspects of the Mesozoic Marine Revolution. *Paläontol. Z.* 76, 57. doi:10.1007/BF02988185

Paladino, F. V., O'Connor, M. P., and Spotila, J. R. (1990). Metabolism of Leatherback Turtles, Gigantothermy, and Thermoregulation of Dinosaurs. *Nature* 344, 858–860. doi:10.1038/344858a0

Radley, J. D. (2010). Grazing Bioerosion in Jurassic Seas: a Neglected Factor in the Mesozoic Marine Revolution? *Hist. Biol.* 22, 387–393. doi:10.1080/08912961003673079

Reijmer, J. J. G. (2021). Marine Carbonate Factories: Review and Update. *Sedimentology* 68, 1729–1796. doi:10.1111/sed.12878

Rezende, E. L., Bacigalupe, L. D., Nespolo, R. F., and Bozinovic, F. (2020). Shrinking Dinosaurs and the Evolution of Endothermy in Birds. *Sci. Adv.* 6, eaaw4486. doi:10.1126/sciadv.aaw4486

Ricqlès, A., Padian, K., Knoll, F., and Horner, J. R. (2008). On the Origin of High Growth Rates in Archosaurs and Their Ancient Relatives: Complementary Histological Studies on Triassic Archosauriforms and the Problem of a 'phylogenetic Signal' in Bone Histology. *Ann. Paléontol.* 94, 57. doi:10.1016/j.annpal.2008.03.002

Ridgwell, A. (2005). A Mid Mesozoic Revolution in the Regulation of Ocean Chemistry. *Mar. Geol.* 217, 339–357. doi:10.1016/j.margeo.2004.10.036

Roghi, G., Gianolla, P., Minarelli, L., Pilati, C., and Preto, N. (2010). Palynological Correlation of Carnian Humid Pulses throughout Western Tethys. *Palaeogeogr. Palaeoclimatol. Palaeoecol.* 290, 89–106. doi:10.1016/j.palaeo.2009.11.006

Romano, C. (2021). A Hiatus Obscures the Early Evolution of Modern Lineages of Bony Fishes. *Front. Earth Sci.* 8, 618853. doi:10.3389/feart.2020.618853

Romano, C., Koot, M. B., Kogan, I., Brayard, A., Minikh, A. V., Brinkmann, W., et al. (2016). Permian-Triassic Osteichthyes (Bony Fishes): Diversity Dynamics and Body Size Evolution. *Biol. Rev.* 91, 106–147. doi:10.1111/brv.12161

Salamon, M. A., Niedźwiedzki, R., Gorzelak, P., Lach, R., and Surmik, D. (2012). *Bromalites* from the Middle Triassic of Poland and the Rise of the Mesozoic Marine Revolution. *Palaeogeogr. Palaeoclimatol. Palaeoecol.* 321-322, 142–150. doi:10.1016/j.palaeo.2012.01.029

Sander, P. M., Griebeler, E. M., Klein, N., Juarbe, J. V., Wintrich, T., Revell, L. J., et al. (2021). Early Giant Reveals Faster Evolution of Large Body Size in Ichthyosaurs Than in Cetaceans. *Science* 374, eabf5787. doi:10.1126/science.abf5787

Schaeffer, B., and Rosen, D. E. (1961). Major Adaptive Levels in the Evolution of the Actinopterygian Feeding Mechanism. *Am. Zool.* 1, 187–204. doi:10.1093/icb/1.2.187

Scheyer, T. M., Romano, C., Jenks, J., and Bucher, H. (2014). Early Triassic Marine Biotic Recovery: The Predators' Perspective. *PLoS ONE* 9 (3), e88987. doi:10.1371/journal.pone.0088987

Schlager, W. (2005). *Carbonate Sedimentology and Sequence Stratigraphy*. Tulsa, Oklahome: Society for Sedimentary Geology, 200.

Schweitzer, C. E., and Feldmann, R. M. (2010). The Decapoda (Crustacea) as Predators on Mollusca through Geologic Time. *Palaios* 25, 167–182. doi:10.2110/palo.2009.p09-054r

Sepkoski, J. J., Jr. (1984). A Kinetic Model of Phanerozoic Taxonomic Diversity. *Paleobiology* 10, 246

Seymour, R. S., Bennett-Stamper, C. L., Johnston, S. D., Carrier, D. R., and Grigg, G. C. (2004). Evidence for Endothermic Ancestors of Crocodiles at the Stem of Archosaur Evolution. *Physiological Biochem. Zoology* 77, 1051–1067. doi:10.1086/422766

Seymour, R. S. (2013). Maximal Aerobic and Anaerobic Power Generation in Large Crocodiles *versus* Mammals: Implications for Dinosaur Gigantothermy. *PLoS ONE* 8 (7), e69361. doi:10.1371/journal.pone.0069361

Simms, M. J., and Ruffell, A. H. (1989). Synchroneity of Climatic Change and Extinctions in the Late Triassic. *Geol.* 17, 265–268. doi:10.1130/0091-7613(1989)017<0265:soccae>2.3.co;2

Smith, R. M. H., and Botha-Brink, J. (2011). Morphology and Composition of Bone-Bearing Coprolites from the Late Permian Beaufort Group, Karoo Basin, South Africa. *Palaeogeogr. Palaeoclimatol. Palaeoecol.* 312, 40–53. doi:10.1016/j.palaeo.2011.09.006

Stanley, S. M. (1968). Post-paleozoic Adaptive Radiation of Infaunal Bivalve Molluscs: A Consequence of Mantle Fusion and Siphon Formation. *J. Paleontol.* 42, 214

Stanley, S. M. (1977). "Chapter 7 Trends, Rates, and Patterns of Evolution in the Bivalvia," in *Patterns of Evolution as Illustrated by the Fossil Record*. Editor A. Hallam (Amsterdam): Elsevier), 209–250. doi:10.1016/s0920-5446(08)70327-3

Stubbs, T. L., and Benton, M. J. (2016). Ecomorphological Diversifications of Mesozoic Marine Reptiles: the Roles of Ecological Opportunity and Extinction. *Paleobiology* 42, 547–573. doi:10.1017/pab.2016.15

Suchéras-Marx, B., Mattioli, E., Allemand, P., Giraud, F., Pittet, B., Plancq, J., et al. (2019). The Colonization of the Oceans by Calcifying Pelagic Algae. *Biogeosciences* 16, 2501. doi:10.5194/bg-16-2501-2019

Sullivan, C. (2015). "Evolution of Hind Limb Posture in Triassic Archosauriforms," in *Great Transformations in Vertebrate Evolution*. Editors K. P. Dial, N. Shubin, and E. L. Brainerd (Chicago: University of Chicago Press), 107

Tackett, L. S., and Bottjer, D. J. (2016). Paleoecological Succession of Norian (Late Triassic) Benthic Fauna in Eastern Panthalassa (Luning and Gabbs Formations, West-Central Nevada). *Palaios* 31, 190–202. doi:10.2110/palo.2015.070

Tackett, L. S. (2016). Late Triassic Durophagy and the Origin of the Mesozoic Marine Revolution. *Palaios* 31, 122–124. doi:10.2110/palo.2016.003

Tackett, L. S., and Tintori, A. (2019). Low Drilling Frequency in Norian Benthic Assemblages from the Southern Italian Alps and the Role of Specialized Durophages during the Late Triassic. *Palaeogeogr. Palaeoclimatol. Palaeoecol.* 513, 25–34. doi:10.1016/j.palaeo.2018.06.034

Tanner, A. R., Fuchs, D., Winkelmann, I. E., Gilbert, M. T. P., Pankey, M. S., Ribeiro, Â. M., et al. (2017). Molecular Clocks Indicate Turnover and Diversification of Modern Coleoid Cephalopods during the Mesozoic Marine Revolution. *Proc. R. Soc. B* 284, 20162818. doi:10.1098/rspb.2016.2818

Tintori, A., and Sassi, D. (1992). ThoracopterusBronn (Osteichthyes: Actinopterygii): A Gliding Fish from the Upper Triassic of Europe. *J. Vertebrate Paleontology* 12, 265–283. doi:10.1080/02724634.1992.10011459

Twitchett, R. J., and Oji, T. (2005). Early Triassic Recovery of Echinoderms. *Comptes Rendus Palevol* 4, 531–542. doi:10.1016/j.crpv.2005.02.006

van Eldijk, T. J. B., Wappler, T., Strother, P. K., van der Weijst, C. M. H., Rajaei, H., Visscher, H., et al. (2018). A Triassic-Jurassic Window into the Evolution of Lepidoptera. *Sci. Adv.* 4, e1701568. doi:10.1126/sciadv.1701568

Van Valen, L. M. (1984). A Resetting of Phanerozoic Community Evolution. *Nature* 307, 50–52. doi:10.1038/307050a0

Vermeij, G. J. (2008). Escalation and its Role in Jurassic Biotic History. *Palaeogeogr. Palaeoclimatol. Palaeoecol.* 263, 3–8. doi:10.1016/j.palaeo.2008.01.023

Vermeij, G. J., Schindel, D. E., and Zipser, E. (1981). Predation through Geological Time: Evidence from Gastropod Shell Repair. *Science* 214, 1024–1026. doi:10.1126/science.214.4524.1024

Vermeij, G. J. (1977). The Mesozoic Marine Revolution: Evidence from Snails, Predators and Grazers. *Paleobiology* 3, 245–258. doi:10.1017/s0094837300005352

Walker, S. E., and Brett, C. E. (2002). Post-paleozoic Patterns in Marine Predation: Was There a Mesozoic and Cenozoic Marine Predatory Revolution? *Paleontol. Soc. Pap.* 8, 119–194. doi:10.1017/s108933260000108x

Waller, T. R. (2006). Phylogeny of Families in the Pectinoidea (Mollusca: Bivalvia): Importance of the Fossil Record. *Zool. J. Linn. Soc.* 148, 313342. doi:10.1111/j.1096-3642.2006.00258.x

Wang, B., Xu, C. P., and Jarzembowski, E. A. (2022). Ecological Radiations of Insects in the Mesozoic. *Trends. Ecol. Evol.* doi:10.1016/j10.1016/j.tree.2022.02.007

Watson, D. M. S. (1931). On the Skeleton of a Bauriamorph Reptile. *Proc. Zool. Soc. Lond.*, 35

Watson, D. M. S. (1913). XXV.-Further Notes on the Skull, Brain, and Organs of Special Sense ofDiademodon. *Ann. Mag. Nat. Hist.* 12, 217–228. doi:10.1080/00222931308693389

Westerhold, T., Marwan, N., Drury, A. J., Liebrand, D., Agnini, C., Anagnostou, E., et al. (2020). An Astronomically Dated Record of Earth's Climate and its Predictability over the Last 66 Million Years. *Science* 369, 1383–1387. doi:10.1126/science.aba6853

Wintrich, T., Hayashi, S., Houssaye, A., Nakajima, Y., and Sander, P. M. (2017). A Triassic Plesiosaurian Skeleton and Bone Histology Inform on Evolution of a Unique Body Plan. *Sci. Adv.* 3 (12), e1701144. doi:10.1126/sciadv.1701144

Wu, F. X., Sun, Y. L., Hao, W. C., Jiang, D.-Y., and Sun, Z. Y. (2015). A New Species of *Saurichthys* (Actinopterygii; Saurichthyiformes) from the Middle Triassic of Southwestern China, with Remarks on Pattern of the Axial Skeleton of Saurichthyid Fishes. *njgpa* 275, 249–267. doi:10.1127/njgpa/2015/0462

Wu, F. X., Chang, M.-m., Sun, Y. L., and Xu, G. H. (2013). A New Saurichthyiform (Actinopterygii) with a Crushing Feeding Mechanism from the Middle Triassic of Guizhou (China). *Plos One* 8 (12), e81010. doi:10.1371/journal.pone.0081010

Wu, F. X., Sun, Y. L., Xu, G. H., Hao, W. C., Jiang, D. Y., and Sun, Z. Y. (2011). New Saurichthyid Actinopterygian Fishes from the Anisian (Middle Triassic) of Southwestern China. *Acta Palaeontol. Pol.* 56, 581. doi:10.4202/app.2010.0007

Wu, F. X., Sun, Y. L., and Fang, G. (2018). A New Species of *Saurichthys* from the Middle Triassic (Anisian) of Southwestern China. *Vertebr. PalAsiat.* 56, 273. doi:10.19615/j.cnki.1000-3118.171023

Xu, G.-H. (2020). *Feroxichthys yunnanensis* gen. et sp. nov. (Colobodontidae, Neopterygii), a large durophagous predator from the Middle Triassic (Anisian) Luoping Biota, eastern Yunnan, China. *PeerJ* 8, e10229. doi:10.7717/peerj.10229

Xu, G.-H., Zhao, L.-J., Gao, K.-Q., and Wu, F.-X. (2013). A New Stem-Neopterygian Fish from the Middle Triassic of China Shows the Earliest Over-water Gliding Strategy of the Vertebrates. *Proc. R. Soc. B* 280, 20122261. doi:10.1098/rspb.2012.2261

Xu, X., Zhou, Z., Dudley, R., Mackem, S., Chuong, C.-M., Erickson, G. M., et al. (2014). An Integrative Approach to Understanding Bird Origins. *Science* 346, 1253293. doi:10.1126/science.1253293

Yang, Z., Jiang, B., McNamara, M. E., Kearns, S. L., Pittman, M., Kaye, T. G., et al. (2019). Pterosaur Integumentary Structures with Complex Feather-like Branching. *Nat. Ecol. Evol.* 3, 24–30. doi:10.1038/s41559-018-0728-7

Zachos, J., Pagani, M., Sloan, L., Thomas, E., Billups, K., Pagani, M., et al. (2001). Trends, Rhythms, and Aberrations in Global Climate 65 Ma to Present. *Science* 292, 686–693. doi:10.1126/science.1059412

Zheng, D., Chang, S. C., Wang, H., Fang, Y., Wang, J., Feng, C., et al. (2018). Middle-Late Triassic Insect Radiation Revealed by Diverse Fossils and Isotopic Ages from China. *Sci. Adv.* 4, eaat1380. doi:10.1126/sciadv.aat1380

Conflict of Interest: The authors declare that the research was conducted in the absence of any commercial or financial relationships that could be construed as a potential conflict of interest.

frontiers | Frontiers in Earth Science

ORIGINAL RESEARCH
published: 24 June 2022
doi: 10.3389/feart.2022.897396

Increased Terrigenous Supply to the Pelagic Panthalassa Superocean Across the Carnian Pluvial Episode: A Possible Link With Extensive Aridification in the Pangean Interior

Tenichi Cho[1]*, *Masayuki Ikeda*[2] and *Tohru Ohta*[3]

[1]Graduate School of Creative Science and Engineering, Waseda University, Shinjuku, Japan, [2]Department of Earth and Planetary Science, The University of Tokyo, Bunkyo, Japan, [3]Department of Earth and Sciences, Faculty of Education and Integrated Arts and Sciences, Waseda University, Shinjuku, Japan

OPEN ACCESS

Edited by:
Jacopo Dal Corso,
China University of Geosciences
Wuhan, China

Reviewed by:
Or M. Bialik,
University of Malta, Malta
Paul Wignall,
University of Leeds, United Kingdom

***Correspondence:**
Tenichi Cho
tianct@fuji.waseda.jp

Specialty section:
This article was submitted to Sedimentology, Stratigraphy and Diagenesis, a section of the journal Frontiers in Earth Science

Received: 16 March 2022
Accepted: 16 May 2022
Published: 24 June 2022

Citation:
Cho T, Ikeda M and Ohta T (2022) Increased Terrigenous Supply to the Pelagic Panthalassa Superocean Across the Carnian Pluvial Episode: A Possible Link With Extensive Aridification in the Pangean Interior. Front. Earth Sci. 10:897396. doi: 10.3389/feart.2022.897396

In the Late Triassic, a global environmental change called the Carnian Pluvial Episode (CPE) emerged, causing major biological turnover. The CPE has been recognized by siliciclastic input to sedimentary basins, multiple carbon isotope perturbations, and climate proxies for humidification. The CPE is considered to have been associated with increased atmospheric pCO_2 from eruptions of large igneous provinces. However, the nature of this global environmental perturbation on the continents is still not well understood. Here we present a geochemical analysis of a pelagic deep-sea bedded chert sequence across the CPE in the Jurassic accretionary complex of Mino terrane, central Japan. Fluctuations in terrigenous material supply were reconstructed using Principal Component Analysis of major element compositions. The first principal component positively correlates with elements enriched in clay minerals such as Al_2O_3, whereas it negatively correlates with CaO, P_2O_5, and MnO, derived from apatite and manganese. A sudden increase in terrigenous supply was detected around the Julian/Tuvalian boundary, suggesting that CPE-related siliciclastic input also occurred in the abyssal plain environment. The terrigenous supply returned to the pre-CPE state in the Tuvalian. Since the terrigenous material supplied to the abyssal plain is thought to be derived from eolian dust blown from continental arid regions, the increasing terrigenous supply detected in the pelagic deep-sea chert succession may indicate extensive aridification. This result seems to conflict with the common view of the CPE as a humidification event. This contradiction possibly suggests that the extensive aridification occurred within the interior of the supercontinent Pangea, while hydrological circulation enhanced on the coastal region during the CPE.

Keywords: CPE, bedded chert, eolian dust, abyssal plain, pangea, panthalassa, compositional data analysis, major element

1 INTRODUCTION

1.1 Carnian Pluvial Episode

The Carnian Pluvial Episode (CPE) was a time of global environmental perturbations with significant biological turnover both in the ocean and on land (e.g., Simms and Ruffell, 1989; Dal Corso et al., 2020). The CPE was initially recognized in many European sedimentary basins as drastic lithologic changes, such as the demise of carbonate platforms and increased siliciclastic input (e.g., Gattolin et al., 2015). Multiple negative shifts of $\delta^{13}C$ are recognized across the CPE, suggesting a link with volcanic activity of Wrangellia LIPs (e.g., Dal Corso et al., 2018). Recent studies revealed that the intensification of the hydrological cycle also occurred not only in the western Tethys realm but in worldwide sedimentary basins (e.g., North China Plate; Lu et al., 2021; Boreal realm; Mueller et al., 2016; Gondwana region; Bernardi et al., 2018).

In contrast, the terrestrial records of the Pangean inland region are still controversial. Paleoclimate proxies, such as clay mineral profiles and paleosols, suggest only minor climate change with a generally arid to semi-arid background climate across the CPE from the United Kingdom (Baranyi et al., 2019a) and from Spain (Barrenechea et al., 2018), while data from the Germanic Basin and the Danish Basin did not show any humidity signal across the CPE (Visscher et al., 1994; Lindström et al., 2017). Enhanced continental weathering related to a more humid climate is only suggested for the early stages of the CPE in the Julian 2 (Baranyi et al., 2019b). Such observed discrepancies in the environmental signal across the CPE seem to be related to the contrasts in the

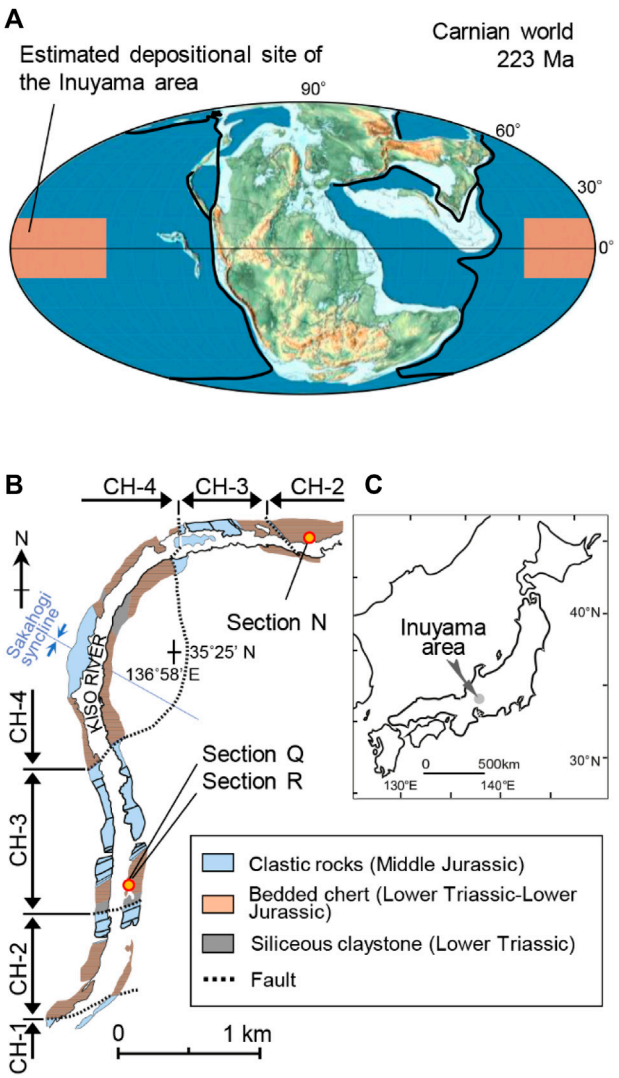

FIGURE 1 | (A) Carnian paleogeography (modified after Scotese, 2014). The shaded region shows a possible area within which the Inuyama succession was likely deposited. Subduction zones are shown in black lines (from Matthews et al., 2016) **(B)** Geologic map and **(C)** location map showing the location of the Carnian bedded chert successions in Inuyama area, central Japan (modified after Kimura and Hori, 1993).

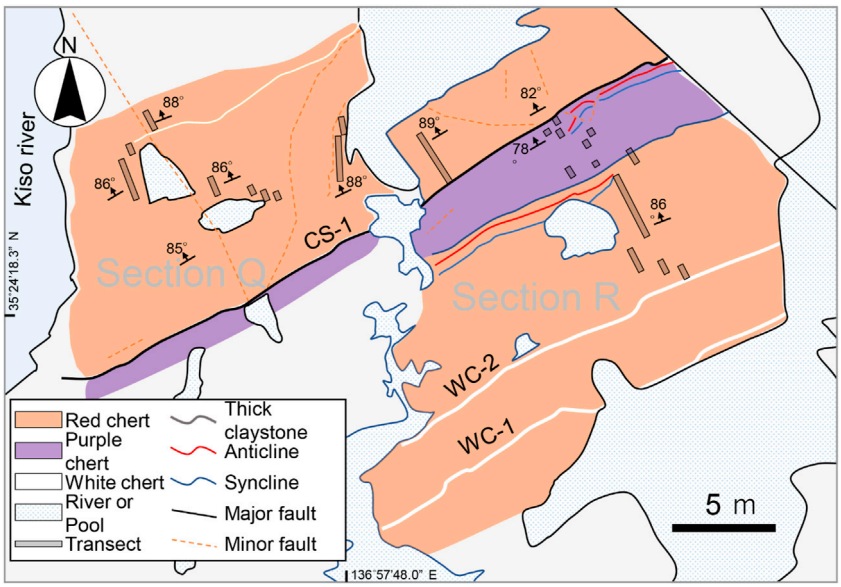

FIGURE 2 | Detailed geologic map of Section R and Section Q of Sugiyama (1997). Continuous composite lithostratigraphy was described in grey lines.

climate of different regions and the limited age constraint of the terrestrial strata.

Abyssal deep-sea sediment provides a relatively continuous and consistent archive (e.g., Ikeda and Tada., 2014). An increase in the relative abundance of smectite among Fe-bearing minerals was detected in Japanese pelagic deep-sea chert across Julian/Tuvalian boundary (Nakada et al., 2014). Studies of Cenozoic sediments show that the terrigenous materials supplied to abyssal plains are mostly eolian dust generated from continental arid regions (e.g., Asahara, 1999). It is also noteworthy that a relatively thick, muddy silicious claystone interval (CS-1; Sugiyama, 1997) is observed within the smectite interval (Nakada et al., 2014). Along with the presence of CS-1, the thickness of intercalated mudstones drastically increased above the CS-1, and this can be correlated at least regionally (Sugiyama, 1997; Sugiyama et al., 2001). Because chert mainly consists of radiolarian tests and eolian mudstone (e.g., Hori et al., 1993), such an increase in mudstone may be related to increased eolian supply and/or decreased productivity (Sugiyama, 1997). The paleoenvironmental significance of these lithologic changes in the Carnian bedded cherts remains unclear.

In this study, the Carnian bedded cherts from the type section of Japanese radiolarian zones were investigated in order to elucidate the influence of the CPE on the Pangean interior. We seek to extract terrestrial environmental conditions by investigating the geochemistry of the intercalated mudstone of the bedded cherts, which concentrate terrigenous materials much higher than chert layers. The terrigenous content fluctuation was reconstructed throughout the Carnian by multivariate statistical analyses of major element composition. The increase of terrigenous materials flux implying reinforcement of eolian supply occurred. Our results thus firstly provide evidence that extensive aridification occurred in the inland of the Pangea across the CPE.

2 GEOLOGICAL SETTING AND LITHOLOGY DESCRIPTION

2.1 Geological Background

Early Triassic to Early Jurassic bedded chert is exposed in the Inuyama area, central Japan, as a part of the Mino-Tamba belt, Jurassic accretionary complex (**Figure 1**). The bedded cherts and the overlying Middle Jurassic clastic rocks are repeatedly exposed as a chert-clastic sequence truncated by bedding-parallel thrusts (**Figure 1B**; Yao et al., 1980; Matsuda and Isozaki, 1991). Since this bedded chert had an extremely slow sedimentation rate of 1–3 mm/kyr, and lacks coarse-grained terrigenous material for over 60 Myr, it is considered to have been deposited in a distal setting (Matsuda and Isozaki, 1991; Hori et al., 1993). The latitude of the depositional site was estimated as 12.3° ± 5.6°N or S and 19.0° ± 10.5°N or S for 237 Ma and 223.5 Ma, respectively based on the inclination of magnetic component of hematite (**Figure 1A**; Oda and Suzuki, 2000).

Bedded cherts are composed of rhythmic alteration of chert layers (cm scale) and intercalated mudstones. Chert layers are mainly composed of microcrystalline quartz and biogenic siliceous tests, whereas intercalated mudstones are mainly composed of clay minerals derived from eolian dust brown from the continental region (Hori et al., 1993). The relationship of chemical composition of chert layers and intercalated mudstones has been recognized as silica dilution by radiolarian test through the observation of negative correlation of SiO2 with other elements (e.g., Hori et al., 2000).

Bedded cherts are considered to be formed by a diagenetic segregation process as silica dissolution and transportation (Tada, 1991). The lithology of bedded cherts in the Inuyama area is mainly divided into two types: F type and B type which denote “fine grained quartz” and “biogenic clasts”, respectively (Imoto 1983; Sugiyama, 1997). F-type cherts show a few siliceous biogenic tests scattered in

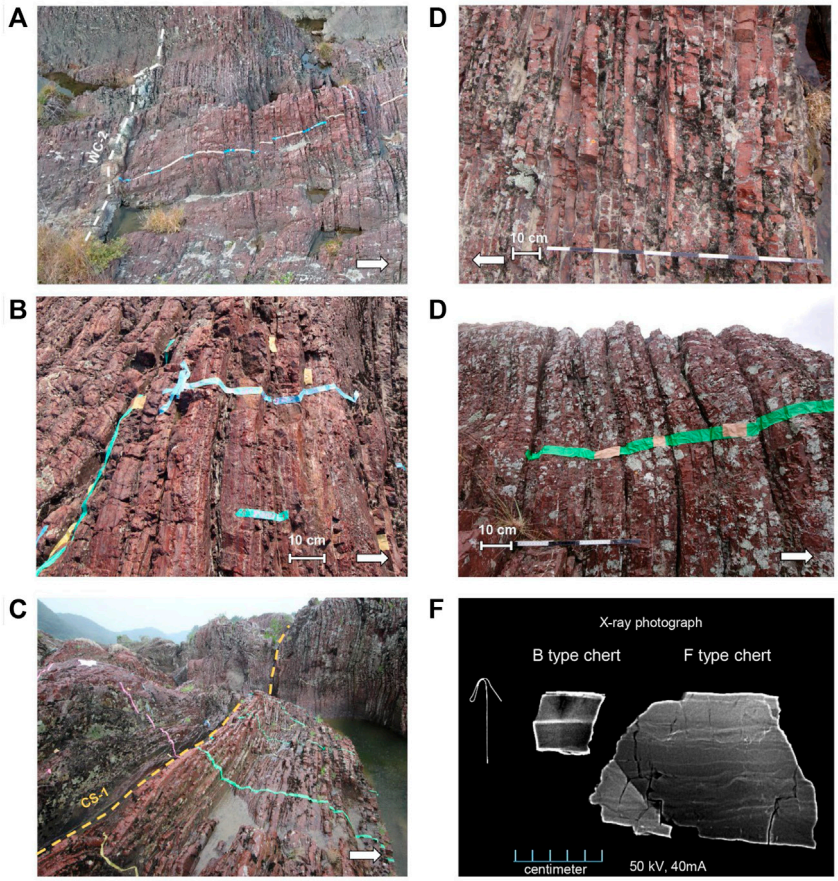

FIGURE 3 | Representative outcrop photographs of the Carnian bedded cherts **(A)** White chert WC-2 and Julian F-type red chert. The boundary of red and purple chert can be seen on the right side of the photograph. **(B)** Close-up of Julian F-type purple chert. Millimeter to cm scale lamination and bedding is observed as changes in color and silica content **(C)** Thick claystone layer CS-1 located at the boundary of F-type purple chert and B-type red chert. **(D)** Close-up of the B-type red chert (Julian-Tuvalian) with relatively thick intercalated mudstones. **(E)** Close-up of the F-type red chert (Tuvalian). The Intercalated mudstones of the F-type cherts are very thin (<5 mm). **(F)** Soft X-ray photograph of B-type (Julian-Tuvalian) and F-type (Tuvalian) chert. Thick intercalated mudstones are observed on the B-type chert whereas millimeter scale lamination can be seen on the F-type chert. Tape width in **(A,C,E)** is 5 cm. Scale bars are 10 cm. The white arrows indicate way-up.

the fine-grained quartz matrix under microscopic observation with very thin (*ca.* 0.5–2 mm) intercalated mudstone layers and laminations. B-type cherts show concentrated biogenic tests under microscopic observation and are usually associated with thick (*ca.* 2–20 mm) intercalated mudstones. The difference in their formation mechanism may be related to changes in silica and terrigenous contents of the precursor sediment of bedded chert, formed by cyclic changes of sedimentary environments and/or diagenetic conditions (Sugiyama, 1997).

In this study, Section R and Section Q of Sugiyama (1997) in the Inuyama area are selected for detailed geological mapping and geochemical study in order to reconstruct paleoclimatic conditions of the entire Carnian stage (**Figures 1**, **2**). Section R is the type section of Japanese radiolarian zone TR5A, which contains the most complete and unaltered sequence of the TR5A zone (Sugiyama, 1997). Section Q is located to the west of Section R and is one of the most complete and unaltered sequences of TR5B zone in Inuyama area (Sugiyama, 1997).

The depositional age of the Carnian bedded chert is constrained by radiolarian and conodont biostratigraphy, cyclostratigraphy, and carbon isotope stratigraphy (Sugiyama, 1997; Ikeda and Tada., 2014; Nakada et al., 2014; Yamashita et al., 2018; Tomimatsu et al., 2021). Sugiyama (1997) correlated interval (*ca.* 20 m thick) from the upper part of the radiolarian zone TR4B (*Spongoserrula delhi*) to the lower part of TR6A (*Capnodoce–Trialatus*) based on the first occurrence (FO) of the Carnian radiolaria *Praeheliostaurus laevis*, the FO of Carnian conodont *Neogondolella foliata*, and the FO of Norian radiolaria *Capnodoce gilis* in Sections N, R and Q in Inuyama area. Nakada et al. (2014) assigned the Julian/Tuvalian boundary within the *Elbistanium gracile* radiolarian zone between their samples R3-1 and R5-3. Tomimatsu et al. (2021) detected two negative excursions in carbon isotopes, NCIE-α and NCIE-β, in

TABLE 1 | Major element composition of bedded chert samples collected in this study.

	Height	Lithology	Color	SiO2	TiO2	Al2O3	Fe2O3	MnO	MgO	CaO	Na2O	K2O	P2O5	LOI_{550}	LOI_{950}
sample	(mm)			(wt%)	(wt%)	(wt%)	(wt%)	(wt%)	(wt%)	(wt%)	(wt%)	(wt%)	(wt%)	(wt%)	(wt%)
WC2	0	Intercalated mudrock	red	56.04	1.61	21.91	8.68	0.470	3.94	0.92	0.24	5.07	0.525	3.36	1.77
Ra3.9	841	Intercalated mudrock	red	61.39	1.34	17.21	8.84	1.243	3.41	0.67	0.19	4.46	0.338	3.85	1.61
Ra4	875	Intercalated mudrock	red	55.78	1.16	19.82	10.87	0.408	5.00	0.59	0.19	4.80	0.253	4.33	1.60
Ra8.2	1,594	Intercalated mudrock	red	55.49	1.07	18.43	12.07	0.665	7.06	0.49	0.14	3.68	0.254	5.27	1.38
Ra9.9	2,273	Intercalated mudrock	red	49.05	2.27	22.66	11.04	0.346	3.97	1.75	0.24	6.52	1.142	4.14	1.82
Ra12	3,122	Intercalated mudrock	red	55.82	1.79	19.63	9.61	0.201	3.61	0.84	0.24	6.16	0.558	3.95	1.36
Ra14	3,540	Intercalated mudrock	red	54.79	1.33	19.63	10.00	0.160	3.84	1.32	0.24	6.37	0.773	4.01	1.60
Ra16	4,019	Intercalated mudrock	red	59.27	1.33	17.83	9.66	0.158	3.31	0.65	0.22	5.73	0.367	3.59	1.51
Ra18	4,511	Intercalated mudrock	red	54.71	1.10	19.16	10.85	0.184	5.47	0.82	0.19	5.61	0.374	4.42	1.63
Ra18.2	4,630	Intercalated mudrock	red	52.97	1.36	20.34	12.08	0.180	4.90	1.10	0.28	5.51	0.595	4.36	2.39
Ra20	4,975	Intercalated mudrock	red	57.37	1.04	18.13	10.43	0.230	5.51	0.69	0.16	5.24	0.273	3.78	1.91
Ra22	5,342	Intercalated mudrock	red	71.54	0.92	12.68	6.98	0.126	2.05	0.36	0.20	4.02	0.170	3.05	1.51
Ra24	5,532	Intercalated mudrock	red	65.58	1.11	15.64	7.57	0.329	2.61	0.36	0.21	5.22	0.157	2.82	1.59
Ra26	5,956	Intercalated mudrock	purple	58.56	1.15	18.89	8.42	0.255	4.06	0.70	0.22	5.99	0.311	3.44	2.07
Ra28	6,774	Intercalated mudrock	purple	62.06	1.25	16.95	8.26	0.170	3.37	0.59	0.21	5.61	0.328	3.14	1.89
Ra30	7,276	Intercalated mudrock	purple	55.63	1.05	19.67	8.90	0.467	5.90	0.70	0.20	5.62	0.278	4.31	2.14
Ra33.9	7,404	Intercalated mudrock	purple	67.83	1.40	15.03	6.96	0.219	2.97	0.44	0.22	4.05	0.187	3.04	1.70
Ra32	7,790	Intercalated mudrock	purple	65.72	0.90	16.40	5.81	0.098	3.06	0.58	0.20	5.48	0.235	3.45	1.76
Ra35.9	7,893	Intercalated mudrock	purple	55.32	1.38	20.33	8.83	0.176	3.50	1.09	0.20	6.99	0.649	3.20	1.95
Ra36	7,999	Intercalated mudrock	purple	67.16	1.14	14.06	8.18	0.142	2.75	0.58	0.17	4.54	0.336	2.70	1.87
Ra37	8,117	Intercalated mudrock	purple	67.25	1.17	14.66	7.99	0.097	2.43	0.66	0.20	4.79	0.321	2.77	1.79
Ra39-1	8,839	Intercalated mudrock	purple	63.87	0.83	14.60	6.53	0.134	2.62	4.35	0.28	4.27	2.768	3.43	2.10
Ra39-2	8,840	Intercalated mudrock	purple	47.25	0.87	17.61	4.88	0.085	3.10	11.12	0.27	6.27	7.475	2.70	2.41
Ra40	8,865	Intercalated mudrock	purple	60.18	0.97	15.51	7.52	0.189	2.91	3.72	0.25	5.50	2.391	2.90	2.19
CS1	9,024	Intercalated mudrock	red	63.8	0.91	16.23	8.02	0.146	3.30	0.35	0.22	5.65	0.095	3.36	1.38
R1	9,053	Intercalated mudrock	red	59.52	1.05	17.44	10.98	0.360	4.29	0.32	0.15	4.90	0.122	3.05	1.54
R4	9,137	Intercalated mudrock	red	58.25	1.25	19.13	9.44	0.185	3.77	0.41	0.23	5.97	0.127	3.85	2.10
R8	9,369	Intercalated mudrock	red	55.62	1.17	19.51	11.02	0.274	5.14	0.40	0.20	5.41	0.117	4.03	2.28
R9	9,383	Intercalated mudrock	red	54.12	1.40	20.18	11.14	0.281	4.61	0.48	0.22	6.18	0.158	3.54	2.04
R10	9,426	Intercalated mudrock	red	51.06	1.22	20.22	12.89	0.443	8.10	0.60	0.14	3.90	0.151	4.82	2.44
R13	9,545	Intercalated mudrock	red	53.31	1.61	20.93	11.51	0.449	4.66	0.47	0.23	5.74	0.163	3.90	2.21
R15	9,610	Intercalated mudrock	red	60.72	1.02	17.72	9.66	0.210	3.89	0.45	0.17	4.95	0.180	3.03	1.56
R16	9,642	Intercalated mudrock	red	75.31	0.59	11.59	5.41	0.163	2.01	0.21	0.11	3.72	0.073	1.77	1.17
R19	9,678	Intercalated mudrock	red	61.85	1.41	17.39	10.66	0.220	2.83	0.41	0.18	5.35	0.286	2.72	1.86
R22	9,778	Intercalated mudrock	red	69.69	0.73	14.13	6.66	0.229	2.61	0.34	0.13	4.67	0.161	2.20	1.30
R23	9,791	Intercalated mudrock	red	64.33	1.05	15.70	9.15	0.329	3.28	0.37	0.14	4.78	0.182	2.86	1.58
R24	9,824	Intercalated mudrock	red	64.44	0.85	15.51	9.36	0.325	3.11	0.40	0.13	5.17	0.181	2.44	1.51
R25	9,866	Intercalated mudrock	red	64.82	0.99	15.44	8.92	0.292	2.76	0.39	0.15	5.11	0.177	2.20	1.44
R26	9,917	Intercalated mudrock	red	57.14	1.14	19.82	10.26	0.478	3.65	0.46	0.20	6.41	0.213	2.85	1.62
R27	9,925	Intercalated mudrock	red	61.71	1.15	16.59	10.43	0.371	5.09	0.39	0.10	3.98	0.178	3.31	1.53
R28	9,952	Intercalated mudrock	red	57.70	0.99	19.52	9.42	0.290	3.74	0.46	0.18	6.30	0.188	3.01	1.80
R29	9,980	Intercalated mudrock	red	61.34	0.92	18.63	8.55	0.243	3.54	0.34	0.17	6.16	0.137	2.60	1.84
R30	10,012	Intercalated mudrock	red	61.43	0.96	18.29	8.98	0.272	3.26	0.35	0.18	5.87	0.151	2.64	1.44
R31	10,080	Intercalated mudrock	red	61.41	1.00	19.26	9.37	0.185	3.55	0.39	0.19	6.18	0.126	2.67	1.70
R32	10,121	Intercalated mudrock	red	54.39	1.15	21.13	10.44	0.192	4.06	0.59	0.22	6.82	0.280	2.98	1.84
R36	10,179	Intercalated mudrock	red	54.77	1.03	20.74	9.69	0.367	4.11	0.63	0.18	6.98	0.287	3.16	1.99
R37	10,189	Intercalated mudrock	red	58.08	1.03	18.26	9.80	0.257	3.57	0.91	0.16	6.35	0.505	2.71	1.82
R38	10,217	Intercalated mudrock	red	56.16	1.10	19.43	9.80	0.463	4.85	0.63	0.16	6.01	0.281	3.22	1.93
R39	10,255	Intercalated mudrock	red	55.61	1.14	19.35	10.55	0.334	4.88	0.69	0.18	5.82	0.326	3.12	2.08
R40	10,325	Intercalated mudrock	red	57.33	0.96	18.68	10.49	0.311	4.04	0.51	0.17	6.30	0.225	2.91	1.81
R41	10,354	Intercalated mudrock	red	61.12	1.00	19.88	9.42	0.262	4.17	0.48	0.18	6.34	0.210	2.74	1.88
R42	10,390	Intercalated mudrock	red	58.50	0.95	19.15	9.86	0.309	4.42	0.72	0.16	6.04	0.352	2.86	1.95
R44	10,421	Intercalated mudrock	red	63.28	0.91	17.19	8.58	0.267	3.98	0.44	0.16	5.59	0.183	2.54	1.74
R45	10,449	Intercalated mudrock	red	65.36	0.89	15.44	8.88	0.357	4.21	0.50	0.13	4.63	0.236	2.59	1.52
R46	10,481	Intercalated mudrock	red	78.00	0.58	9.20	6.87	0.501	2.16	0.31	0.09	2.70	0.141	2.18	1.36
R47	10,508	Intercalated mudrock	red	60.80	1.04	17.66	10.31	0.329	3.90	0.48	0.13	5.46	0.218	2.59	1.73
R49	10,567	Intercalated mudrock	red	62.91	0.93	17.27	9.09	0.302	3.51	0.69	0.14	5.42	0.349	2.54	1.72
R50	10,587	Intercalated mudrock	red	67.84	0.88	13.36	9.85	0.622	2.78	0.45	0.12	4.27	0.227	2.41	1.57
R51	10,605	Intercalated mudrock	red	63.81	0.98	16.15	9.55	0.446	3.46	0.68	0.14	4.88	0.361	2.43	1.58
R52	10,641	Intercalated mudrock	red	63.34	0.89	16.19	9.85	0.495	3.76	0.60	0.14	4.85	0.296	2.45	1.72
R53	10,670	Intercalated mudrock	red	76.63	0.57	10.34	6.34	0.439	2.50	0.39	0.10	3.03	0.184	1.68	1.22
R54	10,689	Intercalated mudrock	red	59.55	0.99	17.85	10.92	0.503	4.04	0.59	0.15	5.35	0.288	2.80	1.75
R55	10,714	Intercalated mudrock	red	60.42	1.05	17.57	10.44	0.575	3.65	0.55	0.15	5.39	0.251	2.72	1.68

(Continued on following page)

TABLE 1 | (*Continued*) Major element composition of bedded chert samples collected in this study.

	Height	Lithology	Color	SiO2	TiO2	Al2O3	Fe2O3	MnO	MgO	CaO	Na2O	K2O	P2O5	LOI_{550}	LOI_{950}
R56	10,742	Intercalated mudrock	red	67.34	0.95	14.08	8.95	0.732	3.19	0.51	0.13	4.10	0.248	2.48	1.40
R59	10,817	Intercalated mudrock	red	72.54	0.8	10.98	8.51	0.937	2.93	0.40	0.10	3.02	0.187	2.16	1.11
R64	10,885	Intercalated mudrock	red	48.64	1.31	19.08	13.75	4.624	5.78	0.94	0.20	4.68	0.349	4.48	2.57
R81	11,021	Intercalated mudrock	red	61.28	1.19	15.02	10.96	0.707	3.61	0.77	0.19	4.68	0.422	2.97	1.71
R82	11,032	Intercalated mudrock	red	58.11	1.25	16.94	11.48	0.541	3.39	0.75	0.22	5.55	0.388	3.11	1.98
R84	11,049	Intercalated mudrock	red	52.80	1.4	20.14	12.24	0.934	4.08	0.82	0.24	5.56	0.395	3.47	2.07
R85	11,085	Intercalated mudrock	red	49.64	1.63	20.03	14.82	0.996	3.94	1.17	0.25	5.65	0.656	3.48	2.04
Q-2	11,954	Intercalated mudrock	red	51.05	2.08	22.46	12.16	0.422	3.20	0.26	0.31	6.10	0.212	3.70	2.13
Q-1	12,255	Intercalated mudrock	red	52.67	1.48	19.81	13.95	0.717	3.98	0.66	0.23	5.15	0.350	3.17	1.84
Q0	13,008	Intercalated mudrock	red	55.88	1.1	18.99	10.36	0.403	3.76	0.83	0.23	6.54	0.506	4.08	1.63
Q1	13,112	Intercalated mudrock	red	50.97	1.46	21.51	12.58	0.694	4.50	0.55	0.28	5.86	0.271	3.59	2.17
Q2	13,924	Intercalated mudrock	red	59.43	1.35	16.31	12.66	0.689	3.98	0.44	0.20	4.10	0.230	3.52	2.03
Q3	14,301	Intercalated mudrock	red	70.16	1.17	11.91	9.12	0.363	2.37	0.66	0.17	3.29	0.373	1.48	1.49
Q4	14,865	Intercalated mudrock	red	50.73	1.8	20.64	14.17	0.672	3.92	0.55	0.26	5.50	0.382	4.12	2.18
Q5	15,411	Intercalated mudrock	red	58.52	1.76	14.83	13.78	2.134	2.93	0.66	0.19	3.98	0.427	3.66	1.89
Q6	15,839	Intercalated mudrock	red	52.78	1.53	19.41	13.66	2.819	3.73	0.50	0.23	4.69	0.233	4.37	2.32
Q7	16,525	Intercalated mudrock	red	80.79	0.78	7.96	5.33	0.670	1.88	0.32	0.11	1.87	0.135	0.77	1.08
Q7.9	17,382	Intercalated mudrock	red	52.02	1.33	21.84	11.90	0.516	3.96	0.52	0.20	6.12	0.339	4.02	2.06
Q10	18,464	Intercalated mudrock	red	56.34	1.46	17.86	11.24	1.315	3.26	0.48	0.22	5.97	0.302	3.95	1.64

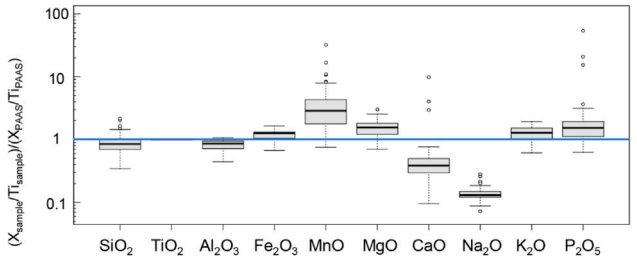

FIGURE 4 | PAAS (Post-Archean Australian Shale)-normalized elemental abundance of the intercalated mudstone of the bedded chert from Section R and Section Q. Boxes indicate the 25th and 75th percentiles. The horizontal line in each box marks the median value. Whiskers represent the 1.5 times the interquartile range of the data. Open circles represent data outliers. Note that the vertical axis is a logarithmic scale. PAAS data are from Taylor and McLennan (1985).

the TR5A zone within the *Nicoraella*? *budaensis* conodont zone in Section N, and correlated them to the global carbon isotopic excursion across the CPE.

2.2 Field Description

We conducted a detailed three-dimensional outcrop observation and constructed a bed-by-bed scale continuous lithostratigraphy to avoid missing or duplicating the strata (**Figure 3**). The lithological column was made from the lower part of Section R to the upper part of Section Q, in ascending order. The F-type red chert is dominant with a white chert bed WC-2 of Sugiyama (1997) at the base. About 900 cm above WC-2, the chert changes to *ca.* 300 cm purple laminated interval. Above the purple chert interval, *ca.* 200 cm B-type chert is intercalated with the *ca.* 20 cm siliceous claystone bed CS-1 of Sugiyama (1997) at the base. The CS-1 between F-type chert to B-type chert is widely recognized, not only in Inuyama area, but also in Hisuikyo area, which is 25 km north to Inuyama area (Sugiyama, 1997; Sugiyama et al., 2001).

3 MATERIALS AND METHODS

3.1 Geochemical Analysis

Eighty-one intercalated mudstone samples were collected from Sections R and Q to cover the Carnian interval (**Figure 2**). Fresh samples were handpicked for geochemical analyses. After cleaning in an ultrasonic bath, the samples were crushed using a tungsten carbide mortar and pestle then pulverized in an agate ball mill. The samples were heated at 550°C for 4 h and 950°C for 2 h to decompose organic matter and carbonate material respectively prior to analysis of major elements and loss on ignition was measured.

Major elements (SiO_2, TiO_2, Al_2O_3, Fe_2O_3, MnO, MgO, CaO, Na_2O, K_2O, and P_2O_5) were analyzed by X-ray fluorescence (ZSX Primus II, Rigaku Co., Japan) at Waseda University. To minimize matrix effects and mineral effects, the fused disk method was used with a sample to lithium borate flux ratio of 1:10. Calibration lines were created using reference samples GSJ (JDo-1, JSd-1, JSd-2, JSd-3, JSI-2, JLk-1, JCh-1, JA-2, JA-3, JB-1a, JB-2, JB-3, JG-1a, JG-2, JG-3, JGb-1, JP-1, JR-1, JR-2). The accuracy of calibration lines for all elements was better than 0.6%. The sample R39, which is located on *ca.* 60 cm below the bottom of CS-1, was hand-picked and measured twice because it showed very high CaO and P_2O_5 concentrations.

Some mudstone samples were observed using scanning electron microscopy (SEM-EDS, Hitachi S-3400N, Japan) at the Waseda University with an accelerating voltage of 15 kV. Soft X-ray photography was employed using a Naomi NX digital X-ray Transmission System (RF Co., Ltd, Japan) with tube voltage of 50 kV and tube current of 40 mA at the Waseda University.

3.2 Multivariate Statistics

3.2.1 Hierarchical Cluster Analysis

Q-mode cluster analysis was conducted to classify the compositional behavior of major elements. Variation matrix (Aitchison, 1986), which consists of variances of all possible

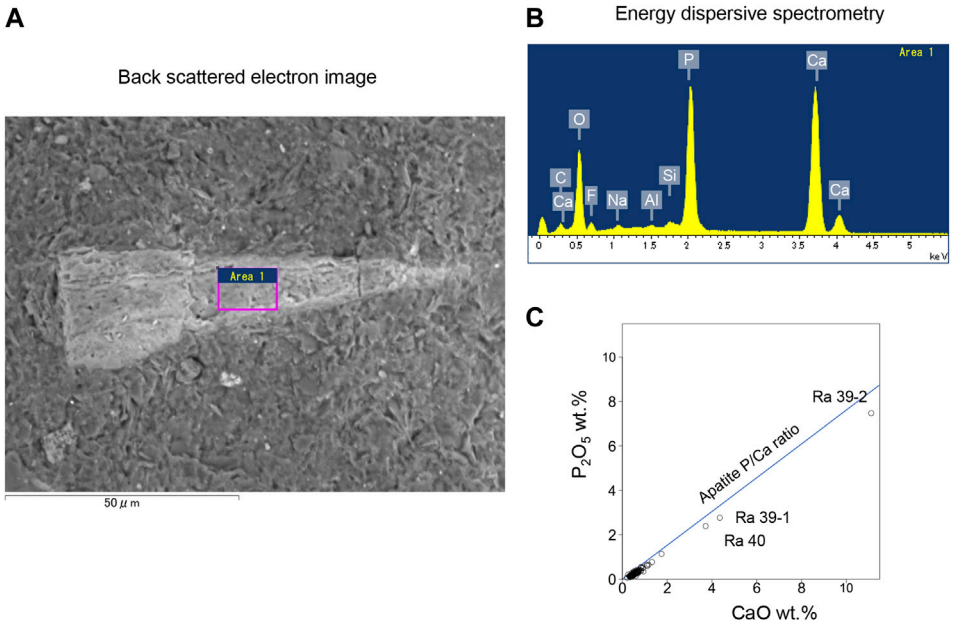

FIGURE 5 | (A) Scanning electron microscopy (SEM) image of the intercalated mudstone. Purple square indicates the region within an apatite for the Energy dispersive spectrometry (EDS) analysis. **(B)** Energy dispersive spectrometry of the apatite fragment. **(C)** Scatter plot of CaO and P_2O_5 of the whole-rack chemical compositions. The variation of the samples is along with the apatite P/Ca ratio.

logratios among components, was used as a distance matrix. Ward algorithm, which hierarchically groups the cluster by minimizing the total within-cluster variance, was used for the clustering criteria.

3.2.2 Principal Component Analysis

To investigate the latent variables that underlie the multivariate data, principal component analysis (PCA) was performed on the major element chemistry. PCA extracts the direction of maximum variance of the input dataset. Prior to PCA, the compositional data of 10 major elements are transformed to centered logratio (clr) space to avoid constant-sum constraint during the calculation without causing an increase in the dimension of the dataset (Aitchison, 1982; Ohta and Arai, 2007). The equation for clr transformation of major element compositional data $x = (SiO_2, TiO_2, \ldots, P_2O_5)$ is as follows:

$$\mathrm{clr}(x) = \left[\ln\frac{SiO_2}{(SiO_2 \times TiO_2 \times \cdots \times P_2O_5)^{1/10}}, \ln\frac{TiO_2}{(SiO_2 \times TiO_2 \times \cdots \times P_2O_5)^{1/10}}, , \cdots, \ln\frac{P_2O_5}{(SiO_2 \times TiO_2 \times \cdots \times P_2O_5)^{1/10}}\right]$$

To obtain robust results in the presence of outliers, robust PCA ('Hubert method', Hubert et al., 2005) were used for the current study. In the current dataset, some samples show a high abundance of specific elements (e.g., CaO, P_2O_5), indicating the anomalously high concentration of some mineral(s). Since PCA captures the direction of the highest variance of the given dataset, avoiding outliers before analysis is indispensable for investigating the latent variables, if any, of the structure of the dataset. The minimum covariance determinant method was adopted for outlier detection on the current dataset and the correlation matrix was used for the PCA calculation. Shapiro-Wilk test was used to evaluate normality of the clr variables after removing detected outliers.

The R package "compositions" (van den Boogaart and Tolosana-Delgado, 2008) and "rrcov" (Filzmoser and Todorov, 2013) were used for the cluster analysis and principal component analysis calculations.

4 RESULT

4.1 Major Element Geochemistry

The result of major element composition of the intercalated mudstone samples and data normalized by PAAS (Post Archean Australian Shale; Taylor and McLennan, 1985) are shown in **Table 1** and **Figure 4**, and **Supplementary Figure S1**. To avoid the false correlation effect of silica dilution, TiO_2 was used to normalize the major element concentrations. The elemental abundance of the intercalated mudstones relative to TiO_2 is generally similar to PAAS, except for CaO, Na_2O, MnO (**Figure 4**). The value of MnO/TiO_2 of the studied samples is higher than that of PAAS, whereas CaO/TiO_2 and Na_2O/TiO_2 are distinctively depleted.

The presence of apatite has a significant effect on the CaO and P_2O_5 concentration. **Figure 5** shows the Back Scatter Electron (BSE) image, Energy dispersive spectrometry, and scatter plot of CaO and P_2O_5 of the intercalated mudstones. Apatite fragments were observed in SEM. The concentration of CaO and P_2O_5 shows a clear positive correlation along with the

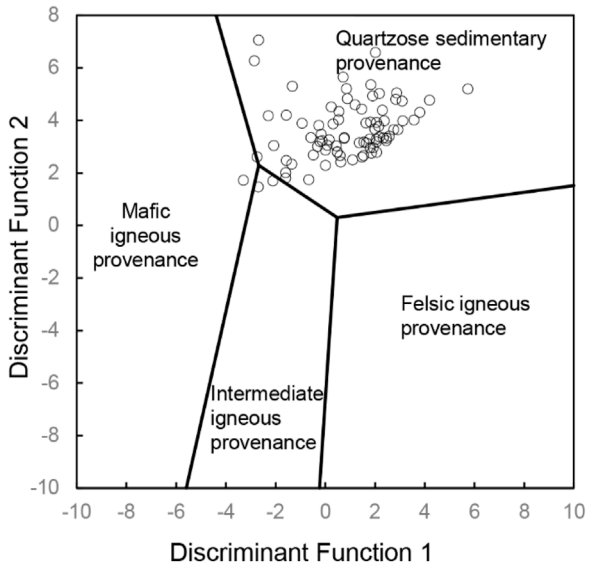

FIGURE 6 | Plot of the provenance discrimination diagram of Roser and Korsch (1988) for the studied mudstones. The Al-normalized version of the diagram of Roser and Korsch (1988) was adopted to avoid dilution effect of non-terrigenous materials. Samples are generally plotted within the "Quartzose sedimentary provenance" region, implying a source area of the intercalated mudstones located in a continental interior. Discriminant Function 1: 30.638×TiO2/Al2O3 – 12.541×Fe2O3/Al2O3 + 7.329×MgO/Al2O3 +12.031×Na2O/Al2O3 + 35.402×K2O/Al2O3 - 6.382. Discriminant Function 2: 56.500×TiO2/Al2O3 – 10.879×Fe2O3/Al2O3 + 30.875×MgO/Al2O3 – 5.404×Na2O/Al2O3 + 11.112×K2O/Al2O3 – 3.809.

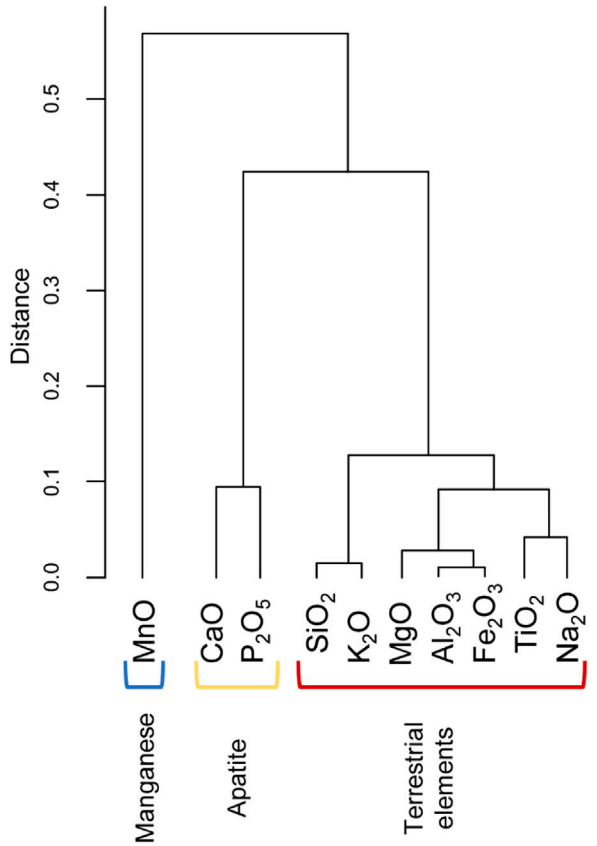

FIGURE 7 | Cluster analysis of the major element composition of intercalated mudstones in Section R and Section Q. Variation matrix (Aitchison, 1986) and Ward method was used for the distance. Three components that control the bulk chemical composition of the intercalated mudstone are classified ("manganese"; "apatite"; "terrestrial elements").

P_2O_5/CaO of 0.75, the ratio of apatite (e.g. Takiguchi et al., 2006).

To evaluate the possible provenance of the studied materials, provenance discrimination diagram of Roser and Korsch (1988) were adopted (**Figure 6**). Almost all samples are plotted in the "Quartzose sedimentary provenance".

To identify groups of elements with the same behavior, Q-mode cluster analysis were performed on the bulk chemical composition of the studied mudstones (**Figure 7**). Results of a cluster ordination of the different variables point to the different grouping of elements associated with siliciclastics (SiO_2, K_2O, MgO, Al_2O_3, Fe_2O_3, TiO_2, and Na_2O) and apatite elements (CaO and P_2O_5) along with MnO, which solely consists of a cluster.

4.2 Principal Component Analysis

To investigate latent information of the bulk chemical composition of the studied samples, PCA was performed (**Table 2**; **Figure 8**). The *p*-values of the Shapiro-Wilk test are 0.35 for clr (SiO_2), 0.44 for clr (TiO_2), 0.14 for clr (Al_2O_3), 0.45 for clr (Fe_2O_3), 0.86 for clr (MnO), 0.70 for clr (MgO), 0.09 for clr (CaO), 0.59 for clr (Na_2O), 0.04 for clr (K_2O), and 0.84 for clr (P_2O_5).

PC1 accounts for 38.9% of the variance of the clr-transformed dataset. PC1 has positive loading from Al_2O_3, K_2O, Na_2O, MgO, SiO_2, TiO_2, and Fe_2O_3, whereas it has negative loading from MnO, P_2O_5, and CaO. Elements positively loaded on PC1 belong to the siliciclastic cluster of above mentioned Q-mode cluster analysis. On the contrary, the elements belonging to the other two clusters (the cluster of manganese and apatite minerals) show negative loadings on PC1.

TABLE 2 | Results of principal component analysis.

	PC1	PC2	PC3	PC4
SiO_2	0.211	–0.200	0.289	–0.835
TiO_2	0.176	0.052	–0.634	–0.042
Al_2O_3	0.526	–0.040	0.091	0.207
Fe_2O_3	0.119	–0.364	–0.184	0.136
MnO	–0.305	–0.508	–0.221	0.028
MgO	0.315	-0.233	0.269	0.450
CaO	–0.179	0.396	0.226	0.095
Na_2O	0.333	0.420	–0.474	–0.143
K_2O	0.469	0.127	0.236	0.025
P_2O_5	–0.282	0.401	0.142	0.078
Eigen value	3.012	1.789	1.239	0.847
Variance explained	38.89	23.10	16.00	10.93
Cumulative variance	38.89	61.99	77.99	88.92

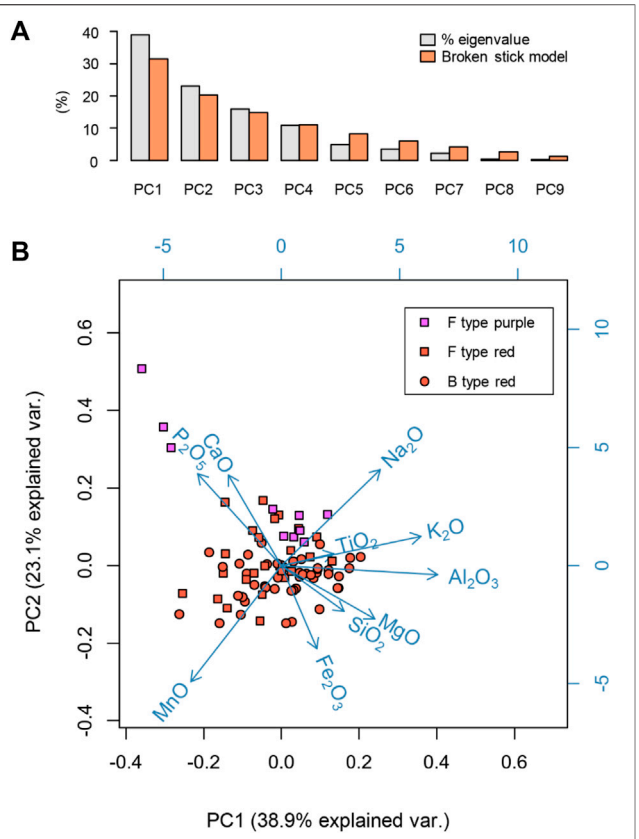

FIGURE 8 | (A) Scree plot of the PCA result and the Broken-Stick model (MacArthur, 1957) for the clr-transformed dataset of intercalated mudstones of Section R and Section Q. **(B)** Biplot of principal component scores and loadings for the PC1 and PC2.

Stratigraphic variations of PC1 and Al_2O_3/TiO_2 ratio are shown in **Figure 9**. The PC1 and Al_2O_3/TiO_2 show a weak positive correlation (R = 0.3). Al_2O_3/TiO_2 ratio increased across the CS-1, and then decreased across the B type/F type boundary but this trend is within the fluctuation throughout the studied section. The stratigraphic variation of PC1 along with the other elemental percent data is shown in **Supplementary Table S1**.

PC2, which is statistically orthogonal with PC1, accounts for 23.1% of the variance of the clr-transformed dataset. PC2 is characterized by high positive loading from P_2O_5, CaO, and Na_2O, and negative loading from MnO and Fe_2O_3.

5 DISCUSSION

5.1 Characterization of Intercalated Mudstone in the Bedded Cherts

The depositional site of the studied bedded chert is located on the deep-sea plane, which was isolated from continental fluvial transportation by trench (**Figure 1**; Matsuda and Isozaki, 1991). Thus, terrigenous materials contained by the bedded cherts are considered to supplied from aeolian transportation (Asahara, 1999). The provenance discrimination diagram of Roser and Korsch (1988) suggests that the provenance of the studied samples is from "Quartzose sedimentary provenance" (**Figure 6**). This result is concordant with the supposed transportation mode of the bedded cherts, that is, the terrigenous materials were blown in from continental interiors (Hori et al., 1993).

The major elemental compositions of the studied intercalated mudstone samples reflect the varying proportions of lithogenic, biogenic, and hydrogenic components in the sediments. The results of Q-mode cluster analysis point to the different grouping of "manganese" (Mn), "apatite" (Ca, P), and "terrestrial" elements (SiO_2, K_2O, MgO, Al_2O_3, Fe_2O_3, TiO_2, and Na_2O) (**Figure 7**).

Mn in our samples is enriched relative to PAAS (**Figure 4**). MnO along with Fe_2O_3 shows large negative loadings in PC2. Mn hydroxides or oxides (e.g., MnO_2) are deposited rapidly in particulate form under oxic conditions, whereas under suboxic and anoxic conditions Mn is reduced to divalent (Mn^{2+}) and forms soluble cations (Sholkovitz et al., 1992; Calvert and Pedersen, 1993). It is thus suggested that the enrichment of Mn may reflect an oxic depositional environment of this section. Alternatively, additional Mn may form under surface oxidized Mn-rich zones during diagenesis (e.g., Pedersen et al., 1986).

The variation of CaO and P_2O_5 in our dataset is controlled by apatite content because of the strong positive correlation of CaO and P_2O_5 with the P_2O_5/CaO ratio of 0.27–0.69 similar to apatite (**Figure 5**). Takiguchi et al. (2006) interpreted the main carrier of apatite in this succession was authigenic in origin and formed during early diagenesis based on their P_2O_5/CaO ratio lower than that of conodont apatite (~0.74; e.g., Ruttenberg and Berner, 1993; Van Cappellen and Berner, 1991). The variation of CaO, P2O5, and MnO characterize PC2, which contains 23.1% of the total variance of the studied dataset. CaO and P_2O_5 show large positive loading whereas MnO shows negative loading, indicating the opposite influence of phosphate and manganese. This relation agrees with the chemistry variation under manganese redirection (Dickens and Owen, 1994; Betzler et al., 2016; Bialik et al., 2020).

The total concentrations of "manganese" and "apatite" elements are generally less than 5%, except for the extremely low PC1 samples at *ca.* 20 cm below the thick claystone CS-1 (Sample Ra39-1, Ra39-2, Ra40). These levels correspond to the unusually high values of CaO and P_2O_5 contents with "apatite" elements content of ca. 7–18%, which can be recognized as an event bed (**Figure 5** and **Figure 9**). The P_2O_5/CaO ratio of these three samples are within 0.6–0.7, lower than that of conodont apatite (Takiguchi et al., 2006). This unusually high apatite concentration may be caused by a pelagic marine environmental shift which led to precipitate abiotic apatite in the sediments, but this topic remains outside the scope of this paper.

For "terrestrial" elements, although biogenic Si is the main component of radiolarian chert, Si in intercalated mudstone is considered to be mainly derived from siliciclastic materials due to migration of biogenic silica to adjacent chert during diagenesis segregation (e.g., Tada, 1991). During this diagenetic segregation,

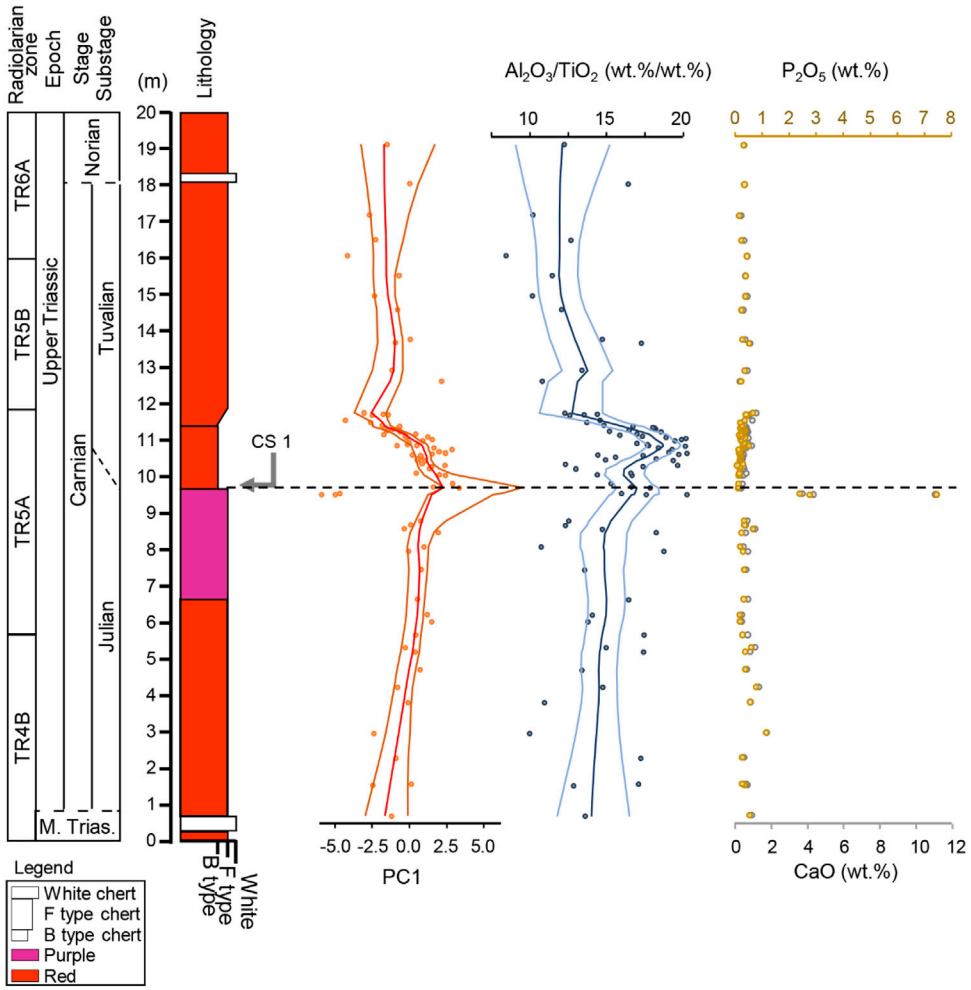

FIGURE 9 | The stratigraphic profile of principal component 1 (PC1) scores and Al_2O_3/TiO_2 ratios. Lines indicate LOWESS fitting and 95% confidence intervals. The relatively high PC1 interval (*ca*. 1 m thick) can be seen above the CS-1. The outstandingly low PC1 observed just below the CS1 corresponds to the high CaO and P_2O_5 samples (Ra39-1, Ra39-2, Ra40).

opal-A in siliceous fossils are extensively dissolved and reprecipitated as tiny opal-CT particles within the pore space mainly in higher dissolved Si area, and thus Si migrated from proto-mudstone intervals to adjacent proto-chert intervals (e.g., Tada, 1991). We cannot rule out contamination of biogenic Si in the intercalated mudstones, but the contribution should be negligible because only well-sorted mudstones were selected for the geochemical analysis.

5.2 Reconstruction of Terrigenous Fluctuations to the Panthalassa Superocean Through the Carnian

PC1 gradually increases below CS-1 from -1.5 to 1, except for the extremely negative values *ca.* 20 cm below the CS-1 (Sample Ra39-1, Ra39-2, Ra40). The PC1 score suddenly increases to 3.4 at the CS-1 horizon and remains constantly high values around 1.5 at the following *ca*. 1 m thick B-type bedded chert interval. The PC1 values decrease across the B type and F type boundary, and then seem to maintain a steady-state with higher variations than Julian to the end of Tuvalian.

Since PC1 has positive loading on all the "terrestrial" elements and negative loading on "manganese" and "apatite" elements, PC1 can be regarded as a latent variable that denotes the degree of relative contribution of terrigenous materials against marine-derived components. Besides, PC1 scores do not show a negative correlation with Al_2O_3/TiO_2 ratio ($R = 0.3$). Al_2O_3/TiO_2 ratio is known to reflect biological productivity on the abyssal fine-grained marine sediments since excess Al is scavenged by the biological pump (Murray and Leinen, 1996; Dymond et al., 1997). The studied bedded cherts are estimated to be deposited at the low latitude of abyssal deep-sea Panthalassa (Ando et al., 2001; Uno et al., 2015) thus the fluctuation of Al_2O_3/TiO_2 ratio of the

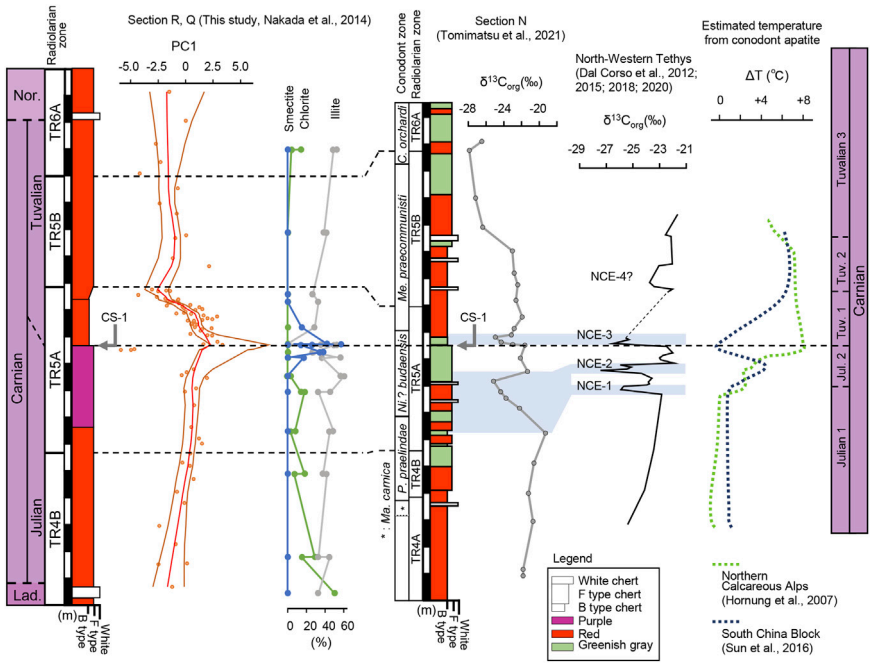

FIGURE 10 | The comparison of PC1 with compositional variation of Fe-bearing minerals and paleotemperature across the CPE. The occurrence of smectite (Nakada et al., 2014) overlaps with the high PC1 interval. Section R and Section N of Inuyama area are correlated by radiolarian biozone and CS-1 as a key bed (Sugiyama, 1997). The conodont and carbon isotope correlations are based on Dal Corso et al. (2020) and Tomimatsu et al. (2021). Paleotemperature profiles are calculated from oxygen isotope of conodont apatite from the western Tethys and the South China Block (Hornung et al., 2007; Sun et al., 2016; redrawn from; Dal Corso et al., 2018).

current dataset is expected to reflect productivity. Therefore, the non-negative correlation observed between PC1 and Al_2O_3/TiO_2 suggests that the changes in PC1 are not mainly regulated by biological productivity fluctuations.

In addition, lithology of the bedded chert suddenly changes from F-type to B-type just above CS-1, with corresponding increased mudstone thickness (Sugiyama, 1997) and an increase in PC1 (**Figure 9**). Two possible factors that regulate the type of bedded chert (F type or B type) that is, the changes in burial flux of biogenic silica and/or siliciclastics (Sugiyama, 1997). Because of the increased Al_2O_3/TiO_2 ratio across the CS-1, a coincident increase in PC1 score may reflect increased terrigenous supply rather than decreased productivity (**Figure 9**).

Equally, considering the negligible contribution of "manganese" and "apatite" elements in samples other than Ra39 and Ra40, the increased mudstone bed thickness across CS-1 likely reflects increased flux of terrigenous material, probably eolian dust in the equatorial pelagic Panthalassa (Hori et al., 1993).

5.3 Continental Environmental Condition Inferred by Terrigenous Supply and Clay Mineral Content Fluctuations of Deep-Sea Bedded Chert

The Carnian Pluvial Episode has been characterized by abrupt siliciclastic input in Tethyan regions (Schlager and Schollnberger, 1974; Simms and Ruffell, 1989; Simms and Ruffell, 1990). This study suggests an increased terrigenous input also occurred in the abyssal deep-sea Panthalassa across the CPE. The increases in siliciclastic input at continental and coastal regions are considered to have been a consequence of enhanced hydrological cycling and consequent increased runoff. However, as discussed above, the terrigenous input in the abyssal plane reflects increasing eolian supply (Hori et al., 1993). Since this eolian dust is likely blown from arid continental areas, the increasing terrigenous supply detected in this study may imply the extensive aridification of the Pangean supercontinent.

This idea seems to contradict the existence of smectite across the CPE which was interpreted as evidence of continental humidification (Nakada et al., 2014). However, a megamonsoonal climate was known to prevail during the Triassic owing to the configuration of supercontinent-superocean (e.g., Kutzbach and Gallimore, 1989). Observational and climate modeling studies at the present day have indicated the humidification of tropical regions and aridification of subtropical regions under global warming (i.e., "Dry gets drier, wet gets wetter"; Held and Soden, 2006). The expansion of arid regions and associated aridification of previously humid regions could account for production of eolian dust containing smectite. The arid and seasonal influences around Carnian are detected in some Gondwana successions (Ruffell et al., 2016).

Expansion of arid regions could have also increased the emission of eolian dust with smectite across CS-1. Eolian

deposits temporarily appeared in the Fundy (Canada), Iberian (Spain) and Argana (Morocco) basins during the Carnian, possibly near the end of the CPE, based on the limited biostratigraphy of terrestrial vertebrates and plant fossils (Arche and López-Gómez, 2014; Sues and Olsen, 2015). Interestingly, the onset of the smectite-rich interval slightly preceded the increased mudstone bed thickness across the CS-1 (**Figure 10**; Sugiyama, 1997; Sugiyama et al., 2001; Nakada et al., 2014). This temporal relation is consistent with the formation of smectite during the CPE and subsequent increase in eolian dust flux owing to the expansion of arid regions in the previously humid regions. Besides, weathering of mafic volcanic sources could also account for the smectite.

Increasing wind gustiness by global cooling and increased latitudinal temperature difference is also known as a main cause of increased eolian flux increase on glacial-interglacial timescales (e.g., McGee et al., 2010). Across the CPE, high-resolution sea surface temperature profile derived from oxygen-isotope of conodont apatite show a possible two-pulse warming event in the Nanpanjiang Basin in South China Block (Sun et al., 2016), while other low-resolution records from western Tethys show only one pulse (e.g., Hornung et al., 2007). In the South China Block, the onset of the CPE, namely NCIE-1, coincided with the first pulse of warming of ~4°C, and followed by a short cooling phase across the Julian/Tuvalian boundary, and then by a prolonged and more intense second phase of warming (**Figure 10**; Sun et al., 2016). According to the biostratigraphy and carbon isotope correlation (**Figure 10**; Tomimatsu et al., 2021), the CS-1 level can be correlated with this short cooling phase across the Julian/Tuvalian boundary. Thus, cooling and associated wind gustiness, in addition to the expansion of arid regions, could have also enhanced the eolian dust emission recorded as the lithologic change in this study section (Sugiyama, 1997).

6 CONCLUSION

The cluster analysis and principal component analysis for the major element composition of intercalated mudstone within bedded chert were performed to investigate the continental environment fluctuation in the Carnian. The PC1 represents the terrigenous content fluctuation whereas PC2 reflects the relative contribution of manganese over apatite. The stratigraphic variation of PC1, coupled with an increase in mudstone thickness, suggests that terrigenous content in abyssal deep-sea sediments from Japan increased at around the Julian/Tuvalian boundary (i.e., across the CPE), and then return to pre-CPE level in Tuvalian. A delayed increase in dust flux relative to an increase in smectite content in deep-sea chert implied expansion of arid regions and associated aridification of previously humid regions. The appearance of eolian successions in low-latitude Pangea are consistent with this idea, but these age models have large uncertainty. This study thus provides deep-sea evidence for widespread aridification that occurred in the Pangean interior across the Julian/Tuvalian boundary, potentially related to CPE.

In addition, an event bed with very high apatite content was found immediately before the high terrigenous supply interval, implying environmental perturbation occurred in pelagic Panthalassa, potentially related to the CPE.

DATA AVAILABILITY STATEMENT

The original contributions presented in the study are included in the article/**Supplementary Material**, further inquiries can be directed to the corresponding author.

AUTHOR CONTRIBUTIONS

TC, MI, and TO contributed to the design and implementation of the research, to the fieldwork, to the analysis of the results and to the writing of the manuscript.

FUNDING

This project was financially supported by Japan Society for the Promotion of Science (21J10870), Fukada geological institute (Grant-in-Aid for feildwork), Waseda Research Institute for Science and Engineering (Grant-in-Aid for Young Scientists: Early-Bird; BD070Z003800).

ACKNOWLEDGMENTS

Thanks go to Yoshiaki Suzuki, Arisa Nakano, Shun Ebisawa and Taro Higuchi for help in the fieldwork, laboratory work, and fruitful discussions. We are grateful to David B. Kemp for fruitful comments, which greatly enhanced the quality of this work. We also thank two reviewers for their helpful and thoughtful reviews.

SUPPLEMENTARY MATERIAL

The Supplementary Material for this article can be found online at: https://www.frontiersin.org/articles/10.3389/feart.2022.897396/full#supplementary-material

REFERENCES

Aitchison, J. (1982). The Statistical Analysis of Compositional Data. *J. R. Stat. Soc. Ser. B Methodol.* 44, 139–160. doi:10.1111/j.2517-6161.1982.tb01195.x

Aitchison, J. (1986). *The Statistical Analysis of Compositional Data/J. Aitchison*. London: Chapman & Hall.

Ando, A., Kodama, K., and Kojima, S. (2001). Low-latitude and Southern Hemisphere Origin of Anisian (Triassic) Bedded Chert in the Inuyama Area, Mino Terrane, Central Japan. *J. Geophys. Res.* 106, 1973–1986. doi:10.1029/2000jb900305

Arche, A., and López-Gómez, J. (2014). The Carnian Pluvial Event in Western Europe: New Data from Iberia and Correlation with the Western Neotethys and Eastern North America-NW Africa Regions. *Earth-Science Rev.* 128, 196–231. doi:10.1016/j.earscirev.2013.10.012

Asahara, Y. (1999). 87Sr/86Sr Variation in North Pacific Sediments: a Record of the Milankovitch Cycle in the Past 3 Million Years. *Earth Planet. Sci. Lett.* 171, 453–464. doi:10.1016/s0012-821x(99)00158-2

Baranyi, V., Miller, C. S., Ruffell, A., Hounslow, M. W., and Kürschner, W. M. (2019a). A Continental Record of the Carnian Pluvial Episode (CPE) from the Mercia Mudstone Group (UK): Palynology and Climatic Implications. *J. Geol. Soc.* 176, 149–166. doi:10.1144/jgs2017-150

Baranyi, V., Rostási, Á., Raucsik, B., and Kürschner, W. M. (2019b). Palynology and Weathering Proxies Reveal Climatic Fluctuations during the Carnian Pluvial Episode (CPE) (Late Triassic) from Marine Successions in the Transdanubian Range (Western Hungary). *Glob. Planet. Change* 177, 157–172. doi:10.1016/j.gloplacha.2019.01.018

Barrenechea, J. F., López-Gómez, J., and De La Horra, R. (2018). Sedimentology, Clay Mineralogy and Palaeosols of the Mid-carnian Pluvial Episode in Eastern Spain: Insights into Humidity and Sea-Level Variations. *J. Geol. Soc.* 175, 993–1003. doi:10.1144/jgs2018-024

Bernardi, M., Gianolla, P., Petti, F. M., Mietto, P., and Benton, M. J. (2018). Dinosaur Diversification Linked with the Carnian Pluvial Episode. *Nat. Commun.* 9, 1499. doi:10.1038/s41467-018-03996-1

Betzler, C., Eberli, G. P., Kroon, D., Wright, J. D., Swart, P. K., Nath, B. N., et al. (2016). The Abrupt Onset of the Modern South Asian Monsoon Winds. *Sci. Rep.* 6, 29838. doi:10.1038/srep29838

Bialik, O. M., Reolid, J., Betzler, C., Eberli, G. P., and Waldmann, N. D. (2020). Source Shifts to Periplatform Deposits during the Early to Middle Miocene in Response to Climatic and Oceanographic Forcing, Maldives, Western Indian Ocean. *Palaeogeogr. Palaeoclimatol. Palaeoecol.* 559, 109969. doi:10.1016/j.palaeo.2020.109969

Calvert, S. E., and Pedersen, T. F. (1993). Geochemistry of Recent Oxic and Anoxic Marine Sediments: Implications for the Geological Record. *Mar. Geol.* 113, 67–88. doi:10.1016/0025-3227(93)90150-t

Cappellen, P. V., and Berner, R. A. (1991). Fluorapatite Crystal Growth from Modified Seawater Solutions. *Geochimica Cosmochimica Acta* 55, 1219–1234. doi:10.1016/0016-7037(91)90302-l

Dal Corso, J., Mietto, P., Newton, R. J., Pancost, R. D., Preto, N., Roghi, G., et al. (2012). Discovery of a Major Negative 13C Spike in the Carnian (Late Triassic) Linked to the Eruption of Wrangellia Flood Basalts. *Geology* 40, 79–82. doi:10.1130/g32473.1

Dal Corso, J., Gianolla, P., Newton, R. J., Franceschi, M., Roghi, G., Caggiati, M., et al. (2015). Carbon Isotope Records Reveal Synchronicity between Carbon Cycle Perturbation and the "Carnian Pluvial Event" in the Tethys Realm (Late Triassic). *Glob. Planet. Change* 127, 79–90. doi:10.1016/j.gloplacha.2015.01.013

Dal Corso, J., Gianolla, P., Rigo, M., Franceschi, M., Roghi, G., Mietto, P., et al. (2018). Multiple Negative Carbon-Isotope Excursions during the Carnian Pluvial Episode (Late Triassic). *Earth-science Rev.* 185, 732–750. doi:10.1016/j.earscirev.2018.07.004

Dal Corso, J., Bernardi, M., Sun, Y., Song, H., Seyfullah, L. J., Preto, N., et al. (2020). Extinction and Dawn of the Modern World in the Carnian (Late Triassic). *Sci. Adv.* 6, eaba0099. doi:10.1126/sciadv.aba0099

Dickens, G. R., and Owen, R. M. (1994). Late Miocene-Early Pliocene Manganese Redirection in the Central Indian Ocean: Expansion of the Intermediate Water Oxygen Minimum Zone. *Paleoceanography* 9, 169–181. doi:10.1029/93pa02699

Dymond, J., Collier, R., McManus, J., Honjo, S., and Manganini, S. (1997). Can the Aluminum and Titanium Contents of Ocean Sediments Be Used to Determine the Paleoproductivity of the Oceans? *Paleoceanography* 12, 586–593. doi:10.1029/97pa01135

Filzmoser, P., and Todorov, V. (2013). Robust Tools for the Imperfect World. *Inf. Sci.* 245, 4–20. doi:10.1016/j.ins.2012.10.017

Gattolin, G., Preto, N., Breda, A., Franceschi, M., Isotton, M., and Gianolla, P. (2015). Sequence Stratigraphy after the Demise of a High-Relief Carbonate Platform (Carnian of the Dolomites): Sea-Level and Climate Disentangled. *Palaeogeogr. Palaeoclimatol. Palaeoecol.* 423, 1–17. doi:10.1016/j.palaeo.2015.01.017

Held, I. M., and Soden, B. J. (2006). Robust Responses of the Hydrological Cycle to Global Warming. *J. Clim.* 19, 5686–5699. doi:10.1175/jcli3990.1

Hori, R. S., Cho, C.-F., and Umeda, H. (1993). Origin of Cyclicity in Triassic-Jurassic Radiolarian Bedded Cherts of the Mino Accretionary Complex from Japan. *Isl. Arc* 2, 170–180. doi:10.1111/j.1440-1738.1993.tb00084.x

Hori, S. R., Higuchi, Y., and Fujiki, T. (2000). Chemical Composition and Their Environmental Records of Bedded Cherts from Accretionary Complexes in Japan. *Mem. Geol. Soc. Jpn.* 55, 43–59. (in Japanese).

Hornung, T., Brandner, R., Krystyn, L., Joachimski, M. M., and Keim, L. (2007). Multistratigraphic Constraints on the NW Tethyan "Carnian Crisis". *Glob. Triassic* 41, 59–67.

Hubert, M., Rousseeuw, P. J., and Vanden Branden, K. (2005). ROBPCA: a New Approach to Robust Principal Component Analysis. *Technometrics* 47, 64–79. doi:10.1198/004017004000000563

Ikeda, M., and Tada, R. (2014). A 70 Million Year Astronomical Time Scale for the Deep-Sea Bedded Chert Sequence (Inuyama, Japan): Implications for Triassic-Jurassic Geochronology. *Earth Planet. Sci. Lett.* 399, 30–43. doi:10.1016/j.epsl.2014.04.031

Imoto, N. (1983). "Chapter 22 Sedimentary Structures of Permian-Triassic Cherts in the Tamba District, Southwest Japan," in *Anonymous Developments in Sedimentology* (Elsevier), 377–393. doi:10.1016/s0070-4571(08)70101-8

Kimura, K., and Hori, R. (1993). Offscraping Accretion of Jurassic Chert-Clastic Complexes in the Mino-Tamba Belt, Central Japan. *J. Struct. Geol.* 15, 145–161. doi:10.1016/0191-8141(93)90092-o

Kutzbach, J. E., and Gallimore, R. G. (1989). Pangaean Climates: Megamonsoons of the Megacontinent. *J. Geophys. Res.* 94, 3341–3357. doi:10.1029/jd094id03p03341

Lindström, S., Erlström, M., Piasecki, S., Nielsen, L. H., and Mathiesen, A. (2017). Palynology and Terrestrial Ecosystem Change of the Middle Triassic to Lowermost Jurassic Succession of the Eastern Danish Basin. *Rev. Palaeobot. Palynol.* 244, 65–95. doi:10.1016/j.revpalbo.2017.04.007

Lu, J., Zhang, P., Dal Corso, J., Yang, M., Wignall, P. B., Greene, S. E., et al. (2021). Volcanically Driven Lacustrine Ecosystem Changes during the Carnian Pluvial Episode (Late Triassic). *Proc. Natl. Acad. Sci. U. S. A.* 118, 5118. doi:10.1073/pnas.2109895118

MacArthur, R. H. (1957). On the Relative Abundance of Bird Species. *Proc. Natl. Acad. Sci. U.S.A.* 43, 293–295. doi:10.1073/pnas.43.3.293

Matsuda, T., and Isozaki, Y. (1991). Well-documented Travel History of Mesozoic Pelagic Chert in Japan: From Remote Ocean to Subduction Zone. *Tectonics* 10, 475–499. doi:10.1029/90tc02134

Matthews, K. J., Maloney, K. T., Zahirovic, S., Williams, S. E., Seton, M., and Müller, R. D. (2016). Global Plate Boundary Evolution and Kinematics since the Late Paleozoic. *Glob. Planet. Change* 146, 226–250. doi:10.1016/j.gloplacha.2016.10.002

McGee, D., Broecker, W. S., and Winckler, G. (2010). Gustiness: The Driver of Glacial Dustiness? *Quat. Sci. Rev.* 29, 2340–2350. doi:10.1016/j.quascirev.2010.06.009

Mueller, S., Hounslow, M. W., and Kürschner, W. M. (2016). Integrated Stratigraphy and Palaeoclimate History of the Carnian Pluvial Event in the Boreal Realm; New Data from the Upper Triassic Kapp Toscana Group in Central Spitsbergen (Norway). *J. Geol. Soc.* 173, 186–202. doi:10.1144/jgs2015-028

Murray, R. W., and Leinen, M. (1996). Scavenged Excess Aluminum and its Relationship to Bulk Titanium in Biogenic Sediment from the Central Equatorial Pacific Ocean. *Geochimica Cosmochimica Acta* 60, 3869–3878. doi:10.1016/0016-7037(96)00236-0

Nakada, R., Ogawa, K., Suzuki, N., Takahashi, S., and Takahashi, Y. (2014). Late Triassic Compositional Changes of Aeolian Dusts in the Pelagic Panthalassa: Response to the Continental Climatic Change. *Palaeogeogr. Palaeoclimatol. Palaeoecol.* 393, 61–75. doi:10.1016/j.palaeo.2013.10.014

Oda, H., and Suzuki, H. (2000). Paleomagnetism of Triassic and Jurassic Red Bedded Chert of the Inuyama Area, Central Japan. *J. Geophys. Res.* 105, 25743–25767. doi:10.1029/2000jb900267

Ohta, T., and Arai, H. (2007). Statistical Empirical Index of Chemical Weathering in Igneous Rocks: A New Tool for Evaluating the Degree of Weathering. *Chem. Geol.* 240, 280–297. doi:10.1016/j.chemgeo.2007.02.017

Pedersen, T. F., Vogel, J. S., and Southon, J. R. (1986). Copper and Manganese in Hemipelagic Sediments at 21 °N, East Pacific Rise: Diagenetic Contrasts. *Geochimica Cosmochimica Acta* 50, 2019–2031. doi:10.1016/0016-7037(86)90256-5

Roser, B. P., and Korsch, R. J. (1988). Provenance Signatures of Sandstone-Mudstone Suites Determined Using Discriminant Function Analysis of Major-Element Data. *Chem. Geol.* 67, 119–139. doi:10.1016/0009-2541(88)90010-1

Ruffell, A., Simms, M. J., and Wignall, P. B. (2016). The Carnian Humid Episode of the Late Triassic: a Review. *Geol. Mag.* 153, 271–284. doi:10.1017/s0016756815000424

Ruttenberg, K. C., and Berner, R. A. (1993). Authigenic Apatite Formation and Burial in Sediments from Non-upwelling, Continental Margin Environments. *Geochimica Cosmochimica Acta* 57, 991–1007. doi:10.1016/0016-7037(93)90035-u

Schlager, W., and Schöllnberger, W. (1974). Das Prinzip stratigraphischer Wenden in der Schichtfolge der Nördlichen Kalkalpen. *Mitt. Geol. Ges. Wien*. 66, 165–193.

Scotese, C. R. (2014). Atlas of Middle & Late Permian and Triassic Paleogeographic Maps. *Paleomap Proj.* 3, 49. doi:10.13140/2.1.2609.9209

Sholkovitz, E. R., Shaw, T. J., and Schneider, D. L. (1992). The Geochemistry of Rare Earth Elements in the Seasonally Anoxic Water Column and Porewaters of Chesapeake Bay. *Geochimica Cosmochimica Acta* 56, 3389–3402. doi:10.1016/0016-7037(92)90386-w

Simms, M. J., and Ruffell, A. H. (1989). Synchroneity of Climatic Change and Extinctions in the Late Triassic. *Geol* 17, 265–268. doi:10.1130/0091-7613(1989)017<0265:soccae>2.3.co;2

Simms, M. J., and Ruffell, A. H. (1990). Climatic and Biotic Change in the Late Triassic. *J. Geol. Soc.* 147, 321–327. doi:10.1144/gsjgs.147.2.0321

Sues, H., and Olsen, P. (2015). Stratigraphic and Temporal Context and Faunal Diversity of Permian-Jurassic Continental Tetrapod Assemblages from the Fundy Rift Basin, Eastern Canada. *Atl. Geol.* 51, 139–205.

Sugiyama, K., Kawakami, S., and Takano, M. (2001). *Aerial Photograph and Stratigraphic Correlation of the Triassic to Lower Jurassic Siliceous Claystone and Bedded Chert Units of the Inuyama and Hisuikyo Areas, Central Japan*. Osaka, Japan: News of Osaka Micropaleontologists, 145–157.

Sugiyama, K. (1997). Triassic and Lower Jurassic Radiolarian Biostratigraphy in the Siliceous Claystone and Bedded Chert Units of the Southeastern Mino Terrane, Central Japan. *Bull. Mizunami Fossil Mus.* 24, 79–193.

Sun, Y. D., Wignall, P. B., Joachimski, M. M., Bond, D. P. G., Grasby, S. E., Lai, X. L., et al. (2016). Climate Warming, Euxinia and Carbon Isotope Perturbations during the Carnian (Triassic) Crisis in South China. *Earth Planet. Sci. Lett.* 444, 88–100. doi:10.1016/j.epsl.2016.03.037

Tada, R. (1991). in *Compaction and Cementation in Siliceous Rocks and Their Possible Effect on Bedding Enhancement. Cycles and Events in Stratigraphy*. Editor G. Einsele, et al. (New York: Springer-Verlag), 480–491.

Takiguchi, T., Sugitani, K., Yamamoto, K., and Suzuki, K. (2006). Biogeochemical Signatures Preserved in Ancient Siliceous Sediments; New Perspectives to Triassic Radiolarian Bedded Chert Compositions. *Geochem. J.* 40, 33–45. doi:10.2343/geochemj.40.33

Taylor, S. R., and McLennan, S. M. (1985). *The Continental Crust: Its Composition and Evolution*. Oxford: Blackwellk, 312.

Tomimatsu, Y., Nozaki, T., Sato, H., Takaya, Y., Kimura, J.-I., Chang, Q., et al. (2021). Marine Osmium Isotope Record during the Carnian "Pluvial Episode" (Late Triassic) in the Pelagic Panthalassa Ocean. *Glob. Planet. Change* 197, 103387. doi:10.1016/j.gloplacha.2020.103387

Uno, K., Yamashita, D., Onoue, T., and Uehara, D. (2015). Paleomagnetism of Triassic Bedded Chert from Japan for Determining the Age of an Impact Ejecta Layer Deposited on Peri-Equatorial Latitudes of the Paleo-Pacific Ocean: A Preliminary Analysis. *Phys. Earth Planet. Interiors* 249, 59–67. doi:10.1016/j.pepi.2015.10.004

Van den Boogaart, K. G., and Tolosana-Delgado, R. (2008). "compositions": A Unified R Package to Analyze Compositional Data. *Comput. Geosciences* 34, 320–338. doi:10.1016/j.cageo.2006.11.017

Visscher, H., Van Houte, M., Brugman, W. A., and Poort, R. J. (1994). Rejection of a Carnian (Late Triassic) "Pluvial Event" in Europe. *Rev. Palaeobot. Palynology* 83, 217–226. doi:10.1016/0034-6667(94)90070-1

Yamashita, D., Kato, H., Onoue, T., and Suzuki, N. (2018). Integrated Upper Triassic Conodont and Radiolarian Biostratigraphies of the Panthalassa Ocean. *Paleontological Res.* 22, 167–197. doi:10.2517/2017pr020

Yao, A., Mtsuda, T., and Isozaki, Y. (1980). *Triassic and Jurassic Radiolarians from the Inuyama Area, Central Japan*. Osaka, Japan: Journal of Geosciences Osaka City University, 135–154.

Conflict of Interest: The authors declare that the research was conducted in the absence of any commercial or financial relationships that could be construed as a potential conflict of interest.

frontiers | Frontiers in Earth Science

ORIGINAL RESEARCH
published: 11 July 2022
doi: 10.3389/feart.2022.900586

An Exceptionally Preserved Terrestrial Record of LIP Effects on Plants in the Carnian (Upper Triassic) Amber-Bearing Section of the Dolomites, Italy

Guido Roghi[1], *Piero Gianolla*[2], *Evelyn Kustatscher*[3,4,5], *Alexander R. Schmidt*[6] *and Leyla J. Seyfullah*[7]*

[1]Institute of Geosciences and Earth Resources (IGG-CNR), Padova, Italy, [2]Department of Physics and Earth Sciences, University of Ferrara, Ferrara, Italy, [3]Museum of Nature South Tyrol, Bolzano, Italy, [4]Department für Geo– und Umweltwissenschaften, Paläontologie und Geobiologie, Ludwig–Maximilians–Universität, Munich, Germany, [5]Bayerische Staatssammlung für Paläontologie und Geologie, Munich, Germany, [6]Department of Geobiology, University of Göttingen, Göttingen, Germany, [7]Department of Palaeontology, University of Vienna, Vienna, Austria

The Carnian Pluvial Episode (CPE) has been recognized as a time of plant radiations and originations, likely related to observed swift changes from xerophytic to more hygrophytic floras. This suggests that the increasing humidity causally resulting from LIP volcanism was the trigger for these changes in the terrestrial realm. Understanding the cause and effects of the CPE on the plant realm, requires study of well-preserved floras that are precisely aligned with the CPE. We therefore focus on the best age-constrained section within the CPE for the terrestrial to marginal marine environment to understand the floristic composition at the early CPE. This is found in the Dolomites, Italy, and is remarkable for the preservation of the oldest fossiliferous amber found in the rock record. An integrated study of palynomorphs and macro-remains related to the conifer families of the fossil resin bearing level brings together the floral components from this section. This observed mixture of different taxa of extinct and modern conifer families underlines firmly the effects of the LIP-induced CPE on the evolution and radiation of conifers.

Keywords: Carnian Pluvial Episode (CPE), palynomorphs, plant fossils, amber, paleoenvironmental reconstruction, conifer evolution and radiation

OPEN ACCESS

Edited by:
Sara Callegaro,
University of Oslo, Norway

Reviewed by:
Daoliang Chu,
China University of Geosciences Wuhan, China
Grzegorz Pacyna,
Jagiellonian University, Poland

***Correspondence:**
Leyla J. Seyfullah
leyla.seyfullah@univie.ac.at

Specialty section:
This article was submitted to Paleontology, a section of the journal Frontiers in Earth Science

Received: *20 March 2022*
Accepted: *01 June 2022*
Published: *11 July 2022*

Citation:
Roghi G, Gianolla P, Kustatscher E, Schmidt AR and Seyfullah LJ (2022) An Exceptionally Preserved Terrestrial Record of LIP Effects on Plants in the Carnian (Upper Triassic) Amber-Bearing Section of the Dolomites, Italy. Front. Earth Sci. 10:900586. doi: 10.3389/feart.2022.900586

INTRODUCTION

The Triassic is generally considered as having hothouse conditions with no polar icecaps. The presence of the supercontinent Pangaea over the paleoequator led to a drier continental interior despite a strong monsoonal system (Tanner, 2018). This allowed two main floristic provinces to develop, one in the Northern Hemisphere (Laurussia) and the other in the Southern Hemisphere (Gondwana). During the Late Triassic (237–201 Ma), Pangaea started to fragment, and the floras show increased provincialism in addition to compositional shifts in reaction to major climatic pulses (Buratti and Cirilli, 2007; Preto et al., 2010; Kustatscher et al., 2018; Tanner, 2018). Palynofloras divide Gondwana in to two sub-provinces: the cooler and perhaps more humid *Falcisporites* (Umkomasiales) dominated Ipswich Sub-province found between 90° and 40°S paleolatitude, and the warmer and more diverse Onslow Sub-province found around 45° to 20°S paleolatitude (Dolby

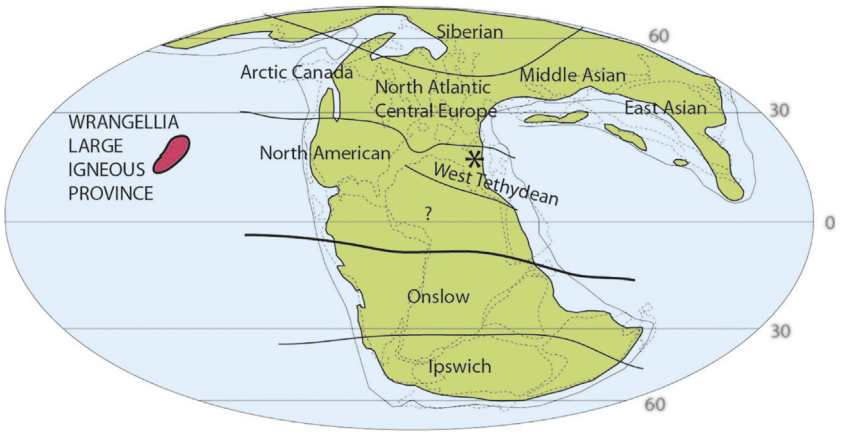

FIGURE 1 | Pangaean floristic subprovinces during the Late Triassic (modified from Kustatscher et al., 2018). The red area marks the likely paleogeographic position of the Wrangellia LIP volcanism, linked to the CPE. Thicker line indicates the divide between the Laurussian and Gondwanan areas. Star indicates the paleogeographic position of the Dolomites area, the question mark indicates area with no data.

and Balme, 1976; Césari and Colombi, 2013; Kustatscher et al., 2018). In Laurussia, seven floral sub-provinces have been recognized, linked to the more varied regional environmental and climate conditions (Kustatscher et al., 2018; **Figure 1**).

During the Carnian (237–227 Ma, early Late Triassic), profound changes are observed in both the marine and terrestrial realms. These changes have been linked to a global climate upheaval termed the Carnian Pluvial Episode (CPE) that occurred around 234 to 232 Ma (Simms and Ruffell, 1989; Simms and Ruffell, 1990; Simms et al., 1995; Dal Corso et al., 2020; Colombi et al., 2021). The increased hydrological cycle and weathering resulted in increased siliciclastic input into the basins (Rigo et al., 2007; Dal Corso et al., 2015; Dal Corso et al., 2020).

The isotopic analyses of these multiple siliciclastic occurrences in the Tethys area define the presence of global negative carbon isotopic excursions (NCIEs) linked to large, pulsed injections of isotopically depleted CO_2. The carbon isotopic perturbations suggest that the CPE was caused by LIP volcanism repeatedly injecting vast amounts of ^{13}carbon depleted carbon dioxide in to the Carnian atmosphere-ocean system warming the world, with the Wrangellia LIP thought to be the major source for these carbon injections (Dal Corso et al., 2012; Dal Corso et al., 2015; Sun et al., 2016; Miller et al., 2017; Dal Corso et al., 2018; Dal Corso et al., 2020; Lu et al., 2021; Mazaheri-Johari et al., 2021; Tomimatsu et al., 2020; Dal Corso et al., 2022). Palynological analyzes of the levels with the NCIEs allow the definition of discrete humid impulses based on the dominance of hygrophytic elements in the palyno-assemblages (Roghi et al., 2010; Mueller et al., 2016a; Mueller et al., 2016b; Baranyi et al., 2019). The Heiligkreuz and Travenanzes formations of the Dolomites (Italy) were the key in linking the NCIEs and the increased siliciclastic occurrences with the signals observed from the plants (e.g., Preto and Hinnov, 2003; Breda et al., 2009; Roghi et al., 2010; Stefani et al., 2010; Dal Corso et al., 2015; Dal Corso et al., 2018). The warmer, wetter climate enhanced the hydrological cycle, resulting in large quantities of terrigenous material and nutrients entering the sea basins. The duration of the entire CPE event is estimated to be around 1.2 Myr (Zhang et al., 2015; Miller et al., 2017; Bernardi et al., 2018; Lu et al., 2021).

This time of significantly increased global rainfall (Preto et al., 2010) even resulted in substantial coal deposits in geographically distinct areas i.e., in Laurussia (Austria, Svalbard, Sweden, China) and in Gondwana (Australia, South Africa), as summarized by Retallack et al. (1996) and Ruffell et al. (2016). The CPE has been related to a major extinction event with subsequent biotic radiations, resulting from an abruptly warmed climate. Many key groups that dominate modern ecosystems appear to have undergone an explosive diversification due to the CPE leading to the "dawn of the modern world" (Dal Corso et al., 2020).

The plant fossil record is intermittent for the Late Triassic and is often only resolved to stage level, meaning that identifying within-stage floral responses such as to the CPE (late Tuvalian to Julian substages of the Carnian) is not always clear-cut (Kustatscher et al., 2018; Dal Corso et al., 2020). There are, however, clear switches to humid elements in the late early Carnian floras, with a return to floras characterized by drier elements during the late Carnian (e.g., Roghi et al., 2010; Kustatscher et al., 2018; Baranyi et al., 2019; Kustatscher et al., 2019). Also, paleosol analysis from Italy (Dolomites) and Spain highlight more humid conditions during the CPE than before and after it (Breda et al., 2009; Barrenechea et al., 2018). The CPE is thought to have led to the diversification of some key Mesozoic plant groups such as the Bennettitales, plus the origination and radiation of several modern fern and conifer families (Kustatscher et al., 2018; Dal Corso et al., 2020). Amber, fossilized plant resin, is also a distinct feature of some Carnian floras (Roghi et al., 2006a; Schmidt et al., 2006; Schmidt et al., 2012; Seyfullah et al., 2018a; Seyfullah et al., 2018b). Although trace amounts of amber are found in earth history from the Carboniferous onwards, these are microscopic amounts from within the plant tissues (Seyfullah et al., 2018a; Seyfullah et al., 2018b). The first appearance of significant amounts of amber in the fossil record is during the Carnian (Seyfullah et al., 2018a;

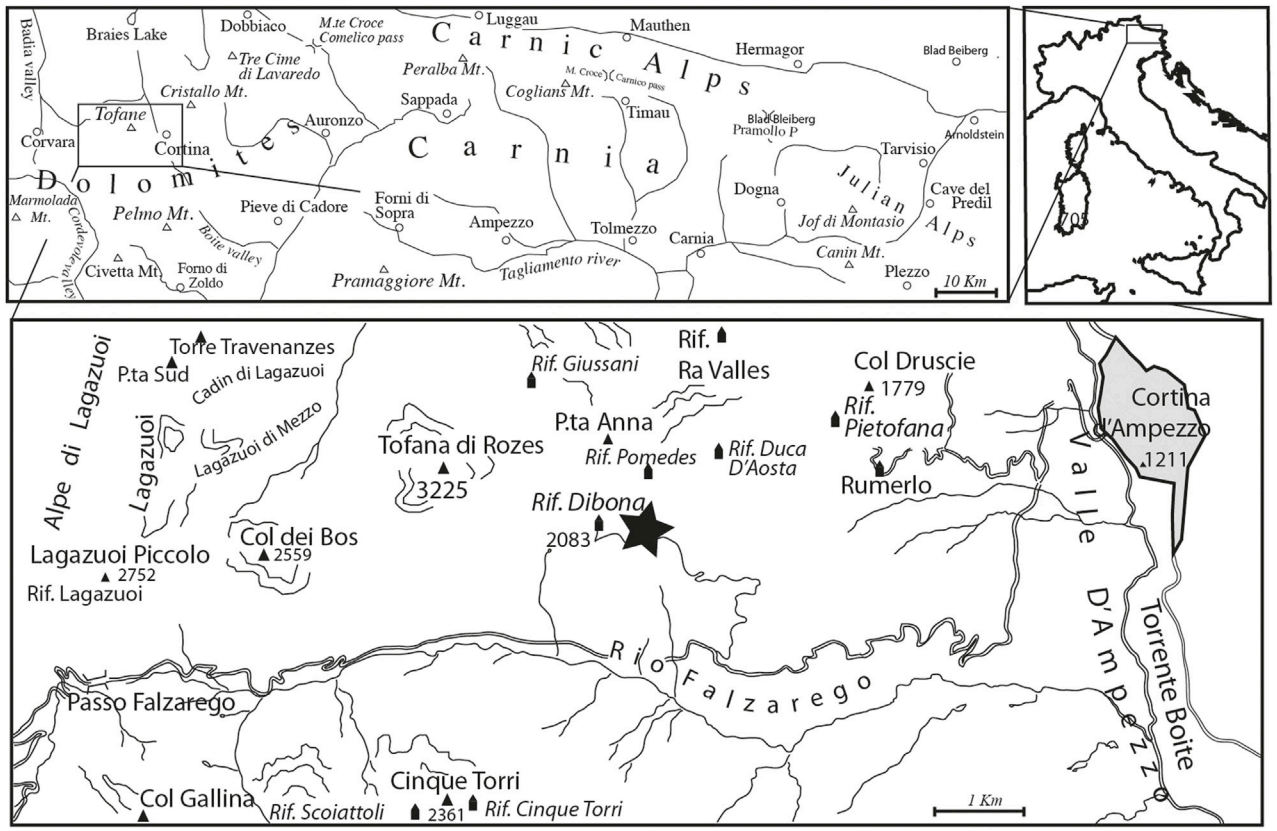

FIGURE 2 | Geographical map of the position of the studied Rifugio Dibona area (star on lower map), near Cortina d'Ampezzo.

Seyfullah et al., 2018b). It is hypothesized that the resin outpourings preserved as amber deposits indicate environmental stresses on the terrestrial environment (Gianolla et al., 1998a; Roghi et al., 2006a; Seyfullah et al., 2018a; Seyfullah et al., 2018b).

Carnian amber has yielded the oldest inclusions in amber in the fossil record. Although the search for inclusions also in other Triassic ambers is promising (Stilwell et al., 2020), a substantial amount is only found from the Heiligkreuz Fm., in the Italian Dolomites, so far. Also, here a large volume of small amber droplets is preserved in paleosols (Preto and Hinnov, 2003; Schmidt et al., 2006; Breda et al., 2009; Schmidt et al., 2012). The entrapped organisms span plant remains, including pollen and spores, invertebrate remains and microorganisms, giving us a rare insight into the terrestrial realm during the CPE and telling us at a very fine scale the incredibly local interaction of the plants and the surrounding biota (Schmidt et al., 2006; Schmidt et al., 2012; Sidorchuk et al., 2015). This amber deposit is the largest by volume of amber of all the Carnian-aged deposits (Seyfullah et al., 2018a). To understand the responses of the plants to the CPE we focus on the best age-constrained section exposing the CPE: the Rifugio Dibona section near the town of Cortina d'Ampezzo, Dolomites, Italy (**Figure 2**). The section of the Rifugio Dibona is one of the most continuous, complete, and best studied outcrops of the Heiligkreuz Formation, the lithostratigraphic unit that

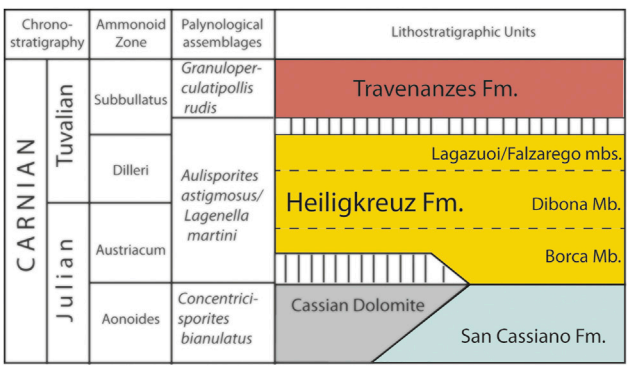

FIGURE 3 | Stratigraphic reconstructions of the Upper Triassic Formations in the area near Rifugio Dibona.

records the CPE in the Dolomites (De Zanche et al., 1993; Gianolla et al., 1998b; Preto and Hinnov, 2003; Breda et al., 2009; Maron et al., 2017) and can be easily correlated with other sections of the same unit in the Dolomites (Neri et al., 2007).

In addition to the amber-rich paleosols, macro- and microfloral remains have also been recovered from the Heiligkreuz Fm. at the Rifugio Dibona section (Roghi et al., 2006a; Dal Corso et al., 2011). Here we focus on these three

botanical indicators: Plant macrofossils, palynomorphs and amber, to show the effects on the flora during the CPE. Particularly interesting are the gymnospermous plant remains since those have a reduced taphonomic and collecting bias compared to the sporing plants (e.g., Nowak et al., 2018).

GEOLOGICAL INFORMATION

In the upper Carnian of the Dolomites, the passage from the carbonate-siliciclastic sediments of the heteropic San Cassiano Formation/Cassian Dolomite, to the Heiligkreuz Formation. is well documented. (see Dürrenstein Fm. in Bosellini, 1984; De Zanche et al., 1993; Gianolla et al., 1998a; Gianolla et al., 1998b; Keim and Brandner, 2001; Keim et al., 2001; Neri et al., 2007; Gattolin et al., 2015) (**Figure 3**).

The lower portion of the Heiligkreuz Fm., also known as Borca Mb. (Neri et al., 2007; Breda et al., 2009; Gattolin et al., 2015; Dal Corso et al., 2018) consists of terrigenous-carbonate facies with well-stratified dolomitic limestones, arenaceous dolomites and hybrid arenites with frequent pelitic intervals. At the base of the Heiligkreuz Fm. there are biostromes with diversified colonial corals, stromatoporoids and sponges, often well preserved in aragonite both in the Alpe di Specie/Seelandalpe and Dibona areas (Scherer, 1977; Russo et al., 1991; Senowbari-Daryan et al., 2001; Neri et al., 2007; Gianolla et al., 2018). The corals that make up these structures, which will never form the edges of large platforms, are of the modern type (Stanley, 2003).

The upper portion of the Borca Mb. is frequently made up of ooliths and peritidal stromatolitic dolomites covered by polycyclic paleosols levels typical of humid climates (Preto and Hinnov, 2003; Breda et al., 2009). In the middle part of the Heiligkreuz Fm. there is a transgressive unit rich in silicoclastics: Calcarenites and biocalcarenites, sometimes oolithic, which make up the Dibona Mb. (Bosellini et al., 1982; Preto and Hinnov, 2003; Neri et al., 2007) and which upwards become nodular hemipelagic limestones. In those lower siliciclastic facies and in the pelitic-clayey levels of paleosols there is a large quantity of fossil resin together with abundant plant remains (Gianolla et al., 1998b; Roghi et al., 2006a).

The top of the Heiligkreuz Fm., called the Lagazuoi Mb., consists of shallow water bioclastic carbonates, which pass laterally to terrigenous sediments (Falzarego Mb. in Neri et al., 2007). On the top there is a discordant surface consisting of dolomitic breccias (Keim and Brandner, 2001). With the deposition of the Lagazuoi Mb., the paleotopography of the area is definitively flattened. Subsequently there are transgressive alluvial and muddy facies of Tuvalian age (Travenanzes Fm.) which are superimposed by a Heiligkreuz Fm. discordance and are in turn covered by carbonate peritidal cycles of the Hauptdolomit/Dolomia Principale (Breda and Preto, 2011).

Near the base of the Heiligkreuz Fm. the *Aulisporites astigmosus* and *Lagenella martini* sporomorph association was identified, and the presence of the ammonoids *Austrotrachyceras* sp. and *Sirenites senticosus* confirm the base of the Julian 2 stage (Breda et al., 2009). In the middle part of the Heiligkreuz Fm. the sporomorph *Lagenella martini* Assemblage (Roghi et al., 2010) defines the Julian 2–Tuvalian 1 age (Roghi et al., 2010; Maron et al., 2017). In the upper part of the Heiligkreuz Fm., together with the ammonoids *Shastites* cfr. *pilari* and cfr. *Jovites* sp., the conodonts *Paragondolella noah* and *Metapolygnathus praecommunisti*, confirm a Tuvalian 1 age (Breda et al., 2009; Maron et al., 2017). The Julian-Tuvalian boundary is thus located in the upper part of Heiligkreuz Fm., where the Tuvalian ammonoids are found, and is marked by a NCIE. The section with the amber-bearing paleosols exposed at the Rifugio Dibona area has been dated to a Julian 2–Tuvalian 1 (late early–early late Carnian; *Austrotrachyceras austriacum–Tropites dilleri* ammonoid zones) of the Heiligkreuz Fm. using ammonoids, conodonts and sporomorphs (Gianolla et al., 1998b; Gianolla et al., 2003; De Zanche et al., 2000; Neri et al., 2007; Roghi et al., 2010; Dal Corso et al., 2015).

The succeeding Travenanzes Fm. is assigned to the Tuvalian 2 by the presence of the *Granuloperculatipollis rudis* assemblage, which is calibrated in the Julian Alps to Tuvalian 2–3 (Roghi, 2004). The Julian 2–Tuvalian 1 interval, well identified in the Heiligkreuz Fm.–Travenanzes Fm. succession, by ammonoids, conodonts and palynomorphs, and is characterized by strong variations in the isotope ratio of organic carbon organized in different events often associated with macroscopic siliciclastic inputs (Dal Corso et al., 2015; Dal Corso et al., 2018). In particular, in the Heiligkreuz Fm., exposed right at the Rifugio Dibona (**Figure 4**), various NCIEs have been identified both with carbon isotopes of the dispersed organic matter, biomarkers and isotopes of the organic carbon of wood present along the entire section. The first of these excursions allow us to define the onset of the CPE whereas two other NCIE events along the sections, and always within the CPE, were also identified. The last shift is present at the base of the Travenanzes Fm. Since the carbon isotopic variation affects both marine and terrestrial fossil molecules, this isotopic variation has its origin in changes of atmospheric, and consequently, terrestrial and marine environments (Dal Corso et al., 2012).

MATERIALS AND METHODS

Plant Macrofossils

Plant macrofossils are composed mainly of impressions and compressions, with occasional small fragments of charcoal; 29 specimens have been collected and deposited at the Museum of Nature South Tyrol, where they are stored by consecutive numbers prefixed by the acronym "PAL". Specimens were photographed with a Canon EOS D550 digital camera and measured using the free software ImageJ64® (National Institute of Health, Bethesda, MD).

Paleosols

Paleosol beds (**Figure 4**) were recognized and followed along different points of the Rifugio Dibona section. The thin (few cm thick) paleosols are usually found lying over karstified surfaces

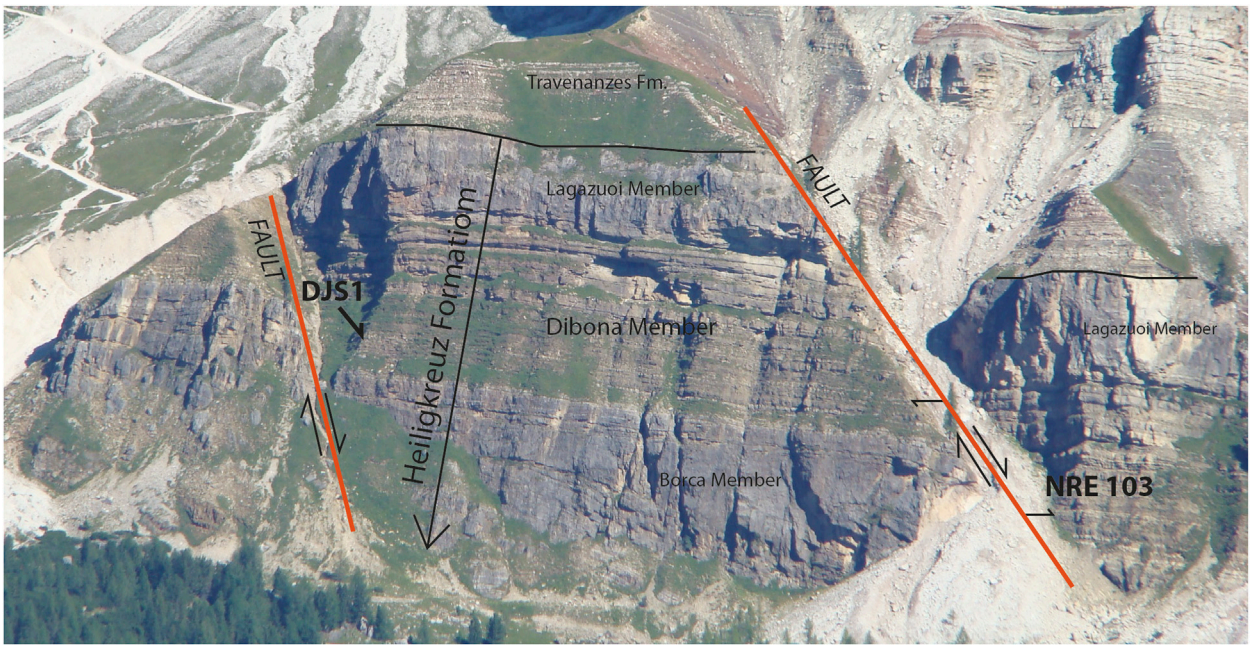

FIGURE 4 | The main outcrops of the Heiligkreuz Fm. exposed at the Refugio Dibona section and the position of the levels of the palynological samples DJS 1 and NRE 103. The paleosol rich in amber crops out at level NRE 103. The distance between the two sampling sites is approximately 250 m, for scale.

(Preto and Hinnov, 2003; Gattolin et al., 2013) with a spodic (Fe-alluvial) horizon under an overlying histic (rich in organic matter) horizon. Breda et al. (2009) used these features to infer that the soil developed in a humid climate during the CPE. One of the paleosols was sampled and subsets were processed for palynological and amber studies (see below).

Pollen

In order to best identify the diversity of plant communities during the CPE, the paleosol level containing a large amount of fossil resin was sampled for the palynological analyses at two different positions of the Rifugio Dibona section, at a distance of about 250 m, respectively DJS 1 and NRE 103 (**Figure 4**). Both qualitative and quantitative analyses (two slides for each sample) were performed showing a high similarity in qualitative and quantitative composition on the microassemblages. Specimens were photographed with a DFC300 camera at a Leica DMLB microscope. The studied material is housed at the Institute of Geosciences and Earth Resources (IGG-CNR), Padova. Additional palynomorphs are present as amber inclusions and are housed at the Museum of Geology and Paleontology, University of Padova.

Amber

The amber droplets were elutriated from the paleosol in water and any adhered plant remains removed. The clean droplets were placed on hollowed glass microscope slides (Menzel Inc.) immersed in water, covered by a glass coverslip and screened for inclusions under a Carl Zeiss AxioScope A1 compound microscope as described by Schmidt et al. (2012).

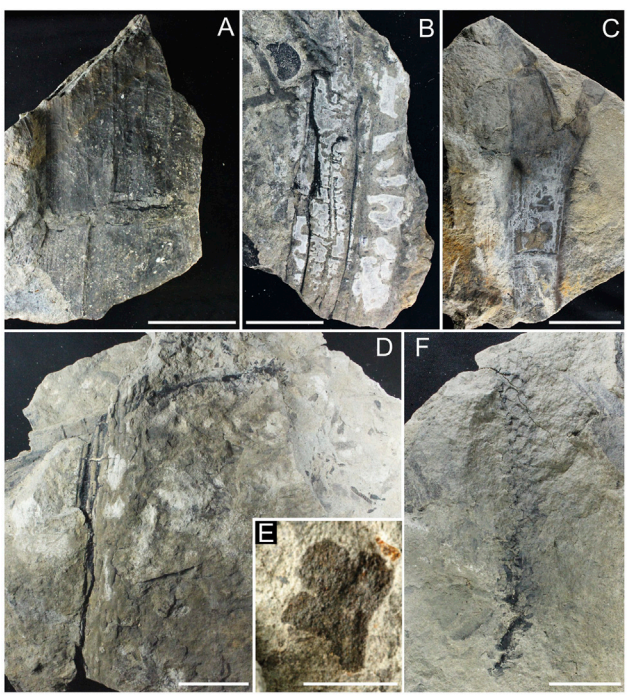

FIGURE 5 | Plant macrofossils of the Heiligkreuz Fm. **(A)** Sphenophyte, PAL 4121 NRE103 72; **(B)** Sphenophyte, PAL 4100 NRE103 52; **(C)** Undeterminated stem, PAL 4112 NRE103; **(D)** *Voltzia* sp., PAL 4107 NRE103 60; **(E)**. Trilobate leaf; **(F)**. *Voltzia* sp., PAL 4111 NRE103 61. Scale bars: 5 cm **(A–D,F)**; 1 cm **(E)**.

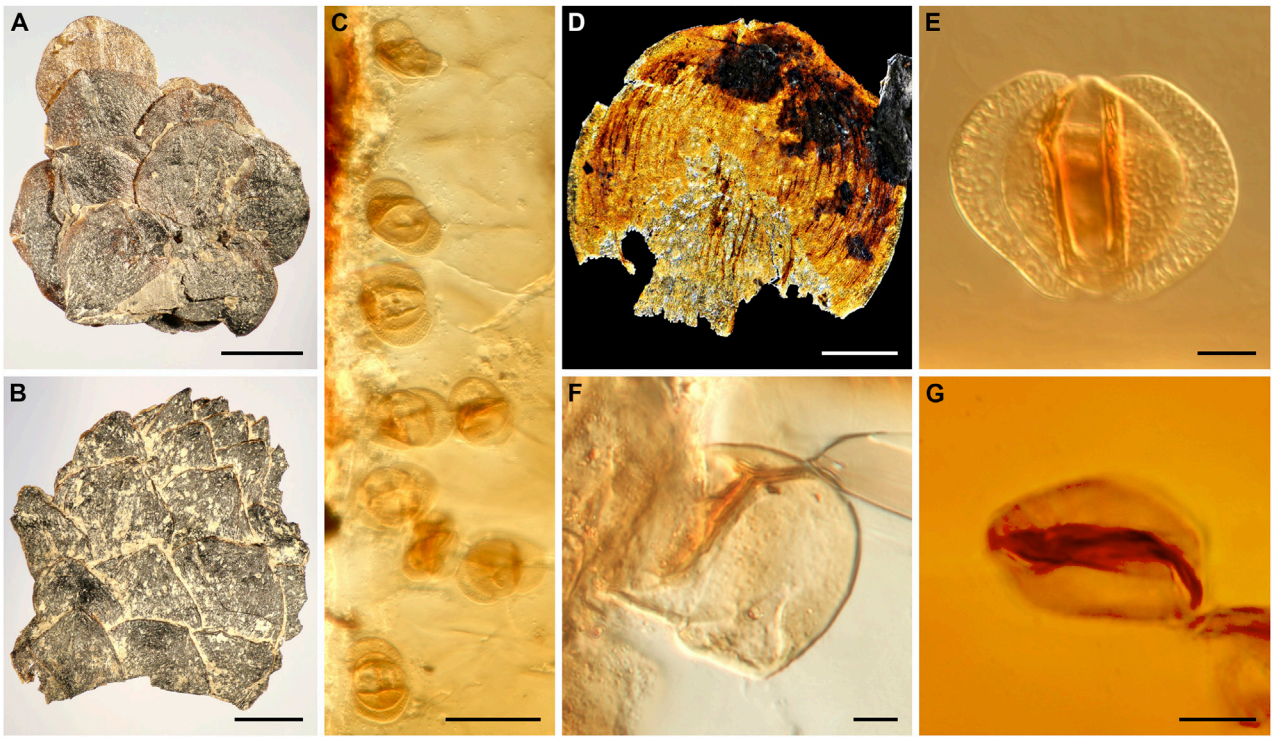

FIGURE 6 | Fossil plant remains **(A,B,D)** and palynomorphs enclosed in the amber droplets **(C,E–G)** recovered from the paleosol. **(A)** Leafy shoot fragment. **(B)** Conifer cone fragment. **(C)** Cluster of *Lueckisporites* pollen grains preserved towards the surface of an amber droplet. **(D)** Fragment of a conifer leaf from the paleosol. **(E–G)** Pollen grains preserved in amber, **(E)** *Lueckisporites* pollen grain. **(F)** Spore. **(G)** Circumpollen grain. Scale bars: 2 mm **(A,B)**, 50 µm **(C)**, 1 mm **(D)**, 10 µm **(E–G)**.

The millimetre-sized amber droplets containing palynomorphs and plant remains were embedded in a high-grade 'glass conservation' epoxy (EpoTek 301-2, Epoxy Technology) and subsequently ground and polished to bring the inclusions close to the surface of the preparation, for enhanced imaging (refer to Sadowski et al., 2021, for protocols).

Prepared specimens were placed on a glass microscope slide with a drop of water applied to the upper surface of the amber, covered with a glass coverslip. This reduces light scattering from fine surface scratches and improves optical resolution. Specimens were photographed with a Carl Zeiss AxioScope A1 compound microscope, using up to 640 magnification and differential interference contrast (DIC) illumination.

RESULTS

Plants of the Heiligkreuz Fm.: Macrofossils

The macrofossil plant assemblage is composed mainly by sphenophyte stem fragments, stem, shoot, leaves and cone fragments of conifers, seeds, a putative axis fragment of a lycophyte, some less well-defined stem fragments that occasionally bifurcate, fragments of charcoal, and amber dispersed among and/or attached to the top of the plant remains (**Figure 5**).

The sphenophyte stem fragments are up to 300 mm long and 150 mm wide. Most fossils are composed by impressions or compressions of the stems with visible impressions of the vascular bundles, often also with desiccation cracks perpendicular to the axes. Internal casts of the stems, diaphragm fragments and rhizome fragments with attachment of the arising subaerial axis are preserved. Elongate structures, up to 230 mm long and 13 mm wide, with a thick central vein/midvein could also belong to this group, as smaller axes.

The conifer fragments are generally small and often represented by up to 200 mm long and 35 mm wide stem fragments of the *Endolepis* type characterized by a knotty surface of the stem. Conifer shoots are up to 160 mm long and 20 mm wide, partly defoliated. Leaves are falcate in lateral view, 7–13 mm long and 1.8–2.5 mm wide with a rounded apex. In frontal view they are lanceolate, the leaf scar impression is almost rhombohedral in shape with a diameter of 6.8–7 mm. One trilobate ovuliferous scale is also preserved; it is less than 10 mm long and wide.

Smaller plant remains include a dispersed seed of up to 16 mm diameter with a slightly pointed apex. The outer layer, preserved only as carbonate material, is about 1 mm thick. A very small plant fragment is composed of bifurcating axis fragments, up to 30 mm long and 2–2.5 mm wide. The single leaves are ovate to scale-like, less 1–1.5 mm long and 1 mm wide, and closely

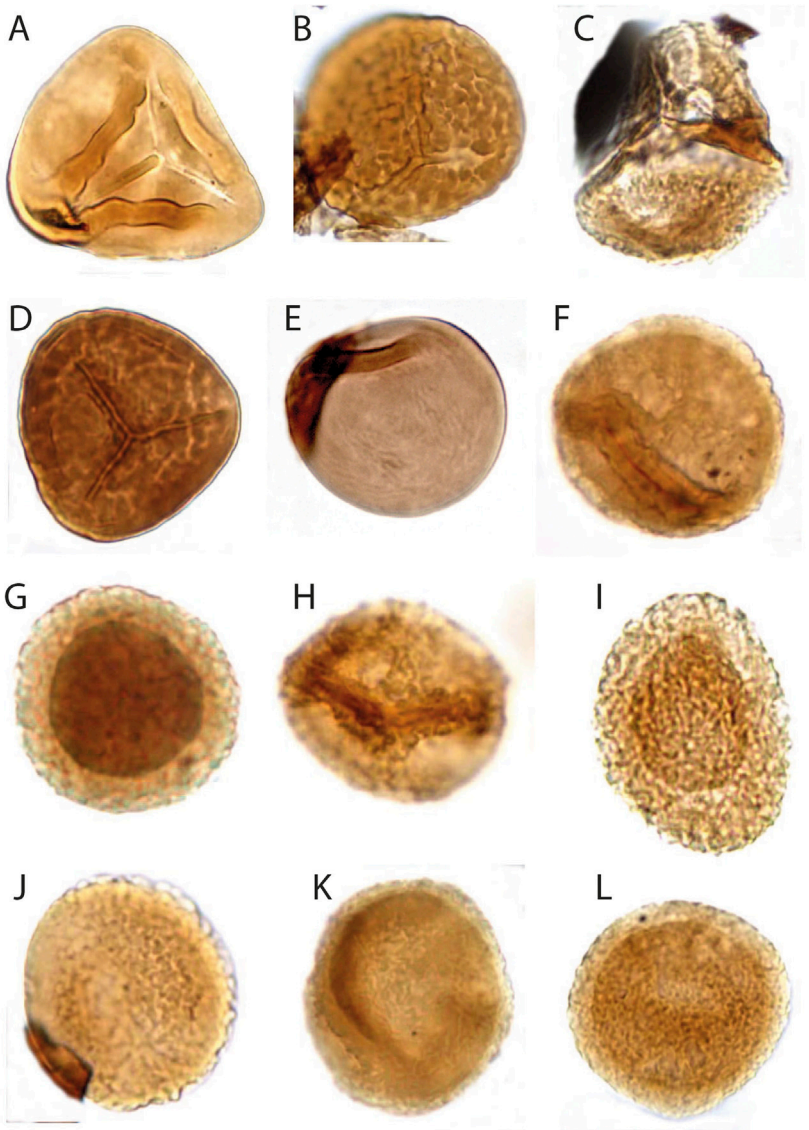

FIGURE 7 | Palynomorphs of the Heiligkreuz Fm., part I. **(A)** *Concavisporites toralis*; slide DJS1A III; O29/3; 57 µm height. **(B)** *Convolutispora* sp. A; slide DJS1A III; O54/1; 46,4 µm diameter. **(C)** *Kraeuselisporites* sp.; NRE103A IV; L24; 52 µm height. **(D)** *Convolutispora* sp. Ind.; DJS1A III; S53/2; 43 µm diameter. **(E)** *Leschikisporites aduncus*; NRE103B III, H32; 35 µm diameter. **(F)** *Aratrisporites scabratus*; DJS1A III; R52/2; 34 µm diameter. **(G)** *Vallasporites ignacii*; DJS1A III, L33/4; 28,8 µm diameter. **(H)** *Vallasporites ignacii*; DJS1A III, N29/2; 32 µm diameter. **(I)** *Patinasporites* cf. *P. densus*; DJS1A II, J43/1; 40 µm height. **(J)** *Haberkornia parva*; DJS1A III, O51; 32 µm diameter. **(K)** *Enzonalasporites vigens*; DJS1A III, N24; 40 µm diameter. **(L)** *Enzonalasporites vigens*; DJS1A II, J43/1; 43 µm diameter.

imbricated. This fragment could represent a lycophyte-type of plant such as *Selaginellites*.

Plants of the Heiligkreuz Fm.: Mesofossils

The paleosol yielded a rich assemblage of dispersed leaves and small conifer shoot and cone fragments with exceptionally well-preserved cuticles (**Figures 6A,B,D**). The leaf fragments are broadly lanceolate with a rounded apex, up to 2–2.5 mm long and 3 mm wide. They are partly macerated, showing the rows of the stomata. The base and attachment area of the leaves is irregular, suggesting that the leaves were not naturally shed but defoliated during transport and deposited in the paleosol. The general shape and dimension of the leaves as well as the cuticles suggest that they belong to the conifers.

Plants of the Heiligkreuz Fm.: Palynomorphs

The palynological analyses of the samples taken at levels DJS 1 and NRE 103 yielded a rich and diverse assemblage of spores, pollen,

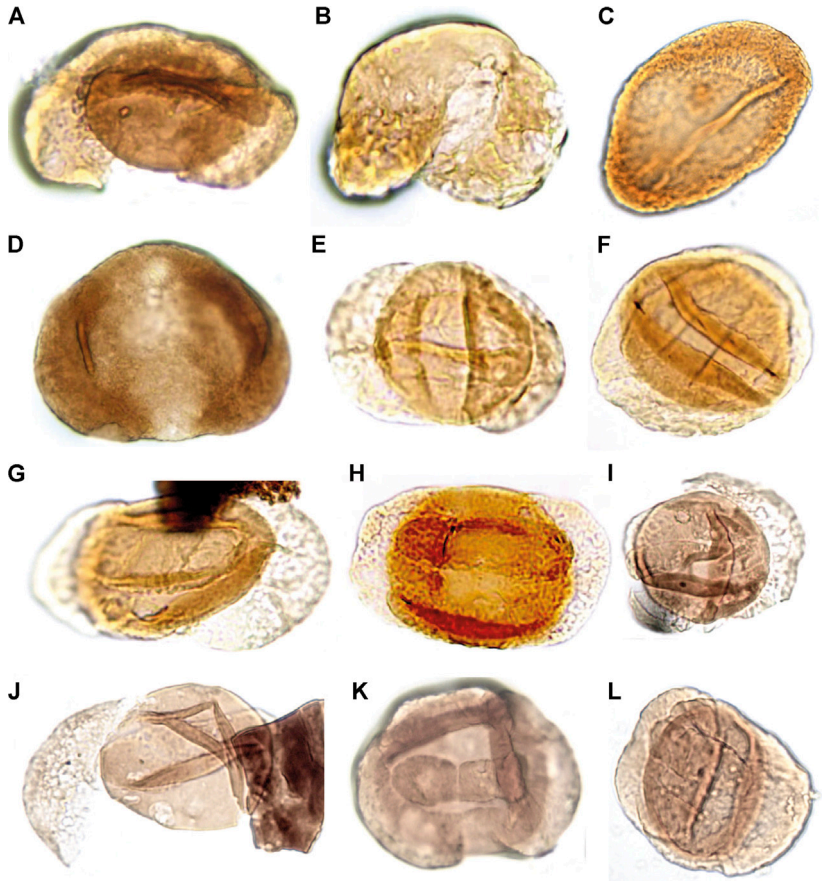

FIGURE 8 | Palynomorphs of the Heiligkreuz Fm., part II. **(A)** *Samaropollenites speciosus*; DJS1A I, J38/1, 55 µm width. **(B)** *Abietineaepollenites* sp.; DJS1A I, T45/3, 46 µm width. **(C)** *Chordasporites* sp.; NRE103B II, S48, 83 µm width. **(D)** *Klausipollenites schaubergeri*; DJS1A I, Q29/2, 72 µm width. **(E)** *Lunatisporites acutus*; DJS1A III, H45/2, 46 µm width. **(F)** *Lueckisporites junior*; NRE103B I, N40/3, 52 µm width. **(G)** *Taeniato* sp. 1; NRE103B III, R33/2, 48 µm height. **(H)** *Lueckisporites junior*; DJS1A I, J52/4, 72 µm length. **(I)** *Samaropollenites* sp.; DJS1A II, L33, 37 µm corpus diameter. **(J)** *Samaropollenites* sp.; DJS1A II, L33, 36 µm corpus diameter. **(K)** *Taeniato* sp. 2, DJS1A I, G36/4, 50 µm width. **(L)** *Lunatisporites acutus*; NRE103B III, S35/3, 51 µm height.

cuticle fragments and amber. The most diverse are the pollen grains with about 30 different forms, whereas the spores are less diverse with eight different types. The spores are represented by trilete laevigate (e.g., *Concavisporites, Calamospora*), trilete ornamented (e.g., *Osmundacidites, Convolutispora*) and monolete cavate (e.g., *Aratrisporites*) forms. The pollen grains include a variety of bisaccate taeniate (e.g., *Lunatisporites, Lueckisporites*), bisaccate non-taeniate (e.g., *Klausipollenites, Triadispora*), monosaccate (e.g., *Enzonalasporites*, *Patinasporites*), circumpollen (e.g., *Duplicisporites*, *Paracirculina*), and alete forms (e.g., *Araucariacites*) (**Figures 7**–**9**).

The two samples DJS 1 and NRE 103 are relatively uniform in their quantitative composition (**Figure 10**). The sporomorph assemblage of sample DJS 1 is dominated by bisaccate taeniate pollen grains (69%). Second in order of abundance are the monosaccate pollen grains (13%), trilete spores (5%), bisaccate alete pollen grains (5%), and circumpollen (6%). Rare are alete pollen grains (1%) and marine sporomorphs (1%), whereas bisaccate trilete pollen grains are missing. The sporomorphs of the sample NRE 103 are dominated by bisaccate taeniate pollen grains (61%). Second in order of abundance are the trilete spores (13%), circumpollen (12%), and monosaccate pollen grains (7%). More rare are the bisaccate trilete (3%), bisaccate alete, and alete pollen grains, and marine sporomorphs (each 2%).

If the botanical affinites of the sporomorphs are considered, the conifer pollen grains are the most represented and diverse group (19/30 genera). For most conifer pollen grains, with the exception of *Klausipollenites* and perhaps *Lunatisporites*, an affinity with conifers has been suggested or proven by *in situ* findings (**Table 1**). Most of the conifer pollen are related to the Majonicaceae (4/19 genera), Cheirolepidiaceae (4/19 genera), and Voltziaceae (3/19 genera). However, also the families Podocarpaceae (*Samaropollenites*), Araucariaceae (*Araucariacites*), Pinaceae (*Abietinaepollenites*) are represented in the palynological record. The monosaccate pollen grains are assigned to the Voltziales but without any detailed botanical affinity since the so far only *in situ* record is that of the putative

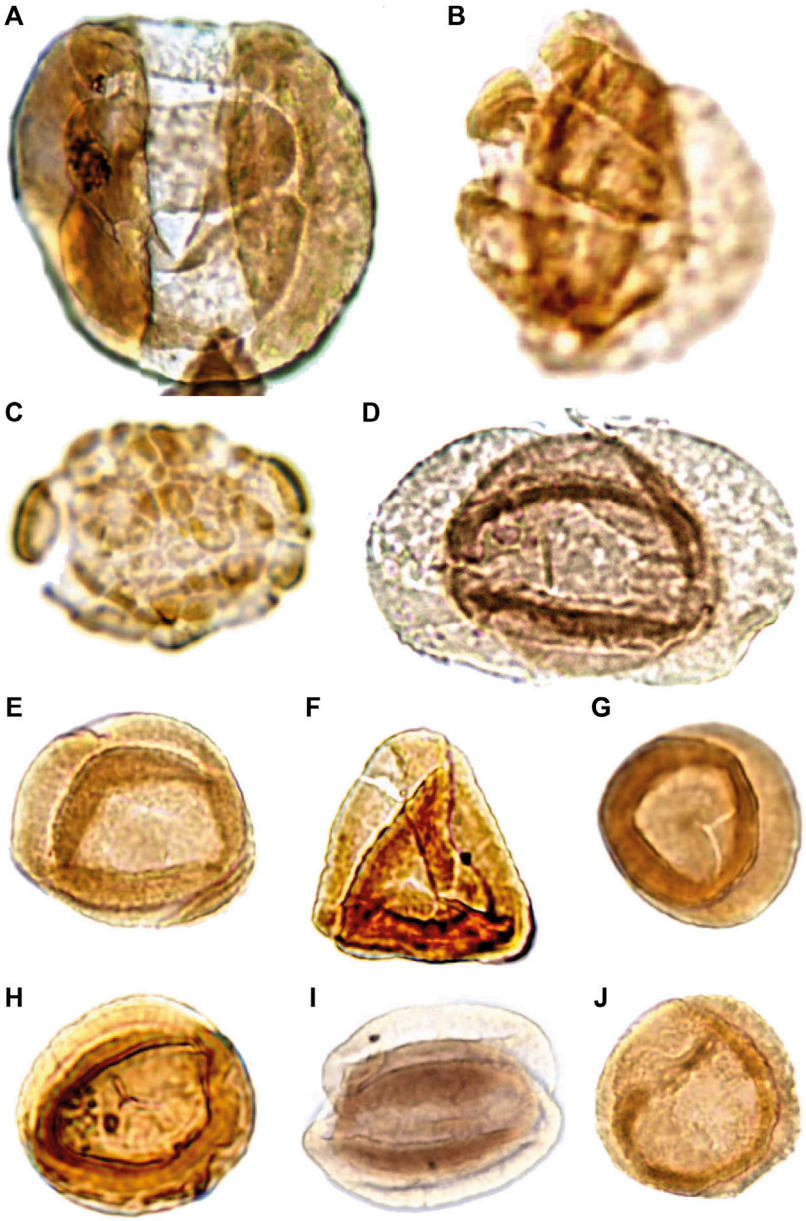

FIGURE 9 | Palynomorphs of the Heiligkreuz Fm., part III. **(A)** *Infernopollenites sulcatus*; DJS1A I, G34/1; 50 µm heigth. **(B)** *Infernopollenites* sp.; DJS1A I, F47/3; 48 µm height. **(C)** *Camerosporites secatus*; DJS1A I, N24, 27 µm diameter. **(D)** *Lueckisporites* cf. *L. virkkiae*; NRE103B III, J27, 51 µm width. **(E)** *Duplicisporites granulatus*; DJS1A II, O28/1, 32 µm diameter. **(F)** *Duplicisporites granulatus*; NRE103A IV; X38, 35 µm height. **(G)** *Duplicisporites granulatus*; DJS1A III, H42/2, 32 µm diameter. **(H)** *Paracirculina maljawkinae*; NRE103B I, D37/4, 29 µm diameter. **(I)** *Duplicisporites granulatus*; NRE103B III, S34/4, 36 µm diameter. **(J)** *Duplicisporites granulatus*; DJS1A II, K36, 32 µm diameter.

voltzialean *Patokaea silesiaca* (Pacyna et al., 2017). Among the spores dominate those of the lycophytes (4/10 genera) and the ferns (4/10 genera).

Observing the ecological distribution of the potential parent plants (**Table 1**), many taxa belong to plants typical of coastal environments (11/30 genera), which include conifers of the families Cheirolepidiaceae, Araucariaceae and Majonicaceae, as well as lycophytes (**Table 1**). Also well represented are elements typical of the lowland (9/30). This environment is mostly represented by hygrophytic elements (5/10 genera) that include representatives of the ferns and lycophytes, as well as more xerophytic elements (4/10 genera) that include seed ferns, putative conifers and/or cycadophytes. Less diverse are the hinterland elements (5/30 genera), which are mostly represented by Voltziaceae and Pinaceae conifers. The most humid areas as inferred from the palynology are interpreted as

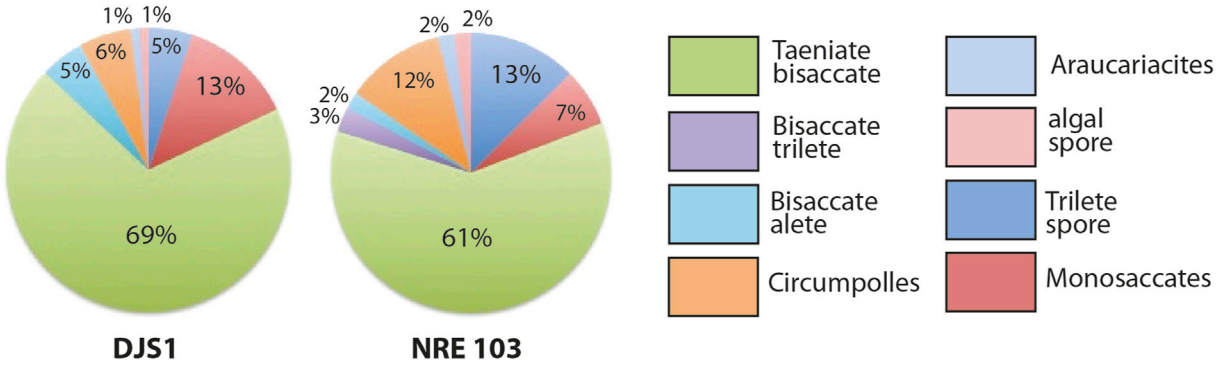

FIGURE 10 | Quantitative palynological composition of the two samples taken at the localities DJS 1 and NRE 103 (shown in **Figure 4**).

having standing fresh water (5/30 genera) and were occupied by sphenophytes, Podocarpaceae (conifers) and Schizaeaceae (ferns).

Considering the relative abundance of the sporomorphs it becomes evident that the most abundant group is that of the hinterland elements, plants that live in environments above the permanent ground water level. This is why they are often indicated as "upland" elements, although this term can be misleading and here does not refer to any sporomorphs originating from areas with significant elevation, only to those from drier environments. They reach 69% in sample DJS 1 and about 64% in NRE 103. The coastal elements are second in order of abundance, with 15–24% in DJS 1 and 21% in NRE 103. Rarer are the lowland dry elements (2–8%) and wet elements typical of standing water bodies (4–8% in DJS 1 and 13% in NRE 103).

Amber

Carnian ambers are the oldest in the fossil record with inclusions. The most abundant and diverse inclusions are from the thousands of the usually 2–6 mm sized amber droplets, discovered in the paleosols exposed at the Rifugio Dibona section (**Figure 11A**). The droplets comprise 2–5% by volume of the paleosol which is equivalent to several thousand droplets per square metre, underlining the phenomenal amber richness of the paleosols (Schmidt et al., 2006; Schmidt et al., 2012; Seyfullah et al., 2018a). The amber source plant for these droplets has been previously identified as members of the Cheirolepidiaceae (e.g., Schmidt et al., 2012).

The amber droplets are famous for its inclusions of microorganisms and small arthropods. From the amber droplets have been described perfectly preserved unicellular organisms such as algal and fungal spores, bacteria, ciliate protozoans and testate amoebae (Schmidt et al., 2006), a nematoceran fly and highly specialized phytophagous mites (Schmidt et al., 2012). The mites are four-legged and represented by four distinct morphologies. They were assigned to the new superfamily Triasacaroidea, which is probably a sister group to the Eriophyoidea (extant gall mites) (Sidorchuk et al., 2015). It was also possible to show that the fossil resin was also preserved as blebs inside the conifer leaves (**Figure 11B**). During the Late Triassic the insects developed herbivorous modes similar to the modern ones, at least at the level of leaf piercing and sucking, and chewing causing evident signs of irritation (Labandeira, 2006). Examples of this chewing damage is also observed in the dispersed plant cuticles found in the Rifugio Dibona paleosol discussed above.

However also pollen and spores were found entrapped in the amber (**Figures 6C,E–G**). The preservation is three-dimensional permitting a comparison with dispersed pollen grains extracted from the samples NRE 103 and DJS 1. Most of the amber-preserved pollen grains are bisaccate (**Figures 6C,E**), whereas spores (**Figure 6F**) and circumpollen grains (**Figure 6G**) are rare. An exceptional group of eight bisaccate pollen grains inside the amber (**Figure 6C**) belongs all to the genus *Lueckisporites*, and appear to be mature grains.

The occurrence of several very similar pollen grains of *Lueckisporites* close to the edge of the amber in a three-dimensional state excludes a previous notion that similar grains found dispersed in the sediment could be reworked from the Permian (Balme, 1979; Utting, 2004). Pollen grains of the *Lueckisporites*-type were only found *in situ* in Permian Majonicaceae conifer cones so far (e.g., Clement-Westerhof, 1974). The presence of Majonicaceae-type of conifers has been already proposed based on a similar cuticle structure of conifer shoot fragments from the Carnian of Dogna (Roghi et al., 2006b). The presence of genuine *Lueckisporites* pollen in the Triassic has been demonstrated lately also by the presence of *in situ* pollen in Anisian conifer cones (Forte et al[1]). Our new findings demonstrate that Majonicaceae-type of conifers were an inherent part of the Triassic floras at least until the Carnian in the low latitudes in the peri-Tethyan areas.

[1]Forte, G., Kustatscher, E., Nowak, H., Van Konijnenburg-Van Cittert, J. H. A. Conifer Cone and Dwarf Shoot Diversity in the Anisian (Middle Triassic) of Kühwiesenkopf/Monte Prà Della Vacca (Dolomites, NE Italy). Int. J. Pl. Sc. in revision.

TABLE 1 | The palynoflora from the paleosols exposed at the Rifugio Dibona, with inferred ecological preferences SEG, Sporomorph Eco Group; CO, Coastal; HL, Hinterland; LD, Dry Lowland; RI, River; LW, Wet Lowland.

Pollen/Spore	Botanical affinity	Ecology	SEG
Araucariacites	Conifer, Araucariaceae (Balme, 1995)	Xerophyte	CO
Abietineaepollenites	Conifer, Pinaceae (Zhang et al., 2021)	Xerophyte	HL
Brachysaccus	Conifer of uncertain affinity (Baranyi et al., 2019)	Xerophyte	LD
Camerosporites	Conifers, Cheirolepidiaceae (Baranyi et al., 2019)	Xerophyte	CO
Chordasporites	Conifers, perhaps Voltziaceae (Balme, 1995; Zhang et al., 2021)	Xerophyte	HL
Duplicisporites	Conifers, Cheirolepidiaceae (Baranyi et al., 2019)	Xerophyte	CO
Enzonalasporites	Conifers, Voltziales (Pacyna et al., 2017)	Intermediate	CO
Haberkornia	Conifer of uncertain affinity	Xerophyte	LD
Infernopollenites	Conifers, perhaps Majonicaceae (Zhang et al., 2021)	Intermediate	CO
Klausipollenites	Seed ferns (Franz et al., 2014)	Xerophyte	LD
Lueckisporites	Conifers, Majonicaceae, Voltziaceae (Clement-Westerhof, 1974; Baranyi et al., 2019)	Intermediate	CO
Lunatisporites	Conifers (Clement-Westerhof, 1974), seed ferns, Peltaspermales (Looy et al., 2001)	Intermediate	HL
Ovalipollis	Conifers, Voltziaceae (Baranyi et al., 2019), Cycadophyta (Barrón et al., 2006)	Xerophyte	LD
Paracirculina	Conifers, Cheirolepidiaceae Zhang et al., 2021)	Xerophyte	CO
Partitisporites	Conifers, Cheirolepidiaceae (Baranyi et al., 2019)	Xerophyte	CO
Patinasporites	Conifers, Majonicaceae (Baranyi et al., 2019)	Intermediate	CO
Quadraeculina	Conifer of uncertain affinity (Barrón et al., 2006)	Xerophyte	HL
Samaropollenites	Conifers, Podocarpaceae (Bonis and Kürschner, 2012)	Hygrophyte	RI
Triadispora	Conifers, Voltziaceae, *in situ* in *Sertostrobus, Darneya* (Grauvogel - Stamm, 1978)	Xerophyte	HL
Vallasporites	Conifers, Majonicaceae (Baranyi et al., 2019)	Intermediate	CO
Aratrisporites	Lycophytes, *in situ* in *Cyclostrobus, Lycostrobus* (Helby and Martin, 1965), *Lepacyclotes zeilleri* (Grauvogel - Stamm and Duringer, 1983)	Hygrophyte	CO
Calamospora	Sphenophytes, Equisetales, *in situ* in *Equisetites arenaceus* (Kelber and Van Konijnenburg - Van Cittert, 1998)	Hygrophyte	RI
Concavisporites	Ferns, Dicksoniaceae and Matoniaceae (Balme, 1995; Baranyi et al., 2019)	Hygrophyte	LW
Concentricisporites	Ferns of unknown botanical affinity (Kustatscher et al., 2010)	Hygrophyte	LW
Convolutispora	Ferns, Schizaeaceae (Barrón et al., 2006)	Hygrophyte	RI
Kraeuselisporites	Lycophytes, Lycopodiales (Balme, 1995)	Hygrophyte	LW
Leschikisporites	Lycophytes, Lycopodiales (Balme, 1995)	Hygrophyte	LW
Osmundacidites	Ferns, Osmundaceae (Balme, 1995)	Hygrophyte	LW
Simplicisporites	Lycophytes of uncertain affinity	Hygrophyte	RI
Trilites	Spore of unknown botanical affinity (Kustatscher et al., 2010)	Hygrophyte	RI

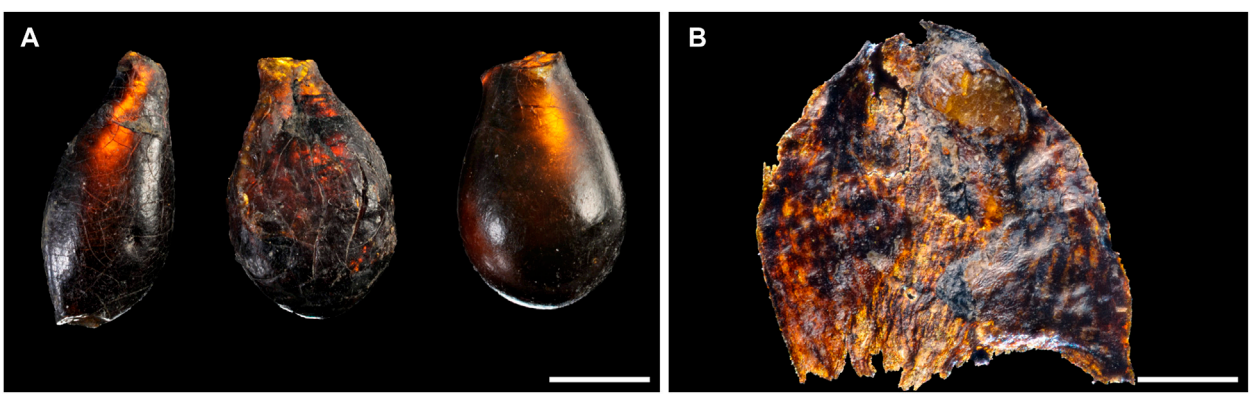

FIGURE 11 | Amber drops from the Rifugio Dibona Section **(A)** and fossil resin exuded inside the conifer leaves from the NRE 103 amber-rich paleosol **(B)**. Scale bars: 2 mm **(A)** and 1 mm **(B)**.

DISCUSSION

The Conifers of Rifugio Dibona

Plants experienced a major evolutionary radiation during the Carnian, with the co-occurrence of a mixture of primitive (Paleozoic) and modern (Mesozoic and Cenozoic) plant groups (Dal Corso et al., 2020) (**Figure 12**). One of the groups, affected more deeply by this radiation, is that of the conifers.

At the Rifugio Dibona macro-, meso-, and microplant remains show a distinct co-occurrence of a series of different conifer families. This includes the Majonicaceae represented by pollen

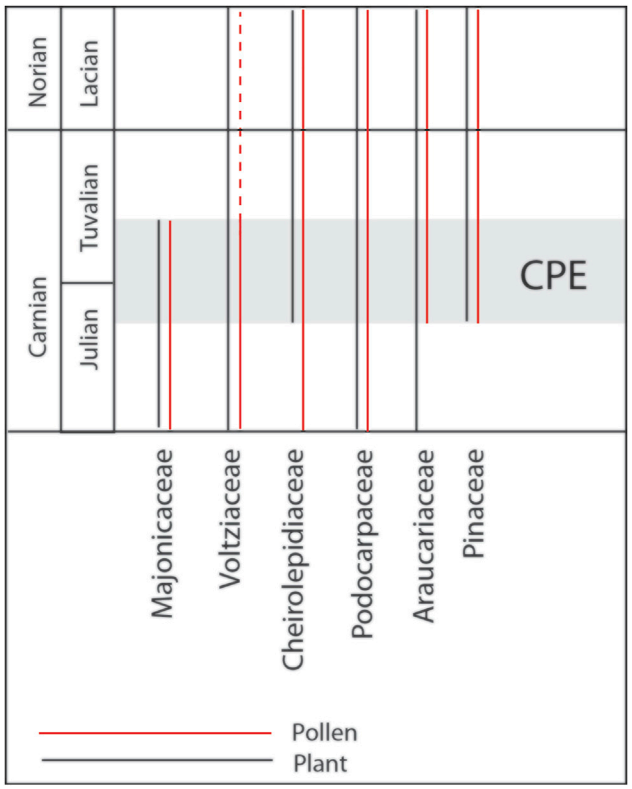

FIGURE 12 | Conifer family distributions along the Carnian based on macro- and micro fossil remains, see text for information.

grains dispersed in the sediment (*Lueckisporites* and *Lunatisporites*) and as inclusions in the amber. This conifer family is considered a typical element in the Southern Alps during the Permian (Clement Westerhof, 1987; Forte et al., 2017). It has been putatively described from the Carnian of the Julian Alps (Roghi et al., 2006b) and lately confidently recorded also from the early Middle Triassic (Anisian) of the Dolomites (Forte et al.[1]). Also, the associated monosaccate pollen grains (e.g., *Enzonalasporites* and *Patinasporites*) were probably produced by primitive voltzialean conifers, although *in situ* findings are still missing and, thus, their specific affinity is still unknown.

Typical Triassic elements are the Voltziaceae (e.g., *Triadispora*), well-represented in the microflora by bisaccate, trilete pollen grains and in the macrofossil record by small conifer shoots. Amber was not found attached to any of the voltziacean conifer shoots from Rifugio Dibona, but small amounts of amber from the Middle Triassic in the northern Dolomites demonstrated that also the Voltziaceae were resin-producers during humid climate shifts (Roghi et al., 2017; Forte et al., 2022).

[1]Forte, G., Kustatscher, E., Nowak, H., Van Konijnenburg-Van Cittert, J. H. A. Conifer Cone and Dwarf Shoot Diversity in the Anisian (Middle Triassic) of Kühwiesenkopf/Monte Prà Della Vacca (Dolomites, NE Italy). Int. J. Pl. Sc. in revision.

The circumpollen belongs to the family Cheirolepidiaceae (e.g., Roghi et al., 2006a; Kustatscher et al., 2011). The dispersed cuticles and small shoot fragments from the paleosol belong to this conifer family as well as the thousands of amber droplets that were collected from the paleosol. Summarizing, it can be said that the dominating element in the paleosol is the Cheirolepidiaceae family.

Three modern conifer families with extant representatives co-occur in the microflora of Rifugio Dibona. These are the Araucariaceae (*Araucariacites*), the Pinaceae (*Abietineaepollenites*) and the Podocarpaceae (*Samaropollenites*). This is not the oldest record of those conifer families. Several macro- and mesoremains putatively assignable to these families were indicated already before. This includes putative araucariaceous seeds already from the Early Permian of Texas (DiMichele et al., 2001) and putative needles and cuticles of podocarpacean conifers from the Permian of Jordan (Blomenkemper et al., 2018). The so far oldest confirmed macrofossil record of Pinaceae is from the Late Jurassic (Rothwell et al., 2012). Here, a mixture of macrofossil (Voltziaceae, Majonicaceae and Cheirlepidiaceae) and pollen (Voltziaceae, Majonicaceae, Araucariaceae, Pinaceae and Podocarpaceae) is presented. This diversity of different taxa of extinct and modern conifer families strongly underlines the pronounced effect of the CPE on the evolution and radiation of the conifers.

The amber-preserved microflora (**Figure 5**) provides an array of paleobotanical insights. The cluster of *Lueckisporites* grains (**Figure 5C**) inside the amber droplet but close to its surface suggests that these grains were most likely stuck to the resin surface when the resin leaked either near the pollen cone or that the droplet oozed from the cone itself. Other findings of spores and circumpollen represent isolated grains that accidentally got stuck to the resin, perhaps transported there by wind or even animals or, for circumpollen (**Figure 5**), from the same tree where the pollen was produced (Cheirolepidiaceae conifer). Studies on this material are ongoing given the high potential for paleobiological insights.

Late Triassic Amber Deposits and the Significance of Amber From the Heiligkreuz Fm.

The oldest major outpouring of amber preserved in the fossil record is associated with the CPE, and the greatest volume reported so far comes from the paleosols at Rifugio Dibona section (Roghi et al., 2006a; Seyfullah et al., 2018a). During this climate crisis, increased storm and fire events cause physical damage, so a climate change towards humid conditions were additional stressors that affected the entire terrestrial plant ecosystem triggering an increase in resin production by conifers (Seyfullah et al., 2018b).

Triassic amber is documented in some localities around the world (Seyfullah et al., 2018a) which are restricted roughly to a latitude band between 5°N and 30°N. In Europe the amber coincides well with the various pulsations of the CPE (**Figure 13**). In Italy, besides the amber from the Heiligkreuz Fm. (e.g., Rifugio Dibona, Heiligkreuz/Santa Croce, Rio

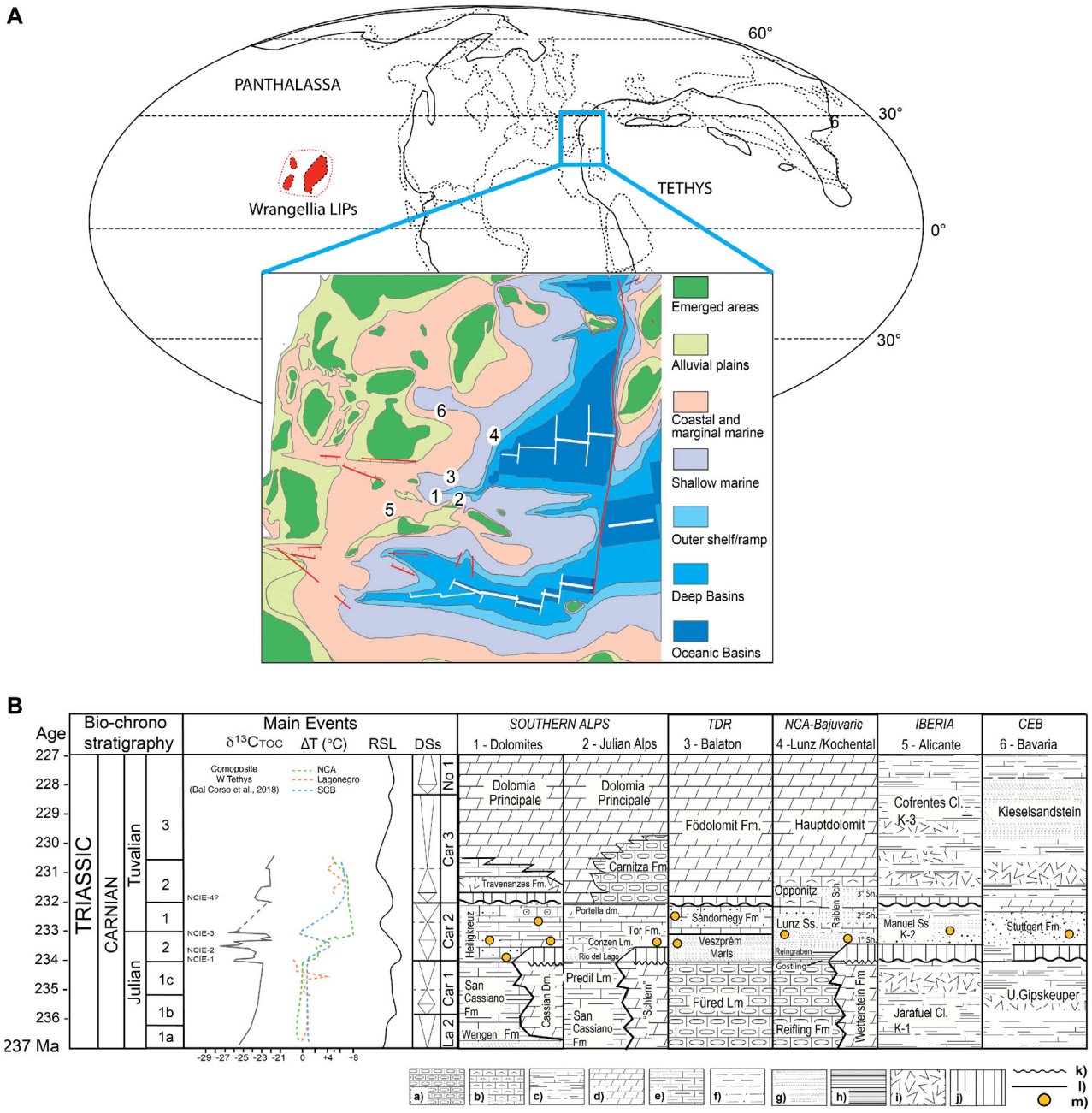

FIGURE 13 | Stratigraphic chart of CPE-aged amber deposits. **(A)** Late Triassic palaeogeography and position of the localities with amber: 1 = Dolomites; 2 = Julian Alps; 3 = Transdanubian Range; 4 = Northern Calcareous Alps; 5 = Iberia; 6 = Bavaria; the map is after Bernardi et al., 2018, **(B)** Lithostratigraphic scheme for the Carnian formations with amber findings. Julian 1a = *Daxatina canadensis* subzone, 1b = *Trachyceras aon* subzone, 1c = *Trachyceras aonoides* subzone; Julian 2 = *Austrotrachyceras austriacum* zone; Tuvalian 1 = *Tropites dilleri* zone, Tuvalian 2 = *Tropites subbullatus* zone, Tuvalian 3 = *Anatropites spinosus* zone. Lithology: **(a)** = Cherty limestone, **(b)** = Bioclastic limestone, **(c)** = Limy marlstone, **(d)** = Dolostone, **(e)** = Marly limestone, **(f)** = Siltstone, **(g)** = Sandstone, **(h)** = Black shale, **(i)** = Evaporites, **(j)** = Hiatus, **(k)**= Unconformity, **(l)** = Conformity, **(m)** = Amber.

Falzarego, Rif. San Marco, Rifugio Mietres, and Rumerlo sections), amber is also found in the Dogna Valley (Julian Alps) from Tor Fm. (Gianolla et al., 1998a; Preto et al., 2005; Roghi et al., 2006a), both are Julian in age. Small amounts of Carnian amber have been reported from Austria, from the Lunz Fm. at Lunz (Vávra, 1984; Vávra, 2005; Roghi et al., 2010; Fischer

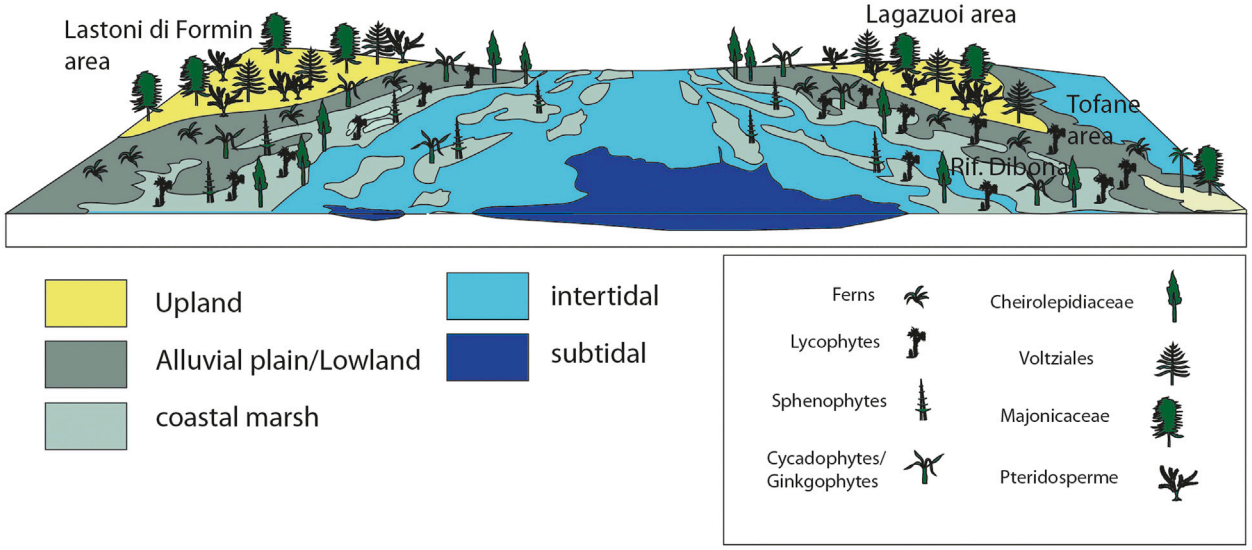

FIGURE 14 | Reconstruction of the environment and the vegetation at the time of origin of the amber-rich paleosol.

et al., 2017), in the Raibler Schichten in Kochental (Pichler, 1868; Gianolla et al., 1998b) and in the Stuttgart Fm. near Neuwelt (Switzerland) (**Figure 13**). Kelber and Hansch (1995) figure amber (p. 89, fig. 180) from the Schilfsandstein (Stuttgart Fm.) of northern Bavaria, Germany. In Hungary, a sole piece has been recorded from a drill core of the Barnag Member of the Sándorhegy Fm. and dated to the early Tuvalian (Csillag and Földvári, 2007) while microscopic droplets in palynological slides are reported from the Julian Veszprem Marls and Tuvalian Sándorhegy Formation from the Zsámbék-14 borehole (Baranyi et al., 2018). Spanish (Alicante) Carnian amber (millimetric droplets) has been reported and figured from the Keuper (K2, Manuel Formation) but no further details are known (Peñalver and Delclòs, 2010).

Triassic amber finding outside of Europe do not have a precise dating until now, or do probably not coincide with the time interval of the CPE. For example, the amber found inside seeds in South Africa (Ansorge, 2007), in the Molteno Formation (Karoo Basin) is slightly younger with respect to the CPE; it is probably Tuvalian in age (Langer, 2005), whereas the amber from the Triassic Blue Mesa Member of the Chinle Formation of Arizona (United States) (Litwin and Ash, 1991) is most likely younger, potentially even Norian in age (Seyfullah et al., 2018a). In the Fingal Valley Upper Triassic Coal Measures of the Upper Parmeener Supergroup, Tasmania, small amounts of ambers with very few miniscule inclusions are reported (Stilwell et al., 2020).

Amber in the Dolomites was found throughout the Heiligkreuz Fm. (Preto and Hinnov, 2003; Roghi et al., 2006a; Breda et al., 2009) as early as the first onset of the CPE as included from the base of the Heiligkreuz Fm., within the Borca member, and becoming very abundant in the upper part of the Formation, in the Dibona sandstones. All these findings allow us to be framed in the two million years that are the time represented by the Heiligkreuz Formation equivalent to the CPE.

Paleoenvironmental Reconstruction

An attempt is made here for the first time to reconstruct the landscape, environment and vegetation at the time of origin of the paleosols of the Heiligkreuz Fm. based on the sedimentological, palynological and paleobotanical content of the studied horizons. The analysis of the facies and the evolution of the environments show that the area between Lastoni di Formin and Lagazuoi were subjected during the deposition of the Borca Member (Heiligkreuz Fm.) to a progressive infilling of residual basinal areas culminated with a regional flattening recorded by the deposition of loferitic dolostones and marly limestones organized in peritidal cyclothems bounded at the top by karstic dissolution and paleosols (Lithofacies D in Preto and Hinnov, 2003).

The emerged land masses, colonized by plants and animals, were almost entirely flat. The area was characterized by an articulated landscape with sub- and intertidal settings as well as coastal marshes (**Figure 14**). The areas, characterized today by the important mountain ridges of Lastoni di Formin, Lagazuoi and Tofane, were covered by a mixture of alluvial plain to lowland settings and some areas that were in a more elevated position, although with a very limited vertical extension above the sea level, the so-called up- or hinterland area. The environment was thus a generally wet but also halophytic environment where water was available the entire year long and the plants were adapted to excessive salt (in the water, soil and in the wind) and experienced, thus some physiological drought. The reconstructed paleotopography, based on

geological and sedimentological data, forms the basis of a vegetation type that rarely has been described from coeval settings. It influences deeply also the understanding of the composition of the vegetation covering it.

The Palynological Climate Signal of the Rifugio Dibona Section

The Rifugio Dibona section is one of the most iconic outcrops for the study of the CPE in a terrestrial/marginal marine setting. Detailed geochemical and sedimentological studies have been carried out (e.g., Gattolin et al., 2013; Dal Corso et al., 2015; Dal Corso et al., 2018) tightly constraining the sedimentological succession corresponding to the CPE.

Additionally, the first studies on Carnian amber and its biological inclusions were carried out (Schmidt et al., 2006; Schmidt et al., 2012; Sidorchuk et al., 2015). Nonetheless, at a first glance the quantitative composition of the macroflora and microflora reported here does not appear to reflect the typical spike in humid elements expected during the CPE. The palynological assemblages are mainly composed of elements from the hinterland and the coastal areas, which are typically xerophytes. However, the lowland elements, living in the environment most sensitive to climate changes, are composed of more abundant hygrophytic than xerophytic elements.

So, does this iconic section exposing the richest amber-bearing paleosol worldwide, constrained by biostratigraphy, geochemistry and sedimentology, in some time not reflect a shift to humid climate? In order to understand the effect of the CPE on the plant communities, the environment and landscape they are living in, as well as the environmental preferences and adaptations of the various plants, has to be taken into account. The landscape reconstructed by the geology and sedimentology is that of a complex coastal and tidal setting. The palynological assemblage is dominated by conifers, which are predominantly considered xerophytic elements. The conifers (e.g., Cheirolepidiaceae, Majonicaceae) had colonized a coastal environment, where water is abundant but not necessarily always available for the plants. Their abundance does, thus, not indicate a drier climate, but rather a xerophytic setting in a local landscape due to a rise in sea water level.

In a larger context, palynological analyses of Carnian (Upper Triassic) successions are well known in the Alpine area from the Dolomites, Carnic Alps, Julian Alps and Northern Calcareous Alps, and the Lunz area, corresponding to the so called northwestern Tethyian margin (Roghi et al., 2010; Mueller et al., 2016b; Dal Corso et al., 2018; Kustatscher et al., 2018). These palynological analyses do provide clear evidence of a shift towards a more humid climatic regime which falls within the framework of the CPE (Dal Corso et al., 2020).

CONCLUSION

The Heiligkreuz Formation at the Rifugio Dibona is very expanded and crops out over a thickness of 160 m. This section has been studied in detail from a sedimentological and geochemical view, making it potentially one of the best preserved and continuous sections in the Dolomites. Since the CPE is so well-constrained sedimentologically and geochemically and clearly delimited, it is possible to reconstruct the flora even if the landscape is untypical and the composition of the flora at a first glance would not automatically indicate a humid event. This shows how important it is to keep in consideration also the landscape setting and requirements when studying climate changes. This case study underlines how climate changes influence the floral and faunal composition but cannot completely override the requirements and restrictions of the landscape itself.

On the other hand, it is possible that it is exactly this complex landscape with a high preservation potential in the paleosol horizons that permits to identify the concurrent presence of ancestral (Majonicaceae), Triassic/Mesozoic (Voltziaceae, Cheirolepidiaceae) and modern conifer families (Araucariaceae, Pinaceae and Podocarpaceae) both among the palynomorphs and the macroremains. A high-resolution palynological study in the future will show whether this co-occurrence is restricted to the CPE only, or is part of a general floral turnover or replacement during the Carnian and if the same type of dynamics can be observed also for the fern group.

One of the causes for the simultaneous occurrence of so many different conifer families could be the latitudinal shifts of the biomes due to the four distinct NCIE shifts linked to different LIP volcanic pulses. These would have affected both the precipitation pattern and mean annual temperature (**Figure 13**) and give origin to migrations fluxes of plants and animals. This theory is supported by the observed immigration pattern of several types of pollen from the high to the low latitudes during the CPE. The extremely dynamic climate and landscape pattern could explain the exceptional mixture of "older" residual and modern conifer families observed in the Rifugio Dibona section. It also would trigger the evolution of the terrestrial and marine plant and animals and increase the origination and speciation rates within the newly developed plant and animal groups (e.g., Dipteridaceae, Bennettitales).

So far the study of the plant fossils is restricted to two main intervals in the Dibona section, the sandstone bank and the paleosols discussed above. The paleosoils yielded amber droplets in association with exceptionally preserved isolated leaf fragments and small shoot and cone fragments. This permits not only to integrate the palynomorph assemblage but shows also the high potential of mesofossil collections. However, it raises also the question whether this association of exceptionally preserved dispersed plant mesofossils with amber droplets is a local effect of the landscape or linked to the extent of the volcanic activity during the CPE.

DATA AVAILABILITY STATEMENT

The original contributions presented in the study are included in the article, further inquiries can be directed to the corresponding author.

AUTHOR CONTRIBUTIONS

All authors listed have made a substantial, direct, and intellectual contribution to the work and approved it for publication.

FUNDING

Funds for open access was provided by the University of Vienna.

ACKNOWLEDGMENTS

We warmly thank Paolo Fedele (Cortina d'Ampezzo) for his enthusiasm and sharing his findings with us. We would wish to thank Miriam A. Slodownik (Göttingen) for preparing amber droplets for microscopic analysis and for detecting plant fossils in the palaeosol samples, and Laura Skadell (Göttingen) for screening numerous amber droplets for inclusions. The reviewers Daoliang Chu (Wuhan) and Grzegorz Pacyna (Kraków) are thanked for their helpful and constructive remarks.

REFERENCES

Ansorge, J. (2007). "Upper Triassic Insects and Amber from Lesotho (South Africa)," in *FossilsX3: Insects, Arthropods, Amber (Abstracts)*. Editor J. Alonso (Spain: Vitoria-Gasteiz), 52–54.

Balme, B. E. (1995). Fossil *In Situ* Spores and Pollen Grains: an Annotated Catalogue. *Rev. Palaeobot. Palynology* 87, 81–323. doi:10.1016/0034-6667(95)93235-x

Balme, B. E. (1979). Palynology of Permian-Triassic Boundary Beds at Kap Stosch, East Greenland. *Meddelelser Om. Grønl.* 200 (6), 1–37.

Baranyi, V., Miller, C. S., Ruffell, A., Hounslow, M. W., and Kürschner, W. M. (2018). A Continental Record of the Carnian Pluvial Episode (CPE) from the Mercia Mudstone Group (UK): Palynology and Climatic Implications. *J. Geol. Soc.* 176, 149–166. doi:10.1144/jgs2017-150

Baranyi, V., Rostási, Á., Raucsik, B., and Kürschner, W. M. (2019). Palynology and Weathering Proxies Reveal Climatic Fluctuations during the Carnian Pluvial Episode (CPE) (Late Triassic) from Marine Successions in the Transdanubian Range (Western Hungary). *Glob. Planet. Change* 177, 157–172. doi:10.1016/j.gloplacha.2019.01.018

Barrenechea, J. F., López-Gómez, J., and De La Horra, R. (2018). Sedimentology, Clay Mineralogy and Palaeosols of the Mid-carnian Pluvial Episode in Eastern Spain: Insights into Humidity and Sea-Level Variations. *J. Geol. Soc.* 175, 993–1003. doi:10.1144/jgs2018-024

Barrón, E., Gómez, J. J., Goy, A., and Pieren, A. P. (2006). The Triassic-Jurassic Boundary in Asturias (Northern Spain): Palynological Characterisation and Facies. *Rev. Palaeobot. Palynology* 138, 187–208. doi:10.1016/j.revpalbo.2006.01.002

Bernardi, M., Gianolla, P., Petti, F. M., Mietto, P., and Benton, M. J. (2018). Dinosaur Diversification Linked with the Carnian Pluvial Episode. *Nat. Commun.* 9, 1499. doi:10.1038/s41467-018-03996-1

Blomenkemper, P., Kerp, H., Abu Hamad, A., DiMichele, W. A., and Bomfleur, B. (2018). A Hidden Cradle of Plant Evolution in Permian Tropical Lowlands. *Science* 362, 1414–1416. doi:10.1126/science.aau4061

Bonis, N. R., and Kürschner, W. M. (2012). Vegetation History, Diversity Patterns, and Climate Change across the Triassic/Jurassic Boundary. *Paleobiology* 38, 240–264. doi:10.1666/09071.1

Bosellini, A., Masetti, D., and Neri, C. (1982). "La geologia del passo del Falzarego," in *Guida alla Geologia del Sudalpino centro-orientale*. Editors A. Castellarin and G. B. Vai (Rome: SOCIETÀ GEOLOGICA ITALIANA), 273–278.

Bosellini, A. (1984). Progradation Geometries of Carbonate Platforms: Examples from the Triassic of the Dolomites, Northern Italy. *Sedimentology* 31, 1–24. doi:10.1111/j.1365-3091.1984.tb00720.x

Breda, A., and Preto, N. (2011). Anatomy of an Upper Triassic Continental to Marginal-Marine System: the Mixed Siliciclastic-Carbonate Travenanzes Formation (Dolomites, Northern Italy). *Sedimentology* 58, 1613–1647. doi:10.1111/j.1365-3091.2011.01227.x

Breda, A., Preto, N., Roghi, G., Furin, S., Meneguolo, R., Ragazzi, E., et al. (2009). The Carnian Pluvial Event in the Tofane Area (Cortina d'Ampezzo, Dolomites, Italy). *Geo.Alp.* 6, 80–115.

Buratti, N., and Cirilli, S. (2007). Microfloristic Provincialism in the Upper Triassic Circum-Mediterranean Area and Palaeogeographic Implication. *Geobios* 40, 133–142. doi:10.1016/j.geobios.2006.06.003

Césari, S. N., and Colombi, C. E. (2013). A New Late Triasssic Phytogeographical Scenario in Westernmost Gondwana. *Nat. Commun.* 4, 1889. doi:10.1038/ncomms2917

Clement-Westerhof, J. A. (1987). Aspects of Permian Palaeobotany and Palynology, VII. The Majonicaceae, a New Family of Late Permian Conifers. *Rev. Palaeobot. Palynology* 52, 375–402. doi:10.1016/0034-6667(87)90066-2

Clement-Westerhof, J. A. (1974). *In Situ* pollen from Gymnospermous Cones from the Upper Permian of the Italian Alps - A Preliminary Account. *Rev. Palaeobot. Palynology* 17, 63–73. doi:10.1016/0034-6667(74)90092-X

Colombi, C., Martínez, R. N., Césari, S. N., Alcober, O., Limarino, C. O., and Montañez, I. (2021). A High-Precision U-Pb Zircon Age Constraints the Timing of the Faunistic and Palynofloristic Events of the Carnian Ischigualasto Formation, San Juan, Argentina. *J. S. Am. Earth Sci.* 111, 103433. doi:10.1016/j.jsames.2021.103433

Csillag, G., and Földvári, M. (2007). "Upper Triassic Amber Fragments from the Balaton Highlands, Hungary," in *Annual Report of the Geological Institute of Hungary 2005* (Budapest: Geological Institute of Hungary), 37–46. [in Hungarian].

Dal Corso, J., Bernardi, M., Sun, Y., Song, H., Seyfullah, L. J., Preto, N., et al. (2020). Extinction and Dawn of the Modern World in the Carnian (Late Triassic). *Sci. Adv.* 6, eaba0099. doi:10.1126/sciadv.aba0099

Dal Corso, J., Gianolla, P., Newton, R. J., Franceschi, M., Roghi, G., Caggiati, M., et al. (2015). Carbon Isotope Records Reveal Synchronicity between Carbon Cycle Perturbation and the "Carnian Pluvial Event" in the Tethys Realm (Late Triassic). *Glob. Planet. Change* 127, 79–90. doi:10.1016/j.gloplacha.2015.01.013

Dal Corso, J., Gianolla, P., Rigo, M., Franceschi, M., Roghi, G., Mietto, P., et al. (2018). Multiple Negative Carbon-Isotope Excursions during the Carnian Pluvial Episode (Late Triassic). *Earth-Science Rev.* 185, 732–750. doi:10.1016/j.earscirev.2018.07.004

Dal Corso, J., Mietto, P., Newton, R. J., Pancost, R. D., Preto, N., Roghi, G., et al. (2012). Discovery of a Major Negative 13C Spike in the Carnian (Late Triassic) Linked to the Eruption of Wrangellia Flood Basalts. *Geology* 40, 79–82. doi:10.1130/g32473.1

Dal Corso, J., Preto, N., Kustatscher, E., Mietto, P., Roghi, G., and Jenkyns, H. C. (2011). Carbon-isotope Variability of Triassic Amber, as Compared with Wood and Leaves (Southern Alps, Italy). *Palaeogeogr. Palaeoclimatol. Palaeoecol.* 302, 187–193. doi:10.1016/j.palaeo.2011.01.007

Dal Corso, J., Song, H. J., Callegaro, S., Chu, D. L., Sun, Y. D., Hilton, J., et al. (2022). Environmental Crises at the Permian–Triassic Mass Extinction. *Nat. Rev. Earth Environ.*. doi:10.1038/s43017-021-00259-4

De Zanche, V., Gianolla, P., Mietto, P., Siorpaes, C., and Vail, P. R. (1993). Triassic Sequence Stratigraphy in the Dolomites (Italy). *Mem. Sci. Geol.* 45, 1–27.

De Zanche, V., Gianolla, P., and Roghi, G. (2000). Carnian stratigraphy in the Raibl/Cave del Predil area (Julian Alps, Italy). *Ecl. Geol. Helv.* 93, 331–347.

DiMichele, W., Mamay, S., Chaney, D., Hook, R., and Nelson, W. (2001). An Early Permian Flora with Late Permian and Mesozoic Affinities From North-Central Texas. *J. Paleontol.* 75 (2), 449–460. doi:10.1666/0022-3360(2001)0752.0.CO;2

Dolby, J. H., and Balme, B. E. (1976). Triassic Palynology of the Carnarvon Basin, Western Australia. *Rev. Palaeobot. Palynology* 22, 105–168. doi:10.1016/0034-6667(76)90053-1

Fischer, T. C., Sonibare, O. O., Aschauer, B., Kleine-Benne, E., Braun, P., and Meller, B. (2017). Amber from the Alpine Triassic of Lunz (Carnian, Austria): a Classic Palaeobotanical Site. *Palaeontology* 60, 743–759. doi:10.1111/pala.12313

Forte, G., Kustatscher, E., Ragazzi, E., and Roghi, G. (2022). Amber Droplets in the Southern Alps (NE Italy): a Link between Their Occurrences and Main Humid Episodes in the Triassic. *Riv. It. Paleontol. Strat.* 128, 69–79. doi:10.54103/2039-4942/15381

Forte, G., Kustatscher, E., Van Konijnenburg-van Cittert, J. H. A., Looy, C. V., and Kerp, H. (2017). Conifer Diversity in the Kungurian of Europe-Evidence from Dwarf-Shoot Morphology. *Rev. Palaeobot. Palynology* 244, 308–315. doi:10.1016/j.revpalbo.2017.01.004

Franz, M., Nowak, K., Berner, U., Heunisch, C., Bandel, K., Röhling, H.-G., et al. (2014). Eustatic Control on Epicontinental Basins: The Example of the Stuttgart Formation in the Central European Basin (Middle Keuper, Late Triassic). *Glob. Planet. Change* 122, 305–329. doi:10.1016/j.gloplacha.2014.07.010

Gattolin, G., Breda, A., and Preto, N. (2013). Demise of Late Triassic Carbonate Platforms Triggered the Onset of a Tide-Dominated Depositional System in the Dolomites, Northern Italy. *Sediment. Geol.* 297, 38–49. doi:10.1016/j.sedgeo.2013.09.005

Gattolin, G., Preto, N., Breda, A., Franceschi, M., Isotton, M., and Gianolla, P. (2015). Sequence Stratigraphy After the Demise of a High-Relief Carbonate Platform (Carnian of the Dolomites): Sea-Level and Climate Disentangled. *Palaeogeogr. Palaeoclimatol. Palaeoecol.* 423, 1–17.

Gianolla, P., De Zanche, V., and Mietto, P. (1998b). "Triassic Sequence Stratigraphy in the Southern Alps (Northern Italy): Definition of Sequences and Basin Evolution," in *Mesozoic and Cenozoic Sequence Stratigraphy of European Basin* (Tulsa/Oklahoma: SEPM Special Publication), 719–747.

Gianolla, P., De Zanche, V., and Roghi, G. (2003). An Upper Tuvalian (Triassic) Platform-Basin System in the Julian Alps: the Start-Up of the Dolomia Principale (Southern Alps, Italy). *Facies* 49, 135–150. doi:10.1007/s10347-003-0029-7

Gianolla, P., Morelli, C., Cucato, M., and Siorpaes, C. (2018). Note Illustrative della Carta Geologica d'Italia alla scala 1:50.000, Foglio 016, Dobbiaco, ISPRA, 2018, Roma. *Systemcart*, 1–283.

Gianolla, P., Roghi, G., and Ragazzi, E. (1998a). Upper Triassic Amber in the Dolomites (Northern Italy). A Paleoclimatic Indicator? *Riv. It. Paleontol. Strat.* 104, 381–390.

Grauvogel-Stamm, L. (1978). *La flore du Grès à Voltzia (Buntsandstein supérieur) des Vosges du Nord (France). Morphologie, anatomie, interprétations phylogénique et paléogéographique (= Université Louis Pasteur de Strasbourg*. Strasbourg: Université Louis Pasteur

Grauvogel-Stamm, L., and Duringer, P. (1983). Annalepis zeilleri Fliche 1910 emend., un organe reproducteur de Lycophyte de la Lettenkohle de l'Est de la France. Morphologie, spores in situ et paléoécologie. *Geologische Rundschau* 72, 23–51.

Helby, R. J., and Martin, A. R. H. (1965). Cyclostrobus gen. nov., Cones of Lycopsidean Plants from the Narrabeen Group (Triassic) of New South Wales. *Aust. J. Botany* 13, 389–404.

Keim, L., and Brandner, R. (2001). Facies Interfingering and Synsedimentary Tectonics on Late Ladinian-Early Carnian Carbonate Platforms (Dolomites, Italy). *Int. J. Earth Sci.* 90, 813–830. doi:10.1007/s005310000192

Keim, L., Brandner, R., Krystyn, L., and Mette, W. (2001). Termination of Carbonate Slope Progradation: an Example from the Carnian of the Dolomites, Northern Italy. *Sediment. Geol.* 143, 303–323. doi:10.1016/S0037-0738(01)00106-3

Kelber, K.-P., and Hansch, W. (1995). Keuperpflanzen. Die Enträtselung einer über 200 Millionen Jahre alten Flora. *Museo* 11, 1–157.

Kelber, K.-P., and Van Konijnenburg-Van Cittert, J. H. A. (1998). Equisetites arenaceus from the Upper Triassic of Germany with Evidence for Reproductive Strategies. *Rev. Palaeobot. Palynol.* 100, 1–6.

Kustatscher, E., Ash, S. R., Karasev, E., Pott, C., Vajda, V., Yu, J., et al. (2018). "Flora of the Late Triassic," in *The Late Triassic World*. Editor L. H. Tanner (Cham: Springer), Vol. 46, 545–622. Topics in Geobiology. doi:10.1007/978-3-319-68009-5_13

Kustatscher, E., Bizzarrini, F., and Roghi, G. (2011). Plant Fossils in the Cassian Beds and Other Carnian Formations of the Southern Alps (Italy). *Geo.Alp.* 8, 146–155.

Kustatscher, E., Michael, W., and Van Konijnenburg-Van Cittert, J. H. A. (2010). Lycophytes from the Middle Triassic (Anisian) Locality Kühwiesenkopf (Monte Prà della Vacca) in the Dolomites (Northern Italy).. *Palaeontology* 53, 595–626. doi:10.1111/j.1475-4983.2010.00948.x

Kustatscher, E., Nowak, H., Forte, G., Roghi, G., and Van Konijnenburg-Van Cittert, J. H. A. (2019). Triassic Macro- and Microfloras of the Eastern Southern Alps. *Geo.Alp.* 16, 5–43.

Labandeira, C. C. (2006). The Four Phases of Plant-Arthropod Associations in Deep Time. *Geol. Acta* 4, 409–438.

Langer, M. C. (2005). Studies on Continental Late Triassic Tetrapod Biochronology. II. The Ischigualastian and a Carnian Global Correlation. *J. South Am. Earth Sci.* 19, 219–239

Litwin, R. J., and Ash, S. R. (1991). First Early Mesozoic Amber in the Western Hemisphere. *Geol* 19, 273–276. doi:10.1130/0091-7613(1991)019<0273:femait>2.3.co;2

Looy, C. V., Twitchett, R. J., Dilcher, D. L., Van Konijnenburg-Van Cittert, J. H., and Visscher, H. (2001). Life in the End-Permian Dead Zone. *Proc. Natl. Acad. Sci. U.S.A.* 98 (14), 7879–7883. doi:10.1073/pnas.131218098

Lu, J., Zhang, P., Dal Corso, J., Yang, M., Wignall, P. B., Greene, S. E., et al. (2021). Volcanically Driven Lacustrine Ecosystem Changes during the Carnian Pluvial Episode (Late Triassic). *Proc. Natl. Acad. Sci. U.S.A.* 118 (40), e2109895118. doi:10.1073/pnas.2109895118

Maron, M., Muttoni, G., Dekkers, M. J., Mazza, M., Roghi, G., Breda, A., et al. (2017). Contribution to the Magnetostratigraphy of the Carnian: New Magneto-Biostratigraphic Constraints from Pignola-2 and Dibona Marine Sections, Italy. *nos* 50, 187–203. doi:10.1127/nos/2017/0291

Mazaheri-Johari, M., Gianolla, P., Mather, T. A., Frieling, J., Chu, D., and Dal Corso, J. (2021). Mercury Deposition in Western Tethys during the Carnian Pluvial Episode (Late Triassic). *Sci. Rep.* 11, 17339. doi:10.1038/s41598-021-96890-8

Miller, C. S., Peterse, F., da Silva, A.-C., Baranyi, V., Reichart, G. J., and Kürschner, W. M. (2017). Astronomical Age Constraints and Extinction Mechanisms of the Late Triassic Carnian Crisis. *Sci. Rep.* 7, 2557. doi:10.1038/s41598-017-02817-7

Mueller, S., Hounslow, M. W., and Kürschner, W. M. (2016a). Integrated Stratigraphy and Palaeoclimate History of the Carnian Pluvial Event in the Boreal Realm; New Data from the Upper Triassic Kapp Toscana Group in Central Spitsbergen (Norway). *J. Geol. Soc.* 173, 186–202. doi:10.1144/jgs2015-028

Mueller, S., Krystyn, L., and Kürschner, W. M. (2016b). Climate Variability during the Carnian Pluvial Phase - A Quantitative Palynological Study of the Carnian Sedimentary Succession at Lunz Am See, Northern Calcareous Alps, Austria. *Palaeogeogr. Palaeoclimatol. Palaeoecol.* 441, 198–211. doi:10.1016/j.palaeo.2015.06.008

Neri, C., Gianolla, P., Furlanis, S., Caputo, R., and Bosellini, A. (2007). *Carta Geologica d'Italia Alla Scala 1:50000, Foglio 29 Cortina d'Ampezzo, and Note Illustrative*. Roma: APAT, 200.

Nowak, H., Schneebeli-Hermann, E., and Kustatscher, E. (2018). Correlation of Lopingian to Middle Triassic Palynozones. *J. Earth Sci.* 29, 755–777. doi:10.1007/s12583-018-0790-8

Pacyna, G., Barbacka, M., Zdebska, D., Ziaja, J., Fijałkowska-Mader, A., Bóka, K., et al. (2017). A New Conifer from the Upper Triassic of Southern Poland Linking the Advanced Voltzialean Type of Ovuliferous Scale with *Brachyphyllum - Pagiophyllum* -like Leaves. *Rev. Palaeobot. Palynology* 245, 28–54. doi:10.1016/j.revpalbo.2017.05.015

Peñalver, E., and Delclòs, X. (2010). "Spanish Amber," in *Biodiversity of Fossils in Amber from the Major World Deposits*. Editor D. Penney(Manchester, UK: Siri Scientific Press), 236–270.

Pichler, A. (1868). Beiträge zur Geognosie Tirols. XI. Fossiles Harz. *J. K.-k. Geol. Reich.* 18, 45–52.

Preto, N., and Hinnov, L. A. (2003). Unraveling the Origin of Carbonate Platform Cyclothems in the Upper Triassic Durrenstein Formation (Dolomites, Italy). *J. Sediment. Res.* 73, 774–789. doi:10.1306/030503730774

Preto, N., Kustatscher, E., and Wignall, P. B. (2010). Triassic Climates - State of the Art and Perspectives. *Palaeogeogr. Palaeoclimatol. Palaeoecol.* 290, 1–10. doi:10.1016/j.palaeo.2010.03.015

Preto, N., Roghi, G., and Gianolla, P. (2005). Carnian Stratigraphy of the Dogna Area (Julian Alps, Northern Italy): Tessera of a Complex Palaeogeography. *Boll. Soc. Geol. It.* 124, 269–279.

Retallack, G. J., Veevers, J. J., and Morante, R. (1996). Global Coal Gap between Permian-Triassic Extinction and Middle Triassic Recovery of Peat-Forming Plants. *Geol. Soc. Am. Bull.* 108, 195–207. doi:10.1130/0016-7606(1996)108<0195:gcgbpt>2.3.co;2

Rigo, M., Preto, N., Roghi, G., Tateo, F., and Mietto, P. (2007). A Rise in the Carbonate Compensation Depth of Western Tethys in the Carnian (Late Triassic): Deep-Water Evidence for the Carnian Pluvial Event. *Palaeogeogr. Palaeoclimatol. Palaeoecol.* 246, 188–205. doi:10.1016/j.palaeo.2006.09.013

Roghi, G., Gianolla, P., Minarelli, L., Pilati, C., and Preto, N. (2010). Palynological Correlation of Carnian Humid Pulses throughout Western Tethys. *Palaeogeogr. Palaeoclimatol. Palaeoecol.* 290, 89–106. doi:10.1016/j.palaeo.2009.11.006

Roghi, G., Kustatscher, E., Ragazzi, E., and Giusberti, L. (2017). Middle Triassic Amber Associated with Voltzialean Conifers from the Southern Alps of Italy. *Riv. It. Paleontol. Strat.* 123, 193–202.

Roghi, G., Kustatscher, E., and van Konijnenburg-van Cittert, J. H. A. (2006b). Late Triassic Plants from Julian Alps (Italy). *Boll. Soc. Paleont. It.* 45, 133–140.

Roghi, G. (2004). Palynological investigations in the Carnian of the Cave del Predil area (Julian Alps, NE Italy). *Rev. Palaeobot. Palynology* 132, 1–35. doi:10.1016/j.revpalbo.2004.03.001

Roghi, G., Ragazzi, E., and Gianolla, P. (2006a). Triassic Amber of the Southern Alps (Italy). *Palaios* 21, 143–154. doi:10.2110/palo.2005.p05-68

Rothwell, G. W., Mapes, G., Stockey, R. A., and Hilton, J. (2012). The Seed Cone Eathiestrobus Gen. nov.: Fossil Evidence for a Jurassic Origin of Pinaceae. *Am. J. Bot.* 99, 708–720. doi:10.3732/ajb.1100595

Ruffell, A., Simms, M. J., and Wignall, P. B. (2016). The Carnian Humid Episode of the Late Triassic: A Review. *Geol. Mag.* 153, 271–284. doi:10.1017/S0016756815000424

Russo, F., Neri, C., Mastandrea, A., and Laghi, G. (1991). Depositional and diagenetic history of the Alpe di Specie (Seelandalpe) fauna (Carnian, northeastern Dolomites). *Facies* 25, 187–210. doi:10.1007/bf02536759

Sadowski, E.-M., Schmidt, A. R., Seyfullah, L. J., Solórzano-Kraemer, M. M., Neumann, C., Perrichot, V., et al. (2021). Conservation, Preparation and Imaging of Diverse Ambers and Their Inclusions. *Earth-Sc. Rev.* 220, 103653. doi:10.1016/j.earscirev.2021.103653

Scherer, M. (1977). Preservation, Alteration and Multiple Cementation of Aragonitic Skeletons from the Cassian Beds (U. Triassic, Southern Alps): Petrographic and Geochemical Evidence. *Neues Jb. Geol. Paläontol. Abh.* 154, 213–262.

Schmidt, A. R., Jancke, S., Lindquist, E. E., Ragazzi, E., Roghi, G., Nascimbene, P. C., et al. (2012). Arthropods in Amber from the Triassic Period. *Proc. Natl. Acad. Sci. U.S.A.* 109, 14796–14801. doi:10.1073/pnas.1208464109

Schmidt, A. R., Ragazzi, E., Coppellotti, O., and Roghi, G. (2006). A Microworld in Triassic Amber. *Nature* 444, 835. doi:10.1038/444835a

Senowbari-Daryan, B., Flügel, E., and Preto, N. (2001). *Tethysocarnia Cautica* N. Gen. N. sp., a Sessile Foraminifer from Late Ladinian and Carnian Reefs of the Western and Southern Tethys. *Geol. Paleontol.* 35, 105–119.

Seyfullah, L. J., Beimforde, C., Dal Corso, J., Perrichot, V., Rikkinen, J., and Schmidt, A. R. (2018b). Production and Preservation of Resins - Past and Present. *Biol. Rev.* 93, 1684–1714. doi:10.1111/brv.12414

Seyfullah, L. J., Roghi, G., Corso, J. D., and Schmidt, A. R. (2018a). The Carnian Pluvial Episode and the First Global Appearance of Amber. *J. Geol. Soc.* 175, 1012–1018. doi:10.1144/jgs2017-143

Sidorchuk, E. A., Schmidt, A. R., Ragazzi, E., Roghi, G., and Lindquist, E. E. (2015). Plant-feeding Mite Diversity in Triassic Amber (Acari: Tetrapodili). *J. Syst. Palaeontol.* 13, 129–151. doi:10.1080/14772019.2013.867373

Simms, M. J., and Ruffell, A. H. (1990). Climatic and Biotic Change in the Late Triassic. *J. Geol. Soc.* 147, 321–327. doi:10.1144/gsjgs.147.2.0321

Simms, M. J., Ruffell, A. H., and Johnson, L. A. (1995). "Biotic and Climatic Changes in the Carnian (Triassic) of Europe and Adjacent Areas," in *The Shadow of the Dinosaurs: Early Mesozoic Tetrapods*. Editors N.C. Fraser and H. D. Sues (Cambridge: Cambridge University Press), 352–365.

Simms, M. J., and Ruffell, A. H. (1989). Synchroneity of Climatic Change and Extinctions in the Late Triassic. *Geol* 17, 265–268. doi:10.1130/0091-7613(1989)017<0265:soccae>2.3.co;2

Stanley, G. D., Jr. (2003). The Evolution of Modern Corals and Their Early History. *Earth-Science Rev.* 60, 195–225. doi:10.1016/s0012-8252(02)00104-6

Stefani, M., Furin, S., and Gianolla, P. (2010). The Changing Climate Framework and Depositional Dynamics of Triassic Carbonate Platforms from the Dolomites. *Palaeogeogr. Palaeoclimatol. Palaeoecol.* 290, 43–57. doi:10.1016/j.palaeo.2010.02.018

Stilwell, J. D., Langendam, A., Mays, C., Sutherland, L. J. M., Arillo, A., Bickel, D. J., et al. (2020). Amber from the Triassic to Paleogene of Australia and New Zealand as Exceptional Preservation of Poorly Known Terrestrial Ecosystems. *Sci. Rep.* 10, 5703. doi:10.1038/s41598-020-62252-z

Sun, Y. D., Wignall, P. B., Joachimski, M. M., Bond, D. P. G., Grasby, S. E., Lai, X. L., et al. (2016). Climate Warming, Euxinia and Carbon Isotope Perturbations during the Carnian (Triassic) Crisis in South China. *Earth Planet. Sci. Lett.* 444, 88–100. doi:10.1016/j.epsl.2016.03.037

Tanner, L. H. (2018). "Climates of the Late Triassic: Perspectives, Proxies and Problems," in *The Late Triassic World*. Editor L. H. Tanner (Cham.: Springer), 59–90. Topics in Geobiology 46. doi:10.1007/978-3-319-68009-5_3

Tomimatsu, Y., Nozaki, T., Sato, H., Takaya, Y., Kimura, J. I., Chang, Q., et al. (2020). Marine Osmium Isotope Record during the Carnian "Pluvial Episode" (Late Triassic) in the Pelagic Panthalassa Ocean. *Glob. Planet. Ch.* 197, 103387. doi:10.1016/j.gloplacha.2020.103387

Utting, J. (2004). Reworked Miospores in the Upper Paleozoic and Lower Triassic of the Northern Circum-Polar Area and Selected Localities. *Palynology* 28, 75–119. doi:10.2113/28.1.75

Vávra, N. (2005). Bernstein und verwandte Organische Minerale aus Österreich. *Beitr. Paläont.* 29, 255280.

Vávra, N. (1984). Reich an armen Fundstellen: Übersicht über die fossilen Harze Österreichs. *Stuttg. Beiträge zur Naturkd. Ser. C* 18, 9–14.

Zhang, J., Lenz, O. K., Wang, P., and Hornung, J. (2021). The Eco-Plant Model and its Implication on Mesozoic Dispersed Sporomorphs for Bryophytes, Pteridophytes, and Gymnosperms. *Rev. Palaeobot. Palynology* 293, 104503. doi:10.1016/j.revpalbo.2021.104503

Zhang, Y., Li, M., Ogg, J. G., Montgomery, P., Huang, C., Chen, Z.-Q., et al. (2015). Cycle-calibrated Magnetostratigraphy of Middle Carnian from South China: Implications for Late Triassic Time Scale and Termination of the Yangtze Platform. *Palaeogeogr. Palaeoclimatol. Palaeoecol.* 436, 135–166. doi:10.1016/j.palaeo.2015.05.033

Conflict of Interest: The authors declare that the research was conducted in the absence of any commercial or financial relationships that could be construed as a potential conflict of interest.

Publisher's Note: All claims expressed in this article are solely those of the authors and do not necessarily represent those of their affiliated organizations, or those of the publisher, the editors and the reviewers. Any product that may be evaluated in this article, or claim that may be made by its manufacturer, is not guaranteed or endorsed by the publisher.

frontiers | Frontiers in Earth Science

TYPE Original Research
PUBLISHED 04 August 2022
DOI 10.3389/feart.2022.914432

OPEN ACCESS

EDITED BY
Haijun Song,
China University of Geosciences
Wuhan, China

REVIEWED BY
Mao Luo,
Nanjing Institute of Geology and
Paleontology (CAS), China
Feifei Zhang,
Nanjing University, China

*CORRESPONDENCE
Xiaolin Zhang,
zhxl2012@ustc.edu.cn
Menghan Li,
limh@ustc.edu.cn

SPECIALTY SECTION
This article was submitted to
Geochemistry,
a section of the journal
Frontiers in Earth Science

RECEIVED 06 April 2022
ACCEPTED 11 July 2022
PUBLISHED 04 August 2022

CITATION
Huang X, Li D, Zhang X, Xu Y, Sun L, Li M and Shen Y (2022), High resolution C-isotopic data from microbialites in the aftermath of the end-Permian mass extinction in South China.
Front. Earth Sci. 10:914432.
doi: 10.3389/feart.2022.914432

High resolution C-isotopic data from microbialites in the aftermath of the end-Permian mass extinction in South China

Xiemin Huang, Dandan Li, Xiaolin Zhang*, Yilun Xu, Lilin Sun, Menghan Li* and Yanan Shen

School of Earth and Space Sciences, University of Science and Technology of China, Hefei, China

Globally, Late Permian to Early Triassic carbonate rocks record several pronounced positive and negative C-isotope excursions, indicating a dramatic reorganization of the global carbon cycle. These C-isotopic anomalies provide important constraints on environmental changes that occurred during the end-Permian extinction and the subsequent delayed biotic recovery. In this study, we present high-resolution carbonate C-isotopic data ($\delta^{13}C_{carb}$) spanning the Permian-Triassic transition at Dajiang, South China. Our results reveal a general decrease in $\delta^{13}C_{carb}$ of ~3.3‰ during the microbialite formation which was followed by an increase. C-isotopic chemostratigraphic correlation between the Dajiang section and the Global Boundary Stratotype Section and Point (GSSP) at Meishan suggest a hiatus of several thousands of years between the pre-extinction skeletal limestones and the microbialite deposition in the aftermath of the end-Permian extinction in South China. We suggest that multiple sources of ^{13}C-depleted dissolved carbon are required to explain the negative $\delta^{13}C_{carb}$ excursions as well as the $\delta^{13}C_{carb}$ differences among microbialites deposited in various paleogeographic locations. Our study shows that carbon cycles during the formation of microbialite may have been more complex than previously thought, and cessation of microbialite formation may have been controlled by both global and local environmental changes.

KEYWORDS

Carbon isotopes, End-Permian mass extinction, Microbialite, ^{13}C-depleted carbon, South China

Introduction

The end-Permian mass extinction (~252 Ma), was the most severe biotic crisis of the Phanerozoic, which eliminated over 90% of marine species and fundamentally altered marine ecosystems (Knoll et al., 2007; Song et al., 2012, 2018). It is generally accepted that environmental deterioration, triggered by the eruption of the Siberian Traps Large Igneous Province, may have led to the end-Permian mass extinction (Kamo et al., 2003; Svensen et al., 2009; Grasby et al., 2011; Shen et al., 2011; Burgess et al., 2017; Zhang

et al., 2017; Fielding et al., 2019; Li et al., 2021, 2022). C-isotopic changes in space and time have been instrumental in understanding the environmental changes that occurred during Late Permian–Early Triassic transition (e.g., Grasby and Beauchamp, 2008; Meyer et al., 2011; Grasby et al., 2013; Song et al., 2013). Existing data show large perturbations of global carbon cycles during the end-Permian mass extinction and the delayed Early Triassic biotic recovery (e.g., Payne et al., 2004; Xie et al., 2007). For example, a pronounced negative C-isotopic excursion coincided with the end-Permian extinction worldwide (Holser et al., 1989; Cao et al., 2002, 2009). The sources of the ^{13}C-depleted carbon causing this global negative C-isotopic excursion are argued to have come from volcanic emissions of CO_2 (Payne and Kump, 2007; Cao et al., 2009), the oxidation of methane (Ryskin, 2003), the increase of ^{12}C-enriched organic carbon weathering due to eustatic sea-level fall (Holser et al., 1989), the incursion of ^{12}C-enriched dissolved carbon in anoxic/euxinic deep water into the shallow marine environment (Riccardi et al., 2007; Zhang et al., 2021), amongst others. However, $\delta^{13}C$ data from the Permian-Triassic transition indicate that $\delta^{13}C_{carb}$ compositions continued to decrease following the end-Permian mass extinction level, when microbialites were deposited (Krull et al., 2004; Mu et al., 2009; Wang et al., 2009; Liao et al., 2010; Liu et al., 2010; Luo et al., 2010, 2011; Yang et al., 2011; Wu et al., 2017).

Permian-Triassic microbialites are carbonates rich in microbial structures and cements of various forms including stromatolites, thrombolites and dendrolites, that were deposited in the aftermath of the end-Permian mass extinction (Lehrmann 1999; Wang et al., 2005; Baud et al., 2007; Kershaw et al., 2007, 2012; Yang et al., 2011; Wang et al., 2019). Most of the Permian-Triassic microbialites were developed in the low-latitude Tethys Ocean, especially in South China where many excellent sections are exposed. Extensively multidisciplinary studies have greatly improved our knowledge about the age, microbial structure, genesis, and environmental implications of these microbialites (Wang et al., 2005; Luo et al., 2010; Wang et al., 2016; Deng et al., 2017; Pei et al., 2019). For example, all of the C-isotopic profiles from South China have shown that the $\delta^{13}C_{carb}$ compositions continue to decrease from pre-extinction bioclastic limestones enriched in benthic fossils to the overlying microbialites (e.g., Yang et al., 2011).

In this study, we report high-resolution $\delta^{13}C_{carb}$ data of microbialites from the Dajiang section in South China. The microbialite interval is about 14.5 m in the Dajiang section and might be the thickest in South China, which could reveal more details of C-isotopic variations during this period. We aim to better understand environmental significance of C-isotopic variations in microbialites and their possible link to the delayed biotic recovery from the end-Permian mass extinction.

Geological background and stratigraphy

During the Permian-Triassic transition, the South China craton, including the Yangtze and Cathaysia blocks, was situated north of the paleo-equator in the eastern part of the Paleotethys Ocean (Figure 1A). The Nanpanjiang Basin is a deep-marine embayment in the Yangtze Platform, which opened south-eastward to the Panthalassa Ocean (Lehrmann, 1999). The Great Bank of Guizhou, which evolved as an isolated carbonate platform within the Nanpanjiang Basin, preserved continuous shallow marine deposition from the late Permian to the middle Triassic (Lehrmann et al., 2003). There are many outstanding sections that preserved microbialites in the Nanpanjiang Basin (Luo et al., 2011, 2014). In part because of its thickness and excellent exposure, the Dajiang microbialites were the focus of this study.

The Dajiang section (106°39′49″E, 25°33′47″N) is located in Bianyang town, Luodian County, Guizhou Province. Paleogeographically, the study section was situated on the Great Bank of Guizhou and was deposited at a water depth possibly less than 100 m (Song et al., 2013) (Figure 1B). The Dajiang section comprises, in ascending order, the upper Permian Wujiaping Formation and the lower Triassic Daye Formation (Figure 2). The uppermost Wujiaping Formation is characterized by skeletal limestone, and contains abundant shallow-marine fossils such as fusulinids, foraminifera, brachiopods, and calcareous algae (Lehrmann et al., 2003). At the base of the Daye Formation, a 14.5 m thick microbialite was deposited, which is mainly composed of laminar or spotted thrombolites (Figure 2). The microbialite deposit is overlain by grainstone and packstone (Jiang et al., 2014).

It is widely accepted that the end-Permian extinction level is correlated with bed 25 in the GSSP at Meishan, South China and the Permian-Triassic boundary (PTB) is correlated with bed 27c at Meishan, indicated by the first appearance datum (FAD) of the conodont species *Hindeodus parvus* (Yin et al., 2001). However, the position of the FAD of *H. parvus* in the Dajiang section was placed at different levels, and therefore the exact placement of the PTB remains debated (Jiang et al., 2014; Lehrmann et al., 2015; Zhang et al., 2020). The PTB has been placed either at the uppermost of the Wujiaping Formation (Jiang et al., 2014) or within the microbialite (Lehrmann et al., 2015; Zhang et al., 2020). In this study, we follow the scheme of Jiang et al. (2014) (Figure 2). Regardless of the precise PTB level, there is little doubt that the microbialites at Dajiang were deposited in the aftermath of the end-Permian mass extinction.

Materials and methods

A total of 100 bulk samples were collected continuously over ~23.4-m of strata across the PTB in the Dajiang section. All

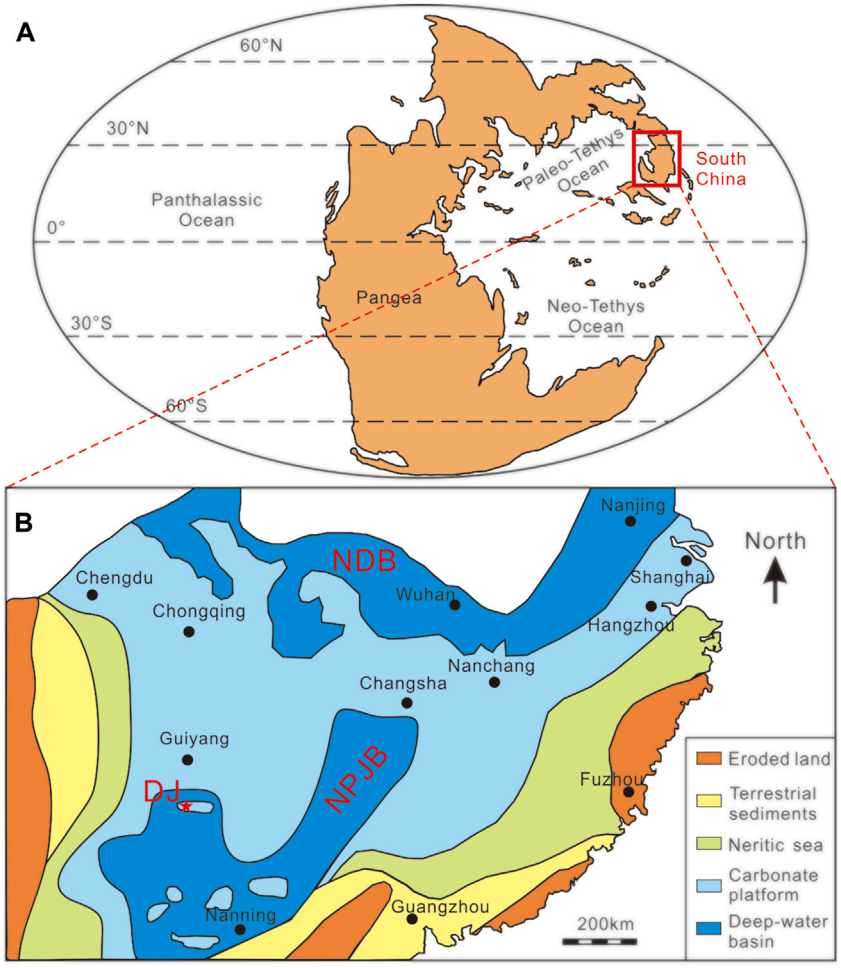

FIGURE 1
Permian-Triassic paleogeographic sketch map of the world **(A)** and the South China Craton **(B)**. Inset red rectangle in **(A)** shows the area of the South China Craton. The red star in **(B)** shows the location of the Dajiang section. Paleogeography of the world is revised from Shen et al. (2015), and the map of the South China Craton is modified from Xie et al. (2010) and Yin et al. (2014). DJ: Dajiang section; NDB: Northern Deepwater Basin; NPJB: Nanpanjiang Basin.

sample depths are measured relative to the PTB. Among them, 16 samples are from the skeletal limestone interval (−3.1–0 m), 66 samples are from the microbialite interval (0–14.5 m), and 18 samples are from the grainstone and packstone (14.5–20.3 m) (Figure 2). Prior to isotopic analysis, any weathered surfaces and visible calcite veins were trimmed off. Pieces of the crushed samples were then ground to fine powders (<200 mesh) using an automated agate mortar and pestle device. Sample preparation and analyses were performed in the Biogeochemical Laboratory at University of Science and Technology of China.

For $\delta^{13}C_{carb}$ and $\delta^{18}O_{carb}$ analysis, approximately 150 μg of sample powder was reacted with 102–105% anhydrous phosphoric acid at 70°C in a Kiel IV carbonate device to generate CO_2. The evolved CO_2 gas was purified in a cryogenic cleaning device and then measured on a ThermoFinnigan MAT 253 Mass Spectrometer. The carbon and oxygen isotope compositions are expressed in the conventional delta notation as per mil (‰) deviations relative to the V-PDB standard. Analytical reproducibility was monitored by replicate analysis of a Chinese national standard GBW04416 ($\delta^{13}C_{carb}$ = +1.61‰, $\delta^{18}O_{carb}$ = −11.59‰), and was better than ±0.05‰ for $\delta^{13}C_{carb}$ and ±0.06‰ for $\delta^{18}O_{carb}$.

Results and data evaluation

The $\delta^{13}C_{carb}$ data show large variations during the Permian–Triassic transition in the Dajiang section, ranging from −0.44‰ to +2.87‰ (Supplementary Table S1; Figure 2). Post-depositional diagenetic processes can alter the primary

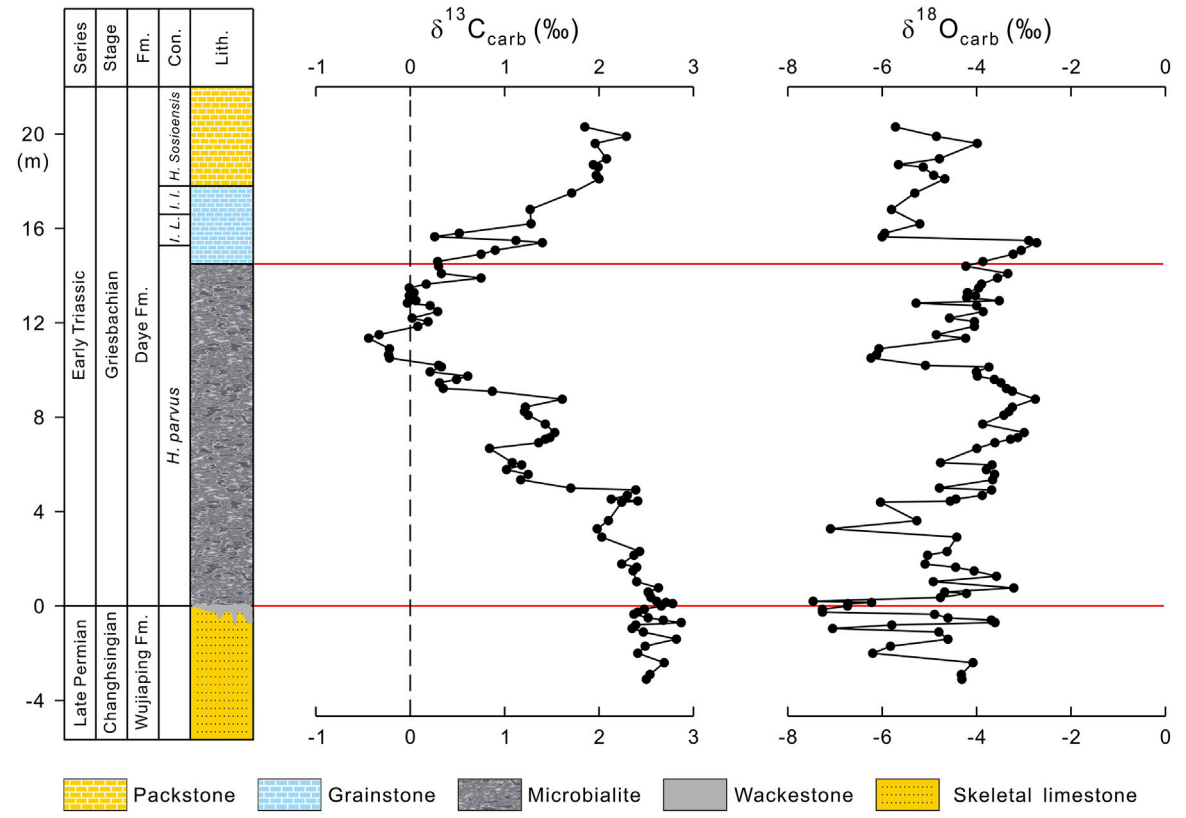

FIGURE 2
Profiles of $\delta^{13}C_{carb}$ and $\delta^{18}O_{carb}$ from the Dajiang section. Conodont zones are from Jiang et al. (2014). Abbreviations: *H. parvus* = *Hindeodus parvus* zone; *I. L.* = *Isarcicella lobate* zone; *I. I.* = *Isarcicella isarcica* zone; *H. sosioensis* = *Hindeodus sosioensis* zone; Fm. = Formation; Con. = Conodont zone; Lith. = Lithology.

C-isotopic compositions of sedimentary carbonates (Kaufman and Knoll, 1995). Therefore, diagenetic effects must be evaluated prior to the interpretation of the isotope data. It has been shown that diagenetic fluids enriched in organic-derived carbon can simultaneously alter the carbonate $\delta^{13}C$ and $\delta^{18}O$ towards more negative values, and as such, the positive correlation between $\delta^{13}C_{carb}$ and $\delta^{18}O_{carb}$ may be indicative of significant diagenetic alteration (Kaufman and Knoll, 1995). Extreme negative $\delta^{18}O_{carb}$ values (<−10‰) have also been suggested to be an additional indicator of diagenetic alteration (Kaufman and Knoll, 1995). However, the $\delta^{18}O_{carb}$ compositions from the Dajiang section range from −2.7‰ to −7.5‰, implying the primary nature for $\delta^{13}C_{carb}$.

The plot of $\delta^{13}C_{carb}$ and $\delta^{18}O_{carb}$ show moderate correlation (R^2 = 0.4653) for the pre-extinction skeletal limestone (Figure 3A). This could suggest diagenetic alteration of the primary isotopic compositions. However, the narrow $\delta^{13}C_{carb}$ range from +2.35‰ to +2.87‰ suggest that the $\delta^{13}C_{carb}$ compositions were not significantly changed and they are of primary isotopic significance, although the $\delta^{18}O_{carb}$ compositions could be altered. There is little correlation between $\delta^{13}C_{carb}$ and $\delta^{18}O_{carb}$ for the microbialites and overlying grainstones and packstones, suggesting that the primary $\delta^{13}C_{carb}$ compositions were well preserved (Figures 3B,C). Similarly, the plot between $\delta^{13}C_{carb}$ and $\delta^{18}O_{carb}$ for all samples from Dajiang shows little correlation, reinforcing the primary nature for $\delta^{13}C_{carb}$ (Figure 3D).

It is worthy to note that a preliminary $\delta^{13}C_{carb}$ study on the Dajiang section was carried out by Krull et al. (2004) (Figure 4). In general, the two datasets are consistent. However, our high-resolution sampling and precise measurements reveal more details about C-isotopic changes. As shown in Figure 2, the $\delta^{13}C_{carb}$ values of the pre-extinction skeletal limestone range from +2.35‰ to +2.87‰, with an average of +2.55‰. There is not much change in $\delta^{13}C_{carb}$ in the pre-extinction interval, although there is a slight $\delta^{13}C_{carb}$ increase from +2.41‰ to +2.78‰ (Figure 4).

After the end-Permian extinction event, the $\delta^{13}C_{carb}$ data display a broad decrease through the microbialite interval, with $\delta^{13}C_{carb}$ decreasing from +2.78‰ to −0.44‰ (Figure 2). Following this the $\delta^{13}C_{carb}$ data recover from the nadir

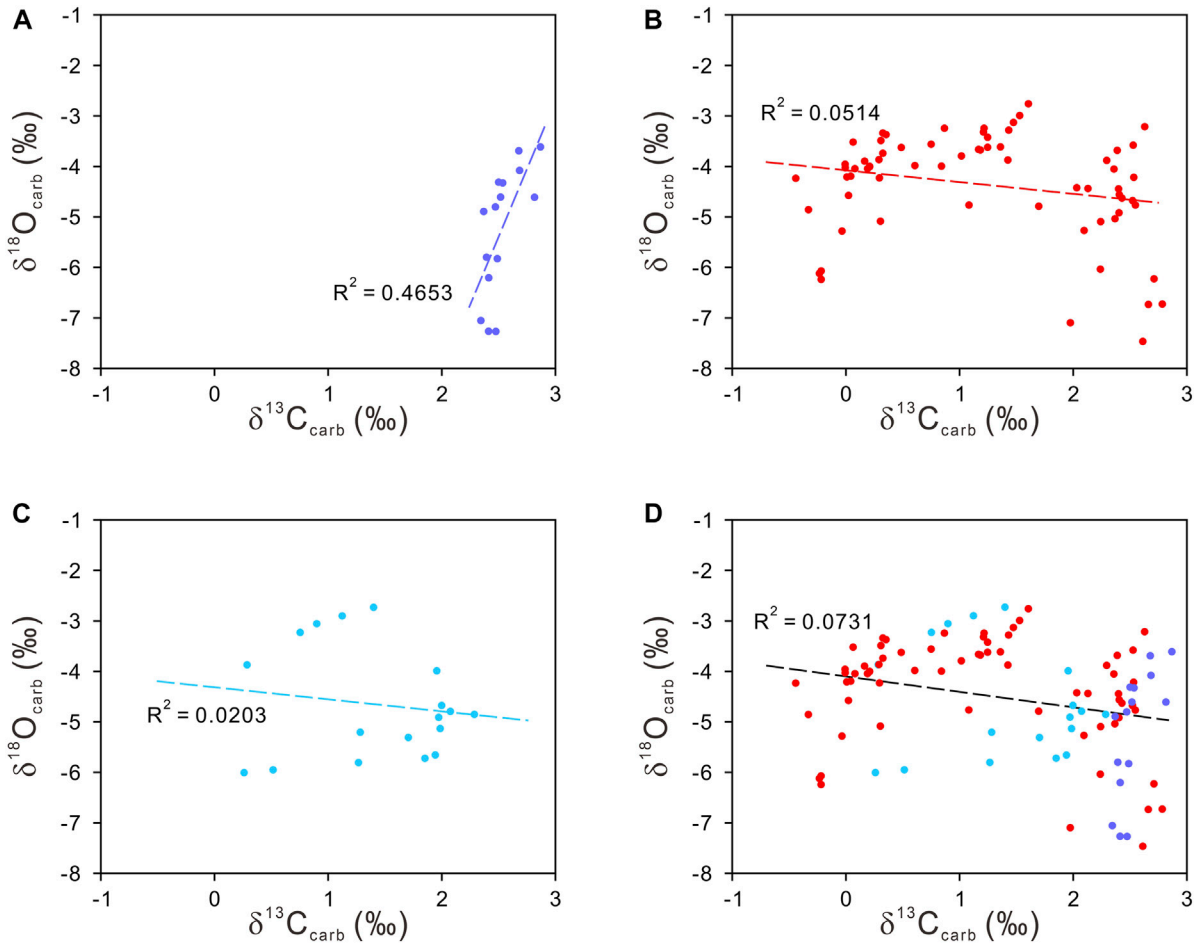

FIGURE 3
Cross-plot of $\delta^{13}C_{carb}$ and $\delta^{18}O_{carb}$ for pre-extinction skeletal limestone **(A)**, microbialites **(B)**, overlying grainstones and packstones **(C)**, and all samples from the Dajiang section **(D)**.

of −0.44‰ to +0.29‰ in the uppermost part of the microbialite interval, and continue to rise to +2.29‰ in the overlying grainstones and packstones (Figure 2).

Our high-resolution C-isotope data reveal that the broad $\delta^{13}C_{carb}$ decrease in the microbialite interval consists of three consecutive episodes (Figure 2). During episode I, $\delta^{13}C_{carb}$ slightly decreases from +2.78‰ to +1.98‰ followed by a recovery to +2.39‰ at 4.92 m (Figure 2). The $\delta^{13}C_{carb}$ continues to decrease from +2.39‰ to +0.84‰ at the height of 6.68 m during episode II, followed by an increase to +1.61‰ at 8.76 m (Figure 2). Episode III shows a $\delta^{13}C_{carb}$ decrease from +1.61‰ to the minimal value of −0.44‰ at 11.35 m in the microbialite interval (Figure 2). The $\delta^{13}C_{carb}$ increases from −0.44‰ to +0.30‰ at the uppermost of the microbialite interval and continues to increase to +2.29‰ in the overlying grainstones and packstones though a sharp negative shift from +1.40‰ at 15.4 m to +0.26‰ at 15.65 m is shown (Figure 2).

Discussion

$\delta^{13}C$ stratigraphic correlation between Dajiang and GSSP Meishan section

Microbialites were deposited immediately following the end-Permian extinction in a shallow marine carbonate environment. Like Dajiang, observations from many sections in South China indicate an erosional surface between the underlying skeletal packstone and overlying microbialite (Jiang et al., 2014) (Figure 2). This has been interpreted as submarine chemical dissolution due to ocean acidification (Payne et al., 2007; Lehrmann et al., 2015) or subaerial erosion due to the major global regression near the extinction event (e.g., Wignall et al., 2009). However, both models could work depending on the paleotopography and accommodation space of the studied section (Yin et al., 2014). It was estimated that a hiatus between the skeletal limestone and the basal microbialite may

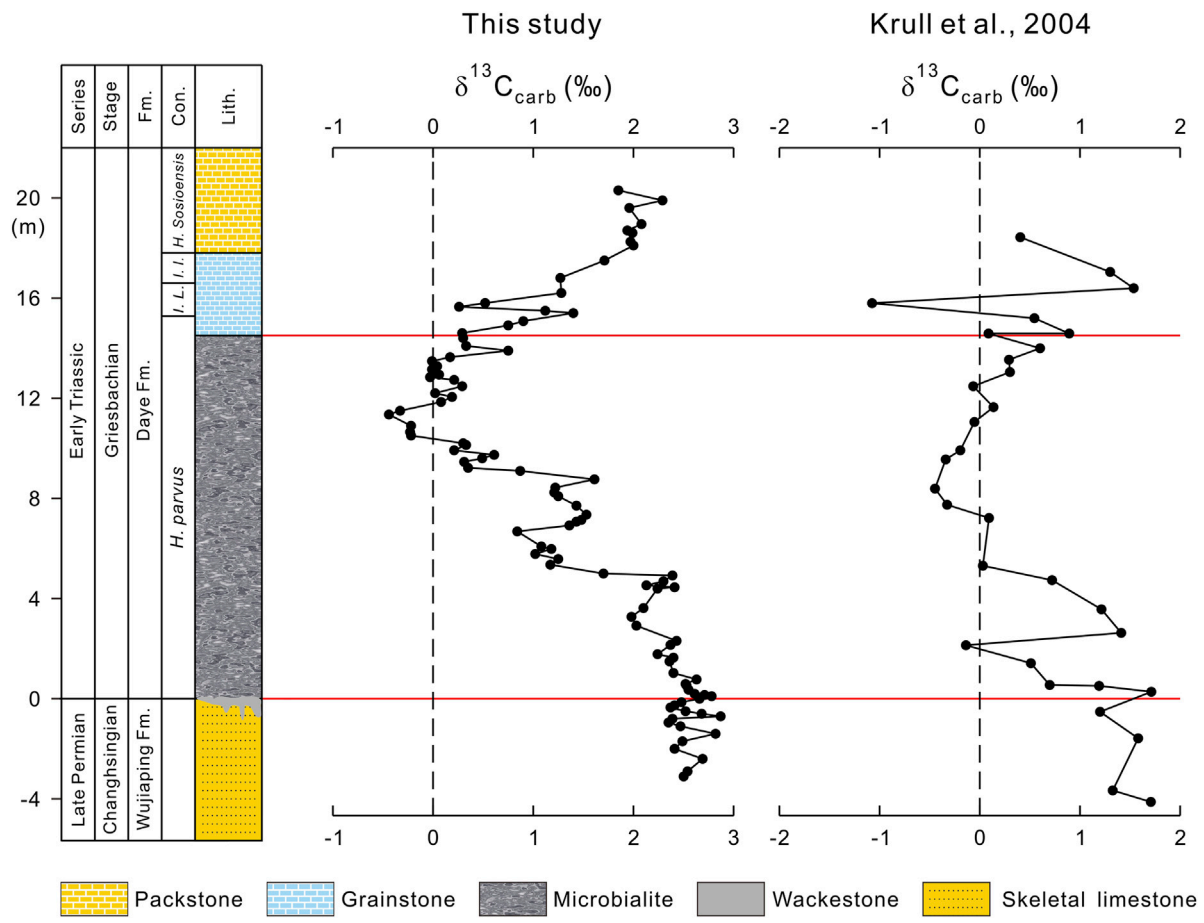

FIGURE 4
Comparison of $\delta^{13}C_{carb}$ records of the Dajiang section from this study and Krull et al. (2004).

be 50–100 ky (Yin et al., 2014). The $\delta^{13}C$ stratigraphic correlation between Dajiang and GSSP Meishan section suggest that the deposition from the skeletal packstone to the overlying microbialite at Dajiang may be not continuous (Figures 2, 5).

At Dajiang, there is minor $\delta^{13}C_{carb}$ increase from +2.37‰ to +2.78‰ from the top of the packstone to the basal microbialite (Figure 5). In contrast, a gradual $\delta^{13}C_{carb}$ decrease from the bed 23 to bed 24e, followed by another $\delta^{13}C_{carb}$ decrease of about 4‰, occurs at the extinction level at bed 25 at Meishan (Cao et al., 2002) (Figure 5). After the extinction, the $\delta^{13}C_{carb}$ at Meishan increases about 3‰, gradually from bed 25 to beds 28–29 (Cao et al., 2002) (Figure 5). However, the $\delta^{13}C_{carb}$ continues to decrease from the packstone to microbialite at Dajiang (Figures 2, 5). The Meishan section may be a condensed section which may have not recorded all of the C-isotopic changes during Permian-Triassic transition. However, the $\delta^{13}C_{carb}$ from Dajiang missed several significant $\delta^{13}C_{carb}$ changes in Meishan and elsewhere. Therefore, our $\delta^{13}C_{carb}$ data from Dajiang support that the microbialites were deposited in the aftermath of the end-Permian extinction and that the deposition of several thousands of years was probably missing prior to the microbialite formation.

$\delta^{13}C$ stratigraphic correlations of microbialites between Dajiang and elsewhere in South China

The correlations between the Dajiang section and Zuodeng and Taiping sections in the same Nanpanjiang Basin show similarities as well as differences in $\delta^{13}C$ variations (Figure 6). The $\delta^{13}C_{carb}$ from all three sections show decreasing values in the microbialite interval and increasing values after the deposition of microbialites (Figure 6). The minimal $\delta^{13}C_{carb}$ values at Dajiang, Zuodeng, and Taiping are −0.44‰, +0.3‰, and −0.7‰, respectively (Figure 6). Unlike Dajiang, the $\delta^{13}C_{carb}$ profiles of the microbialites from Zuodeng and Taiping remain relatively stable after the $\delta^{13}C_{carb}$ decrease from the pre-

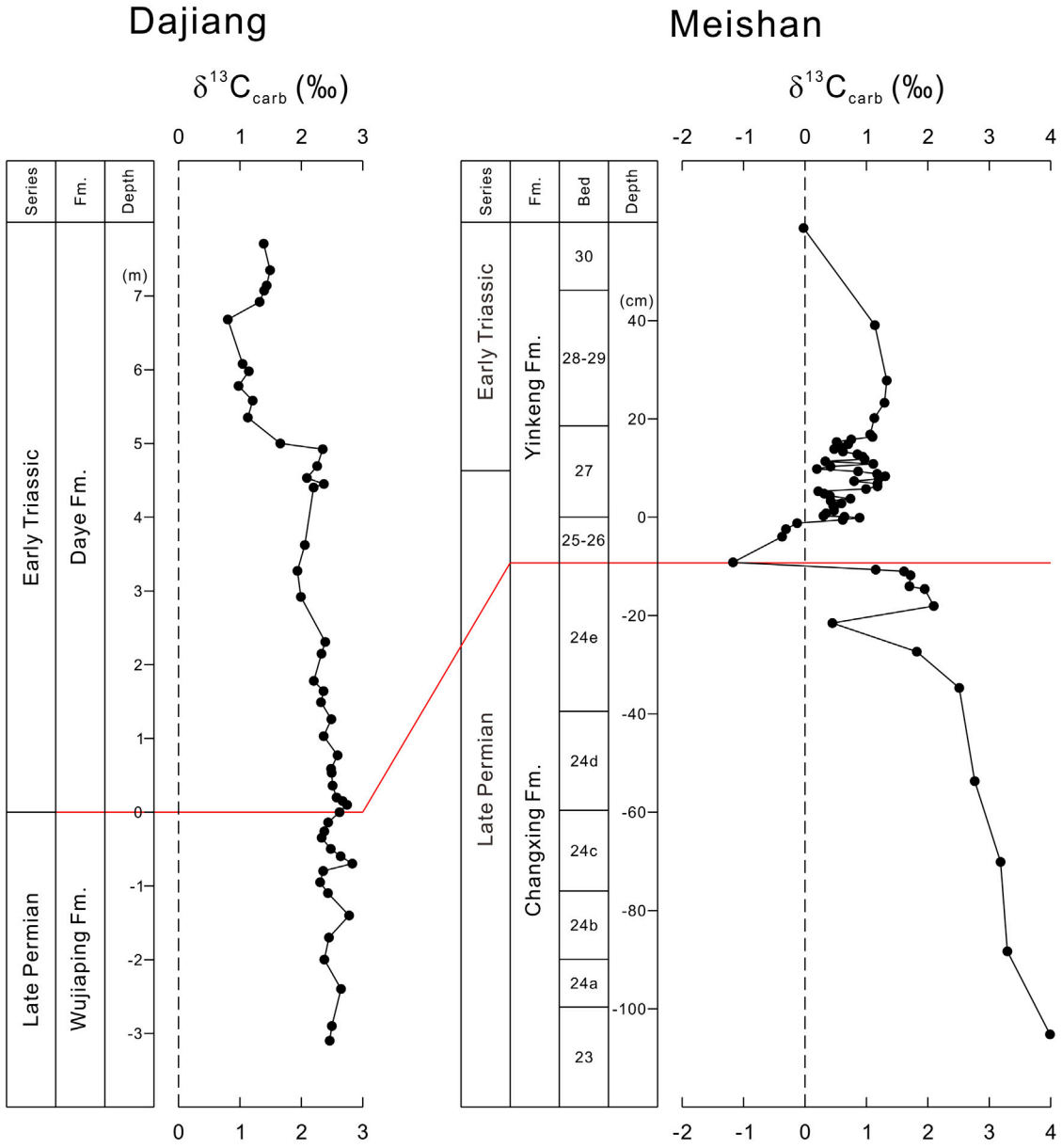

FIGURE 5
Comparison of $\delta^{13}C_{carb}$ records from the Dajiang (this study) and Meishan section (Cao et al., 2002).

extinction skeletal limestones, reflecting complexities of carbon cycling in the basin (Figure 6). The correlations between Dajiang and Cili and Chongyang sections add more complexities of carbon cycling as the late two sections were also deposited in a carbonate platform close to the Northern Deepwater Basin (Luo et al., 2014). Like the Dajiang section, the $\delta^{13}C_{carb}$ profile at Cili shows a general decrease to −0.4‰ and consists of three minor negative $\delta^{13}C_{carb}$ excursions (Figure 6). However, the Chongyang section, which was deposited in a similar environment as the Cili section (Luo et al., 2014), shows relatively stable $\delta^{13}C_{carb}$ values around −0.3‰, after the decrease of about 2‰ from the pre-extinction skeletal limestones (Figure 6).

It appears that there is a general $\delta^{13}C_{carb}$ decrease from the pre-extinction skeletal limestones to the microbialites in all studied sections, although the absolute $\delta^{13}C_{carb}$ decrease varies between each section (Figure 6). After this general $\delta^{13}C_{carb}$ decrease, the $\delta^{13}C_{carb}$ profile of the microbialite either remains relatively stable or continues to decrease (Figure 6). The $\delta^{13}C_{carb}$ value then increases starting from either within the microbialite or after

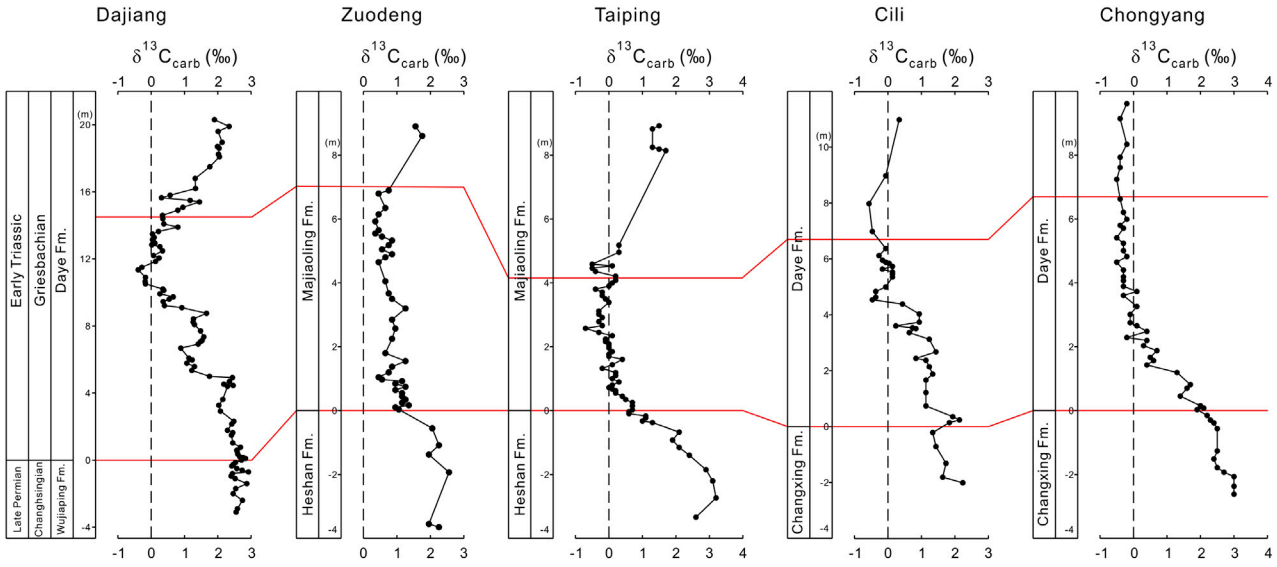

FIGURE 6
Comparison of $\delta^{13}C_{carb}$ records during the Permian-Triassic transition in South China. The data are from the Dajiang (this study), Zuodeng (Luo et al., 2011), Taiping (Luo et al., 2011), Cili (Luo et al., 2011), and Chongyang (Luo et al., 2011) section. The red lines indicate the onset and termination of the microbialite interval.

the microbialite deposition (Figure 6). However, this $\delta^{13}C_{carb}$ increase was not shown in the Chongyang section (Figure 6).

Regardless, the significant $\delta^{13}C_{carb}$ decrease from the pre-extinction skeletal limestones to the microbialites in all studied sections requires inputs of ^{13}C-depleted dissolved carbon. Continental weathering of ^{13}C-depleted carbon was unlikely a major source as a large amount of clastic inputs would have inhibited the growth of microbialite. Likewise, dissociation of methane hydrates was unlikely a major source considering the continuous decreasing $\delta^{13}C_{carb}$ compositions as at Dajiang, as well as the very shallow water environment for precipitation of microbialites. There are possible ^{13}C-depleted sources that could help to explain the decreasing $\delta^{13}C_{carb}$ values for the microbialites. Emission of CO_2 and possibly methane as well by the Siberian Traps magmatism could provide ^{13}C-depleted carbon, producing the negative $\delta^{13}C_{carb}$ excursion (Burgess and Bowring, 2015). Upwelling of anoxic deep water into the photic zone could also contribute ^{13}C-depleted carbon during the microbialite formation (e.g., Kershaw et al., 2007). As well, low productivity could possibly lead to ^{13}C-depleted isotopic values in surface waters. However, evidence for either of the mechanisms may be circumstantial and neither of them can independently explain the negative $\delta^{13}C_{carb}$ excursion from the pre-extinction skeletal limestone to the microbialite level, as well as the differences in $\delta^{13}C_{carb}$ minimums amongst the microbialites deposited in various paleogeographic locations (Figure 6).

The general increasing $\delta^{13}C_{carb}$ profiles within the microbialite interval at Dajiang or after the deposition of the microbialtes elsewhere (Figure 6) suggest changes of carbon cycling in the post-microbialite oceans. Increasing primary productivity and/or anoxia could facilitate enhanced burial of organic carbon, resulting in the increasing $\delta^{13}C_{carb}$ compositions. We speculate that the cessation of microbialites in South China may be linked to the changes of carbon cycling which may have controlled by global and local environmental changes.

Conclusion

The $\delta^{13}C_{carb}$ data from the Dajiang section reveal a general decrease of ~3.2‰ from pre-extinction skeletal limestone to the microbialite deposition. Unlike the $\delta^{13}C_{carb}$ data from many sections in South China, the decreasing $\delta^{13}C_{carb}$ at Dajiang is followed by an increasing $\delta^{13}C_{carb}$ profile. We suggest that multiple sources of ^{13}C-depleted dissolved carbon may be possibly required to explain the decreasing $\delta^{13}C_{carb}$ during the microbialite formation. There is little doubt that carbon cycling during the microbialite precipitation are more complex than previously thought. Though great details about morphology and mineralogical compositions have been studied, local environments for microbialite formation have not been well reconstructed. Future studies should focus on environmental reconstruction for microbialite formation and their possible link to the delayed recovery from the end-Permian mass extinction.

Data availability statement

The original contributions presented in the study are included in the article/Supplementary Material, further inquiries can be directed to the corresponding authors.

Author contributions

YS conceived the study. XZ and YS collected samples. XH, XZ, and ML wrote the manuscript with inputs from DL, YX, LS, and YS.

Funding

This study was supported by the National Natural Science Foundation of China (41721002 and 41890842) and the 111 project (B14026).

Acknowledgments

We dedicated this paper to the late Yongbiao Wang for his pioneering work on the microbialite in South China and his help in collecting samples from Dajiang. We thank Steve Grasby, Haishui Jiang and the reviewers for their constructive comments.

Conflict of interest

The authors declare that the research was conducted in the absence of any commercial or financial relationships that could be construed as a potential conflict of interest.

Publisher's note

All claims expressed in this article are solely those of the authors and do not necessarily represent those of their affiliated organizations, or those of the publisher, the editors and the reviewers. Any product that may be evaluated in this article, or claim that may be made by its manufacturer, is not guaranteed or endorsed by the publisher.

Supplementary material

The Supplementary Material for this article can be found online at: https://www.frontiersin.org/articles/10.3389/feart.2022.914432/full#supplementary-material.

References

Baud, A., Richoz, S., and Pruss, S. (2007). The lower Triassic anachronistic carbonate facies in space and time. *Glob. Planet. Change* 55, 81–89. doi:10.1016/j.gloplacha.2006.06.008

Burgess, S. D., and Bowring, S. A. (2015). High-precision geochronology confirms voluminous magmatism before, during, and after Earth's most severe extinction. *Sci. Adv.* 1, e1500470. doi:10.1126/sciadv.1500470

Burgess, S. D., Muirhead, J. D., and Bowring, S. A. (2017). Initial pulse of Siberian Traps sills as the trigger of the end-Permian mass extinction. *Nat. Commun.* 8, 164. doi:10.1038/s41467-017-00083-9

Cao, C., Love, G. D., Hays, L. E., Wang, W., Shen, S., Summons, R. E., et al. (2009). Biogeochemical evidence for euxinic oceans and ecological disturbance presaging the end-Permian mass extinction event. *Earth Planet. Sci. Lett.* 281, 188–201. doi:10.1016/j.epsl.2009.02.012

Cao, C., Wang, W., and Jin, Y. (2002). Carbon isotope excursions across the permian-triassic boundary in the meishan section, zhejiang Province, China. *Chin. Sci. Bull.* 47, 1125–1129. doi:10.1360/02tb9252

Deng, B., Wang, Y., Woods, A., Li, S., Li, G., Chen, W., et al. (2017). Evidence for rapid precipitation of calcium carbonate in South China at the beginning of Early Triassic. *Palaeogeogr. Palaeoclimatol. Palaeoecol.* 474, 187–197. doi:10.1016/j.palaeo.2016.06.007

Fielding, C. R., Frank, T. D., McLoughlin, S., Vajda, V., Mays, C., Tevyaw, A. P., et al. (2019). Age and pattern of the southern high-latitude continental end-Permian extinction constrained by multiproxy analysis. *Nat. Commun.* 10, 385. doi:10.1038/s41467-018-07934-z

Grasby, S. E., Beauchamp, B., Embry, A., and Sanei, H. (2013). Recurrent early triassic ocean anoxia. *Geology* 41, 175–178. doi:10.1130/G33599.1

Grasby, S. E., and Beauchamp, B. (2008). Intrabasin variability of the carbon-isotope record across the permian-triassic transition, sverdrup basin, arctic Canada. *Chem. Geol.* 253, 141–150. doi:10.1016/j.chemgeo.2008.05.005

Grasby, S. E., Sanei, H., and Beauchamp, B. (2011). Catastrophic dispersion of coal fly ash into oceans during the latest Permian extinction. *Nat. Geosci.* 4, 104–107. doi:10.1038/ngeo1069

Holser, W. T., Schonlaub, H. P., Attrep, M., Boeckelmann, K., Klein, P., Magaritz, M., et al. (1989). A unique geochemical record at the Permian-Triassic boundary. *Nature* 337, 39–44. doi:10.1038/337039a0

Jiang, H., Lai, X., Sun, Y., Wignall, P. B., Liu, J., Yan, C., et al. (2014). Permian-Triassic conodonts from Dajiang (Guizhou, South China) and their implication for the age of microbialite deposition in the aftermath of the end-Permian mass extinction. *J. Earth Sci.* 25, 413–430. doi:10.1007/s12583-014-0444-4

Kamo, S. L., Czamanske, G. K., Amelin, Y., Fedorenko, V. A., Davis, D., Trofimov, V., et al. (2003). Rapid eruption of Siberian flood-volcanic rocks and evidence for coincidence with the Permian-Triassic boundary and mass extinction at 251 Ma. *Earth Planet. Sci. Lett.* 214, 75–91. doi:10.1016/S0012-821X(03)00347-9

Kaufman, A. J., and Knoll, A. H. (1995). Neoproterozoic variations in the C-isotopic composition of seawater: Stratigraphic and biogeochemical implications. *Precambrian Res.* 73, 27–49. doi:10.1016/0301-9268(94)00070-8

Kershaw, S., Crasquin-soleau, S., Li, Y., Collin, P-Y., Forel, M-B., Mu, X., et al. (2012). Microbialites and global environmental change across the permian-triassic boundary: A synthesis. *Geobiology* 10, 25–47. doi:10.1111/j.1472-4669.2011.00302.x

Kershaw, S., Li, Y., Crasquin-soleau, S., Feng, Q., Mu, X., Collin, P-Y., et al. (2007). Earliest triassic microbialites in the South China block and other areas: Controls on their growth and distribution. *Facies* 53, 409–425. doi:10.1007/s10347-007-0105-5

Knoll, A. H., Bambach, R. K., Payne, J. L., Pruss, S., and Fischer, W. W. (2007). Paleophysiology and end-Permian mass extinction. *Earth Planet. Sci. Lett.* 256, 295–313. doi:10.1016/j.epsl.2007.02.018

Krull, E. S., Lehrmann, D. J., Druke, D., Kessel, B., Yu, Y., Li, R., et al. (2004). Stable carbon isotope stratigraphy across the Permian-Triassic boundary in shallow marine carbonate platforms, Nanpanjiang Basin, south China. *Palaeogeogr. Palaeoclimatol. Palaeoecol.* 204, 297–315. doi:10.1016/S0031-0182(03)00732-6

Lehrmann, D. J., Bentz, J. M., Wood, T., Goers, A., Dhillon, R., Akin, S., et al. (2015). Environmental controls on the Genesis of marine microbialites and dissolution surface associated with the end-permian mass extinction: New sections and observations from the Nanpanjiang Basin, south China. *Palaios* 30, 529–552. doi:10.2110/palo.2014.088

Lehrmann, D. J. (1999). Early triassic calcimicrobial mounds and biostromes of the Nanpanjiang Basin, south China. *Geology* 27, 359–362. doi:10.1130/0091-7613(1999)027<0359:etcmab>2.3.co;2

Lehrmann, D. J., Payne, J. L., Felix, S. V., Dillett, P. M., Wang, H., Yu, Y., et al. (2003). Permian-triassic boundary sections from shallow-marine carbonate platforms of the Nanpanjiang Basin, south China: Implications for oceanic conditions associated with the end-permian extinction and its aftermath. *Palaios* 18, 138–152. doi:10.1669/0883-1351(2003)18<138:pbsfsc>2.0.co;2

Li, M., Frank, T. D., Xu, Y., Fielding, C. R., Gong, Y., Shen, Y., et al. (2022). Sulfur isotopes link atmospheric sulfate aerosols from the Siberian Traps outgassing to the end-Permian extinction on land. *Earth Planet. Sci. Lett.* 592, 117634. doi:10.1016/j.epsl.2022.117634

Li, M., Grasby, S. E., Wang, S., Zhang, X., Wasylenki, L. E., Xu, Y., et al. (2021). Nickel isotopes link Siberian Traps aerosol particles to the end-Permian mass extinction. *Nat. Commun.* 12, 2024. doi:10.1038/s41467-021-22066-7

Liao, W., Wang, Y., Kershaw, S., Weng, Z., and Yang, H. (2010). Shallow-marine dysoxia across the permian-triassic boundary: Evidence from pyrite framboids in the microbialite in South China. *Sediment. Geol.* 232, 77–83. doi:10.1016/j.sedgeo.2010.09.019

Liu, H., Wang, Y., Yuan, A., Yang, H., Song, H., Zhang, S., et al. (2010). Ostracod fauna across the Permian-Triassic boundary at Chongyang, Hubei Province, and its implication for the process of the mass extinction. *Sci. China Earth Sci.* 53, 810–817. doi:10.1007/s11430-010-0045-8

Luo, G., Algeo, T. J., Huang, J., Zhou, W., Wang, Y., Yang, H., et al. (2014). Vertical $\delta^{13}C_{org}$ gradients record changes in planktonic microbial community composition during the end-Permian mass extinction. *Palaeogeogr. Palaeoclimatol. Palaeoecol.* 396, 119–131. doi:10.1016/j.palaeo.2014.01.006

Luo, G., Kump, L. R., Wang, Y., Tong, J., Arthur, M. A., Yang, H., et al. (2010). Isotopic evidence for an anomalously low oceanic sulfate concentration following end-Permian mass extinction. *Earth Planet. Sci. Lett.* 300, 101–111. doi:10.1016/j.epsl.2010.09.041

Luo, G., Wang, Y., Yang, H., Algeo, T., Kump, L., and Huang, J. (2011). Stepwise and large-magnitude negative shift in $\delta^{13}C_{carb}$ preceded the main marine mass extinction of the Permian-Triassic crisis interval. *Palaeogeogr. Palaeoclimatol. Palaeoecol.* 299, 70–82. doi:10.1016/j.palaeo.2010.10.035

Meyer, K. M., Yu, M., Jost, A. B., Kelley, B. M., and Payne, J. L. (2011). $\delta^{13}C$ evidence that high primary productivity delayed recovery from end-Permian mass extinction. *Earth Planet. Sci. Lett.* 302, 378–384. doi:10.1016/j.epsl.2010.12.033

Mu, X., Kershaw, S., Li, Y., Guo, L., Qi, Y., Reynolds, A., et al. (2009). High-resolution carbon isotope changes in the Permian-Triassic boundary interval, Chongqing, South China; implications for control and growth of earliest Triassic microbialites. *J. Asian Earth Sci.* 36, 434–441. doi:10.1016/j.jseaes.2007.08.004

Payne, J. L., and Kump, L. R. (2007). Evidence for recurrent Early Triassic massive volcanism from quantitative interpretation of carbon isotope fluctuations. *Earth Planet. Sci. Lett.* 256, 264–277. doi:10.1016/j.epsl.2007.01.034

Payne, J. L., Lehrmann, D. J., Follet, D., Seibel, M., Kump, L. R., Riccardi, A., et al. (2007). Erosional truncation of uppermost Permian shallow-marine carbonates and implications for Permian Triassic boundary events. *Geol. Soc. Am. Bull.* 119, 771–784. doi:10.1130/B26091.1

Payne, J. L., Lehrmann, D. J., Wei, J. Y., Orchard, M. J., Schrag, D. P., Knoll, A. H., et al. (2004). Large perturbations of the carbon cycle during recovery from the end-Permian extinction. *Science* 305, 506–509. doi:10.1126/science.1097023

Pei, Y., Chen, Z., Fang, Y., Kershaw, S., Wu, S., Luo, M., et al. (2019). Volcanism, redox conditions, and microbialite growth linked with the end-Permian mass extinction: Evidence from the Xiajiacao section (Western Hubei Province), South China. *Palaeogeogr. Palaeoclimatol. Palaeoecol.* 519, 194–208. doi:10.1016/j.palaeo.2017.07.020

Riccardi, A., Kump, L. R., Arthur, M. A., and D'Hondt, S. (2007). Carbon isotopic evidence for chemocline upward excursions during the end-Permian event. *Palaeogeogr. Palaeoclimatol. Palaeoecol.* 248, 73–81. doi:10.1016/j.palaeo.2006.11.010

Ryskin, G. (2003). Methane-driven oceanic eruptions and mass extinctions. *Geology* 31, 741–744. doi:10.1130/G19518.1

Shen, J., Schoepfer, S. D., Feng, Q., Zhou, L., Yu, J., Song, H., et al. (2015). Marine productivity changes during the end-Permian crisis and Early Triassic recovery. *Earth. Sci. Rev.* 149, 136–162. doi:10.1016/j.earscirev.2014.11.002

Shen, Y., Farquhar, J., Zhang, H., Masterson, A., Zhang, T., Wing, B. A., et al. (2011). Multiple S-isotopic evidence for episodic shoaling of anoxic water during Late Permian mass extinction. *Nat. Commun.* 2, 210. doi:10.1038/ncomms1217

Song, H., Tong, J., Algeo, T. J., Horacek, M., Qiu, H., Song, H., et al. (2013). Large vertical $\delta^{13}C_{DIC}$ gradients in Early Triassic seas of the South China craton: Implications for oceanographic changes related to Siberian Traps volcanism. *Glob. Planet. Change* 105, 7–20. doi:10.1016/j.gloplacha.2012.10.023

Song, H., Wignall, P. B., and Dunhill, A. M. (2018). Decoupled taxonomic and ecological recoveries from the Permo-Triassic extinction. *Sci. Adv.* 4, eaat5091. doi:10.1126/sciadv.aat5091

Song, H., Wignall, P. B., Tong, J., and Yin, H. (2012). Two pulses of extinction during the Permian-Triassic crisis. *Nat. Geosci.* 6, 52–56. doi:10.1038/ngeo1649

Svensen, H., Planke, S., Polozov, A. G., Schmidbauer, N., Corfu, F., Podladchikov, Y. Y., et al. (2009). Siberian gas venting and the end-Permian environmental crisis. *Earth Planet. Sci. Lett.* 277, 490–500. doi:10.1016/j.epsl.2008.11.015

Wang, L., Wignall, P. B., Wang, Y., Jiang, H., Sun, Y., Li, G., et al. (2016). Depositional conditions and revised age of the permo-triassic microbialites at gaohua section, Cili county (hunan Province, south China). *Palaeogeogr. Palaeoclimatol. Palaeoecol.* 443, 156–166. doi:10.1016/j.palaeo.2015.11.032

Wang, Q., Tong, J., Song, H., and Yang, H. (2009). Ecological evolution across the permian/triassic boundary at the kangjiaping section in Cili county, hunan Province, China. *Sci. China Ser. D-Earth. Sci.* 52, 797–806. doi:10.1007/s11430-009-0077-0

Wang, T., Burne, R. V., Yuan, A., Wang, Y., and Yi, Z. (2019). The evolution of microbialite forms during the early triassic transgression: A case study in Chongyang of hubei Province, south China. *Palaeogeogr. Palaeoclimatol. Palaeoecol.* 519, 209–220. doi:10.1016/j.palaeo.2018.01.043

Wang, Y., Tong, J., Wang, J., and Zhou, X. (2005). Calcimicrobialite after end-Permian mass extinction in South China and its palaeoenvironmental significance. *Chin. Sci. Bull.* 50, 665–671. doi:10.1360/982004-323

Wignall, P. B., Kershaw, S., Collin, P. Y., and Crasquin, S. S. (2009). Erosional truncation of uppermost permian shallow-marine carbonates and implications for permian-triassic boundary events: Comment. *Geol. Soc. Am. Bull.* 121, 954–956. doi:10.1130/B26424.1

Wu, S., Chen, Z., Fang, Y., Pei, Y., Yang, H., Ogg, J., et al. (2017). A Permian-Triassic boundary microbialite deposit from the eastern Yangtze Platform (Jiangxi Province, South China): Geobiologic features, ecosystem composition and redox conditions. *Palaeogeogr. Palaeoclimatol. Palaeoecol.* 486, 58–73. doi:10.1016/j.palaeo.2017.05.015

Xie, S., Pancost, R. D., Huang, J., Wignall, P. B., Yu, J., Tang, X., et al. (2007). Changes in the global carbon cycle occurred as two episodes during the Permian-Triassic crisis. *Geology* 35, 1083–1086. doi:10.1130/G24224A.1

Xie, S., Pancost, R. D., Wang, Y., Yang, H., Wignall, P. B., Luo, G., et al. (2010). Cyanobacterial blooms tied to volcanism during the 5 m.y. Permo-Triassic biotic crisis. *Geology* 38, 447–450. doi:10.1130/g30769.1

Yang, H., Chen, Z., Wang, Y., Tong, J., Song, H., Chen, J., et al. (2011). Composition and structure of microbialite ecosystems following the end-Permian mass extinction in South China. *Palaeogeogr. Palaeoclimatol. Palaeoecol.* 308, 111–128. doi:10.1016/j.palaeo.2010.05.029

Yin, H., Jiang, H., Xia, W., Feng, Q., Zhang, N., Shen, J., et al. (2014). The end-Permian regression in South China and its implication on mass extinction. *Earth. Sci. Rev.* 137, 19–33. doi:10.1016/j.earscirev.2013.06.003

Yin, H., Zhang, K., Tong, J., Yang, Z., and Wu, S. (2001). The global stratotype section and point (GSSP) of the Permian-Triassic boundary. *Episodes* 24, 102–114. doi:10.18814/epiiugs/2001/v24i2/004

Zhang, G., Zhang, X., Hu, D., Li, D., Algeo, T. J., Farquhar, J., et al. (2017). Redox chemistry changes in the Panthalassic Ocean linked to the end-Permian mass extinction and delayed Early Triassic biotic recovery. *Proc. Natl. Acad. Sci. U. S. A.* 114, 1806–1810. doi:10.1073/pnas.1610931114

Zhang, G., Zhang, X., and Shen, Y. (2021). Quantitative constraints on carbon cycling and temporal changes in episodic euxinia during the end-Permian mass extinction in South China. *Chem. Geol.* 562, 120036. doi:10.1016/j.chemgeo.2020.120036

Zhang, X., Zheng, Q., Li, Y., Yang, H., Zhang, H., Wang, W., et al. (2020). Polybessurus-like fossils as key contributors to Permian-Triassic boundary microbialites in South China. *Palaeogeogr. Palaeoclimatol. Palaeoecol.* 552, 109770. doi:10.1016/j.palaeo.2020.109770

frontiers | Frontiers in Earth Science

TYPE Brief Research Report
PUBLISHED 31 July 2023
DOI 10.3389/feart.2023.747059

OPEN ACCESS

EDITED BY
Ángel Puga-Bernabéu,
University of Granada, Spain

REVIEWED BY
Annette Goetz,
State Authority for Mining, Energy and Geology, Germany
Wolfram Michael Kürschner,
University of Oslo, Norway

*CORRESPONDENCE
Agostino Merico,
agostino.merico@leibniz-zmt.de

RECEIVED 25 July 2021
ACCEPTED 17 July 2023
PUBLISHED 31 July 2023

CITATION
Hohn S, Dal Corso J, Hoke KL, Thoms S and Merico A (2023), Environmental and physiological conditions that led to the rise of calcifying nannoplankton in the Late Triassic.
Front. Earth Sci. 11:747059.
doi: 10.3389/feart.2023.747059

Environmental and physiological conditions that led to the rise of calcifying nannoplankton in the Late Triassic

Sönke Hohn[1], Jacopo Dal Corso[2], Kim Lisa Hoke[3], Silke Thoms[4] and Agostino Merico[1,5]*

[1]Leibniz Centre for Tropical Marine Research (ZMT), Department of Integrated Modelling, Bremen, Germany, [2]State Key Laboratory of Biogeology and Environmental Geology, China University of Geosciences, Wuhan, China, [3]Department of Biology, Colorado State University, Fort Collins, CO, United States, [4]Division of Biosciences, Alfred Wegener Institute for Polar and Marine Research (AWI), Bremerhaven, Germany, [5]School of Science, Constructor University, Bremen, Germany

The rise of calcifying nannoplankton in the Late Triassic (237–201 Ma) had profound consequences for the carbonate buffering capacity of the ocean. Research on the appearance of calcification typically focuses on the reasons that made this process successful on a global scale. The underlying environmental and physiological conditions that led to its appearance, therefore, are still obscure. Here we show that the rise of intracellular calcification is intrinsically linked to cellular calcium metabolism and to the prevention of calcium accumulation in the cytoplasm. Using gene tree analysis, we present evidence that the physiological machinery for calcification was already present in non-calcifying ancestor cells. Additionally, by modelling the energy demands for calcium transport in calcifying and non-calcifying cells, we demonstrate that intracellular calcification does not require additional energy investments. Since all eukaryotic cells export calcium across the plasma membrane, our findings indicate that the onset of intracellular calcification in Earth's history required only the activation of calcium transport proteins during their passage to the plasma membrane. Hence, intracellular calcification could have occurred at any time in the geological past because physiological preconditions were already present, but a combination of favourable environmental factors may have helped calcifying nannoplankton to spread at the beginning of the Mesozoic, a time of catastrophic climate changes and mass extinctions that reshuffled life on Earth.

KEYWORDS

calcareous nannoplankton, unicellular eukaryotes, calcium homeostasis, ion transport, Carnian, coccolithophores

1 Introduction

Pelagic nannoplankton calcifiers appeared in the Late Triassic (Bralower et al., 1991; Bown, 1998; Bown et al., 2004; Onoue and Yoshida, 2010; Gardin et al., 2012; Preto et al., 2013b; a), Figure 1. The first were probably small calcareous dinoflagellates that produced simple calcispheres (on average about 10 μm in diameter) composed of sub-micron scale calcium carbonate crystals, which appeared during the Carnian, about 233 Ma, when modern marine fauna was rising in the aftermath of the most catastrophic mass extinction event of the entire Phanerozoic Eon at the Permian-Triassic boundary

(Janofske, 1992; Onoue and Yoshida, 2010; Preto et al., 2013b; Preto et al., 2013a; Dal Corso et al., 2021), Figure 1. Coccolithophores, which are haptophyte algae and secrete complex ornamented calcite plates (Young, 2003; Young et al., 2005), appeared in the middle-late Norian, about 215–210 Ma (Gardin et al., 2012; Demangel et al., 2020), and spread after the Triassic-Jurassic mass extinction event (e.g.,: Bown et al., 2004), Figure 1. Before the emergence of pelagic nannoplankton calcification, the biological precipitation of calcium carbonate was dominated by metazoans and microbial mats that calcified extracellularly in a medium isolated from seawater (Lowenstam and Margulis, 1980; Kaźmierczak et al., 1985; Knoll, 2003). In contrast, calcareous nannoplankton, such as calcareous dinoflagellates (calcispheres) and coccolithophores, calcify inside intracellular compartments called vesicles and extrude the accreted crystals via exocytosis (Inouye and Pienaar, 1983; Paasche, 2002; Brownlee et al., 2015; Jantschke et al., 2020). The emergence of intracellular calcification allowed biocalcification to expand into the surface waters of the open ocean, marking the transition from the so-called "Neritan" ocean to the "Cretan" ocean (Zeebe and Westbroek, 2003; Ridgwell, 2005; de Vargas et al., 2007), Figure 1. This expansion produced a much more efficient regulation of the global carbon cycle and changed the marine calcium carbonate saturation state, transforming the entire ocean carbonate chemistry (Zeebe and Westbroek, 2003; Ridgwell, 2005; Ridgwell and Zeebe, 2005). The production of intracellular platelets that are then extruded onto the outer cell surface led to a completely new phenotype with respect to non-calcifying nannoplankton. The emergence of pelagic calcareous nannoplankton is, thus, one of the most important evolutionary innovations in Earth's history but how and why it originated is still unclear. The mechanisms driving evolutionary innovations are mutation and selection. Therefore, before identifying the benefits that could have selected intracellular calcification to make it a successful innovation at a global scale, it is important to understand the physiological characteristics (or mutations) required for its emergence.

While the evolution of extracellular calcification was likely an adaptive response to rising calcium concentrations in the ocean (Kaźmierczak et al., 1985; Kaźmierczak and Kempe, 2004), the appearance of intracellular calcification does not clearly correlate with changes in ocean chemistry (Figure 1). For example, a temporal coincidence between a Late Triassic drastic drop in atmospheric pCO_2, resulting from global carbon-climate numerical modelling, and the primary radiation of calcareous nannoplankton, inferred from the fossil record, has been observed but a cause-and-effect link between the two events could not be proven (Goddéris et al., 2008).

Moreover, when intracellular calcification emerged, the concentration of calcium in the ocean was approximately 30 mM, dissolved inorganic carbon (DIC) was 5,000 μM, and ocean pH was about 7.8 (Figure 1). These conditions would have led to a carbonate concentration of 160 μM and a calcite saturation state of 10. Although such chemical conditions would be favourable to calcification and could therefore positively select for this innovation, they alone are not sufficient to explain the appearance of intracellular calcification because the ocean experienced similar conditions 80–100 million years before the first evidence of pelagic nannoplankton calcification appears in the geological record (Late Triassic-Jurassic). The ocean experienced even higher calcium concentrations (from 50 to almost 60 mM) from the Cambrian to the Carboniferous and calcite saturation reached almost 15 in the Carboniferous and Permian. Therefore, it is plausible to assume that the emergence of intracellular calcification was most likely a consequence of random changes in cellular physiology rather than a response to external environmental factors such as changes in ocean carbonate chemistry. Using new energy budget calculations and gene analyses, we investigate here the underlying mechanisms and prerequisites that allowed intracellular calcification to appear. More explicitly, we investigate if the proteins and ion transporters involved in intracellular calcification were present in non-calcifying ancestors or appeared coincidentally with the emergence of intracellular calcification. Furthermore, we explore if intracellular calcification is indeed energetically costly as proposed by Monteiro et al. (2016) so that secondary evolutionary benefits must compensate for the energy invested into calcification. This is done by calculating the amounts of energy required to pump calcium ions into the calcifying vesicles in comparison to maintaining calcium homeostasis in all (calcifying and non-calcifying) cells.

2 Materials and methods

2.1 Analysis of environmental data

We calculated the carbonate chemistry parameters from reconstructed historic ocean pH and DIC (Ridgwell, 2005) using the standard software CO2sys, version 1.01 (Lewis and Wallace, 1998). Calculated ocean carbonate concentrations and reconstructed calcium concentrations (Stanley and Hardie, 1998) were used to determine the calcite saturation state. Atmospheric pCO_2 was obtained from previous reconstructions (Berner and Kothavala, 2001). We compared the carbonate chemistry parameters with the fossil record of pelagic calcifying nannoplankton (Bown et al., 2004) to identify the environmental conditions under which intracellular calcification emerged (Figure 1). The primary objective of this analysis is to compare, in qualitative terms, the reconstructed carbonate chemistry of the ocean with the appearance of calcareous nannoplankton. A precise, quantitative reconstruction of the carbonate chemistry throughout the Phanerozoic goes beyond the scope of our study. However, from a visual inspection, the data we compiled using literature sources and CO2sys are consistent with recent reconstructions (Witkowski et al., 2018; Montañez et al., 2016).

2.2 Calcium-transporter gene tree analysis

To examine the evolutionary history of calcification-related proteins, we identified proteins across lineages and created gene trees of relevant protein families. We downloaded protein databases from the National Center for Biotechnology Information (NCBI) genome browser for taxa represented in the phylogeny of Read et al. (2013), Supplementary Table S1. To account for differences in annotation completeness in each protein database, we used BLAST to identify homologs of *Gephyrocapsa huxleyi* proteins in each taxon. We searched the *G. huxleyi* protein database for annotated sequences

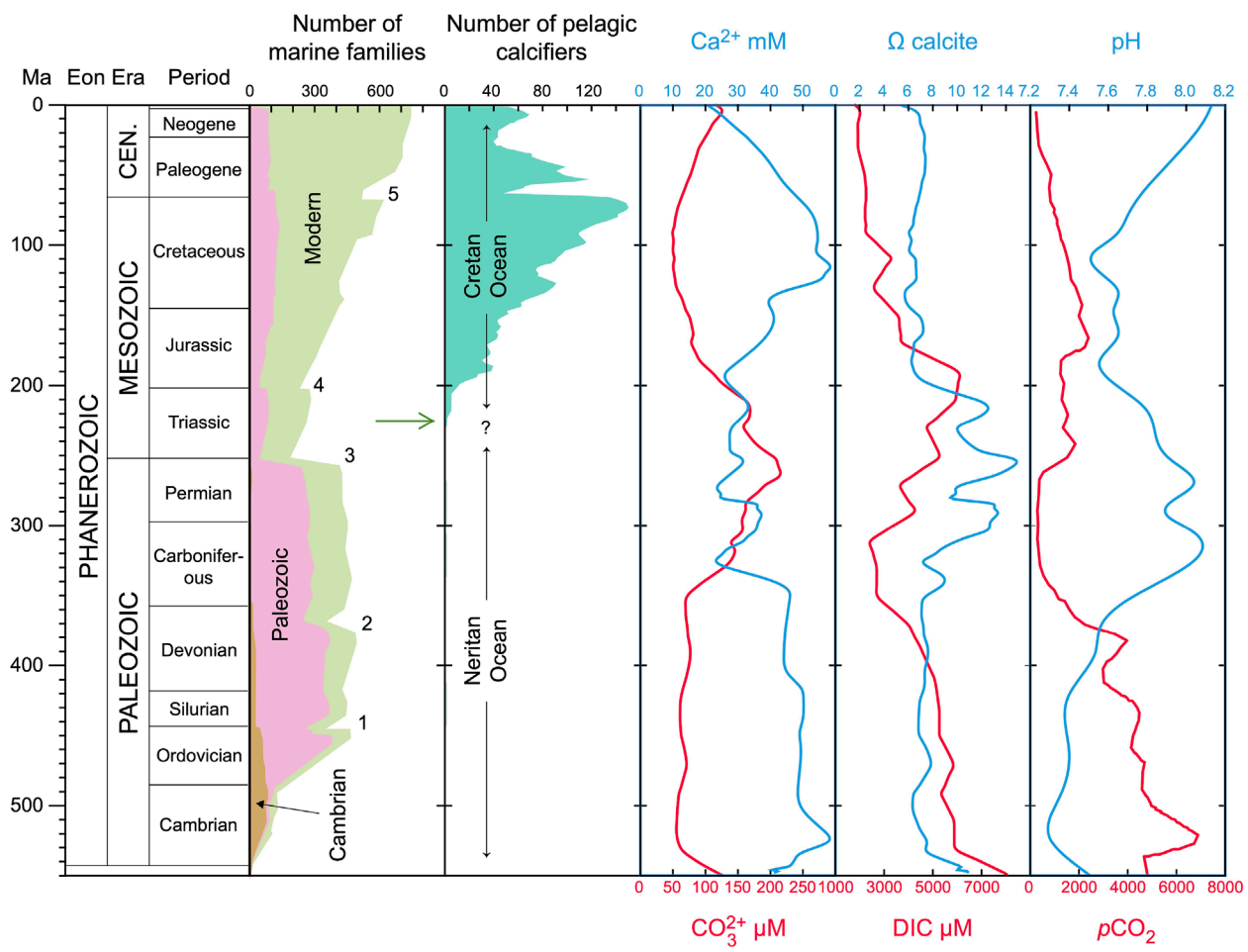

FIGURE 1
Fossil record of pelagic calcifiers and paleoceanographic carbonate chemistry over the past 550 Myr. The number of marine families and evolutionary faunas throughout the Phanerozoic are from Raup and Sepkoski Jr (1982) and Sepkoski and Ausich (1990). The numbers indicate the 5 major mass extinction events (1 = Ordovician–Silurian Extinction; 2 = Late Devonian Extinction; 3 = Permian–Triassic Extinction; 4 = Triassic–Jurassic Extinction; 5 = Cretaceous–Paleogene Extinction). The number of pelagic nannoplankton calcifiers is reconstructed by Bown et al. (2004). Note, however, that the data in Bown et al. (2004) include pelagic calcifiers in general and not exclusively nannoplankton. The concentration of calcium is taken from Stanley and Hardie (1998) and atmospheric pCO_2 from Berner and Kothavala (2001). Dissolved inorganic carbon (DIC) and ocean pH were reconstructed by Ridgwell (2005). The calcite saturation state ($\Omega_{calcite}$) was calculated, using the standard software CO2sys (Lewis and Wallace, 1998), from Ca^{2+} and CO_3^{2-} based on ocean temperature (Royer et al., 2004). The emergence of intracellular calcification (indicated by the green arrow) is marked by the rise of calcareous dinoflagellates in the early Late Triassic (Preto et al., 2013b) and was followed by the appearance of coccolithophores in the latest Triassic. Unidentified, very rare calcispheres are found in the Silurian, Devonian, and Carboniferous but are of uncertain origin (Kaźmierczak and Kremer, 2005).

in each protein family implicated in calcification (Benner et al., 2013) to use as query sequences (Supplementary Table S2). We then used pBLAST to identify all sequences in the protein database that matched these query sequences with probabilities less than e-6. After discarding duplicates, we aligned the BLAST results for each protein family in Geneious 11.1.3, (Kearse et al., 2012), http://www.geneious.com, using the Geneious global alignment with cost matrix Blosum62, gap open penalty 12, and gap extension penalty 3. We created gene trees using Jukes-Cantor genetic distance module and the UPGMA tree building method in Geneious. We then inspected trees for phylogenetic representation and patterns of protein family expansion. Because the BLAST output results for calcium channels included both cation channels and calmodulin, we split these sequences into two subtrees for better visualization of the relationships among calmodulin-related proteins. Supplementary Figures S1 – S7 show the resulting gene trees.

2.3 Calculation of energy invested into intracellular calcification

We calculated the energy required for calcium transport into Golgi-derived vesicles as part of the energy invested to maintain calcium homeostasis. In our calculations, we neglect the costs associated to the transport of golgi vesicles because these vesicles are transported by both calcifying and non-calcifying cells. We also neglect the costs required for the production of polysaccharides

and for exocytosis, the process for the secretion of polysaccharides by haptophytes, because also these costs are inccurred by non-calcifying cells and, thus, do not constitute and additional energy requirement for calcifying cells. In order to achieve intracellular calcium homeostasis, total calcium transport out of the cytoplasm has to equal the passive influx via calcium channels. The passive, diffusive uptake via the calcium channels is driven by the difference between the calcium concentration at the cell surface (Ca_{surf}) and the calcium concentration in the cytoplasm (Ca_{cyt}). Thus, knowing the calcium gradient across the plasma membrane, the energy required to achieve calcium homeostasis (E_{ATP}) can be calculated by

$$E_{ATP} = P_{Ca} \cdot A_{cell} \cdot \left(Ca_{surf} - Ca_{cyt}\right) \cdot \Psi^{\frac{ATP}{Ca}}, \quad (1)$$

where P_{Ca} is the apparent membrane permeability per cell surface area (A_{cell}) and $\Psi^{\frac{ATP}{Ca}}$ is the amount of ATP required per calcium ion transported. The consumption of one ATP molecule for transporting two calcium ions through the membrane is a functional property of the reaction loop of the Ca-ATPase (Toyoshima and Inesi, 2004; Winther et al., 2013) and is independent if transport is over the vesicle or plasma membrane. Without net calcium influx into the cell, Ca_{surf} is equal to the calcium concentration in the bulk medium (Ca_{out}). However, fluxes of calcium into intracellular compartments, such as vesicles, create a concentration gradient across the cell membrane with $Ca_{surf} < Ca_{out}$. With the total flux of calcium into the vesicles ($Q_{vesicle}$), and thus into the cell, the integration of the spherical diffusion equation in the cell environment gives the following concentration at the cell surface:

$$Ca_{surf} = Ca_{out} - \frac{Q_{vesicle}}{4 \cdot \pi \cdot r_{cell} \cdot D_{Ca}}, \quad (2)$$

where D_{Ca} is the diffusion coefficient of calcium in seawater and r_{cell} is the cell radius. Here, we assume that the transport of calcium into vesicles represents a fixed fraction of total calcium transport (f_v) as compared to the transport over the plasma membrane ($1 - f_v$), i.e.,:

$$Q_{vesicle} = f_v \cdot P_{Ca} \cdot A_{cell} \cdot \left(Ca_{surf} - Ca_{cyt}\right). \quad (3)$$

In other words, we assume that while calcium is rushing in through the ion channels, ATPases pump calcium back through the cell membrane into the extracellular medium but at the same time also into the vesicles. The volume inside the vesicle, however, can be regarded as outside of the cytoplasm from a thermodynamical point of view. In order to maintain calcium homeostasis, the flux into the cytoplasm has to be balanced by the fluxes out of the cytoplasm. Inserting the expression for $Q_{vesicle}$ into Eq. 2 and subtracting Ca_{cyt} from both sides of Eq. 2 results in an implicit equation for the concentration difference Ca_{surf} - Ca_{cyt}, which has the solution:

$$Ca_{surf} - Ca_{cyt} = \frac{Ca_{out} - Ca_{cyt}}{1 + \frac{f_v \cdot P_{Ca} \cdot A_{cell}}{4 \cdot \pi \cdot r_{cell} \cdot D_{Ca}}} \quad (4)$$

Replacing in Eq. 1 the concentration difference $Ca_{surf} - Ca_{cyt}$ with Eq. 4 gives E_{ATP} as a function of the relative fraction of calcium transport into the calcifying vesicles:

$$E_{ATP} = P_{Ca} \cdot A_{cell} \cdot \frac{Ca_{out} - Ca_{cyt}}{1 + \frac{f_v \cdot P_{Ca} \cdot A_{cell}}{4 \cdot \pi \cdot r_{cell} \cdot D_{Ca}}} \cdot \Psi^{\frac{ATP}{Ca}} \quad (5)$$

This equation shows that the higher f_v, the lower the absolute requirements for cellular energy. In order to quantify how much the cellular energy consumption can potentially be reduced by intracellular calcification, we calculate the energy requirements to maintain calcium homeostasis as a function of f_v from 0 (non-calcifying cell) to 1 (Supplementary Figure S8). The coccolithophore *Gephyrocapsa huxleyi* produces approximately 1 coccolith per hour (Paasche, 1962) and one coccolith contains around 22 fmol of $CaCO_3$ (Young and Ziveri, 2000). This results in a calcification flux ($Q_{vesicle}$) of about $6.11 \cdot 10^{-18}$ mol s^{-1} (see: Holtz et al., 2013). Since the permeability of the plasma membrane for calcium ions is not known in coccolithophores, we estimate a permeability that is based on the conductance of calcium channels (Lux and Nagy, 1981) and measured densities of calcium channels in cell membranes of snail axons (Krishtal et al., 1981; Tsien, 1983). All the parameter values used to calculate the extra energy required by intracellular calcification are reported in Supplementary Table S3. We provide the numerical code for calculating the energy required to maintain calcium homeostasis by single-celled calcifying nannoplankton as open-source software (https://github.com/systemsecologygroup/Calcisphere) so that it can be used, modified, and redistributed freely.

2.4 Calculation of intracellular calcium poisoning

The energy for the Ca^{2+} pumping ATPase is provided by the hydrolysis of ATP at a high ATP/ADPxPi ratio in the cytosol with a free energy gain, ΔG, of 15 kcal/mol (Meldolesi and Pozzan, 1998). Cooperative binding of 2 Ca^{2+} per ATPase implies a Ca^{2+}/ATP coupling ratio of 2 (Inesi and Tadini-Buoninsegni, 2014). We assume an electroneutral $Ca^{2+}/2H^{+}$ co-transport for the Ca^{2+} pump and a physiological pH at both sides of the Ca^{2+} pump. If all of the free energy available from ATP hydrolysis is stored in the concentration gradient of Ca^{2+} between the cytosol and its environment, i.e.,: $\Delta G = 2RT \cdot \ln(Ca_{surf}/Ca_{cyt})$, the calcium gradient can be up to 10^5. If the Ca-ATPases work near this thermodynamic limit, the cytosolic Ca^{2+} concentration of 0.1 μmol L^{-1} and the gradient of 10^5 yields a Ca^{2+} concentration of 10 mM at the cell surface, which is, in fact, exactly the Ca^{2+} concentration in today's ocean (Langer et al., 2006). Ca^{2+} transport near the thermodynamic limit would have the advantages that: 1) pumping Ca^{2+} from the cytosol to the environment proceeds with a minimum dissipation of energy in ATP consumption, and 2) a steep Ca^{2+} gradient provides fast influx in cell signaling. We therefore postulate that a constant Ca^{2+}-gradient close to the thermodynamic limit represents a part of calcium homeostasis. Moreover, the Ca^{2+}-gradient across the plasma membrane should be quite independent of the bulk Ca^{2+} concentration in seawater.

Assuming that the Ca^{2+}-gradient across the plasma membrane is maintained at 10^5 by the Ca^{2+}-ATPase, the intracellular calcium concentration will respond to variations in extracellular calcium concentration as experienced during Earth's history (Stanley and Hardie, 1998), Figure 1. The intracellular concentration of calcium (Ca_{cyt}), however, generates a constraint on the intracellular phosphate concentration (PO_{cyt}) because calcium and phosphate precipitate to $Ca_3(PO_4)_2$ when the ion product

exceeds the solubility product $K_{sp}^{Ca_3(PO_4)_2} = PO_{cyt} \cdot Ca_{cyt}$. We can therefore calculate the maximum possible intracellular phosphate concentration for any intracellular calcium concentration as follows:

$$PO_{cyt} = \sqrt{\frac{K_{sp}^{Ca_3(PO_4)_2}}{Ca_{cyt}}}. \quad (6)$$

3 Results and discussion

3.1 Calcium metabolism

Calcium ions play important roles in the physiology of eukaryotic cells, including control of DNA synthesis, chromosomal configuration, and signal transduction (Marcum et al., 1978; Boynton et al., 1980; Krishtal et al., 1981; Lux and Nagy, 1981; Tsien, 1983; Poenie et al., 1985; Carafoli, 1987; Steinhardt and Alderton, 1988; Hepler, 1994; Sanders et al., 2002; Verret et al., 2010). Calcium ions enter the cell passively via channels (Gussone et al., 2006; Verret et al., 2010) that allow for a diffusive influx driven by a steep concentration gradient across the plasma membrane (Langer et al., 2006). Excess intracellular Ca^{2+} is then actively removed by calcium-binding proteins (e.g., calmodulin) and transport proteins (Ca^{2+}-ATPase and Na^+/Ca^{2+} exchanger) with different calcium affinities and maximum transport rates (Carafoli, 1987). The Ca^{2+} concentration inside the cell has to be tightly regulated (calcium homeostasis) at around 0.1 μmol L^{-1} (Brownlee et al., 1995) for optimal cell functioning (Carafoli, 1987) and to avoid cell poisoning (Simkiss, 1977; Orrenius et al., 1989; Müller et al., 2015).

The same proteins that maintain intracellular calcium homeostasis in non-calcifying cells (Figure 2A) are implicated in intracellular calcification (Figure 2B). To determine whether an expansion of protein families coincides with the emergence of intracellular calcification, we compared all gene families involved in the precipitation of calcium carbonate (von Dassow et al., 2009) in a large number of eukaryotes (Read et al., 2013). These genes include Ca^{2+} transporting ATPases, HCO_3^- transporters, Ca^{2+} channels, calmodulin, carbonic anhydrase, Ca^{2+}/H^+ exchangers, Na^+/Ca^{2+} exchangers, and vacuolar H^+-ATPases. The presence of calcium transport proteins in all eukaryotes clearly indicates that these genes are not unique to intracellular calcification. We found no evidence that diversification of these gene families could explain the appearance of nannoplankton calcification (Supplementary Figures S1 – S7).

The most significant difference between calcifying and non-calcifying cells is that calcium carbonate precipitates inside Golgi-derived vesicles. The vesicles fuse with the plasma membrane and the calcium carbonate is extruded outside the cell where it remains attached to the extracellular organic matrix. The same vesicular pathway is used in non-calcifying cells to produce new membrane material and to transport proteins to the plasma membrane (Figure 3). All ion transporters and channels that help establish calcium homeostasis in non-calcifying cells, therefore, reach the plasma membrane via Golgi-derived transport vesicles (Pfeffer and Rothmann, 1987). However, the Ca^{2+} transporting ATPase initially occurs in its auto-inhibited form and becomes activated by the presence of calmodulin (Tidow et al., 2012) at the plasma membrane. We thus argue that the emergence of intracellular calcification was triggered by the activation of calcium pumps during the passage of transport vesicles from the Golgi apparatus to the plasma membrane, following the accumulation of calcium in the transport vesicles. This explanation is consistent with the simple structure of sub-micron scaled calcite crystals of proto-calcispheres found in previous studies and attributed to calcareous dinoflagellates (Janofske, 1992; Preto et al., 2013b; Dal Corso et al., 2021). The activation of the calcium transport inside the Golgi apparatus would later lead to the formation of more elaborated coccolith-like platelets due to the specific endomembranous structure of the Golgi apparatus (Figure 3). This is also in line with the finding that inhibition of the cytoskeleton and microtubule formation induces malformations in modern coccolith (Langer et al., 2010).

Such a change in timing of activation would not be detected in gene sequence comparison, as they require protein functional assays. We conclude, however, that all components necessary for the emergence of intracellular calcification were already present in non-calcifying ancestor cells and that no major modifications of cellular physiology and structure were required to induce intracellular calcification. An alternative and speculative hypothesis to the activation of calcium pumps could be that those pumps were already active and that the precipitation of calcium carbonate in the vesicles was prevented by inhibitors, which were subsequently lost thus leading to the emergence of intracellular calcification. But also in this alternative case, the emergence of intracellular calcification would not require major innovations in cellular structure, which is our main argument here.

3.2 Energy requirements

Since ion transport requires energy, a previous study (Monteiro et al., 2016) assumed that intracellular calcification is energetically costly, thus implying the presence of associated benefits to overcome natural selection. But because non-calcifying cells also export calcium from their cytoplasm, the energetic costs of calcification have to be quantified by comparing the costs required for ion transport into vesicles in calcifying cells versus those required by ion transport across the plasma membrane (to maintain calcium homeostasis) in both calcifying and non-calcifying cells. We therefore assessed the energetic costs of intracellular calcification by calculating the total energy required by cellular calcium transport to maintain calcium homeostasis. Our calculations indicate that the precipitation of $CaCO_3$ inside the vesicle removes calcium from the solution and generates a sink that depletes calcium around the cell, Eq. 2. Consequently, the gradient across the plasma membrane that drives the diffusive calcium influx through the channel is reduced with respect to non-calcifying cells, Eq. 4, thus fewer ions have to be transported out of the cytoplasm in order to maintain calcium homeostasis, Eq. 5. Since the energy required for active calcium transport out of a calcifying cell is negligibly lower than that required in non-calcifying cells (Supplementary Figure S8), we conclude that extra energy is not needed to transport calcium for intracellular calcification.

10.3389/feart.2023.747059

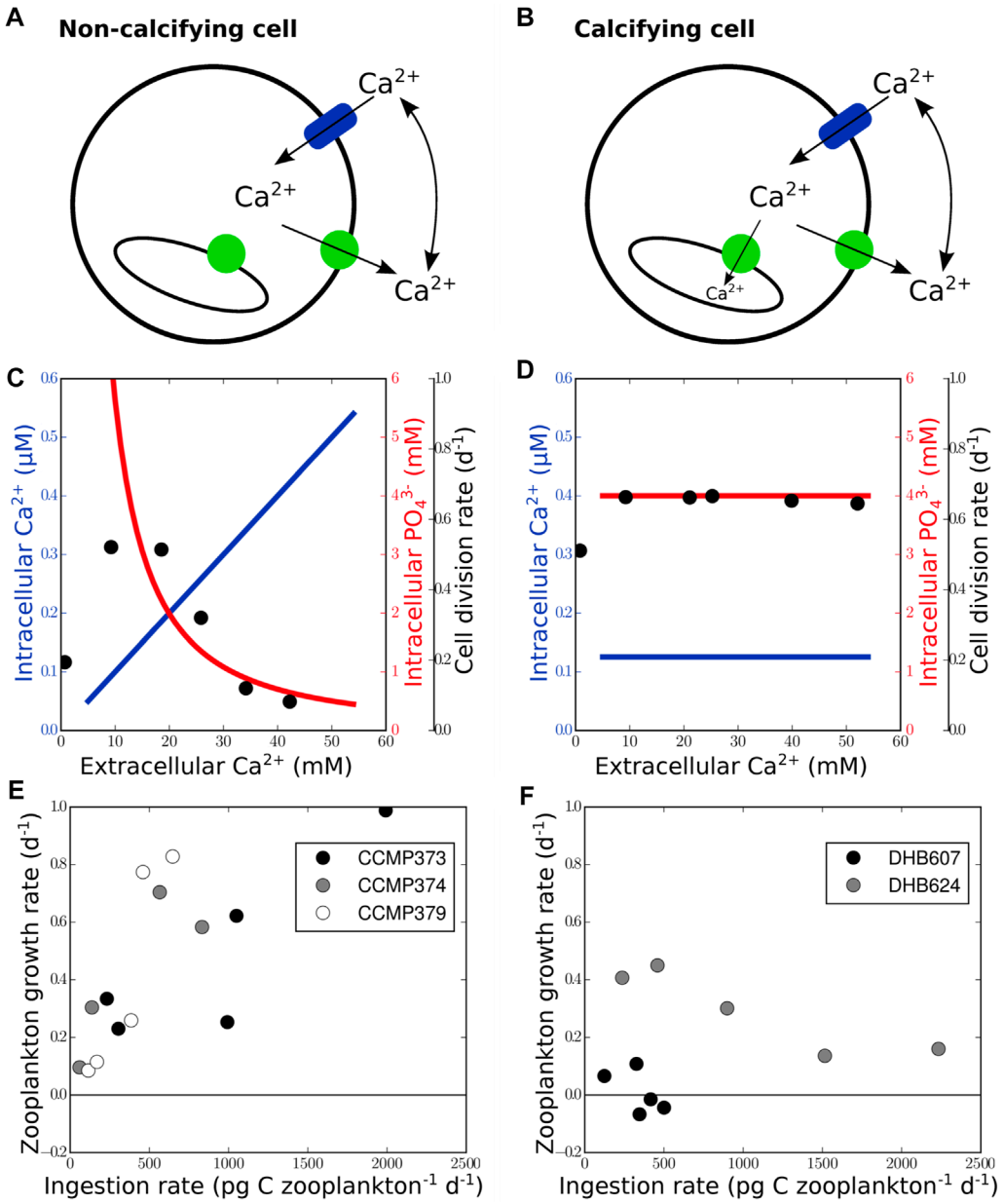

FIGURE 2
Physiological and ecological benefits of intracellular calcification. Calcifying cells **(B)** differ from non-calcifying cells **(A)** by the presence of intravesicular calcium accumulation in Golgi-derived transport vesicles (green circles represent Ca^{2+} pump/ATPase; blue cylinder indicates calcium channel). Calcium transport into vesicles allows maintenance of calcium homeostasis under elevated extracellular calcium concentrations **(D)** and prevents drawdown of intracellular phosphate **(C)** due to precipitation of $Ca_3(PO_4)_2$ in the cytosol. Therefore, cell division rates, black dots in **(C)** and **(D)**, redrawn from Müller et al. (2015), remain unaffected by extracellular calcium concentrations in calcifying cells contrary to non-calcifying cells. The growth rate of zooplankton fed with calcifying cells **(F)** is generally lower than that of zooplankton fed with non-calcifying cells **(E)**, data taken from Harvey et al. (2015) and originally produced from batch cultures in exponential growth phase by Strom et al. (2003).

However, our energy calculations also show that the reduction in energy requirements is very small because the calcification flux is slow compared to extracellular calcium diffusion so that no significant diffusive boundary layer develops at the cell surface. If all calcium ions were transported into the vesicles and no calcium were exported through the plasma membrane, $f_v = 1.0$ in Eq. 5, the energy requirements would only be 0.16 percent less than if no calcium were transported into vesicles and all ions were exported through the plasma membrane, $f_v = 0.0$ in Eq. 5.

Besides calcium ions, also carbonate ions are needed in the vesicle to sustain calcification. The transport of carbon could thus be another process requiring energy. However, the transport of hydrogen ions that is coupled to calcium transport creates an alkaline medium inside the calcifying vesicle that shifts the

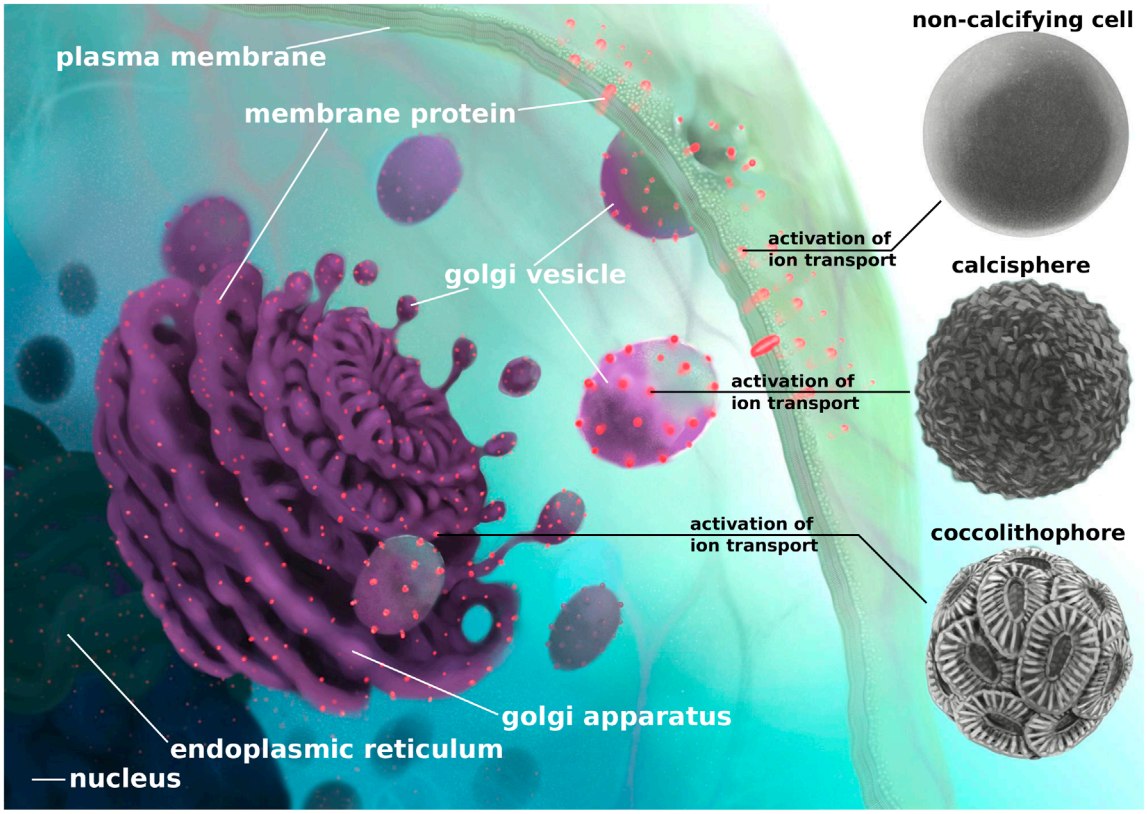

FIGURE 3
Schematic reconstruction of the steps that, based on our findings, would have led to the emergence of nannoplankton calcification. After transcription from DNA to mRNA in the nucleus, gene copies are translated into proteins in the endoplasmic reticulum. Proteins that are bound to the plasma membrane are incorporated into the ER membrane and are transported via vesicles to the Golgi apparatus. Golgi-derived vesicles are then transported to the plasma membrane where the vesicles fuse and shed their content to the extracellular space. The vesicle membrane, including all membrane proteins, becomes part of the plasma membrane. We suggest that, in a non-calcifying cell, the activation of calcium transporters occurs at the plasma membrane. Earlier activation of calcium transporters in transport vesicles would allow precipitation of sub-micron scale crystals inside the vesicles that could have led to the formation of proto-calcispheres by calcareous dinoflagellates (Janofske, 1992; Preto et al., 2013b; Dal Corso et al., 2021). The activation of calcium transporters, in the more structurally complex endomembranous systems like the Golgi apparatus, could explain the formation of delicate coccoliths and the emergence of modern-like coccolithophores. The chronological order of the appearance of calcispheres and coccolithophores shown in the diagram (from top to bottom) does not necessarily represent direct evolutionary steps regarding the activation of calcium transporters but may represent parallel origins of early Ca^{2+} transport activation that happened independently (Meier et al., 2007).

equilibrium of the carbonate system towards carbonate ions and lowers the CO_2 concentration (Holtz et al., 2013; Holtz et al., 2015). CO_2 can, therefore, passively diffuse through the vesicle membrane to replenish the carbonate ions consumed by calcification, thus sustaining calcification at moderate rates (see Figure 3 and Table 4 in Holtz et al., 2013) without additional metabolic costs. Additional carbon transport into the vesicles may only be required to sustain higher calcification rates, as observed in some coccolithophore species (e.g., *G. huxleyi*) that appeared later in the geological records. Data in support of these arguments can be found in Paasche (1962) and in Young and Ziveri (2000). Since the bicarbonate concentration in the calcifying vesicle is higher than in the cytoplasm, bicarbonate would then need to be transported actively under consumption of metabolic energy (Holtz et al., 2015). However, the bicarbonate gradient across the vesicle membrane is much smaller than the calcium gradient and CO_2 can freely diffuse across the membrane, thereby functioning as a major source of carbon to the calcifying vesicle (Holtz et al., 2015) and, thus, preventing additional energetic requirements for bicarbonate transport.

3.3 Evolutionary success

Because of its low metabolic requirements, intracellular calcification does not require secondary evolutionary benefits to emerge. Yet, a number of hypotheses in relation to potential benefits of intracellular calcification have been proposed to explain both emergence and success of coccolithophores. These hypotheses include the potential enhancement of photosynthesis via the removal of carbonate ions (Nielsen, 1966; Paasche, 2002), protection against photoinhibition, advantages in hydrodynamic control, and protection against viruses, bacteria, and grazing (Monteiro et al., 2016). However, enhanced calcification does not enhance photosynthesis (Herfort et al., 2004; Trimborn et al., 2007)

and non-calcifying coccolithophore cells can grow even faster than calcifying cells (Rost and Riebesell, 2004). Non-calcifying strains appear also not affected by photo-inhibition at high irradiances (Nanninga and Tyrrell, 1996). Additionally, coccolithophores use non-calcifying haploid stages to escape viral infections of calcified diploid cells (Frada et al., 2008), also questioning the relevance of calcification for viral protection. All these cases cast doubts on the assumption that calcification presents relevant physiological advantages.

Previous experiments (Müller et al., 2015) showed that calcifying cells can grow faster than non-calcifying cells when exposed to elevated calcium concentrations, indicating that intracellular calcification may protect against calcium poisoning (Simkiss, 1977). Our calculations show that the Ca^{2+}-ATPase can transport ions against a gradient of up to 10^5 (see Supplementary Material S1). In non-calcifying cells, an increase of extracellular Ca^{2+} concentrations yields an increase of intracellular Ca^{2+} (Figure 2C). Since intracellular phosphate concentrations are usually around 4–5 mM (Auesukaree et al., 2004), cells operate at calcium and phosphate concentrations just below the solubility product of $Ca_3(PO_4)_2$ (Chow, 2001). Increasing intracellular calcium concentrations, therefore, lead to precipitation with phosphate due to the low solubility of $Ca_3(PO_4)_2$ (Pytkowicz and Kester, 1967; Chow, 2001). The decrease of cellular phosphate impedes cell growth in non-calcifying cells (Figure 2C). In calcifying cells, calcium transport into intracellular vesicles can still occur under elevated extracellular calcium concentrations because the calcium concentration inside the vesicle (ranging from 0.5 to 10 mM Holtz et al., 2013; Holtz et al., 2015) required for the precipitation of calcium carbonate is lower than outside the cell. The calcium gradient at the vesicle membrane therefore permits Ca^{2+}-ATPase activity and allows maintenance of calcium homeostasis even under elevated extracellular calcium concentrations (Figure 2D). Cell division of calcifying cells remains unaffected (Müller et al., 2015).

Another benefit proposed for intracellular calcification is protection against zooplankton grazing (Jaya et al., 2016; Monteiro et al., 2016). However, coccolithophores are grazed by copepods without any significant sign of saturation of ingestion rates at increasing coccolithophore densities (Harris, 1994). This indicates that calcification and thus mechanical stability does not necessarily protect against copepod grazing. Calcification can, however, have an indirect negative effect on zooplankton grazing. Culture experiments (Harvey et al., 2015) showed that ingestion of calcifying cells reduces the growth rate of the grazers (Figure 2F), whereas ingestion of non-calcifying cells leads to an incrase in zooplankton growth rate (Figure 2E). A reduction of coccolithophore grazing mortality would thus provide calcifying cells with a competitive advantage against non-calcifying cells (Monteiro et al., 2016). Though not relevant for the emergence of pelagic nannoplankton calcification, the potential chemical protection against grazing may have contributed to its ecological success.

4 Conclusion

In summary, our analyses indicate that the first appearance of intracellular calcification is intrinsically linked to cellular calcium metabolism and to the prevention of calcium accumulation in the cytoplasm. This process did not require major physiological mutations or extra energy but only a very minor change, that is the activation of calcium transport proteins during their passage from the endoplasmic reticulum to the plasma membrane. Therefore, this innovation could have occurred at any time in the geologic past because preconditions were favourable, in line with evidence suggesting unrelated appearances in different lineages. A combination of environmental factors, such as chemical conditions and ecological interactions, may have subsequently helped calcifying nannoplankton to become abundant at a global scale. Therefore, nannoplankton calcifiers rose in pelagic environments during a time, the beginning of the Mesozoic, of profound changes in the structure of Earth's ecosystems, marked by major climate changes and biological crises (i.e., the Permian–Triassic mass extinction, the Carnian Pluvial Episode and the Triassic-Jurassic mass extinction), which wiped out most of the Palaeozoic life and paved the way to the emergence of modern organisms. Within these new ecosystems, calcifying nannoplankton spread.

Data availability statement

The original contributions presented in the study are included in the article/Supplementary Material, further inquiries can be directed to the corresponding author.

Author contributions

SH, JDC, and AM conceived the idea of the study. SH and ST performed the energy budget calculations. KLH compiled the genetic information and performed the gene tree analysis. All authors contributed to the interpretation of the results. SH and AM wrote the manuscript with contributions from all authors. All authors contributed to the article and approved the submitted version.

Funding

Hanse-Wissenschaftskolleg (HWK) provided visiting fellowships to JDC and KLH.

Acknowledgments

We gratefully acknowledge the Hanse-Wissenschaftskolleg (HWK), Delmenhorst, Germany, for providing visiting fellowship to JDC and KLH and thus for creating the opportunity to bring together the multidisciplinary expertise necessary for this study.

Conflict of interest

The authors declare that the research was conducted in the absence of any commercial or financial relationships

that could be construed as a potential conflict of interest.

Publisher's note

All claims expressed in this article are solely those of the authors and do not necessarily represent those of their affiliated organizations, or those of the publisher, the editors and the reviewers. Any product that may be evaluated in this article, or claim that may be made by its manufacturer, is not guaranteed or endorsed by the publisher.

Supplementary material

The Supplementary Material for this article can be found online at: https://www.frontiersin.org/articles/10.3389/feart.2023.747059/full#supplementary-material

References

Auesukaree, C., Homma, T., Tochio, H., Shirakawa, M., Kaneko, Y., and Harashima, S. (2004). Intracellular phosphate serves as a signal for the regulation of the PHO pathway in *Saccharomyces cerevisiae*. *J. Biol. Chem.* 279, 17289–17294. doi:10.1074/jbc.M312202200

Benner, I., Diner, R. E., Lefebvre, S. C., Li, D., Komada, T., Carpenter, E. J., et al. (2013). *Emiliania huxleyi* increases calcification but not expression of calcification-related genes in long-term exposure to elevated temperature and pCO_2. *Philosophical Trans. R. Soc. B* 368, 20130049. doi:10.1098/rstb.2013.0049

Berner, R. A., and Kothavala, Z. (2001). Geocarb III: A revised model of atmospheric CO_2 over phanerozoic time. *Am. J. Sci.* 301, 182–204. doi:10.2475/ajs.301.2.182

Bown, P. R. (1998). *Calcareous nannofossil biostratigraphy*. Dordrecht: Springer.

Bown, P. R., Lees, J. A., and Young, J. R. (2004). "Calcerous nannoplankton evolution and diersity through time," in *Coccolithophores. From molecular processes to global impact* (Springer Berlin), 481–508.

Boynton, A. L., Whitfield, F. F., and MacManus, J. P. (1980). Calmodulin stimulates DNA synthesis by Rat Liver cells. *Biochem. Biophysical Res. Commun.* 95, 745–749. doi:10.1016/0006-291x(80)90849-9

Bralower, T. J., Bown, P. R., and Siesser, W. G. (1991). Significance of upper triassic nannofossils from the southern hemisphere (ODP leg 122, wombat plateau, NW Australia). *Mar. Micropaleontol.* 17, 119–154. doi:10.1016/0377-8398(91)90025-2

Brownlee, C., Davies, M., Nimer, N., Dong, L., and Merrett, M. (1995). Calcification, photosynthesis and intracellular regulation in Emiliania huxleyi. *Bull. l'institute Océanogr. Monaco* 14, 19–36.

Brownlee, C., Wheeler, G. L., and Taylor, A. R. (2015). Coccolithophore biomineralization: New questions, new answers. *Seminars Cell and Dev. Biol.* 46, 11–16. doi:10.1016/j.semcdb.2015.10.027

Carafoli, E. (1987). Intracellular calcium homeostasis. *Ann. Rev. Biochem.* 56, 395–433. doi:10.1146/annurev.bi.56.070187.002143

Chow, L. (2001). Solubility of calcium phosphates. *Octacalcium Phosphate* l, 94–111. doi:10.1159/000061650

Dal Corso, J., Preto, N., Agnini, C., Hohn, S., Merico, A., Willems, H., et al. (2021). Rise of calcispheres during the carnian pluvial Episode (late triassic). *Glob. Planet. Change* 200, 103453. doi:10.1016/j.gloplacha.2021.103453

de Vargas, C., Aubry, M. P., Probert, I., and Young, J. (2007). Origin and evolution of coccolithophores. From coastal hunters to oceanic farmers. *Evol. Prim. Prod. Sea* 2007, 251–285. doi:10.1016/B978-012370518-1/50013-8

Demangel, I., Kovács, Z., Richoz, S., Gardin, S., Krystyn, L., Baldermann, A., et al. (2020). Development of early calcareous nannoplankton in the late triassic (northern calcareous alps, Austria). *Glob. Planet. Change* 193, 103254. doi:10.1016/j.gloplacha.2020.103254

Frada, M., Probert, I., Allen, M. J., Wilson, W. H., and de Vargas, C. (2008). The Cheshire Cat escape strategy of the coccolithophore Emiliania huxleyi in response to viral infection. *Proc. Natl. Acad. Sci.* 105, 15944–15949. doi:10.1073/pnas.0807707105

Gardin, S., Krystyn, L., Richoz, S., Bartolini, A., and Galbrun, B. (2012). Where and when the earliest coccolithophores? *Lethaia* 45, 507–523. doi:10.1111/j.1502-3931.2012.00311.x

Goddéris, Y., Donnadieu, Y., Vargas, C. D., Pierrehumbert, R. T., Dromart, G., and van de Schootbrugge, B. (2008). Causal or casual link between the rise of nannoplankton calcification and a tectonically-driven massive decrease in Late Triassic atmospheric CO_2? *Earth Planet. Sci. Lett.* 267, 247–255. doi:10.1016/j.epsl.2007.11.051

Gussone, N., Langer, G., Thoms, S., Nehrke, G., Eisenhauer, A., Riebesell, U., et al. (2006). Cellular calcium pathways and isotope fractionation in Emiliania huxleyi. *Geology* 34, 625–628. doi:10.1130/G22733.1

Harris, R. P. (1994). Zooplankton grazing on the coccolithophore Emiliania huxleyi and its role in inorganic carbon flux. *Mar. Biol.* 119, 431–439. doi:10.1007/BF00347540

Harvey, E. L., Bidle, K. D., and Johnson, M. D. (2015). Consequences of strain variability and calcification in *Emiliania huxleyi* on microzooplankton grazing. *J. Plankton Res.* 37, fbv081–1148. doi:10.1093/plankt/fbv081

Hepler, P. K. (1994). The role of calcium in cell division. *Cell Calcium* 16, 322–330. doi:10.1016/0143-4160(94)90096-5

Herfort, L., Loste, E., Meldrum, F., and Thake, B. (2004). Structural and physiological effects of calcium and magnesium in Emiliania huxleyi (Lohmann) Hay and Mohler. *J. Struct. Biol.* 148, 307–314. doi:10.1016/j.jsb.2004.07.005

Holtz, L. M., Thoms, S., Langer, G., and Wolf-Gladrow, D. A. (2013). Substrate supply for calcite precipitation in Emiliania huxleyi: Assessment of different model approaches. *J. Phycol.* 49, 417–426. doi:10.1111/jpy.12052

Holtz, L. M., Wolf-Gladrow, D., and Thoms, S. (2015). Numerical cell model investigating cellular carbon fluxes in Emiliania huxleyi. *J. Theor. Biol.* 364, 305–315. doi:10.1016/j.jtbi.2014.08.040

Inesi, G., and Tadini-Buoninsegni, F. (2014). Ca^{2+}/H^{+} exchange, lumenal Ca^{2+} release and Ca^{2+}/ATP coupling ratios in the sarcoplasmic reticulum ATPase. *J. Cell Commun. Signal.* 8, 5–11. doi:10.1007/s12079-013-0213-7

Inouye, I., and Pienaar, R. N. (1983). Observations on the life cycle and microanatomy of Thoracosphaera heimii (Dinophyceae) with special reference to its systematic position. *S. Afr. Tydskr. Plantk.* 2, 63–75. doi:10.1016/S0022-4618(16)30147-4

Janofske, D. (1992). Kalkiges Nannoplankton, insbesondere Kalkige Dinoflagellaten-Zysten der alpinen Ober-Trias: Taxonomie, Biostratigraphie und Bedeutung für die Phylogenie der Peridiniales. *Berl. Geowiss. Abh. Reihe E* 4, 53.

Jantschke, A., Pinkas, I., Schertel, A., Addadi, L., and Weiner, S. (2020). Biomineralization pathways in calcifying dinoflagellates: Uptake, storage in mgcap-rich bodies and formation of the shell. *Acta Biomater.* 102, 427–439. doi:10.1016/j.actbio.2019.11.042

Jaya, B. N., Hoffmann, R., Kirchlechner, C., Dehm, G., Scheu, C., and Langer, G. (2016). Coccospheres confer mechanical protection: New evidence for an old hypothesis. *Acta Biomater.* 42, 258–264. doi:10.1016/j.actbio.2016.07.036

Kaźmierczak, J., Ittekkot, V., and Degens, E. T. (1985). Biocalcification through time: Environmental challenge and cellular response. *Paläontologische Z.* 59, 15–33. doi:10.1007/BF02985996

Kaźmierczak, J., Kempe, (2004). "Calcium build-up in the precambrian sea," in *Origins: Genesis, evolution and diversity of life* (Springer), 329–345.

Kaźmierczak, J., and Kremer, B. (2005). Early post-mortem calcified Devonian acritarchs as a source of calcispheric structures. *Facies* 51, 554–565. doi:10.1007/s10347-005-0071-8

Kearse, M., Moir, R., Wilson, A., Stones-havas, S., Cheung, M., Sturrock, S., et al. (2012). Geneious Basic: An integrated and extendable desktop software platform for the organization and analysis of sequence data. *Bioinformatics* 28, 1647–1649. doi:10.1093/bioinformatics/bts199

Knoll, A. H. (2003). Biomineralization and evolutionary history. *Rev. Mineralogy Geochem.* 54, 329–356. doi:10.2113/0540329

Krishtal, O. A., Pidoplichko, V. I., and Shakhovalov, Y. A. (1981). Conductance of the calcium channel in the membrane of snail neurones. *J. physiology* 310, 423–434. doi:10.1113/jphysiol.1981.sp013558

Langer, G., De Nooijer, L. J., and Oetjen, K. (2010). On the role of the cytoskeleton in coccolith morphogenesis: The effect of cytoskeleton inhibitors. *J. Phycol.* 46, 1252–1256. doi:10.1111/j.1529-8817.2010.00916.x

Langer, G., Gussone, N., Nehrke, G., Riebesell, U., Eisenhauer, A., Kuhnert, H., et al. (2006). Coccolith strontium to calcium ratios in Emiliania huxleyi: The dependence on seawater strontium and calcium concentrations. *Limnol. Oceanogr.* 51, 310–320. doi:10.4319/lo.2006.51.1.0310

Lewis, E., and Wallace, D. (1998). *CO2SYS program. Tech. Rep., carbon dioxide information analysis center*. Oak Ridge, Tennessee: Oak Ridge National Laboratory Environmental Sciences Division.

Lowenstam, H. A., and Margulis, L. (1980). Evolutionary prerequisites for early phanerozoic calcareous skeletons. *BioSystems* 12, 27–41. doi:10.1016/0303-2647(80)90036-2

Lux, H. D., and Nagy, K. (1981). Single Channel Ca^{2+} currents in helix pomatia neurons. *Pflügers Archiv Eur. J. Physiology* 391, 252–254. doi:10.1007/bf00596179

Marcum, J. M., Dedman, J. R., Brinkley, B. R., and Means, A. R. (1978). Control of microtubule assembly-disassembly by calcium-dependent regulator protein. *Proc. Natl. Acad. Sci.* 75, 3771–3775. doi:10.1073/pnas.75.8.3771

Meier, K. J., Young, J. R., Kirsch, M., and Feist-Burkhardt, S. (2007). Evolution of different life-cycle strategies in oceanic calcareous dinoflagellates. *Eur. J. Phycol.* 42, 81–89. doi:10.1080/09670260600937833

Meldolesi, J., and Pozzan, T. (1998). The endoplasmic reticulum Ca^{2+} store: A view from the lumen. *Trends Biochem. Sci.* 23, 10–14. doi:10.1016/S0968-0004(97)01143-2

Montañez, I. P., McElwain, J. C., Poulsen, C. J., White, J. D., DiMichele, W. A., Wilson, J. P., et al. (2016). Climate, p_{co2} and terrestrial carbon cycle linkages during late palaeozoic glacial–interglacial cycles. *Nat. Geosci.* 9, 824–828. doi:10.1038/ngeo2822

Monteiro, F. M., Bach, L. T., Brownlee, C., Bown, P., Rickaby, R. E. M., Poulton, A. J., et al. (2016). Why marine phytoplankton calcify. *Sci. Adv.* 2, e1501822. doi:10.1126/sciadv.1501822

Müller, M. N., Barcelos E Ramos, J., Schulz, K. G., Riebesell, U., Kaźmierczak, J., Gallo, F., et al. (2015). Phytoplankton calcification as an effective mechanism to alleviate cellular calcium poisoning. *Biogeosciences* 12, 6493–6501. doi:10.5194/bg-12-6493-2015

Nanninga, H. J., and Tyrrell, T. (1996). Importance of light for the formation of algal blooms by Emiliania huxleyi. *Mar. Ecol. Prog. Ser.* 136, 195–203. doi:10.3354/meps136195

Nielsen, E. S. (1966). The uptake of free CO_2 and HCO_3^- during photosynthesis of plankton algae with special reference to the coccolithophorid coccolithus huxleyi. *Physiol. Plant.* 19, 232–240. doi:10.1111/j.1399-3054.1966.tb09095.x

Onoue, T., and Yoshida, A. (2010). Depositional response to the Late Triassic ascent of calcareous plankton in pelagic mid-oceanic plate deposits of Japan. *J. Asian Earth Sci.* 37, 312–321. doi:10.1016/j.jseaes.2009.08.013

Orrenius, S., McConkey, D. J., Bellomo, G., and Nicotera, P. (1989). Role of Ca^{2+} in toxic cell killing. *Trends Pharmacol. Sci.* 10, 281–285. doi:10.1016/0165-6147(89)90029-1

Paasche, E. (2002). A review of the coccolithophorid Emiliania huxleyi (Prymnesiophyceae), with particular reference to growth, coccolith formation, and calcification-photosynthesis interactions. *Phycologia* 40, 503–529. doi:10.2216/i0031-8884-40-6-503.1

Paasche, E. (1962). Coccolith Formation. *Nature* 193, 1094–1095. doi:10.1038/1931094b0

Pfeffer, S. R., and Rothmann, J. E. (1987). Biosynthetic protein transport and sorting by the endoplasmic reticulum and golgi. *Annu. Rev. Biochem.* 56, 829–852. doi:10.1146/annurev.bi.56.070187.004145

Poenie, M., Alderton, J., Tsien, R. Y., and Steinhardt, R. A. (1985). Changes of free calcium levels with stages of the cell division cycle. *Nature* 315, 147–149. doi:10.1038/315147a0

Preto, N., Agnini, C., Rigo, M., Sprovieri, M., and Westphal, H. (2013a). The calcareous nannofossil Prinsiosphaera achieved rock-forming abundances in the latest Triassic of Western Tethys: Consequences for the δ13C of bulk carbonate. *Biogeosciences* 10, 6053–6068. doi:10.5194/bg-10-6053-2013

Preto, N., Willems, H., Guaiumi, C., and Westphal, H. (2013b). Onset of significant pelagic carbonate accumulation after the carnian pluvial event (CPE) in the Western tethys. *Facies* 59, 891–914. doi:10.1007/s10347-012-0338-9

Pytkowicz, R. M., and Kester, D. R. (1967). Relative calcium phosphate saturation in two regions of the north pacific ocean. *Limnol. Oceanogr.* 12, 714–718. doi:10.4319/lo.1967.12.4.0714

Raup, D., and Sepkoski, J., Jr (1982). Mass extinctions in the marine fossil record. *Science* 215, 1501–1503. doi:10.1126/science.215.4539.1501

Read, B. A., Kegel, J., Klute, M. J., Kuo, A., Lefebvre, S. C., Maumus, F., et al. (2013). Pan genome of the phytoplankton Emiliania underpins its global distribution. *Nature* 499, 209–213. doi:10.1038/nature12221

Ridgwell, A. (2005). A Mid Mesozoic Revolution in the regulation of ocean chemistry. *Mar. Geol.* 217, 339–357. doi:10.1016/j.margeo.2004.10.036

Ridgwell, A., and Zeebe, R. E. (2005). The role of the global carbonate cycle in the regulation and evolution of the Earth system. *Earth Planet. Sci. Lett.* 234, 299–315. doi:10.1016/j.epsl.2005.03.006

Rost, B., and Riebesell, U. (2004). "Coccolithophores and the biological pump: Responses to environmental changes," in *Coccolithophores: From molecular processes to global impact*. Editors H. R. Thierstein, and J. R. Young (Springer Berlin), 99–125. doi:10.1007/978-3-662-06278-4_5

Royer, D. L., Berner, R. A., Montañez, I. P., Tabor, N. J., and Beerling, D. J. (2004). CO_2 as a primary driver of Phanerozoic climate. *Geol. Soc. Am. Today* 14, 4–10. doi:10.1130/1052-5173(2004)014<4:caapdo>2.0.co;2

Sanders, D., Pelloux, J., Brownlee, C., and Harper, J. F. (2002). Calcium at the crossroads of signaling. *Plant Cell* 14 (l), S401–S417. doi:10.1105/tpc.002899

Sepkoski, J. J., and Ausich, W. I. (1990). "Evolutionary faunas," in *Palaeobiology: A synthesis*. Editors D. E. G. Briggs, and P. R. Crowther (Oxford: Blackwell Scientific Publications), 37–41.

Simkiss, K. (1977). Biomineralization and detoxification. *Calcif. Tissue Res.* 24, 199–200. doi:10.1007/BF02223316

Stanley, S. M., and Hardie, L. A. (1998). Secular oscillations in the carbonate mineralogy of reef-building and sediment-producing organisms driven by tectonically forced shifts in seawater chemistry. *Palaeogeogr. Palaeoclimatol. Palaeoecol.* 144, 3–19. doi:10.1016/S0031-0182(98)00109-6

Steinhardt, R. A., and Alderton, J. (1988). Intracellular free calcium rise triggers nuclear envelope breakdown in the sea urchin embryo. *Nature* 332, 364–366. doi:10.1038/332364a0

Strom, S., Wolfe, G., Holmes, J., Stecher, H., Shimeneck, C., and Sarah, L. (2003). Chemical defense in the microplankton i: Feeding and growth rates of heterotrophic protists on the dms-producing phytoplankter emiliania huxleyi. *Limnol. Oceanogr.* 48, 217–229. doi:10.4319/lo.2003.48.1.0217

Tidow, H., Poulsen, L. R., Andreeva, A., Knudsen, M., Hein, K. L., Wiuf, C., et al. (2012). A bimodular mechanism of calcium control in eukaryotes. *Nature* 491, 468–472. doi:10.1038/nature11539

Toyoshima, C., and Inesi, G. (2004). Structural basis of ion pumping by Ca^{2+}-ATPase of the sarcoplasmic reticulum. *Annu. Rev. Biochem.* 73, 269–292. doi:10.1146/annurev.biochem.73.011303.073700

Trimborn, S., Langer, G., and Rost, B. (2007). Effect of varying calcium concentrations and light intensities on calcification and photosynthesis in Emiliania huxleyi. *Limnol. Oceanogr.* 52, 2285–2293. doi:10.4319/lo.2007.52.5.2285

Tsien, R. W. (1983). Calcium channels in excitable cell membranes. *Annu. Rev. Physiology* 45, 341–358. doi:10.1146/annurev.ph.45.030183.002013

Verret, F., Wheeler, G., Taylor, A. R., Farnham, G., and Brownlee, C. (2010). Calcium channels in photosynthetic eukaryotes: Implications for evolution of calcium based signalling. *New Phytol.* 187, 23–43. doi:10.1111/j.1469-8137.2010.03271.x

von Dassow, P., Ogata, H., Probert, I., Wincker, P., Da Silva, C., Audic, S., et al. (2009). Transcriptome analysis of functional differentiation between haploid and diploid cells of Emiliania huxleyi, a globally significant photosynthetic calcifying cell. *Genome Biol.* 10, R114. doi:10.1186/gb-2009-10-10-r114

Winther, A.-M. L., Bublitz, M., Karlsen, J. L., Møller, J. V., Hansen, J. B., Nissen, P., et al. (2013). The sarcolipin-bound calcium pump stabilizes calcium sites exposed to the cytoplasm. *Nature* 495, 265–269. doi:10.1038/nature11900

Witkowski, C. R., Weijers, J. W., Blais, B., Schouten, S., and Sinninghe Damsté, J. S. (2018). Molecular fossils from phytoplankton reveal secular Pco2 trend over the Phanerozoic. *Sci. Adv.* 4, eaat4556. doi:10.1126/sciadv.aat4556

Young, J. R. (2003). Biomineralization within vesicles: The calcite of coccoliths. *Rev. Mineralogy Geochem.* 54, 189–215. doi:10.2113/0540189

Young, J. R., Geisen, M. P. I., and Probert, I. (2005). A review of selected aspects of coccolithophore biology with implications for paleobiodiversity estimation. *Micropaleontology* 51, 267–288. doi:10.2113/gsmicropal.51.4.267

Young, J. R., and Ziveri, P. (2000). Calculation of coccolith volume and it use in calibration of carbonate flux estimates. *Deep-Sea Res. Part II Top. Stud. Oceanogr.* 47, 1679–1700. doi:10.1016/S0967-0645(00)00003-5

Zeebe, R. E., and Westbroek, P. (2003). A simple model for the $CaCO_3$ saturation state of the ocean: The Strangelove, the Neritan, and the Cretan Ocean. *Geochem. Geophys. Geosystems* 4. doi:10.1029/2003GC000538

Frontiers in Earth Science

Investigates the processes operating within the major spheres of our planet

Advances our understanding across the earth sciences, providing a theoretical background for better use of our planet's resources and equipping us to face major environmental challenges.

Discover the latest Research Topics

See more →

Frontiers

Avenue du Tribunal-Fédéral 34
1005 Lausanne, Switzerland
frontiersin.org

Contact us

+41 (0)21 510 17 00
frontiersin.org/about/contact